From Dopant to Source: The Use of Zinc as an Enabler in the Synthesis of Nanostructures by Metalorganic Vapour Phase Epitaxy

Timothy Burgess

June 2017

A THESIS SUBMITTED FOR THE DEGREE OF

DOCTOR OF PHILOSOPHY

OF THE AUSTRALIAN NATIONAL UNIVERSITY

Australian National University

Department of Electronic Materials Engineering

Research School of Physics and Engineering

College of Physical and Mathematical Sciences

The Australian National University

Declaration

This thesis, to the best of my knowledge and belief, does not contain any results previously published by another person or submitted for a degree or diploma at any university except where due reference is made in the text.

Tim Burgess

Department of Electronic Materials Engineering
Research School of Physics and Engineering
Australian National University Canberra,
ACT 2601, Australia
20th June 2017

Acknowledgments

This thesis would not have been possible without the support and guidance of many individuals and organisations. I am sincerely grateful to all of them.

I would especially like to thank my supervisory panel which consisted of Prof. Chennupati Jagadish, Prof. Hark Hoe Tan, A/Prof. Jennifer Wong-Leung Dr. Michael Gao and Dr. Philippe Caroff. I am deeply grateful to Prof. Jagadish for encouraging me to pursue this PhD and continuing to support me over the many years it has taken me to complete it. He is one of the most generous and patient men I know. He always makes time and I never cease to be amazed by the speed with which he replies to emails. I similarly wish to thank Prof. Tan for his ongoing support throughout my PhD. He is one of a rare breed of senior academics who is equally at home changing a phosphine bottle as correcting a manuscript. I will miss his sense of humour most of all. I will also miss working with A/Prof. Jennifer Wong-Leung who was a very patient TEM tutor. I want to thank her for instilling in me the importance of scientific rigour and for the many chats we've had. I am similarly grateful to Dr. Gao for training me in MOVPE growth and guiding me through the early stages of my research. Finally, my heartfelt thanks go to Dr. Caroff who took over as chair of panel someway into my research program. His enthusiasm for science and willingness to think outside the box has been infectious. He has been both a mentor and a friend and this work would not have been possible without his guidance.

In addition to my supervisory panel, I would also like to thank the many other academics who have been part of the journey. These include Dr. Sudha Mokkapati and A/Prof. Lan Fu from my own department with whom I collaborated on the nanowire laser work, Prof. Jin Zou from the University of Queensland who has been a long-time TEM partner of our research group, Dr. Baptiste Gault A/Prof. Rongkun Zheng, and Prof. Simon Ringer from Sydney University with whom I collaborated on the atom probe tomography work, Dr. Douglas Little and Prof. Kane from Macquarie University with whom I collaborated on the phase-stepping interferometry work, Profs Leigh Smith and Howard Jackson from the University of Cincinnati with whom I collaborated on a range of optical characterisation including the II-V work, Prof. Michael Johnson of Oxford University with whom I collaborated on the terahertz characterisation of

nanowires and A/Prof. Anna Foncuberta I Morral with whom I am currently collaborating on the growth of II-V materials. I would also like to thank the postdoctoral staff who have been part of laboratory over the course of my PhD. These include Drs Steffen Breuer, Yanan Guo, Fan Wang, Pawel Sajewicz and Patrick Parkinson

Experimental equipment is only as good as its technical staff and I am grateful to the excellent scientists who have both provided training and maintained the many facilities I have had available for my use. My thanks go to all the staff of the Australian national fabrication facility (ANFF) including Drs Fouad Karouta, Mykhaylo Lysevych, Kaushal Vora, Jie Tian, Li Li, Naeem Shahid and Mark Lockrey. I am especially grateful to Drs Frank Brink, Animesh Basak, Hua Chen and Mr. David Llewellyn of the centre for advanced microscopy for providing training in SEM and TEM respectively. I would also like to acknowledge the many technical and administrative staff of my research school including, Tom Kitchen, Josh Carr, Dane Kelly, Michael Aggett, Scott Yates, Julie Arnold, Liudmila Mangos, Karen Nulty, Karen Scholte and Liz Micallef.

I have shared this journey with many fellow students who have been both friends and collaborators. These include Ahmed Alabadla, Amira Ameruddin, Aruni Fonseka, Bekele Badada, Bijun Zhao, Daniel Pyke, Daniel Schauries, Dipankar Chugh, Hannah Joyce, Hongyi Xu, Ian McKerracher, James Miloš, Jaret Lee, Jung-Hyun Kang, Keng Chan, Kun Peng, Li Zhe, Naiyin Wang, Nian Jiang, Prakash Prasai, Qian Gao, Reddy Narangari, Sahar Mirzaei, Sam Turner, Sichao Du, Teng Shi, Thomas Bierschenk, Xiaoming Yuan, Yesaya Wenas, Yuda Wang, Yujie Chen.

Research would not be possible without funding and I thank the Australian Government and ANU for the scholarships I received during my PhD: Australian Postgraduate Award, ANU Supplementary Scholarship and Postgraduate Research Scholarship. I acknowledge the National Computational Infrastructure (NCI) for providing computing resources. I also acknowledge Australian National Fabrication Facility (ANFF) and the Australian Microscopy and Microanalysis Research Facility (AMMRF) for access to facilities. My sincere gratitude goes to the staff and management of University House at the ANU who made me feel at home during my research.

Finally, I thank my friends and family for their love and support throughout this journey.

Abstract

As conventional methods of semiconductor fabrication approach fundamental physical limits, new paradigms are required for progress. One concept with the potential to deliver such a paradigm shift is the bottom-up synthesis of semiconductor nanostructures. Beyond further scaling, bottom-up methods promise novel geometries and heterostructures unavailable by conventional top-down methods. This is particularly true in the case of nanostructure growth by the vapour-liquid-solid (VLS) method. Commonly realised using existing vapour phase epitaxy techniques, a range of high-performance VLS devices have now been demonstrated including photovoltaic cells, lasers and high-frequency-transistors.

In this dissertation, selected applications of diethylzinc (DEZn) are used to step through a range of opportunities and challenges arising from the VLS synthesis of semiconductor nanostructures by metal-organic vapour phase epitaxy (MOVPE). These applications are broadly grouped into four chapters focusing on the use of zinc firstly as a dopant and then morphological agent, internal quantum efficiency (IQE) enhancer and finally, source.

In the context of doping, relatively high DEZn flows are shown to alter the morphology of GaAs nanowires by introducing planar defects, kinking and seed-splitting. Growth studies are used to establish the threshold for these effects and thus the range of DEZn flows suitable for doping. Successful incorporation of up to 5×10^{20} Zn/cm^3 is demonstrated through atom probe tomography (APT) and electrical characterisation.

Building on these results, DEZn is then used to generate periodic twinning in GaAs nanowires. The morphology and overgrowth of these twinning superlattice (TSL) nanowires is studied. Unlike for other III-V materials, twin spacing is found to be a linear function of nanowire diameter. By analysing the probability of twin formation, this result is related to the relatively high twin plane and solid-liquid interface energies of GaAs. Values for the wetting angle and supersaturation of the seed particle during growth are also extracted.

In addition to acting as a dopant, zinc is also shown to produce an orders of magnitude increase in the IQE of GaAs nanowires. Performance gains are quantified by measuring

the absolute efficiency of individual nanowires. This increase in IQE with doping enables room-temperature lasing from unpassivated GaAs nanowires. The performance of doped nanolasers, including the transition to lasing, is fully characterised. In addition to increasing radiative efficiency, Zn doping also increases differential gain while reducing the transparency carrier density. The threshold pump power of a Zn doped nanowire is thus shown to be less than that of an equivalent AlGaAs passivated structure.

In the final chapter, DEZn is used as a source for the growth of ZnAs, ZnP and ZnSb nanostructures by MOVPE. A range of growth conditions, substrates and seed materials are investigated. Individual nanostructures of both ZnAs and ZnP are shown to exhibit excellent optoelectronic performance with emission from individual nanostructures at 1.0 and 1.5 eV respectively.

Overall, this thesis underlines the vast range of possibilities offered by VLS growth and opens to the door to both a variety of new techniques and new family of semiconductor nanomaterials.

Publications

Journal articles

1. Burgess T., Jagadish C. Nanoscale Materials: How Small is Big. *P Ieee* 2008, **96**(12)**:** 1895-1897.

2. Xu H. Y., Guo Y. N., Sun W., Liao Z. M., Burgess T., Lu H. F., Gao Q., Tan H. H., Jagadish C., Zou J. Quantitative study of GaAs nanowires catalyzed by Au film of different thicknesses. *Nanoscale Res Lett* 2012, **7**(1)**:** 589.

3. Guo Y. N., Xu H. Y., Auchterlonie G. J., Burgess T., Joyce H. J., Gao Q., Tan H. H., Jagadish C., Shu H. B., Chen X. S., Lu W., Kim Y., Zou J. Phase separation induced by Au catalysts in ternary InGaAs nanowires. *Nano Lett* 2013, **13**(2)**:** 643-650.

4. Du S., Burgess T., Tjing Loi S., Gault B., Gao Q., Bao P., Li L., Cui X., Kong Yeoh W., Hoe Tan H., Jagadish C., Ringer S. P., Zheng R. Full tip imaging in atom probe tomography. *Ultramicroscopy* 2013, **124**(0)**:** 96-101.

5. Burgess T., Breuer S., Caroff P., Wong-Leung J., Gao Q., Hoe Tan H., Jagadish C. Twinning Superlattice Formation in GaAs Nanowires. *ACS Nano* 2013, **7**(9)**:** 8105-8114.

6. Du S., Burgess T., Gault B., Gao Q., Bao P., Li L., Cui X., Kong Yeoh W., Liu H., Yao L., Ceguerra A. V., Hoe Tan H., Jagadish C., Ringer S. P., Zheng R. Quantitative dopant distributions in GaAs nanowires using atom probe tomography. *Ultramicroscopy* 2013, **132**(0)**:** 186-192.

7. Little D. J., Kuruwita R. L., Joyce A., Gao Q., Burgess T., Jagadish C., Kane D. M. Phase-stepping interferometry of GaAs nanowires: Determining nano-wire radius. *Appl Phys Lett* 2013, **103**(16)**:** 161107.

8. Guo Y. N., Burgess T., Gao Q., Tan H. H., Jagadish C., Zou J. Polarity-driven nonuniform composition in InGaAs nanowires. *Nano Lett* 2013, **13**(11)**:** 5085-5089.

9. Wang Y., Jackson H. E., Smith L. M., Burgess T., Paiman S., Gao Q., Tan H. H., Jagadish C. Carrier Thermalization Dynamics in Single Zincblende and Wurtzite InP Nanowires. *Nano Letters* 2014, **14**(12)**:** 7153-7160.

10. Burgess T., Caroff P., Wang Y., Badada B. H., Jackson H. E., Smith L. M., Guo Y., Tan H. H., Jagadish C. Zn3As2 Nanowires and Nanoplatelets: Highly Efficient Infrared Emission and Photodetection by an Earth Abundant Material. *Nano Lett* 2015, **15**(1)**:** 378-385.

11. Burgess T., Saxena D., Mokkapati S., Li Z., Hall C. R., Davis J. A., Wang Y., Smith L. M., Fu L., Caroff P., Tan H. H., Jagadish C. Doping-enhanced radiative efficiency enables lasing in unpassivated GaAs nanowires. *Nat Commun* 2016, **7:** 11927.

12. Chen Y., Burgess T., An X., Mai Y. W., Tan H. H., Zou J., Ringer S. P., Jagadish C., Liao X. Effect of a High Density of Stacking Faults on the Young's Modulus of GaAs Nanowires. *Nano Lett* 2016, **16**(3)**:** 1911-1916.

13. Qu J., Du S., Burgess T., Wang C., Cui X., Gao Q., Wang W., Tan H. H., Jagadish C., Zhang, Y., Chen H., Khan M., Ringer S., Zheng R. 3D Atomic-Scale Insights into Anisotropic Core–Shell-Structured InGaAs Nanowires Grown by Metal–Organic Chemical Vapor Deposition. *Advanced Materials* 2017, **29**(31): 1701888.

14. Sun Z., Burgess T., Tan H. H., Jagadish C., & Kogan A. (2018). Temperature effects in contacts between a metal and a semiconductor nanowire near the degenerate doping. *Nanotechnology* 2018, 29(16) 165202.

Conference papers and proceedings

1. Burgess T., Gao Q., Tan H. H., Jagadish C. High Temperature Zinc Doping of GaAs Nanowires. *ICONN 2012*; Perth, WA, Australia; 5-9 Feb., 2012.

2. Burgess T., Du S., Gault B., Gao Q., Tan H. H., Zheng R., Jagadish C. Quantification of the zinc dopant concentration in GaAs nanowires. *Optoelectronic and Microelectronic Materials & Devices (COMMAD)*; Melbourne, VIC, Australia; 12-14 Dec., 2012. p. 41-42.

3. Guo Y., Zou J., Burgess T., Gao Q., Tan H. H., Jagadish C. Shell formation in InGaAs nanowires driven by lattice latching and polarity effect. *Optoelectronic and Microelectronic Materials & Devices (COMMAD)*; Melbourne, VIC, Australia; 12-14 Dec., 2012. p. 51-52.

4. Badada B., Smith L. M., Jackson H., Yarrison-Rice J., Burgess T., Jagadish C. Photocurrent spectroscopy of single ZB GaAs and GaAs/AlGaAs core-shell nanowires. *APS March Meeting 2013*; Baltimore, MD, USA; March 18-22, 2013. p. 22009.

5. Montazeri M., Wang Y., Jackson H. E., Smith L. M., Yarrison-Rice J. M., Burgess T., Tan H. H., Gao Q., Jagadish C. Picosecond carrier dynamics within the band structure of single InP nanowires with zincblende and wurtzite symmetries. *APS March Meeting 2013*; Baltimore, MD, USA; March 18-22, 2013. p. 22003.

6. Sun Z., Kogan A., Burgess T., Jagadish C. Electric transport in Individual GaAs nanowires. *APS March Meeting 2013*; Baltimore, MD, USA; March 18-22, 2013. p. 20004.

7. Little D. J., Kuruwita R. L., Joyce A., Gao Q., Burgess T., Jagadish C., Kane D. M. Nanoparticle Measurement in the Optical Far-Field. *The European Conference on Lasers and Electro-Optics and the International Quantum Electronics Conference 2013*; Munich, Germany; 12-16 May, 2013.

8. Burgess T., Breuer S., Caroff P., Wong-Leung J., Gao Q., Tan H. H., Jagadish C. Twinning superlattices in p-doped GaAs nanowires. *NanoS-E3 2013*; Airlie Beach, QLD, Australia; 15 - 20 Sep., 2013.

9. Wang Y., Montazeri M., Jackson H., Smith L., Yarrison-Rice J., Burgess T., Jagadish C. Transient Rayleigh Spectroscopy measure of Carrier Dynamics in Wurtzite and Zincblende InP nanowires. *2013 Annual Fall Meeting of the APS Ohio-Region Section* Cincinnati, OH, USA; October 4–5, 2013.

10. Smith L. M., Shi T., Badada B., Jackson H. E., Yarrison-Rice J., Burgess T., Gao Q., Tan H. H., Jagadish C. Probing the electronic structure in GaAs nanowire rotational twin superlattices. *SPIE Micro+Nano Materials, Devices, and Applications 2013 Conference*; Melbourne, VIC, Australia; 8-11 Dec., 2013.

11. Burgess T., Breuer S., Caroff P., Wong-Leung J., Gao Q., Tan H. H., Jagadish C. Twinning Superlattices in p-type GaAs Nanowires. *ICONN2014*; Adelaide, SA, Australia; 2-6 Feb., 2014.

12. Sun Z., Kogan A., Burgess T., Jagadish C. Temperature dependence of electron transport in GaAs nanowires. *APS March Meeting 2014*; Denver, CO, USA; March 3-7, 2014.

13. Wang Y., Montazeri M., Jackson H., Smith L., Yarrison-Rice J., Burgess T., Paiman S., Tan H., Gao Q., Jagadish C. Transient Rayleigh Scattering Spectroscopy measurement of Carrier Dynamics in Zincblende and Wurtzite Indium Phosphide nanowires. *APS March Meeting 2014*; Denver, CO, USA; March 3-7, 2014.

14. Shi T., Badada B., Wang Y., Jackson H. E., Smith L. M., Burgess T., Gao Q., Tan H. H., Jagadish C. Optical and electronic signatures of very high hole concentrations in degenerately doped GaAs rotational twin nanowire superlattices. *ICPS 2014*; Austin, TX, USA; 10-15 Aug., 2014.

15. Burgess T., Guo Y., Wang Y., Babada B., Smith L. M., Jackson H. E., Wong-Leung J., Gao Q., Caroff P., Tan H. H., Jagadish C. Zn_3As_2 nanowires and nanoplatelets grown by MOVPE: an earth abundant 1.0 eV optoelectronic nanomaterial. *2014 MRS Fall Meeting & Exhibit*; Boston, MA, USA; 30 Nov.-5 Dec., 2014.

16. Burgess T., Caroff P., Wang Y., Badada B. H., Jackson H. E., Smith L. M., Guo Y., Tan H. H., Jagadish C. Introducing the II-V family at the nanoscale with high quality Zn_3As_2 and Zn_3P_2. *2015 MRS Spring Meeting and Exhibit*; San Francisco, CA, USA; 6-10 Apr, 2015.

17. Burgess T., Caroff P., Friedl M., Wang Y., Badada B. H., Jackson H. E., Smith L. M., Fontcuberta i Morral A., Guo Y., Tan H. H., Jagadish C. Introducing nanoscale II-V materials by MOCVD with high quality Zn_3As_2 and Zn_3P_2. *18th International Conference on Metal Organic Vapor Phase Epitaxy*; San Diego, CA, US; 10-15 July, 2016.

18. Daniil A., Burgess T., Steinvall S. E., Tan H. H., Jagadish C., Caroff P., Fontcuberta i Morral A. Characterisation of earth abundant semiconductor nanostructures based on zinc phosphide and zinc arsenide. *10th Nanowire Growth Workshop*; Lund, Sweden; 29 May-2 Jun., 2017.

List of acronyms and common symbols

APT	atom probe tomography
ASE	amplified spontaneous emission
BSE	back-scattered electrons
CBE	chemical beam epitaxy
CMOS	complementary metal-oxide-semiconductor
CVD	chemical vapour deposition
CW	continuous-wave
DEZn	diethylzinc
DFT	density functional theory
DMZn	dimethylzinc
EBIC	electron beam induced current
EBL	electron beam lithography
EDXS	energy dispersive X-ray spectrometry
EQE	external quantum efficiency
FDTD	finite different time domain
FEM	field emission microscopy
FET	field emission microscopy
FFT	field -effect transistor
FIB	focused ion beam
FIM	field ion microscopy
FWHM	full width at half maximum
GS-MBE	gas source molecular beam epitaxy
HAADF	high angle annular dark field
HRTEM	high resolution transmission electron microscopy
ICF	image compression factor
IQE	internal quantum efficiency
IR	infrared
ITO	indium tin oxide

LEAP	local electrode atom probe
LED	light emitting diode
MBE	molecular beam epitaxy
MOVPE	metal-organic vapour phase epitaxy
MS	mass spectrometry
MSM	metal-semiconductor-metal junction
NEMS	nanoelectromechanical systems
PL	photoluminescence
PLL	poly-L-lysine
PV	photovoltaic
SAE	selective area epitaxy
SAED	selected area electron diffraction
sccm	standard cubic centimetres per minute
SEM	secondary electron microscopy
SIMS	secondary ion mass spectroscopy
slm	standard litres per minute
SPM	scanning probe microscopy
SPP	surface plasmon polariton
SRH	Shockley-Read-Hall
SRV	surface recombination velocity
STEM	scanning transmission electron microscopy
STM	scanning tunnelling microscopy
TCSPC	time correlated single photon counting
TEM	transmission electron microscopy
TESn	tetraethyltin
TMAl	trimethylaluminium
TMB	trimethylboron
TMGa	trimethylgallium
TEGa	triethylgallium
TMIn	trimethylindium
TMSb	trimethylantimony
TOF-MS	time-of-flight mass spectrometry
TRPL	time resolved photoluminescence

TRS	transient Rayleigh scattering
TSL	twinning superlattice
UV	ultraviolet
VLS	vapour-liquid-solid
VS	vapour-solid
VSS	vapour-solid-solid
WZ	wurtzite
XRD	X-ray diffraction
ZB	zincblende
A	non-radiative recombination coefficient
B	radiative recombination coefficient
c	vacuum speed of light
C	auger recombination coefficient
D	nanowire diameter
e	charge on an electron
E	energy
E_g	bandgap
f_p	pump frequency
h	spacing between bilayers in the growth direction
$\hbar$	reduced Planck constant
g	gain
g_0	gain coefficient
g_{th}	threshold gain
L	cavity length
m_0	electron mass
m_e^*	effective electron mass
m_{lh}^*	effective light hole mass
m_{hh}^*	effective heavy hole mass
$\lvert M\rvert^2$	momentum matrix element
n_r	effective index
n_g	group index
n_0	equilibrium donor concentration
N	carrier concentration
$\mathrm{N_0}$	equilibrium carrier concentration
$\mathrm{N_A}$	acceptor concentration

N_A^-	ionised acceptor concentration
N_D^+	ionised donor concentration
N_{th}	threshold carrier concentration
N_{tr}	transparency carrier density
p_0	equilibrium acceptor concentration
P	pump power
P_p	peak pump power
P_{th}	threshold pump power
R	mode reflectance
S	surface recombination velocity
S_b	photon density in the b^{th} cavity mode
t	time
T	temperature
V_a	active volume
α_i	internal cavity loss
α_m	mirror loss
β	wetting angle of the seed particle
β	fraction of spontaneous emission coupled into the lasing modes
γ_{Nl}	nucleus-liquid interface energy
γ_{NV}	nucleus-vapour interface energy
γ_{LV}	liquid-vapour interface energy
γ_{SL}	solid-liquid interface energy
γ_{SV}	solid-vapour interface energy
γ_T	twin plane interface energy
Γ	mode confinement factor
Γ	effective interfacial energy barrier to nucleus formation
ε_0	vacuum permittivity
η_{IQE}	internal quantum efficiency
η_p	pumping efficiency
λ	wavelength
$\rho_r(E)$	3D reduced density of states
τ_{mc}	minority carrier lifetime
τ_{nr}	lifetime of non-radiative recombination
τ_r	lifetime of radiative recombination

Table of Contents

List of Figures

List of Tables

1

Introduction

1.1 Nanowires and other nanostructures

With the performance of many conventional semiconductor fabrication technologies rapidly approaching fundamental physical limits, new paradigms are required for further technological progress.[69-71] One alternative to current 'top-down' methods is the use of nanomaterials as building blocks for the 'bottom up' approach to device design. Particular attention has focused on the development of 1D nanomaterials such as nanowires. [70, 72-74] Typically characterised by diameter of less than 100 nm and a length of at least 1 μm, nanowires are commonly synthesised by the vapour-liquid-solid (VLS) or selective area epitaxy (SAE) methods.[75-77] Relative to traditional planar structures, the nanowire geometry offers significant advantages including the opportunity for both two and three dimensional quantum confinement,[78-83] superior light trapping[84-88] and a high surface-to- volume ratio for nanoelectromechanical systems (NEMS)[89-91] and chemical sensing.[92-97] A full range of nanowire based devices have now been demonstrated including field-effect transistors (FET),[98-103] Esaki diodes,[104-107] light emitting diodes (LED),[108-111] lasers,[25, 112-118] photodetectors,[119-122] photovoltaic devices (PV),[85, 86, 123-125] single electron and photon devices,[79, 103, 126-129] field-emission sources[130, 131] and chemical[96, 97] and biological[93-95] sensors. Beyond miniaturization, nanowires offer a unique platform for realising novel heterostructure. Growth may be directed in either the radial or axial directions,[132, 133] and as cross-sectional area is limited, relatively large lattice mismatches may be elastically accommodated.[134-140] Of particular significance is the potential for heterostructures combining silicon with higher mobility direct band gap compound semiconductors.[99, 141-144] The nanowire also provides unique opportunities for engineered homostructure. Unlike most bulk semiconductor materials, crystal phase may be controlled during nanowire growth to give novel structures such as the crystal phase quantum dot.[145-148] This precise control over growth to produce superior quality 1D semiconductor materials has further enabled a range of fundamental experiments in physics including the search for the Majorana fermion.[149-151] As a fresh approach to semiconductor device fabrication, the nanowire

and other related nanostructures thus hold promise for both fundamental research and consumer technologies.

1.1.2 Nanowire growth by MOVPE

Metalorganic vapour phase epitaxy (MOVPE) is one of the most common epitaxial growth methods.[152-154] Capable of delivering high quality material and abrupt interfaces, MOVPE has proven a popular route to nanowire synthesis.[75, 155-157] Growth is usually by either the VLS or SAE methods and relies on achieving anisotropy in growth rate. In the case of VLS, crystal growth occurs preferentially at the interface between a semiconductor material and a 'seed particle'. The deposition of material moves this interface in the direction of its normal to give a 1D structure having a cross-section equal in size to the interface itself. The VLS mechanism has proven highly versatile and has been successfully applied to wide range of seed-material combinations.[73, 75-77, 155, 158] While the seed particle is a liquid in the case of VLS growth, a similar mechanism has also been shown to operate for solid seed particles and is termed vapour-solid-solid (VSS) growth.[159-162] In both cases, the seed particle is not usually thought of as a chemical catalyst *per se*, but rather as a conduit or reservoir for the reactants. Noble metals, such as Ag,[163-165] Pt[166-168] and particularly Au, have proven particularly popular as seed materials although research into alternatives such as Al,[169, 170] Sn[171-173] and Ni[174-179] is ongoing.[77] Where one or more reactants form a suitable seed material, such as In in the case of InP,[180-182] these may also act as a seed in what is termed self-catalysed growth.[77, 183, 184] While highly versatile, the VLS method also introduces a range of unique challenges. Significant alloying between the seed particle and reactants can reduce the abruptness of interfaces in what is termed the 'reservoir effect'.[185-187] Here a reactant continues to be supplied from the seed particle even after its vapour phase source is terminated. Interactions between the seed and the reactants can also lead to variations between gas and solid phase compositions. Such issues are particularly problematic in the case of doped materials[188] and semiconductor alloys[189, 190]. There is furthermore often significant compositional variation between material deposited axially through VLS growth and material simultaneously deposited radially by vapour-solid (VS) mechanisms leading to unintentional 'core-shell' nanowire structures.[189, 191-195] Such difficulties are generally avoided in the case of SAE growth. A combination of both top-down and bottom-up methods, SAE growth is templated using a lithographically defined mask.[196-199] Most often an oxide, the mask contains holes from

which nanowires emerge. Anisotropy in growth rate is usually considered to be facet-limited although recent work has questioned the possible operation of (self-catalysed) seed particles.[200] Growth likely occurs by a VS mechanism similar to that responsible for standard planar epitaxy with reactant supply being both by surface diffusion across the mask and direct impingement.[201-203] Being a similar growth mechanism to that of standard epitaxy processes, doping and alloying are less problematic for nanowires grown by SAE relative to VLS.[99, 204-206] The lithographic requirements for SAE growth are however challenging and the growth temperatures employed are generally higher than those required for VLS growth.

1.1.3 Impurity doping of nanostructures

Impurity doping is fundamental to controlling the carrier concentration and therefore electrical properties of semiconductor materials. There remain however, serious challenges to the realization of uniform and reproducible impurity doping in semiconductor nanostructures.[207-210] The first and perhaps most fundamental of these challenges is non-uniformity arising from statistical fluctuations in dopant concentration. As the dimensions of a nanostructure are reduced, the absolute number of dopant atoms is also reduced and shot or Poisson noise in this number becomes significant. These statistical fluctuations are further compounded by the need to increase the dopant concentration to account for reductions in contact size which leads to dopant clustering and deactivation.[209] Of more elementary concern however are difficulties with dopant incorporation itself. Often termed ‘self-purification’,[211, 212] difficulties with the incorporation of impurity species into nanostructures have been related to a range of thermodynamic and kinetic effects.[211, 213-218] In the case of nanostructures grown by the VLS method, the operation of multiple incorporation pathways has been shown to result in a potentially inhomogeneous dopant distribution.[218-220] Even when successfully incorporated, many impurity species are predicted to segregate within nanostructures[221-224] while confinement is further predicted to increase the ionization energy of these impurities[225] and reduce the maximum carrier concentration which may be achieved through doping[214]. Exploring these effects experimentally is complicated by difficulties in metrology.[209, 226] The small volume of individual nanostructures coupled with the relatively low chemical concentration of typical dopant species precludes the use of many common analytical techniques such as secondary ion mass spectrometry (SIMS).[227] For chemical analysis, researchers have turned to methods such as scanning

tunnelling microscopy (STM),[228, 229] and atom probe tomography (APT)[218, 220, 230] while electrical activity has been measured using scanning probe techniques,[231] specially fabricated Hall effect setups[232, 233] and electron holography[234, 235]. Despite these challenges there exists a large body of work reporting on the synthesis of doped nanostructures. Much of this work has focused on *in situ* doping, encompassing techniques such as MOVPE,[132, 236, 237] MBE[238, 239] and solvothermal synthesis[240]. While controllable doping has been reported for a number of systems, the introduction of impurities during growth has also been observed to affect parameters such as morphology,[35, 241] crystal phase[242-244] and growth rate[245, 246]. In some cases the role of impurity doping has expanded from simply modifying carrier concentration to also controlling the crystal phase and morphology of the doped nanostructures.[244, 247]

1.2 The element zinc in MOVPE growth

Zinc is one of the most common p-type dopants used in the growth of III-V materials by MOVPE.[154, 248, 249] Unlike several other common p-type dopants such as beryllium and cadmium, elemental zinc has relatively low toxicity. A shallow substitutional acceptor with ionization energies of approximately 25-30 meV in GaAs[250, 251] and 47 meV in InP,[252, 253] zinc exhibits high electrical activity without auto-compensation enabling hole concentrations in excess of 1 x10^{20} /cm^3 to be achieved.[249, 254] Although abrupt zinc profiles may be generated,[255] the diffusion coefficient of zinc in III-V materials increases with zinc concentration.[256, 257] Zinc is furthermore characterized by a relatively high vapour pressure and incorporation is reduced at temperatures above 575 °C.[249, 258] Common metalorganic sources of zinc include dimethylzinc [DMZn - $(CH_3)_2Zn$], diethylzinc [DEZn - $(C_2H_5)_2Zn$] and, to a lesser extent, dimethylzinc-triethylamine [DMZn-TEN - (CH3)2Zn-$N(C_2H_5)_3$]. The latter of these is an adduct used particularly for the growth of Zn-VI compounds where the premature reaction of precursors can be problematic. Examples of Zn-VI semiconductor compounds which have been demonstrated by MOVPE include: ZnO,[259] ZnS,[260] ZnSe[261] and ZnTe[262]. There have also been a limited number of reports detailing the planar growth of Zn-V semiconductor materials by MOVPE.[263]

1.2.1 Applications of zinc to nanostructure growth by MOVPE

Zinc has proven to have a variety of applications to nanostructure growth by MOVPE. The first of these is as a p-type dopant of III-V nanostructures. Successful Zn doping

has been now been shown for almost the entire III-V family of semiconductor materials.[111, 246, 264-266] Both *in situ*[246, 267] and *ex situ*[265, 268] doping methods have been reported with researchers achieving acceptor concentrations of up to, and in excess,[105, 269, 270] of 1×10^{19} /cm^3 as determined through both electrical[105] and optical[270] characterization means. Zinc doping has further been used to enable a range of nanowire devices including photovoltaic cells,[86, 271] photodetectors[272], light emitting diodes[110, 111, 273] and Esaki dioides[273]. Beyond application as a dopant, zinc has also been found to be a powerful morphological agent for nanowires grown by the VLS method. In the case of Au-catalysed nanowires, the addition of zinc has been shown to promote the zincblende phase in preference to wurtzite for a number of III-V materials.[35, 243] This shift is often accompanied with a transition to {111} type faceting.[24, 35] Being non-parallel to the growth direction, {111} faceting has been further shown to generate a twinning superlattice structures whereby periodic twin planes are inserted into the zincblende structure.[24, 35] Further zinc addition often leads to more dramatic morphological effects including kinking and seed-splitting.[237] The mechanism for this morphological action has been related to changes in relevant surface energies[24, 35, 243, 274] with one *ex-situ* study[243] showing zinc doping to alter the contact angle and size of the seed particle. The final application of zinc to nanostructure growth by MOVPE is as a primary source. A number of II-VI nanostructures including, ZnO, ZnS have now been synthesised by MOVPE. The growth of II-V nanostructures by MOVPE remains however to be reported.

1.2.2 The II-V semiconductor family

The II-V family of semiconductors encompasses a range of unique materials offering significant opportunities for both fundamental research and commercial application. In contrast to well-known II-VI semiconductors such as ZnO and CdS, there are relatively few publications focusing on II-V materials and only a handful of reports describing their growth by MOVPE.[263, 275-285] This is despite the II-V family including materials that hold promise for earth-abundant PV (Zn_3P_2, ZnP_2, Zn_3As_2),[277, 286-290] one of the best performing thermoelectric materials (Zn_4Sb_3)[19] and the first reported topological semimetal (Cd_3As_2).[291-293] Significant diversity exists among II-V materials due in part to the multiple equilibrium stoichiometries that exist in many binary systems. While some II-V materials are normal valence compounds (eg Zn_3As_2), others are polyanionic (anion-anion bonding; eg ZnP_2) and still others, electron poor (eg ZnSb).[294] The band-

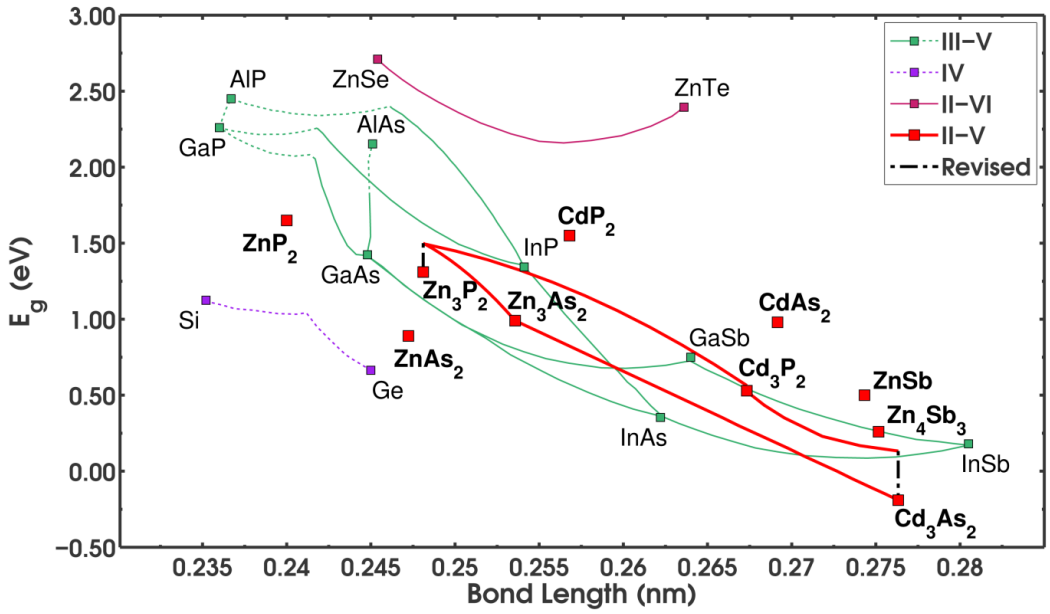

Figure 1-1 | Bandgap vs. bond length for selected semiconductor compounds. Data for compounds of Zn-As, Zn-P and Zn-Sb is from Tables 2-1, 2-2 and 2-3 respectively. Data for CdP_2 and $CdAs_2$ is from Aleinikova et al.[18], Sobolev et al.[29] and Morozova et al.[38]. Data for Cd_3As_2 is from Ali et al.[43] and Aubin et al.[47] and for Cd_3P_2, from Palkina et al.[52] and Gelten et al.[57] Data for Zn_3As_2-Cd_3As_2 is from Caron et al.[59], Zn_3As_2-Zn_3P_2, Im et al.[63], Cd_3P_2-Zn_3P_2, Pawlikowski[64] and Cd_3P_2-Cd_3As_2, Radoff and Bishop[66].

structure and physical properties of the electron poor compounds are particularly intriguing as the existence of a band-gap in these materials is unexpected and, at present, not fully understood.[295-297]

In a similar manner to other better known compound semiconductor systems, the II-V family forms a variety of alloys with scope for band-gap and lattice parameter tuning. Figure 2-2 plots the bandgap and average bond length of some relatively well characterized II-V materials along with some other well known III-V, IV and II-VI materials. The II-V alloys are seen to span an energy range from the semimetal (Cd_3As_2[66]) to around 1.5 eV (Zn_3P_2[45] and ZnP_2[29]). Zinc nitride (Zn_3N_2), with an average II-V bond length of 0.212 nm,[298] is further reported to emit in the UV. Some confusion remains regarding its bandgap which has been placed at values ranging from 1.0 to 3.2 eV.[299-304] Similar confusion also remains regarding the band structure of many other

better characterized II-V materials including Zn_3P_2 and Zn_3As_2.[45, 305-308 49, 277, 309, 310] II-V semiconductors are often p-type materials which in the case of Zn_3P_2 has been related to the formation of charged phosphorus interstitial defects.[311] The p-type nature of many II-V materials has lead to interest in their integration with n-type materials and heterostructures of Zn_3P_2 with ZnO,[287, 312] CdS,[287] ZnSe[281, 287] and ZnS[313] have been reported as potential PV candidates. The band-gap and earth abundance of Zn_3As_2 (1.0 eV) and Zn_3P_2 (1.5 eV) are particularly attractive for such applications.[277, 313] Due to similarities in crystal structure, lattice spacing and composition there is also considerable potential for the realization of II-V/III-V heterostructures. The epitaxial growth of Zn_3As_2 on InP[49, 263, 276, 314-316] (lattice mismatch 0.5%), GaAs[49 276, 314, 317] (lattice mismatch 4%) and InAs[318, 319] (lattice mismatch 3.8%) has been reported. Zn_3P_2 has similarly been grown on GaAs[280, 286, 320-322] (lattice mismatch 1%) and formed on InP through Zn diffusion.[323, 324] Recent work has focused particularly on the synthesis of II-V nanostructures with nanowires and other nano-geometries of Zn_3As_2,[63, 277, 325] Zn_3P_2,[63, 326-341] Cd_3P_2,[326, 327] Cd_3AS_2,[292, 342-345] and Zn_xSb_y[341, 346, 347] being grown, generally by thermal evaporation methods. Nanostructured II-V materials hold potential in both enabling heterostructure[63, 331, 333] and capitalizing on the excellent thermoelectric properties of many II-V compounds.[341, 348, 349] Continued work is required to both understand the unique properties of II-V semiconductors and realize their potential in commercial devices.

1.3 Thesis Synopsis

This dissertation investigates several potential applications of the element zinc to nanostructure growth by MOVPE. These applications encompass roles as a dopant, morphological agent, radiative enhancer and finally, primary source. Before proceeding to the contributions of this work, Chapter 2 surveys relevant publications. Details of the experimental techniques used in this work and the theory underlying their operation are further given in Chapter 3.

Chapter 4 explores the role of zinc as a dopant of Au-seeded GaAs nanowires. Zinc incorporation is established using both energy dispersive x-ray spectroscopy (EDXS) and atom probe tomography (APT) while electrical measurements provide evidence for dopant activity. The spatial distribution of zinc in regards to axial core and radial shell growth is explored along with the effect of II/III ratio on nanowire morphology.

Crucially, growth conditions are outlined to enable effective p-type doping of GaAs nanowires.

The morphological action of zinc on Au-seeded GaAs nanowires is further explored in Chapter 5. By considering both reactor temperature and V/III ratio, growth conditions suitable for generating a twinning superlattice (TSL) structure are identified. The morphology of this structure is then further investigated and its transformation with overgrowth analysed. Variation of twinning period with nanowire diameter is measured and modelling thereof is used to calculate supersaturation in the Au-seed during growth.

Chapter 6 investigates the use of zinc as an enhancer of radiative efficiency in GaAs nanowires. Efficiency gains of over two orders of magnitude are measured in doped nanowires. Rate equation modelling is used to relate these gains to an increase in the rate of radiative recombination. Room-temperature lasing is then shown for unpassivated Zn-doped GaAs nanowires. Analysis shows that doping acts to increase differential gain and reduce the transparency carrier density.

The use of zinc as a source for the growth of Zn-V nanostructures by MOVPE is considered in Chapter 7. The growth windows for three distinct Zn-V compounds, Zn_3As_2, Zn_3P_2 and Zn_xSb_y are identified with the aid of various thermodynamic analyses. Both 1D and 2D nanomaterials are synthesised using various different seed-metals substrates. Efficient photoemission and detection is shown for single Zn_3As_2 nanostructures at around 1.0 eV while room-temperature emission from Zn_3P_2 nanowires is located at 1.5 eV.

Conclusions and recommendations for future work are given in Chapter 8.

2

Literature Review

2.1 Introduction

Filamentary crystal growth has a long association with electronic technologies. The spontaneous formation of 'whiskers' between soldered joints was a particular problem in the valve era.[350] Later studies of compound semiconductor growth used same 'whisker' terminology to describe unwanted filamentary growth which, in the case of III-V materials, often formed due to an excess supply of the group III element.[351-353] The VLS mechanism of directed or filamentary growth was first introduced by Wagner and Ellis in 1964.[354] Initial studies focused largely on silicon whiskers[355-359] although Barns and Ellis did show the VLS growth of GaAs and GaP whiskers in 1965.[360] Givargizov later made significant contributions particularly in regards to morphology,[361-364] control[365, 366] and fundamental understanding[367, 368]. The field underwent a renaissance in the early 1990s with the work of Hiruma and others at the Hitachi corporation,[369-374] followed later by the Lieber,[375-378] Samuelson[72, 379-381] and Bakkers[382-384] groups. It was around this time that the term 'whisker' or 'nanowhisker' was replaced with 'nanowire'.[369, 375, 379, 380]

2.2 Impurity doping of nanowires grown by VLS

2.2.1 Modelling

2.2.1.1 Dopant Incorporation & Segregation

A variety of analytical approaches to dopant incorporation *via* VLS have been explored. For growth conditions approaching local equilibrium, Schwalbach *et al.*[385] has shown that incorporation is not only a function of the steady-state seed composition but also the relative flux of dopant atoms. Variation with factors such as dopant solubility, diffusivity and the kinetics of incorporation was more recently considered by Dubrovskii[386] who found a diameter dependence to incorporation. Highly non-equilibrium incorporation has further been modelled in terms of solute trapping by Moutanabbir *et al.*[387] while inhomogeneities within the liquid catalyst have been

considered by Connell *et al.*[218] who found a significant local increase in dopant concentration at the triple phase line.

Dopant segregation in nanowires has been considered by density functional theory (DFT) methods for a wide range of host materials including Si,[221, 222, 388-395] $Si_{1-x}Ge_x$,[396] Ge,[397] GaAs,[398-402] InP,[403, 404] InAs[399, 401, 405, 406] and even an Au seed particle[407]. In most cases authors have found a driving force for the segregation of dopants to the sidewalls of nanowire structures. Segregation to the core has also been reported in a limited number of cases such as the Be doping of GaAs nanowires.[399] Segregation behaviour has generally been found to be highly sensitive to surface termination[406] with surface dangling bonds acting to promote segregation[222] by combining with dopants to form electronically inactive complexes.[221, 222, 389, 393, 400, 402, 408, 409] The influence of other factors such as codoping,[221] surface termination[222, 389] and even applied electric field[392] has also been investigated. Where the host semiconductor is polymorphic, crystal phase must also be considered,[410] and Galicka *et al.*[399] has reported that the driving force for segregation is generally greater in zincblende (ZB) relative to wurtzite (WZ) III-V nanowires. In the case of amphoteric dopants, variation between host lattice sites has also been identified with calculations showing a greater driving force for the segregation of group-III relative to group-V substituted Si[398, 399] and Sn[399] in GaAs nanowires. While the results of DFT simulations were initially applied to nanowires of up to 20 nm in diameter,[221, 389] Leao *et al.*[390] later calculated that segregation would be negligible for diameters in excess of 3 nm. A similar conclusion was reached by Chan *et al.*[411] who found the many-body interactions of several dopant species in silicon nanowires to be short range in nature. Experimental verification of dopant segregation within ultrathin nanowires remains however difficult and while surface rich dopant distributions have been reported for doped nanowires, such inhomogeneity has generally been related to parasitic sidewall growth.[219, 231, 412, 413]

2.2.1.2 Dopant Activity

Both quantum and dielectric confinement may reduce doping efficiency by increasing the ionization energy of dopants. Quantum confinement is, however, only significant where the diameter of a nanowire approaches the Bohr radius of an impurity and is therefore typically limited to ultrathin wires. In contrast, dielectric confinement arises from the dielectric mismatch between the nanowire and its surrounds and may be relevant for diameters of several tens of nanometres.[414, 415]

Early studies of quantum confinement in one-dimensional semiconductor systems found an inverse relationship between impurity ionization energy and wire radius.[416-418] For a GaAs/AlGaAs core/shell system, reduction in wire diameter was shown to result in carrier leakage with a sharp transition from quasi-one-dimensional to three-dimensional behaviour.[416] Using the amphoteric defect model, Khanal *et al.*[214] has further shown that quantum confinement will lead to an appreciable reduction in maximum achievable dopant density for wires with a diameter of less than 5 nm.

In parallel with studies of dopant segregation, DFT methods have also been used to calculate the binding energy of impurities in nanowire structures.[388, 390, 394, 419-425] While DFT calculations often shown an increase in ionization energy with reduced nanowire diameter, these increases have only been significant for nanowire diameters of less than a few nanometres.[388, 390] Increases in ionization energy for diameters of up to 10 nm have however been found using a hybrid functional.[419] Similar results were found by the tight binding approach, with Delerue and co-workers[426, 427] finding a 50% reduction in doping efficiency for a 9 nm diameter Si nanowire. While this reduction showed only a weak dependence on dopant placement and identity, other authors have suggested that distortion of the donor wavefunction at the nanowire surface could work to counteract increases in ionization energy.[428] The tight binding model has also been applied to the activation of donors by a gate voltage.[429]

The relationship between dopant density and carrier mobility may also differ in nanowire systems relative to the bulk.[430-437] Rather than point-like scattering centres, impurity cross sections become comparable to the physical nanowire cross section for diameters of 10 nm and less.[438] Combining DFT and a Green's function approach, early work by Fernández-Serra *et al.*[389] showed both B and P to induce strong backscattering in ultrathin Si nanowires at resonance energies dependant on radial placement. Later work found a similar result for several of the metals used to catalyse the VLS process[439] with authors generally determining scattering to be greatest when impurities are located at the centre of nanowires.[439-442] Ionization state is also critical with Rurali *et al.*[389] calculating a 1000 times increase in minority carrier scattering for a charged versus neutral impurity. Interestingly, the application of dielectric coatings appears to somewhat mitigate these mobility issues.[441, 443]

2.2.2 Synthesis

2.2.2.1 Group IV Materials

2.2.2.1.1 Silicon

Early reports of *in situ* VLS doping relate to Si whisker synthesis. In this context, Wagner and Doherty[359] employed phosphorus trichloride as a chemical marker to investigate growth while Komatsu *et al.*[357] observed rectification in Si whisker devices doped using boron tribromide (BBr_3). Several years after this initial work, Givargizov[363] made one of the first observations of *in situ* doping affecting growth morphology.

Phosphorus in the form of phosphine is one of the most widely reported n-type dopants of Si nanowires.[188, 444-451] Under typical growth conditions, P has been shown to incorporate at a similar concentration to the ratio of PH_3:SiH_4 in the gaseous phase,[444] before reaching the solid solubility limit of P in Si ($1.5x10^{20}$ /cm^3).[445] Annealing has been reported to increase the efficiency of P doping.[450] Phosphine addition does not appear to have any significant morphology effects,[444-453] although Schmid *et al.*[445] did find that high concentrations may inhibit nanowire nucleation. Phosphine has further been reported to favour the cubic phase.[454] Scanning probe methods have shown that P incorporation is generally greater towards the sidewalls.[219, 231, 455] Growth conditions leading to reduced radial growth and post-growth annealing may both ameliorate radial inhomogeneity.[412] Axial inhomogeneity resulting from the reservoir effect[456] may further be reduced by reduced growth rates and low reactor pressures.[188] Other reported n-type dopants include Sb and As. Antinomy in the forms of TMSb and Triethylantimony (TESb) and particularly As in the forms of AsH_3 and Triethylarsenic (TEAs) have all been shown to significantly reduce nanowire growth rate and affect nanowire morphology.[104, 457, 458] Interestingly, Sb introduced by a pre-growth deposition process showed no such effect.[459]

Boron introduced as either diborane (B_2H_6)[132, 242, 245, 448, 451-453, 460-468] or less commonly, trimethylboron (TMB) [449, 461, 469] or BBr_3[470-472] is one of the most commonly reported p-type dopants of Si nanowires. Diborane in particular, has been found to be a successful p-type dopant across a range of growth conditions[451, 460-462, 464, 465] and is capable of being incorporated in concentrations of at least $1x10^{20}$ /cm^3.[467] Incorporation approximates the gas phase ratio (B_2H_6:SiH_4) at lower concentrations before reaching an upper limit.[461] Unlike phosphine, diborane has been found to induce radial

growth,[132, 242, 245, 461, 463] and has even been used to form core/shell structures.[132] At (B_2H_6:SiH_4) ratios of 1:70 and higher, an amorphous shell has been observed to form[132, 245, 463] with concurrent sidewall serration,[466] kinking, reduction in axial growth rate and Au decoration of the sidewalls.[242] Authors have generally related this to the catalytic effect of B_2H_6 on SiH_4 decomposition.[132, 242, 245, 463, 473] Strategies to mitigate or circumvent unwanted sidewall growth have included using a local substrate heater and H_2 carrier gas,[448] *in-situ* etching,[462] post growth annealing[132] and post growth B_2H_6 plasma treatment.[463] Interestingly Al catalyzed Si nanowires appeared not to show a morphological effect of diborane addition. As for phosphine, incorporation appears to be inhomogeneous with both Raman spectroscopy[464] and APT[230, 468] finding a greater concentration of B atoms towards the surface of doped nanowires. In contrast to B_2H_6, neither TMB[449, 461, 469] nor BBr3[470-472] have been reported to affect Si nanowire morphology.

Aluminium seeding of Si nanowire growth has been found to deliver highly p-type material.[170, 474-476] Carrier concentrations of approximately $1x10^{19}$ /cm^3 have been demonstrated by electrical characterization, [474-476] while APT analysis has shown that incorporation is homogenous and may produce concentrations significantly above equilibrium solid solubility levels.[387] The use of trimethylaluminium (TMAl) during the Au seed growth of Si nanowires has also been investigated but was found to significantly alter morphology generating tapering and dendritic structures.[477]

2.2.2.1.2 Germanium

One of the earliest reports detailing the *in situ* doping of germanium structures grown by the VLS mechanism is by Givargizov and Sheftal[362] who employed As ($AsCl_3$) as a morphological agent. Later studies have focused on the use of P and B doping to fabricate Ge nanowire devices including transistors[478-480] and photodetectors.[481] As in Si, P is an n-type dopant. The introduction of P in the form of phosphine does not generally alter Ge nanowire morphology[482-484] although Dayeh et al.[485] reported an increased growth rate for smaller diameter nanowires which they related to a reduction in the vapour-solid interface energy. Electron concentrations in excess of $1x10^{18}$ /cm^3 have been regularly achieved by phosphorus doping.[218, 480, 482, 483, 485-488] Incorporation is again inhomogeneous with both electrical characterization[487] and later atom probe tomography (APT)[218, 220] showing greater dopant incorporation towards the sidewalls of P doped nanowires. Hole doping of Ge nanowires is often achieved using B and the

performance of B_2H_6 as an *in-situ* dopant of Ge nanowires is also similar to that found for Si.[241, 478, 480, 483, 489] While hole concentrations[241, 480, 483] in excess of $1x10^{18}$ /cm^3 and a relatively high hole mobility figure of 600 cm^2/Vs have been achieved,[478, 489] an increase in tapering and radial growth has also been noted.[241, 487] Surface termination is a particular issue for Ge nanowires with Wang *et al.*[478, 486] reporting that n-type nanowires oxidise faster than p-type. Lauhon and colleagues[488] have further shown that P concentrations of up to $1x10^{18}$ /cm^3 may be fully compensated by surface states.

2.2.2.2 III-V Materials

2.2.2.2.1 InP

Reported InP nanowire dopants include sulfur,[105, 110, 236, 244, 490-495] tin,[246, 271, 272, 496, 497] silicon,[273, 498] zinc[35, 86, 105, 110, 243, 246, 271, 273, 497, 499-505] and beryllium[506, 507]. Doping of smaller diameter nanowires is complicated in the presence of the native oxide which tend to pin the Fermi level close to the conduction band.[497, 508]

Sulphur in the form of hydrogen sulphide (H_2S) has been widely used as both an n-type dopant[105, 110, 232, 236, 244, 490, 493-495, 505, 509, 510] and WZ promoter[244, 491, 492] for InP nanowire growth by MOVPE. Controllable carrier concentrations of up to $2x10^{19}$ /cm^3 are regularly achieved, with associated electron mobilities varying between 150 and 450 cm^2/Vs.[232, 244, 490] In the case of mixed phase structures, electron trapping[490] often results in a non-linear relationship between H_2S flow and carrier concentration.[244, 490] Sulphur doping has further been hypothesised to introduce non-radiative trap states.[511] The observation of a memory effect, which would be unique to InP nanowire growth, has been related to interaction between S and the Au particles used to seed growth.[509] Several morphological effects have also been noted with H_2S doping acting to increase both WZ content and growth rate and decrease nanowire diameter.[105, 110, 236, 244, 490-492] Interestingly, *in situ* etching with HCl appears to somewhat reverse these morphological effects.[490] Measuring the seed contact angle post growth, Wallentin *et al.*[244] hypothesised that H_2S acted to promote WZ formation through a reduction in the ratio between the interfacial energy of the seed and nanowire and the surface energy of the seed (γ_{LS}/γ_{LV}).

Tin introduced as tetraethyltin (TESn) has also been investigated as an n-type dopant for MOVPE growth.[246, 271, 272, 496, 497, 512] Similarly to H_2S, carrier concentrations ranging from $1x10^{17}$ up to $1x10^{19}$ /cm^3 and electron mobilities of approximately 200 cm^2/Vs

have been measured.[246] Unlike H_2S however, no significant morphological effects have been reported for axial growth, only a slight decrease in growth rate.[246] Carrier concentration has been furthermore found to increase in a linear fashion with increasing TESn flow.[246] Silicon has also been reported as an n-type dopant. A silane (SiH_4) source has been used for MOVPE growth,[273] while Si doping by MBE has been found to decrease the axial growth rate and incorporation by VLS was determined to be relatively poor[498].

Zinc is commonly used to p-dope InP nanowires. For laser assisted techniques, zinc or zinc phosphide has typically been introduced into the target material ablated during growth.[499-502] In the case of MOVPE synthesis, two metalorganic precursors have been investigated: dimethylzinc (DMZn) and diethylzinc (DEZn). While successful p-type doping has been reported for DMZn doping,[246, 497] carrier concentration decreases at higher DMZn flows[246]. Significant morphological effects have also been observed with DMZn doping leading to an increased axial growth rate and a reduction in nanowire tapering. Borgström *et al.*[246] related these effects to an action of DMZn in passivating the substrate surface and thereby increasing the In diffusion distance. Doping with DEZn is more widely reported and has been employed in a range of device applications.[86, 105, 110, 271, 273, 503, 504] Controllable carrier concentrations approaching the limit of solid solubility ($\sim 5 \times 10^{19}$ /cm^3) have been determined from electrical[105, 110, 503, 510] and APT measurements[513]. Incorporation *via* VLS has further been demonstrated by both post growth[236] and *in situ* sidewall etching[503, 513]. Diethylzinc has been found to promote the ZB phase[35] and, at relatively high partial pressures, generate a twinning superlattice structure (TSL)[35]. Authors have related this to an increase in the solid vapour surface energy[35, 243, 505] with Wallentin *et al.*[243] reporting a systematic increase in contact angle with increased DEZn flow. At the highest of flows both DMZn[246] and DEZn[243] inhibit InP nanowire growth.

Other reported p-type dopants include beryllium[506, 507] and magnesium[514]. Beryllium doping was reported for InP nanowire growth by gas source molecular beam epitaxy (GS-MBE) where relatively high doping concentrations were found to inhibit growth.[506] In the case of growth by MOVPE, carbon incorporation may further act as an unintentional source of p-type doping.[513, 515]

2.2.2.2.2 GaAs

A range of dopants have been reported for GaAs nanowire growth including, Sn,[173, 237, 270, 516-522] Te,[227, 239, 523-527] Si,[239, 370, 528-537] Zn,[105, 235, 237, 265, 269, 270, 516, 517, 519, 520, 538-544] Be[85, 526, 534, 536, 545, 546] and C[370, 521, 531, 541, 542, 547, 548]. As for InP nanowires, surface states are expected to have significant influence on carrier type and concentration.[267, 520] In the case of Au-seeded GaAs nanowires there has further been some concern regarding the possible effects of Au impurities.[549] While Au concentrations of up to $1x10^{19}$ /cm^3 have been measured from transmission electron microscopy (TEM) studies,[550] more recent work demonstrating nanosecond carrier lifetimes in Au-seeded GaAs nanowires suggests that Au impurities likely do not act as non-radiative recombination centres.[551, 552]

As for InP, Sn has been widely employed as an n-type dopant of GaAs nanowires.[173, 237, 270, 516-522] Two distinct approaches to incorporation have been investigated; precursor supply[237, 270, 516, 517, 519-522] and seed or self-doping whereby GaAs nanowires are grown using Sn seeds[173, 518]. In the case of MOVPE growth, Sn doping has commonly been achieved using tetraethyltin (TESn).[270, 516, 517, 519-522] Tetraethyltin supply does not appear to have any structural affects on GaAs nanowire growth and has been used to achieve doping concentrations of up to $1x10^{18}$ /cm^3.[237, 522] An accumulation effect has, however, been noted with higher conductivity being found towards the tip of Sn doped nanowires, despite Sn not being detected in the Au seed post-growth.[237, 522] Interestingly, heavy Sn doping has been correlated with an orders of magnitude increase in carrier lifetime which is likely due to a confinement effect.[517, 531, 553] For Sn seeded GaAs growth, TESn has been used for the initial seed formation step.[173, 518] Carrier concentrations in excess of $1x10^{19}$ /cm^3 have been estimated from PL spectra[173] while variation in growth temperature has been observed to alter nanowire resistivity[518]. For some growth conditions, Sn seeded nanowires have been shown to behave as Esaki diodes which was related to C incorporation in VS shell growth.[518]

Tellurium has also been employed as an n-type dopant of GaAs nanowires.[227, 235, 523-527] In the case of growth by gas source molecular beam epitaxy (GS-MBE) doping has generally been achieved using a GaTe effusion cell.[227, 523, 526, 527] For this experimental setup, tellurium doping has been observed to increase nanowire diameter and to reduce the axial growth rate.[527] Carrier concentrations of up to $2x10^{18}$ /cm^3 have been measured by secondary ion mass spectroscopy (SIMS).[227] Tellurium doping has also been

achieved in nanowires grown by MOVPE using diethyltellurium (DETe).[235, 524, 525] Carrier concentrations of up to $9x10^{17}$ /cm^3 and n-type behaviour have been observed.[524, 525]

Silicon is amphoteric in III-V materials and has been employed as both an n[370, 530, 533, 538] and a p-type[239, 528, 532, 534-537] dopant for GaAs nanowire growth. In the case of self-seeded MBE growth, Raman spectroscopy has shown that Si is initially incorporated as an acceptor on the Si_{As} site.[239, 528, 534, 535] At concentrations of greater than $1.4x10^{18}$ /cm^3, compensation by pair formation occurs. Silicon doping does not appear to alter the structure of GaAs nanowires[530, 534] although incorporation has been found to be greater at the sidewalls[239]. Carrier concentrations of up to $7.4x10^{18}$ /cm^3 have been achieved with an associated hole mobility of 31 cm^2/Vs.

Zinc has been widely employed as a p-type dopant in GaAs nanowires.[105, 237, 265, 269, 270, 516, 517, 519, 520, 538-544] The majority of this work has reported on nanowires grown by MOVPE where the zinc source has been DEZn. As for InP nanowire growth, increasing concentrations of DEZn have been associated with a variety of morphological effects. These include an increase in growth rate,[540] the promotion of the ZB phase,[105] an increase in the planar defect density,[269, 539, 540] kinking,[269, 539, 540, 543] seed-splitting[269, 543] and, at the highest of DEZn flow rates, the inhibition of growth.[269, 543] Gutsche *et al.*[269] have further reported that these effects are more pronounced for larger diameter nanowires and scale with II/III ratio[237, 269, 543]. Interestingly, similar behaviour has also been found for DEZn doped planar GaAs nanowire growth.[541, 542] These effects can likely be related to changes in the relevant surface and supersaturation energies.[540] A significant concentration of zinc may furthermore build up in the Au seed particle during growth[539] and a reservoir effect has been observed[237, 520]. Controllable hole concentrations of up to $1x10^{20}$ /cm^3 have been achieved *via* zinc doping.[105, 235, 269, 538, 539, 541]

Be has been employed as a p-type dopant in several MBE GaAs nanowire studies.[85, 526, 534, 536, 545, 546] High Be concentrations have been shown to cause kinking and tapering.[534] Incorporation is initially on Be_{Ga} sites and then, at higher concentrations, at interstitial sites.[534] Casadei *et al.*[546] found incorporation to be poor by VLS. Despite this, hole concentrations of up to $1x10^{20}$ /cm^3 have been reported.[545] Carbon has also been employed as a p-type dopant of GaAs nanowires.[370, 521, 531, 541, 542, 547, 548] In the case of

MOVPE growth, carbon tetrabromide (CBr_4) has generally been used as the dopant precursor.[521, 541, 542, 548] Salehzadeh *et al.*[548] observed a dramatic reduction in growth rate with C doping at low V/III ratios which they related to competition between C and As for incorporation. Morphological effects similar to those generated by Zn, including twinning and kinking have further been reported for planar nanowires. Controllable hole concentrations of between $4x10^{18}$ and $1x10^{19}$ /cm^3 have been reported for C doping.

2.2.2.2.3 InAs

The doping of InAs nanowires has been investigated by several authors. A particular emphasis has been placed on n-type doping as InAs is both a high electron mobility material and p-type doping is difficult to achieve due to surface pinning.[268, 554-558] One approach to p-type doping has been the VS growth of a doped shell on VLS nanowires to achieve modulation doping.[559, 560] In the case of Au-seeded growth, APT has measured significant Au impurity incorporation ($1x10^{18}$ /cm^3) which may be of concern for high mobility applications.[561]

Silicon has been widely investigated as an n-type dopant of InAs nanowires.[557, 562-568] Several different sources have been investigated including disilane (Si_2H_6)[563, 565, 569] and silicon tetrabromide ($SiBr_4$)[562, 563, 565] for MOVPE growth and elemental Si for MBE growth.[557, 564, 566-568] High silicon concentrations have generally been found to increase the radial growth while reducing nanowire length.[562, 563, 565, 566] Authors have related this to an action of Si in reducing the diffusion length of In. [562, 563, 565, 566] Structural effects are usually absent, [562, 563, 565, 566] but the promotion of ZB may occur under some growth conditions.[567, 568] Incorporation is similarly variable with Si being found to be primarily incorporated in the sidewalls by some authors[556, 566] and in the core by others[569]. Raman spectroscopy has shown Si to be incorporated as Si_{Ga}. Electron concentrations of up $2x10^{18}$ /cm^3 and mobilities of up to $2x10^3$ cm^2/Vs have been measured with Si doping.

Selenium has also been employed as an n-type dopant in InAs nanowires.[562, 570, 571] The precursor ditertiarybutyl selenide (DtBSe) has been used for both chemical beam epitaxy (CBE)[562, 571] and MOVPE[562, 570]. Selenium doping has been observed to increase nanowire diameter and promote the ZB phase. In the case of MOVPE growth, radial overgrowth has been found to be Se-rich (3 at.%).[562] Controllable doping[571] delivering electron concentrations of up to $1.2x10^{20}$ /cm^3 and mobilities of up to $1x10^4$ cm^2/Vs have been reported. [562, 571] Tin the form of TESn has also been reported as an n-type

dopant.[562, 570] At higher molar fractions TESn has been observed to increase radial overgrowth.[562, 570] Electron concentrations of up to $1x10^{19}$ /cm^3 have been reported. [562]

Both zinc and beryllium have been investigated as p-type dopants of InAs nanowires.[556-558] As for other III-V nanowires, higher concentrations of zinc in the form of DEZn have been reported to cause kinking.[558] Ambipolar behaviour has been reported for Be doped InAs nanowires [556, 557] with measured hole concentrations of up to $3x10^{18}$ /cm^3.[556]

In addition to binary InAs, the doping of several InAs rich ternary alloys has also been reported.[264, 572, 573] While the doping of ternary nanowires has been observed to produce similar morphological effects to those observed for binary,[264, 572] an effect on alloy composition has additionally been observed for $In_xGa_{1-x}P$ nanowires[572].

2.2.2.2.4 GaP

There have been relatively few reports of doped GaP nanowires.[24, 574-578] Zinc introduced as DEZn has been found to have similar morphological effects in GaP to those reported for InP and GaAs nanowires.[24, 576, 578] Hole concentrations of up to $1x10^{18}$ /cm^3 and mobilities of up to 9 cm^2/Vs have however been achieved without kinking.[578] Zinc pre-doping has also proven useful for the growth of GaP nanowires on graphite.[576] Interestingly, electron holography revealed a core-shell structure in DEZn doped GaP nanowires.[577] This was related to Zn and C having different rates of incorporation into the VLS mechanism (core) relative to the VS mechanism (shell).

2.3 Crystal structure tuning and twin-plane superlattices in III-V nanowires

2.3.1 Crystal structure tuning

III-V semiconductors typically crystallize in either a ZB or a WZ structure. These two structures are closely related with ZB consisting of two cubic close packed sublattices and WZ, two hexagonal close packed sublattices. As such, both structures exhibit tetragonal coordination and vary in spacing for only the third nearest neighbours or subsequent. Structural preference is generally related to the bond ionicity of a compound. For compounds exhibiting bonding of a more covalent nature, ZB is generally favoured for its higher symmetry. Where bonding is more ionic, WZ will be favoured as the third-nearest-neighbour spacing is slightly shorter reducing the Coulomb interaction energy. The WZ structure further allows for greater distortion

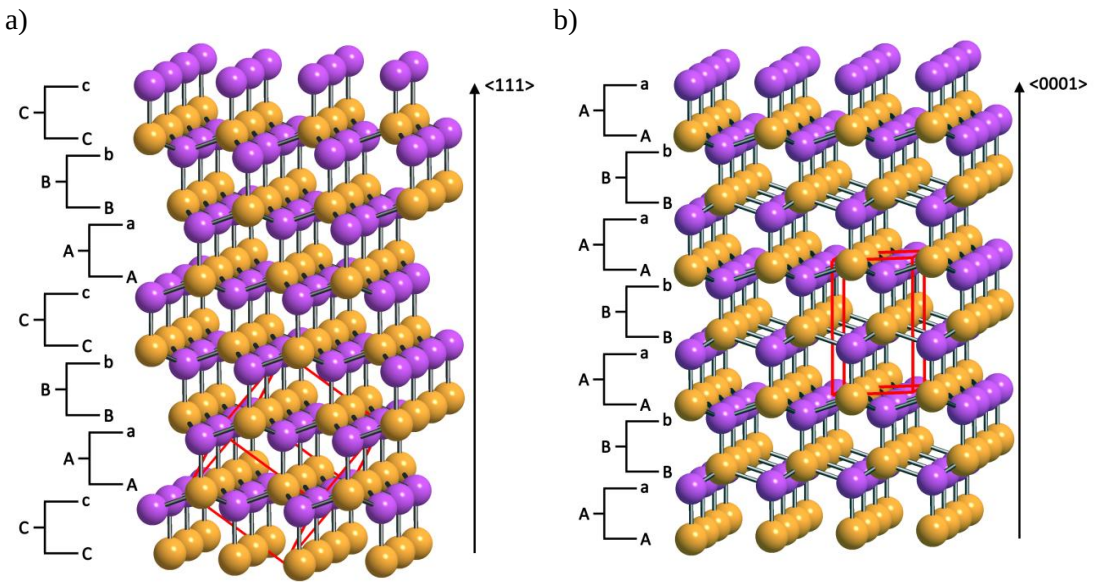

Figure 2-1 | Illustration of the a) Zincblende and b) Wurtzite lattice structures. Each atomic species is represented by a different colour. The stacking direction of each structure (<111> and <0001> respectively) is in the vertical. Note that the Zincblende structure repeats every third layer while that of Wurtzite repeats for every second layer. Unit cells are indicated by the red outlines.

away from regular tetragonal bonding.[579, 580] As such, most III-V semiconductors favour the ZB structure with the notable exception of the nitrides which favour WZ.[579, 581] Despite the difference in formation energy between these structures generally being small (typically < 25 meV per atomic pair)[579, 581, 582] bulk III-V semiconductors can normally only be synthesised in their equilibrium phase.

The difference between ZB and WZ is best appreciated by considering the stacking sequence of the close packed planes (<111> for ZB; <0001> for WZ). Figure 2-1(a) and (b) presents ball and stick models of ZB and WZ respectively. Both models are oriented such that a set of close packed planes are stacked in the vertical direction. This direction is sometimes termed the 'stacking direction'. Examining Figure 2-1(a) and (b), it is apparent that some of the close packed planes have atoms at equivalent horizontal positions. If such planes are considered to be equivalent, the ZB sequence is seen to repeat at every third plane, whereas that of WZ repeats at every second. These sequences are commonly described alphabetically in terms of bilayers (ABCABCA for zincblende and ABABA for wurtzite) or atomic layers (AaBbCcAaBbCcAa for

zincblende and AaBbAaBbAa for wurtzite). Crystal structures differing only in stacking sequence are termed ‘polytypes’ and the presence of multiple stacking types within a single crystal, ‘polytypism’.

Interruptions to a stacking sequence are known as ‘planar defects’. Where an interruption introduces only a local disruption, it is described as a ‘stacking fault’ [Figure 2-2(a)]. An interruption introducing extended disruption in the form of a symmetry operation is known as a twin plane. Where the symmetry operation is a rotation the defect is termed a rotational or ‘ortho’ twin plane [Figure 2-2(b)]. In the case of a reflection, the defect is termed a mirror or ‘para’ twin plane (sequence:).[583, 584] Stacking faults are commonly observed in WZ III-V nanowires while ortho-twin planes are common in ZB III-V nanowires. Para-twin planes involve a reversal of crystal polarity and have not been reported for III-V nanowires.[583-585] Sections of crystal either side of a twin plane are termed ‘twins’ while the presence of multiple twin planes is known as ‘twinning’.

Planar defects are frequently observed in nanowires due to the nature of the VLS growth mechanism itself. VLS growth most commonly occurs along the stacking direction[586] (<111> for ZB; <0001> for WZ) by the nucleation and flow of atomic planes or bilayers across the solid-liquid interface.[587-596] In this geometry, each nucleation event has a certain probability of altering the stacking sequence.[35, 597, 598] Given that the energy difference between cubic and hexagonal stacking is generally small,[579, 581, 582] the

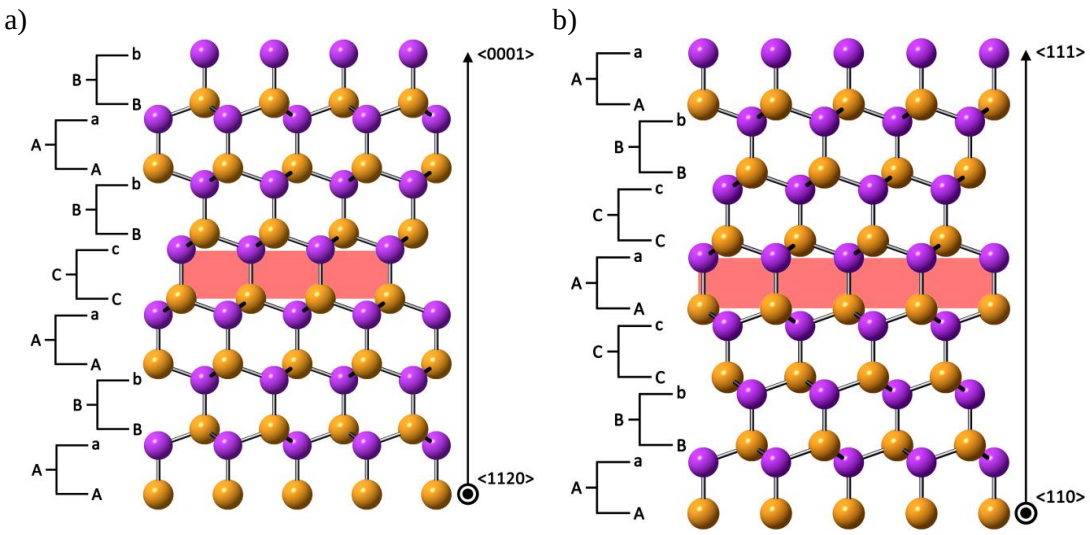

Figure 2-2 | Illustration of a) a stacking fault in Wurtzite and b) a rotational twin plane in Zincblende. The stacking direction in each case is in the vertical.

probability of planar defect formation is relatively high but may also be readily manipulated.[35, 597, 598] The susceptibility of nanowires to variation in stacking order is thus a double edged sword. Random planar defects are generally undesirable as they can have a number of detrimental effects on nanowire growth and performance. Some of these effects include altering radial overgrowth and therefore morphology,[148, 599, 600] the scattering of charge carriers[601-607] and phonons,[608-610] charge trapping[611] and altering the bandgap[612-614]. Where the stacking sequence is, however, controlled, all of these effects may be employed advantageously and the door is opened to crystal phase engineering.

The ability to engineer the crystal phase of nanowires provides a unique opportunity to explore non-equilibrium III-V phases. The combination of multiple polytypes in a single semiconductor structure further raises the possibility of homostructure devices. III-V nanowires exhibiting random polytypism were first reported by researchers at the Hitachi corporation in 1992[615] while controlled polytypism was later achieved by Caroff *et al.*[616] in 2009. Since then, controlled polytypism has been shown for many III-V nanowire materials including, GaAs,[598, 617-622] InAs,[148, 598, 616, 618, 623] and GaP[618, 624]. Band structure varies with phase due to the differences in crystal symmetry. In the case of the non-nitride III-V materials, WZ structures have generally been found to have slightly wider band-gaps than those of the equilibrium ZB phases. The band alignment between the ZB and WZ phases is further generally staggered (type II) with WZ having a positive offset.[146, 625-628] This arrangement enables the realization of crystal phase quantum dots with hole confinement for short segments of WZ in ZB and electron confinement for short segments of ZB in WZ.[145-147, 622, 625, 628-631] Confinement energies may further be tailored by varying the length of these segments.[147, 622, 625, 626, 628, 630-633] There has, however, been considerable confusion in the literature regarding the bandstructure of the non-equilibrium III-V phases. In the case of WZ GaAs, authors have reported bandgap energies ranging from 1.44 through 1.54 eV. [632, 634-637] The most recent reports suggest that the bandgap is actually within 1 meV of that of ZB GaAs[627, 636] and that the valence band offset is approximately 115 meV[622, 627]. Effective electron and hole masses of 0.15 and 0.5 m_0, respectively, have also been recently reported.[622, 638] There is less confusion regarding the bandgap of WZ InP which has generally been found to be around 70 meV greater than that of the ZB phase.[491, 613, 639-642] Theoretical calculations suggest conduction and valence band offsets of 129 and 65 meV respectively.[625, 643] Orientation dependant effective masses of between 0.078-0.093 and

0.25-0.81 m_0 for electrons and holes respectively have been reported.[644] The bandgap of InAs has been measured to be approximately 60 meV wider in the WZ relative to the ZB phase.[628, 645, 646] The offset between the conduction bands of these two phases was recently reported to be 135 meV.[647] In contrast to the other III-V materials, the bandgap of ZB GaP is indirect while that of WZ GaP is direct.[648-651] Room temperature PL emission from WZ GaP nanowires has been measured at 2.22 eV.[648, 650] GaP is also closely lattice matched to Si and the realisation of WZ GaP has further enabled the synthesis of hexagonal Si which was grown as a shell on WZ GaP nanowires.[652]

A variety of models have been developed to describe polytypic nanowire growth. Amongst these, most find the high surface to volume ratio of nanowires to be responsible for the appearance of non-equilibrium phases. Several earlier authors took a total energy approach to III-V nanowire polytypism.[582, 653-656] Using both first-principles and semi-empirical methods, the lower surface energy of WZ structured nanowires was found to define a critical diameter that below which, the WZ structure would be energetically favoured. Yamashita *et al.*[656] calculated for instance, that WZ GaAs with {1120} faceting would be energetically favoured relative to ZB with {110} faceting for diameters of less than 29 nm. The critical diameters predicted by such total energy approaches were found, however, the significantly underestimate experimental results.[598, 616, 657] Dubrovskii and Sibirev later pointed to the high surface to volume ratio

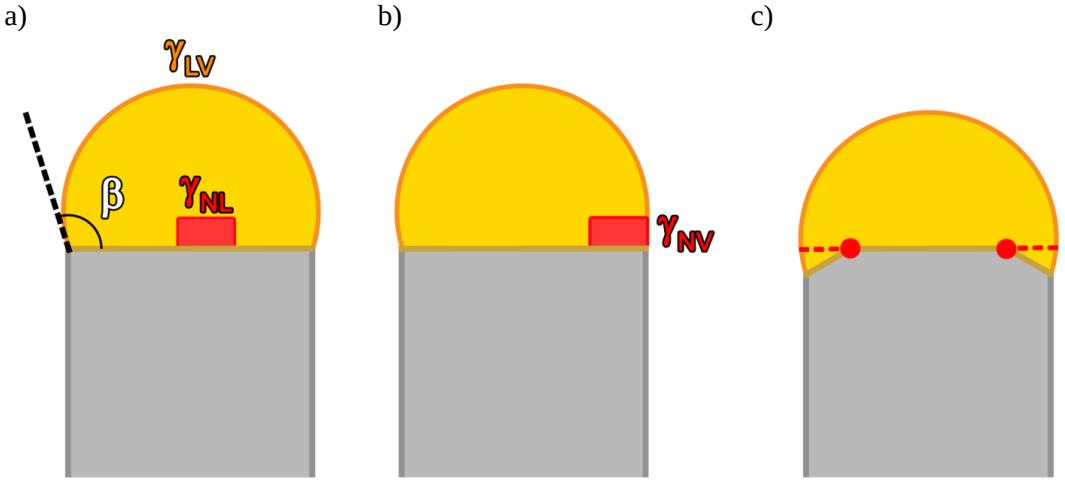

Figure 2-3 | Schematic illustration of VLS nucleation sites: a) within the droplet; b) at the triple phase line; c) at the junction of the top and edge facets (indicated by the red dots).

of nanowire structures as evidence of the VLS process being controlled by kinetics rather than thermodynamics.[658]

The majority of authors seeking to describe VLS nanowire growth have modelled the nucleation process.[583, 592, 593, 595, 598, 659-663] As discussed above, in most regimes, VLS growth is expected to proceed by the nucleation and flow of individual planes in a layer by layer process. As such, each plane is expected to form from a single nucleation event. Nucleation itself may be imagined to occur at two distinct locations: within the nanowire seed [Figure 2-3(a)] or at the triple phase line [Figure 2-3(b)].

Nucleation at the triple phase line may, however, be considered the more likely option as the energy inherent to generating the nucleus interface is partly offset by the removal of an area of the liquid-vapour interface. More formally, Glas *et al.*[591] found that nucleation at the triple phase line may be expected when:

$$\gamma_{NV} - \gamma_{NL} - \gamma_{LV}\beta < 0 \qquad \ldots(2\text{-}1)$$

where γ_{NV}, γ_{NL} and γ_{LV} are the nucleus-vapour, nucleus-liquid and liquid vapour interface energies respectively and β is the wetting angle of the seed particle [see Figure 2-3(a)] . The change in Gibbs free energy for a 2D nucleus forming at this location may be written as:

$$\Delta G = -Ah\Delta\mu + A\gamma_T + lh\Gamma \qquad \ldots(2\text{-}2)$$

where A is the area of the nucleus, h is the planar bilayer spacing, $\Delta\mu$ is the difference in chemical potential between components in the seed and in the nanowire, γ_T is the surface energy of a planar defect, l is the sidewall length of the nucleus and Γ is the effective interfacial energy barrier to nucleus formation. By considering the critical nucleus size and energy, the following conditions for non-equilibrium WZ formation may be formulated[591]:

$$\gamma_{NV,WZ} < \gamma_{NV,ZB};\ \Delta\mu > \frac{1}{1 - \left(\frac{\Gamma_{WZ}}{\Gamma_{ZB}}\right)^2}\frac{\gamma_T}{h} \qquad \ldots(2\text{-}3)$$

where $\gamma_{NV,WZ}$ is the edge energy of a WZ nucleus and $\gamma_{NV,ZB}$ is the edge energy of ZB nucleus. Nucleation of non-equilibrium WZ is thus favoured where the edge energy of

WZ is lower than that of ZB and the supersaturation in the seed particle is sufficient to overcome the creation of a stacking fault. As the facets relating to non-equilibrium WZ growth are usually considered to be lower energy than those of ZB, nucleation models generally predict WZ growth at higher supersaturation levels. Authors have continued to refine the above nucleation model by considering details including supersaturation as a function of both group III and V,[598] distortion of the seed particle[598, 663], the angle of the nucleus edge[659] and contributions from mass transport and the Gibbs-Thomson effect[592, 595, 660]. Earlier modelling generally assumed each nucleation event to be independent giving Poissonian statistics. More recent experimental evidence from *in situ* TEM studies[587-589, 664-666] and growth marker analysis[667] has shown that nucleation events are, in fact, anticorrelated. The small volume of the seeds used for nanowire growth results in a significant reduction in supersaturation with each nucleation event. As such, the seed particles must refill between nucleation events producing nucleation antibunching. This oscillation in supersaturation is further manifested in an oscillation of the growth front. *In situ* TEM studies have shown that, under some growth conditions, an 'edge facet' forms subsequent to each nucleation event as shown in

Figure 2-3(c).[587-589, 664-666] This edge facet then gradually fills in as supersaturation increases before the next nucleation event. Interestingly, Jacobsson *et al.*[589] observed only ZB growth in the presence of an edge facet likely due to nucleation away from the TPL at the vertex between the edge and top facets. Nucleation away from the TPL leading to ZB may also be expected at high supersaturations.[596] In this way, a series of transitions from ZB to WZ and back to ZB again may be expected with increasing supersaturation. Such a series of transitions was recently shown[621] with increasing V/III ratio for MOVPE and may explain the opposing V/III trends previously reported for MOVPE[198, 583, 598, 618, 619, 648, 668-674] and MBE[591, 675-678] growth.

2.3.2 Twinning superlattices in nanowires

A particular example of sub-Poissonian nucleation statistics occurs for twinning-superlattice nanowire growth. Unlike most nanowires, TSL structures are characterised by {111} sidewalls which are non-parallel to the growth direction. [24, 35, 366, 515, 600, 616, 679-681] As such, the shape of the liquid-solid interface varies away from equilibrium with growth. At some point, it becomes energetically favourable to introduce a twin plane and reverse the polarity of the sidewall facets. This process is illustrated in . Starting at

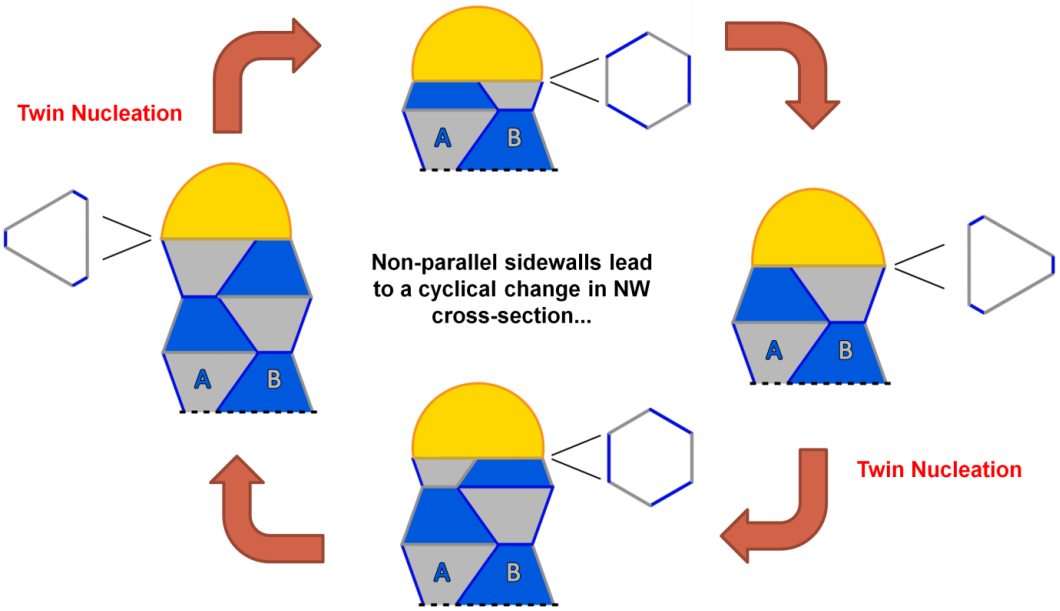

Figure 2-4 | Illustration of the a) Zincblende and b) Wurtzite lattice structures. Each atomic species is represented by a different colour. The stacking direction of each structure (<111> and <0001> respectively) is in the vertical. Note that the Zincblende structure repeats every third layer while that of Wurtzite repeats for every second layer. Unit cells are indicated by the red outlines.

the topmost figure where the nanowire has a hexagonal cross-section, further growth leads to triangular cross-section and distortion of the seed particle. At some point the contact angle of the seed particle is altered such that the nucleation of twin-plane is favoured.[35] The cross section of the nanowire then tends back towards an equilibrium hexagonal shape. Further growth leads again to the distortion of the seed particle and another twin plane which returns the crystal to its original orientation. This process produces periodically spaced twin planes and is dependant on both the relevant interfacial energies and the energetic barrier to twinning. Generally the period between twins is an increasing function of nanowire diameter.

Twinning superlattice structures are of interest for fundamental growth studies,[24, 35] electronic band structure engineering,[682-687] and thermoelectric[609, 610, 688-690] and mechanical applications[691, 692]. The use of periodic twinning to introduce miniband structure is, however, challenging as a period of several nanometres or less is likely needed for appreciable effects. [682-687]

2.4 Nanoscale and subwavelength scale lasers

Nanoscale lasers hold promise for a range of applications including integrated photonics and biological sensing.[693-695] The majority of current designs may be classified as either plasmonic or photonic. A relatively recent development,[113, 696, 697] plasmonic lasers or 'spasers' employ surface plasmon-polariton (SPP) modes at the interface between a dielectric and a conductor. As a high effective index may be achieved for SPP modes, the spatial dimensions of plasmonic devices may be significantly less than their operating wavelength. Absorption in the metal cavity is, however, also high and these devices are characterised by relatively large losses and low quality factors.[698-701] Superior performance is generally obtained from nanoscale photonic lasers in terms of lower threshold, longer photon lifetime and increased quality factor.[693] Dielectric contrast confines photonic modes and scaling is, in principle, diffraction limited. Many such photonic nanolasers represent an evolution of more traditional designs such as VCSELs[702, 703] and microdisk lasers[704].

Semiconductor nanowires are a popular platform for realizing nanoscale lasers as they offer the combination of a high quality gain medium with a tailored optical cavity. Photonic modes may propagate along the length of a nanowire to give a Fabry-Pérot type cavity[25, 114, 705-707] or around the circumference in a whispering gallery type arrangement[118, 708]. The dielectric contrast between nanowires and their surrounding medium (usually air) usually results in excellent confinement. In the case of a Fabry-Pérot type cavity, high end reflectivity may further be achieved for certain wavelength-diameter combinations as the reduced diameter of nanowire structures causes the end facets to behave like localised scattering centres. The reduced diameter of nanowire structure further enables the integration of lattice mismatched materials to give possibilities including the growth of III-V nanowire lasers on silicon.[118, 709]

Lasing has now been reported for semiconductor nanowires from a number of material systems including, II-VI compounds such as ZnO[112, 115, 710-715], CdS[713, 716-722] and CdSe[705, 723-726], III-V materials such as InP,[706, 727, 728] GaAs,[25, 116, 729-732] GaSb,[733] GaN[707, 713, 722, 734-742] and several ternary alloys such as CdSSe[743-746] and InGaAs[118, 708, 747]. While most authors have shown lasing from nanowires lying on low-index substrates, several strategies to achieve lasing from as-grown standing nanowires have also been demonstrated.[118, 708, 728, 732] Early work focused on semiconductor materials characterised by high exciton binding energies with optically pumped ZnO nanowire

lasers[112, 710] and electrically pumped CdS nanowire lasers[114] being reported in 2001 and 2003 respectively. An unambiguous transition from amplified spontaneous emission (ASE) to lasing was later shown for ZnO nanowires by Capasso and co-authors[748] in 2008. Near-infrared III-V nanowire lasers took longer to develop due to difficulties with material quality and, surface and Auger recombination.[733, 749] Descriptions of room temperature operation appear from 2013 for both GaAs[25] and InP[728]. In the case of GaAs nanowire lasers, surface recombination was a particular issue with the development of a high quality AlGaAs passivation being required for room temperature operation. [25] The ability to create both radial and axial heterostructures in nanowire has recently enabled the demonstration of multi-quantum well and dot nanowire lasers.[730, 731, 741, 747, 750]

The limits to photonic nanolaser scaling may be better understood by considering the balance between modal gain and losses in a Fabry-Pérot type optical cavity. At the threshold for lasing, the round-trip model modal gain will be balanced by the round trip losses:

$$\Gamma g_{th} = \alpha_i + \alpha_m \qquad \ldots(2\text{-}4)$$

where Γ is the mode confinement factor, g_{th} is the threshold gain and α_i and α_m are the internal cavity and mirror losses respectively. In a Fabry-Pérot type optical cavity, mirror losses may be estimated in the following fashion:

$$\alpha_m = \frac{1}{L}\ln\left(\frac{1}{\sqrt{R_1 R_2}}\right) \qquad \ldots(2\text{-}5)$$

where L is the cavity length and R_1 and R_2 are the reflectance of the two ends of the cavity. Combining equations 2-4 and 2-5 and considering that, at threshold, the electric field at any point in the cavity will return to the same value for a round-trip of the propagating mode gives two expressions for the length of the Fabry-Pérot cavity:

$$L = -\frac{1}{2}\frac{\ln(R_1 R_2)}{\Gamma g_{th} - \alpha_i}, \qquad L = \frac{\lambda}{2n_r}m \qquad \ldots(2\text{-}6)$$

where L is length, n is the effective index of the propagating mode and m is an integer. Given that that cavity length, L, is inversely related to threshold gain, g_{th}, it is apparent that a reduction in the cavity length will increase the threshold gain requirement of a

Fabry-Pérot type laser. The mode confinement factor, Γ, is similarly inversely related to cavity length and a reduction in this variable must be offset by an increase in cavity length or threshold gain. As such, it may be appreciated that reducing the dimensions of a laser is a trade off between size and threshold gain. Reducing the width of the cavity below the wavelength leads to a dramatic reduction in confinement and is usually unfeasible. From the second equation for length it is further noted that the minimum cavity length of a Fabry-Pérot laser is half of the propagating wavelength.

The threshold for an optically pumped laser may further be considered in terms of steady-state operation:

$$P_{th} = \frac{\hbar\omega V_a}{\eta_p}\left[\left(1-\beta(N_{th})\right)BN_{th} + AN_{th}\right] \qquad \ldots(2\text{-}7)$$

where P_{th} is the threshold pump power, $\hbar\omega$ is the photon energy of the pump source, V_a is the active volume of the laser, η_p is the pumping efficiency, β is the fraction of spontaneous emission coupled into the lasing modes, N_{th} is the threshold carrier concentration, R_{sp} is the spontaneous or radiative recombination rate and R_{nr} is the non-radiative recombination rate. Examining equation 2-7, several observations can be made. Firstly, it is noted that the threshold pump power, P_{th}, is seen to scale with the active volume, V_a. This relationship is well known from quantum well[751, 752] and dot[753-755] lasers and is a major motivation for the continued development of nanoscale lasers. The fraction of light coupling into the lasing modes, β, represents a further advantage of nanowire lasers as β is increased due to both the excellent confinement discussed above and the small diameter of these structures which acts to reduce the number of allowable modes.[732] Finally, it is seen that $P_{th}$is positively correlated with the non-radiative recombination rate R_{nr}. Given the high surface to volume ratio of nanowire structures, the significance of non-radiative surface recombination may be appreciated.

2.5 Zn-V Semiconductors

2.5.1 The Zn-V semiconductor family

The earliest publications describing the structure and properties of the various Zn-V compounds date from the late nineteenth through early twentieth centuries.[756-761] Optoelectronic studies appeared in the literature from the late nineteen fifties on, with much of the pioneering work originating from the IBM Corporation[62, 762, 763] and the

Institute of Technology Wrocław Poland[764, 765]. Early reviews of Zn-V work include Turner *et al.*[766] in 1961, Nasledov and Shevchenko[767] in 1973 and Żdanowicz and Żdanowicz[768] in 1975. Material synthesis during this early period was generally from the melt[32, 54, 763, 764, 769-778] with single crystals being grown by Bridgman-type methods[61, 763, 778-782]. Physical vapour deposition methods gained popularity from the nineteen seventies on[45, 63, 284, 325-327, 329, 331, 333-340, 774, 777, 783-800] with MBE[49, 287, 314, 316, 321] and MOVPE[263, 276, 280, 282-285, 308, 801, 802] growth of Zn-Vs first being described in the nineteen eighties. In the case of MBE, major contributions include the work of Bell laboratories on Zn_3As_2[49, 314, 316, 803] and, more recently, the work of the Atwater group at the California Institute of Technology on Zn_3P_2[286, 287, 313, 320, 321]. Major contributions to the MOVPE growth of Zn-Vs include the work of the University of Port Elizabeth, South Africa which focussed on Zn_3As_2[263, 276, 308, 315] and that of Suda *et al.* from Japan which focussed on Zn_3P_2[280-283, 802]. Growth by both MBE and MOVPE has most commonly been on III-V substrates [typically GaAs or InP(100)],[49, 263, 276, 280, 282, 286, 287, 308, 313-316, 320, 321, 802, 803] although glass[283] graphite, mica and steel substrates have also been reported.[289, 801] This century has seen a shift in interest away from bulk and planar Zn-V materials towards nanostructures. Most commonly grown by physical vapour deposition methods, various nano-geometries of Zn_3As_2,[63, 277, 325-327, 338, 796, 804, 805] Zn_3P_2,[63, 278, 328-340] Zn_xSb_y[346, 349, 798, 799, 806-809] have now been reported. Professor Guozhen Shen of China has been particularly active in this field publishing first from the National Institute for Materials Science in Japan[326, 327, 335, 336, 338-340] and then later from the Huazhong University of Science and Technology[325, 329].

In addition to the binary Zn-V compounds, the synthesis and properties of the various Zn-V alloys has also been an ongoing subject of research.[810, 811] The ternary alloy $Cd_{(3-x)}Zn_xAs_2$ has received particular attention,[65, 764, 769, 770, 772, 779, 780, 782, 812-830] due initially to a combination of high electron mobility (the electron mobility of Cd_3As_2 can exceed 10^4 $cm^2V^{-1}s^{-1}$ at room temperature)[293, 831, 832] and convenient band-gap (0-1.0 eV)[59], and more recently, the newly established topological semimetal behaviour of Cd_3As_2.[291-293] Other Zn-V alloys reported in the literature include $Cd_{(3-x)}Zn_xP_2$[64, 830, 833-838], $Zn_3As_{(2-x)}P_x$[830, 839], $Cd_{(1-x)}Zn_xAs_2$[819, 822, 823, 826, 828, 833, 840-844] and $Cd_{(1-x)}Zn_xP_2$[833, 834, 841, 844] (published values of bandgap as a function of composition are shown in Figure 1-1). Ternary $Zn_3As_{(2-x)}P_x$ nanowires were recently described by Im *et al.*[63] who found negative bowing in the relationship between bandgap and composition.

Electrical characterization of Zn_3As_2,[263, 310, 314, 317, 319, 325, 763, 764, 769, 779, 814, 845] Zn_3P_2[280, 282, 284, 285, 321, 329, 332, 335-337, 786, 787, 789, 793, 800-802, 834, 846, 847] and Zn_xSb_y[46, 61, 279, 778, 808, 848-852] has almost universally found p-type behaviour regardless of synthesis method. In the case of Zn_3As_2 this has been related to shallow-level[310] native defects.[263] In Zn_3P_2 these defects have been identified as P interstitials[311, 321, 777, 787] while the p-type character of Zn_xSb_y is thought to derive from Zn vacancies[853-855]. Despite the III and VI elements In[781, 782, 856] and Se[779, 845, 856] being shown to act as effective n-type dopants there are few

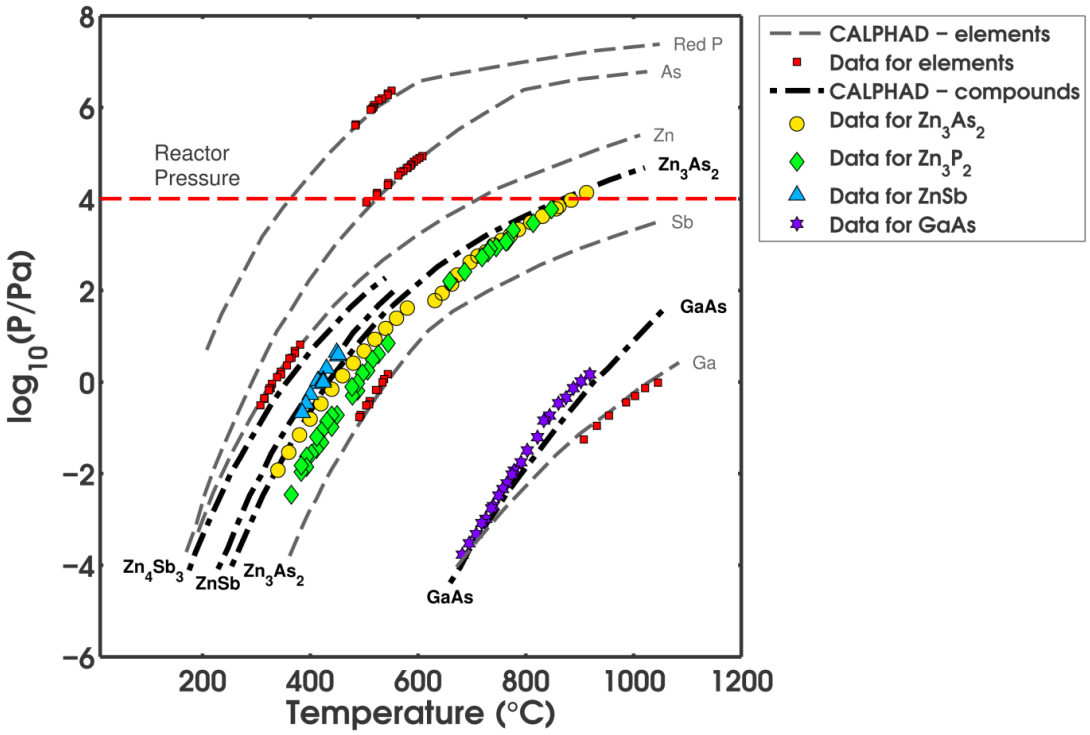

Figure 2-5 | Vapour pressure of selected elements (l,s) and compounds (s). Lines show the results of modelling by the CALPHAD method, points show experimental data from the literature. Thermodynamic data for elements in the condensed phases was taken from Dinsdale[6] and for gaseous species, Ansara *et al.*[26]. Experimental data for elemental Phosphorus is from Bachmann and Buehler[34], Arsenic: Lisak and Fitzner[44], Zinc: Klimova *et al.*[48] and Aldred and Pratt[53], Antimony: Aldred and Pratt[53] and Gallium: Munir and Searcy[60]. Experimental data for ZnSb is from Hirayama[32] and thermodynamic data for the calculations was taken from Li *et al.*[17]. Experimental data for Zn_3As_2 and $Zn_3P_2$is from Schoonmaker and Lemmerman[31, 67] and Greenberg *et al.*[28, 39] and thermodynamic data for Zn_3As_2 was taken from Ghasemi and Johansson[13]. Experimental data for GaAs is from Richman[68] and the thermodynamic data was taken from Ansara *et al.*[26].

generally accepted reports of n-type Zn-V material due most likely to a self-compensatory effect.[311, 857, 858] Earlier work described the formation of p-n junctions in Zn_3P_2 through Mg in-diffusion[857, 859] but more recent research has questioned this result.[860] There are also several reports of n-type ZnP_2 but this behaviour has been related to relatively deep level defects.[861, 862] Alloying with Cd produces n-type material for Cd-rich compositions.[764, 769, 779, 838] Silver has been widely employed as p-type dopant[781, 782, 863, 864] being used particularly to increase the conductivity of Zn_3P_2 samples.[863, 864]

Posing a particular challenge for material synthesis and annealing, the Zn-V semiconductor family is characterized by relatively high equilibrium vapour pressures.[28, 31, 32, 39, 67, 68] Figure 2-5 plots equilibrium vapour pressure as a function of temperature for several Zn-V compounds and the III-V semiconductor GaAs. As may be observed, the equilibrium vapour pressures of the Zn-V materials are significantly greater than that of GaAs. At 650 °C, a typical growth temperature for GaAs, the difference is some five orders of magnitude. Equilibrium vapour pressure is furthermore observed to increase with group V atomic number such that Zn_3P_2 is seen to exhibit the lowest vapour pressure and ZnSb the highest.[28, 31, 32, 39, 67] Where these materials are nanostructured, the Gibbs-Thompson effect will act to further increase equilibrium vapour pressure.

The high equilibrium vapour pressure of the Zn-V materials present a particular challenge for growth at reduced ambient pressures. In the case of MBE, previous authors have found substrate temperature to be limited by product decomposition and the highest reported growth temperatures for Zn_3As_2[49, 314] and Zn_3P_2[320, 321] are 360 °C and 275 °C respectively. Higher maximums of up to 600 °C[801] have been achieved using MOVPE although decomposition remains limiting and growth temperatures of between 200 to 400 °C are more common.[263, 283, 802] As precursor decomposition becomes limiting at these lower temperatures researchers have investigated the application of both thermal and photochemical pre-cracking to Zn-V MOVPE growth.[263, 280-283, 315, 802] While relatively low growth temperatures have been reported to reduce physical cracking in Zn-V layers grown on III-V substrates,[282, 284] crystal quality suffers.[49, 263, 276, 284, 314, 865] In the case of MOVPE growth, Scriven *et al.*[263] and Kakishita *et al.*[282] both found that a temperature of at least 350 °C is required for single crystalline growth. Unlike typical III-V growth where Group V re-evaporation dominates, the re-

evaporation of both elemental reactants must be considered with increasing temperature. Figure 2-5 plots the elemental vapour pressures of selected Groups II, III and V elements where it can be seen that the vapour pressure of Zn is orders of magnitude greater than that of Ga. In the case of zinc antimonide, elemental zinc actually exhibits a higher elemental vapour pressure than that of the group V element, antimony (see Figure 2-5).[48, 53] Previous authors have employed V/II ratios as low as 0.56 for the growth of Zn-V materials.[282]

2.5.2 Zinc – Arsenic binary system

The Zn-As binary system contains two intermediate compounds and three eutectic points.[866] The intermediate compounds, $ZnAs_2$ and Zn_3As_2, melt congruently at temperatures of 1043 and 1288 K respectively (770 and 1015 °C) while the three eutectic points are located at 21.0, 41.0 and 99.8 at.% Zn and 997, 1021 and 690 K (724, 748, 417 °C).[866] The system was first assessed by Heike[757] in 1921 with significant later contributions from Lazarev *et al.*[36] and Yamaguchi *et al.*[867]. These previous studies are well summarized by Okamoto[866] and a CALPHAD-type assessment

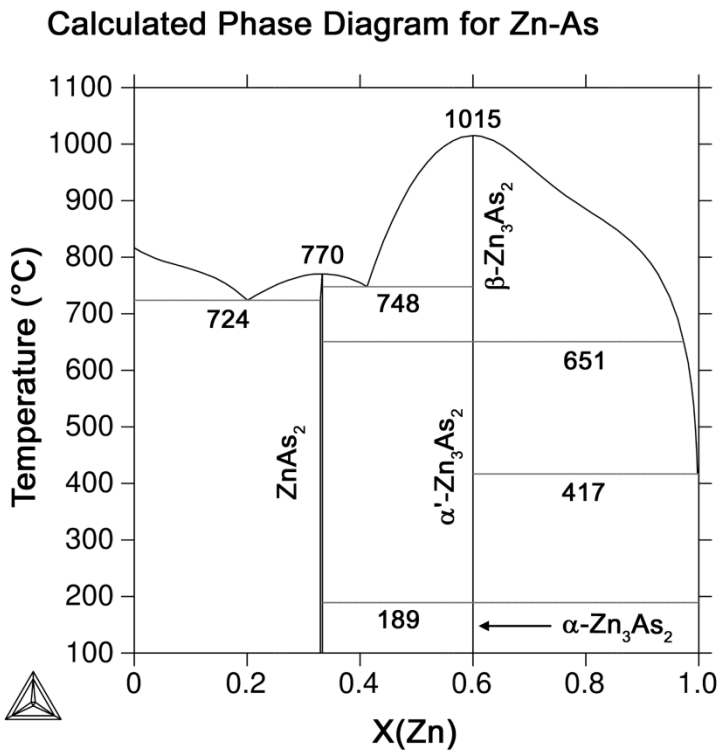

Figure 2-6 | Binary phase diagram for Zn-As constructed by the CALPHAD method using the data of Ghasemi *et al.*[13].

was recently published by Ghasemi and Johansson[13]. The phase diagram that may be calculated using this CALPHAD assessment is shown in Figure 2-6. Gaseous phases were excluded from this diagram as the mixing enthalpy reported for the liquid phase gives an unphysical liquid phase stability region.

Zinc diarsenide ($ZnAs_2$) is characterised by a large monoclinic cell where each Zn atom is tetrahedrally bonded to four As atoms and each As atom is tetrahedrally bonded to two Zn atoms and two As atoms.[54, 58] In this arrangement the As atoms form semi-spiral chains parallel to the c-axis. [54, 58] A narrow region of solid solubility exists from 33.0 to 33.5 at.% Zn at 550 °C.[58] Congruent melting occurs at 1043 K (770 °C) under an As overpressure of 3.3 x10^5 Pa with incongruent dissociation at pressures below this to give Zn_3As_2 and As_4.[62] The low symmetry of the monoclinic cell leads to large anisotropies of up to ten times in Hall coefficient,[845, 868, 869] resisitivity[845, 868, 869] and Seebeck coefficient[870]. Unintentionally doped specimens are slightly p-type with carrier mobilities of up to 100 cm^2/Vs.[845, 869] The optical properties of $ZnAs_2$ are also highly anisotropic with an indirect bandgap of 0.89 eV in the **E∥c** direction and a direct gap of 0.97 eV in the **E⊥c** direction.[65, 871] Specimens have generally been produced by direct synthesis with an excess of As.[54, 774]

At room temperature the Zn_3As_2 α phase is tetragonal and consists of a distorted face centred cubic As sublattice interpenetrated by a 75% filled simple cubic Zn sublattice.[9, 22, 872] In this arrangement each arsenic atom is surrounded by six zinc atoms and two zinc vacancies whereas each zinc atom is surrounded by four arsenic atoms. A slight

Table 2-1 | Selected properties of the compounds of Zn and As at 300 K

	Crystal System and Space Group	Lattice Parameters	Melting Temperature	Bandgap
Zn_3As_2	Tetragonal $I4_1cd$ (De Vries '89)[9]	a=b= 11.7823(6) c= 23.6385(24) (De Vries '89)[9]	$T_{m,congruent}$=1015 °C (Lazarev '81)[36]	$E_{g,dir}$=0.99 eV (Pawlikowski '79)[42] $E_{g,indir}$=0.992 eV (Chelluri '86)[49]
$ZnAs_2$	Monoclinic P21/c (Fleet '74)[54]	X(Zn)=33.3 a= 9.200 b= 7.664 c= 7.985 β= 102.47° (Lazarev '79)[58]	$T_{m,congruent}$=768 °C (Lyons '59)[62]	$E_{g,dir}$=0.97 eV (**E⊥c**) $E_{g,indir}$=0.89 eV (**E∥c**) (Morozova '07)[65]

reordering of the zinc sublattice produces the α' phase at 463 K (190 °C)(see Figure 7-12).[22, 866] Above 924 K (651 °C) Zn_3As_2 transforms into the cubic β phase.[873] This transformation was identified as incongruent by Greenberg *et al.*[874] who measured 0.01 at.% As enrichment. Like the other Zn-V materials, Zn_3As_2 has universally been reported to behave as a p-type material with hole mobilities of up to 300 cm^2Vs.[49, 317, 325, 781, 875] An optical transition at an energy of approximately 1.0 eV has variously been identified as both an indirect and a direct bandgap.[42, 49] Samples have been synthesised by a variety of methods including direct synthesis,[763, 769, 770] CVD,[325, 326, 338] LPE,[317-319] MBE[49, 314] and MOVPE[263]. As an earth abundant material with strong absorption around 1.0 eV, Zn_3As_2 has potential for various applications in optoelectronics including photovoltaics and optical telecommunications.

2.5.3 Zinc – Phosphorus binary system

Relative to the Zn-As system the Zn-P binary is less well characterized with experimental data being available for only a limited compositional range (0-66 at.% P).[40] Significant experimental studies include those of Ugay *et al.*,[876] Berak and Pruchnik,[877] Schneider and Krumnacker,[878] and Liu *et al.*[30]. As for the Zn-As binary, the Zn-P system contains two intermediate compounds. Both ZnP_2 and Zn_3P_2 are thought to melt congruently at temperatures of 1035 and 1170 °C respectively (1308 and 1443 K) although there remains some confusion regarding the equilibrium phase of ZnP_2.[30, 40, 877, 878] The eutectic between these two compounds is located at 45 at.% Zn and 980 °C.[877] The eutectic between Zn and Zn_3P_2 was originally reported to be at 97.5 at.% Zn by Ugay *et al.*[876], but has more recently been calculated to occur at a lower zinc concentration and a temperature of 689 K (416 °C).[30, 37] A CALPHAD-type assessment of the Zn-P system was first reported by Tu et al.[16] and then later refined by Liu *et al.*[30] who removed an unphysical liquid immiscibility gap. The phase diagram which may be calculated from these assessments is shown in Figure 2-7. Gaseous phases were excluded from this diagram as the thermodynamic function provided for Zn_3P_2 gives an unphysical sublimation point. Polymorphism was not considered in either assessment and is shown in Figure 2-7 by dashed lines.

Zinc diphosphide (ZnP_2) is known to take several different structural forms although there remains some confusion regarding the relationship between these phases.[820, 879-882] Early work identified the tetragonal α phase (also known as red ZnP_2) as the low

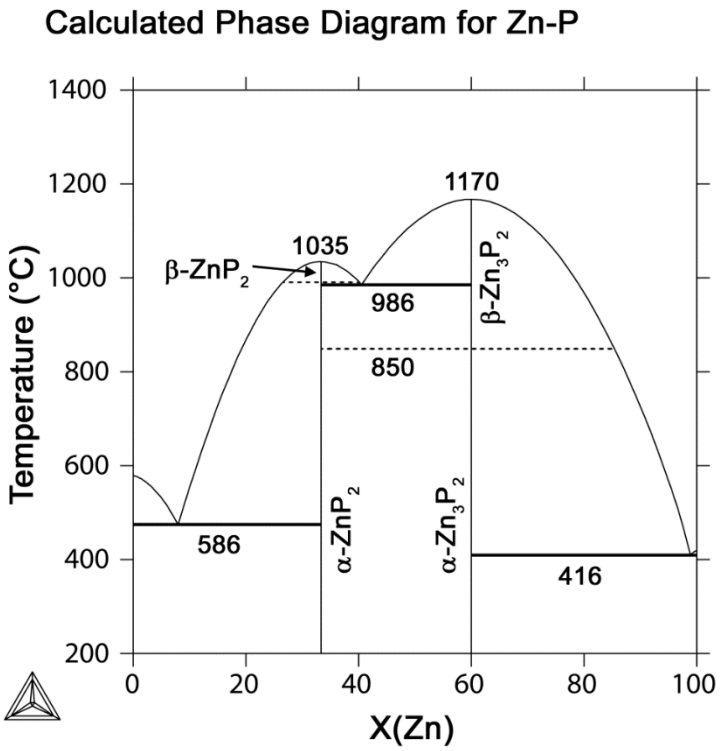

Figure 2-7 | Binary phase diagram for Zn-P constructed by the CALPHAD method using the data of Tu *et al.*[16] and Liu *et al.*[30]. Polymorphic transformations were not taken into account in the thermodynamic modelling and are instead shown as dashed lines following the results of Dutkiewicz[40].

temperature polymorph with a transformation to the monoclinic β phase (black ZnP_2 - isomorphic to $ZnAs_2$) at 990 °C.[877] More recent studies have, however, suggested that the tetragonal phase is metastable.[820, 879-882] A cubic variant has further been identified at high pressures.[879] The melting behaviour of ZnP_2 is also poorly understood but the process is generally reported to be congruent.[877, 883] Interestingly, n-type ZnP_2 has been reported by several authors.[861, 862, 884, 885] Like the other Zn-V compounds, ZnP_2 has usually been found to be intrinsically p-type[861, 886] but almost uniquely to this compound, successful n-type doping has been reported for both the tetragonal and monoclinic phases using Ga, Te and Sn.[861, 884, 885] Several authors have, however, related this n-type behaviour to deep-level defects rather than shallow-level impurity-related donor states.[861, 862] Isomorphic to $ZnAs_2$, monoclinic ZnP_2 also exhibits highly anisotropic behaviour.[887-889] The bandgap in the **E∥c** direction has been found to be 1.32 eV and indirect while there is a direct forbidden transition at approximately 1.42 eV in

Table 2-2 | Selected properties of the compounds of Zn and P at 300 K				
	Crystal System and Space Group	Lattice Parameters	Melting Temperature	Bandgap
Zn_3P_2	Tetragonal $P4_2/nmc$ (Zanin '04)[12]	a=b= 8.0785(2) c= 11.3966(4) (Zanin '04)[12]	$T_{m,congruent}$=1173 °C (Dutkiewlcz '91)[37]	$E_{g,dir}$= 1.50 eV $E_{g,indir}$= 1.38 eV (Kimball '09)[45]
ZnP_2 (Red)	Tetragonal $P4_12_12$ (Hegyi '63)[50]	a=b= 5.0661 c= 18.532 (Zanin '03)[55]	$T_{m,congruent}$=1040 °C (Dutkiewlcz '91)[37]	$E_{g,dir}$= 2.18 eV $E_{g,indir}$= 1.65 eV (Sobolev '71)[29]

the **E⊥c** direction.[889] In contrast to the 'black' monoclinic phase, the 'red' tetragonal phase has a significantly wider direct bandgap of 2.18 eV.[29, 890] Indirect transitions with anisotropic energies ranging from 1.65 to 1.97 eV have been reported at lower energies.[18, 29] Zinc diphosphide has usually been grown by a combination of direct synthesis and CVD-type methods.[884, 885, 891]

The room temperature α phase of Zn_3P_2 belongs to the tetragonal $P4_2/nmc$ space group with a=b=8.09 Å and c=11.45 Å.[12, 23] As for Zn_3As_2, the Zn_3P_2 lattice can be considered as a slightly distorted defective antifluorite structure consisting of a distorted face centred cubic P sublattice interpenetrated by a 75% filled simple cubic Zn lattice. Above 1123 K (850 °C) Zn_3P_2 transforms into the cubic cF12 β phase.[877, 892] Electrical characterization has found unintentionally doped samples to be moderately p-type with hole mobilities of 30 to 100 cm^2/Vs.[329, 787, 863, 864] The existence of a direct bandgap of 1.50 eV at room-temperature is well accepted,[893] but confusion remains regarding a transition around 1.38 eV which has variously been ascribed to an indirect transition[305, 306] or defect states[307, 777]. Zn_3P_2 has been synthesised by a variety of methods including direct synthesis,[777, 894, 895] CVD,[338, 339, 786] MBE[320, 321] and MOVPE[282, 802]. As an earth abundant material with an optimal bandgap, Zn_3P_2 is considered a particular candidate for photovoltaic applications.[281, 286, 288-290, 312, 321, 329, 333, 896-901]

2.5.4 Zinc – Antimony binary system

Despite being a subject of ongoing research since the middle of the nineteenth century,[758, 760, 902-904] confusion remains regarding the nature of the Zn-Sb binary.[20, 41, 905, 906] The system is significantly more complex than that of both Zn-As and Zn-P with at least three accepted intermediate phases: ZnSb, Zn_4Sb_3 and Zn_3Sb_2. Further

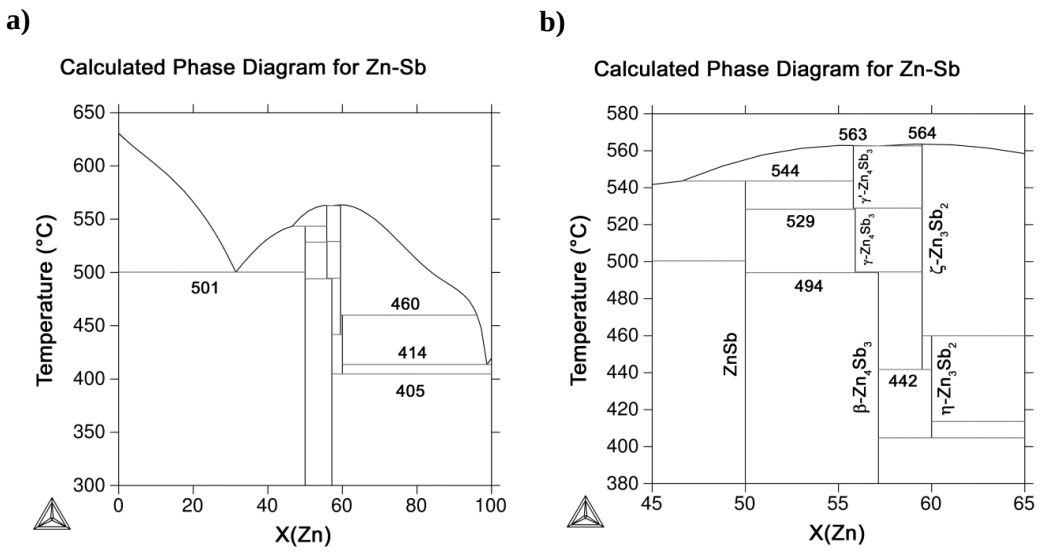

Figure 2-8 | Binary phase diagram for Zn-Sb constructed by the CALPHAD method using the data of Li *et al.*[17]. a) Full compositional range b) magnified region of the diagram.

stoichiometries in the literature include Zn_6Sb_5 which was previously considered an equilibrium phase[907, 908] but is now no longer accepted[905] and recent work reporting the synthesis of Zn_8Sb_7.[27, 349, 909, 910] Both Zn_4Sb_3 and Zn_3Sb_2 melt congruently at temperatures of 839 and 841 K respectively (566 and 568 °C)[41] while ZnSb decomposes in a peritectic reaction at 779 K (506 °C) to give a liquid and Sb_3Zn_4.[20, 41, 904, 911] Below 633 K Zn_3Sb_2 also decomposes to give Zn_4Sb_3 and Zn. There are two further eutectic reactions in the binary, one between Sb and ZnSb at 32 at.% Zn and 779 K (506 °C) and another between zinc and Sb_2Zn_3 at 99 at.% Zn and 687 K (414 °C).[41] Differences in stoichiometry between the polymorphs of Zn_4Sb_3 and Zn_3Sb_2 give rise to several eutectoids and peritectoids. A variety of thermodynamic assessments of the system have been previously undertaken[17, 20, 912, 913] with the most recent at the time of writing being that of Gierlotka.[906, 914]

Unlike the other compounds in the Zn-Sb phase diagram, ZnSb does not undergo any polymorphic transformations. An orthorhombic structure which may be visualised as layers of Zn_2Sb_2 rhomboid rings, the unit cell contains eight formula units and is stoichiometric with relatively little structural disorder.[56, 295, 296, 775] While ZnSb is a semiconductor, its mechanical, thermal and chemical properties approach those of a metal.[915] Previous authors have reported unintentionally doped samples to be p-type,[766,

Table 2-3 | Selected properties of the compounds of Zn and Sb at 300 K

	Crystal System and Space Group	Lattice Parameters	Melting Temperature	Bandgap
β-Zn_4Sb_3	Rhombohedral R-3c (Snyder '04)[19]	a= 12.2282(3) c= 12.4067(4) (Snyder '04)[19]	γ-Zn_4Sb_3 $T_{m,congruent}$=563 °C (Adjadj '07)[41]	$E_{g,dir}$= 0.33 eV $E_{g,indir}$= 0.26 eV (Qiu '10)[46] *Calculation
ZnSb	Orthrhombic Pbca (Mozharivsky '04)[11]	a= 6.20393(8) b= 7.7408(1) c= 8.0977(1) (Carter '64)[56]	$T_{m,incongruent}$=544 °C (Adjadj '07)[41]	$E_{g,dir}$= 0.99 eV $E_{g,indir}$= 0.5 eV (Komiya 64)[61]

[916] behaviour which has been linked to an acceptor band likely arising from intrinsic point defects.[297, 850] The bandgap is indirect and approximately 0.5 eV at 300 K,[61, 766, 917] with the threshold for direct transitions at this temperature being 0.99 eV.[61] Specimens have generally been synthesised from the melt[56, 297, 915, 918] with examples of Bridgman-type processes for single crystal growth[61]. There is one report of the MOVPE growth of ZnSb films in the literature.[279] The excellent thermoelectric performance of the compounds of zinc and antimony are well known having been reported by Seebeck in his original work on thermoelectricity.[919] Commercial application of ZnSb as a p-type thermoelectric dates from the nineteen fifties when it was often used in conjunction with constantan.[915] Thermoelectric figures of merit (ZT) approaching 1.0 have been achieved at temperatures around 700 K.[915, 920, 921]

Zn_4Sb_3 exists in a variety of polymorphs. While the structure of both the γ and γ' phases remain to be solved,[14, 19] the stoichiometry of both the α and β phases is now known to be closer to $Zn_{13}Sb_{10}$.[14, 296] The low temperature α polymorph (not shown in Figure 2-8) is triclinic[14] and transforms *via* a reversible order-disorder transformation into the rhombohedral β phase around 260 K (-13 °C).[11]

In a similar fashion to ZnSb, both phases can be considered as being constructed from Zn_2Sb_2 rhomboid (diamond) rings.[14, 296] In the β phase these diamonds are linked in chains to give columns of Sb atoms along the c-axis (the structure of β-Zn_4Sb_3 is illustrated in Figure 7-49).[19] A Zn deficiency is thought[922] to be responsible for the highly p-type behaviour of β-Zn_4Sb_3 with the conductivity of unintentionally doped

material generally approaching 5-10 inverse ohm metres.[922-924] Phonon conductivity is conversely low,[922, 923, 925-927] which has been related particularly to the presence of disordered zinc interstitials in the structure.[19, 296] Together these two factors work to give β-Zn_4Sb_3 the highest known thermoelectric figure of merit for temperature range of approximately 150 to 400 °C.[19] Authors have sought to further improve this performance through nanoscaling.[346, 349, 798, 806, 808, 921, 928-930]

Synthesis of bulk Zn_4Sb_3 samples has generally been from the melt with some authors employing quenching[923, 931, 932] or gradient freeze methods[19, 923, 933] in order to obtain β-Zn_4Sb_3. Both CVD-type[798, 799] and liquid phase[346, 349, 806-808] techniques have been used in order to obtain nanostructured samples. No optical spectroscopy of Zn_4Sb_3 has been performed to date but an indirect bandgap of 0.26 eV was calculated by Qui *et al.*[46] from first principle methods.

3

Experimental Methods

3.1 Metal organic vapour phase epitaxy (MOVPE)

Metal organic vapour phase epitaxy (MOVPE) is a chemical vapour deposition technique used for the growth of compound semiconductor materials such as GaAs, InP and GaN. The technique is common in commercial settings and involves the introduction of gaseous precursors into a heated reaction vessel where they undergo pyrolysis and react in a complex series of both homogenous and heterogeneous reactions. As the atmosphere in the reaction vessel is continuously flowing, MOVPE is

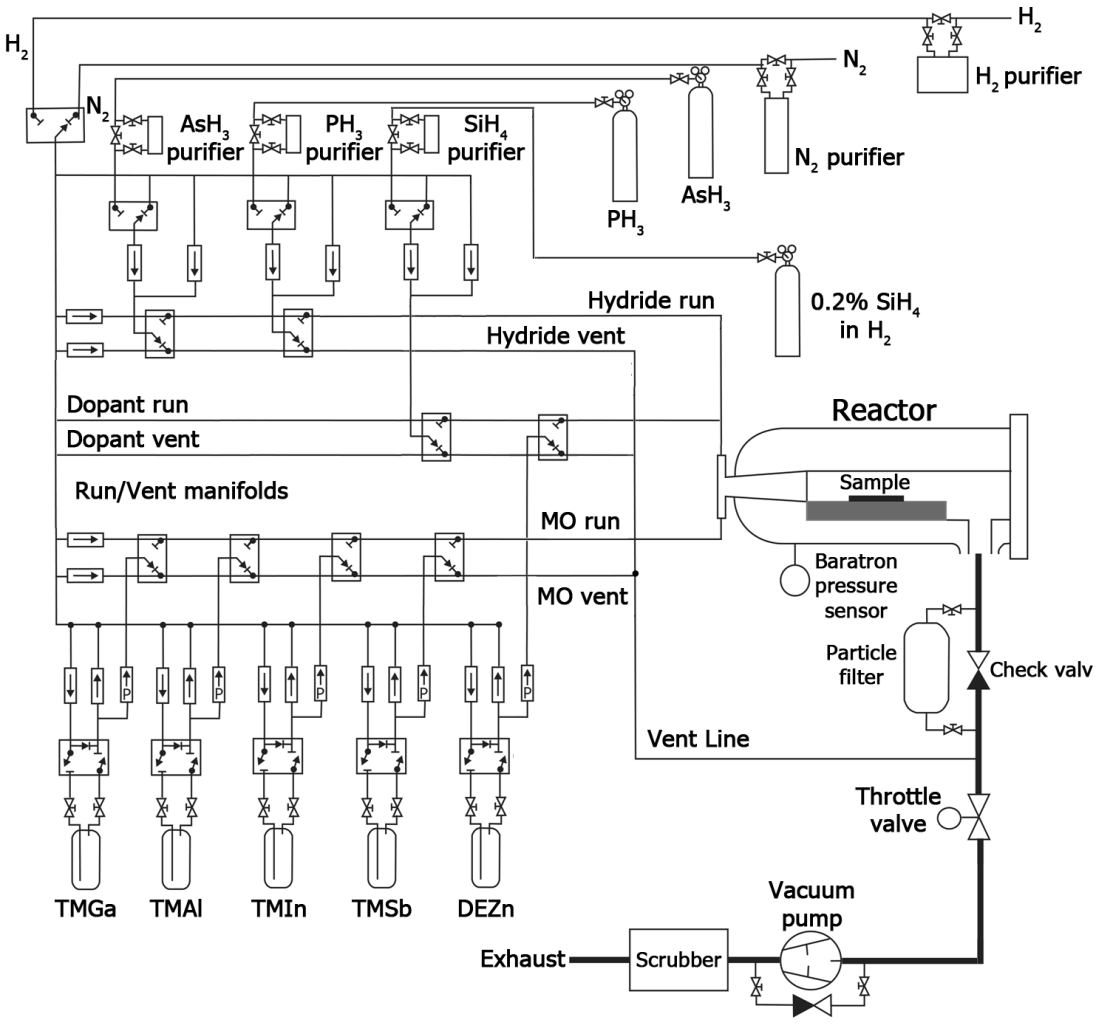

Figure 3-1 | Schematic illustration of the MOVPE reactor used in this work.

characterised by an excellent degree of control over the growth process and is capable of delivering atomically abrupt heterostructures. A wide variety of binary semiconductors (III-V, II-VI) and alloys may be grown by the technique, and the process is readily scalable. Development of MOVPE methods date from at least the 1960s with pioneering contributions coming from the groups of Didchenko[934] and Manasevit[935-937]. A comprehensive publication on the subject of MOVPE growth has been authored by Stringfellow[152].

The samples analysed in this work were grown using an AIXTRON 200/4 horizontal flow MOVPE reactor. A schematic illustration of the setup is shown in Figure 3-1. As can be seen, the group V elements and Si were introduced as the hydrides arsine (AsH_3), phosphine (PH_3) and silane (SiH_4, 0.2% in H_2). These gases were stored in pressurised cylinders. The metalorganic sources included trimethylgallium [$Ga(CH_3)_3$, TMGa], trimethylindium [$In(CH_3)_3$,TMIn], trimethylaluminium [$Al(CH_3)_3$, TMAl], trimethylantimony [$Sb(CH_3)_3$, TMSb] and Diethylzinc [$Zn(C_2H_5)_2$, DEZn]. Each was stored in a temperature controlled bath at a temperature of 17 °C except TMGa which was stored at 5 °C. At these temperatures, TMIn was the only solid metalorganic source with the remainder being liquids. Ultra-high purity hydrogen was used as the carrier gas after being filtered through a proprietary membrane material. All flows were metered using electronic flow controllers. The susceptor was silicon carbide coated graphite configured in a 3x2-inch arrangement with both planetary and satellite gas foil rotation. Heating was provided by a three-zone infrared lamp setup with a thermocouple placed in the susceptor. Growth was conducted at 100 mbar using a standard flow rate of 15 slm. Vent and exhaust gases were passed through an activated carbon scrubber.

3.1.1 Substrate preparation

A variety of substrate types and orientations were investigated in this work. Prior to VLS growth, either metallic nanoparticles or a metallic thin film were deposited on the substrate. Two different types of metallic nanoparticles were investigated, Au and Ag, with both being obtained as citrate stabilised colloidal solutions (Ted Pella, Inc.). In this form, individual nanoparticles carry a net negative charge and do not naturally adhere to III-V substrates. The substrates were therefore treated with an aqueous 0.1 % solution of poly-L-lysine (PLL) before nanoparticle deposition.[938, 939] This involved immersion in the solution for 60 seconds before washing with deionised (DI) water and drying with a nitrogen (N_2) gas gun. A colloidal solution containing metallic nanoparticles was then

Table 3-1 | Concentration of colloidal solutions			
Colloidal Au Solutions		**Colloidal Ag Solutions**	
Diameter /nm	**Nanoparticles /ml**	**Diameter /nm**	**Nanoparticles /ml**
10	5.7×10^{12}	60	1.70×10^{10}
30	2.0×10^{11}	80	1.70×10^{9}
50	4.5×10^{10}		
80	1.1×10^{10}		
100	5.6×10^{9}		
150	1.7×10^{9}		
200	7.0×10^{8}		
250	3.6×10^{8}		

applied by dropper to the face of the substrates and allowed to sit for another 60 seconds before further washing and drying. The concentration of the colloidal solutions varied by nanoparticle diameter as supplied (see Table 7-3), and in some cases, was further reduced by dilution with DI water immediately prior to application.

Thin films were deposited using either electron-beam physical vapour deposition (Temescal BJD-2000 E-beam/Thermal Evaporator) or thermal evaporation (Kurt J. Lesker Nano 36). The nominal thickness was 0.5 nm in all cases.

3.2 Electron microscopy

Electron microscopy takes advantage of the wave-like nature of electrons to achieve spatial resolutions far in excess of those which may be achieved using conventional light microscopy. While the wavelength of visible light varies from approximately 400 to 700 nm, that of an electron accelerated by 200 kV is approximately 2.5 pm. The possibility of using electrons for imaging was first suggested with de Broglie's work on wave-particle duality in 1924,[940] and the first electron microscope was developed soon after by Ruska and Knoll[941] in 1931. Development of electron microscopy was rapid with some of the first commercial systems being offered by Siemens in 1939.

In operation, electron microscopes direct a high energy electron beam towards a sample. Upon entering the sample, scattering leads to the formation of an interaction volume which is significantly larger than the initial beam diameter. A range of signals are generated from across this interaction volume as shown schematically in Figure 3-2.

These signals include both electrons and electromagnetic radiation with a range of energies. Differing signals provide complimentary information relating to features such as geometry, composition and electronic band structure.

Secondary electrons (SE) are produced by inelastic scattering and represent the lowest energy electron signal (typically < 50 eV for secondary electron imaging). Being low energy, SE have a short escape depth and carry information about surface topography. While most SE are the product of multiple scattering events, those which are the product of a single scattering event also carry information about the composition of the surface and are termed Auger electrons (AE). Elastically scattered electrons have a higher energy and therefore longer escape depth relative to secondary electrons. As the probability of backscattering increases with atomic mass, backscattered electrons (BSE) carry compositional information from a depth of up to several microns. Structural information is further present where these electrons are coherently scattered.

A range of electromagnetic radiation is also produced by the inelastic scattering of the primary beam with particularly important information appearing as X-rays. Characteristic X-rays with energies corresponding to the atoms from which they are

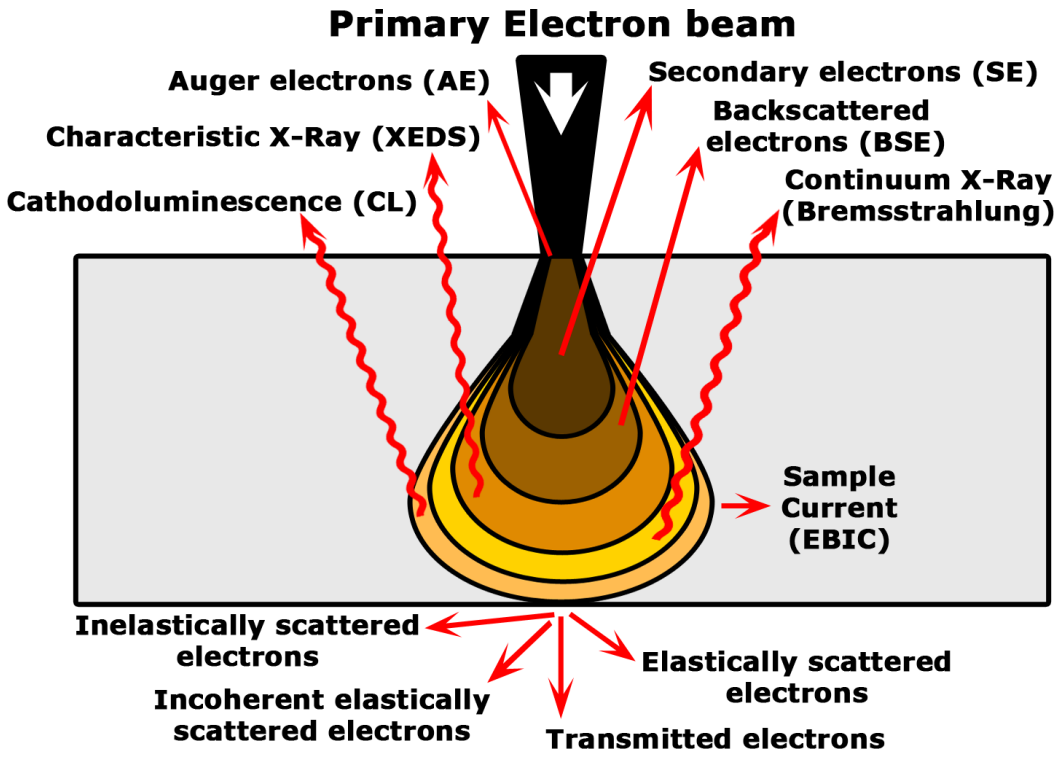

Figure 3-2 | Schematic illustration showing the interaction of an energetic electron beam with a sample and some of the signals which may be produced.

emitted provide compositional information in a similar manner to Auger electrons. The collection of this spectrum is termed X-ray energy dispersive spectroscopy (XEDS). Background Bremsstrahlung X-ray radiation further provides information about the average atomic mass of the sample in a similar fashion to the BSE signal. As the X-ray absorption length is relatively long these signals are generated from throughout the interaction volume.

Scattering events may also generate electron hole pairs which can provide information about the electronic structure of a sample. The application of voltage leads to electron beam induced current (EBIC) while radiative recombination gives cathodoluminescence.

3.2.1 Scanning electron microscopy (SEM)

Scanning electron microscopy (SEM) methods are characterised by the rastering of an electron beam across the sample. Relatively low beam energies are employed (1 – 30 kV) and the signal is usually collected in a backscatter geometry. Variation in signal with beam raster is used to generate the image. The most commonly analysed signal is SE yield with all SEM images in this work being SE images except where otherwise noted. Contrast arises in these images as the volume of material contributing to the SE signal varies with topography. As shown schematically in Figure 3-3, steep gradients in

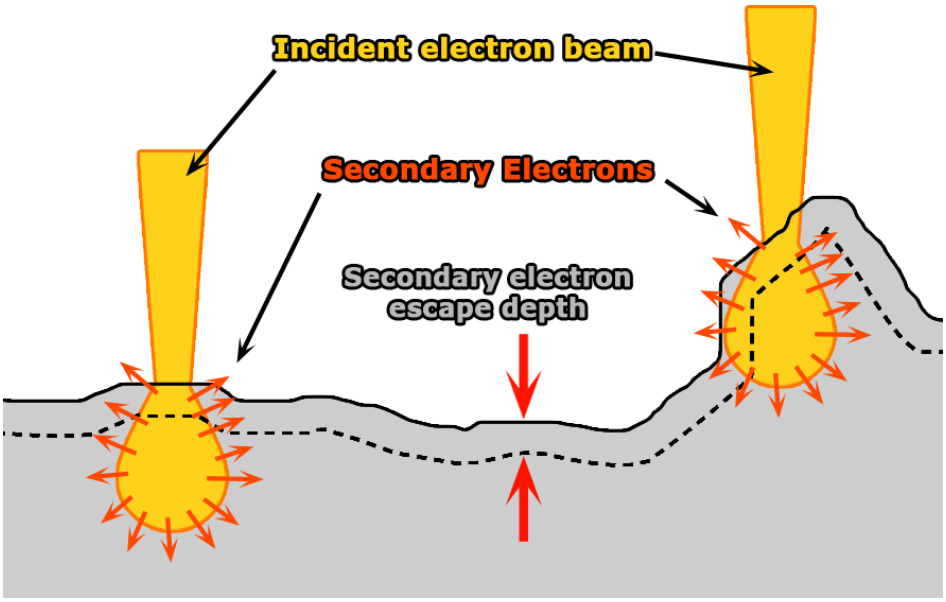

Figure 3-3 | Schematic illustration of the effect of surface topography on secondary electron yield.

depth produce more secondary electrons and will appear brighter relative to flatter areas. Secondary electrons are typically collected by a positively charged grid before being accelerated towards a detector.

SEM is a highly versatile technique with the primary sample requirement being one of conductivity. Non-conductive sample may be imaged by firstly depositing a thin film of a conductive material such as Au or C. Such coating was unnecessary for the semiconductor samples studied in this thesis. A variety of different SEMs were used in this work with imaging primarily conducted at accelerating voltages of 3 kV or less. SEM imaging was primarily employed to investigate the morphology of synthesised nanowires.

3.2.2 Transmission electron microscopy (TEM)

In contrast to SEM, transmission electron microscopy (TEM) techniques usually employ significantly higher accelerating voltages (hundreds of kV) and the signal is collected in a forward scatter or 'transmitted' geometry. The optical path in a TEM is conceptually similar to that of traditional transmission light microscope with the beam being shaped and directed onto the sample by a condenser lens system. An image of the sample is then formed by the objective, intermediate and projector lens systems. At lower magnifications, this image is most commonly formed from the direct (unscattered) beam with contrast here largely representing differences in atomic mass (Z-contrast) or sample thickness.

In addition to imaging the sample, the diffraction pattern formed at the back focal plane of the objective lens may also be imaged by adjusting the strength of the intermediate lens system. Ray diagrams for these two imaging modes are shown schematically in Figure 3-4. The diffraction pattern arises from coherent elastic scattering and reveals crystallographic information about the sample. It may further be used to orient the sample onto a particular zone axis. When oriented on a zone axis, high-resolution TEM (HRTEM) imaging may be performed where the difference between the direct and diffracted beams is used to form an interference image showing individual columns of atoms.

As TEM methods collect signals in the forward scatter geometry, relatively thin (typically < 100 nm) or 'electron transparent' samples are required. For many materials, extensive sample preparation work is required to meet this requirement. In the case of

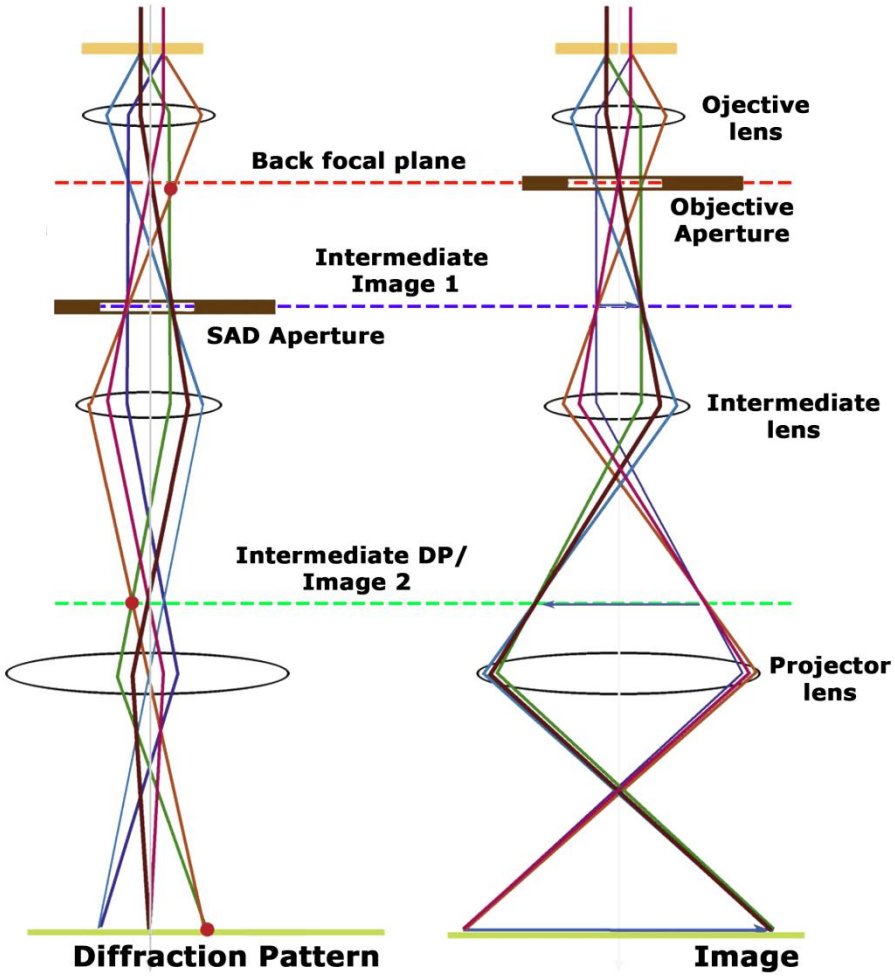

Figure 3-4 | Ray diagrams for a TEM in a) diffraction mode and b) Imaging mode. Adapted from Williams and Carter.[5]

the current work, however, the majority of samples were already characterised by a critical size of less than 100 nm and sample preparation consisted of mechanically dispersing the nanowires onto a holey carbon coated copper grid. The one exception to this was the analysis of nanowire cross sections which were prepared by ultra-microtomy. The samples for cross section were firstly embedded in Spurr resin[942] before being baked at 70 °C for 24 hours. The growth substrate was then removed by immersion in liquid N_2. Cross-sectional lamella with a thickness of approximately 40 nm were then cut using a diamond knife and placed on carbon coated copper grids.

3.3 Atom probe tomography (APT)

Atom probe tomography (APT) combines field emission microscopy (FEM) with time of flight mass spectroscopy (TOF-MS) to generate an atomic scale, 3D map of a

sample. The technique employs needle-shaped specimens (with a radius < 100 nm) which are placed in a strong electric field (typically 1-2 kV). Voltage or laser pulsing is then used to extract individual ions which are swept along electric field lines towards a 2D sensor. The position at which an ion is detected may then be mapped back a position on the sample surface with depth information being calculated from the atomic volume. Time of flight corresponds to the time between pulsing and detection. The whole process is performed under ultra high vacuum conditions (typically 10^{-8} to 10^{-10} Pa) and at cryogenic temperatures (typically 10-100 K). A schematic illustration of the experimental apparatus is shown in Figure 3-5.

APT traces its origins to the early work of Müller who developed the FEM in 1936[943] and in 1956 became the first to directly observe atoms[944] by using a variant of FEM known as field ion microscopy (FIM). The concept of combining FEM and TOF-MS was introduced by his colleague Panitz in 1973.[945] Early APT systems were often limited to voltage pulsing and thus the analysis of conductive metallic samples. With the development of laser pulsing a wider range of materials including semiconductors and insulators may now be imaged.[946, 947] Several different types of artefact affect APT analysis. Chief among these are difficulties with the 3D reconstruction process. Most reconstruction models assume a spherical tip shape and broadly uniform field distribution. These assumptions often, however, break down due to faceting of the tip or the presence of inhomogeneities such as precipitates or heterostructure. Methods to

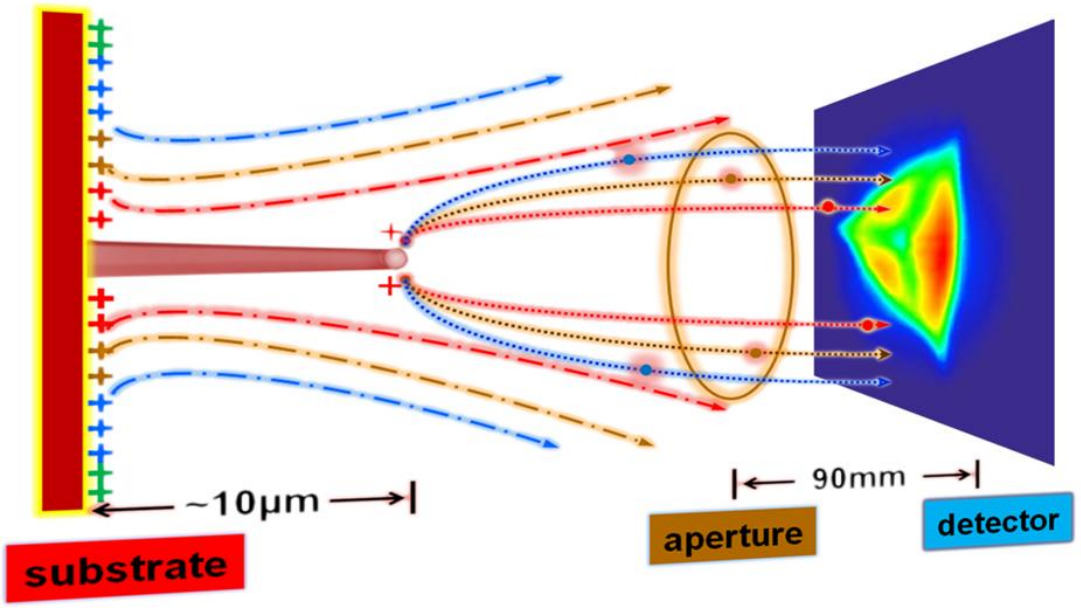

Figure 3-5 | Schematic illustration of the APT process.

correct for tip shape include imaging the real tip shape by electron microscopy both before and after APT and using known values such as plane spacing. There are furthermore plans to combine APT with electron microscopy in the one instrument so that the tip shape may be imaged during the APT process.[946] Another potential artefact is the migration of surface atoms before ionisation. Migration may be particularly problematic for dilute species with higher ionization potential than that of the host matrix. Finally, the ionisation of multiple ions or clusters can generate ambiguity in identifying the evaporated species. A comprehensive book on the subject of APT has been written by Gault et al.[948] The current study employed a laser-assisted local-electrode atom probe system (LEAP) (Cameca 3000X Si λ= 532 nm, repetition rate 200 kHz, pulse length 10 ps) equipped with a position-sensitive, wide field-of-view detector and a micro-electrode for ion extraction. Characterization was performed at 20 K using laser energies ranging between 10 and 100 pJ.

3.4 Photoluminescence spectroscopy (PL)

Photoluminescence spectroscopy (PL) describes the measurement and analysis of optical emission generated by optical excitation. In the case of semiconductor materials, photons with an energy greater than that of the bandgap are used to generate electron hole pairs. Emission by subsequent radiative recombination reveals information relating to the electronic structure of the material. Where a microscopic feature or material is of interest, PL may be performed with the aid of an optical microscope in what is known as micro-photoluminescence spectroscopy (μ-PL). A full review of the topic of PL has been written by Gilliland.[949]

The custom μ-PL setup used in the current work was built in-house and is illustrated in Figure 3-6. Optical excitation was provided by a pulsed diode pumped solid-state (DPSS) laser (femtoTRAIN IC-Yb-2000, λ = 1044 nm, repetition rate 20.8 MHz, pulse length 400 fs, 3 W maximum output), which was frequency doubled to 522 nm. The excitation intensity was controlled by neutral density filters. Individual nanowires were imaged and excited using an optical microscope (Nikon Eclipse L150) equipped with a motorised stage and a high magnification lens (Nikon LU Plan 100x/0.9NA). Photoluminescence was collected through the same objective lens before being spectrally filtered (550 nm longpass) to remove the laser wavelength. The spectrometer (Acton, SpectraPro 2750) contained two selectable gratings (150 lines /mm or

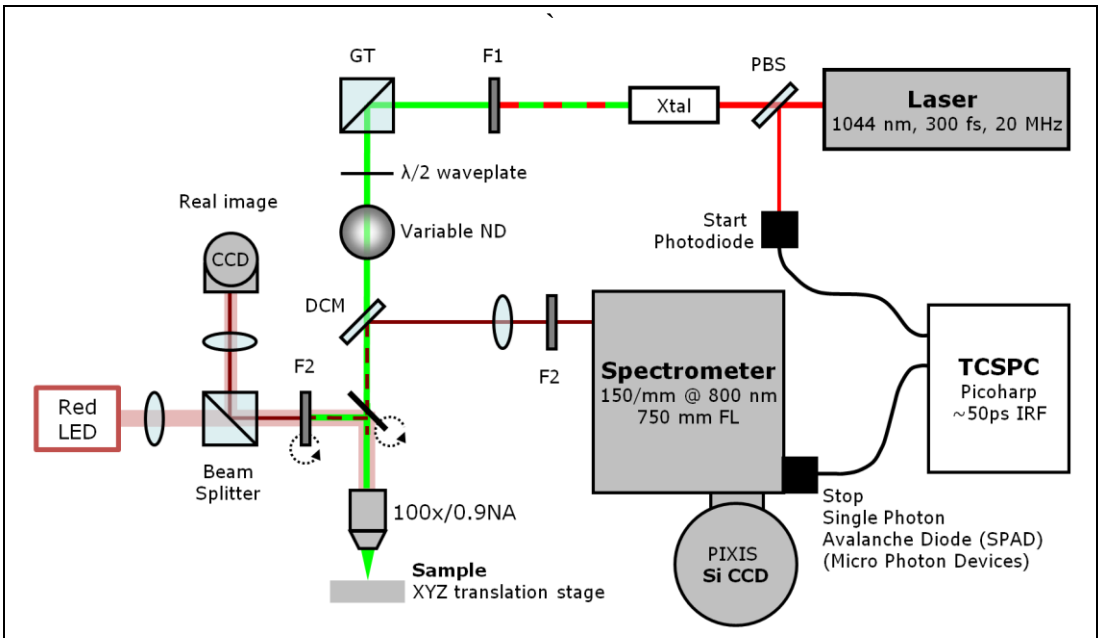

Legend

PBS	Partial Beam splitter (~4%)	LP	Linear polariser
Xtal	LBO non-linear doubling crystal	GT	Glan-Thompson polariser
F1	522nm bandpass filter	DCM	Dichroic Mirror
F2	550nm longpass filter		Flip mounts

Figure 3-6 | Schematic illustration of the layout used for optical spectroscopy. Adapted with permission from Saxena.[7]

1200 lines /mm) and spectral data was recorded using a Peltier-cooled CCD camera (Princeton Instruments, PIXIS). For low temperature measurements a continuous flow He-cooled cryostat (Janis research) was mounted on the microscope stage. The cryostat featured a 0.5 mm thick chemically polished 0° sapphire window, which was used in conjunction with an aberration-corrected 60x/0.70NA lens (Nikon CFI Plan Fluor).

3.4.1 Time-resolved photoluminescence spectroscopy (TRPL)

Time-resolved photoluminescence spectroscopy (TRPL) methods measure PL emission as a function of time. Transients are usually generated by pulsed excitation and provide an insight into the dynamical behaviour of semiconductor materials. The current study measured the carrier lifetime of individual nanowires using a form of TRPL known as time-correlated single photon counting (TCSPC). TCSPC involves exciting the sample with a pulsed source such that there is less than a few percent chance of detecting

emission for any given cycle. Repeated measurements of the delay between excitation and emission are then used to generate a frequency histogram which corresponds to the recombination dynamics of the sample. The TCSPC setup is shown in Figure 3-6. A partial beam splitter (PBS) is used to generate a reference beam which is directed to a photodiode and provide the start signal. Emission of a selected wavelength is directed to a single photon avalanche diode (SPAD) to generate the stop signal. Signal processing was provided by a Picoharp 300 with a response time of approximately 30 ps. The maximum window for TRPL was limited by the laser repetition rate to approximately 50 ns.

3.4.2 Sample preparation

Samples for PL measurement were firstly transferred onto alternate substrates by mechanical dispersion. This was achieved by gently rubbing the face of the nanowire growth substrate across that of the alternate substrate which was typically Si. Where guided modes and lasing behaviour were of interest, ITO (indium tin oxide, ~ 200 nm thickness) coated SiO_2 substrates were used in place of Si to minimise absorption and leakage. These substrates were firstly patterned with Au markers such that the same nanowires could be repeatedly identified for PL and later SEM analysis. The markers were defined using a standard photolithography process which has been described in detail elsewhere.[7]

4

Zinc as a Dopant: p-type GaAs nanowires

4.1 Introduction

Realizing controlled impurity doping remains a key obstacle to the continued development of semiconductor nanostructures such as nanowires.[211, 213, 226, 950] Particular challenges include incorporation[207, 951] activation[214, 952] and metrology[209, 953, 954]. Reductions in contact size further demand increased dopant concentrations and improved statistical control over doping.[209, 955] These issues are compounded by the unique geometries and nanoscale volumes which preclude or complicate many of the standard quantitative tools of semiconductor engineering such as secondary ion mass spectrometry (SIMS) and Hall measurements.[209, 232, 233, 495] In the context of the aforementioned challenges, there exists a rich body of work reporting on the impurity doping of semiconductor nanowires.[950] Doping has been found to have a variety of potential effects on nanowire growth including altering the growth rate,[220, 244, 246, 449, 498, 956] the stacking fault density and crystal phase,[35, 244, 247, 562] changing the growth direction through kinking and interrupting the VLS process itself.[**237, 445**] The potential for significant dopant inhomogeneity has further been identified with incorporation generally being found to be greater for radial relative to axial growth.[218, 220, 412, 455, 464, 950] Despite these issues, a wide variety of technically relevant doped semiconductor nanowire devices have now been demonstrated including transistors,[99, 377, 470, 499] electrically pumped lasers,[117, 957] light-emitting diodes (LEDs)[110, 499] and photovoltaic devices.[85, 86, 125]

This chapter investigates the Zn doping of Au-seeded GaAs nanowires. Working with the precursor diethylzinc (DEZn), various morphological effects of *in situ* Zn doping are investigated and suitable growth conditions for Zn-doping are identified. The incorporation of Zn and distribution thereof is explored using both EDXS and APT, with APT in particular enabling the quantification of dopant concentrations. The

electrical activity of Zn in GaAs nanowires is then demonstrated through the optoelectronic characterization of nanowire devices. This chapter provides the foundations for the controlled Zn-doping of Au-seeded GaAs nanowires grown by MOVPE.

4.2 Methods

4.2.1 Growth and morphological characterization

The doping studies described in this chapter focus on Au-seeded GaAs nanowires grown under conditions known to promote a zincblende crystal structure and taper-free morphology. [598, 958] Briefly, semi-insulating (111)B oriented GaAs substrates (AXT) were pre-treated with poly-L-lysine (PLL) and various concentrations of 10, 30, 50, 100 and 250 nm colloidal Au solutions (Ted Pella, Inc.) as described in Section 3.1.1. The substrates were then loaded into the MOVPE reactor (Aixtron 200/4) which was operated at a pressure of 100 mbar and a flow of 15 standard litres per minute.[668] After annealing under AsH_3 at 600 °C for 10 minutes, the reactor was cooled to 450 °C for nanowire nucleation. In the case of 'single-temperature' recipes, growth was also carried out at 450 °C for a duration of 20 minutes. 'Two-temperature' recipes employed a lower growth temperature of 375 °C which was selected after a two minute nucleation period at 450 °C. To accommodate the lower growth rates at this temperature, a longer growth time of 45 minutes was employed. Unless otherwise specified the molar fractions of AsH_3 and trimethylgallium (TMGa) were 3.20×10^{-3} and 6.91×10^{-5} respectively giving a V/III ratio of 46.3. In some growths axial GaP segments were inserted as markers by exchanging AsH_3 for PH_3. Where multiple GaP markers were inserted, GaAs segments were grown for four minutes and GaP markers, 2 minutes. The same V/III ratio was maintained throughout growth. For the doping studies, DEZn was introduced in various molar fractions two minutes subsequent to nucleation. In the case of doped heterostructure growth, DEZn was introduced 30 seconds following the initiation of a GaAs segment and paused 15 seconds before GaP growth. Following the termination of growth with the cessation of TMGa and DEZn flow, AsH_3 flow was maintained until the reactor cooled to a temperature of 350 °C. Subsequent investigation by scanning electron microscopy (SEM) was performed utilizing either a Zeiss UltraPlus FESEM or FEI Helios 600 NanoLab Dualbeam (FIB/SEM) which were operated at 10 kV. SEM based EDXS analysis employed an INCA Energy 450 EDXA

system (30mm^2 Si drift detector, Oxford instruments). Characterization by transmission electron microscopy (TEM) was conducted on a Phillips CM300 TEM operating at 300 kV or a JEOL 2100F TEM operating at 200 kV or in one case an FEI Tecnai Osiris operating at 200 kV. Samples for TEM investigation were prepared by mechanical dispersion on copper grids coated by holey carbon films. TEM and STEM based EDXS analysis was conducted on the JEOL 2100F which was equipped with a JED-2300 detector (30mm^2 Si drift detector, JEOL).

4.2.2 Atom probe tomography

Atom probe tomography (APT) employed a laser-assisted local-electrode atom probe system (LEAP) (Cameca 3000X Si λ= 532 nm, repetition rate 200 kHz, pulse length 10 ps) equipped with a position-sensitive, wide field-of-view detector and a micro-electrode for ion extraction. Characterization was performed at 20 K using laser energies ranging between 10 and 100 pJ. Several approaches to sample preparation were investigated including a FIB based pick-and-place procedure before a direct, on-substrate technique was developed.[959] Low areal density samples were grown especially for APT analysis by diluting the Au colloidal solutions used to seed growth by up to 1000 times. With an inter-nanowire spacing of 5 to 10 microns these samples were dilute enough to be characterized directly on substrate, as grown. Sample alignment was achieved by pre-selecting appropriate experimental conditions such as start voltage, base temperature, detection rate and laser pulse energy and then monitoring the rate of ion hits as the stage was moved. Once a nanowire had been located the stage was adjusted so as to move the generated image into the centre of the micro-aperture. The position and energy of the laser beam was then further optimized to maximize the ion detection rate. Nanowires analysed by APT were later imaged by SEM in order to ascertain the final tip shape.

4.2.3 Electrical characterization

For electrical characterisation, nanowires were transferred onto highly doped (p^+), thermally oxidised Si substrates (SiO_2 thickness > 100 nm) by either direct mechanical dispersion or ultrasonication in isopropyl-alcohol (IPA) followed by drop casting. Electron beam lithography (EBL, Raith 150) was used to pattern the substrates. Following development, residual resist and oxides were removed by oxygen plasma and then wet (9% HCl) etching. Metallisation (Ti 10 nm / Au 300 nm) was by electron-

beam evaporation (Temescal BJD-2000 E-beam/Thermal Evaporator). Electrical characterisation employed a Keysight B2902A precision source measure unit (SMU).

4.3 Morphological effects of diethylzinc

4.3.1 GaAs nanowire growth

It is well known that certain dopant precursors have the potential to affect the structure and morphology of III-V nanowires grown by MOVPE.[246, 247, 522] Figure 5-1 reveals some morphological effects of DEZn on the growth of GaAs nanowires at 450 °C. Undoped control structures are shown in Figure 5-1(a-c) with the nominal diameter of Au nanoparticles used to seed growth increasing from 30 to 250 nm left to right. In each case the majority of the imaged nanowires are seen to grow in a single direction, vertical to the substrate. The sidewalls of these nanowires furthermore appear smooth at the resolution of the SEM images. Note that the reduction in nanowire areal density which is seen here to accompany increasing nanowire diameter is a function of the differing concentration of the colloidal solutions used to treat the wafers before growth (see Section 3.1.1).

The introduction of a minimal DEZn flow equating to a molar fraction of 4.72×10^{-7} and DEZn:TMGa of 6.83×10^{-3}, produces no obvious morphological effects in the smaller diameter nanowires with nominal diameters of 30 and 50 nm respectively [Figure 5-1(d,e)]. The largest diameter nanowires are however seen to change diameter and begin growing in random directions with the growth front breaking up to give multiple nanowires [Figure 5-1(f)]. Interestingly, despite DEZn being introduced only two minutes subsequent to nucleation, these effects appear at a significant distance from the substrate surface which is suggestive of a delayed action. With a further increase in DEZn flow to give a molar fraction of 2.05×10^{-6} and DEZn:TMGa of 2.96×10^{-2}, these morphological effects become visible for each of the nanowire diameters [Figure 5-1(g-i)]. The magnitude of these effects further scales with diameter, being greatest for the largest diameter nanowires [Figure 5-1(i)]. Starting first with the smallest diameter nanowires, sidewall banding characteristic[247, 657] of high density twinning is observed [see inset Figure 5-1(g)]. A concomitant shift in sidewall faceting to orientations which are nonparallel to the growth direction is further evident. In some cases such faceting is seen to produce significant quasi-periodic modulations in diameter (see inset). Moving to the intermediate diameter nanowires [Figure 5-1(h)], sidewall roughness is seen to

further increase suggesting an increase in planar defect density. For the largest diameter nanowires [Figure 5-1(i)], a stem is seen to grow vertically from the substrate before kinking to random and continually changing growth directions. The sidewalls of the stem section are again seen to be rough in a manner indicative of a high density of planar defects.

In addition to the morphological effects discussed, the introduction of DEZn is also seen to increase the growth rate of the GaAs nanowires. Comparing the undoped nanowires

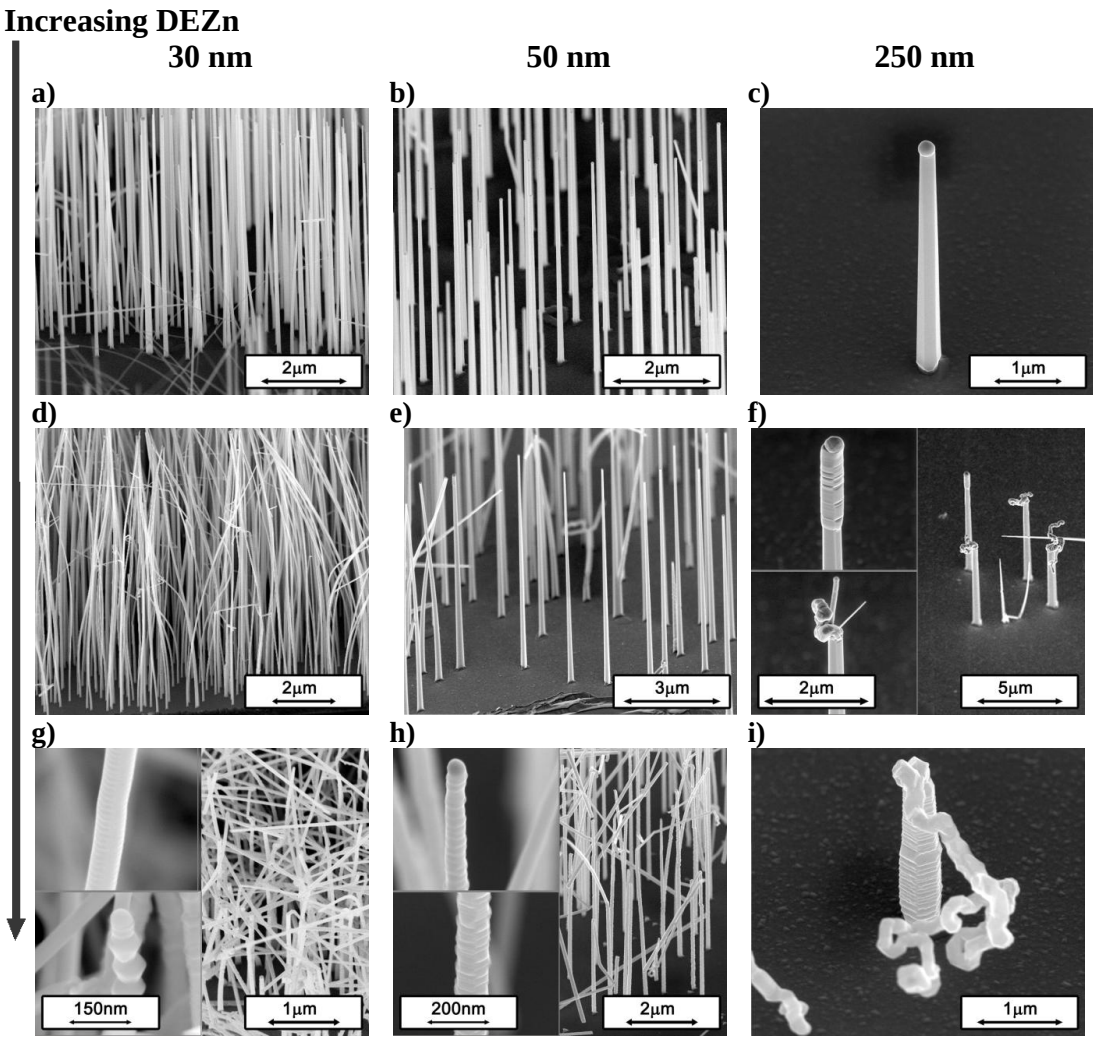

Figure 4-1 | SEM images showing the effects of increasing DEZn molar fraction on the morphology of GaAs nanowires grown at 450 °C, X_{TMGa}= 6.91 ×10^{-5} and V/III=46.3 using Au seed nanoparticles with nominal diameters of 30, 50 nm and 250 nm. (a-c) X_{DEZn}= 0; (d-f) X_{DEZn}= 4.72x10^{-7}, (DEZn/TMGa= 6.83 x10^{-3}); (g-i) X_{DEZn}= 2.05x10^{-6}, (DEZn/TMGa= 2.96 x10^{-2}). (g-h) present magnified images inset.

having a nominal 50 nm diameter [Figure 5-1(b)] to those grown with a minimal DEZn flow [Figure 4 1(d)], an increase in length of some 50 % is evident. A similar increase in length was also found for the nanowires having a nominal diameter of 30 nm, but this increase is somewhat obscured in Figure 5-1(d) due to self-attraction induced bunching[960-964]. Doping was also found to increase the length and therefore growth rate of the largest diameter nanowires but this increase is also obscured in Figure 4 1(f,i) due, in this case, to kinking.

The effects of DEZn doping on the structure of GaAs nanowires are illustrated in Figure 4-2 where a bright field TEM image of an undoped nanowire is contrasted with that of a doped nanowire. Both images are taken along the <110> zone axis. The undoped nanowire here further corresponds to the growth run presented in Figure 5-1(b) and the doped nanowire, Figure 5-1(h). Considering first the undoped nanowire, the only planar defects observed are seen to be located directly below the Au seed and may be related to transients following the termination of group III flow.[598, 657] The imaged profile of the nanowire presents vertical sidewalls. In contrast to Figure 4-2(a), the doped nanowire of Figure 4-2(b) exhibits an extremely high density of planar defects. From the imaged

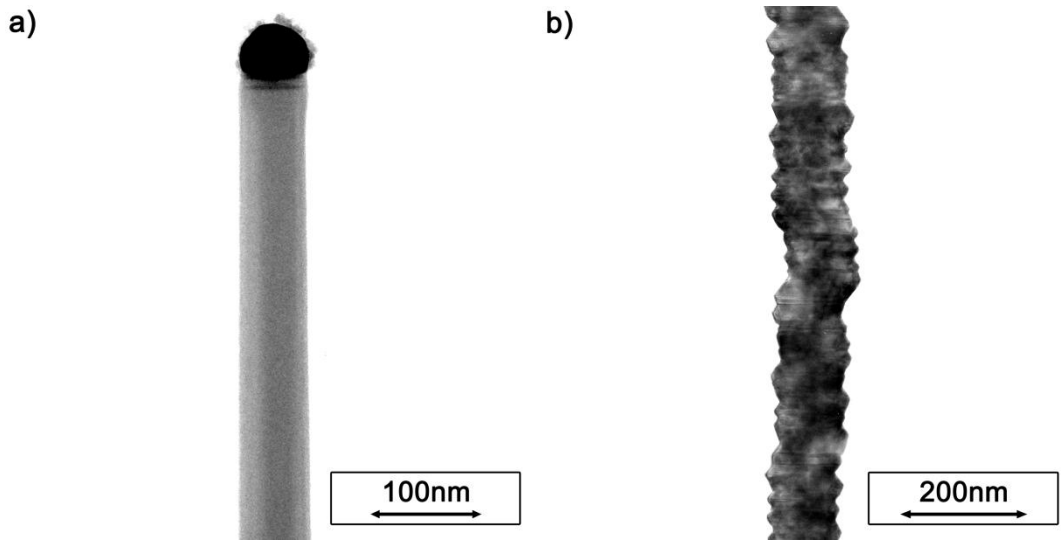

Figure 4-2 | Bright field TEM images showing an increase in planar defect density and changes in sidewall faceting with the introduction of DEZn during GaAs nanowire growth at 450 °C, X_{TMGa}=6.91 ×10^{-5} and V/III=46.3 using Au seed nanoparticles with a nominal diameter of 50 nm. a) X_{DEZn}= 0, b) X_{DEZn}= 2.05 ×10^{-6} (DEZn/TMGa= 2.96 x10^{-2}). Both images were taken on the <110> zone axis.

profile a variety of facet orientations can be identified, many of which being nonparallel to the growth direction. In the same manner that the positioning of planar defects appears random, the sidewall faceting of this nanowire also appears random such that the growth axis of the nanowire does not form a vertical axis from the bottom to the top of the micrograph.

Similar morphological effects of DEZn on the growth of Au-seeded GaAs nanowires have previously been reported in the literature. Growing at a temperature of 400 °C with a V/III ratio of 2.5, Regolin *et al.*[237] reported kinking for II/III ratios of greater than 0.004 and a breaking up of the growth front or 'seed splitting' for II/III ratios of 0.08. In later work at a growth temperature of 470 °C, Haggren *et al.*[540] found kinking for II/V ratios greater than 0.16. DEZn was also found to increase both the density of planar defects and nanowire growth rate. For growth by aerotaxy, Yang et al.[539] also reported DEZn to increase the planar defect density but no kinking was observed for that study's maximum II/III ratio of 0.034. Previous authors have linked these effects to changes in the phase and supersaturation of the Au seed particle.[540] In the case of InP growth where similar effects of DEZn have also been noted, Algra *et al.*[35] hypothesised that the introduction of zinc leads to reordering at the Au-nanowire interface. Wallentin *et al.*[243] have further shown a systematic increase in contact angle with increased zinc flow. Such changes in the contact angle of the seed particle are expected to affect the phase purity and sidewall orientation of the nanowire.[243, 598, 659, 965] Finally, Otnes et al.[572] have speculated that the additional ethyl radicals introduced by DEZn doping may enhance TEGa decomposition leading to increased growth rates and lower effective V/III ratios.

4.3.2 GaAs/GaP heterostructure nanowire growth

The use of marker segments as a means of *ex situ* nanowire growth analysis has been investigated by several authors.[200, 623, 667, 966-968] In the current study, GaP segments were employed as markers in GaAs nanowires during the initial semi-qualitative assessment of the zinc doping parameter space. By delineating different segments of growth, these markers enabled several different doping conditions to be trialled during a single growth run. Group V exchange was chosen here as group III elements are known to accumulate in the Au seed reducing interface abruptness.[185, 969-971] Figure 4-3(a) shows a SEM micrograph of a GaAs nanowire containing eight GaP marker segments. The GaP marker segments can be easily identified due to both a reduction in the nanowire diameter and increased sidewall roughness. Variation in diameter here can be related to

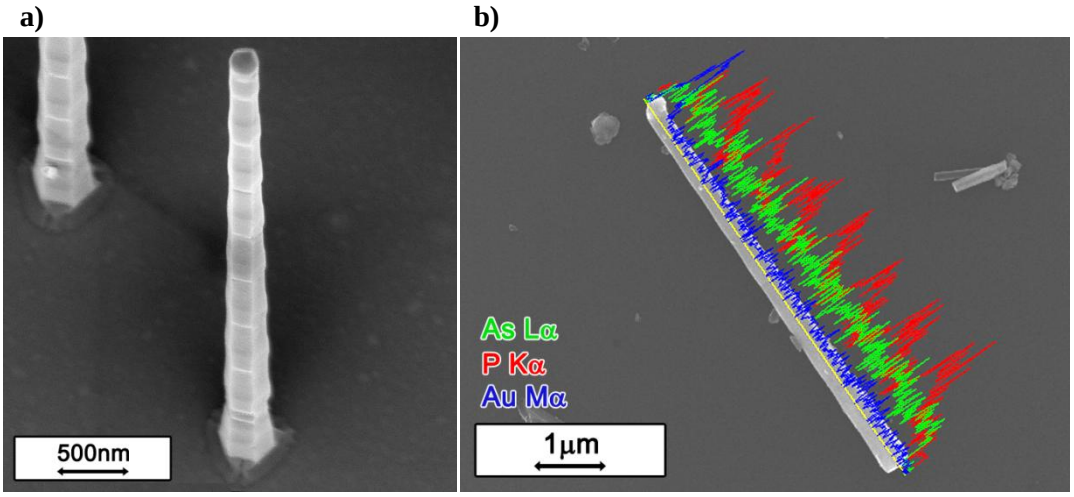

Figure 4-3 | SEM images of GaAs/GaP heterostructure nanowires. a) Nanowire morphology as grown. b) Nanowire transferred to a Si substrate with EDXS line-scan overlaid. P counts are shown in red, As in green and Au in blue.

changes in both the composition and contact angle of the seed particle[972-974] which also affect phase purity and the resulting sidewall faceting of the nanowire. [243, 591, 598, 659, 965] Previous studies of GaAs/GaP heterostructures grown by MOVPE have reported significantly higher planar defect densities in GaP segments.[975, 976] The identity of the various segments may also be identified by EDXS. A SEM EDXS linescan of a nanowire from the same growth is presented in Figure 4-3(b) where the P composition of the nanowire is seen to vary along its length. Interestingly the transition from GaP to GaAs appears more abrupt than the reverse. A similar finding has been made by previous authors who related this difference to the higher vapour pressure of P relative to As.[976-978]

The nature of the interface between GaAs and GaP was further studied by TEM. Figure 4-4 shows a STEM high angle annular dark field (HAADF) image and corresponding EDXS elemental maps of an interface corresponding to a transition from GaP to GaAs (the nanowire growth direction is towards the top of the page). Considering first the HAADF image [Figure 4-4(a)], a relatively abrupt transition in diameter is visible but there is insufficient Z-contrast visible in order to identify the accompanying compositional transition. This transition is however clearly visible from the As and P elemental maps [Figure 4-4(c,d)].

In addition to compositional variation in the axial direction, compositional variation is also visible in the radial direction, particularly to the top right hand side of the maps. Variation here corresponds to material deposited through radial shell growth which will have alternated between GaAs and GaP in the same manner as axial growth. The presence of this radial overgrowth is further responsible for the relatively strong As and P background signals in regions corresponding to GaP and GaAs axial growth respectively. It is interesting to note that shell growth may be identified here by considering the EDXS map of the C distribution [Figure 4-4(e)]. As C is immiscible in Au[548, 979] and low temperature MOVPE growth is known to favour C incorporation,[980-982] material deposited through shell growth is widely expected to contain a significantly higher C concentration relative to axial VLS growth.[518, 983, 984] The C signal to the top left of the map not corresponding to the nanowire originates with the holey carbon support film. In addition to the maps of the As and P distributions, a linescan was also conducted as presented in Figure 4-4(f). Considering the P Kα signal, the transition region is seen to appear exponential and to cover a length of some 60 nm.

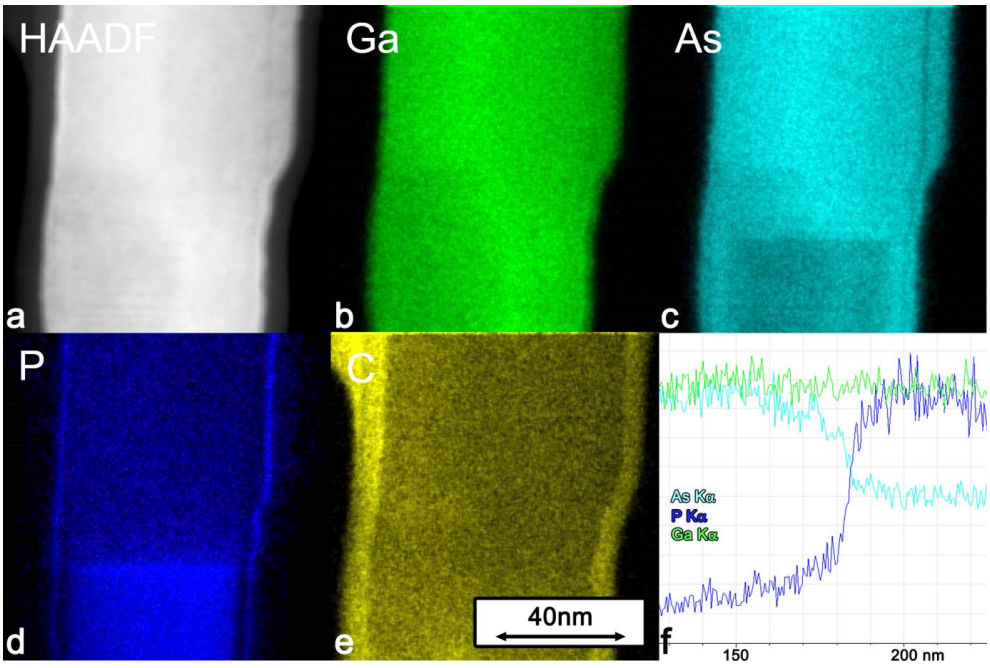

Figure 4-4 | STEM EDXS maps showing the GaP to GaAs interface (growth direction bottom to top) in a GaAs/GaP heterostructure nanowire. a) HAADF stem image; b) Ga map; c) As map; d) P map; e) C map; f) corresponding EDXS linescan for As, P and Ga. Maps were collected with a 50 μsec dwell time and 1 nA beam current on a FEI Technai Osiris STEM.

A further benefit of the GaP marker segments was a dramatic reduction in tapering and commensurate increase in the axial growth rate at relatively high growth temperatures. Figure 4-5 contrasts a GaAs nanowire [Figure 4-5(a)] grown at 550 °C with a GaAs/GaP heterostructure nanowire [Figure 4 5(b)] grown under the same conditions. While the GaAs nanowire is pyramidal in shape, the GaAs/GaP nanowire retains a high aspect ratio. Interestingly, the upper portion of the GaAs nanowire is hexagonal and not triangular in cross section as is usually observed for ZB GaAs nanowire overgrowth.[985, 986] Given that the radial growth rate here is inconsistent with a WZ crystal structure,[264, 600, 618, 987] the observed morphology suggests that for large taper angles total energy considerations favour a hexagonal rather than triangular ZB cross-section. Unlike the GaAs nanowire, the GaAs/GaP heterostructure does not present a constant taper angle but displays abrupt variations in diameter located at regular intervals along the nanowire (see inset). These abrupt variations in diameter can be linked with the location of the GaP marker segments. It is likely that lattice mismatch between the GaAs and GaP segments[988, 989] significantly altered the kinetics of adatom diffusion and shell growth[990, 991] leading to an increased axial growth rate and the rough sidewall morphology observed.

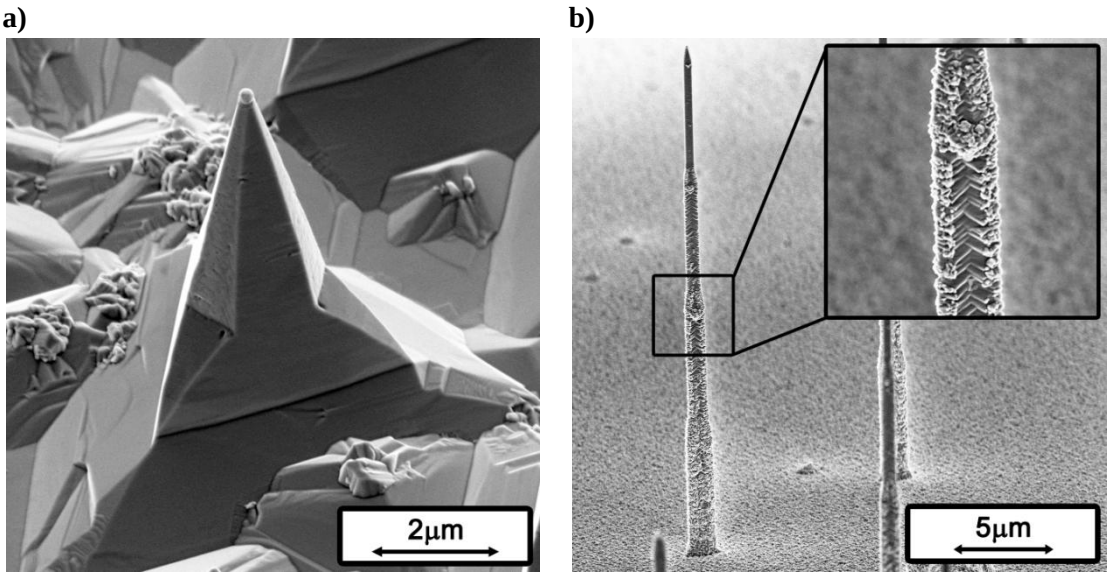

Figure 4-5 | SEM images showing the reduction in overgrowth with the introduction of GaP marker segments to GaAs nanowires grown at 550 °C, X_{TMGa}= 2.59 ×10^{-4} and V/III=46.3 using Au seed nanoparticles with a nominal diameter of 250 nm. a) GaAs nanowire b) GaAs/GaP heterostructure nanowire with magnified image inset.

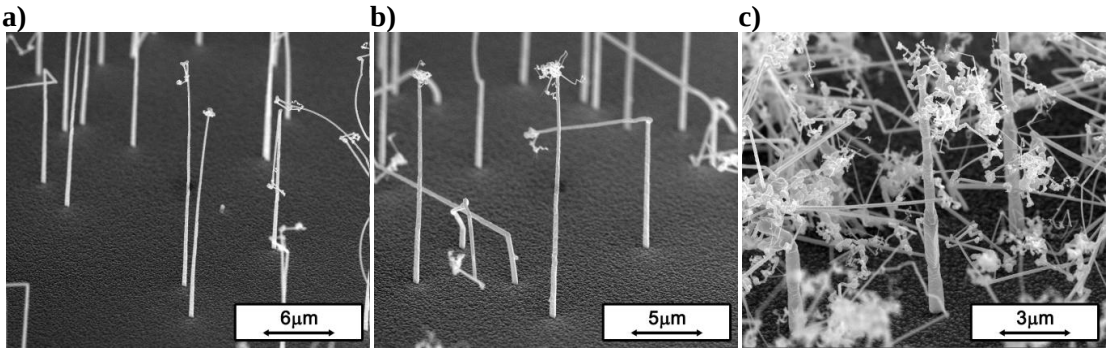

Figure 4-6 | SEM images of GaAs x9 /GaP x8 heterostructure nanowires grown at 450 °C, TMGa= 6.91×10^{-5} and V/III=46.3 using Au seed nanoparticles with nominal diameters of a) 30 nm, b) 50 nm and (c) 250 nm. X_{DEZn} was increased for each GaAs segment from 0 through 5.19×10^{-7}, 6.65×10^{-7}, 1.02×10^{-6}, 2.41×10^{-6}, 3.88×10^{-6}, 5.28×10^{-6}, 6.61×10^{-6}, 8.05×10^{-6}.

Use of GaAs/GaP heterostructures as a means to efficiently assess the DEZn doping parameter space is shown in Figure 4-6. The nanowires here are seen to be predominantly vertical before the growth fails due to kinking and eventually seed splitting. The recipe for this growth contained eight GaP marker segments with the DEZn molar fraction being increased with each subsequent GaAs segment. By counting the number of marker segments visible before growth fails due to kinking or seed-splitting, a semi-quantitative measure of the DEZn threshold is obtained. As was observed for the GaAs nanowires in Figure 5-1, this threshold appears inversely related to nanowire diameter. Variation further suggests a stochastic nature to kinking and seed-splitting.

The DEZn/TMGa (II/III) threshold for seed-splitting in GaAs/GaP heterostructure nanowires is plotted as a function of nanowire diameter in Figure 4-7(a). Dopant flow is expressed in terms of the II/III ratio here for the sake of consistency with previous publications. Values for growth at 450 °C are shown in black and at 500 °C in red. Error bars represent the total range of values observed. In the case of the smallest diameter nanowires at 500 °C, the maximum II/III ratio investigated did not produce seed-splitting in all nanowires and the upper limit is shown as an arrow. Considering seed-splitting first as function of temperature, the threshold II/III ratio is seen to increase with increasing temperature. Given the significantly higher vapour pressure of Zn relative to

Ga, this behaviour can, in the first instance, be related to a reduction in the effective II/III ratio with increasing temperature. Similar reasoning applies to the observed relationship between seed-splitting and nanowire diameter. Both surface diffusion and the Gibbs-Thomson effect become more significant with decreasing nanowire diameter[992, 993] and both may be expected to reduce the effective II/III ratio. In the case of surface diffusion, the characteristic diffusion length of Zn is shorter than that of Ga due to the relatively higher vapour pressure of Zn.[994] The relatively higher vapour pressure of Zn further leads to a greater absolute increase in partial pressure due to the Gibb-Thomson effect.

While nanowires of differing nominal diameters were generally grown on separate substrates of differing areal density, Figure 4-7(b) demonstrates that these differences in areal density were not entirely responsible for the observed diameter dependence of seed-splitting. Seen in Figure 4-7(b) are several larger diameter nanowires showing

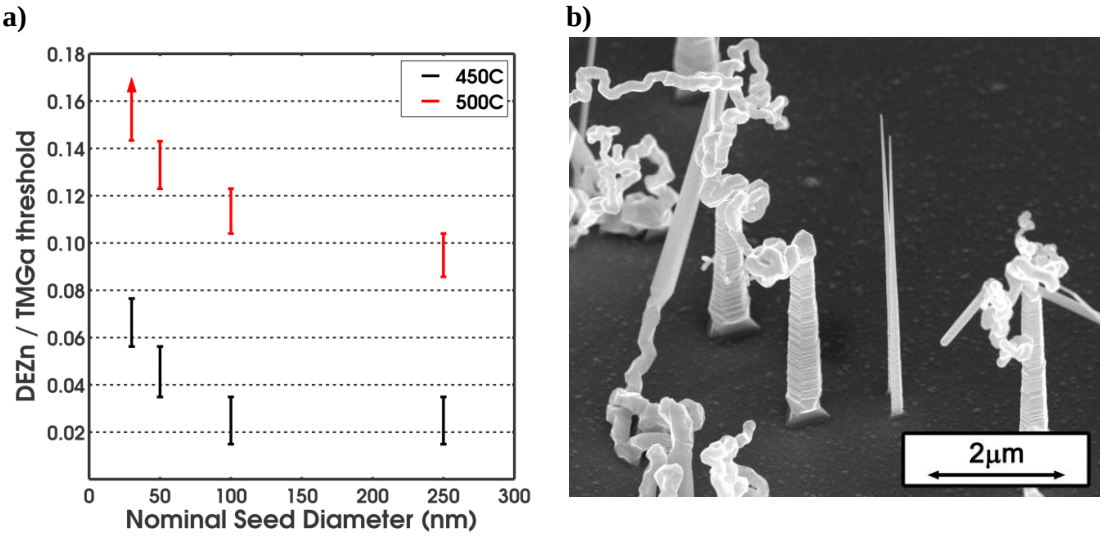

Figure 4-7 | DEZn/TMGa threshold for seed-splitting in GaAs/GaP heterostructure nanowires; TMGa= 6.91×10^{-5} and V/III=46.3. a) Plot showing the DEZn/TMGa ratio at which seed-splitting occurred for GaAs/GaP heterostructure nanowires of various nominal diameters at growth temperatures of 450 and 500 °C. Error bars show variance across a single substrate. In the case of the smallest diameter nanowires at 500 °C, the maximum DEZn/TMGa was insufficient to generate seed-splitting in all nanowires and the upper limit is shown as an arrow. Note the threshold for seed-splitting is increased for smaller diameter nanowires and higher temperatures. b) SEM image illustrating the higher kinking threshold of smaller diameter nanowires.

seed-splitting at a given distance above the substrate. Also visible are two nanowires of smaller diameter that do not display seed-splitting. Thus, while the threshold II/III ratio for seed-splitting has evidently been reached for in the case of the larger diameter nanowires, the smaller diameter nanowires require a higher DEZn flow for seed-splitting. Interestingly, the quantitative results obtained here for GaAs/GaP heterostructures are similar to those reported by other authors for GaAs nanowires. Growing nanowires with a nominal diameter of 100 nm and greater at a temperature of 400 °C and V/III ratio of 2.5, Regolin *et al.*[237] reported the onset of kinking and seed-splitting for II/III ratios greater than 0.004. At a growth temperature of 470 °C, Haggren *et al.*[540] reported the 'continuous kinking' of 50 nm GaAs nanowires at a DEZn/TMGa ratio of 0.16.

4.4 Incorporation

4.4.1 Energy Dispersive X-Ray Spectroscopy

The incorporation of dopant species into nanowires grown by the VLS process often differs from planar growth processes in terms of both distribution and concentration.[220, 237, 246, 269, 455] In the current work, EDXS studies were initially undertaken on Zn-doped GaAs nanowires in order to verify the successful incorporation of Zn. Figure 4-8(a) shows a bright field TEM image of a cross-section taken from near the base of a heavily Zn-doped GaAs nanowire as prepared by ultramicrotomy. The growth direction of this nanowire and the orientation of the cross-section are further confirmed as <111> by the SAED pattern shown in Figure 4-8(b). The successful incorporation of Zn into this nanowire is demonstrated by the EDXS spectra shown in Figure 4-8(c). (For EDXS all nanowire cross-sections were tilted to be slightly off-axis.) While a Zn signal is not detected from near to the centre of the cross-section, a peak corresponding to the Zn K_α line is clearly observed in the spectrum taken from closer to the edge of the cross-section. Radial variation in dopant concentration has been previously reported for a variety of nanowire systems.[220, 231, 413] In the current case, the size of the cross-section relative to the 50 nm nominal diameter of the seeding particles and its truncated triangular shape point to significant radial overgrowth. It is likely that greater Zn incorporation occurred for radial rather than axial growth.[985, 986]

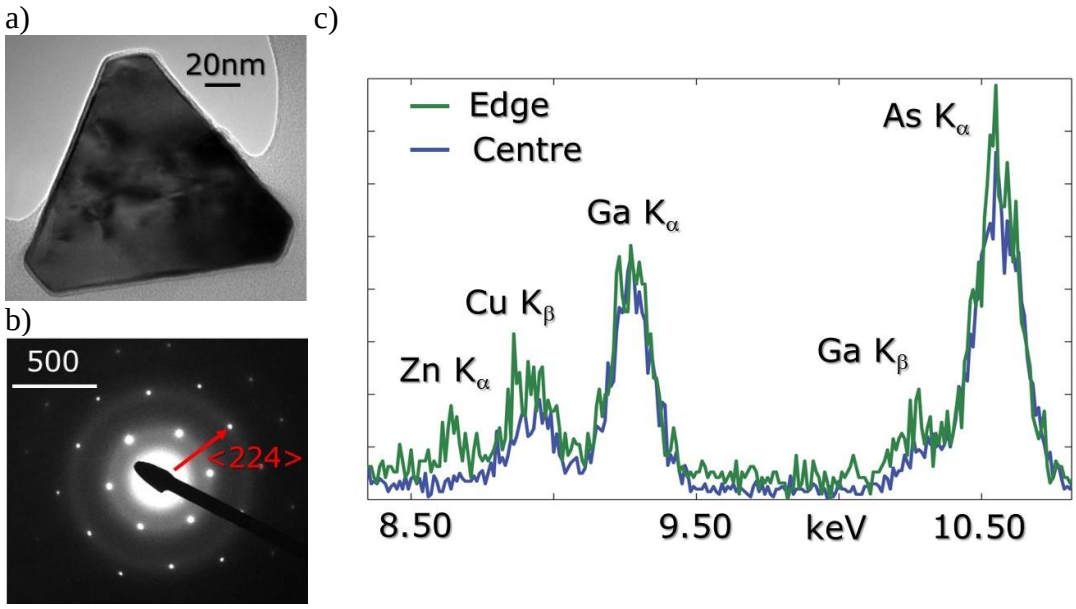

Figure 4-8 | TEM analysis of a cross-section taken from a Zn-doped GaAs nanowire prepared by ultramicrotomy. a) Bright field TEM image of the cross-section. b) SAED pattern of (a) confirming a ⟨111⟩ axis orientation and {112} type faceting. (c) EDXS spectra taken from points close to the centre and edge of the cross-section respectively. Note that the zinc signal is significantly greater near to the edge of the cross-section.

The Zn dopant distribution was further investigated by STEM EDXS mapping. Figure 4-9(a-c) shows a bright field TEM image of a Zn-doped GaAs nanowire cross-section along with a corresponding SAED pattern and bright field STEM image. Contrast variation in the bright field images reflects sample non-uniformity produced by the ultramicrotomy sectioning process. A STEM EDXS map of the Zn distribution is also presented in (d). The Zn distribution shown is normalized by the Ga distribution in order to mitigate the effects of sample non-uniformity. As was observed for the TEM EDXS spectra presented in Figure 4-8, the Zn concentration is seen to be lower at the centre of the nanowire cross-section relative to the edge. Located at the centre of the cross-section is a circular region of low Zn concentration which corresponds to the core of nanowire as deposited by axial VLS growth. Axial VLS growth has generally been reported to contain a lower dopant concentration than radial VS growth.[220, 950, 995, 996] While the central region corresponding to VLS growth appears essentially homogenous,[218] the surrounding shell region exhibits symmetrical variation consistent

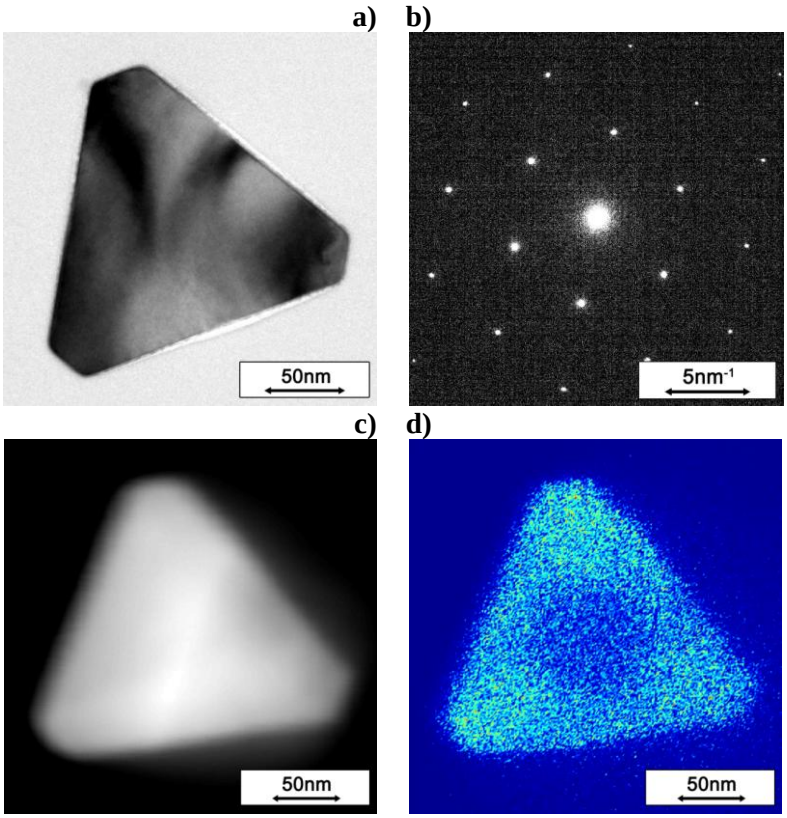

Figure 4-9 | STEM analysis of a cross-section taken from a Zn-doped GaAs nanowire prepared by ultramicrotomy. a) Bright field TEM image of the cross-section. b) SAED pattern of (a) confirming a ⟨111⟩ axis orientation and {112} type faceting. (c) Bright field STEM image of the cross-section. Note that there is a slight rotation between the TEM and STEM images. (d) STEM EDXS mapping of Zn normalized by Ga counts. Light blue indicates the presence of a Zn related signal.

with polarity-driven growth. Material at the vertices of the truncated triangular cross-section is seen to contain a higher Zn concentration relative to that half-way along the longer facets. From previous studies of GaAs nanowire growth these shorter and longer facets can be identified <112>A and <112>B respectively.[985, 986] Interestingly, a similar pattern has been reported for the incorporation of In into GaAs sidewall growth.[997] In that case it was argued that a greater strain energy was associated with impurity incorporation at B-polar versus A-polar group III sites.

4.4.2 Atom Probe Tomography

The use of APT to quantify and map dopant species in semiconductor nanowires has now been reported by several authors.[220, 998-1000] Figure 4-10 presents a mass spectrum

from the APT analysis of a Zn-doped GaAs nanowire. This mass spectrum here represents a dataset of over 150 million ions and was collected over a length of 2.5 μm. The most prominent peaks belong to ^{69}Ga and ^{71}Ga and appear in a ratio of 59.4 : 40.6; close to what may be expected from the natural abundance of these isotopes (60.1 : 39.9). No intermediate peak is observed between these two isotopes indicating that the formation of molecular Ga ions was insignificant. Unlike Ga, a series of peaks corresponding to molecular As ions are observed (As_3^{2+}, As_2^{+}, As_5^{2+}, As_3^{+}). Arsenic is also seen to form molecular ions with other species such as O and Zn. Having only one naturally occurring isotope, the presence of molecular As ions precludes the unambiguous counting of As and the determination of the Ga : As stoichiometry. As such, the possibility of significant As loss[998] cannot be discounted.

Immediately to the left of Ga, four singly charged isotopes of Zn are noted (^{64}Zn, ^{66}Zn, ^{67}Zn and ^{68}Zn). Like Ga, intermediate peaks are not observed and the isotopes appear in a ratio, 57.0 : 27.3 : 1.0 : 14.8, close to what is expected from natural abundance

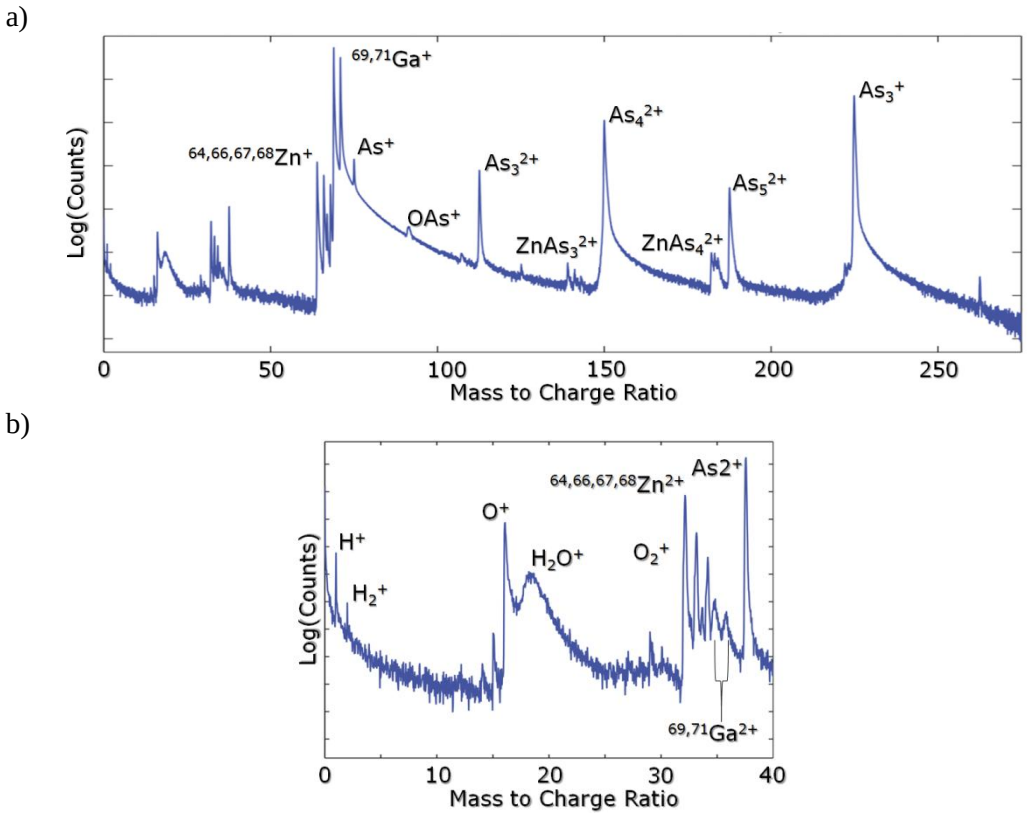

Figure 4-10 | APT mass spectrum for a Zn-doped GaAs nanowire. Peaks are marked by species and ionisation. a) Full data range; b) Magnification of the low mass to charge region of the spectrum.

(49.2 : 27.7 : 4.0 : 18.5). The fifth naturally occurring Zn isotope, ^{70}Zn, is not observed due to both its low abundance (0.6%) and the dominance of the nearby ^{69}Ga and ^{71}Ga peaks.

Examining the magnified section of the mass spectrum shown in Figure 4-10(b) it is interesting to note that C appears to be absent. While C was observed by EDXS in Figure 4-4(e) for a GaAs/GaP nanowire grown under similar conditions, the APT analysis here was only of the tip region and may have therefore included insufficient shell growth to generate a C signal. A significant O signal is however observed which may be associated with the native oxide of GaAs. H_2O likely represents the reaction of hydrogen and O ions rather than adsorbed water. Hydrogen signals here are from the background high vacuum atmosphere. Interestingly, doubly ionized Zn is more abundant than doubly ionized Ga, a fact which suggests a relatively low effective evaporation field of 20 to 25 V / nm.[1001] Dividing the total Zn counts by the total Ga counts and assuming the volume concentration of Ga to be 2.21 x10^{22} /cm^3, gives a zinc

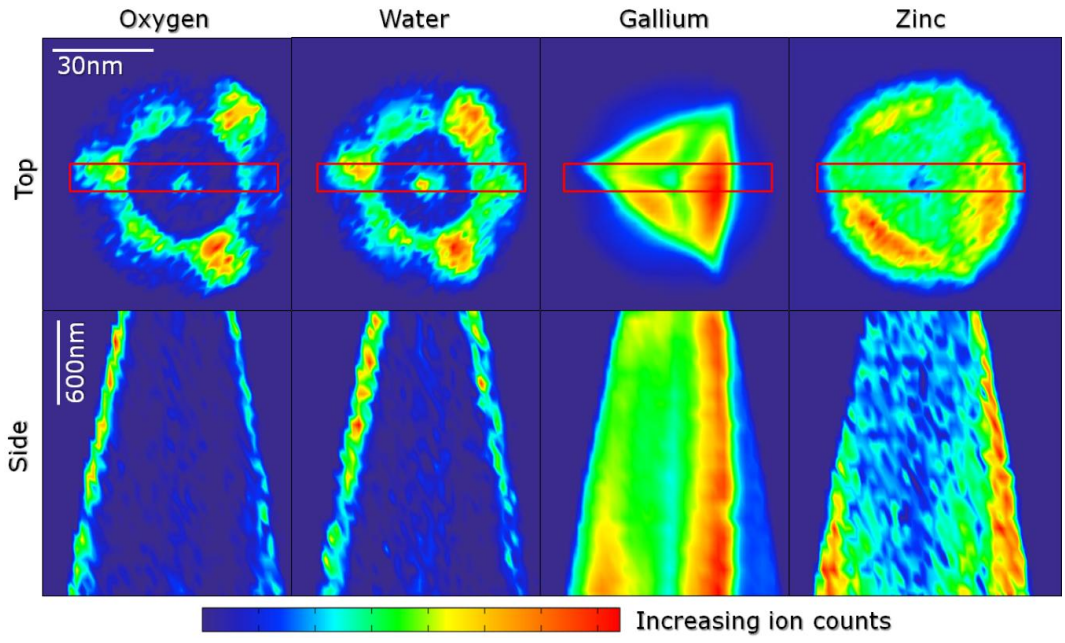

Figure 4-11 | Spatial distribution of ion counts corresponding to the mass spectrum shown in Figure 4-10. Top row shows the cumulative distribution of ions looking along the nanowire growth axis. Bottom row shows the cumulative distribution of ions looking in a direction perpendicular to the growth axis as integrated across the area specified by the red boxes in the top row. Note that the vertical axis is compressed for the images presented in the bottom row.

concentration of 1.9 x10^{20} /cm^3 for the entire volume analysed.

Figure 4-11 presents the reconstructed distribution of several different species. The presence of zone lines and other crystallographic features here is an indicator of the quality of the dataset and lends additional confidence to the calculated image compression factor (ICF).[959, 1000] In the case of the current experiments, the close proximity of substrate surface to the local aperture produced a relatively high ICF enabling the entire cross-section of the nanowire to be analysed.[959] In this way the distribution of Ga counts is seen as a truncated-triangular cross-section as was observed by TEM in Section 4.4.1 and not the circular cross-section of the local aperture. A further indicator of full tip imaging is the presence and distribution of oxygen and water corresponding to the native oxide. Both species are seen as rings in top view and inclined lines in side view which approximately outline the nanowire cross-section as defined by the Ga distribution. Interestingly, strong three fold symmetry is observed for both species in top view which can likely be related to surface migration of these species to crystallographic poles. From the morphology of the Ga distribution, migration to {112}A appears strongest. Oxygen and water counts located at the centre

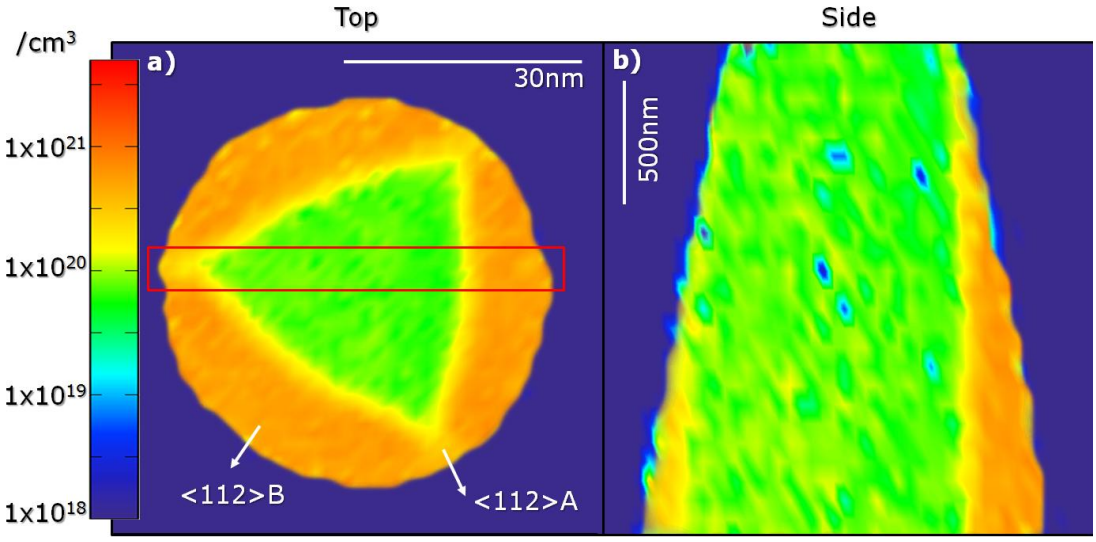

Figure 4-12 | Spatial distribution of Zn counts normalised by the spatial distribution of Ga counts to give a count per cubic centimetre. Result corresponds to the data shown in Figure 4-10 and Figure 4-11. a) Cumulative distribution of Zn looking along the nanowire growth axis. B) Cumulative distribution of Zn looking in a direction perpendicular to the nanowire growth axis as integrated across the area specified by the red box in (a).

of the cross section can similarly be related to surface migration. In the case of Zn, a significant proportion of the counts appear outside the main body of the nanowire as defined by the Ga distribution. The cause of this potentially unphysical reconstruction is likely an artefact of full tip imaging[959] but points to greater Zn incorporation in the nanowire sidewalls.

The Zn distribution found by APT is further explored in Figure 4-12 where volumetric concentration has again been calculated by taking a Ga atomic density of 2.21 $x10^{22}$ /cm^3. Two distinct regions are apparent from both top and side view; a lower concentration core and a higher concentration shell. The difference in Zn concentration between these two regions is roughly an order of magnitude being 6.64 $x10^{19}$ Zn atoms/cm^3 in the core and 5.51 $x10^{20}$ Zn atoms/cm^3 in the shell. In side profile the diameter of the core region appears relatively constant while that of the shell region increases giving apparent taper. Interestingly, the Zn concentration in both the core and shell regions appears constant along the length of the analysed volume which is a testament to the stability of both the VLS growth conditions and the APT evaporation conditions. From top view the cross section of the core region appears triangular while the shell appears circular as apparently limited by the local electrode aperture. This is in contrast to the Zn distribution observed by EDXS in Section 4.4.1 where a circular core was observed inside a triangular shell. Considering that the triangular core region seen by APT corresponds to the region of higher Ga distribution observed in Figure 4-11 it is likely that the Zn distribution observed in Figure 4-12represents an artefact of full-tip imaging with the trajectory of atoms evaporating from the nanowire sidewalls being aberrated.[959] While the spatial distribution of Zn observed in Figure 4-12 is thus likely erroneous it provides a further indication that Zn incorporation is higher at the nanowire sidewalls. There is further no reason to doubt the Zn concentration of 1.9 $x10^{20}$ /cm^3 found for the entire volume analysed. Coupled with the electrical measurements which will be presented in the next section this value enables an estimate of dopant activity.

4.5 Electrical Characterization

4.5.1 IV measurements

In order to confirm that the Zn observed by EDXS and APT was electrically active, a range of GaAs nanowire devices were fabricated and characterised. The contacting of

nanomaterials presents a variety of challenges arising from factors such as non-planar geometries, carrier depletion and the dominance of surface states.[1002, 1003] In the current study, the treatment of nanowire surfaces prior to metallisation was found to be a critical factor in achieving ohmic contact. Figure 4-13 compares the IV characteristic of a nanowire which was not cleaned before metallisation with another from a nanowire which was cleaned by oxygen plasma and wet (HCl) etching. Whereas the IV characteristic of the cleaned nanowire presents linear behaviour, that of the nanowire which was not cleaned is highly non-linear and demonstrates a significantly higher resistance. In the case of GaAs, native oxide films are well known to form under ambient conditions and to affect electrical contacting.[1004-1006] GaAs surfaces are furthermore characterised by a high density of trap states which may act to produce significant carrier depletion and Schottky behaviour in nanowire devices.[1003, 1007-1010]

Figure 4-14 compares the IV characteristic of an undoped GaAs nanowire with several results collected from Zn-doped samples. Strong evidence for the efficacy of Zn-doping is provided by the significantly increased conductance of the doped nanowires relative to the undoped nanowire. Considering firstly the undoped nanowire (nanowire 1, Figure 4-14), a maximum current of only several tens of picoamps is observed. Maximum

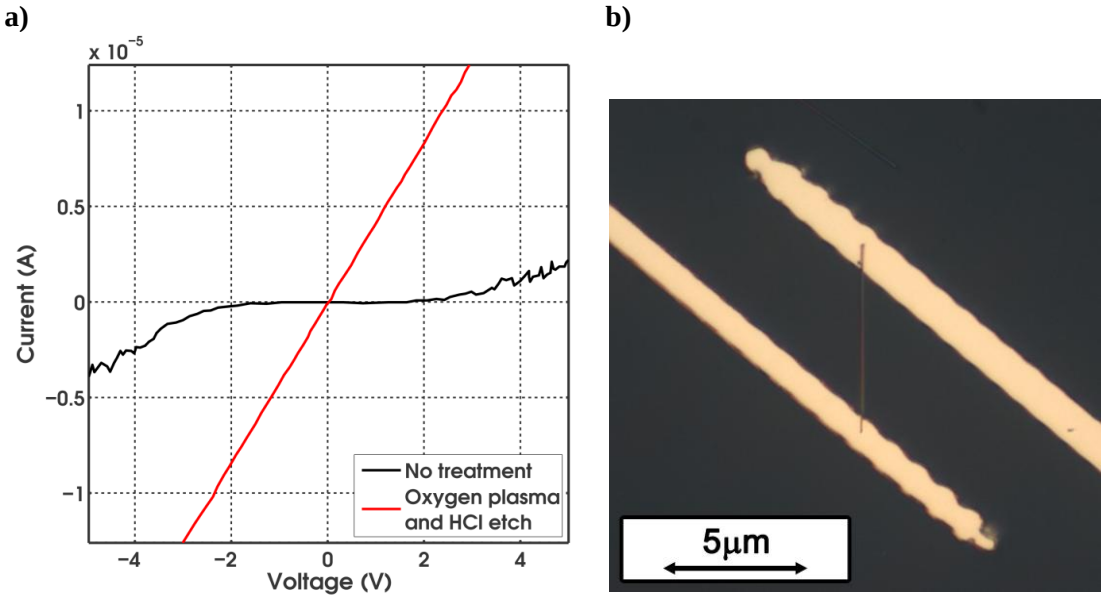

Figure 4-13 | Effect of pre-metallisation cleaning processes on contact performance. a) Room-temperature IV curves contrasting the response of a device fabricated without pre-metallisation cleaning and another which received oxygen plasma and wet etching treatments. b) Optical image of a contacted GaAs nanowire device.

current then increases with both DEZn molar fraction and nanowire diameter although the nature of the increase with DEZn molar fraction is somewhat unexpected.[258, 269]

With the initial introduction of DEZn, the maximum current achieved by nanowire 2 is seen to be 3 orders of magnitude greater than that of nanowire 1. A similar increase is again observed moving to nanowire 3 while the increase moving to nanowire 4 is only around 3 times. This is despite the difference in DEZn molar fraction between nanowires 3 and 4 being significantly greater than that between nanowires 2 and 3. It is likely that the large initial increases in conductance observed here relate to the action of doping in reducing or eliminating carrier depletion.[957, 1007, 1011-1013] With the elimination of carrier depletion conductance then returns to an approximately linear function of DEZn molar fraction as observed for nanowires 3 and 4. The resistivity of the nanowires may be approximated, in the first instance, by neglecting contact resistance and approximating the nanowires as uniform conical conductors. Starting with the undoped nanowire the values found for the devices here are: 1.0 $x10^{4}$, 30.7, 1.9 $x10^{-2}$, 4.8 $x10^{-3}$ and 1.9 $x10^{-2}$ Ωcm. In the case of the doped nanowires these values can further be used to approximate active dopant concentrations.[1014] Beginning with nanowire 2,

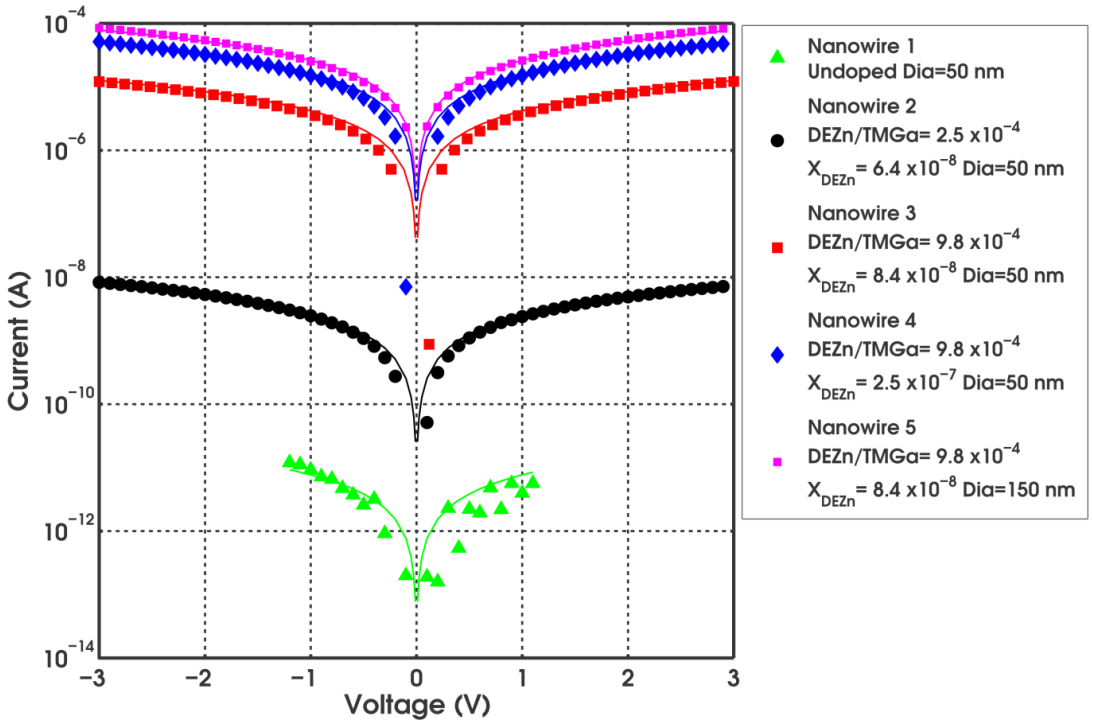

Figure 4-14 | Room-temperature IV curves of selected GaAs nanowires. Data points represent experimentally measured values; lines are linear fits to the data.

the resistivities calculated correspond to p-type doping with the following concentrations: 6.0 x10^{14}, 2.1 x10^{18}, 2.0 x10^{19}, 2.1 x10^{18} /cm^3. It is interesting to note here that despite being different diameters, nanowires 3 and 5, which were grown under the same conditions, give the same dopant density. The value found for nanowire 2 is however somewhat surprising. Despite being grown using a DEZn molar fraction that was only 1.3 times less than that employed for nanowire 3 the carrier concentration found for nanowire 2 is almost 4 orders of magnitude less than that found for nanowire 3. This large difference is consistent with complete carrier depletion as described earlier. Additional doping acted to reduce depletion enabling a channel for conduction through the nanowire. Despite the relatively high dopant concentrations found for nanowires 3, 4 and 5, these values are still an order of magnitude less than that found by APT in Section 4.4.2. While a component of this difference can be related to carrier depletion by surface trapping,[957, 1007, 1011-1013] it is likely that the low areal densities used for APT growth favoured increased Zn incorporation.

4.5.2 Wavelength dependant photocurrent measurements

In addition to the electrical characterisation discussed above, optoelectronic characterisation was also carried out in the form of wavelength-dependant photocurrent measurements. Figure 4-15 compares the low-temperature wavelength-dependant photoresponse of an undoped GaAs nanowire with that of a Zn-doped GaAs nanowire (V_{SD}= 1 V). A clear difference is again observed in the conductance of the two samples with the current carried by the Zn-doped nanowire being an order of magnitude greater than that carried by the undoped nanowire. Interestingly an increasing photocurrent is noted for both samples at photon energies below the bandgap. This behaviour can be related to the combination of both the Franz−Keldysh effect[1015-1017] and the optical excitation of surface states. As was discussed above, GaAs is known to be characterised by a high density of surface states that pin the Fermi-level mid-gap leading to carrier depletion in nanostructures. In the case of p-type GaAs, surface band-bending can be expected to separate optically generated excitons leading to both a photo-gating effect and additional carriers.[957, 1017] By this mechanism, photons with below band-gap energy may generate photocurrent. Despite this background, the position of band-edge is clearly apparent in the case of the undoped nanowire at the expected energy of 1.515 eV. A band-edge is not however apparent in the spectrum of the Zn-doped

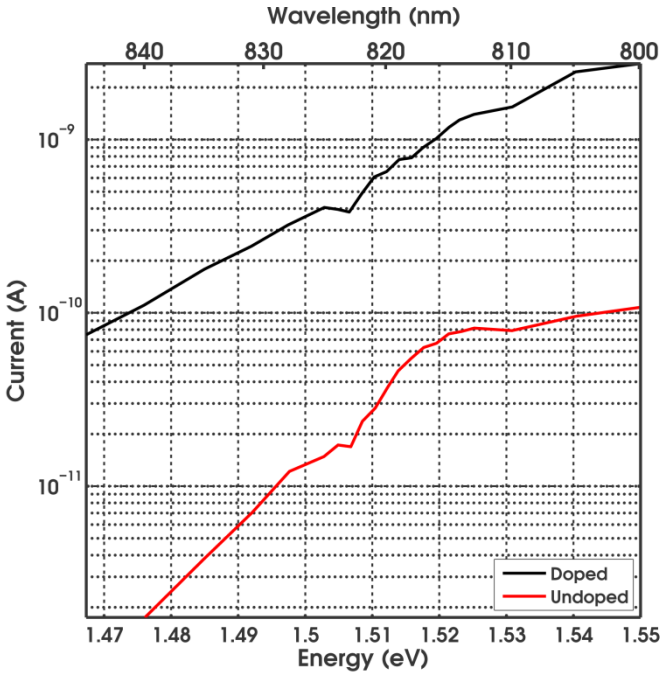

Figure 4-15 | Wavelength dependant photocurrent response of undoped and Zn-doped GaAs nanowires (X_{DEZn}= 8.6 x10^{-8}, DEZn/TMGa=9.8 x10^{-4}) at 10 K (V_{SD}= 1 V).

nanowire with photocurrent seen to increase at a relatively continuous rate across the spectrum. Recalling the high Zn concentrations found both electrically in Section 4.5.1 and analytically in Section 4.4.2, this behaviour can be related to band-narrowing and tailing as expected for p-type GaAs.[1018, 1019]

4.6 Summary

Realising the controlled impurity doping of semiconductor nanostructures remains a challenging proposition. The current chapter has explored some of these challenges as they relate to the *in situ* Zn-doping of Au-seeded GaAs nanowires. The effects of Zn doping on Au-seeded GaAs nanowire growth were firstly examined across a broad parameter space, with high molar fractions of the Zn precursor DEZn being observed to disrupt VLS growth. Effects such as kinking and seed-splitting were found to be more prominent for lower growth temperatures and larger nanowire diameters. Incorporation was then studied with STEM based EDXS mapping revealing the Zn distribution to be inhomogeneous. A higher Zn concentration was found for shell growth relative to axial VLS growth with a further preference for incorporation at the {112}A relative to the {112}B facets. The particular challenge of quantifying Zn incorporation was tackled by

APT analysis which found an overall Zn concentration of 1.9 x10^{20} /cm^3 for the volume analysed. The Zn distribution determined by APT did not however match that seen by EDXS and it is likely that further work is required in properly reconstructing the nanowire geometry. Despite some difficulties in forming Ohmic contact, the electrical activity of Zn in GaAs was confirmed through electrical and optoelectronic measurements. The results of this chapter demonstrate the successful Zn doping of GaAs nanowires and lay the groundwork for achieving a controlled dopant profile. The demonstration of radial inhomogeneity is of particular significance for future device design.

5

Zinc as a morphological agent: Twin-plane superlattices in GaAs nanowires

5.1 Introduction

The control of crystal structure has emerged as a particular focus of III-V semiconductor nanowire research.[598, 657] Unlike bulk material synthesis, the III-V nanowire growth mechanism enables controllable switching between the zincblende and wurtzite crystal structures to give unique polytypic structures. Offering particular novelty is the periodic arrangement of twin planes to give a twin-plane superlattice (TSL). These structures have now been reported for a variety of III-V nanowire systems including InAs,[366, 616, 679-681] InP,[35, 515, 600] GaP[24] and horizontally growing GaAs[542] with similar reports for other semiconductor materials including Zn_3P_2,[336, 680] ZnTe,[1020] ZnSe,[1021-1023] ZnS,[1024] $ZnSnO_4$,[1025], ZnO[1026] and SiC.[1027] Beyond potential for fundamental insight into the growth process,[24] periodic twinning has been predicted to introduce electronic miniband structure, which may be useful for bandgap engineering, as well as direct intersubband optical transitions.[682-687] A reduction in thermal conductivity which has been both modeled[609, 688-690] and demonstrated[610] holds further interest for thermoelectric application while increased mechanical strength has been reported for twinned metallic nanowires[691, 692]

The element zinc is a well known to promote the formation of TSL nanowire structures.[24, 35, 246, 271, 515, 542] In their pioneering work on TSL formation in InP nanowires, Algra *et al.*[35] discussed several possible actions of zinc. Taking both the results of modelling and the observation that zinc addition did not affect nanowire diameter, the authors suggested the most significant role of zinc was in reordering the Au-nanowire interface. Working again with InP nanowires, Wallentin *et al.*[243] have contrastingly reported a systematic increase in contact angle with increased zinc flow, explaining the discrepancy between works with reference to differing reactor cooling rates. Assuming a constant solid vapour surface energy, zinc addition was related to an increase in the ratio between the liquid solid and liquid vapour surface energies.

This chapter investigates the growth of vertically freestanding GaAs twinning superlattice structures as enabled by zinc. Nanowire morphology is reported for a range of diameters and a correlation between diameter and superlattice period is identified. Qualitative difference between the relationship found in this chapter and that reported previously for GaP and InP is explained with reference to expected differences in chemical potential and relevant surface energies.

5.2 Methods

5.2.1 Growth and morphological characterization

Nanowires were grown *via* horizontal flow metalorganic vapour phase epitaxy (MOVPE) utilizing an Aixtron 200/4 reactor operating at a pressure of 100 mbar and a flow of 15 standard litres per minute.[668] A growth temperature of 575 °C was used in conjunction with AsH_3 and trimethylgallium (TMGa) molar fractions of 1.43×10^{-5} and 1.04×10^{-5} respectively to give a V/III ratio of approximately 1.4. Growth time was 60 minutes including a two minute nucleation window before the introduction of diethylzinc (DEZn) at a molar fraction of $1.4\text{x}10^{-4}$ to generate the TSL structure. Following termination of TMGa and DEZn flows, AsH_3 flow was maintained until the reactor reached a temperature of 350 °C. Growth was conducted on semi-insulating GaAs(111)B substrates which had been individually treated with various concentrations of 10, 30, 50, 100 and 250 nm colloidal Au solutions (Ted Pella, Inc.). Dilution of the colloidal Au solutions was achieved using deionised water. Subsequent investigation of the nanowires by scanning electron microscopy (SEM) and transmission electron microscopy (TEM) was performed utilizing a FEI Helios 600 NanoLab Dualbeam (FIB/SEM) operated at 10 kV and a Phillips CM300 TEM operated at 300 kV respectively. Samples for TEM investigation were prepared by mechanical dispersion on copper grids coated with holey carbon films.

The error on nanowire diameter measurements was conservatively estimated at ±10% for diameters of less than 150 nm and ±5% for diameters greater than this. Systematic error is expected in SEM calibration but assuming good astigmatism correction, error should cancel in the ratio of superlattice period to diameter.

5.3 Growth and morphology

5.3.1 Effect of diethylzinc flow

In chapter 4, a high DEZn molar fraction was observed to disrupt GaAs nanowires growth across the conventional low temperature, moderate V/III ratio zincblende regime. Figure 5-1 now explores the effects of increasing DEZn molar fraction on GaAs nanowires grown in the conventional high temperature, low V/III wurtzite regime. Starting with conditions producing a pure wurtzite structure in nanowires seeded using Au nanoparticles with nominal diameters of 30, 50 and 250 nm (left to right), the DEZn molar fraction (X_{DEZn}) is increased top to bottom through 8.2×10^{-5} to 1.1×10^{-4} and finally 1.4×10^{-4}. Despite the relatively small difference between these values, clear trends are observed from the SEM images of the GaAs nanowires grown under each of these molar fractions. Starting with the nanowires seeded by Au nanoparticles of 30 nm nominal diameter [Figure 5-1(a,d,g,j)], an immediate increase in diameter is observed upon the addition of DEZn [Figure 5-1(d)]. Further increase in the DEZn molar fraction is seen to lead to aperiodic and then periodic sidewall modulations [Figure 5-1(g,j)].

A similar pattern is observed for the nanowires seeded by Au nanoparticles of 50 nm nominal diameter [Figure 5-1(b,e,h,k)], excepting that the addition of zinc produces aperiodic sidewall modulations towards the base of the nanowire and periodic modulations towards the tip [Figure 5-1(e)]. With increasing DEZn molar fraction the lengths of these respective segments alter such that segment at the base of the nanowire showing aperiodic modulation reduces in length while that at the tip increases. At the highest DEZn molar fraction, periodic sidewall modulation is observed along the length of the nanowire [Figure 5-1(k].

For nanowires seeded by Au nanoparticles with a nominal diameter of 250 nm [Figure 5-1(c,f,i,l)], DEZn addition is again observed to generate nanowires with aperiodic sidewall modulations towards the base and periodic modulations towards the tip. In this case however, the sidewall modulations become periodic along the length of the entire nanowire at only the second highest DEZn molar fraction [Figure 5-1(i)].

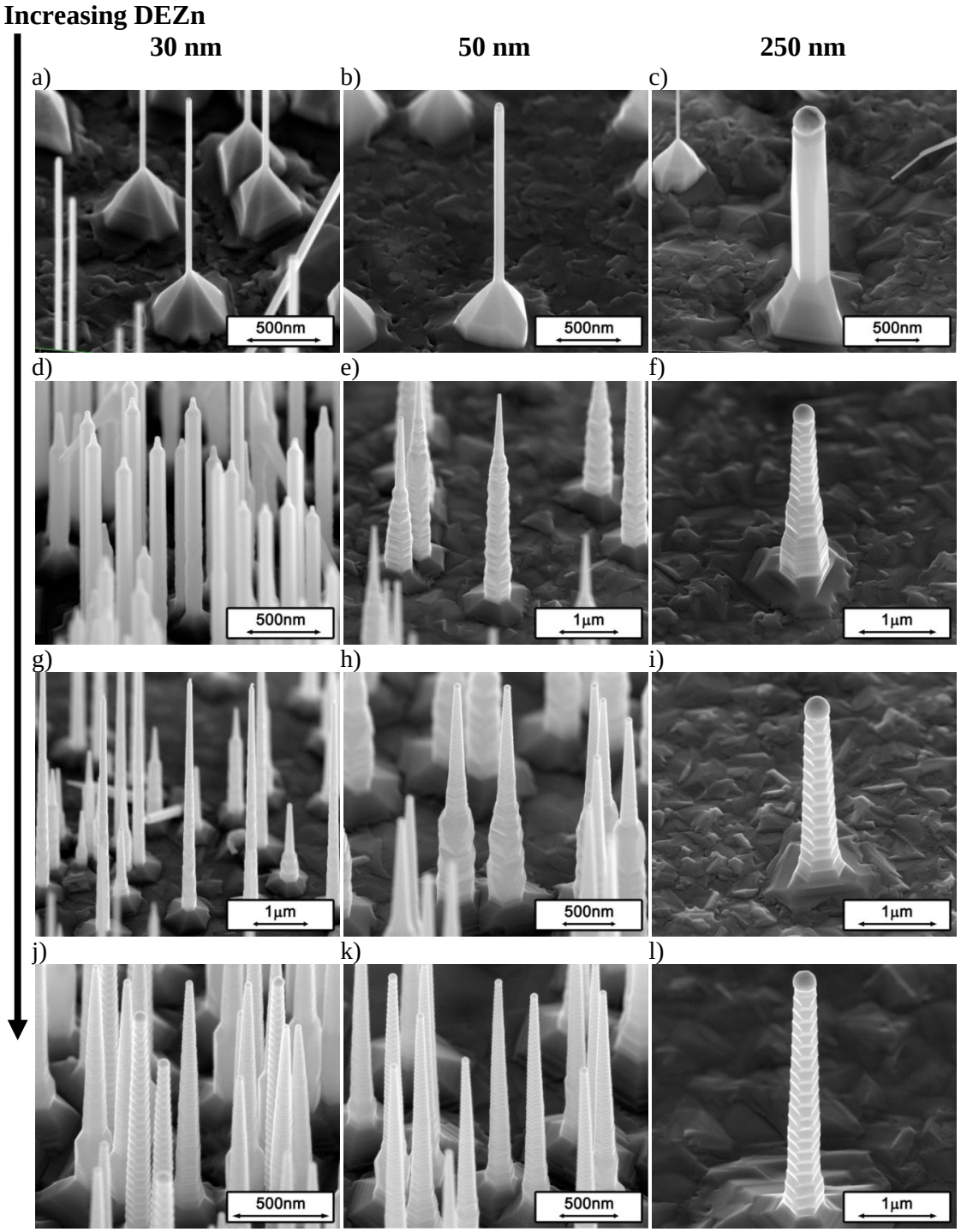

Figure 5-1 | SEM images showing the effects of increasing DEZn molar fraction on the morphology of GaAs nanowires grown at 575 °C, X_{TMGa}= 1.04×10^{-5} and V/III=1.4 using Au seed nanoparticles with nominal diameters of 30, 50 nm and 250 nm. (a-c) X_{DEZn}= 0; (d-f) X_{DEZn}= $8.2\text{x}10^{-5}$; (g-i) X_{DEZn}= $1.1\text{x}10^{-4}$; (j-l) X_{DEZn}= $1.4\text{x}10^{-4}$.

The structural changes responsible for these morphological trends may be understood by considering Figure 5-2 which presents TEM images of nanowires grown under increasing DEZn molar fractions. In the case of the undoped nanowire [Figure 5-2 (a)], a wurtzite structure is observed as is expected for the high temperature, low V/III growth conditions. The sidewall of this undoped nanowire is parallel to the growth direction and may be indexed to the $\{\bar{1}\bar{1}10\}$ plane.[598] With the addition of DEZn flow a variety of planar defects are introduced to give a mixed phase structure [Figure 5-2 (b)]. The sidewalls here are no longer vertical but represent a mixture of {001} and {111}, {111}A and {111}B, or {113} and {111} sidewalls to give the aperiodic modulations observed from the SEM images in Figure 5-1.[598, 985, 1028] Finally, at the highest DEZn molar fraction an almost pure zincblende structure is observed [Figure 5-2 (c)]. The sidewalls here are again not parallel to the growth direction and periodically spaced planar defects in the zincblende structure produce the periodic modulations of the sidewall observed in Figure 5-1.

Having observed the transformation in crystal structure accompanying zinc doping in Figure 5-2, the morphological trends observed in Figure 5-1 can now be better understood. Zinc doping is firstly seen to promote zincblende formation in a progressive manner such that a mixed phase structure results for an intermediate DEZn molar fraction [Figure 5-1(e,f,g,h)] while at high zinc concentrations an almost pure zincblende structure is produced [Figure 5-1(i,j,k,l)]. Interestingly, the transition from

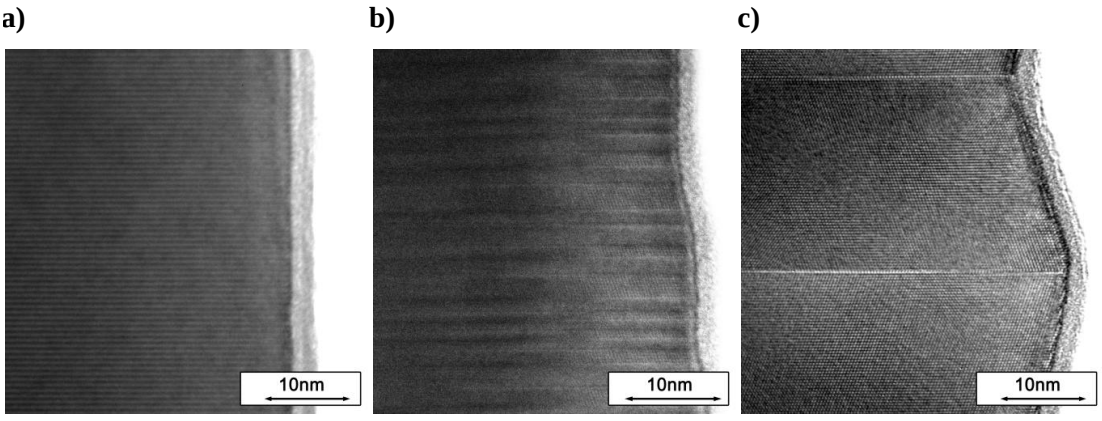

Figure 5-2 | TEM images showing the effects of increasing DEZn molar fraction on the crystal structure of GaAs nanowires grown at 575 °C, $X_{TMGa}=1.04\times10^{-5}$ and V/III=1.4 using Au seed nanoparticles with a nominal diameter of 50 nm. a) $X_{DEZn}= 0$; b) $X_{DEZn}= 8.2x10^{-5}$; c) $X_{DEZn}= 1.4x10^{-4}$.

aperiodic to periodic sidewall modulations occurs closer to the substrate with increasing DEZn molar fraction [Figure 5-1(e,f,h,i)]. One explanation for this behaviour may be variations in reactant supply with nanowire height.[992, 1029-1031] Growth rate has been shown to be non-linear for nanowires shorter than a characteristic diffusion length[992, 1029, 1031, 1032] and it may be hypothesised that conditions closer to the substrate favour the zincblende phase. The transition from aperiodic to periodic sidewall modulations seen in Figure 5-1(e) is however at least two microns above the substrate, a length greater than what would be expected for such a substrate effect. A second possibility could then be a gradual accumulation of zinc in the seed particle during growth. Previously observed transients occurring during nanowire growth have however reached steady state in relatively short periods of time.[185, 667, 1033] The transformation to zincblende is furthermore observed to be diameter dependant with the smaller diameter nanowires requiring a higher DEZn molar fraction for transformation. This observation is best evident for the lowest DEZn molar fraction shown ($8.2x10^{-5}$), where the smallest diameter nanowires [Figure 5-1(d)] are seen to remain as wurtzite while the largest are mixed phase towards the base and zincblende towards their tips. A transition to zincblende with increasing nanowire diameter has been previously reported by several authors.[616, 669, 671, 679, 1034, 1035]

5.3.2 Role of areal density

Further examining Figure 5-1, the areal density of nanowires is seen to be lower for the larger diameter growths [compare Figure 5-1(a) with Figure 5-1(c)]. This trend is a direct result of differences in the concentrations of the colloidal solutions used to seed growth. In order to better understand the effects of areal density on nanowire morphology, Figure 5-3 presents SEM images of nanowires seeded by different concentrations of 30 nm diameter colloidal Au nanoparticles. Beginning with growth under the same conditions and at the same areal density as was employed for the nanowires shown in Figure 5-1(j), periodical modulated sidewalls are noted [Figure 5-3(a)]. Dilution of the colloidal seeding solution by 25 times produces a commensurate reduction in areal density and a significant increase in nanowire length [Figure 5-3(b)]. The sidewalls of these nanowires grown at lower areal density present aperiodic modulations along the majority of their length. A further 10 times dilution leads to a further increase in nanowire length [Figure 5-3(c)]. Aperiodic sidewall modulations are observed along almost the entire length of this nanowire grown at the

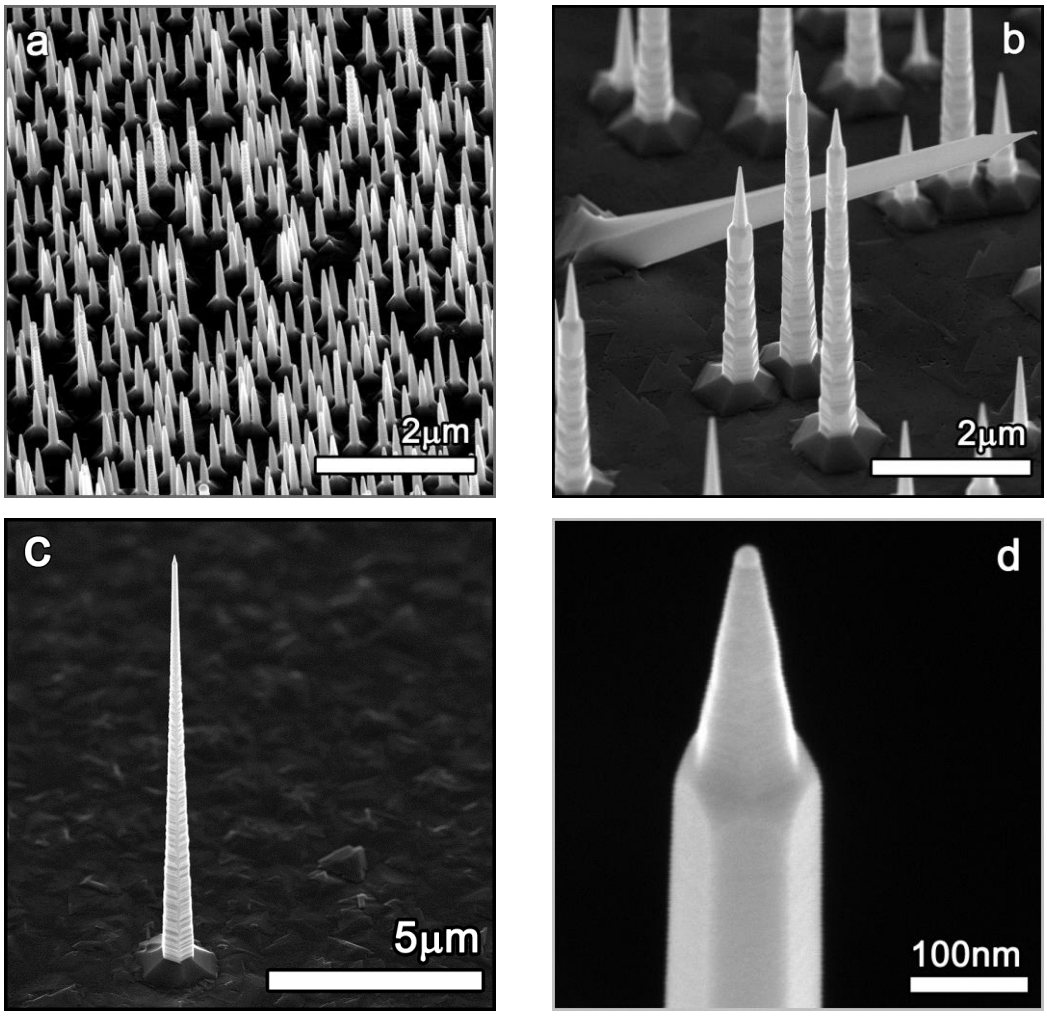

Figure 5-3 | Effects of areal density on the structure and morphology of GaAs nanowires grown using Au seeds with a nominal diameter of 30 nm. a) Growth seeded by a colloidal solution of the standard molar concentration; b) growth seeded by a colloidal solution diluted 25 times from standard; c) growth seeded by a colloidal solution diluted 250 times from standard; d) magnified image of the tip of the nanowire shown in (c).

lowest areal density except for the tip which shows a tapered morphology [Figure 5-3(d)]. It is thus clear that a reduced areal density acts here to increase growth rate and favours a mixed-phase structure.

Where the separation of nanowires is less than the twice the characteristic diffusion length, a reduction in areal density can be expected to increase material supply through surface diffusion.[994, 1036, 1037] An increase in material supply is observed here from the increased length of the nanowires grown at lower areal densities. As the vapour pressure

of both arsenic and zinc is significantly greater than that of gallium, the decrease in areal density will also act to decrease both the effective V/III and II/III ratios while increasing group III supersaturation.[44, 48, 53, 60, 994, 1038]

While a reduction in V/III ratio was recently shown to favour the zincblende phase under a group V limited growth regime, such a regime is characterised by a large seed particle and is not consistent with observed increase in nanowire length at lower areal densities.[621] In the more usual case of group III limited growth the opposite behaviour is expected with a decreasing V/III ratio instead favouring wurtzite.[598, 619, 621] A reduction in II/III ratio also likely favours wurtzite as, in Figure 5-1, an increase in DEZn molar fraction was observed to favour zincblende. An increased supersaturation is also generally thought to promote wurtzite, [591, 593, 598, 679] although several authors have

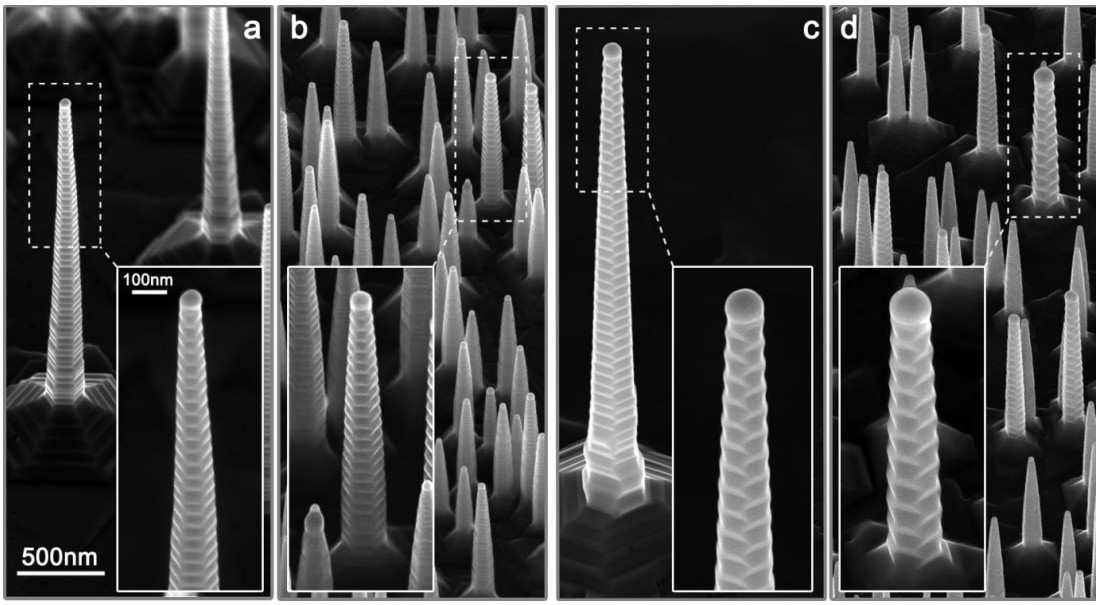

Figure 5-4 | General nanowire morphology showing variation with both nanowire diameter and density: Each SEM image and corresponding inset show the same magnification where the sample substrate is tilted 45° relative to the incident electron beam; (a) Areal density of 0.21 nanowires /μm^2 where inset magnifies an approximately 50 nm diameter nanowire; (b) Areal density of 7.2 nanowires /μm^2 where inset magnifies an approximately 50 nm diameter nanowire; (c) Areal density of 0.09 nanowires /μm^2 where inset magnifies an approximately 100 nm diameter nanowire; (d) Areal density of 7.2 nanowires /μm^2 where inset magnifies an approximately 100 nm diameter nanowire.

reported the opposite trend.[621, 669, 984]

Figure 5-4 presents SEM images of nanowires with periodically modulated sidewalls which were grown at differing areal densities in the same MOVPE growth run. Lower areal densities [Figure 5-4(a)-(c)] are shown to the left of higher [Figure 5-4(b)-(d)], with the insets in the first two panels comparing nanowires that were both seeded by Au particles of approximately 50 nm in diameter [Figure 5-4(a)-(b)] and those in the second two comparing nanowires seeded by Au particles of approximately 100 nm in diameter [Figure 5-4(c)-(d)]. Of immediate note is that period of oscillation appears unaffected by areal density with the low density samples to the left (Figure 5-4(a)-(c)) closely resembling the higher density samples to the right (Figure 5-4(a)-(c)) despite a factor of approximately four difference in total length and therefore growth rate. The spacing between twins is however clearly dependant on diameter with the 100 nm diameter nanowires exhibiting a significantly longer period relative to the 50 nm diameter nanowires.

5.3.3 Structure and growth mechanism

The origin of the observed periodic sawtooth-like sidewall modulations is further explored in Figure 5-5. Figure 5-5(a) presents a ⟨110⟩ zone axis bright field TEM image of a typical GaAs nanowire showing distinct and periodic variations in contrast. Considering the corresponding selected area diffraction pattern [Figure 5-5(b)], this structure can be identified as zincblende with rotational twinning along the ⟨110⟩ growth direction.[598, 1039, 1040] Each contrast level here corresponds to one of the two distinct twin orientations. Taking the known polarity of the substrate[1041, 1042] to index the selected area diffraction pattern [Figure 5-5(b)], enables the sidewall facets of the nanowire to be further identified as {111}-type of alternating polarity [Figure 5-5(a)]. Together these observations equate the structures here with the TSL structures reported previously for other III-V nanowire material systems and growth geometries.[24, 35, 616] An atomic model of the prototype TSL structure is further shown both in orthogonal projection along the $[1\bar{1}0]$ zone axis [Figure 5-5(c)] and in arbitrary perspective [Figure 5-5(d)] to help visualize the unique three-dimensional morphology of these nanowires. The difference in contrast between adjoining facets here illustrates the periodic alternation of sidewall polarity with rotational twinning.

Being polar and non-parallel to the growth direction, {111} oriented sidewalls define a constantly varying nanowire cross section that tends towards triangular as the sidewall of one polarity type grows in area at the expense of the adjoining facets of opposite polarity. Insertion of a rotational twin reverses facet polarity at the twin plane allowing for continuation of growth to produce the well reported truncated octahedron

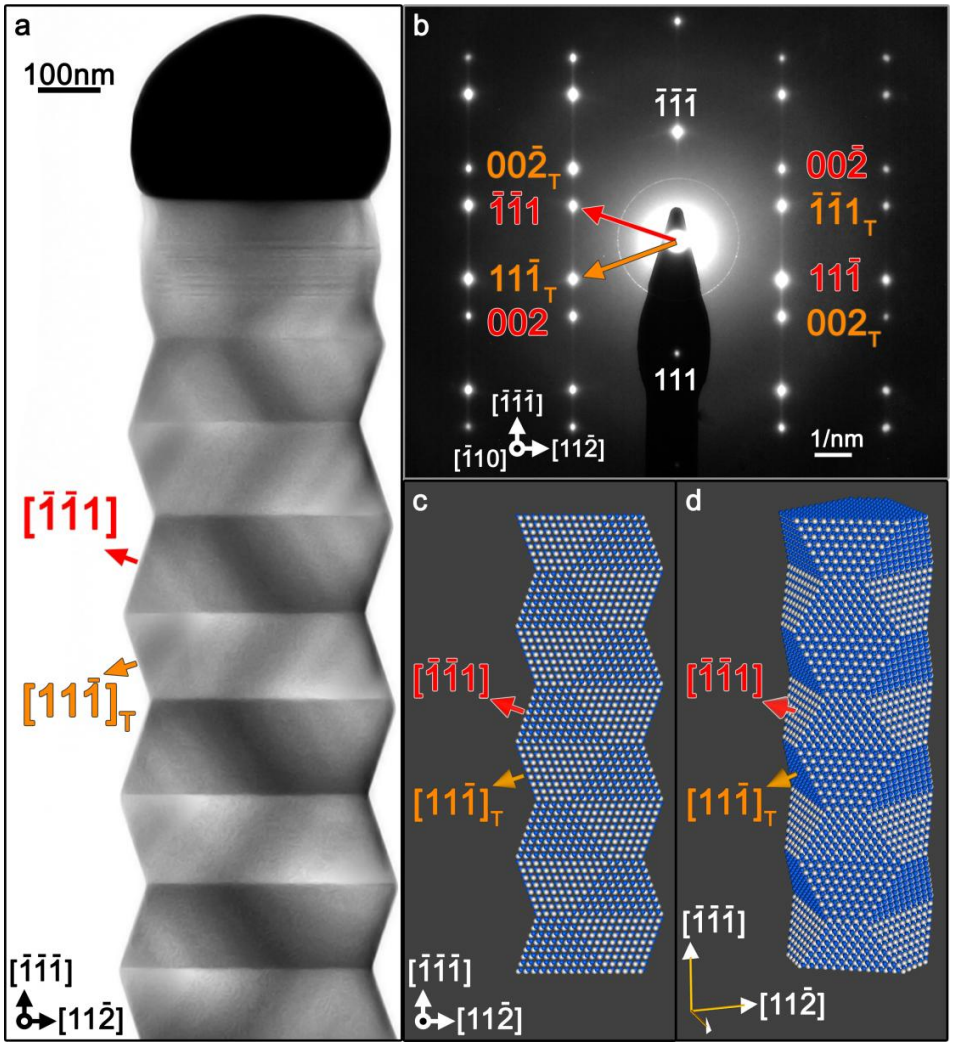

Figure 5-5 | Exploration of the twinning superlattice structure: (a) $[\bar{1}10]$ zone axis bright field TEM image with facet normals shown for two adjoining facets. The subscript T indicates that the second direction arises as a result of crystalline twinning; (b) indexed electron diffraction pattern corresponding to the image shown in (a) where the facet normals may be clearly identified as $[\bar{1}\,\bar{1}1]$ & $[11\bar{1}]_T$; (c) an orthogonal projection of the same model viewed along the $[\bar{1}10]$ zone axis; (d) an atomic model of the twinning superlattice structure in arbitrary perspective illustrating the alternating polarity of adjoining facets.

geometry.[583, 1043] Where the probability of twin formation is low such that it only occurs for a given distortion of the nanowire cross section away from its equilibrium hexagonal shape, periodic twin formation may be expected along the growth direction.[35, 616]

In all the GaAs TSL nanowires investigated by TEM, the interface between rotational twins was found to consist of a single twin plane. Figure 5-6 presents representative HRTEM images of twin planes in TSL nanowires seeded by Au nanoparticles of approximately 50 and 250 nm diameter. The only planar defects visible in both cases are twin planes which are marked in purple [variation in contrast around the twin plane visible in Figure 5-6(a) can be attributed to slight misalignment from the zone axis]. The other close packed direction on this ⟨110⟩ projection axis is ⟨112⟩ and is marked in green for one twin orientation and red for the other. The growth direction is perpendicular to the twin identified planes and was taken to be B polar.[1041, 1042] Interestingly, although the interface between twin orientations is sharp, the convex intersection between {111} sidewalls is not observed to be directly located at this interface. This apparent shift can be related to radial overgrowth and is discussed further in Section 5.3.4.

Figure 5-7 presents SEM (Figure 5-7(a-e)) and TEM (Figure 5-7(f-j)) images of GaAs TSL nanowires seeded by increasing (10, 30, 50, 100, 250 nm) diameter Au

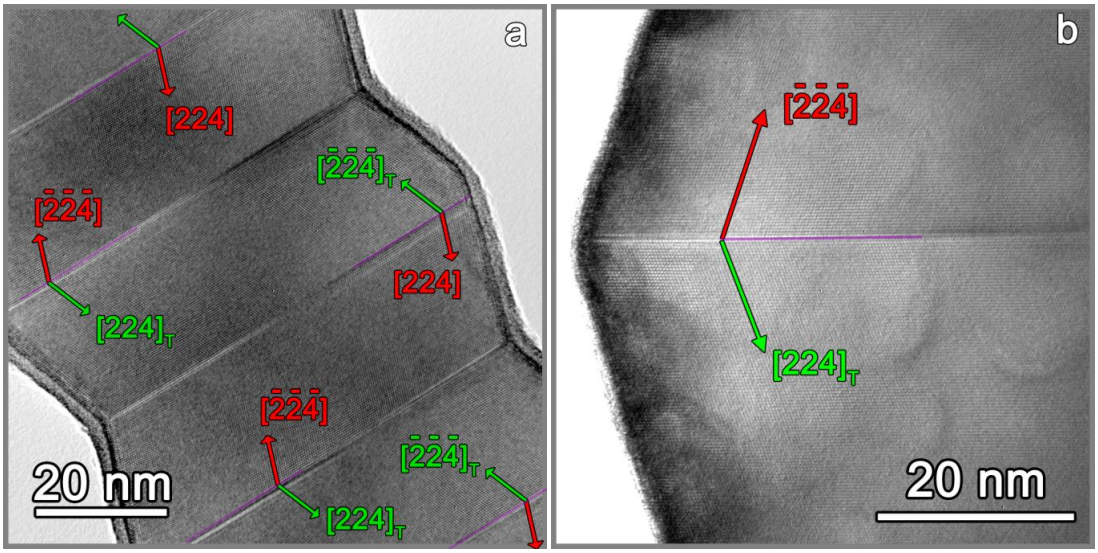

Figure 5-6 | ⟨110⟩ axis high-resolution TEM images of twin boundaries in TSL nanowires seeded by Au nanoparticles of (a) 50 nm and (b) 250 nm diameter. In both cases the transition between twin orientations is abrupt.

nanoparticles and grown under the standard conditions described earlier. From both the sawtooth pattern of the sidewalls (where visible) and the variation in contrast visible in the TEM images, the spacing between twins is seen to be an increasing function of nanowire diameter. Beyond this increase in the period of twinning, the most striking feature observed is a systematic increase in nanowire length with increasing nanowire

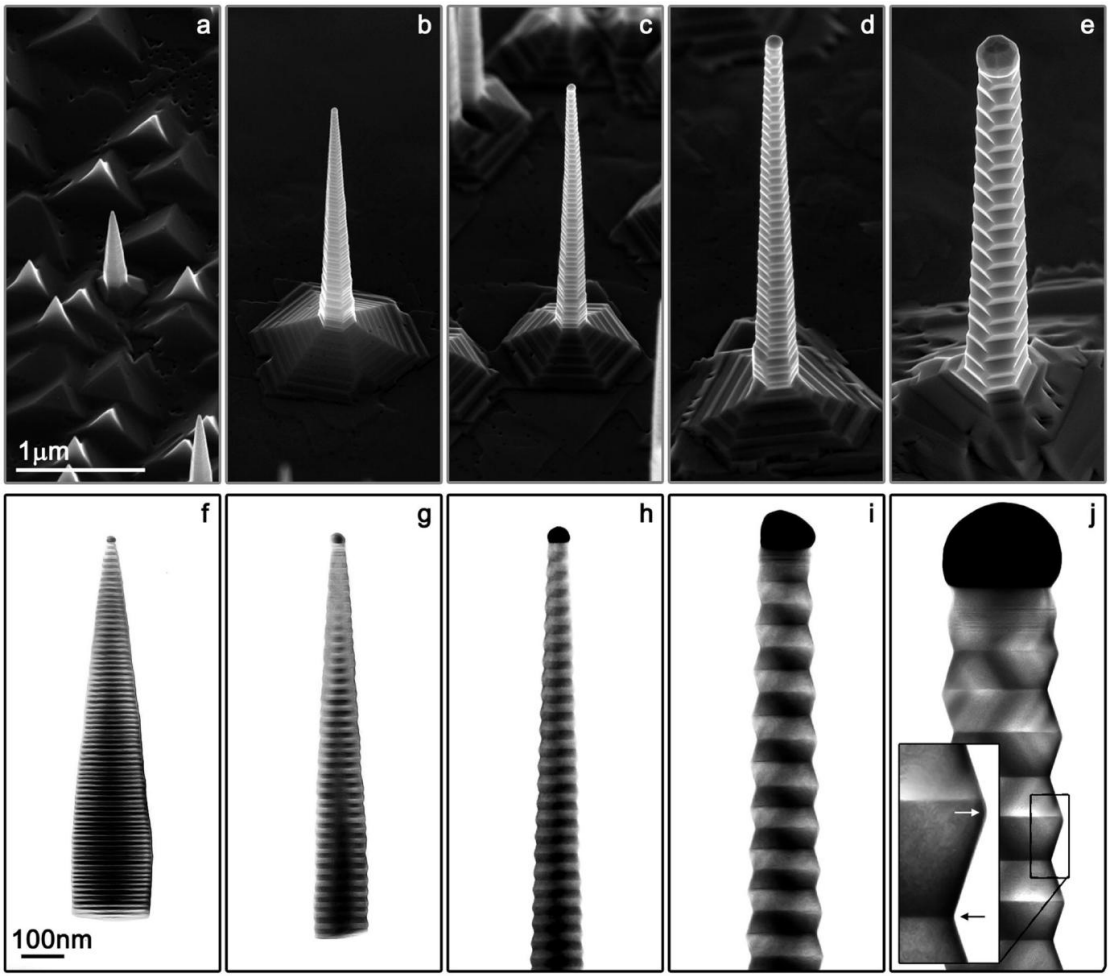

Figure 5-7 | General morphology of the obtained GaAs twinning superlattice structures: Top row presents SEM images for each of the Au colloid diameters, (a) 10, (b) 30, (c) 50, (d) 100, and (e) 250 nm taken at a constant magnification with the sample substrate tilted 45relative to the incident electron beam. Bottom row presents bright field TEM for each of the Au colloid diameters, (f) 10, (g) 30, (h) 50, (i) 100, and (j) 250nm from representative nanowires taken along the ⟨110⟩ zone axis again at a constant magnification. Inset to (j) is a magnified view of the sidewall that demonstrates how the convex meeting point of facets (white arrow) appears below the twin plane with the concave meeting of facets (black arrow) appears at the twin plane.

diameter. This increase can again be related in some part to the areal density of nanowires as observed from the lower magnification SEM images presented inFigure 5-9. Areal density is seen here to mostly decrease with increasing diameter, being 1.73, 0.15, 0.21, 0.09, 0.032 nanowires /μm^2 for the nanowires seeded by 10, 30, 50, 100 and 250 nm Au nanoparticles respectively. Despite areal density decreasing moving from the 100 nm growth to the 250 nm growth, no significant difference in height is observed between the nanowires presented in Figure 5-7(I,j). In this case it is likely that the areal density of the nanowires seeded with the 100 nm diameter Au particles (0.09 nanowires /μm^2) is already below that where the collection area of individual nanowires overlap. A further reduction in areal density below this point cannot deliver additional mass supply to individual nanowires. The trend in areal density moving from the 30 nm growth to the 50 nm growth presents another anomaly. Here nanowire length is seen to increase with increasing areal density.

Additional to the effect of areal density, growth rate may also be a function of the nanowire diameter where the Gibbs Thompson effect is significant in reducing the effective supersaturation of smaller diameter nanowires.[134, 367, 368, 992] Comparing the

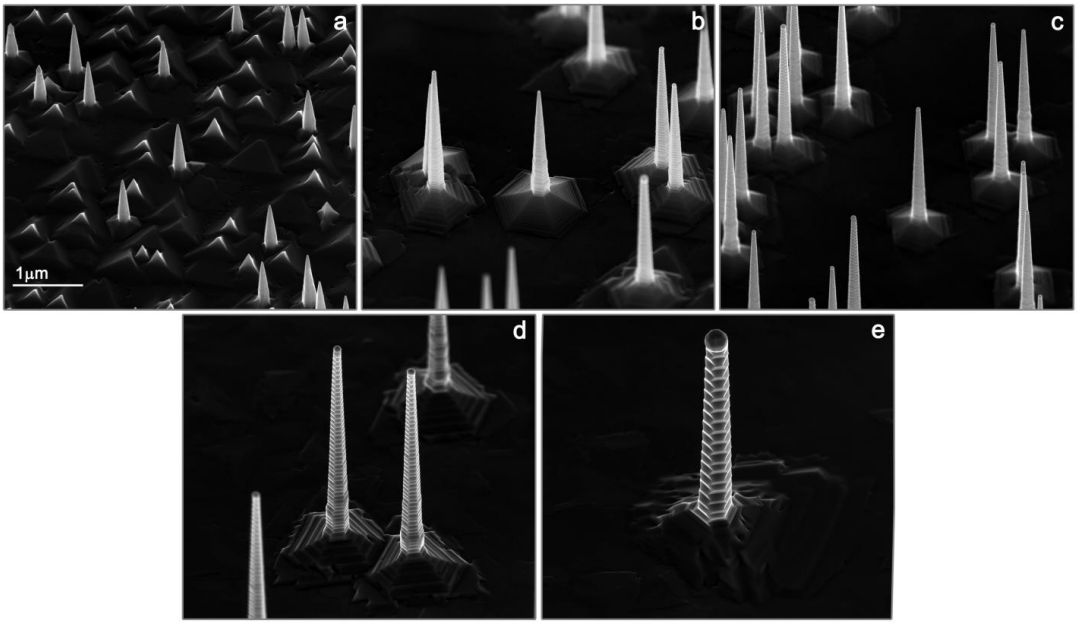

Figure 5-8 | Lower magnification SEM images of the growths presented in Figure 5-7, (a) 10 nm - 1.73 nanowires /μm^2, (b) 30 nm - 0.15 nanowires /μm^2, (c) 50 nm - 0.21 nanowires /μm^2, (d) 100 nm - 0.09 nanowires /μm^2, and (e) 250 nm - 0.032 nanowires /μm^2. All images were taken at a constant magnification with the sample substrate tilted 45° relative to the incident electron beam.

length of the smallest diameter nanowires (Figure 5-7(a)) with those of slightly larger diameter (Figure 5-7(b)) it is clear that the Gibbs-Thomson effect was significant under the current growth conditions for nanowires of 30 nm diameter or less.

Large variation in length is noted within Figure 5-7(a) with pyramidal structures evident where the Au diameter was barely above the diameter threshold for growth. Figure 5-9 investigates the significance of the Gibbs Thompson effect in reducing the effective supersaturation of these smaller diameter nanowires. Seen inset are magnified views of four Au nanoparticles increasing in diameter from left to right. The smallest of these (Figure 5-9 (b)) was below the diameter threshold for growth and has not seeded a nanostructure but has instead formed a pit. The other three larger diameter nanoparticles (Figure 5-9 (c-e)) are seen to have seeded nanostructures which increase significantly in height with small increases in Au nanoparticle diameter.

Turning now to the TEM images shown in Figure 5-7(f)-(j), a region of randomly twinned zincblende is observed directly below the seed particles of two largest diameter

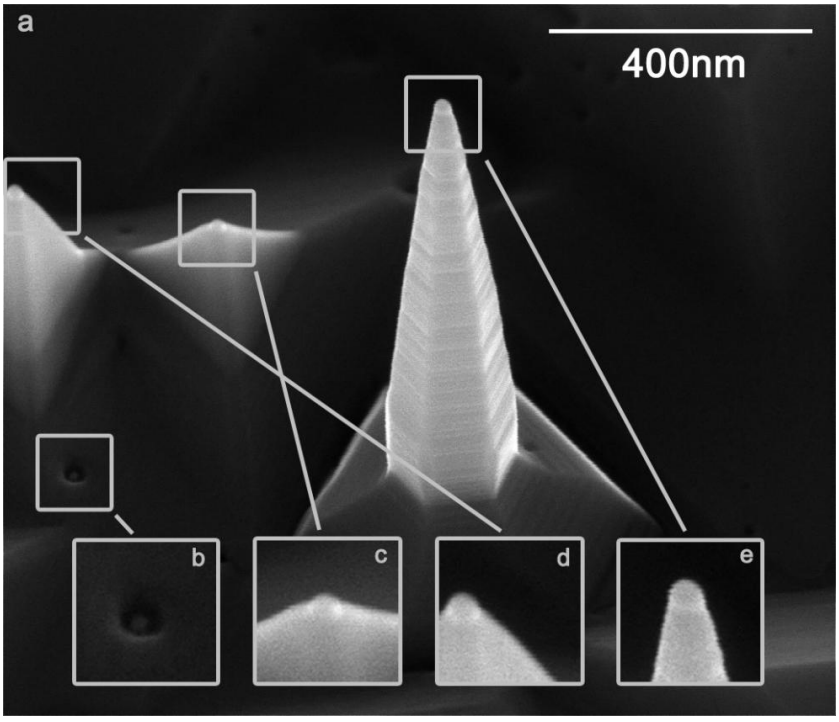

Figure 5-9 | Gibbs Thompson effect; SEM image showing several Au particle sizes, (b) pit formed by Au particle below the threshold for growth, (c-e) increasing nanowire length with increasing Au seed particle diameter. The sample substrate was tilted 45° relative to the incident electron beam.

nanowires. Similar regions can be observed from the HRTEM images presented in Figure 5-10 for the nanowires seeded by 30 nm and 50 nm diameter Au nanoparticles. In all cases the introduction of these additional planar defects can be related to transients in material supply with the termination of growth on cooling.[598, 657]

While direct impingement will cease almost immediately with the termination of group III precursor flow, some surface diffusion continues, more significantly, group III material may precipitate from the seed particle in a process known as the reservoir effect.[185, 186, 188, 496, 1044] This additional group III material can facilitate further nanowire growth at reduced group III supersaturations and increased effective V/III ratios. The material thus produced is termed a 'neck' and is often characterised by a different crystal structure and diameter to growth under steady state conditions.[593, 968, 1033, 1044-1046] Neck structures are particularly prominent in Figure 5-1(d) and Figure 5-4(c,d) where sidewalls of these nanowires shift abruptly from near vertical to a tapered morphology close to their tips. It is likely that the transients in material supply affect the crystal structure and diameter of the tip grown following termination as well as the radial overgrowth on that tip. Also of note in Figure 5-7 is the large increase evident in nanowire tapering with reduction in Au seed size. While radial overgrowth is expected to be a complex function of factors such as nanowire geometry and density, measurement of the difference between base and tip diameters reveals a relatively constant radial growth rate across nanowire diameters. The difference in tapering may thus be related in the first instance to the reduced axial growth rate of the smaller

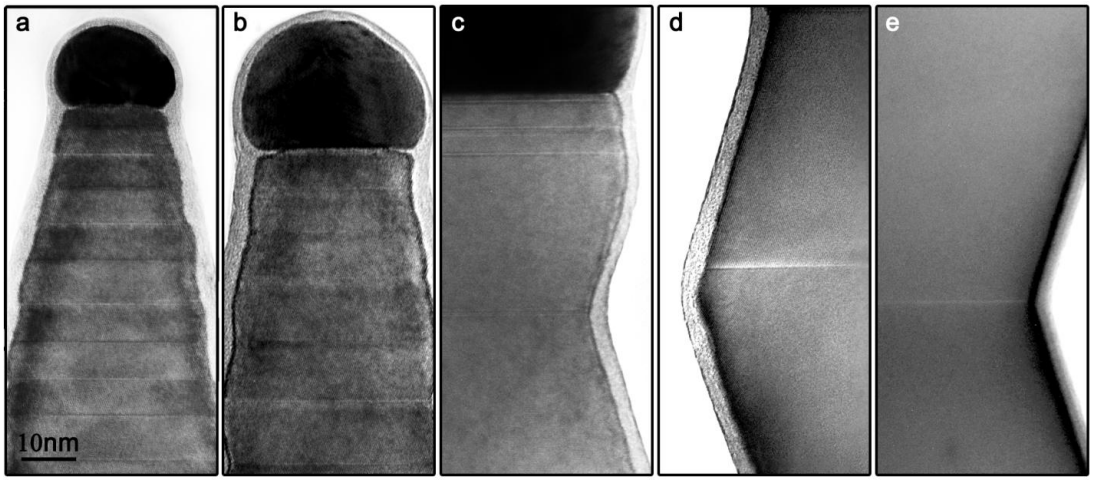

Figure 5-10 | Representative ⟨110⟩ zone axis HRTEM from each of the Au colloid treatments; (a) 10 nm, (b) 30 nm, (c) 50 nm, (d) 100 nm and (e) 250 nm.

diameter nanowires leading to a reduced ratio of axial to radial growth.

5.3.4 Radial overgrowth

As was observed in Figure 5-6, the larger diameter nanowires presented in Figure 5-7(I,j) and Figure 5-10(d) also show a vertical offset between twin planes and the apparent intersection of their sidewall facets [indicated by a white arrow in Figure 5-7(j)]. Where the intersection of the sidewall facets is convex it is observed below the nearest twin plane (in the direction of the substrate) but where the intersection is concave it appears on or very close to the horizontal line of the twin plane. Similar patterns of radial overgrowth are apparent in previous reports of III-V twinning superlattice structures[24, 616, 679] while asymmetry in radial overgrowth leading to the {111}A facets having a larger area than the {111}B facets has been noted for both InAs crystal phase superlattices[1047] and pseudo-periodic $InAs_{(1-x)}Sb_x$ twinning superlattices.[670]

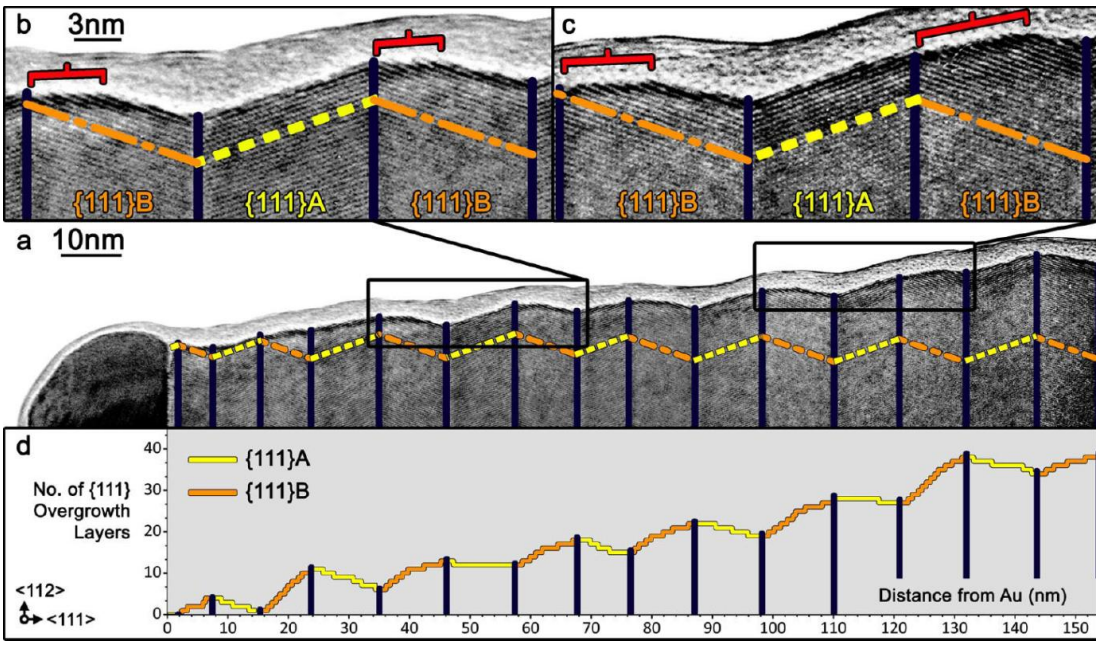

Figure 5-11 | Investigation of sidewall growth: (a) ⟨110⟩ zone axis HRTEM image of an approximately 30 nm diameter nanowire. Twin plane locations are marked with solid dark blue lines while dashed yellow and dashed dotted orange lines show expected {111}A and {111}B sidewall projections, respectively; (b, c) magnified views of (a) where expected sidewall projections are again shown. Regions of the sidewall strongly deviating from the expected {111}B orientation are highlighted with red braces; (d) Plot of the number of {111} bilayers difference between the expected sidewall profile and the actual sidewall.

The asymmetry of radial overgrowth is investigated in Figure 5-11 by overlaying the expected {111} sidewall projection onto a HRTEM image of the observed sidewall. This line construction represents ideal {111} faceting and illustrates the expected sidewall position prior to radial overgrowth with the offset between it and the actual sidewall [Figure 5-11(d)] being representative of tapering due to radial overgrowth.

Taking a magnified view from close to the Au nanoparticle but outside the neck region, Figure 5-11(b) compares the actual sidewall profile of three twin segments with that expected for {111} faceting. While the sidewall profile of the middle segment closely resembles an expected {111}A orientation, those of the adjacent two segments show significant deviation from {111}B. Radial overgrowth appears to have transformed the sidewall profile of both these segments, with two different orientations clearly visible. Whereas the right hand side of each segment (opposite the direction of growth) retains an orientation close to {111}B the left hand side appears close to horizontal in the figure. Counting {111} planes it is apparent that this new sidewall orientation arises from the incomplete extension of {111} planes from the right hand twin boundary to the left. A similar geometry is evident with further radial overgrowth as shown in Figure 5-11(c) though the angle formed by this incomplete extension of planes appears somewhat variable (the distribution of sidewall orientations formed by radial overgrowth on {111}B facets is presented for various nanowire diameters in figure S4 of the supporting information).

Figure 5-11(d) illustrates the above observations by plotting the number of {111} planes from the expected {111} sidewall profile constructed to that of the actual sidewall observed by HRTEM. Steps in this plot represent the origin or termination of {111} bilayers with the gradient, or more specifically the deviation from horizontal, being representative of deviation from a {111} sidewall orientation. An overall increase in the number of counted planes and the related net positive gradient may furthermore be considered indicative of material added through radial overgrowth. This increase is further observed to be pseudo-periodic with a greater number of overgrowth layers at each concave intersection of facets relative to the convex intersection below. Vu *et al.*[515] have previously suggested that radial growth rate is higher at these concave intersections due to the re-entrant geometry.

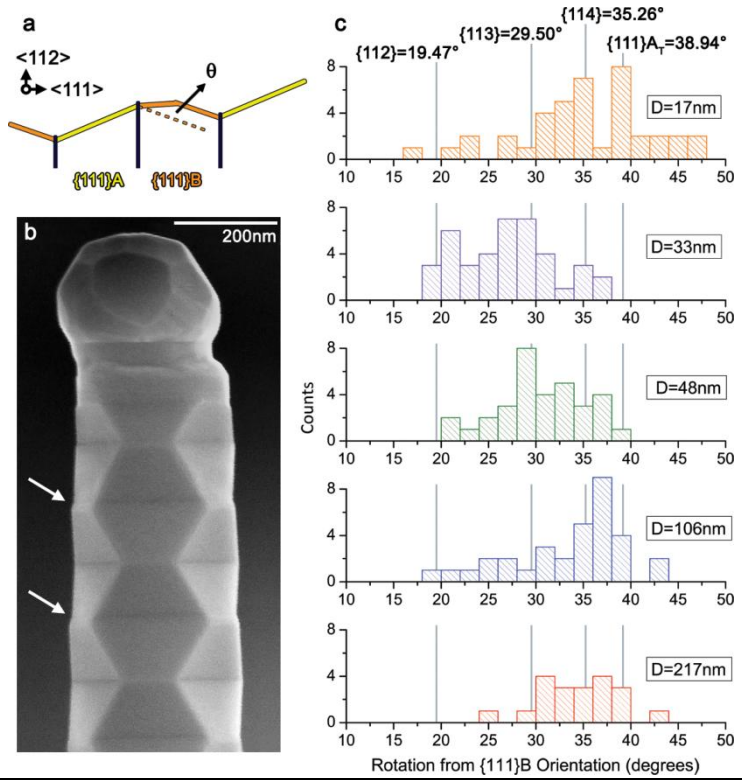

Figure 5-12 | Orientation of {111}B facets following overgrowth: (a) schematic defining the angle of rotation measured; (b) SEM image demonstrating that overgrowth at the convex intersection of facets retains an orientation approximately parallel to the ⟨110⟩ direction; (c) distribution of the orientation of overgrowth as defined by (a) and measured for single nanowires representative of each Au particle size investigated. The {111}A_T plane belongs to the crystal twin.

Returning to Figure 5-11(d) and examining the behaviour of each segment type in turn, it is firstly noted that the {111}A sections of the graph exhibit a low density of steps in agreement with the close to expected orientation already discussed. These steps are furthermore universally related to the termination of {111} bilayers. Such observations contrast with the {111}B sections where a high density of steps is related to the origin of overgrowth planes. Unlike the generally uniform distribution of steps observed for the {111}A segments, there is furthermore a tendency for steps on the {111}B sections to be found more towards the left hand side of these sections (the direction of growth). It is this grouping of steps which is responsible for the apparent change in sidewall orientation and the related asymmetry at the convex intersection of facets.

Taken together these observations are suggestive in the first instance of an energetic instability to the {111}B As terminated facets under the current growth conditions.

While contrasting with previous reports for {112} faceting,[985] detailed DFT calculations[1048] suggest such an analysis would not be unreasonable given the significantly lower V/III ratio used in this work. Overgrowth morphology is however not only a function of the various surface energies but also the total surface area generated. Interpretation is furthermore complicated by the three dimensional nature of radial overgrowth with recent work highlighting the potential complexity of such processes.[1049, 1050]

Figure 5-12 presents the distribution of sidewall orientations as altered from the expected {111}B orientation by overgrowth. The measurements are expressed as the angular difference between the orientation of the sidewall projection at the twin boundary closest to the growth front and a perfect {111}B orientation [shown schematically in Figure 5-12(a)] That the facet orientation remains approximately perpendicular to the ⟨110⟩ zone axis is observed for the case of larger diameter nanowires from Figure 5-12(b). Indicated are two convex intersection of facets where the small edge arising from this intersection is clearly shifted down (opposite the growth direction) relative to the longer adjacent edge arising from the concave intersection facets. In neither case does overgrowth appear to have rotated the facet orientation into the plane of the ⟨110⟩ zone axis. Comparing the distribution of orientations for each of

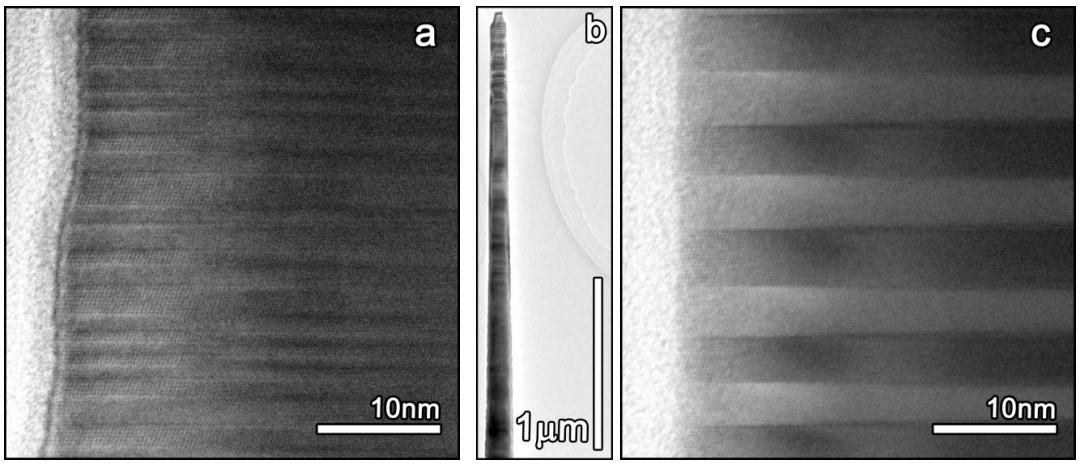

Figure 5-13 | <110> axis TEM images of a GaAs nanowire grown at low areal density showing a transition from mixed phase to TSL. a) HRTEM of the sidewall closer to the base of the nanowire showing a mixed phase structure. b) Low magnification image of the entire TEM sample. c) HRTEM of the sidewall closer to the tip of the nanowire showing a TSL structure.

the representative nanowire diameters it is apparent that the areal density of nanowires (see Section 5.3.2) has affected final orientation with those nanowires grown with higher areal densities (30 and 50 nm samples) exhibiting lower angular variations. Some clustering around significant orientations is also noted.

Interestingly, the final configuration of overgrowth on TSL nanowires appears to be {110} type faceting. Figure 5-13 presents a GaAs nanowire with significant radial overgrowth due to a long growth time and low areal density. Like the nanowires observed in Figure 5-1(e,f,h) this nanowire shows a transition from mixed phase [Figure 5-13(a)] to a TSL structure [Figure 5-13(c)]. While the HRTEM image of the mixed phase segment reveals a complex arrangement of multiple facet orientations, the sidewall of the TSL segment is smooth. A transformation of other III-V TSL nanowires to towards {110} faceting has been reported for InAs[600] and InP[515] twinning superlattice[515] structures as well as regions of pseudo-periodic twinning in $InAs_{(1-x)}Sb_x$ nanowires[670].

5.4 Modelling

5.4.1 Background and motivation

As the physical properties of TSL structures are dependant on period, an ability to tailor this characteristic will be critical for future device applications. It is therefore important that a proper understanding of the relationship between TSL period and several basic growth parameters is developed. Shown in Figure 5-14 is a plot of superlattice period as a function of nanowire tip diameter for the five different colloid treatments as presented in Figure 5-7 and Figure 5-9. Despite each treatment having a different nominal diameter, overlap is observed between the treatments due to the relatively wide distribution of nanoparticle diameters in each treatment. Given that the areal density of each treatment was different (see Figure 5-9), Figure 5-14 is graphical illustration of what was observed earlier from Figure 5-4: that density and growth rate do not significantly affect twin spacing.

The apparent linearity of the result presented in Figure 5-14 is similar to that reported for ZnSe twinning superlattice nanowires[1021] but differs from the clearly non-linear trends reported for other III-V materials, namely InAs,[616] InP[35] and GaP[24]. Most authors have interpreted this relationship as a balance between the energy required for twin

formation and the increased droplet surface energy inherent to deviation from the equilibrium cross sectional shape with the latter being geometrically similar for a given ratio of twin spacing to diameter. For sawtooth faceting in Si nanowires where twinning is absent, Ross *et al.*[1051] equated a barrier to edge creation with the difference in free energy per unit length of growth for two different non-vertical sidewall facet orientations. Facet orientation was considered to change where this difference exceeded the barrier to edge creation giving a linear relationship between facet period and nanowire diameter. A similar total energy approach was also described by Shim *et al.*[1052] for periodic twinning in SiC nanowires. The linear relationship between twin

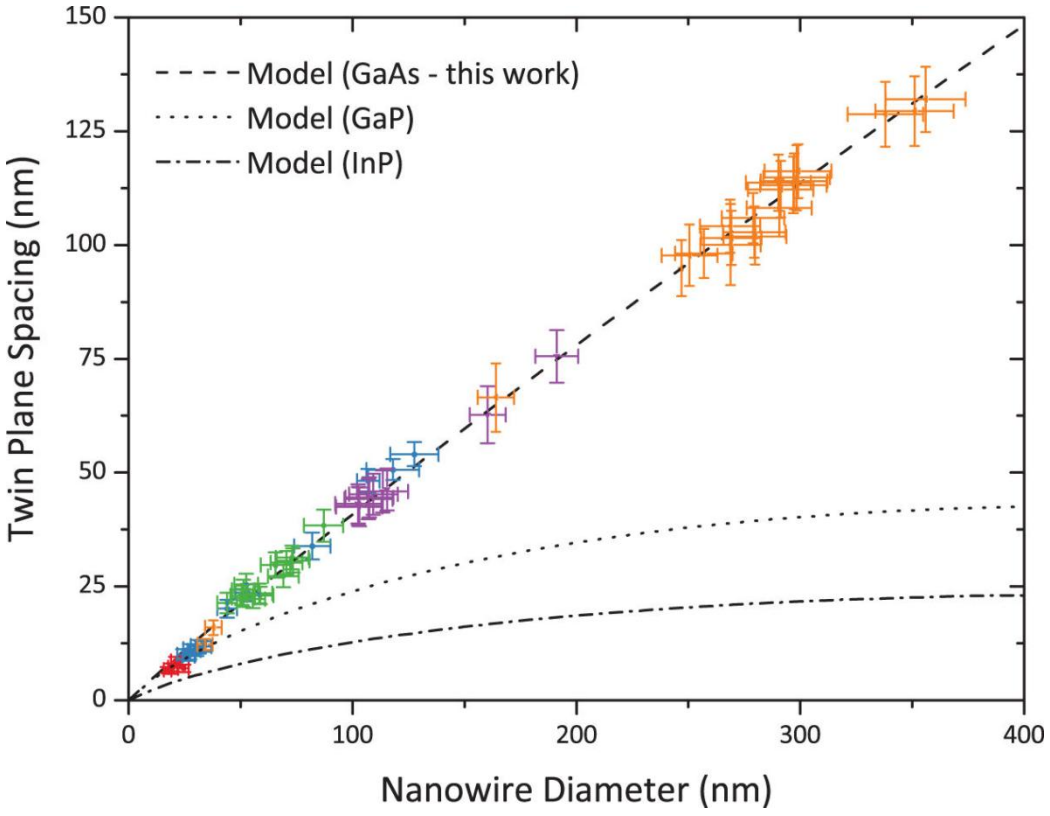

Figure 5-14 | Plot of nanowire twinning superlattice average twin plane spacing as a function of nanowire diameter where results from each of the different colloid treatments are shown in differing colours. The error in diameter is defined as 10% for diameters of less than 150 nm and 5% for values greater than this. Variability in segment length is demonstrated by (1 standard deviation from average). All lines are generated by eq 2, with the dashed line being a fit to the current data and the dotted and dash-dotted lines being representative fits for GaP[24] and InP[35], respectively, from previous publications. Vertical error bars equate to one standard deviation from average.

spacing and nanowire diameter so derived was well matched experimentally and allowed the authors to calculate a dynamic variation of less than 1° in contact angle during growth.

5.4.2 Framework

Algra *et al.*[24, 35] modelled the relationship between nanowire diameter and twin spacing in InP and GaP TSL nanowires by considering individual nucleation events. Relative nucleation probabilities were determined by finding the free energy difference between a facet conserving nucleus and its twin. For the point at which nucleation of either orientation is equally probable a linear relationship was again derived;

$$H_c \cong \frac{b}{h} \frac{\gamma_T}{\gamma_{LV} \sin\delta_0} \left(\frac{\Gamma}{\Delta\mu}\right) \cdot D \qquad \ldots(5\text{-}1)$$

with H_c being the axial distance from the point where the nanowire cross section is hexagonal, b a geometrical constant previously calculated to be 1.16,[24] h the planar bilayer spacing in the $\langle 111 \rangle$ direction, γ_T, γ_{SL}, γ_{SV} and γ_{LV} the surface energies per unit area of a twin plane, the solid-liquid, solid-vapour and liquid-vapour interfaces respectively, δ_0 the angle of the droplet with respect to a {111}B facet at a hexagonal cross section (preferred nucleation sites were analysed for this geometry by Liu *et al.*[1053]), $\Gamma = \gamma_{SL} + 1/6 \cdot [\gamma_{SV} - \gamma_{SL} - \gamma_{LV}\cos(\delta_0)]$ the effective interfacial energy barrier to nucleus formation, $\Delta\mu$ the supersaturation in the Au seed as defined by the difference in chemical potential between III-V pairs in solution relative to those in the solid and D the nanowire diameter Figure 5-15 schematically illustrates these various geometrical and physical parameters.

The length H_c may be considered something of a balance between an increasingly unfavourable contact angle due to the distortion of the seed particle and the energetic barrier to twin formation. As the distortion of the seed particle will be an increasing function of H_c it is perhaps intuitive that an increased resistance to this distortion, γ_{LV}, will reduce H_c while an increased barrier to twin formation, γ_T, will increase it. The barrier to twin formation is furthermore not only a function of γ_T but also the interfacial area between nanowire and nucleus. As Γ will act to increase and $\Delta\mu$ reduce the critical nucleus size [583, 591] an increase in their ratio, $\Gamma/\Delta\mu$, will also act to increase the barrier to twin formation reducing the expected value of H_c.

While H_c gives the point beyond which twin formation is energetically more favourable for an individual nucleation event, the axial distance between twin planes is ultimately the product of multiple nucleation events. Algra *et al.*[24, 35] found a good fit to their non-linear experimental result by calculating the most probable number of uninterrupted facet conserving nucleation events ending in a twin, the total segment length H_s being less than two times the critical distance H_c;

$$H_s = 2H_c\left\{1 + \left(\frac{1}{\Delta}\right)\ln\left[1 - \exp\left(\frac{-\Delta}{H_c/h}\right)\right]\right\} \qquad \ldots(5\text{-}2)$$

$$\Delta = \frac{c^2}{k_B T}\gamma_T\left(\frac{\Gamma}{\Delta\mu}\right)^2 \qquad \ldots(5\text{-}3)$$

where k_B and T have their usual meanings and c is another geometrical constant

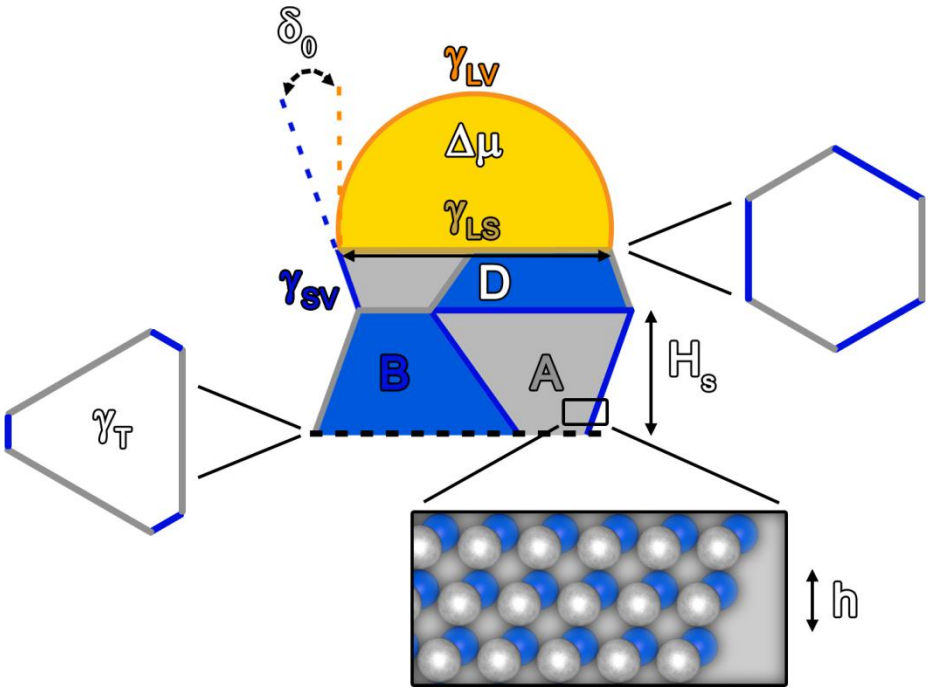

Figure 5-15 | Geometry and physical parameters; γ_T, γ_{SL}, γ_{SV} and γ_{LV} are the surface energies per unit area of a twin plane, the solid-liquid, solid-vapour and liquid-vapour interfaces respectively, $\Delta\mu$ the supersaturation in the Au seed as defined by the difference in chemical potential between III-V pairs in solution relative to those in the solid, δ_0 the angle of the droplet with respect to a {111}B facet at a hexagonal cross section, h the planar bilayer spacing in the ⟨111⟩ direction, D the nanowire diameter.

previously calculated to be 1.98.[24] In Equation 5-2 the term Δ, which represents the energetic barrier to twin formation,[35] is seen to control the deviation of the probabilistic segment length H_s from that calculated geometrical in Equation 5-1. Factors that increase the probability of a twin event (reduce Δ) such as a reduction in the twin plane surface energy, γ_T, or the interfacial area between nanowire and nucleus [proportional to $(\Gamma/\Delta\mu)^2$ for a hexagonal nanowire cross section][35] will act to reduce the linearity of the relationship between TSL segment length, H_s, and diameter, D. Figure 5-16 investigates this behaviour by plotting H_s as a function of D for various different values of the pertinent physical parameters.

The values of these physical parameters and the ranges they describe were chosen here to be both physically relevant to the current work and illustrative of the relevant trends. The supersaturation of the seed particle is firstly seen to have a highly significant effect on H_s, with higher supersaturation increasing the probability of twinning event and therefore reducing the expected length H_s [Figure 5-16(a)]. Increasing twin plane and solid-liquid surface energies both reduce the probability of twinning and produce a more linear relationship between H_s and D [Figure 5-16(b,c)]. The observed significance of the solid-liquid surface energy further reinforces the potential importance of any liquid ordering as was discussed by Algra *et al.*[35] Also reinforced is the importance of correctly defining the equilibrium contact angle which is currently a fitted parameter as both *in situ* measurement and calculation have proven difficult.[243] Finally, the liquid-vapour and solid-vapour surface energies are seen to have an opposite influence on H_s. The effect of the surface-vapour surface energy is, in particular, relatively less significant than some of the other parameters considered.

With a significant barrier to twin formation, Δ, the probability of a twin or facet changing nucleation event is reduced and the likelihood of an uninterrupted sequence of facet conserving nuclei approaching the length H_c predicted through energetics is increased. In the case of GaAs, the twin plane formation energy has been reported[1054] as $2.75\text{x}10^{-2}$ J/m^2 which is higher than the corresponding values of $2.10\text{x}10^{-2}$ J/m^2 and $9.00\text{x}10^{-3}$ J/m^2 reported for GaP[1054] and InP[1054] respectively. Turning to Γ, the dominating contribution to this term is γ_{SL} which for Au on planar GaAs can be approximated by γ_{SV}.[35, 591] For GaAs, γ_{SV} of a {111}B surface under relatively low V/III ratios has been calculated[1048] to be 1.11 J/m^2 which is again higher than the values

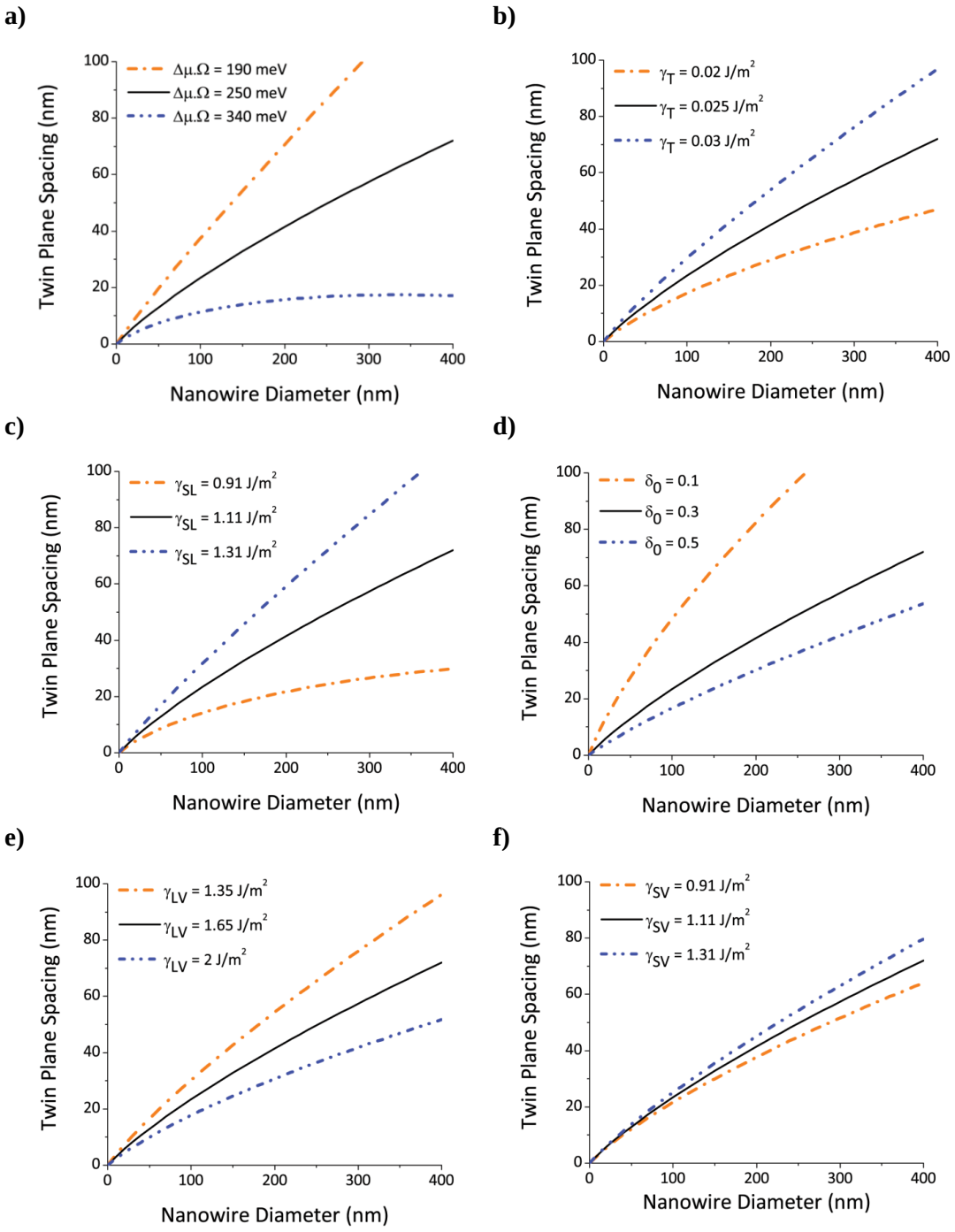

Figure 5-16 | Numerical study of the influence of selected physical parameters on the relationship between twin spacing and nanowire diameter. a) Supersaturation in the seed; b) twin plane energy interfacial energy; c) solid liquid interfacial energy; d) contact angle e) liquid vapour interfacial energy; f) solid vapour interfacial energy. The parameters used for the common curve shown in black are the mid-range values in each case; $\Delta\mu.\Omega = 250meV$, $\delta_0 = 17.2°$, $\gamma_{LV} = 1.65\ \mathrm{J/m^2}$, $\gamma_T = 0.025\ \mathrm{J/m^2}$, $\gamma_{SL} = 1.11\ \mathrm{J/m^2}$, $\gamma_{SV} = 1.11\ \mathrm{J/m^2}$.

of 0.96 J/m^2 and 0.8 J/m^2 reported for GaP[24] and InP[35, 1055] respectively. With higher surface energies related to both twin plane formation and the generation of solid liquid interface it may be thus expected that, as observed experimentally, the relationship between twin spacing and nanowire diameter will better approximate the linear behaviour found for H_s in GaAs relative to both GaP and InP.

5.4.3 Application

Returning to Figure 5-14 a fit of Equation 5-2 to the data in this work is shown where the above values for GaAs have been used in conjunction with the value of γ_{LV} calculated by Algra *et al.*[24] for a trimethylgallium (TMGa) partial pressure most closely matching that used in the current work. The values of the remaining parameters that give the best fit are δ_0 =17° and $\Delta\mu$ =191 meV per pair. The first of these values is only 10° larger than the value extracted for GaP by similar means,[24] while the second fit parameter, supersaturation, is significantly lower than that found for GaP in the same work.[24] The latter trend corresponds well with the work of Glas[1056] who has previously employed chemical thermodynamics to calculate the supersaturation relevant to Au seeded GaP nanowire growth as being higher than that for Au seeded GaAs nanowire growth at the same temperature and seed particle composition (Au, Ga, group V element). Where growth temperature was raised, as is the case for this work relative to the previous reports of twinning superlattice formation in both GaP and InP, the calculated supersaturation was furthermore also found to be lowered. Taking the value of supersaturation found here by fitting, the calculations of Glas[1056] suggest that the Ga content of the Au alloy was between 40-60% during growth, a range similar to that reported and calculated in other work.[536, 678, 1045, 1057]

In making the above fit we have implicitly assumed a constant supersaturation $\Delta\mu$ across all samples. This is perhaps counter-intuitive given the differences in growth rate observed from Figure 5-4. Nucleation probability is however well known to be an exponential function of liquid phase supersaturation.[1058-1060] Where the growth of each bilayer proceeds from a single nucleation event and supersaturation is approximated to be constant, the overall nanowire growth rate becomes proportional to this nucleation rate.[1058] The growth rate in such a nucleation limited growth regime was given by Algra *et al.*[24]:

$$v \cong a \cdot \exp\left(-c_1 \frac{\Gamma^2}{\Delta\mu}\right) \qquad \ldots(5\text{-}4)$$

where a and c_1 are constants for given growth conditions. In such a regime only a small change in supersaturation is required to generate the observed change in growth rate v rendering any related change in superlattice period likely within the error bounds of this work. Alternatively, where supersaturation is considered to periodically fluctuate, as emphasized by small nanowire diameters or low reactant solubility, the strong exponential dependence of nucleation probability effectively defines a constant supersaturation for which nucleation is expected.[1059, 1060] We further note that $\Delta\mu$ has previously been calculated to be only a weak function of gallium supply rate and thus growth rate for GaP twinning superlattice growth under similar reactor conditions.[24] Such a scenario explains our initial observation that the twinning superlattice period is unaffected by density and related growth rate.

Returning to the given equations, it has been noted that $\Delta\mu$ acts to reduce the critical nucleus size and thus appears in the denominator of both Equations 5-1 and 5-3. As such it may be appreciated that the decreased supersaturation value of GaAs in comparison to GaP works to increase both twin spacing and the linearity of the spacing *vs*. diameter relationship. This qualitative difference in behaviour is illustrated in Figure 5-14 where previous fits of Equation 5-2 to both GaP[24] and InP[35] twinning superlattice structures are shown for comparison. The higher twin plane, surface and interfacial energies relevant to GaAs nanowire growth coupled with relatively low chemical potential all act to generate significant difference in superlattice period at larger diameter. Although the relationship between diameter and twin spacing found for GaAs is almost exactly linear, we note that the model presented here (Equations 5-1, 5-2 and 5-3) provides a better fit to the experimental data ($R^2$of 0.998 vs. 0.995) in addition to describing the differences in behaviour between material systems. As the linear fit in this case was constrained to pass through the origin and thus has one less fitting parameter Equation 5-2 is also preferred by the Akaike information criterion.

Being probabilistic in nature, the form of H_s given in Equation 5-2 can also be used to calculate the width of segment length distributions δH_s.

$$\delta H_s = \frac{4H_c(D)}{\Delta} \qquad \ldots(5\text{-}5)$$

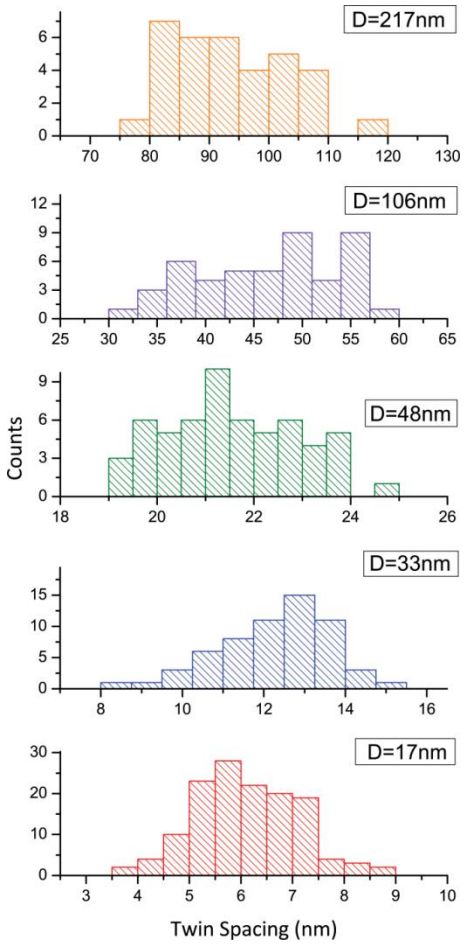

Figure 5-17 | Twin plane spacing distribution as measured by TEM for representative nanowires from each of the colloid treatments,

Figure 5-17 presents twin plane spacing distributions found for each of the colloid treatments which were presented in Figure 5-7 and Figure 5-9. Measured from TEM images of individual nanowires, the distribution and central tendency is seen more clearly for the smaller diameter nanowires as these structures had a greater number of twin planes per wire and therefore larger samples size. Examining each x-axis, it is apparent that the distribution width is an increasing function of nanowire diameter as given by Equation 5-5.

5.5 Summary

In conclusion, this chapter has demonstrated twinning superlattice formation in vertically standing GaAs nanowires. Studying nanowire morphology across a range of diameters and densities it was shown that under the described growth conditions twin plane spacing and, by implication, supersaturation are not strong functions of nanowire

areal density. A polarity dependence to radial overgrowth has also been noted with the orientation of expected {111}B facets being seen to be altered in a specific fashion. Whereas previous studies of periodic twinning in InP[35] and GaP[24] found a non-linear relationship between twin spacing and nanowire diameter, this chapter found an approximately linear relationship for GaAs nanowires . Taking the model used to fit these previous non-linear results we have shown how the higher twin plane and surface energies of GaAs coupled with lower chemical potential may act to generate this behaviour. Beyond growth parameter tuning, the model also provides an indirect measure of some fundamental physical parameters affecting nanowire growth and a method to assess the effect of various growth conditions such as doping on these parameters. The availability of such a model provides a useful tool for the future investigation of the novel electronic, thermal and mechanical properties predicted to arise from periodic twinning.

6

Zinc as an IQE enhancer: Lasing from bare GaAs nanowires

6.1 Introduction

The development of nanoscale lasers promises to enable novel nanophotonic technologies for applications including integrated photonics,[118, 1061] on-chip optical interconnects,[118, 728, 1062] optical switching[1063] and single molecule sensing[713, 1064]. With the potential to act as both a tailored nanoscale cavity and a high-quality gain medium[25, 114, 724, 726], the semiconductor nanowire remains a particularly attractive geometry for realizing these devices. The nanowire geometry is furthermore highly amenable to the definition of complex heterostructure,[117, 709, 730, 741] and as such is a leading candidate for the integration of direct band-gap optoelectronic materials with traditional silicon based CMOS technologies.[118, 709]

In work to date, semiconductor nanowires have been used as a basis for photonic, plasmonic[113, 714, 1065] and polaritonic[1066] nanolaser devices operating at wavelengths ranging from IR through to UV.[25, 112-114, 116-118, 708, 709, 724, 728, 741, 745, 748, 749, 1061, 1066, 1067] Near and mid-infrared operation holds particular relevance for integrated photonics and as such there has been significant interest in III-V nanowire based nanolasers. Recent progress in this field has seen reports of room temperature IR lasing from GaAs,[25, 116, 729, 730] InGaAs[118, 708] and InP[706, 727, 728] nanowires.

Key among the challenges faced in further developing nanolaser designs is improving efficiency.[693] As the reduced dimensions of these devices generally act to increase loss while also reducing round-trip gain, optimizing the performance of the gain medium is an especially critical task. In the case of semiconductor nanowire lasers, emphasis has been placed on reducing non-radiative recombination by reducing defect[117, 1066] and surface state densities[25, 708]. For materials exhibiting a high surface recombination velocity such as GaAs, this has necessitated surface passivation[25, 116, 729, 730, 749, 1068] which adds to the complexity of device fabrication, may be incompatible with other processing steps and can also increase cavity loss through absorption.[25]

This chapter introduces controlled impurity doping as a novel alternative method for increasing the radiative efficiency of nanowires. Building on the framework of previous chapters, the PL emission of zinc-doped GaAs nanowires is compared with that of undoped GaAs nanowires. By quantifying the IQE of individual nanowires, emission from heavily doped nanowires is shown to be orders of magnitude more efficient than that from undoped nanowires. This increase is comparable to current state-of-the-art passivation schemes[25, 116, 729, 730, 749, 1068] and enables the demonstration of room-temperature lasing in unpassivated GaAs nanowires. Time resolved PL and transient Rayleigh scattering spectroscopy further demonstrate that the minority carrier lifetime is unchanged by doping. In this way high IQE is combined with a picosecond carrier lifetime.

Through detailed modelling the increase in IQE with doping is shown to result from an increase in the rate of radiative recombination. This mechanism is generally applicable across device geometries and operating wavelengths. It is furthermore complementary with more conventional strategies such as passivation which rely on reducing the rate of non-radiative recombination. Impurity doping is thus introduced as an effective approach to improving the radiative efficiency of nanostructures.

6.2 Methods

6.2.1 Growth and morphological characterisation

For the experiments described in this chapter, undoped and zinc-doped Au-seeded GaAs nanowires were synthesised via the methods described in Section 3.1. The growth temperature was 575 °C, the V/III ratio 1.4 and the AsH_3 molar fraction 1.43×10^{-5}. Doping was realised by introducing diethylzinc (DEZn) at molar fractions of up to 1.4×10^{-4}. Nanoparticles having nominal diameters of 30, 50 and 250 nm were used to seed growth. Varying areal densities were achieved by diluting the colloidal solutions containing the seed particles with deionised water. Following growth, the nanowires were surveyed by SEM and TEM in order to document their general morphology and crystal structure. Individual nanowires studied by PL were later relocated and imaged by SEM.

6.2.2 Photoluminescence experiments

Power and temperature-dependant single nanowire PL spectra were collected using a 100x/0.9NA objective (Nikon LU Plan) at room-temperature and a longer working

distance aberration corrected 60x/0.70NA lens (Nikon CFI Plan Fluor) at low temperature. The collected light was spectrally filtered to remove the pump wavelength and then dispersed through a 150 lines/mm grating of a 0.75 m spectrometer. For spectra exhibiting fine features such as stimulated emission, a 900 lines/mm grating was employed. Focal plane images were obtained from the zeroth order of the gratings. For lasing nanowires a series of images taken at differing exposures were composited to increase dynamic range.

The spot size was measured for each experimental setup as described in Section 6.2.2.1 and the system was calibrated to give absolute photon count as described in Section 6.2.2.2. Excitation power was measured after the objective using an optical power meter (Thor PM100D) and was varied using a continuously variable neutral density filter wheel (Thor NDM4). The filter wheel was controlled electronically enabling for the automated collection of power dependant data.

Before characterisation by PL, the nanowires were transferred by mechanical dispersion onto SiO_2 substrates. SiO_2 substrates were chosen in preference to Si so to maximize the dielectric contrast between the nanowires and their surrounds. The substrates were further pre-patterned with a photolithographically defined square-grid consisting of Au stripes of around 1 μm thickness with a 20 μm spacing. This grid, in conjunction with optical images of the characterized nanowires allowed for their later identification and

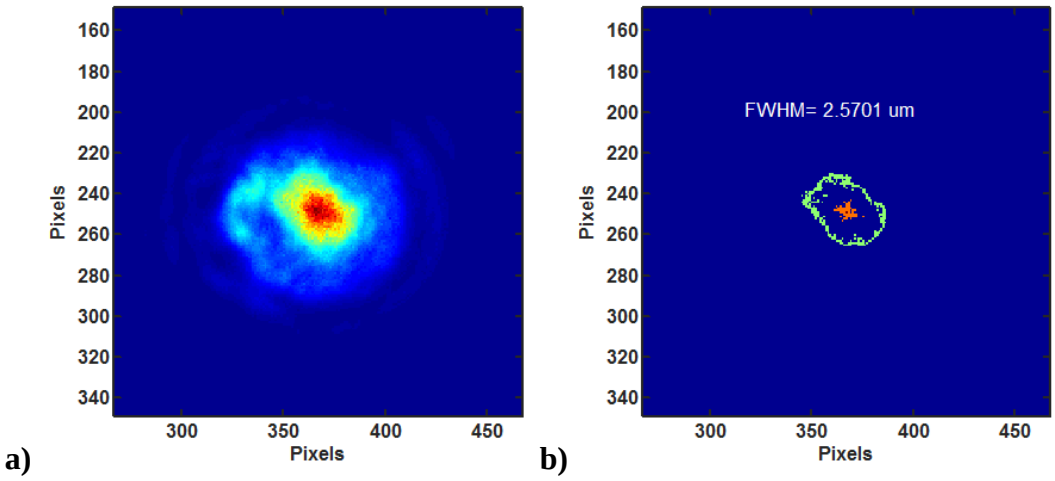

Figure 6-1 | Measurement of excitation spot size. a) A composite image of the reflected laser spot b) Analysis of (a) showing the brightest 50 pixels in orange and pixels with 45-55% brightness in green. The FWHM shown is the mean distance between the green pixels and the centroid of the orange pixels.

morphological characterisation by SEM.

6.2.2.1 Measurement of the excitation spot size

The excitation spot size was measured under various experimental conditions by taking an image of its reflection from a polished silicon surface. The full width at half maximum (FWHM) was then calculated as the mean distance between pixels ranging from 45-55% of maximum brightness and the centroid of the brightest 50 pixels. Distance here was calibrated by imaging nanowires previously measured using a calibrated SEM and by using an optical microscope calibration slide.

6.2.2.2 System calibration

The detection efficiency of the optical system was measured by employing a laser diode operating at 850 nm (TT Electronics OPV302) as a reference source. The output of this reference laser was firstly measured by an optical power meter (Thor PM100D) before its spectra was collected by our system using the same parameters as later photoluminescence experiments. Being of small spatial size and low divergence, the entire reference beam was collected by our system enabling the ratio between photons collected and CCD counts to be measured. When calculating the absolute external quantum efficiency (EQE) of our nanowires light emission was assumed to be isotropic.

6.2.3 Time-resolved measurements

The dynamics of photoexcited carrier decay were studied for doped nanowires using several complementary techniques. Single nanowire studies were conducted by the University of Cincinnati using time correlated single photon counting (TCSPC) at low temperature and transient Rayleigh scattering spectroscopy[1069] at room temperature.

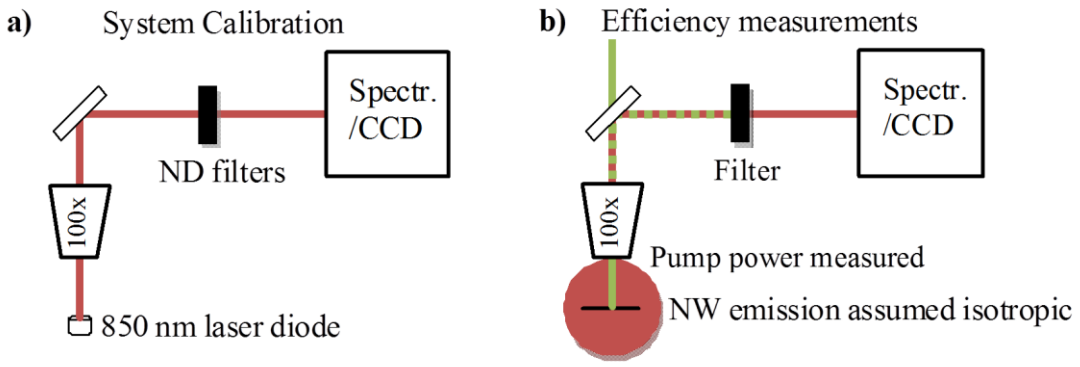

Figure 6-2 | Schematics showing the experimental setup for a) the calibration of CCD sensor sensitivity and b) absolute EQE measurements

Ensemble measurements were undertaken at Swinburne University of Technology through PL up-conversion. For the up-conversion measurements, the sample was excited by 100 μJ pulses from a non-collinear OPA (NOPA) (Light conversion – Orpheus-N) pumped by a Y:KGW amplified laser system (Light Conversion – Pharos). The repetition rate was 125 kHz with a central wavelength of 740 nm. The emission from the nanowire samples was mixed with the gate pulse (from the same source) in a 50 μm-thick type-II BBO crystal. The mixing signal (centred at 402 nm) was spectrally resolved and detected by a CCD. The delay of the gate pulse was scanned in 20 fs steps.

6.2.4 Finite-difference-time-domain simulations

Finite-difference time-domain (FDTD) simulations were performed using a commercial software package (Lumerical FDTD solutions, www.lumerical.com) in order to calculate the absorption and cavity spectrum of individual nanowires. For the absorption simulations, the nanowires were modelled as truncated GaAs cones lying flat on a silica substrate under a Gaussian beam profile. The orientation of individual nanowires relative to the fixed polarisation of the excitation source was measured at the time of the μPL experiments and their dimensions measured later from SEM images. The FWHM of the excitation source was measured as described in Section 7.2.1.

In order to identify the cavity mode with the lowest threshold gain g_{th}, the mode confinement factor Γ and reflectance R of various modes were calculated for a wavelength of 880 nm. As Γ varies along the length of a tapered nanowire, values were taken for the midpoint. Having identified the lasing mode, the cavity spectrum of individual nanowires was simulated by placing a dipole source orientated and positioned in order to excite this lasing mode.[1070] The index of the nanowire and substrate were taken as 3.6 and 1.5, respectively. In these simulations, the electric field was monitored at various positions within the nanowire as a function of time. The cavity spectrum was then determined from the Fourier transform of the signal.

6.2.5 Finite volume modelling of surface depletion

Finite volume modelling was performed using the commercial software package COMSOL Multiphysics in order to assess the effects of surface band-bending on the dynamics of recombination. In an approach that has been previously reported by Li *et al.*[1071], the Poisson, continuity and drift-diffusion equations were solved in 1D to give

electric potential, hole concentration and electron concentration as a function of radial position. Solutions were firstly obtained without illumination for a sequence of eleven different background hole concentrations logarithmically spaced between 2.8 x10^{16} /cm^3 and 2.8 x10^{19} /cm^3. Steady state, spatially uniform carrier generation was then progressively ramped to a maximum value of 1.0 x10^{40} /cm^3. Losses were to surface, Shockley-Read-Hall (SRH) recombination, radiative and Auger recombination with the recombination coefficients being found from the literature as documented in Table 6-1. Relatively high carrier mobilities were used to represent a worst case scenario for surface recombination. Although the use of steady state conditions represents somewhat of a simplification, the results derived held qualitative similarity to rate equation modelling for pulsed excitation (see Section 6.4.2).

Table 6-1 | Model Parameters

Parameter	Value	Refs.
Surface trap density	1 x10^{12} /cm^2	1072-1076
Surface recombination velocity	2.2 x10^6 cm/s	1077, 1078
Electron mobility	8500 cm^2/Vs	1079-1081
Hole mobility	400 cm^2/Vs	258, 1082
Bulk SRH lifetime	10 ns	1083, 1084
Radiative recombination coefficient	Eqn. …(7-1)	8
Auger recombination coefficient	Eqn. …(6-2)	1085-1088

6.2.5.1 Variation of the recombination coefficients with doping

Both the radiative and Auger recombination coefficients, B and C, will vary with dopant concentration.[8, 1085] In the current finite volume modelling these parameters were therefore defined as a function of dopant concentration from empirically determined relationships. In the case of the radiative recombination coefficient B, its variation with doping in *p*-type GaAs was investigated by Nelson and Sobers.[8] The following relationship was obtained from that data:

$$B = -3.47 \times 10^{-11} \ln N_A \, cm^3/s + 1.63 \times 10^{-9} cm^3/s \qquad \ldots(6\text{-}1)$$

The Auger recombination coefficient in GaAs is less well defined with a range of values having been reported.[1086-1088] For p-type doping, Ahrenkiel *et al.*[1085] found the following relationship:

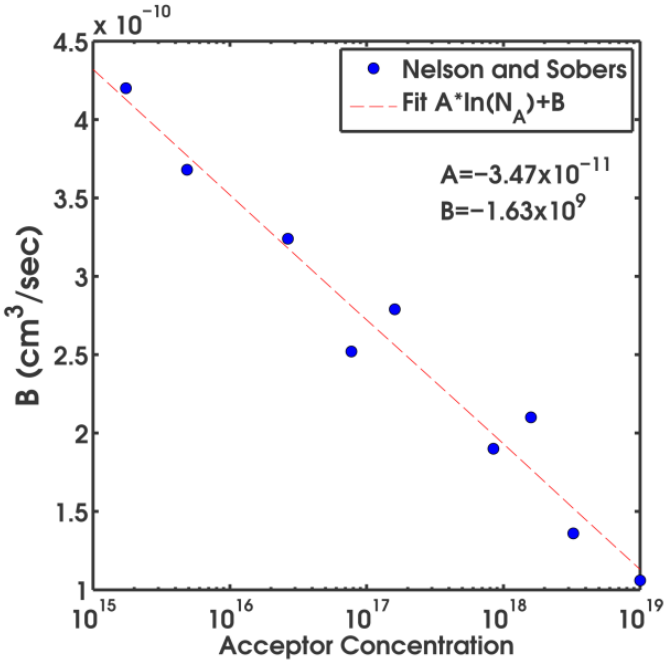

Figure 6-3 | Variation of the radiative recombination coefficient with p-type doping as determined by Nelson and Sobers[8] and the fit used here.

$$C = 3.83 \times 10^{-43} N_A^{0.78} cm^6/s \qquad \ldots(6\text{-}2)$$

For doping levels of below 1.9 x10^{18} /cm^3 where the above relationship intersects with the value reported by Strauss *et al.*[1086] for intrinsic GaAs (7 x10^{-30} /cm^3) C was taken to be constant.

6.3 Increasing quantum efficiency through doping

6.3.1 Effects of heavy zinc doping on structure and photoluminescence

As discussed in Chapter 5, the introduction of zinc can significantly alter the structure and morphology of GaAs nanowires grown by the VLS method. Figure 6-4 documents these effects along with changes in PL for heavy zinc doping (P_{DEZn}= 1.4 Pa), relatively high temperature (575°C) and low V/III ratio (1.4). Considering first the undoped nanowires, a pure wurtzite (WZ) structure is observed from the $[11\bar{2}0]$ zone axis transmission electron microscopy (TEM) images [Figure 6-4(a,b)] and corresponding selected area electron diffraction pattern (SADP) [Figure 6-4(c)]. In contrast to the vertical sidewalls of the undoped, pure WZ nanowires [Figure 6-4(d)], zinc doping is seen to induce sawtooth like faceting [Figure 6-4(f)] corresponding to the formation of a

twining superlattice (TSL) [Figure 6-4(g-i)].[247] This transition was further discussed in Chapter 5.

Figure 6-4 (e) further contrasts the room temperature (RT) PL spectra of a single unpassivated and undoped GaAs nanowire with that of an unpassivated but doped nanowire, where both are acquired under equal pump fluencies of 0.1 μW/cm^2/pulse (SEM images of the two nanowires characterized are presented in Figure 6-5). Emission from the undoped WZ GaAs nanowire is seen to peak at approximately 1.435 eV (865 nm) and give a full width at half-maximum (FWHM) of 44 meV. Some confusion remains in the literature regarding the expected peak position of WZ GaAs,[1089] and the value found here sits between those currently published, being 10 meV greater than[1090] one report and 10-25 meV less than[532, 637, 1091, 1092] several others. Unlike the majority of samples characterized elsewhere, the nanowires characterized here are unpassivated and therefore required relatively high pump powers which may have produced thermal

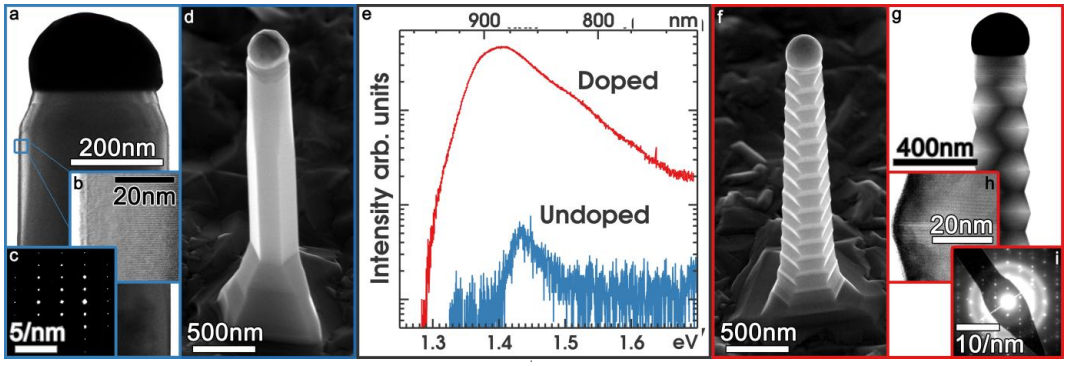

Figure 6-4 | Structure, morphology and photoluminescence (PL) of undoped and doped GaAs nanowires a) Bright field TEM image of an undoped GaAs nanowire. b) HRTEM image of the same undoped GaAs nanowire demonstrating the absence of stacking faults. c) Electron diffraction pattern of an undoped GaAs nanowire corresponding to a pure wurtzite structure. d) SEM image of an undoped GaAs nanowire. e) PL spectra collected from single undoped and doped GaAs nanowires under identical excitation and collection conditions. Emission from the doped nanowire is seen to be orders of magnitude brighter. f) SEM image of a doped GaAs nanowire. g) Bright field TEM image of a doped GaAs nanowire. h) HRTEM TEM image of a doped GaAs nanowire showing a single twin plane. i) Electron diffraction pattern of a doped GaAs nanowire corresponding to a twinned zincblende structure. All TEM images and diffraction patterns were collected from the $\langle 11\bar{2}0\rangle$ /$\langle 110\rangle$ axis.

effects. In comparison to the undoped WZ GaAs nanowires, emission from the doped ZB TSL structures is redshifted and significantly broader, peaking at approximately 1.402 eV (884 nm) and giving a FWHM of 110 meV. Redshift here to energies below that expected for ZB GaAs is related to bandgap narrowing and corresponds in magnitude to a doping density of approximately 10^{19} /cm^3. [1018, 1093, 1094]

Most strikingly, however, Zn doping is observed to radically increase the intensity of PL emission from GaAs nanowires. Comparing the two spectra collected under identical conditions [Figure 6-4(e)], the peak intensity of the doped nanowire is some two orders of magnitude brighter (~4700 counts) than that of the undoped nanowire (~40 counts). This difference is even greater (450x brighter) when integrated intensity is considered as emission from the doped nanowire is also spectrally broader. In addition to being brighter, the doped nanowire is also smaller. While the undoped nanowire has a tip diameter of 340 nm, a base diameter of 390 nm and a length of 2.06 μm the doped nanowire has a tip diameter of 299 nm, a base diameter of 350 nm and a length of 1.52 μm (Figure 6-5). Approximating their geometry as that of a truncated cone, the volume of the doped nanowire is thus 0.13 μm^2, some 40% less than that of the undoped nanowire which is 0.22 μm^2. If absorption is initially assumed to increase linearly with volume, the radiative efficiency of the doped nanowire can thus be approximated as over 750 times that of the undoped nanowire. (more sophisticated FDTD simulations were employed for later modelling as discussed in Section 6.2.4)

Previous studies have found doping to variously increase[517, 540] and decrease[1095] the intensity of PL emission from GaAs nanowires. Increases in emission intensity have

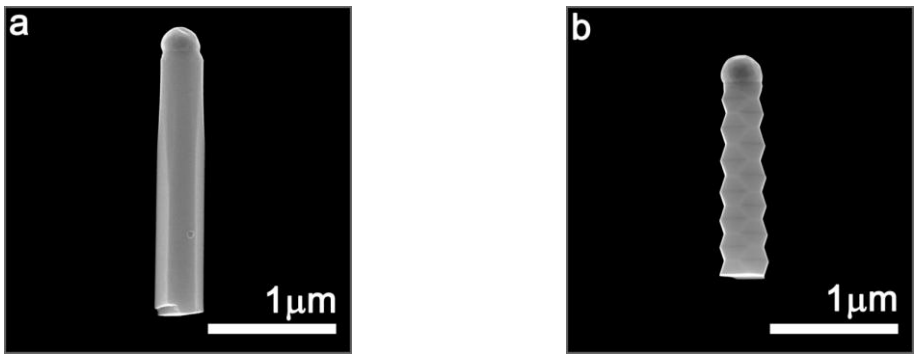

Figure 6-5 | SEM images of the nanowires from which the spectra presented in Figure 6-4(e) were collected. a) undoped wurtzite b) doped twinning superlattice type zincblende.

generally been linked to a mitigation of the carrier depletion arising from surface trapping.[517, 540] An action of band-bending in suppressing surface recombination has also been considered where doping was observed to lengthen minority carrier lifetime.[517]

6.3.2 The minority carrier lifetime of heavily zinc doped nanowires

6.3.2.1 Photoluminescence up-conversion

Despite exhibiting a relatively high radiative efficiency, the minority carrier lifetime of the doped nanowires was found to be only picoseconds in length. Figure 6-6(a) plots the results of up-conversion spectroscopy, mapping the emission intensity of the doped nanowires as a function of energy and time following excitation. The slight redshift and spectral narrowing seen here at early times are attributable to both thermalization and the decaying carrier density. Beyond this, emission remains centred around 1.395 eV (889 nm) and when integrated across time gives a spectrum closely resembling that seen by PL spectroscopy [Figure 6-4(e)]. The intensity of emission is further seen to decay rapidly, reducing by more than two orders of magnitude in less than 15 ps. When integrated in energy, this decay is well described by a single-exponential expression with a time constant of 3.44 ps [Figure 6-6(b)].

A lifetime of 3.44 ps accords well with previous studies of unpassivated GaAs nanowires[517, 1077] and represents one of the shortest carrier lifetimes reported for a semiconductor nanowire. Given the high surface to volume ratio of the nanowire geometry and the high rates of surface recombination known to characterize bare GaAs surfaces, the ultrashort lifetimes of bare GaAs nanowires have usually been associated with non-radiative surface recombination.[517, 1077] In a regime where surface recombination dominates the dynamics of recombination, the surface recombination velocity (SRV) of a nanowire may be related to the minority carrier lifetime τ_{mc} in the following manner:

$$\frac{1}{\tau_{\mathrm{mc}}} \cong \frac{4S}{D} \qquad \ldots(6\text{-}3)$$

where S is the SRV D is the nanowire diameter.[1096] Substituting a diameter of 300 nm into Equation 6-3 gives a SRV of 2.18 x10^6 cm/s. This value is similar to that calculated previously from measurements of minority carrier diffusion length in unpassivated Zn doped GaAs nanowires[517] and towards the higher end of the range expected for bare

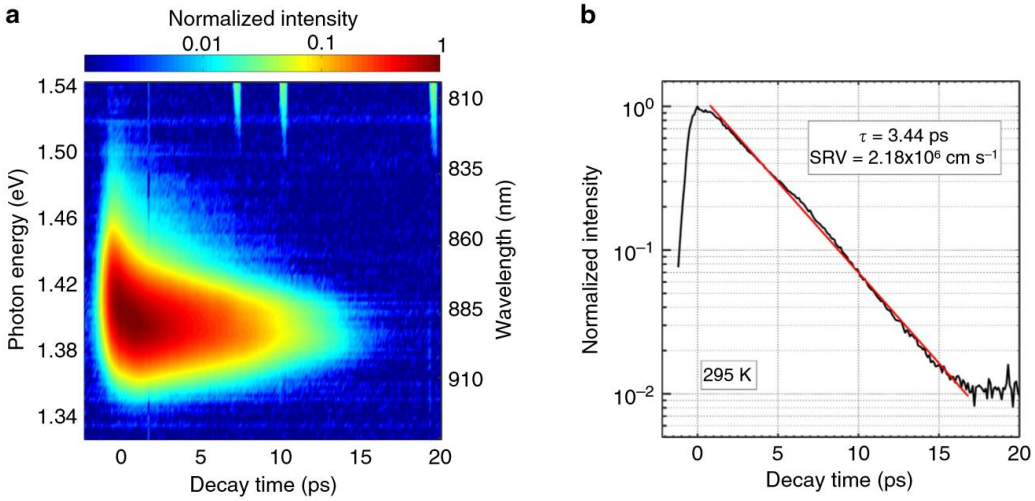

Figure 6-6 | Measurement of carrier lifetime by PL up-conversion a) Emission of doped GaAs nanowires in energy and time. b) Integration of (a) in energy, giving a lifetime of 3.44 ps and a surface recombination velocity of 2.18 x10^6 cm/s.

GaAs surfaces. Although the SRV will depend on multiple factors such as facet orientation and chemical termination, it is interesting to note that an increased SRV has previously been associated with doping.[1078, 1097]Given that the carrier lifetime measured here is both comparable to that of undoped GaAs nanowires[1077] and corresponds to a reasonable value of surface recombination velocity, it may be identified as a non-radiative lifetime dominated by surface recombination. Internal quantum efficiency (IQE), η_{IQE}, is related to both the non-radiative, τ_{nr}, and radiative lifetimes, τ_r, in the following manner:

$$\eta_{IQE} = \frac{\tau_{nr}}{\tau_{nr} + \tau_r} \qquad \ldots(6\text{-}4)$$

As surface recombination is the dominant recombination pathway in GaAs nanowires, previous efforts to increase the η_{IQE} of GaAs nanowires have focused on lengthening τ_{nr} through surface passivation. Here doping has however increased η_{IQE} without significantly affecting the non-radiative lifetime.

6.3.2.2 Transient Rayleigh scattering spectroscopy

The minority carrier lifetime of the doped nanowires was also measured by transient Rayleigh scattering (TRS)[1069]. Figure 6-7(a) plots the photomodulated polarisation

response, $\Delta R'/R' = \Delta(R_{\parallel} - R_{\perp})/(R_{\parallel} - R_{\perp})$, of a single doped TSL nanowire as a function of time and scattered wavelength. Delay time here reflects dispersion in the optics and source laser fibre with zero time being chosen to correspond with the onset of the fundamental band gap response at around 850 nm. The spin-orbit split-off band transition is further observed at around 700nm and appears more pronounced as R' approaches zero at shorter wavelengths. By considering the response at several particular wavelengths close to the band gap [as plotted in Figure 6-7(c)], the minority carrier lifetime is again observed to be picoseconds in length.

Beyond carrier dynamics, TRS spectroscopy also provides insight into band structure as carriers relax towards their equilibrium distributions following excitation.[1098] Figure 6-7(d) plots TRS spectra as a function of wavelength for several particular times following excitation. Given the minority carrier lifetime of approximately 1 ps, the response at 3 ps can be expected to represent carrier concentrations and temperatures

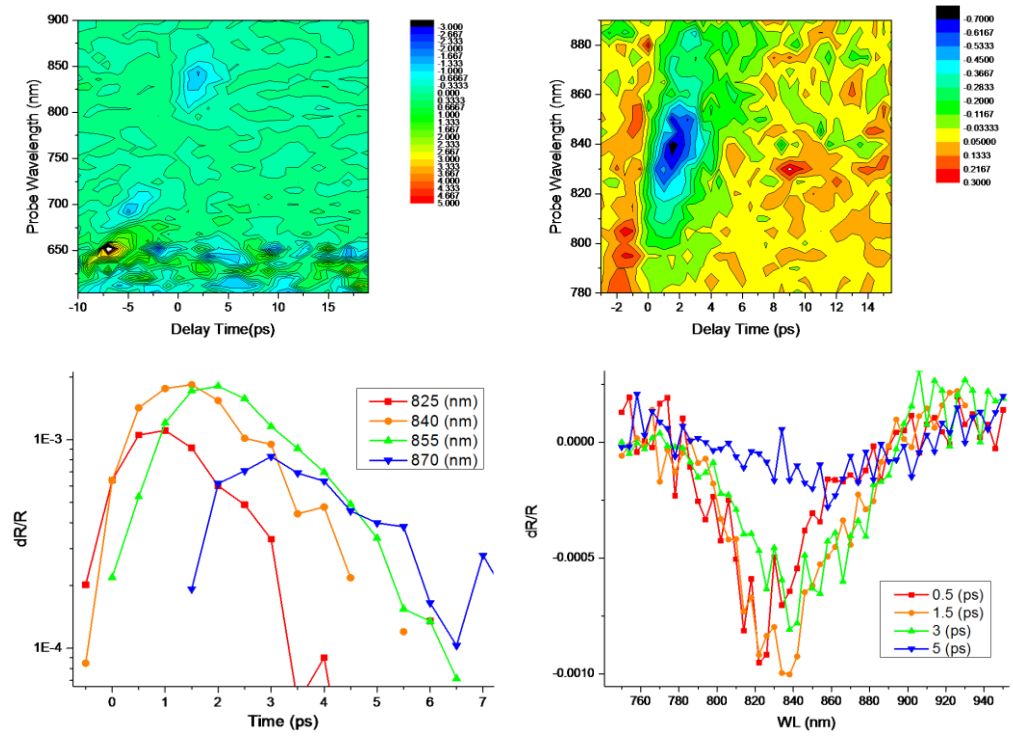

Figure 6-7| TRS characterisation of a single doped GaAs nanowire a) photomodulated polarisation response ΔR'/R' b) a magnified view of (a) close to the band gap c) time dependant photomodulated polarisation response ΔR'/R' for several wavelengths close to the band gap d) wavelength dependant photomodulated polarisation response ΔR'/R' for several times following excitation.

approaching equilibrium. The minimum of this spectrum is observed at around 850 nm (1.46 eV) and corresponds to the transition between valence and conduction band edges. Blueshift here from a wavelength of 872 nm (1.42 eV) in undoped GaAs may be attributed to heavy hole doping having shifted the Fermi level to a position within the valence band. Redshift of the fundamental band gap from 872 nm (1.42 eV) to approximately 880 nm (1.41 eV), as determined from the zero crossing point [Figure 6-7(d)], may further be attributed to band gap renormalisation due to doping.

Taken together the quasi hole Fermi level can thus be taken to be +50 meV. From this energy, a heavy hole doping concentration of at least 2.4 $x10^{19}$ $/cm^3$ and a light hole doping concentration of at least 1.5 $x10^{18}$ $/cm^3$ may be calculated for a temperature of 300K. Similarly, the late time displacement of the split-off band to conduction band transition of +10 meV is indicative of a doping level of at least 1.8 $x10^{18}$ $/cm^3$.

6.3.2.3 Low-Temperature time correlated single photon counting

The efficiency advantage obtained through doping continues at low temperature. Figure 6-8(a) shows PL spectra obtained from single doped and undoped nanowires at 6 K where emission has been normalized to an excitation fluence of 5 $\mu J/cm^2$/pulse. Emission from the doped nanowire is again seen to be orders of magnitude brighter than that from the undoped nanowire.

In all cases the lifetime of PL emission at low temperature was found to be less than the 80 ps system response of the time correlated single photon counting (TCSPC) setup. Such short lifetimes are consistent with previous measurements[1007, 1099-1102] of GaAs nanostructures at low temperature and indicate the continued dominance of a non-radiative recombination pathway. The surface recombination velocity of GaAs has been found[1101-1103] to remain relatively high (>1 $x10^5$ cm/s) at cryogenic temperatures and the lifetime of GaAs nanostructures has previously been linked to surface recombination at these temperatures.[1101, 1103-1105] In the case of InGaAs/InP wires, surface recombination velocity was found to vary as the square root of absolute temperature between 4 and 77 K. This suggests a capture cross section that is independent of temperature. Such behaviour can be expected for traps with a large capture cross section such as those present at the surface of unpassivated GaAs.[1106, 1107]

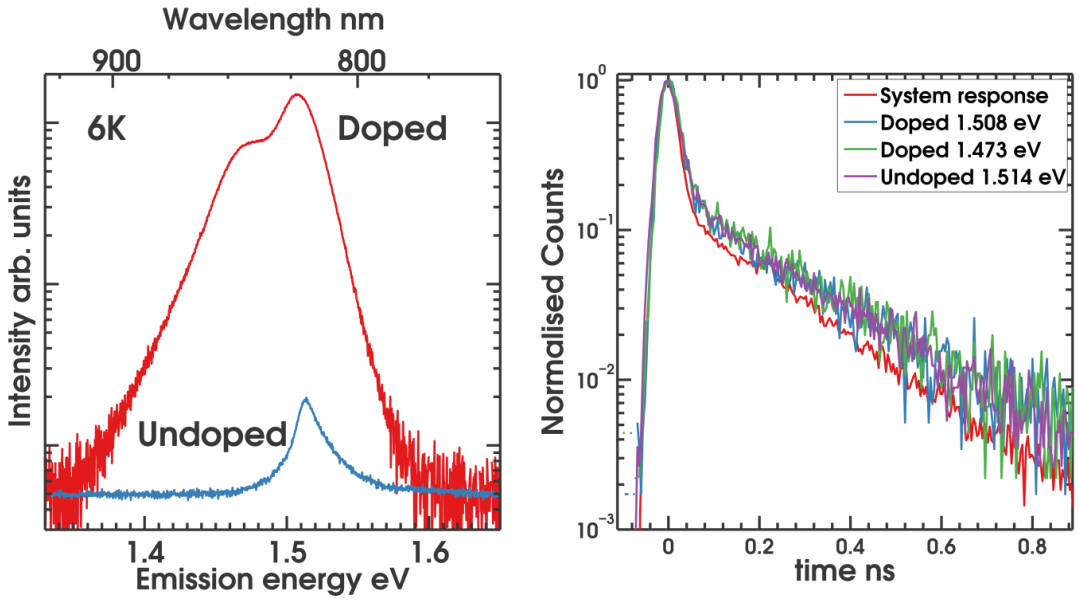

Figure 6-8 |Low temperature (6 K) PL of single nanowires a) Emission spectra normalized to an excitation fluence of 5 μJ/cm^2/pulse b) TCSPC measurements at the energies stated. Data is limited by the system response indicating lifetimes of less than 80 ps.

6.3.3 Effects of heavy zinc doping on quantum efficiency

6.3.3.1 Quantum efficiency as a function of excitation intensity for selected nanowires

In order to further investigate the observed increase in radiative efficiency with doping, Figure 6-9 plots the EQE of four individual nanowires along with corresponding SEM images and selected PL spectra. Considering firstly the undoped WZ GaAs nanowire [Figure 6-9(a,b)], band edge emission is again noted around 1.435 eV (865 nm) with a secondary, higher energy peak appearing at 1.531 eV (810 nm) for photoinjected carrier densities greater than 3 x10^{17} /cm^3. This second peak may be identified as the conduction band to light-hole transition[1091] and its appearance is a result of photoinduced band-filling as suggested by the broadening of emission towards higher energy at increased pump powers. Both peaks are seen to slightly redshift with increasing excitation. As discussed earlier, emission from bare, undoped GaAs nanowires is relatively weak and under the experimental conditions employed here a photoinjected carrier density of at least 1 x10^{17} /cm^3 was required in order to detect a PL signal Figure 6-9(e)]. At this excitation density the nanowire's EQE was determined to

be 0.008% rising to 0.05% for injected carrier densities of 1 x10^{18} /cm^3. (light blue triangles) Saturation of EQE at carrier densities beyond 1 x10^{18} /cm^3 is likely a result of several factors including photoinduced heating and the extensive band-filling.

Unlike emission from the undoped nanowire, that from the first doped nanowire considered here (X_{DEZn} = 1.4 x10^{-4}) [Figure 6-9 (c-d)], shows no appreciable change in lineshape with pump power and no secondary peak at higher pump powers. Doping is again noted to have produced redshift and broadening, with the peak in this case being centred at 1.391 eV (891 nm) across a FWHM of 80 meV. Of greatest significance, however, is the fact that a PL signal can be detected some two orders of magnitude earlier at a photoexcited carrier concentration of 1 x10^{15} /cm^3. The EQE at this carrier density is 0.65%, and in contrast to the behaviour of the undoped nanowires, remains approximately constant with increasing pump power. At the photoexcited carrier concentration where PL is first observed from the undoped nanowire (1x10^{17} /cm^3) the EQE of the doped nanowire is two orders of magnitude greater than that of the undoped

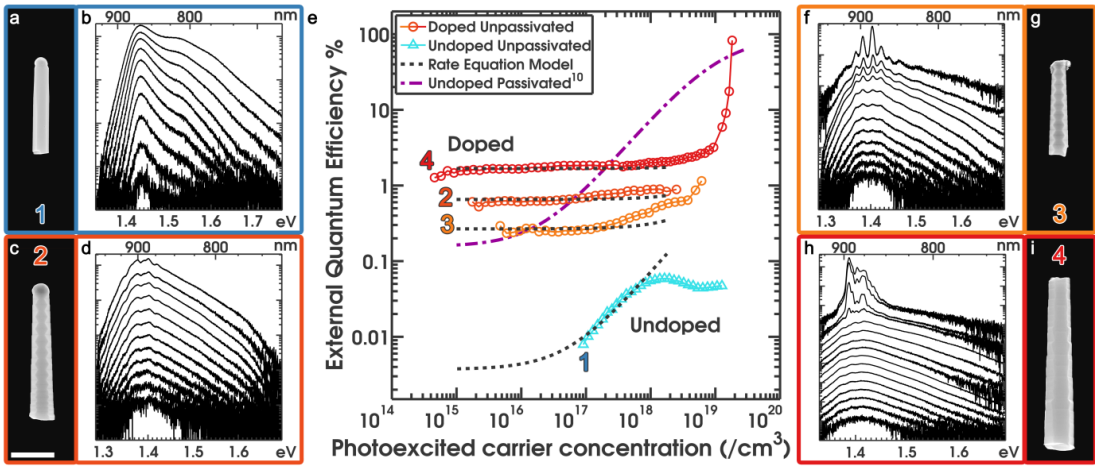

Figure 6-9 | Absolute quantum efficiency measurements a) SEM image of an undoped GaAs nanowire and b) corresponding power dependent PL spectra. c) SEM image of a doped TSL GaAs nanowire and d) corresponding power dependent PL spectra. e) External quantum efficiency of the nanowires shown in (a), (c), (g) and (h). Fits of rate equation modelling are also plotted along with the modelled performance of undoped AlGaAs passivated GaAs nanowires previously shown to lase at RT[25] f) Power dependent PL spectra of a doped TSL GaAs nanowire and g) a corresponding SEM image. h) Power dependent PL spectra of a doped aperiodically twinned GaAs nanowire and i) a corresponding SEM image.

nanowire. Until this carrier density, the EQE of the doped nanowire is also greater than that of AlGaAs passivated GaAs nanowires previously shown to lase.[25] (dash-dotted purple line)

Similarly enhanced values of EQE were found across all the doped (X_{DEZn} = 1.4 x10^{-4}) nanowires investigated regardless of their diameter, morphology or even crystal phase purity. Figure 6-9 presents two further doped nanowires grown under the same reactor conditions as wire 2 [Figure 6-9 (c-d)]. The first is a TSL structure [Figure 6-9 (g)] grown at a standard areal density while the second is a highly defective ZB structure Figure 6-9 (i)] grown at a lower areal density (see Section 5.3.2). The EQE of both nanowires is seen to be around 1% [Figure 6-9 (e)] remaining relatively constant with pump power until the highest of excitation intensities. That the EQE of these two very morphologically different nanowires is comparable, confirms that the changes in crystal phase and morphology observed with doping are not responsible for the increase in IQE. Rate equation fits to the data are discussed in section 6.4.2.

6.3.3.2 Quantum efficiency as a function of diameter

Figure 6-10 plots EQE versus nanowire diameter for both undoped and heavily doped

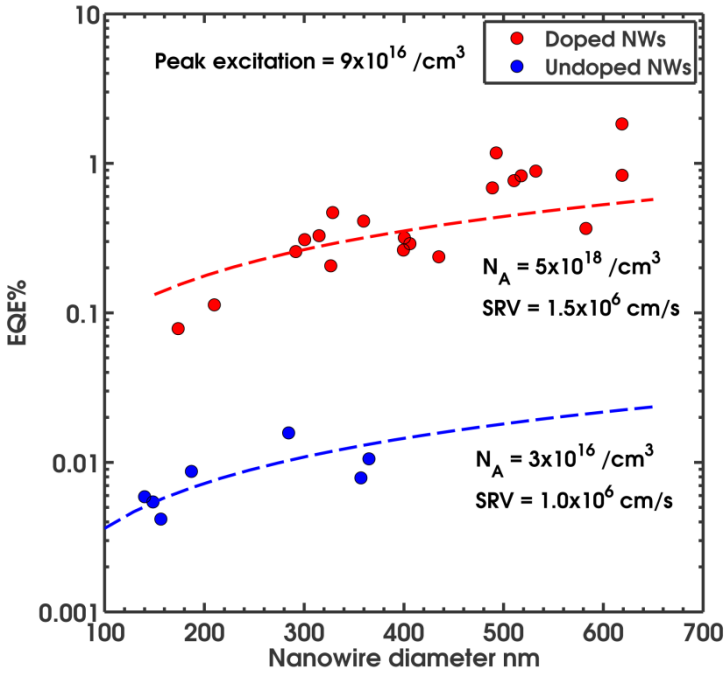

Figure 6-10 | Measured EQE as a function of diameter for doped and undoped nanowires at a peak photoexcitation of 9 x10^{16} /cm^3. Dashed lines present fits of Equation 6-5 with the parameters shown.

nanowires (X_{DEZn} = 1.4 x10^{-4}) at a photoexcitation density of 9 x10^{16} /cm^3. Both datasets show EQE to increase with diameter which is expected where non-radiative surface recombination is the dominant recombination pathway. Combining Equations 6-3 and 6-4, this relationship is further expected to be linear:

$$\eta_{IQE} = \frac{D}{4S} * \frac{1}{\tau_{rad}} = C_1 D \qquad \ldots(6\text{-}5)$$

where C_1 is a constant. Dashed lines show fits of Equation 6-5 to the experimental data. Deviation of the doped nanowire dataset towards a more superlinear relationship may be related in this instance to a variation in effective doping density with varying shell thickness. Unlike previous work by Demichel *et al.*,[1007] the observed increase is steady and presents no evidence for the presence of significant surface Fermi-level pinning across the experimental regime considered.

6.4 Mechanism and modelling

6.4.1 Mechanism

The mechanism by which doping acts to increase IQE may be understood in terms of a reduction in radiative lifetime through doping. As a first approximation, carrier recombination may be considered in terms of non-radiative SRH type and radiative bimolecular recombination:

$$\left(\frac{dN}{dt}\right)_{rad} = -AN - BN(N + N_A) \qquad \ldots(6\text{-}6)$$

where N is the photoexcited carrier density, N_A is the ionized acceptor density and A and B are the non-radiative and radiative recombination coefficients respectively. Inspecting Equation 6-6, it is clear that absolute value of the second term is an increasing function of N_A, and as such doping will act to increase the rate of radiative recombination. Further considering the rate of radiative recombination alone, where N_A dominates the term $(N + N_A)$, the time constant describing radiative recombination, τ_r, will be inversely proportional to N_A (for $N_A \gg N : \tau_r \simeq 1/BN_A$). Recalling Equation 6-4, however, where the non-radiative lifetime dominates, as is the case for our unpassivated nanowires, τ_r will also be inversely proportional to IQE (for $\tau_r \gg \tau_{nr} : \tau_r \simeq \tau_{nr}/\eta_{IQE}$). It may therefore be expected that in a regime where the photoexcited carrier density is lower than the ionized impurity density and the non-radiative lifetime

is shorter than the radiative lifetime, IQE will be directly proportional to N_A (for $N_A \gg N$ & $\tau_r \gg \tau_{nr}$: $\eta_{IQE} \propto N_A$). This derivation accords well with our experimental findings and identifies a reduction in radiative lifetime as the mechanism by which doping acts to increase IQE.

Returning to Equation 6-4, it is noted that where $N \gg N_A$ the rate of radiative recombination will increase as N^2 while that of non-radiative recombination increases as N. In this way, IQE will increase with pump power as is observed for the undoped nanowires. Where the reverse is true, however, and N_A dominates the term $(N + N_A)$, both the radiative and non-radiative recombination rates will increase equally as N. In this scenario IQE will remain constant with pump power as is observed for our doped nanowires. Thus doping is expected to both increase radiative efficiency and alter the power dependence of this parameter.

6.4.2 Rate Equation Modelling

As the pulse duration (approximately 300 fs) was significantly shorter than the decay process (several ps), and the interval between pulses (50 ns) significantly longer, recombination can be considered as decay from an initial excited carrier concentration, N_0, by non-radiative, radiative and Auger loss terms:

$$\frac{dN}{dt} = -AN - BN(N + N_A) - CN(N + N_A)^2 \qquad \ldots(6\text{-}7)$$

where N is the time dependent carrier density, N_A is the ionised acceptor density and A, B and C are the non-radiative, radiative and Auger recombination coefficients respectively. The Auger recombination term is included here as some experiments employed high maximum pump powers and/or high doping densities. Solving Equation 6-7 for a given initial photoexcited carrier concentration, N_0, surface recombination velocity (A*D/4) and acceptor concentration, N_A gives IQE:

$$\eta_{IQE} = \frac{\int BN(t)(N(t) + N_A)dt}{N_0} \qquad \ldots(6\text{-}8)$$

Figure 6-11 plots solutions to Equation 6-8 for GaAs nanowires of 300 nm with a SRV of 2.2×10^6 cm/s. Each curve represents a different doping density. At low photoexcitation it is apparent that IQE increases with doping density from around

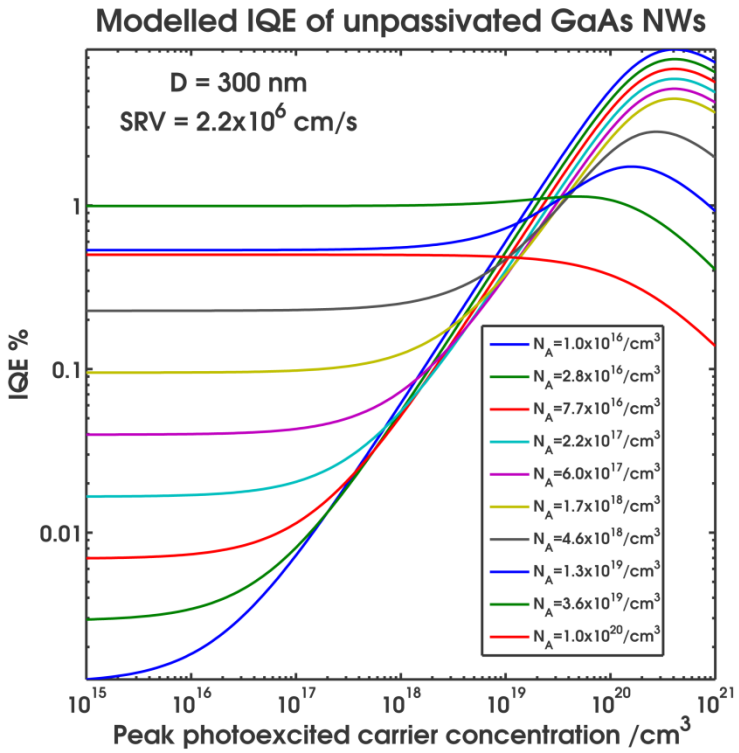

Figure 6-11 | Modelled variation of IQE with peak excitation for variously doped GaAs nanowires of 300 nm diameter characterised by a surface recombination velocity of 2.2 x10^6 cm/s.

0.001% for doping levels of 10^{16} /cm^3 to a peak of 1% for doping levels of 3.6 x10^{19} /cm^3.

The increase in IQE with doping may be attributed to the second term of the differential equation governing recombination, $BN(N + N_A)$, and represents a decreasing radiative lifetime with doping. While $N_A \gg N$, IQE remains constant as the rates of non-radiative, ($\cong AN$), and radiative, ($\cong BN_AN$), recombination both increase linearly with photoexcited carrier concentration. Beyond these pump powers the rate of radiative recombination begins to increase as the square of the photoexcited carrier concentration, ($\cong BN^2$), and IQE increases steadily with excitation.At the highest of pump powers Auger recombination becomes significant and IQE is reduced. The threshold for this efficiency droop shifts to lower pump powers with increasing doping but is only significant at extremely high photoexcited carrier concentrations, >10^{20} /cm^3; well beyond those that were achieved experimentally.

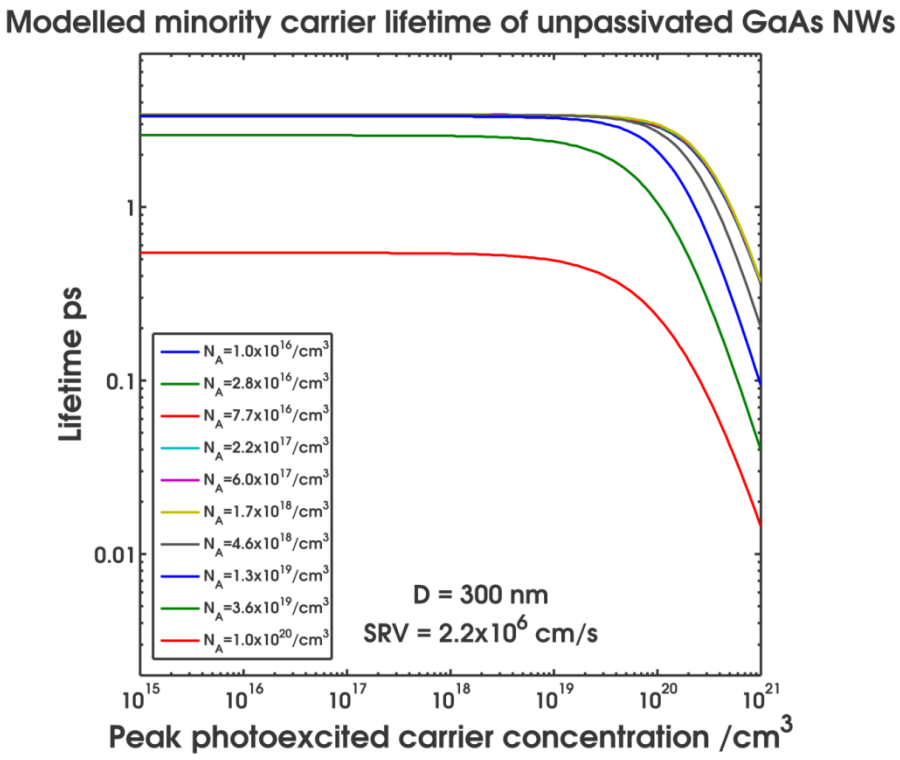

Figure 6-12 | Modelled variation of minority carrier lifetime with excitation for variously doped GaAs nanowires of 300 nm diameter characterised by a surface recombination velocity of 2.2 x10^6 cm/s.

Although peak efficiency is highest (≈9%) for the lowest of doping concentrations, 10^{16} /cm^3, the IQE of this nanowire does not exceed the IQE of a nanowire doped to 3.6 x10^{19} /cm^3 until photoexcited carrier concentrations in excess of 2 x10^{19} /cm^3, a regime where thermal effects are likely to be significant. Importantly, the low excitation increase in IQE with doping shows a peak at around 3.6 x10^{19} /cm^3 beyond which Auger recombination becomes significant with the IQE of a nanowire doped to 1 x10^{20} /cm^3 seen to be less than that of the nanowire doped to 3.6 x10^{19} /cm^3 for all pump powers. Equation 6-7 may also be used to model variation in minority carrier lifetime with doping. Taking again a diameter of 300 nm and a SRV of 2.2 x10^6 cm/s, Figure 6-12 plots the time to achieve a carrier concentration of N_0/e as a function of excitation intensity and doping density. At lower pump powers lifetime is SRV limited (≈3.5 ps) for all but the most highly doped nanowires (>3.6 x10^{19}). Beyond photoexcitation intensities of approximately 2 x10^{19} /cm^3, Auger recombination becomes significant and carrier lifetimes are reduced.

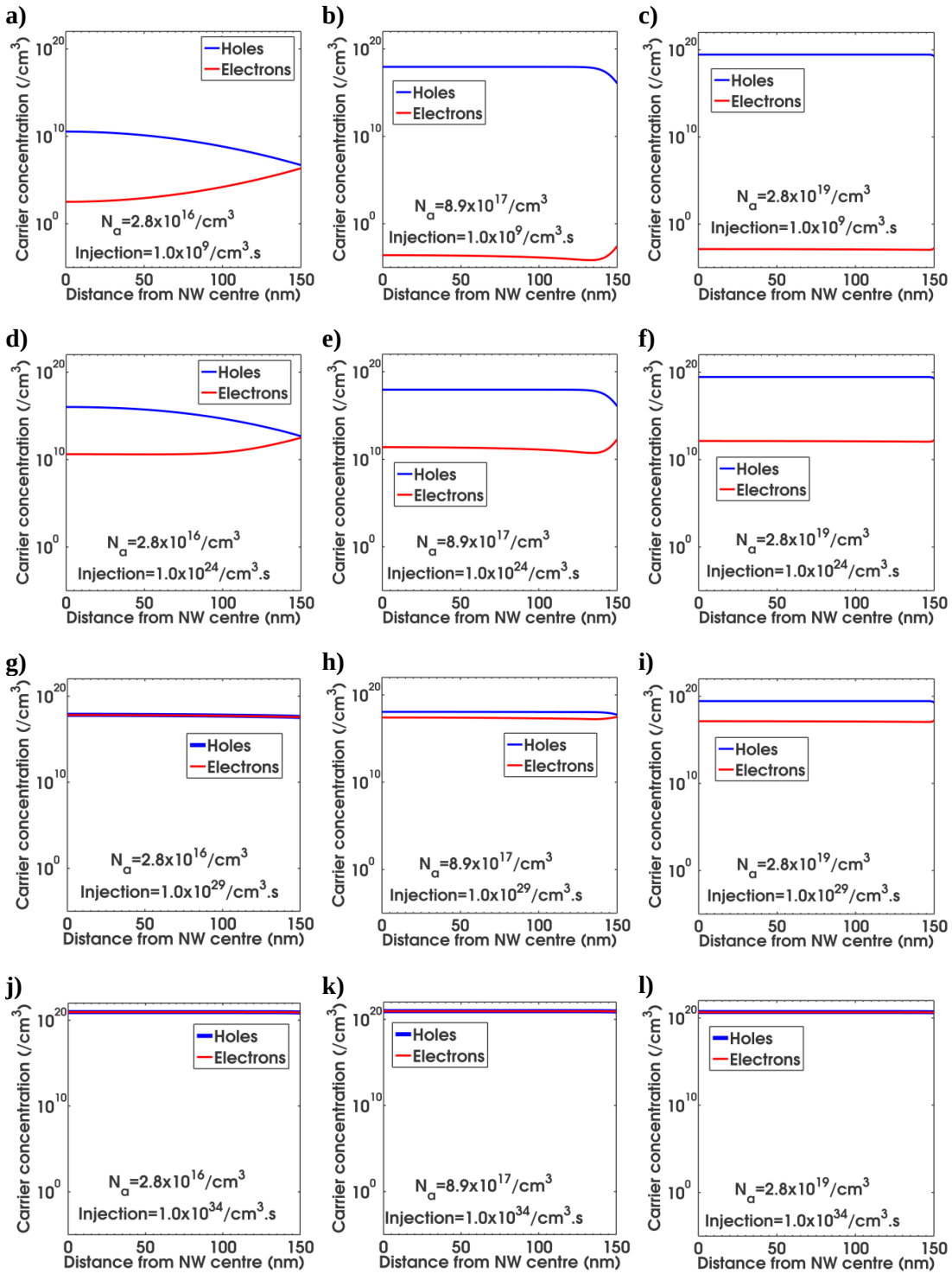

Figure 6-13 | Modelled carrier concentration along the radial direction for various doping densities and carrier generation rates in 300 nm diameter unpassivated GaAs nanowires. Note that band bending is reduced by both increased doping and increased rates of carrier generation.

6.4.3 Finite volume modelling

Unpassivated GaAs is known to be characterised by a high concentration of surface trap states producing surface band-bending and carrier depletion.[1073, 1074, 1108] These effects have been reported to significantly affect emission from unpassivated GaAs nanowires,[1007] will vary with excitation intensity and are not considered by the rate equation analysis discussed in Section 6.4.2.

Figure 6-13 presents finite volume modelling (see Section 6.2.5 for method details) of surface depletion in 300 nm diameter unpassivated GaAs nanowires. The effect of increasing doping density is shown left to right and increasing excitation intensity top to bottom. Beginning with the lowest of doping densities and excitation powers [Figure 6-13(a)], variation in carrier concentration across the entire nanowire profile indicates full depletion. As the excitation intensity is increased, the depletion width is firstly reduced [Figure 6-13(d)], before at the highest of pump powers flat band conditions are approached [Figure 6-13(j)]. With a higher doping density, depletion is only partial at

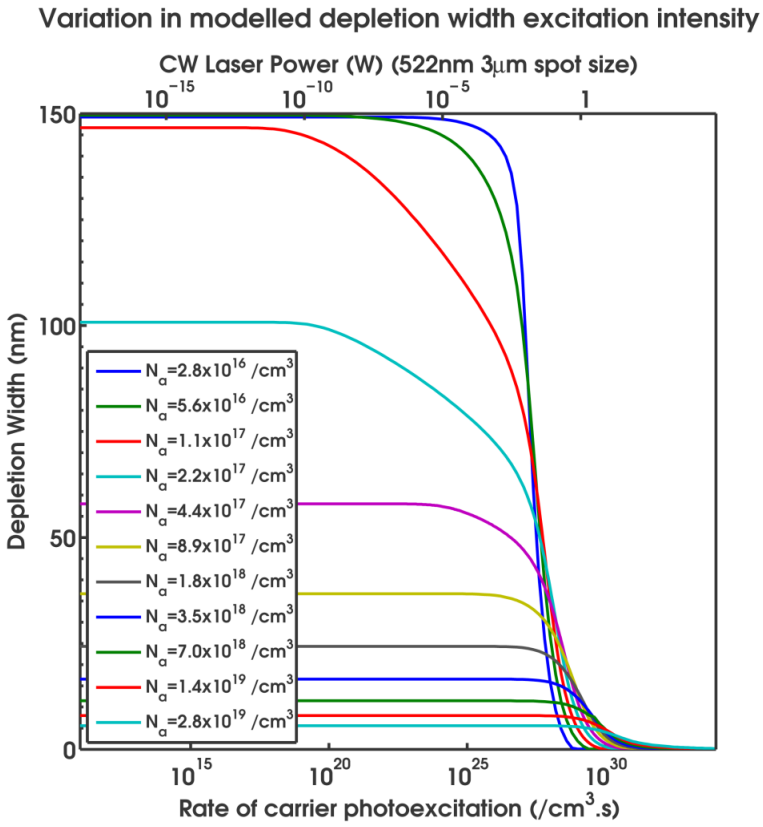

Figure 6-14 | Modelled depletion width (electric field strength of > 0.1 kV/cm) as a function of carrier generation rate for various doping densities.

low excitation [Figure 6-13(b)] and flat-band like conditions are reached at lower excitation intensities. At the highest of doping densities shown, surface band bending is negligible even for the lowest of excitation powers [Figure 6-13(c)]. Considering Figure 6-13 in its entirety, it is apparent that both heavy doping (right of figure) and high excitation (bottom of figure) act to reduce the spatial extent of band bending.

Figure 6-14 plots the spatial extent of surface depletion (defined here as an electric field strength of > 0.1 kV/cm) as a function of photoexcitation intensity for various doping densities. At relatively low photoexcitation intensities, full depletion is observed for lower doping densities (2.8×10^{16} /cm^3, 5.6×10^{16} /cm^3), and only minor depletion (several nms) for higher doping densities (2.8×10^{19} /cm^3). Around a photoexcitation intensity of 1×10^{28} /cm^{3}s the spatial extent of carrier depletion is seen to dramatically reduce in all cases as surface band-bending is screened by the photoinduced carriers. This occurs at higher photoexcitation intensities for higher doping densities as the electric field strengths associated with the space charge region increase with doping.

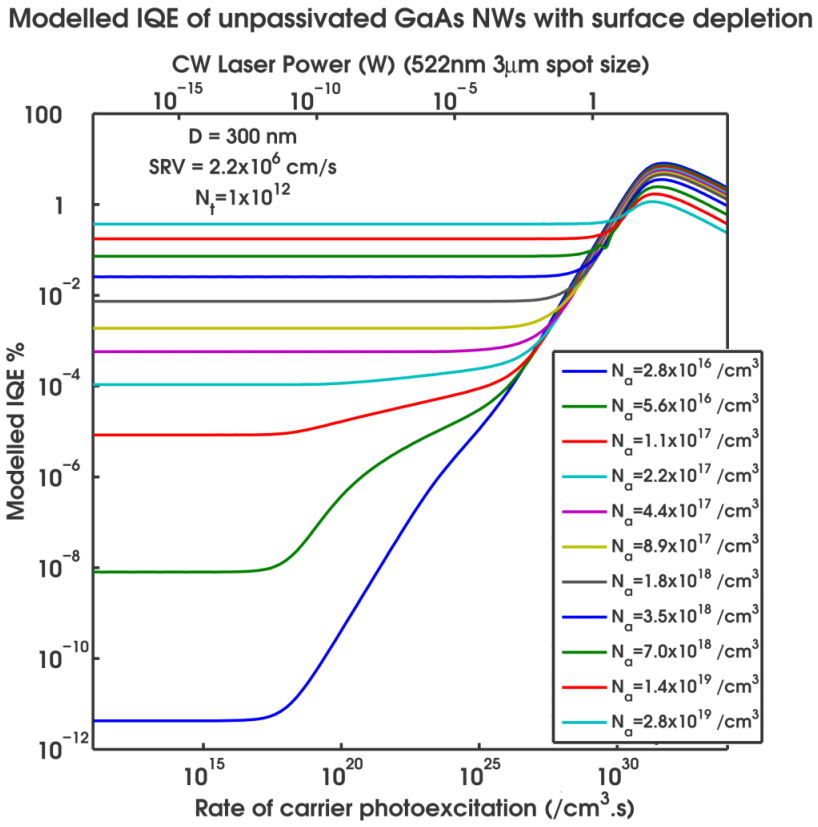

Figure 6-15 | Modelled variation of IQE with carrier generation rate for various doping concentrations.

The x-axis at the top of Figure 6-14 relates the photoexcited carrier densities to equivalent powers of a 522 nm, 3 μm spot-size continuous-wave (CW) pump laser. In most cases the depletion width is not seen to significantly alter until pump powers of around 1 mW suggesting that depletion will be significant across the usual range of powers accessed by CW pumping.

Figure 6-15 plots IQE of as a function of photoexcitation for various doping densities. As was observed for the rate-equation modelling presented in Figure 6-11, IQE remains constant at low excitation before increasing beyond a given excitation threshold level towards a peak value at high excitation. This behaviour may be again related to magnitude of the photoexcited carrier density relative to the background doping density.(See section 6.4.2)

Despite strong qualitative similarities between the results of the two modelling methods, a clear contrast is apparent at low photoexcitation intensities where surface depletion is most significant. Here, the rate equation modelling finds heavy doping ($4x10^{19}$ /cm^3) to

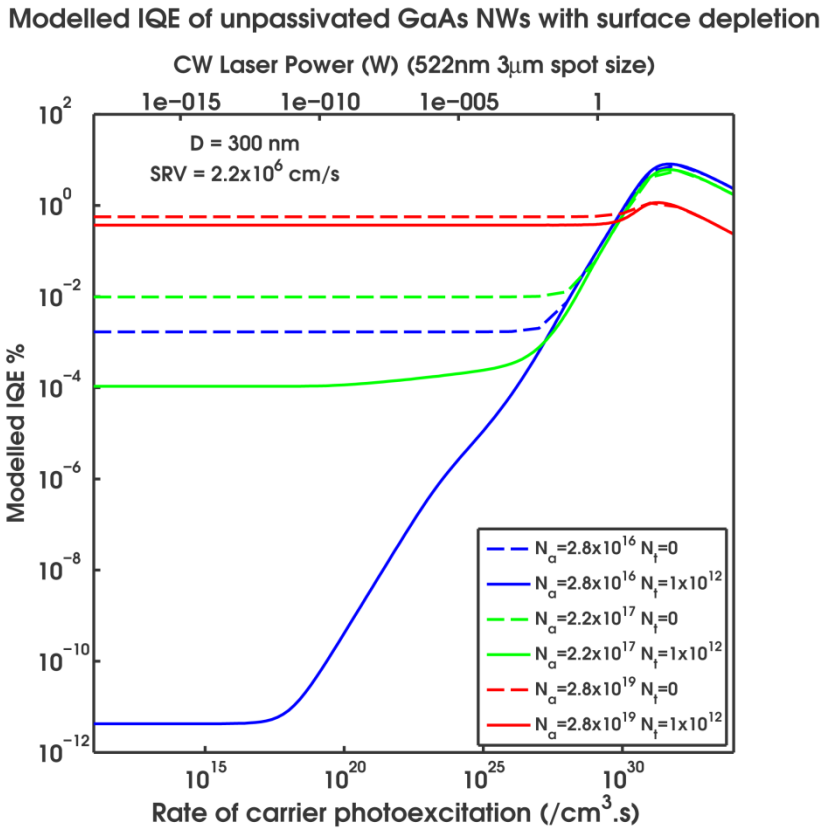

Figure 6-16 | Modelled variation of IQE with carrier generation rate with (N_t=1 x10^{12} /cm^2) and without (N_t=0 /cm^2) surface charge trapping.

increase low excitation IQE by only 3 orders of magnitude (Figure 6-11), while the finite volume modelling finds an increase of closer to 11 orders of magnitude. Surface depletion acts to significantly reduce IQE as the rate of radiative recombination is quadratic in carrier concentration while that of non-radiative recombination is linear (Equation 6-7). As surface depletion is screened by photoexcitation the two approaches converge.

To illustrate the regimes where rate equation analysis can be considered to provide a good estimate of IQE, Figure 6-16 compares finite volume modelling of IQE both with (N_t=1 x10^{12} /cm^3) and without (N_t=0 /cm^3)surface depletion effects. For the lowest doping density of 1.1x10^{16} /cm^3, the inclusion of surface trapping is seen to reduce IQE by around 8 orders of magnitude at low pump powers. At higher pump powers approaching 1mW CW surface depletion effects become negligible and the two results converge. For the highest doping density of 2.8 x10^{19} /cm^3, both results are seen to be similar across all pump powers but only fully converge at a higher rate of photoexcitation relative to the undoped case. The rate equation modelling can thus be expected to provide a good estimate of IQE at high excitation intensities or high doping concentrations.

6.4.4 Fitting the experimental data

Given the nanoscale dimensions of the emitters, self absorption may be neglected and IQE equated with EQE. On this understanding Equation 6-8 was fit to the experimental data presented in Figure 6-9 to give SRV (A*D/4) and N_A. The rate equation analysis is valid here as the data was either collected at high photoexcitation intensity or from highly doped nanowires. Fitting only the rising portion of the dataset collected from the undoped nanowire, gives a SRV of 2.0 x10^6 cm s^{-1}. This velocity is very similar to that determined earlier for the doped nanowires and suggests that p-type doping with zinc does not significantly alter SRV. Taking the SRV found by upconversion and fitting the remaining EQE datasets gives ionised dopant concentrations of 8.4 x10^{18} cm^{-3}, 3.6 x10^{18} cm^{-3} and 2.5 x10^{19} cm^{-3} for the doped nanowires shown in Figure 6-10(c), Figure 6-10(g) and Figure 6-10(i), respectively. Previous nanowire studies have found dopant incorporation to be higher in the radial rather than axial direction[220, 239] and it is therefore interesting to note that the dopant concentrations found here scale with nanowire diameter. (see Section 6.3.3.2)

6.5 Lasing from unpassivated GaAs nanowires

Returning to the power dependent spectra presented for each of the doped nanowires [Figure 6-10(d,f,h)], regular modulations are noted in all spectra. In the case of the last two doped nanowires [Figure 6-10(f,h)], the modulations become increasingly

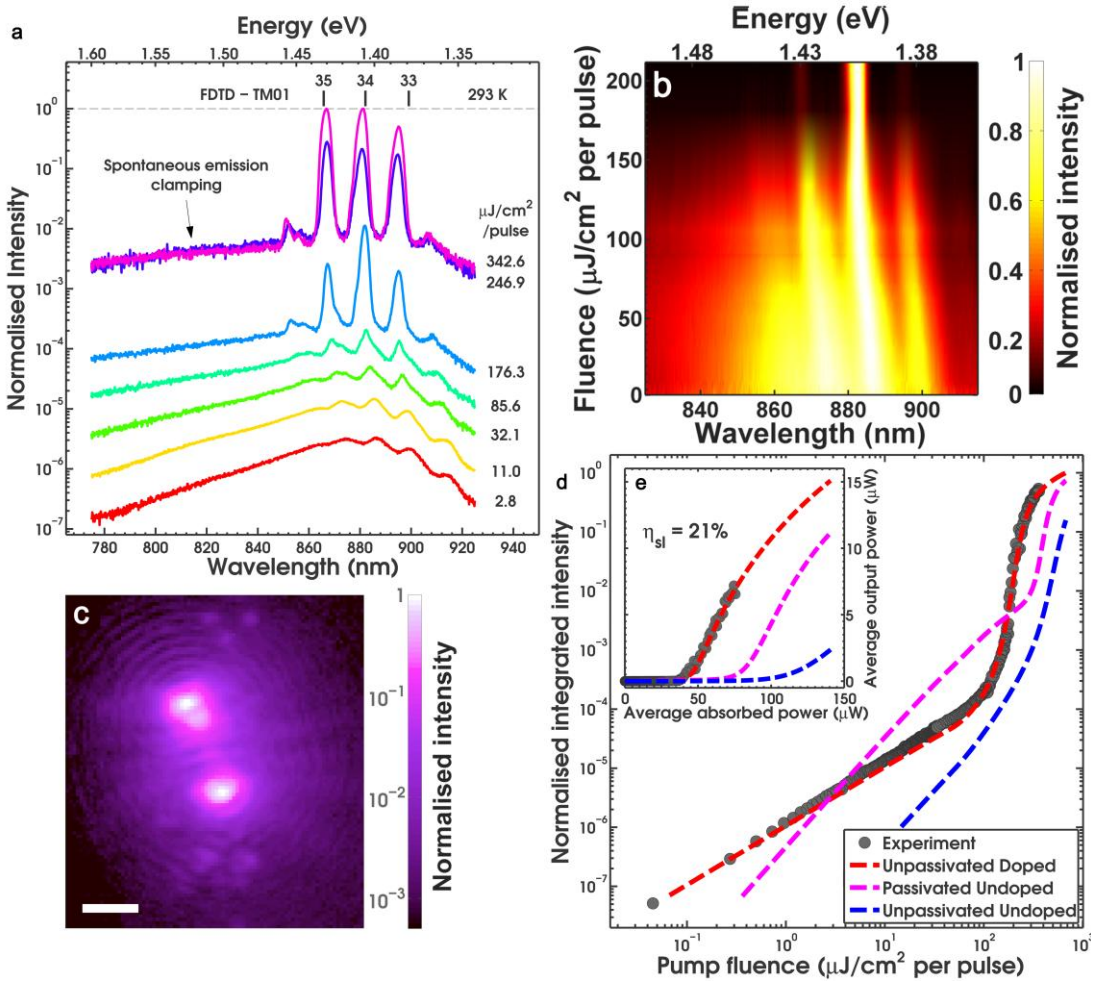

Figure 6-17 | RT characterisation of an unpassivated doped GaAs nanowire nanolaser. a) Power dependant spectra. Note the appearance of ASE from the lowest of pump intensities and the clamping of spontaneous emission at higher pump intensities. b) Normalised spectral map across pump intensities close to threshold c) Logarithmic map of a composite optical image showing the lasing nanowire above threshold d) Logarithmic plot of integrated intensity of emission as a function of pump power. The clear non-linearity here represents a transition to lasing. Also shown is a fit to the experimental data and modelling for undoped nanowires. Normalisation here is by the highest intensity of the modelled fit e) linear scale plot of (d) revealing slope efficiency.

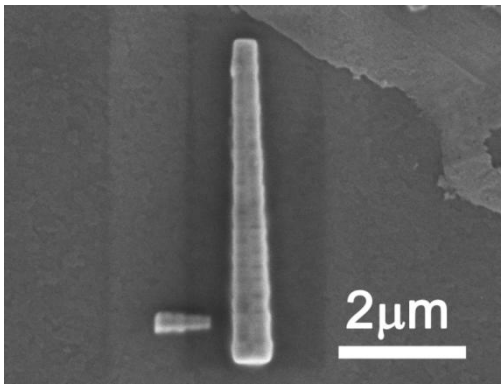

Figure 6-18 | An SEM image of a mixed phase doped GaAs nanowire from which lasing was observed as characterised in Figure 6-17 above.

prominent at higher pump intensities. Taken together, these observations are suggestive of amplified spontaneous emission (ASE) arising from optical feedback within the nanowire cavity.[114, 116, 748] Unlike previous work however,[25, 727] ASE is observed here from relatively low pump intensities. This is because the threshold for ASE scales directly with the radiative lifetime of a material[1109] which in our case has been reduced by several orders of magnitude by doping.

Around the same photoexcited carrier concentration (~1.0 x10^{19} cm^{-3}) that ASE becomes more prominent in the spectra of nanowire 4 [Figure 6-10(h)] a superlinear increase in EQE is also noted [Figure 6-10(e)]. This superlinear increase marks a transition from spontaneous emission to lasing and was observed at RT for many of the doped nanowires analysed. Figure 6-17 investigates this transition and the subsequent laser action of one particular doped nanowire (an SEM image of this nanowire is shown in Figure 6-18). Considering first the emission from this nanowire at a relatively low pump power (2.7 μJ cm^{-2} per pulse), a broad spectrum (full width at half-maximum (FWHM) ~100 meV) centred around 1.407 eV (881 nm) is noted [Figure 6-17 a)]. Despite the low pump intensity, modulations corresponding to ASE (Δλ ~12 nm, FWHM ~6 nm) are clearly apparent. Initial increases in excitation produce spectral blueshift [Figure 6-17(a,b)] which can be attributed to a carrier induced change in refractive index. On a log-log plot, integrated intensity rises linearly with pump power in this low excitation regime [Figure 6-17(d)] as is expected for spontaneous emission (SE). Optical images collected in this regime show emission to be uniform along the length of the nanowire (Figure 6-19)

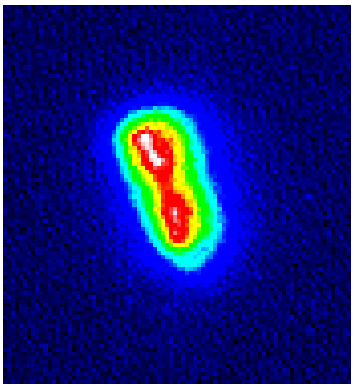

Figure 6-19 | An optical image of emission from the nanowire below threshold.

From a pump fluence of approximately 65 μJ cm^{-2} per pulse, the peaks corresponding to ASE are seen to experience gain, spectrally narrowing and increasing in intensity more rapidly than the broad SE background. This process becomes especially pronounced around a pump fluence of 165 μJ cm^{-2} per pulse as the lasing threshold is approached. Around threshold, integrated intensity is seen to exhibit a superlinear relationship to pump fluence. For pump fluences greater than ~200 μJ cm^{-2} per pulse the broad SE background becomes clamped and lasing is observed from three cavity modes located at 867, 881, 895 nm (FWHM ~2.6 nm). The relationship between integrated intensity and pump power is again linear in this regime with the gradient here corresponding to a slope efficiency of 21% [Figure 6-17(e)]. An optical image of the nanowire lasing [Figure 6-17(c)] shows emission to be predominantly from the ends of the nanowire in the manner of a Fabry-Pérot type cavity. The observed interference fringes indicate that the emission from these two ends is spatially coherent.

6.6 Modelling doped nanowire lasers

6.6.1 Lasing mode and threshold gain

The lasing mode of the nanolaser characterized in Figure 6-17 was identified by calculating the mode with the minimum threshold gain requirement. Finite-difference time-domain (FDTD) simulations (see Section 6.2.4), were used to calculate the mode confinement factor and end reflectance of each of the modes supported by the nanowire. The threshold gain requirement of each mode was then found from the following expression:

$$\Gamma g_{th} \sim \frac{1}{L} \ln \frac{1}{R} \qquad \ldots(6\text{-}9)$$

where Γ is the mode confinement factor, g_{th} is the threshold gain, L is the cavity length and R is the geometric mean of the mode reflectance from each end facet. Values of 3390, 3450, 1140, 2570, 2480, 1050, 1700 and 1600 cm^{-1} were calculated for the $HE11_a$, $HE11_b$, TE01, $HE21_a$, $HE21_b$, TM01, $EH11_a$, and $EH11_b$ modes, respectively. The relatively low threshold gain requirements of the TE01 and, in particular, TM01 modes suggest that the lasing spectrum observed in Figure 6-17 was from one of the these two modes.

6.6.2 Cavity spectrum

To further verify the identity of the lasing mode observed in Figure 6-17, both TE01 and TM01 mode cavity spectra were calculated for comparison with the experimental spectrum. Excitation was by a dipole source orientated and positioned along the axis of the nanowire in order to excite the appropriate guided modes.[1070] Cavity spectra [shown for the TM01 resonant modes in Figure 6-20(a)] were then calculated from the Fourier transform of the electric field strength as measured at various locations within the nanowire. The cavity spectrum found for the TM01 guided modes provided the best fit

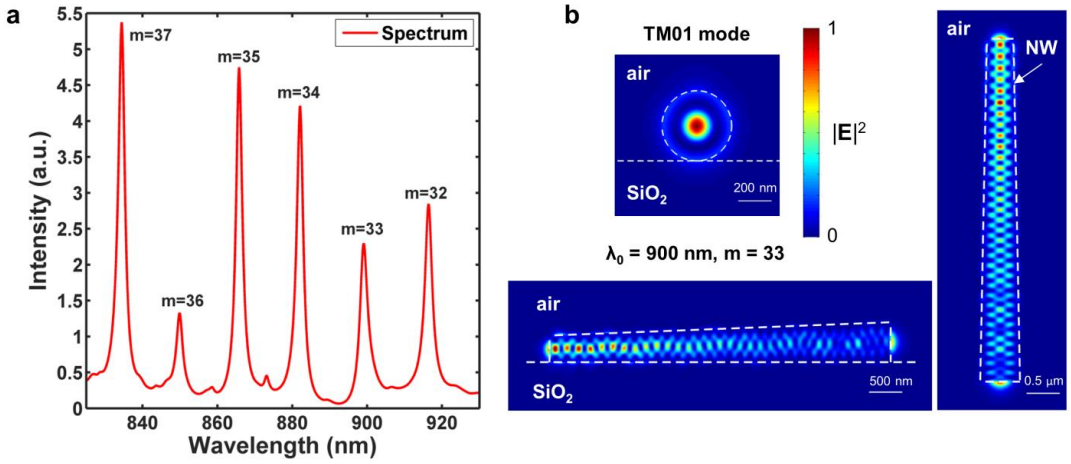

Figure 6-20 | FDTD simulation. a) Cavity spectrum calculated from FDTD simulation, showing the spectral position of TM01 resonant modes supported in the nanowire laser. The axial order (m) is denoted above each peak. b) Electric field intensity profiles in the cross-section of the nanowire at wavelength of 900 nm. The field profiles show that the resonant mode at 900 nm corresponds to the TM01 mode with m=33.

to the experimental data.

Figure 6-20(b) shows the electric field intensity profile in the cross-section of the nanowire at wavelength of 900 nm, corresponding to the spectral position of one of the resonant modes. The field profile in the cross-section transverse to the nanowire axis resembles the profile of the TM01 guided mode and the field profiles in the cross-sections parallel to the nanowire axis show that the resonant mode has an axial order (m) of 33. The mode type and axial order of the resonant modes at other spectral positions was identified from field profiles in a similar way. The axial order of the TM01 resonant modes is denoted above the peaks in Figure 6-20(a). As shown in Figure 6-17, modes of axial order 33-35 provide a close match to the experimentally observed lasing peaks. The simulated Q factor for these modes (Q≈250-300) is furthermore in good agreement with the experimentally measured FWHM.

Analysis of the simulated cavity spectrum also enables the group index of the lasing mode to be estimated. The wavelength separation between resonant modes in a Fabry-Pérot type cavity is given by:

$$\Delta\lambda = \frac{\lambda^2}{2Ln_g} \qquad \ldots(6\text{-}10)$$

where λ is the wavelength, L is the cavity length and n_g is the group index of the mode. Using Equation 6-10 n_g of the mode at 883 nm is estimated to be 4.44.

6.6.3 Effect of doping on optical gain

Optical gain in a direct band gap bulk semiconductor can be modelled using the following equation:

$$g(\hbar\omega) = \frac{\pi e^2}{n_r c \varepsilon_0 m_0^2 \omega} |M|^2 \int \rho_r(E)\big(f_c(E) - f_v(E)\big)\,\ell(E - \hbar\omega)\,dE \qquad \ldots(6\text{-}11)$$

$$\ell(E - \hbar\omega) = \frac{1}{\pi\gamma}\,\mathrm{sech}\left(\frac{E - \hbar\omega}{\gamma}\right)$$

where e, n_r, c, ε_0, m_0, $\hbar\omega$ and $|M|^2$ are electron charge, refractive index, vacuum speed of light, vacuum permittivity, electron mass, photon energy and the momentum matrix element. In the integrand, $\rho_r(E)$ is the 3D reduced density of states function, $f_{c,v}(E)$ is the Fermi-Dirac distribution for conduction/valance band and $\ell(E - \hbar\omega)$ is the lineshape broadening function which accounts for the energy broadening of

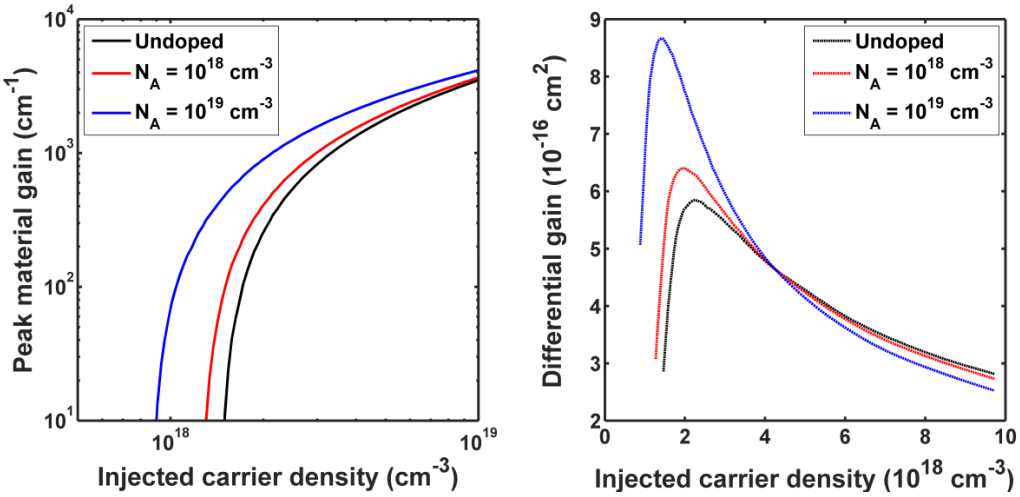

Figure 6-21 | Peak material gain(left) and differential gain (right) as function of injected carrier density for p-type doped and undoped bulk GaAs.

electron-hole states. The sech lineshape function used here prevents unphysical absorption below the band gap, with γ having the dimensions of energy.

Taking Equation 6-11 and the material parameters listed in Table 7-3, the gain spectrum of p-type GaAs was calculated for different doping concentrations and photoexcitation intensities. Intrinsic carrier concentrations were first firstly calculated for the specified temperature using Fermi-Dirac statistics and the charge neutrality condition: $n_0 + N_A^- = p_0 + N_D^+$, where n_0 and p_0 are the intrinsic electron and hole concentrations and N_A^- and N_D^+ are the ionised acceptor and donor concentrations. Quasi-Fermi levels were then calculated for the given injected carrier density, i.e. at electron concentration of $n + n_0$ and hole concentration of $p + p_0$, where n and p are the injected electron and hole

Table 6-2 | Parameters used for gain model	
m_e^*	0.067 m_0 kg
m_{lh}^*	0.087 m_0 kg
m_{hh}^*	0.51 m_0 kg
$\lvert M\rvert^2/m_0$	4.8 eV
E_g	$1.519 - 5.405{\cdot}10^{-4}{\cdot}T^2/(T{+}204)$ eV
E_A	24 meV
n_r	3.6
γ	6.6 meV
T	300 K

concentrations. Figure 6-21(a) shows peak material gain as a function of injected carrier density for undoped and p-doped GaAs. Peak gain is seen to significantly increase with p-type doping as the downward shift in the quasi-Fermi levels with p-type doping acting to reduce the injected carrier density required to achieve gain.[1110] From Figure 6-21(b), p-type doping is also seen to increase differential gain which may again be related to the realignment of the quasi-Fermi levels with the band edges.[1110]

6.6.4 Rate equation modelling

Rate equation modelling was used to fit the experimental L-L curve shown in Figure 6-17 and thereby estimate the doping concentration, N_A, threshold gain, g_{th}, and spontaneous emission factor, β. As three lasing modes are observed in the lasing spectra, the data was fit with multimode rate equations. The rate equations for the carrier density in the active region, N, and photon density in the b^{th} cavity mode, S_b, can be expressed as follows:

$$\frac{dN}{dt} = \frac{\eta_p P}{\hbar\omega V} - AN - BN(N+N_A) - CN(N+N_A)^2 - \sum_{b=1}^{3} v_g g S_b \qquad \text{…(6-12)}$$

$$\frac{dS_b}{dt} = \Gamma v_g (g - g_{th}) S_b + \Gamma\beta \cdot BN(N+N_A)$$

Here $\eta_p P/\hbar\omega V$ is the carrier generation rate, with η_p, $\hbar\omega$, P and V being the fraction of pump power absorbed, energy of pump photon, optical pump power used and volume of the nanowire, respectively. η_p was estimated from FDTD simulations to be 1%.

As P is a time-dependent function of the form $P_p\, sech^2(1.76t/\Delta t)$, where P_p is the peak power of the pulse and Δt = 400 fs is the pulse width, P_p was calculated from the average power of the pump laser using $P_p \Delta t = P_{ave}/f_p$, where f_p= 20.8 MHz is the frequency of the pulsed laser. The volume of the nanowire was calculated using $V = \pi L/12\,(d_1^2 + d_2^2 + d_1 d_2)$, where $d_1 = 400$ nm, $d_2 = 600$ nm and $L = 5.15$ μm are the measured dimensions of the nanowire laser. (See Figure 6-18)

Table 6-3 | Gain function parameters for different doping densities

	N_A= 1×10^{18} cm^{-3}	N_A= 1×10^{19} cm^{-3}	N_A= 2×10^{19} cm^{-3}	N_A= 5×10^{19} cm^{-3}
g_0	950 cm^{-1}	835 cm^{-1}	780 cm^{-1}	700 cm^{-1}
N_{tr}	2.55×10^{18} cm^{-3}	2.0×10^{18} cm^{-3}	1.75×10^{18} cm^{-3}	1.4×10^{18} cm^{-3}
N_s	-1.1×10^{18} cm^{-3}	-1.1×10^{18} cm^{-3}	-1.1×10^{18} cm^{-3}	-1.1×10^{18} cm^{-3}

The non-radiative recombination coefficient A was found from Equation 6-3 using the minority carrier lifetime determined from Figure 7-21 while B and C were calculated from the Equations 7-1 and 6-2 respectively.

Material gain was modelled as described in Section 6.6.3 with a three-parameter logarithmic model being used for the gain function: $g(N) = g_0 \ln(N + N_s/N_{tr} + N_s)$, where g_0 is the gain coefficient, N_{tr} is the transparency carrier density and N_s is the shift parameter. The gain function parameters for different doping concentrations are shown in Table 6-3. The temperature and lineshape broadening parameter (γ=18.8 meV) were estimated by modelling the spontaneous emission spectrum and fitting its shape with the photoluminescence spectrum of the nanowire laser. Finally, g_{th} and β, v_g and Γ were assumed to be equal for each of the three lasing modes. Values of $v_g = c/4.44$ and $\Gamma = 1.2$ were taken from FDTD simulations (see Section 6.6.2).

Equation 6-12 was solved for the duration of one duty cycle of the pump laser with initial estimates for N_A, g_{th} and β. The total photon density ($S(t) = \sum_b S_b$) was then evaluated and the average photon density was calculated by integrating over time and dividing by the time span. The normalised average photon density as a function of the average pump power (P) is shown on a log-log scale in Figure 6-22, together with the

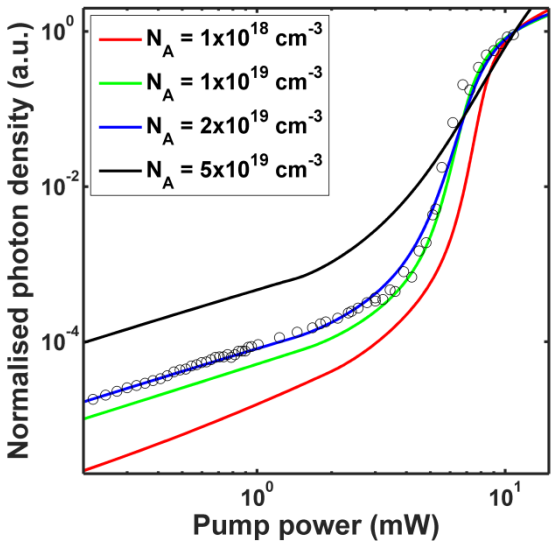

Figure 6-22 | L-L curves obtained from rate equation modeling, for different doping concentrations, with g_{th}=1300 cm^{-1} and β=0.015. The experimental data is superimposed (open circles).

experimental data.

Figure 6-22 compares fits to the experimental data for four different doping concentrations: N_A = 0.1, 1, 2 and 5 $\times 10^{19}$ cm^{-3}. The curve that with the best fit corresponds to an ionised doping concentration of 2.0 x10^{19} cm^{-3}, a beta factor (β) of 0.015 and g_{th} of 1300 cm^{-1}. These estimates are consistent with the fits to the data presented in Figure 6-9 (N_A = 3.6 x10^{18} - 2.5 x10^{19} cm^{-3}, see Section 6.4.4), previous publications (Reference 10: $\beta = 0.015$, $g_{\mathrm{th}} = 1820$ cm^{-1}) and the FDTD threshold gain modelling ($g_{\mathrm{th}} = 1050$ cm^{-1}, see Section 6.6.1).

For the purposes of comparison, the power dependent emission behaviour of undoped nanowires equal in size to the lasing nanowire [Figure 6-17(d,e)] was also modelled. In the case of the undoped and unpassivated nanowire (dashed blue line), poor IQE was found to preclude laser action with the threshold pump fluence being calculated to be greater than that required for thermal vaporisation. Surface passivation enables lasing (dashed pink line), but despite a relative advantage in IQE, the threshold is seen to be at a higher pump fluence than that of our doped but unpassivated nanowire. This may be related to the action of p-type doping in increasing differential gain and reducing the transparency carrier density. (see Section 6.6.3). A further effect of this increase in differential gain is seen in the superior slope efficiency of the doped nanowire [Figure 6-17(e)] Despite being unpassivated the doped nanowire laser is thus expected to outperform undoped GaAs/AlGaAs heterostructure nanolasers of similar dimensions.

6.7 Summary

In this chapter controlled impurity doping has been used to enable room-temperature lasing in unpassivated GaAs nanowires. Doping here acts to radically increase the radiative efficiency while also increasing differential gain and reducing the transparency carrier density. Unlike many previous attempts to improve the efficiency of semiconductor nanomaterials by reducing the rate of non-radiative recombination, the improvement here is related to an enhanced rate of radiative recombination. Due to the fundamental nature of the presented approach it has general applicability to semiconductor nanomaterials regardless of device geometry or operating wavelength and is complementary with more conventional strategies such as passivation. In a device context, doping is important for achieving electrical injection and an enhanced rate of radiative recombination promises an increased modulation bandwidth.[693, 1111] Controlled

impurity doping is thus introduced as a simple and convenient tool for improving the radiative efficiency and performance of semiconductor nanomaterials.

7

Zinc as a source: Zn-V nanostructures by MOVPE

7.1 Introduction

The explosion in demand for electronic goods has placed increasingly unsustainable pressure on a variety of scarce materials used in their production.[1] While the most commonly used semiconductor material, silicon, is of high earth abundance, its indirect bandgap is unsuited to many important applications. In contrast to silicon, the majority of commercialised direct bandgap semiconductors including members of the III-V family, cadmium telluride and copper indium gallium selenide/sulfide (CIGS) contain elements of low earth abundance. As a result, there is an ongoing need for alternate semiconductor materials combining superior optoelectronic performance with earth abundance. Promising examples include copper zinc tin sulfide (CZTS),[4, 5] the organic-inorganic pervoskites[6, 7] and Zn_3P_2.[2, 3]

An attractive material for PVs, Zn_3P_2 is part of the relatively unexplored II-V family of semiconductors. Other examples include Zn_4Sb_3 which is among the most efficient of thermoelectric materials[8, 9] and Cd_3As_2 which was recently identified as one of the few known examples of a three-dimensional topological Dirac semimetal.[10, 11] Less well studied, Zn_3As_2 is an earth abundant semiconductor with a band gap around 1.0 eV[12, 13] and the potential to realize high carrier mobilities.[14, 15, 16] Of key importance for possible optoelectronic applications, these II-V compounds form alloys enabling band-gap tuning between Zn_3P_2 (1.5 eV),[17, 18] Zn_3As_2 with Cd_3As_2 (semimetal). Heteroepitaxy between II-V and III-V materials is also possible due to their close structural similarity and, in the case of Zn_3As_2 and InP, a lattice mismatch of only 0.5%.[19, 20]

In this chapter we synthesise both nanowires and nanoplatelets of the zinc-based II-V compound semiconductor materials Zn_3As_2, Zn_3P_2 and Zn_xSb_y. Zinc is an earth abundant element and we use a standard DEZn source in a metal organic vapour phase epitaxy (MOVPE) reactor compatible with commercial production of III-V materials. We firstly discuss relevant growth conditions before going on to analyse the structure

and morphology of the product materials. Efficient emission is then shown at around 1.0 eV and 1.5 eV for Zn_3As_2 and Zn_3P_2 respectively. These results open the door to the MOVPE/MBE synthesis of nanostructured II−V semiconductor materials, II−V alloys, and novel II−V/III−V heterostructures for applications encompassing optoelectronics, thermoelectrics, high speed nanoelectronics, and topological physics.

7.2 Methods

7.2.1 Growth and morphological characterization

Being an exploratory work, the growth of II-V semiconductors was assessed across a wide parameter space. The variables considered included precursor flow rates and ratios, reactor temperature, growth time, substrate type and orientation and seed material. As II-V semiconductor materials are known to be characterised by relative high vapour pressures, a maximum flow rate of 2.38 $x10^{-5}$ mol/min was achieved from the DEZn bubbler by increasing the bubbler temperature to 15 °C and reducing the bubbler pressure to 3.55 $x10^{4}$ Pa.

For Au and Ag seeded growth, the substrates were treated with colloidal nanoparticles as described in Section 3.1.1. In the case of Ni and Pt, thin films of 0.5 nm nominal thickness were deposited at a rate of 0.01 nm/s using electron-beam evaporation (Temescal BJD-2000 E-beam/Thermal Evaporator). Sn and Zn films were deposited by thermal evaporation (Kurt J. Lesker Nano 36) at rates of 0.03 nm/s and 0.05 nm/s respectively.

Subsequent investigation by both scanning electron microscopy (SEM) and transmission electron microscopy (TEM) was performed utilising a FEI Helios 600 NanoLab Dualbeam (FIB/SEM) operated at 10 kV and a JEOL 2100F TEM operated at 200 kV. Samples for TEM investigation were prepared by mechanical dispersion on holey carbon copper grids. Particular care was required in regards to the imaging conditions employed for Zn_xP_y and Zn_xSb_y samples as both materials proved to be relatively beam sensitive.

7.2.2 Photoluminescence experiments

Micro-photoluminescence (PL) measurements at wavelengths greater than 1100 nm employed a 50x/0.55NA NIR objective lens (Leica HCX PL Fluotar) with excitation coming from an 830 nm continuous-wave laser (Topica DL100) delivering between

1μW and 8mW at the focal spot (FWHM ≈ 3 μm). The PL was passed through an 830 nm longpass edge filter and then a spectrometer (Horiba T64000) fitted with a 150 lines/mm diffraction grating before being collected on a liquid nitrogen cooled InGaAs 1D array detector. Temperature dependant PL measurements were conducted between 77 and 570 K under nitrogen in a liquid nitrogen cooled cryostat. (Linkham TS1500) For μ-PL measurements at wavelengths of less than 1100 nm, a silicon based focal plane array detector was employed.

The dynamics of photoexcited carrier decay were studied using several complementary techniques. Time-resolved photoluminescence measurements at wavelengths of less than 1100 nm were achieved by time-correlated single photon counting (TCSPC) technique (Picoharp 300) using the experimental setup described in Section 6.2.2.2. For wavelengths beyond 1100 nm, the carrier dynamics were studied by transient Rayleigh scattering spectroscopy.[1069]

7.2.3 Electrical Characterisation

In order to realise the optoelectronic potential of our Zn_3As_2 nanostructures we fabricated single nanowire and single nanoplatelet metal−semiconductor−metal photoconductor devices. The nanostructures were first dispersed from solution onto a highly doped silicon substrate with a thermal oxide thickness of 300 nm. Photolithography followed by the deposition of Ti (20 nm)/Al (500 nm) and lift off were used to define contacts at either end of nanowires. The devices were wire bonded and mounted in an optical cryostat (Attocube) for low temperature photocurrent measurement. Photocurrent measurements were performed using a tunable pulsed light from a super continuum photonic crystal fiber. The laser light was focused onto the nanowire with 50×/0.5NA long working objective and a fixed bias of 5 V applied across the nanowire. We acquired the photocurrent data using a standard lock in technique involving chopping of the laser light. Cooling was provided by a continuous flow of liquid helium.

7.3 Zinc Arsenide

7.3.1 Growth Parameters

7.3.1.1 Absolute diethylzinc flow rate

As discussed in Chapter 2, the thermal stability of the II-V compounds is generally lower than that of III-V compounds. For this reason special care must be taken to prevent thermal decomposition of the product material. Deposition can furthermore only occur where the partial pressures of the reactant gases is greater than that of their equilibrium values.

Figure 7-1 displays the results of two attempts to grow Zn_3As_2 at a temperature of 400 °C and a V/II ratio of 1000. In the case of the first run [Figure 7-1(a)], no growth is observed and the Au seed particles remain as droplets on the substrate surface. With a doubling of the reactant partial pressures micron sized structures are observed [Figure 7-1(b)]. This onset of growth can be related to the partial pressures of the reactant precursors exceeding their equilibrium values. In the current studies, the threshold for growth was found to be sharp, reproducible and highly temperature dependant. As decomposition can be expected to be heterogeneous throughout the temperature range

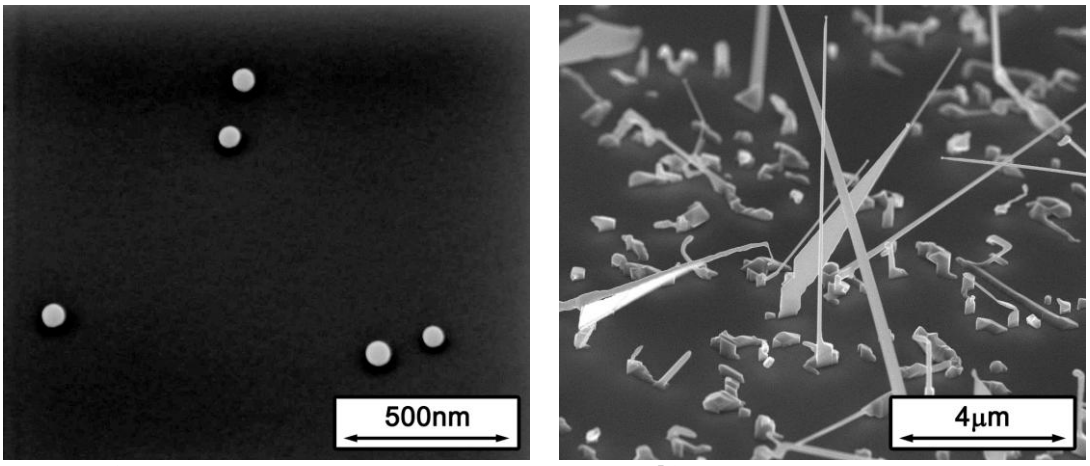

a) **T = 400 °C**
V/II= 1000
P_{DEZn}= 0.025 Pa

b) **T = 400 °C**
V/II= 1000
P_{DEZn}= 0.05 Pa

Figure 7-1 | Sensitivity of Zn_3As_2 growth to the absolute precursor flow rates at a temperature of 400 °C and V/II ratio of 1000. a) DEZn partial pressure less than the equilibrium vapour pressure. b) DEZn partial pressure greater than the equilibrium vapour pressure. Both micrographs show the sample substrate tilted 45 ° to normal.

considered, this threshold was furthermore found to be critically dependant on the condition of the liner and susceptor. A particular example of this is that no Zn-V growth could be obtained without firstly pre-coating a thin film of III-V material on freshly cleaned liners.

Figure 7-2 plots the results of Zn_3As_2 growth at various reactor temperatures and zinc partial pressures. The partial pressure of zinc was chosen as the ordinate here as it expected to exceed the partial pressure of arsenic from both the stoichiometry of the considered compound and the relative propensity of each element to form molecular gases. Such an approach is supported by the CALPHAD modelling discussed below where the partial pressure of zinc in equilibrium with Zn_3As_2 at a temperature of 400 °C was calculated to be more than four times greater than that of the partial pressure of arsenic. Growth was furthermore always conducted at V/II ratios greater than one with

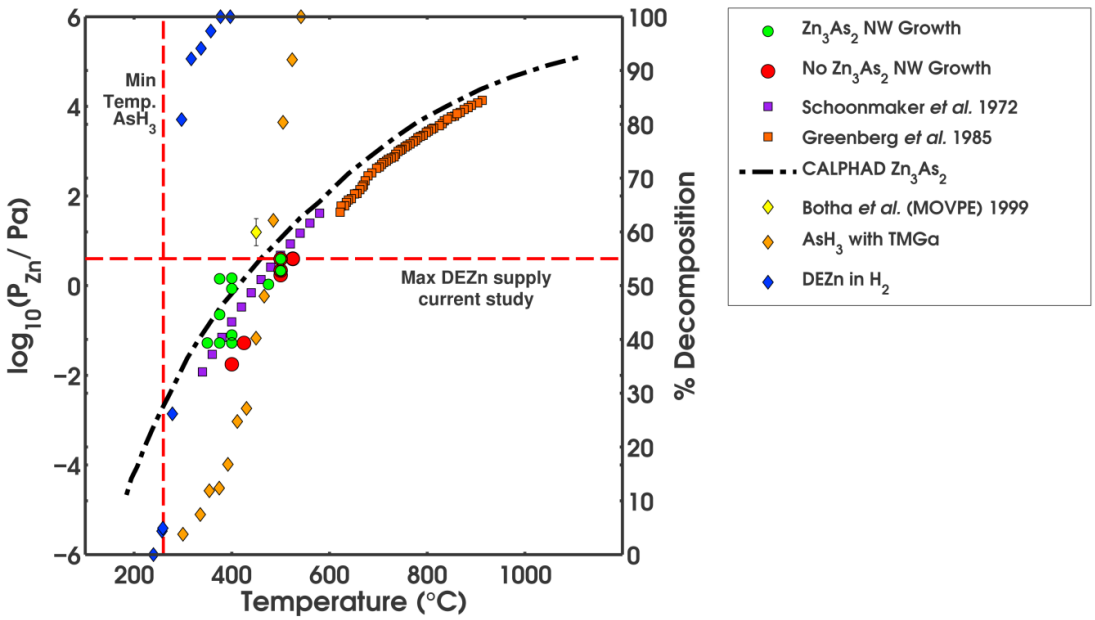

Figure 7-2 | Outcome of Zn_3As_2 nanowire growth under various combinations of zinc partial pressure and temperature. The percentage decomposition of the precursors DEZn in H_2 and AsH_3 with TMGa is further plotted as a function of temperature on the right-hand axis.[1, 3] Also plotted is temperature dependence of zinc partial pressure in equilibrium with Zn_3As_2 as calculated by the CALPHAD method using the thermodynamic data of Ghasemi and Johansson[13] and measured experimentally by Schoonmaker and Lemmerman[31] and Greenberg *et al.*[39]. The expected growth window for the current experimental setup is ~250-500 °C.

zinc therefore expected to be the limiting reactant. The partial pressure of zinc is furthermore equated with the partial pressure of DEZn as complete decomposition can be expected for the majority of the temperatures considered.[1112]

Across Figure 7-2, the smaller green circles indicate growth parameters which led to Zn_3As_2 deposition whereas the larger red circles indicate parameters which did not lead to any deposition. As discussed previously, the zinc partial pressure required for deposition is seen to increase with temperature, doubling around every 25 °C. Close correlation is evident between the partial pressure of zinc required for growth and that in equilibrium with powdered Zn_3As_2 as reported by Schoonmaker and Lemmerman[31]. That the threshold for growth found by the current experiments is at zinc partial pressures slightly lower than those reported for equilibrium may be related to the Gibbs-Thomson effect[993] or difference between the measured susceptor temperature and actual wafer temperature.

The relationship between the zinc partial pressure in equilibrium with Zn_3As_2 and temperature is further extended by the experimental results of Greenberg *et al.*[39] represented by the orange squares and theoretical calculations indicated by the dash-dotted line. The theoretical calculations here were performed using the CALPHAD method with the data for solid Zn_3As_2 being taken from an assessment of the Zn-As system by Ghasemi and Johansson[13] and that for the relevant gaseous species from Ansara *et al*[26]. Together these various results define a stability region for Zn_3As_2, with temperature-pressure combinations appearing above the dash-dotted line being suitable for deposition. The intersection between this curve with the maximum partial pressure that may be obtained by the current experimental setup further defines the maximum attainable growth temperature. In the current case, the maximum achievable partial pressure of around 3.4 Pa is seen to limit growth to temperatures of approximately 500 °C or less.

Also plotted on Figure 7-2 are heterogeneous decomposition curves for the precursors DEZn and AsH_3 as a function of temperature.[1, 3] As material deposition requires some degree of precursor decomposition, these curves define the minimum growth temperature for Zn_3As_2 using the current precursors. In the current case, AsH_3 decomposition is limiting with very little decomposition occurring at less than 300 °C and virtually no decomposition occurring at less than 250 °C.

The minimum growth temperature together with the maximum obtainable zinc partial pressure and Zn_3As_2 decomposition curve form a triangular-like region which serves to define the Zn_3As_2 growth parameter space accessible in the current experiments. This parameter space covers a temperature range from approximately 250-500 °C and zinc partial pressures from around 0.01-3.6 Pa or equivalently, 0.5-136 sccm.

7.3.1.2 Growth Temperature

The effect of reactor temperature on the growth and morphology of Au seeded Zn_3As_2 nanostructures is documented in Figure 7-3. At the lowest of the growth temperatures investigated (350 °C), Zn_3As_2 nanocrystallites formed with an areal density proportional to that of the Au nanoparticle pre-treatment [Figure 7-3(a)]. Growth here was not by the VLS mechanism and the Au nanoparticles could not be located post-growth using standard SEM imaging and analysis techniques. Zinc has previously been shown to disrupt the VLS growth of Au-seeded III-V nanowires leading to kinking, 'seed

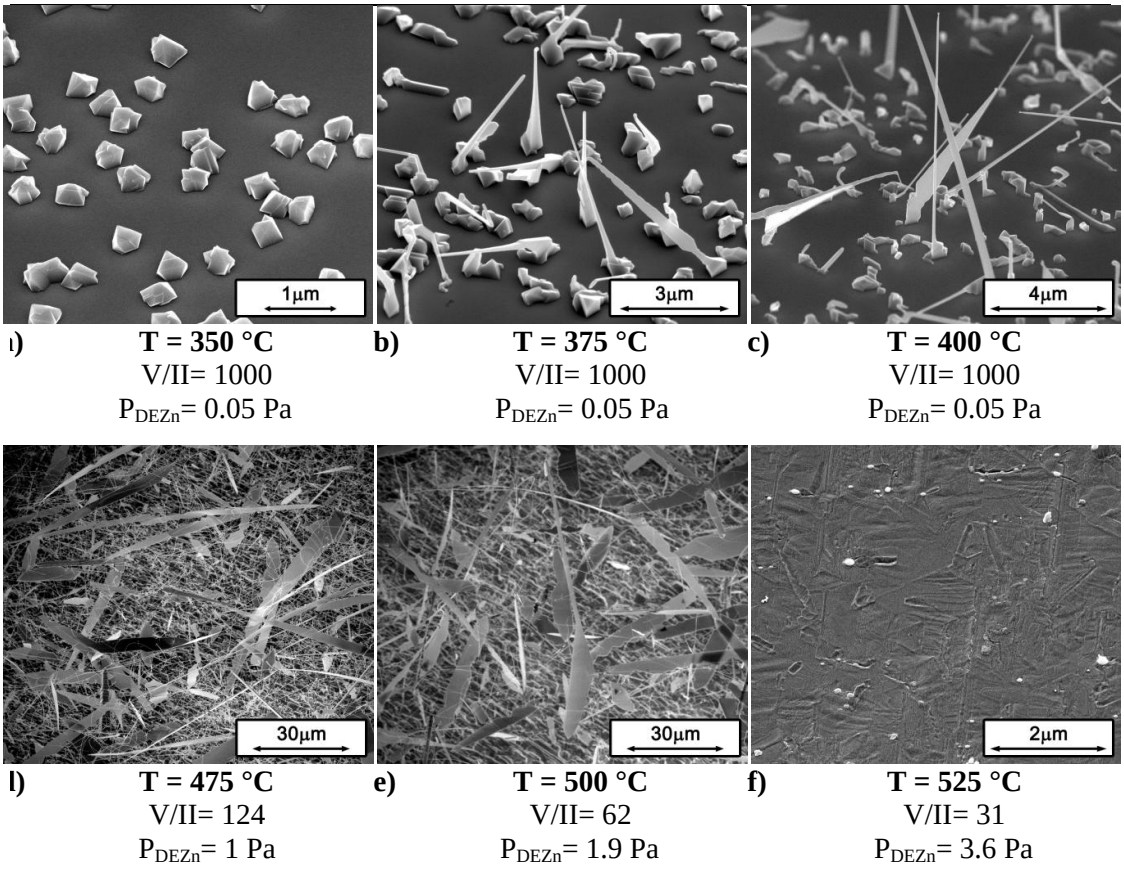

a) **T = 350 °C** V/II= 1000 P_{DEZn}= 0.05 Pa

b) **T = 375 °C** V/II= 1000 P_{DEZn}= 0.05 Pa

c) **T = 400 °C** V/II= 1000 P_{DEZn}= 0.05 Pa

d) **T = 475 °C** V/II= 124 P_{DEZn}= 1 Pa

e) **T = 500 °C** V/II= 62 P_{DEZn}= 1.9 Pa

f) **T = 525 °C** V/II= 31 P_{DEZn}= 3.6 Pa

Figure 7-3 | Effect of growth temperature on the morphology of Zn_3As_2 nanostructures. a) 350 °C; b) 375 °C; c) 400 °C; d) 475 °C; e) 500 °C; f) 525 °C. All micrographs show the sample substrate tilted 45 ° to normal.

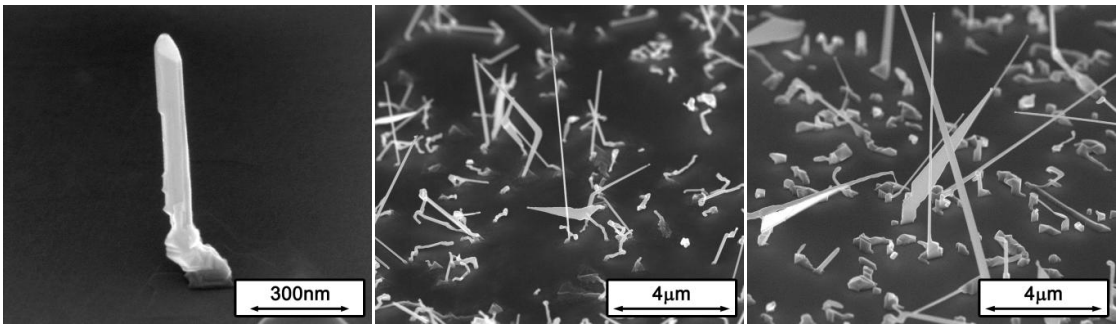

a)	T = 400 °C **V/II= 10** P_{DEZn}= 0.05 Pa	b)	T = 400 °C **V/II= 280** P_{DEZn}= 0.05 Pa	c)	T = 400 °C **V/II= 1000** P_{DEZn}= 0.05 Pa

Figure 7-4 | Effect of V/II ratio on the morphology of Zn_3As_2 nanostructures grown at 400 °C. At the lowest V/II ratios investigated. The growth time in all cases was 20 minutes. a) V/II=10; b) V/II=280; c) V/II=1000. All micrographs show the sample substrate tilted 45 ° to normal.

splitting' and eventually, a failure to grow.[237, 243, 246, 539, 540, 578, 1113] (See Section) Suggested causes include a change in supersaturation,[540] III/V ratio,[246] seed composition[243, 246] and phase[243, 540] and surface energies[35, 243]. The effective partial pressure of zinc is furthermore greater at lower temperature as evaporation is reduced.

Increasing temperature was found to promote VLS growth. At a temperature of 375 °C, around 15 % of structures grew out of the substrate while the other structures retained a crystallite morphology [Figure 7-3(b)]. At 400 °C the proportion of structures growing out of the substrate increased to approximately 20 % with the remainder being planar VLS nanowires [Figure **7-3**(c)]. Among those structures growing away from the substrate at 400 °C, around 70 % were nanowires and 30 % were nanoplatelets. The areal density of VLS structures here of approximately 0.27 nanostructures per square micron was over one order of magnitude less than that observed for GaAs nanowire growth with a similar Au seed pre-treatment (see Section 3.1.1).

At higher temperatures, relatively high DEZn partial pressures were required for growth (see Section 7.3.1.1) and the V/II ratio was limited by the maximum AsH_3 flow of the current experimental setup [Figure 7-3(d-f)]. A significant increase in growth rate was obtained as control over the DEZn partial pressure was necessarily coarser leading to a greater absolute difference between the supplied DEZn partial pressure and the decomposition pressure of Zn_3As_2. As is observed in Figure 7-3(d,e), growth at temperatures around 500 °C produced structures of at least tens of microns in length.

Despite this high growth rate, radial growth was not significant with the diameter of the nanowires and thickness of the nanoplatelets remained between 50 and 100 nm. The areal density of nucleation did however remain low with a large proportion of the VLS growth occurring as planar nanowires. Planar growth was difficult to quantify in this case as many of the planar nanowires coalesced. Growth of Zn_3As_2 was not observed above a temperature of 500 °C using the current experimental setup Figure 7-3(f).

7.3.1.3 V/II ratio

At a growth temperature of 400 °C, a relatively low V/II (<30) was observed to result in poor nucleation, non-uniform faceting and an absence of nanoplatelet structures [Figure

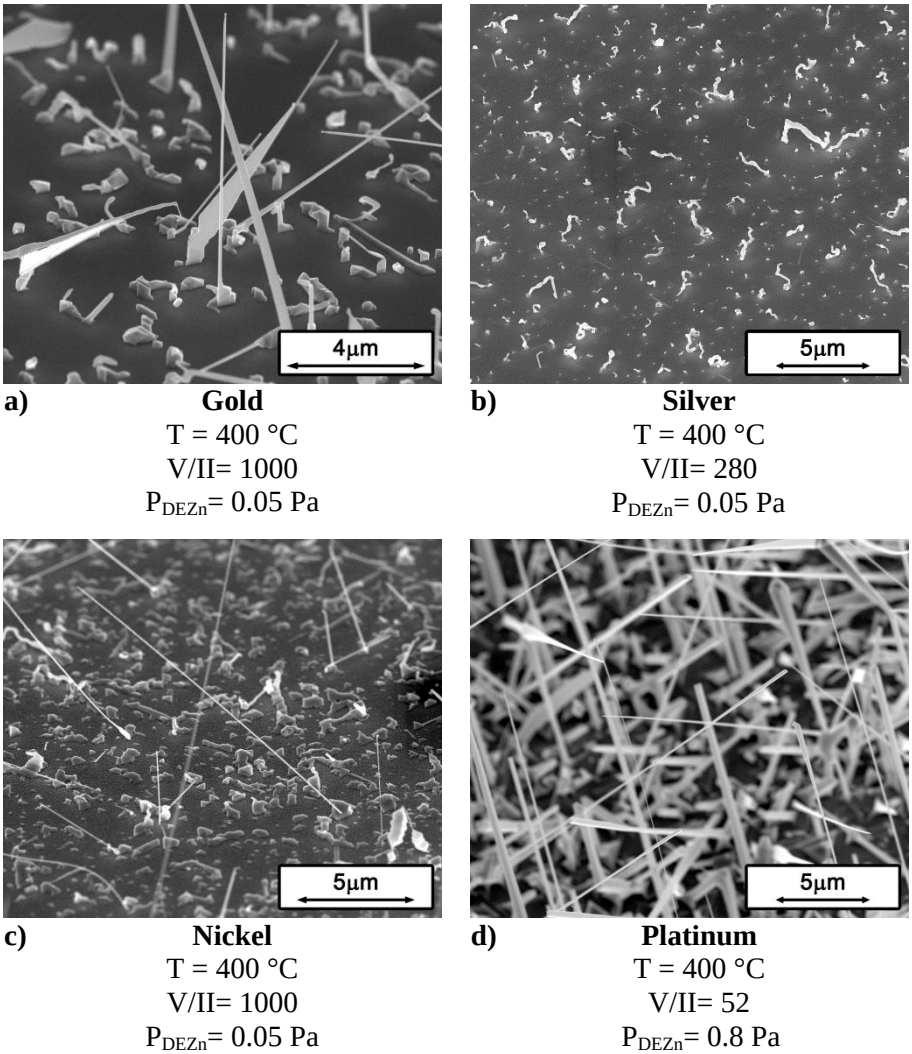

a) **Gold**
T = 400 °C
V/II= 1000
P_{DEZn}= 0.05 Pa

b) **Silver**
T = 400 °C
V/II= 280
P_{DEZn}= 0.05 Pa

c) **Nickel**
T = 400 °C
V/II= 1000
P_{DEZn}= 0.05 Pa

d) **Platinum**
T = 400 °C
V/II= 52
P_{DEZn}= 0.8 Pa

Figure 7-5 | Zn_3As_2 nanostructure growth at 400 °C as seeded by various different metals. a) Gold (60 nm nanoparticles); b) Silver (60 nm nanoparticles); c) Nickel (0.5 nm thin film); d) Platinum (0.5 nm thin film). All micrographs show the sample substrate tilted 45 ° to normal.

7-4(a)]. Here V/II ratio may act to alter relevant surface energies or seed particle phase, with a relatively low ratio disrupting VLS growth as described in Section 7.3.1.2. In the case of III-V nanowires the V/III ratio has been found to affect both crystal structure[616, 657, 668, 1035] and morphology[668, 1035, 1114-1116]. An increasing V/III ratio has been shown to increase radial growth rate and tapering,[983, 1116-1119] while also reducing (increasing) the group III[243, 1056] (V)[1119] concentration in the alloy droplet. A similar result has been reported for the II-VI material, ZnSe, where increasing the VI/II ratio lead to a transition from VLS to VSS growth.[1120]

7.3.1.4 Seed material

Several different metals were investigated as potential seed materials for the VLS-type growth of Zn_3As_2 nanostructures. The current study focuses particularly on the use of gold nanoparticles which were found to deliver the largest and most reproducible parameter space as well as the greatest diversity of structure types. The Au-Zn system contains a variety of intermetallic compounds and a high degree of solid solubility. The lowest liquidus temperature is approximately 420 °C as occurring for pure zinc and it is therefore expected that growth with Au seeds followed a VSS-type mechanism.[159, 183]

As discussed in Section 7.3.1.2, at 400 °C Au seeded growth produced free-standing nanowires, nanoplatelets and planar nanowires although the areal density was relatively low and many nanostructures showed some degree of kinking [Figure 7-5(a)]. Under similar growth conditions, silver nanoparticles also seeded Zn_3As_2 growth but that growth showed significant kinking, poor faceting and a low areal density [Figure 7-5(b)]. Interestingly, these structures appeared morphologically similar to Au seeded growth at low V/II ratios (see Section 7.3.1.3). Silver has previously been investigated as a seed material for GaAs,[163] InSb[164] and InP[165] nanowire growth where variance with Au-seeded growth was suggestive of a differing parameter space for each metal.

The successful VLS-type growth of Zn_3As_2 nanostructures was also realized with thin films of both nickel and platinum. In both cases high aspect ratio nanowire structures grew over a relatively wide temperature range (400-500 °C). (See Section 7.3.6 for an investigation of Ni seeded Zn_3As_2 nanowires.) Platinum was generally found to produce a greater areal density of nanowires which showed greater tapering. Both metals have previously been shown to effectively seed III-nitride growth[167, 168] with nickel also being used for GaAs[174, 175], InAs,[176] Si[177] and Ge[177-179] nanowire growth.

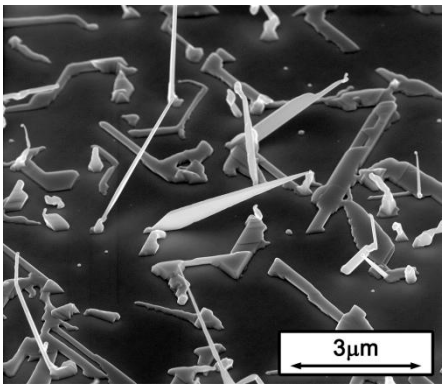

GaAs (111)B
T = 400 °C
V/II=1000
P_{DEZn}=0.05 Pa

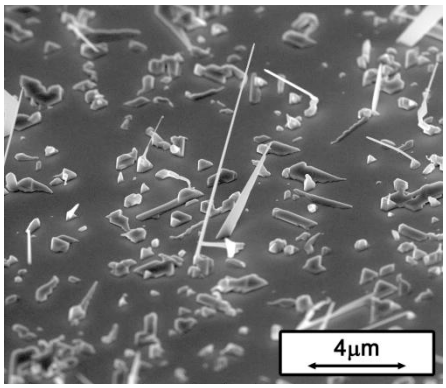

GaAs (111)A
T = 400 °C
V/II=280
P_{DEZn}=0.05 Pa

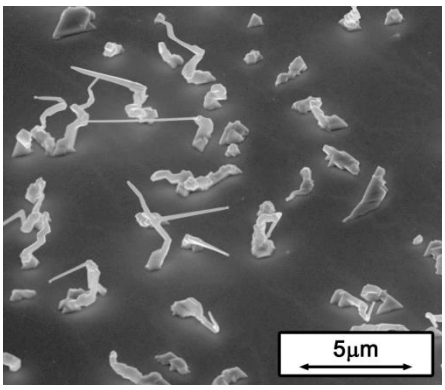

GaAs (100)
T = 400 °C
V/II=1000
P_{DEZn}=0.05 Pa

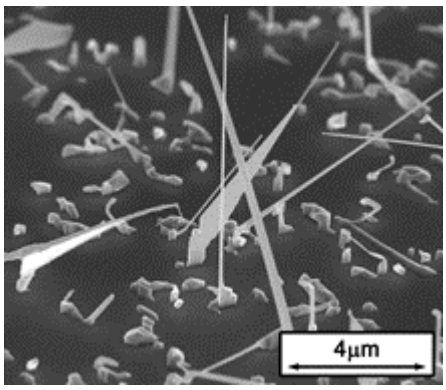

GaAs (110)
T = 400 °C
V/II=52
P_{DEZn}=0.8 Pa

Figure 7-6 | Au seeded Zn_3As_2 nanostructure growth at 400 °C on various GaAs substrate orientations. a) (111)B; b) (111)A; c) (100); d) (100). All micrographs show the sample substrate tilted 45 ° to normal.

Thin films of tin and zinc were not found to seed Zn_3As_2 growth under any of the parameters investigated despite Sn being reported to be an excellent catalyst for both IV and III-V nanostructure growth.[171, 172, 518] While the compound semiconductor Zn-Sn-As_2 is known,[1121, 1122] it was not found to be formed either through Sn seeding or the addition of tetraethyltin (TESn) during growth.

7.3.1.5 Substrate

In the current studies, the growth of Zn_3As_2 was primarily from GaAs substrates. As the most common binary arsenide semiconductor, GaAs was chosen in order to minimize the potential for substrate decomposition and cross-contamination between substrate

and sample. Growth was furthermore investigated on a variety of GaAs substrate orientations including (111)B, (111)A, 100 and 110 both with and without pre-growth annealing. At a growth temperature of 400 °C and using 50 nm Au seeding, subtle differences were evident between substrate orientations, with the greatest amount of planar nanowire growth occurring on the (111)A and (111)B oriented substrates (Figure 7-6).

The only vertical nanowires were those that grew on the (110) oriented substrate, while the nanostructures formed on the (100) substrate showed significant kinking. Pre-growth annealing did not appear to have a significant effect on yield. In the case of III-V nanowires, substrate orientation is well known to affect growth direction and subsequently, morphology and structure.[180, 1123-1126] For differing substrate-nanowire material combinations, planar nanowire growth has been thought to occur where the seed material prefers to wet the substrate rather than nanowire.[1127, 1128]

Where InP was used as a substrate in place of GaAs, a greater proportion of structures were found to nucleate with a nanowire-like morphology (Figure 7-7). An indium background has previously been shown to affect the morphology and structure of Au-

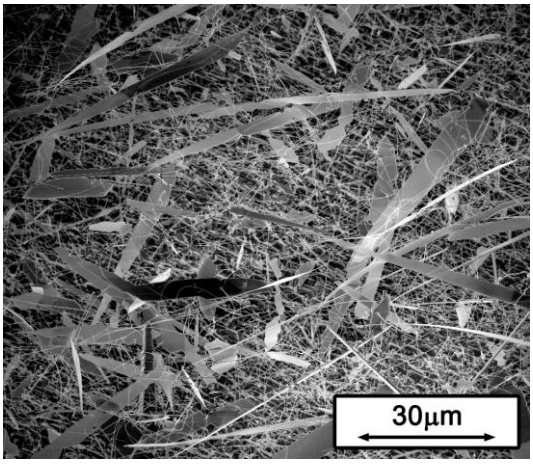

GaAs (110)
T = 475 °C
V/II=124
P_{DEZn}=1 Pa

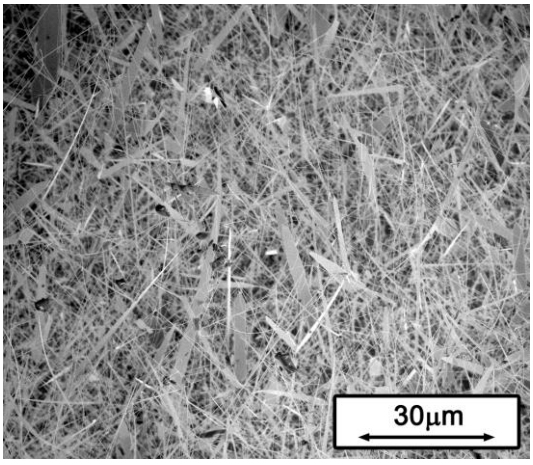

InP (110)
T = 475 °C
V/II=124
P_{DEZn}=1 Pa

Figure 7-7 | Au seeded Zn_3As_2 nanostructure growth at 400 °Con a) a GaAs (110) substrate; b) a InP (110) substrate. A greater proportion of the nanostructures which nucleated on the InP substrate presented a nanowire morphology. Both micrographs show the sample substrate tilted 45 ° to normal.

seeded GaAs nanowires[593, 1129] and it is likely that indium acts here to alter the wetting angle between Zn_3As_2 and the Au alloy seed.[1130, 1131] Interestingly, In has been shown to act as a suitable seed material for the growth of $Zn_3(P_{1-x}As_x)_2$ and Zn_3P_2 by CVD.[63, 336]

7.3.2 Structural Characterisation

7.3.2.1 Morphology

Two distinct Zn_3As_2 nanostructure geometries were synthesised in the current study, nanowires and nanoplatelets. Figure 7-8 presents SEM images showing typical examples of both, which were often observed to grow concurrently. The images here correspond to the Au-seeded growth of Zn_3As_2 at 400 °C on GaAs (110) substrates. Nanowires grew in a vertical direction on the (110) substrates with occasional kinking

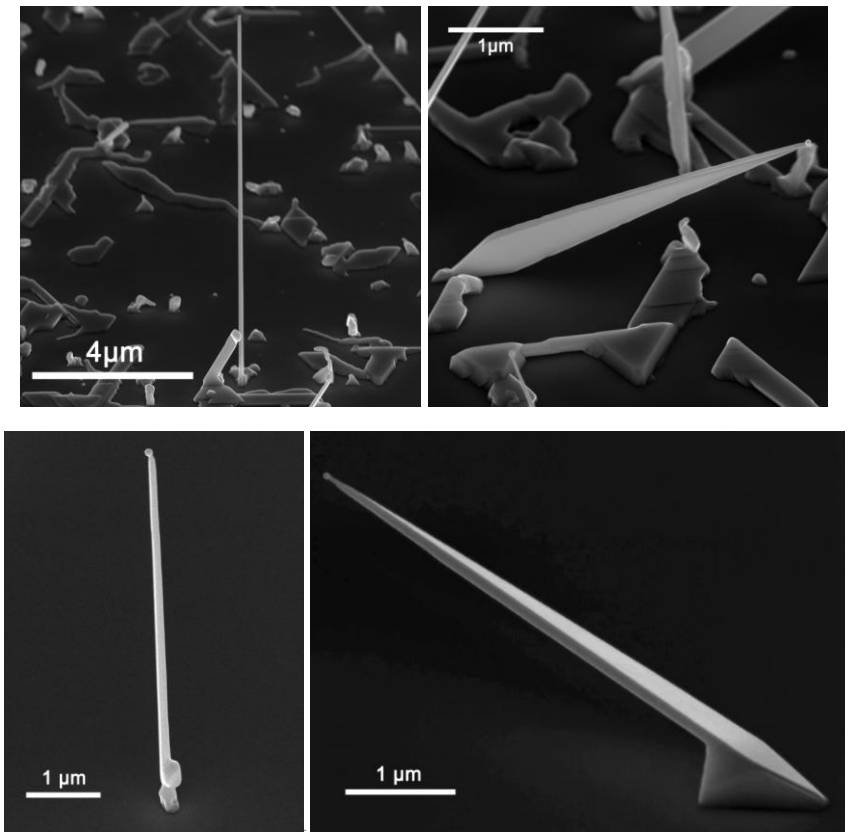

Figure 7-8 | SEM images of the two distinct nanostructures that were observed to form from the Au-seeded growth of Zn_3As_2 on GaAs (110) at 400 °C. a) nanowire vertical from GaAs (110) substrate; b) nanoplatelet at oblique angle to GaAs(110) substrate; c) nanowire with kinking at base; d) platelet showing a thickness of approximately 80 nm.

closer to the substrate Figure 7-8(a,c). The platelets in contrast, which showed a distinct ‘kite’ or ‘tie’ morphology Figure 7-8(b,d), always grew at an oblique angle to the substrate.

Bright field TEM images typical of the two distinct free-standing nanostructure geometries are presented in Figure 7-9(a,b,d,e,g). Each micrograph excepting Figure 7-9(d) depicts the same major zone axis, later determined to be <112>. The apparent length of the nanostructures was maximised in this zone axis and the nanostructures therefore lie in the plane of these images. The nanowire is somewhat longer than the nanoplatelet, being approximately 11.5 µm in length and almost taper free, ranging from 75 to 150 nm in diameter from tip to base. In contrast, the nanoplatelet is approximately 8.5 µm long and its width increases from 50 nm at the tip to a maximum of 1.3 µm near the base to give a necktie-like silhouette. From the SEM images [Figure 7-8(t), Figure 7-9(b,d)] the thickness of the nanoplatelets is seen to be approximately 50-100 nm.

Considering the high-resolution images, [Figure 7-9(b) and Figure 7-9(e)] and their Fourier transforms, [Figure 7-9(c) and Figure 7-9(f)], this difference in morphology is seen to arise from a difference in growth direction. With reference to the expected pseudocubic structure of Zn_3As_2,[9, 22, 263] as identified below, the nanowire may be said to have grown along the equivalent cubic direction <110> and the nanoplatelet: <112>. While these directions differ from the usual <111> VLS growth direction, conditions favouring non-<111> growth have been widely reported in other material systems.[1124, 1130, 1132-1134] Concomitant changes in geometry are also common and may be related to changes in the symmetry of the growth axis.[452, 586, 1131]

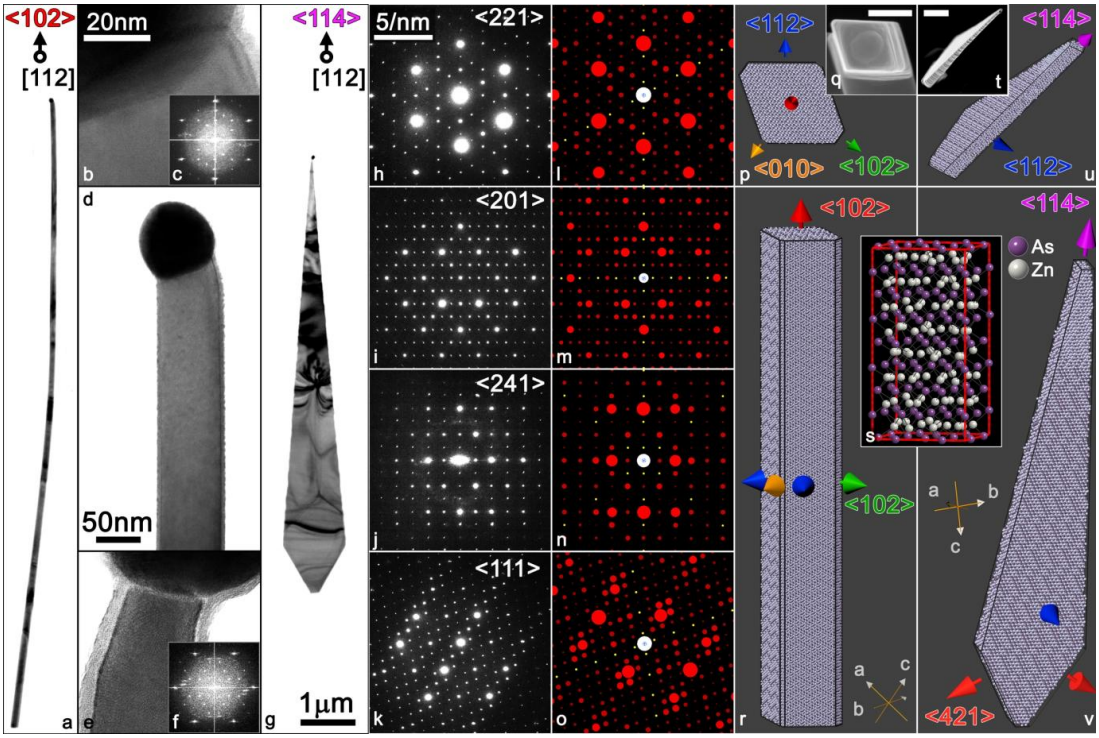

Figure 7-9 | Structure and morphology of the Zn_3As_2 nanowires and nanoplatelets: a) <221> axis bright field TEM image of a nanowire; b) <221> axis HRTEM image of the nanowire / seed particle interface; c) Fourier transform of (b) revealing <110> type growth direction; d) <201> axis TEM image of the nanowire tip; no planar defects are apparent; e) <221> axis HRTEM image of the nanoplatelet / seed particle interface; f) Fourier transform of (e) showing that the growth direction is rotated 60 ° relative to (b); g) <221> axis bright field TEM image of the entire nanoplatelet h) <221> axis diffraction pattern i) <201> axis diffraction pattern j) <241> axis diffraction pattern k) <111> axis diffraction pattern l) simulation of <221> diffraction from α' Zn_3As_2 m) simulation of <201> diffraction from α' Zn_3As_2 n) simulation of <241> diffraction from α' Zn_3As_2 o) simulation of <111> diffraction from α' Zn_3As_2 p) atomic model of the Zn_3As_2 nanowire shown in top view with facet directions marked q) top view SEM image of a Zn_3As_2 nanowire (scale bar 100 nm) r) atomic model of the Zn_3As_2 nanowire shown in side view with facet directions marked s) Schematic model of α' Zn_3As_2 as reported by Pietraszko[22] t) atomic model of the Zn_3As_2 nanoplatelet shown in top view with facet directions marked u) SEM image of a Zn_3As_2 nanoplatelet (scale bar 500 nm) v) atomic model of the Zn_3As_2 nanowire shown in side view with facet directions marked.

7.3.2.2 Crystal Structure

That both nanostructures presented here are single crystalline and appear free from planar defects may be concluded following examination of the images presented in Figure 7-9(a-g) along with similar images from a variety of zone axes (Figure 7-10, Figure 7-11) and representative selected area electron diffraction patterns (SADP) from each of these zones axis [Figure 7-9(h-k), Figure 7-11(b,d,f)]. Interestingly, an absence of planar defects has also been widely noted for III-V nanowires propagating along non-<111>B growth directions.[452, 1134-1136]

Energy dispersive X-ray spectroscopy (EDXS) (Figure 7-15) analysis of the nanostructures identified only zinc and arsenic in an approximate atomic ratio of 3:2 as quantified by the standardless *k*-factor method. Such a ratio is consistent with the compound Zn_3As_2, one of two line compounds in the arsenic-zinc binary system. Zn_3As_2 is known to be tetragonal at room temperature before transforming into a cubic

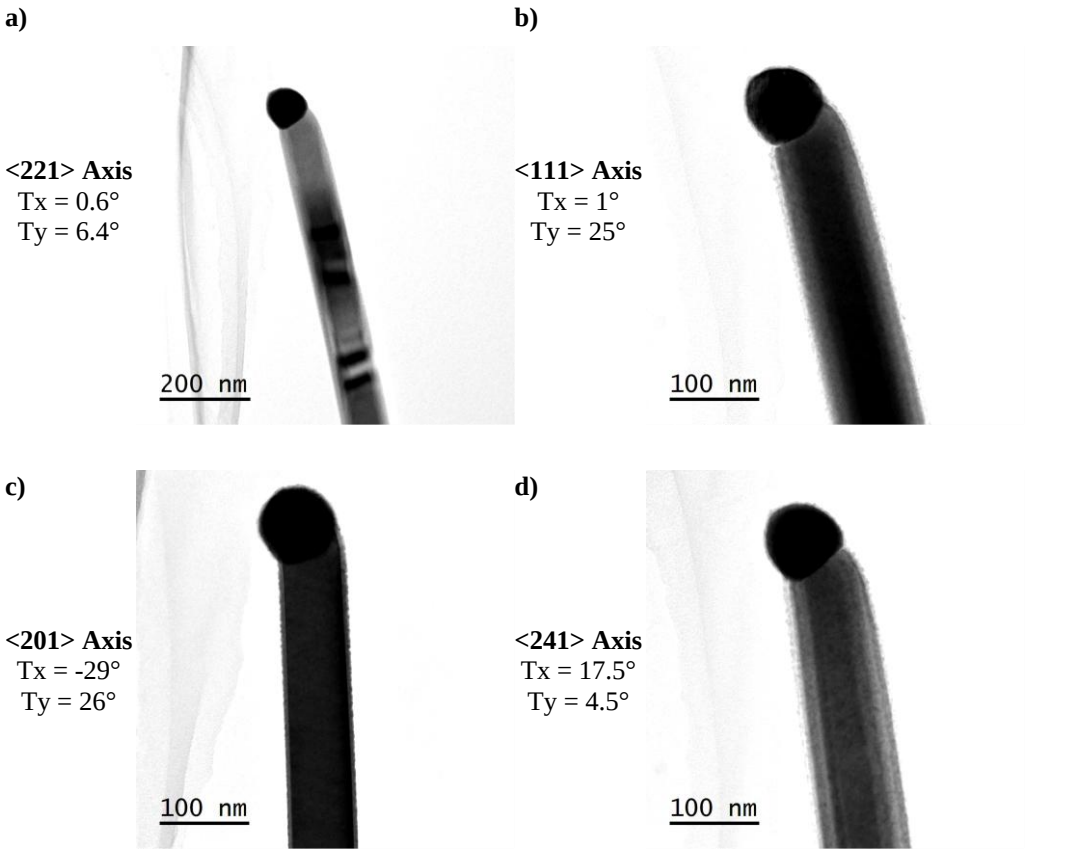

Figure 7-10 | Additional bright field TEM images of the Zn_3As_2 nanowire shown in Figure 7-9(a) as collected on various zone axes; a) <221> axis; b) <111> axis; c) <201> axis; d) <241> axis. Tx and Ty correspond to the specimen tilt.

structure at 651°C.[866]

The room temperature phase α as investigated by both X-ray diffraction[22, 872] and neutron diffraction[9] techniques has been described by a 160 atom unit cell [Figure 7-12(a)]. This cell consists of a distorted face centred cubic As sublattice interpenetrating a 75% filled simple cubic Zn sublattice. In this arrangement each arsenic atom is surrounded by six zinc atoms and two zinc vacancies and each zinc atom is surrounded by four arsenic atoms. A small alteration in the symmetry of the zinc

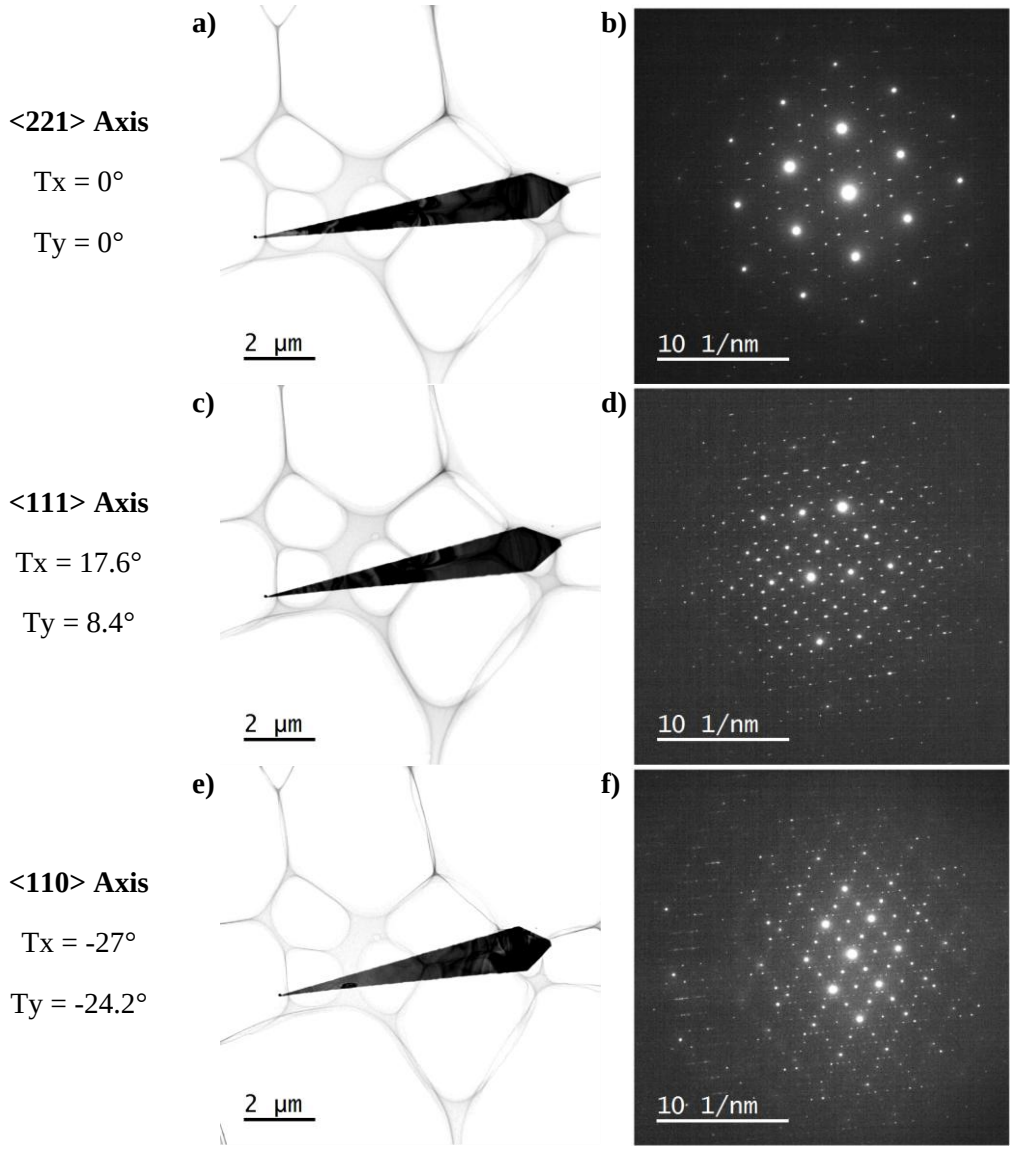

Figure 7-11 | Additional bright field TEM images and corresponding SADPs from the Zn_3As_2 nanoplatelet shown in Figure 7-9(g) as collected on various zone axes; a) <221> axis; c) <111> axis; e) <110> axis. Tx and Ty correspond to the specimen tilt.

vacancies produces the α' phase at 190°C.[22, 866] [Figure 7-12(b)]

Figure 7-9(h-k) presents four zone axis SADPs obtained from the nanowire structure presented in Figure 7-9(a-c, g) which are representative of those obtained from all the nanostructures investigated. A clear pseudocubic symmetry is again apparent. Using the *jems* software package (Pierre Stadelman), we simulated the expected zone axis patterns of various reported α and α' Zn_3As_2 structures.[9, 22] [Figure 7-13(e-h)] The experimental patterns were best replicated by the α' Zn_3As_2[22] phase which is expected to be the most stable phase at the growth temperature. Shown in Figure 7-9(l-o) with the same orientation and scale as the experimental patterns, the α' simulations are seen to replicate all experimentally observed diffraction spots. In contrast, simulation of the α Zn_3As_2 phase[22] showed a space group absence of h=k, l=4n and a lattice absence of h+k+l=2n+1 spots observed in the experimental <221> and <102> axis diffraction

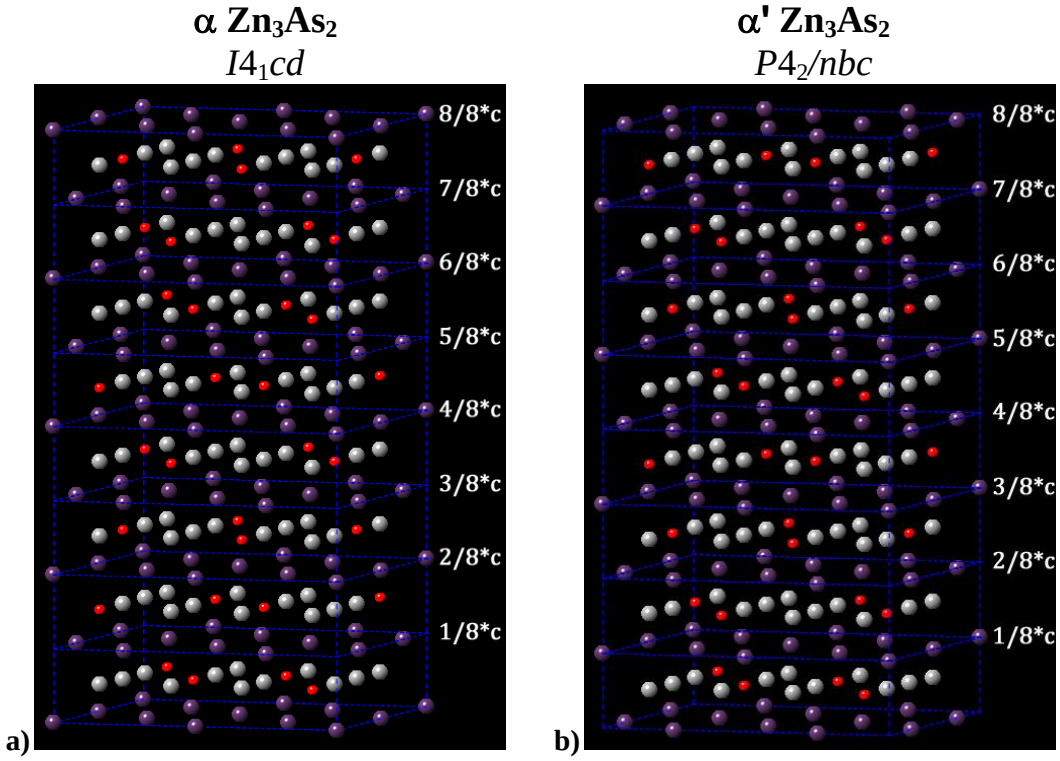

Figure 7-12 | The atomic structures of α and α' Zn_3As_2 and corresponding simulated electron diffraction patterns for selected zone axes. a) The atomic structure of α Zn_3As_2 as described by Pietraszko.[22] b) The atomic structure of α' Zn_3As_2 as described by Pietraszko.[22] In both atomic models zinc vacancies are shown in red. Disorder in the atomic placement of zinc is not shown for clarity.

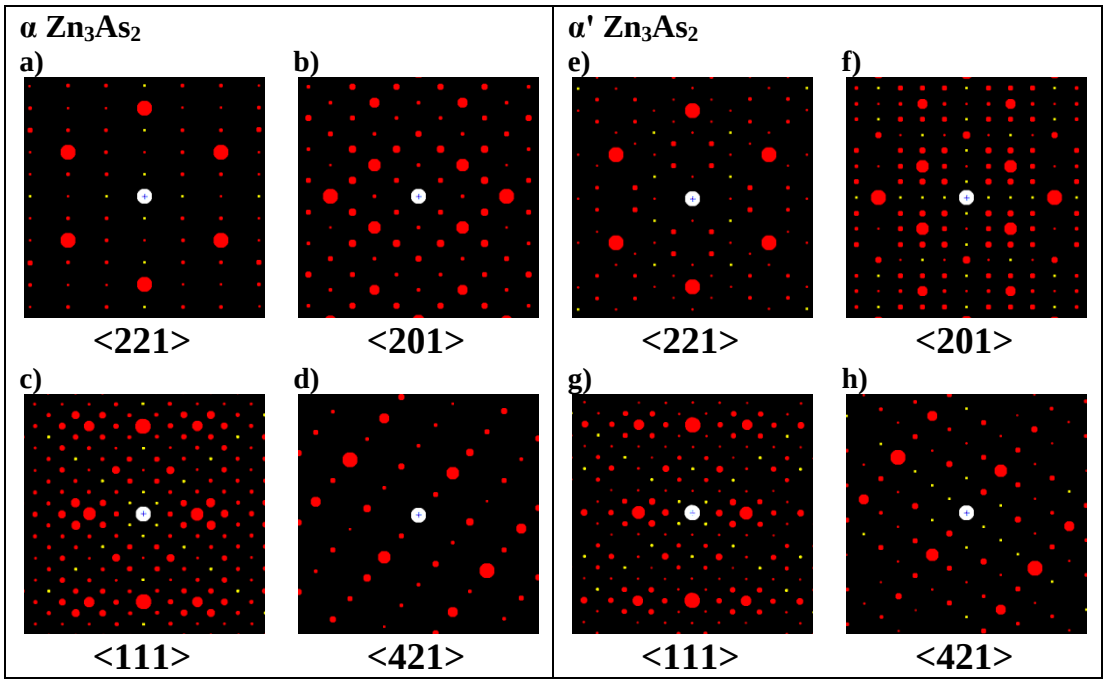

Figure 7-13 | Simulation of diffraction from α Zn_3As_2 and α' Zn_3As_2. (a-d): α Zn_3As_2; a) <221> axis; b) <201> axis; c) <111>; d) <421> axis; (e-h): α' Zn_3As_2; a) <221> axis; b) <201> axis; c) <111>; d) <421> axis. In all cases the patterns are oriented such that projection of the c* axis points left.

patterns. [The corresponding α phase simulations are shown in Figure 7-13(a-d)]

Under most imaging conditions electron diffraction is known to be strongly dynamical, which greatly complicates the analysis of the relative diffracted intensities.[1137] The intensity of the 204 type spot is however observed to be systematically greater than that expected from the modelling shown in Figure 7-9(l-o). One explanation for this difference could be a variation in zinc ordering. Variation from the expected structure[9, 22] has previously been deduced from Raman spectroscopy and is expected to occur with relative ease.[803] An understanding and control of zinc ordering is moreover expected to be crucial in realizing the thermoelectric potential of the Zn-V compounds.[19]

7.3.2.3 Growth direction and faceting

The Zn_3As_2 α' unit cell is shown in Figure 7-9(s) (a simplified representation is also shown in Figure 7-12(b)] with atomic models of the nanowire and nanoplatelet structures constructed from this basis shown in Figure 7-9(p,r) and (u,v), respectively. Figure 7-9(q) and (p) illustrate the diamond shaped cross-section of the nanowire with a top view SEM image of a nanowire looking along the <102> growth axis being inset

into a top view of the atomic model with labelled plane normals. Confirmed by both SEM imaging and TEM measurement of apparent diameter at varying tilts, this shape is formed by the primary sidewall facets of the nanowire which are {112} type or in equivalent cubic terms, {111} type. The vertices of this diamond are blunted by small strips of {102} type (equivalent cubic {110}) and to a lesser extent, {100} type sidewall facets. A similar pattern of faceting has previously been observed for nanowires grown in the cubic <110> direction across a diverse range of materials including oxide assisted silicon,[1138] Au seeded germanium,[1133] and Pd seeded InAs[1134]. Figure 7-9(s) shows the same atomic model in a side profile similar to the orientation of the nanowire in Figure 7-9(g).

In contrast to the 1D geometry found for the <112> growth direction in many other material systems,[452, 1133, 1139] Zn_3As_2 growing along <112> was here found to form 2D-like nanoplatelets. Figure 7-9(u-w) illustrate this geometry with an atomic model of the

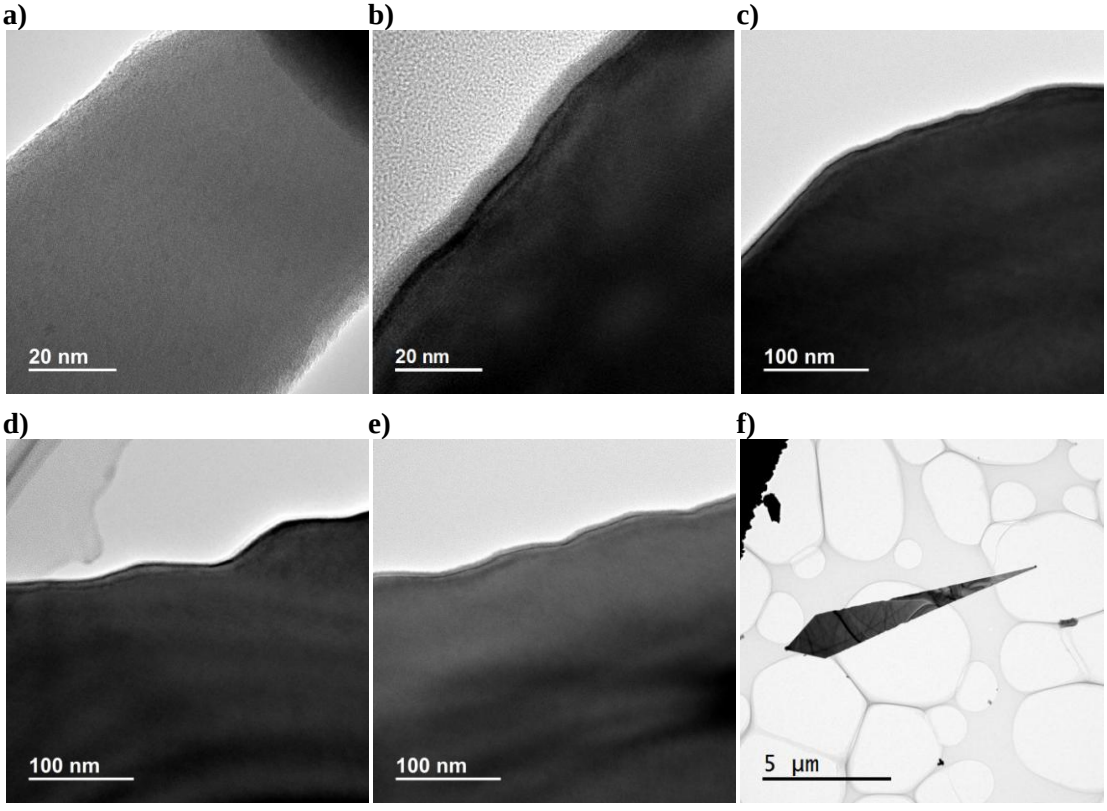

Figure 7-14 | Bright field TEM images showing the sidewall of a nanoplatelet moving from the tip towards the base (a-e) and a low magnification image of the entire platelet (f). The nanoplatelet forms with {110} type sidewalls (a) before overgrowth produces a complex combination of {122} and {110} type facets (b-e).

platelet structure shown from the side [Figure 7-9(v)) and the top (Figure 7-9(u)] with a top view SEM image of a platelet inset [Figure 7-9(t)]. Through a combination of SEM imaging and TEM tilting studies similar to those undertaken for the nanowire, the major facet or face of the nanoplatelet was determined to be {112} type or in equivalent cubic terms, {111} type. The shorter sidewalls perpendicular to the <112> viewing direction in Figure 7-9(g) were thus identified as {122} type or in equivalent cubic terms {112} type. The longer sidewalls meeting at the apex defined by the seed particle are more complex and were observed to vary in angle with the length of the nanoplatelet. (High resolution images of these sidewalls are shown in Figure 7-14 where it may be observed that this longer sidewall is actually a combination of {122} and {110} facets.) Interestingly, the geometry found here is somewhat similar to that reported by Kouklin *et al.*[795] for platelets millimetres in length and microns in thickness grown by thermal evaporation.

7.3.2.4 Composition and crystallography of the seed particle

Figure 7-15(c,d) shows typical EDXS spectra for a Zn_3As_2 nanowire and catalyst where Zn, As and Au are identified along with C and Cu from the specimen holder. EDXS

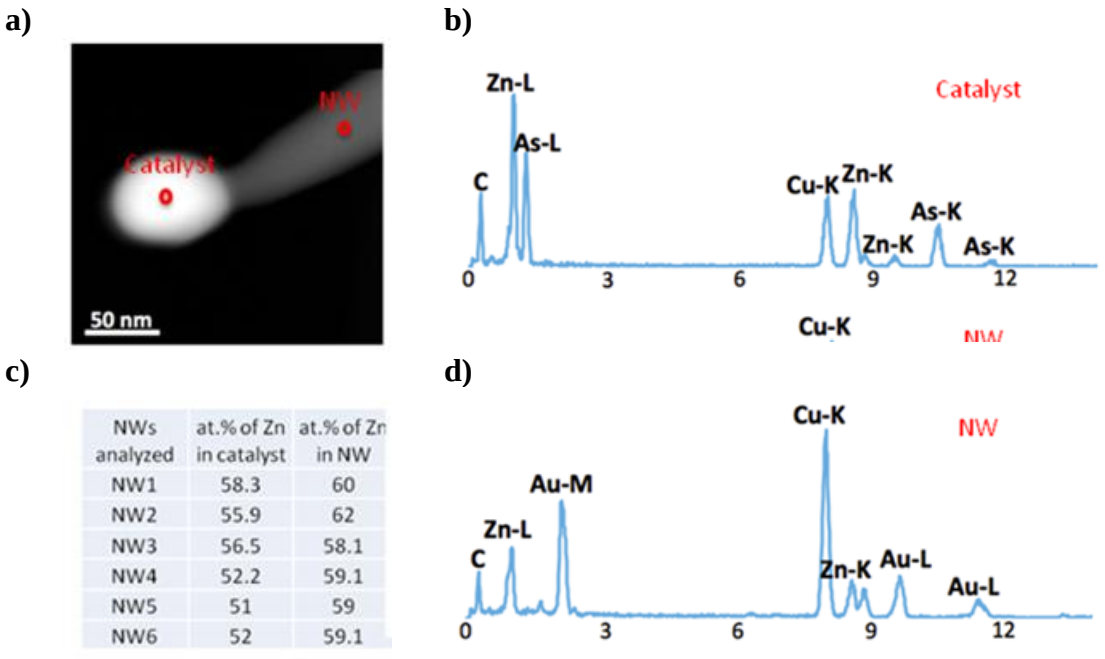

NWs analyzed	at.% of Zn in catalyst	at.% of Zn in NW
NW1	58.3	60
NW2	55.9	62
NW3	56.5	58.1
NW4	52.2	59.1
NW5	51	59
NW6	52	59.1

Figure 7-15 | EDXS Studies. a) typical locations for point EDXS point analysis; b) typical spectra for a seed particle; c) typical spectra for a nanowire; d) quantitative EDXS results for six individual nanowires.

results for several nanowires were analysed quantitatively using K-factors calculated (thin film approximation applied for TEM samples) for Zn-L, As-L and Au-M lines in Analysis Station (JEOL Engineering Co., Ltd). In agreement with the stoichiometry of Zn_3As_2, the nanowires were found to be approximately 60 at.% Zn and 40 at.% As, whereas the catalysts were found to contain over 50 at.% Zn with remainder being Au [Figure 7-15(b)].

Figure 7-16 further presents HRTEM images taken near the tip of a Au seeded platelet and nanowire [Figure 7-16(a) and Figure 7-16(d) respectively], selected area fast Fourier transforms (FFT) of areas corresponding to the seed particle and Zn_3As_2 nanostructures within these images [Figure 7-16(b,e)] and SADPs of the seed particles taken at this same orientation [Figure 7-16(c,f)]. From the FFTs of the seed particles

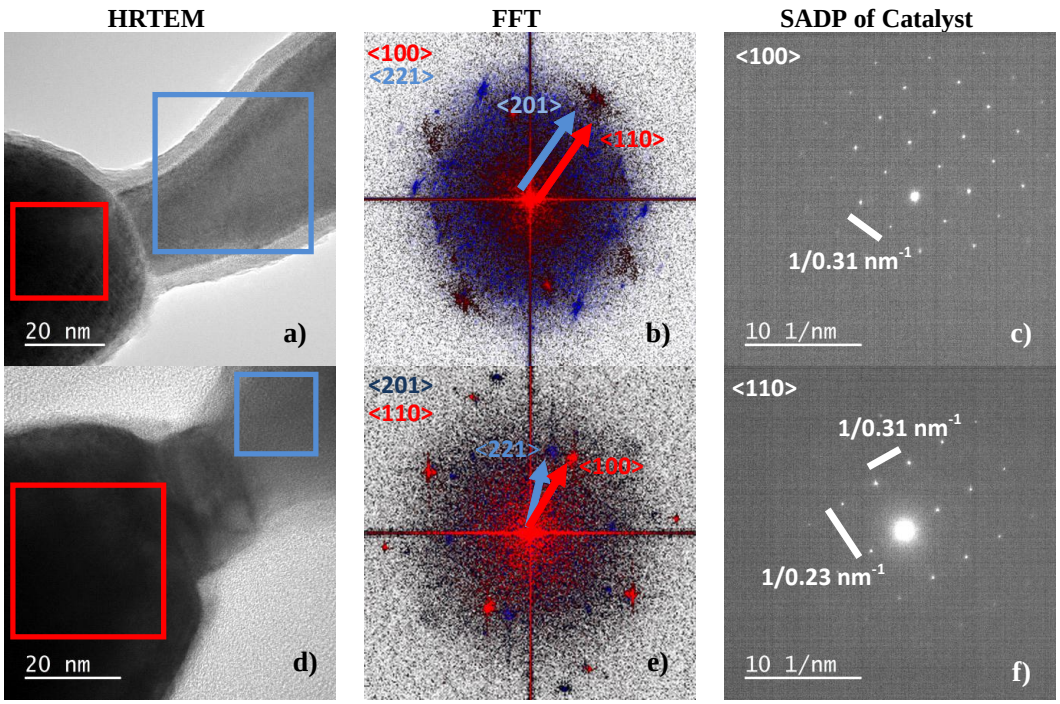

Figure 7-16 | HRTEM, FFT & SADP of Au seed particles. (a) HRTEM of the tip of a platelet showing areas chosen for (b) selected area FFTs where blue corresonds to the platelet (on <221>) and red the seed particle (on <100>). (c) SADP of the seed particle showing a cubic pattern of spacing 3.12 Å. (β' is a cubic phase with lattice parameter of approximately 0.315 Å.[21]) (d) HRTEM of the tip of a nanowire showing areas chosen for (e) selected area FFTs where blue corresponds to the nanowire (on <201>) and red the seed particle (on <110>). (f) SADP of the seed particle on the same orientation.

(shown in red) and more clearly in the SADPs, both seed particles may be indexed to Au-Zn alloy β' which has the chemical formula AuZn.[21] Similar alloying has been reported for the Au-assisted nanowire growth of a variety of zinc based compounds including ZnO and ZnSe.[1021, 1140, 1141]

The AuZn phase was found across the Zn_3As_2 nanostructures studied. Similarly high post growth concentrations of reactants in the seed particle have been widely reported for III-V nanowires.[536, 678, 1045] It is furthermore interesting to consider that the steady state concentration of Zn in the Au seed particle may have significantly exceeded this post growth value of 50 at.%. Also observed from Figure 7-16 is a close orientational relationship between AuZn and Zn_3As_2 phases. For both structures and orientations shown the seed particle and Zn_3As_2 nanostructure are simultaneously on zone. The <221> zone axis of the platelet in Figure 7-16(a-b) corresponding to the <100> zone axis of the AuZn seed particle and the <201> zone axis of the nanowire in Figure 7-16(d-e) corresponding to the <110> zone axis of the AuZn seed particle. In Figure 7-16(b) the <201> direction of the Zn_3As_2 is furthermore observed to align with the <110> direction of the AuZn and in Figure 7-16(b) the <221> direction of the Zn_3As_2 is close to the <110> direction of the AuZn.

7.3.3 Photoluminescence studies

Both the Zn_3As_2 nanowires and nanoplatelets were found to emit a strong photoluminescence (PL) signal in the near-infrared. Figure 7-17(a) shows typical spectra which in this case were obtained from an ensemble of nanostructures over the temperature range of 90 to 330 K. A single peak is observed to narrow and blueshift from 1.0 eV at room temperature to 1.1 eV at 80 K. These energies correspond well to what has previously been described as the band edge emission of bulk Zn_3As_2.[49, 308] The integrated intensities of the PL emission are maximum near room temperature (see Figure 7-18) decreasing relatively slowly with decreasing temperature (activation energy 21.5 meV) and quite quickly (85.3 meV) with increasing temperature. This is in contrast to several earlier reports which did not observe this peak below 100 K.[49, 308] Botha *et al.*[308] for instance, found band-edge emission to become gradually quenched before disappearing altogether at a temperature of approximately 110 K. Various lower energy peaks (0.7 – 1.0 eV), tentatively identified as transitions between the conduction band and acceptor states were instead observed to begin appearing at temperatures as

high as 190 K. The line shapes and relative intensities of these lower energy peaks were furthermore observed to vary with the V/II ratio used for growth and the growth substrate orientation.

A similar result was also found for samples grown by MBE with the additional point that at the lowest of temperatures, 1.85 K, band edge emission was again observed.[49] In both cases the authors attributed the absence of band edge emission at lower temperatures to an indirect bandgap as suggested by previous pseudo-potential modelling of the band structure.[1142] The nature of the bandgap in this system is however contentious as other experimental results have shown the transition to be direct.[875, 1143] We suggest that some of these discrepancies arise from variation in material quality and that in our case the VLS growth method may act to reduce impurity incorporation.[515]

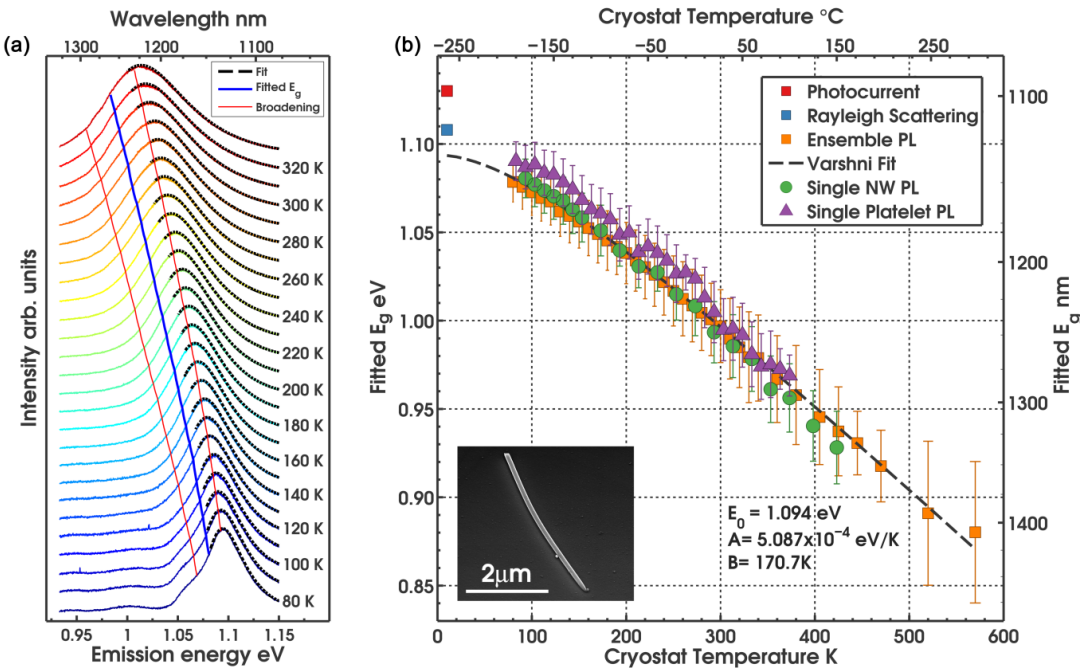

Figure 7-17 | Temperature dependant PL of Zn_3As_2 nanostructures: (a) Temperature dependant PL spectra from an ensemble of Zn_3As_2 nanostructures showing fits (dashed lines) to the high energy tails of the spectra. The fitted bandgap and broadening are also shown. (b) Fitted bandgap and broadening (error bars) as a function of temperature for an ensemble of Zn_3As_2 nanostructures (squares), a single Zn_3As_2 nanowire (circles) and a single Zn_3As_2 platelet (triangles). A fit of the Varshni equation to the ensemble data is also shown (dashed line). An SEM image of the Zn_3As_2 nanowire investigated is inset.

We also recall the planar defect-free nature of our nanostructures.

In order to quantify both band gap and effective spectral broadening the high energy tail of each PL spectrum was fitted with a line shape describing band-to-band emission.[1144] The form chosen describes direct band to band transitions as convolved with a Gaussian distribution:[1144, 1145]

$$I_{PL} = A \int \sqrt{E' - E_0}\, \exp\left(-\frac{E' - E_0}{k_B T}\right) \frac{1}{\sigma} \exp\left(-\frac{(E_0 - E')}{2\sigma^2}\right) dE' + c \qquad \ldots(7\text{-}1)$$

where E_0 is the transition energy, T is the electronic temperature, σ is the standard deviation of the Gaussian convolution, A and c are constants, E' is the dummy variable used for convolution and k_B is Boltzmann's constant. As plotted in Figure 7-17(a), the fits, the extracted band gap and the extracted effective broadening (first standard deviation of the modelled Gaussian distribution) are seen to reproduce both the data and trends discussed. The extracted carrier temperatures [Figure 7-19(b)] are furthermore close to the measured lattice temperatures indicating equilibrium between carriers and

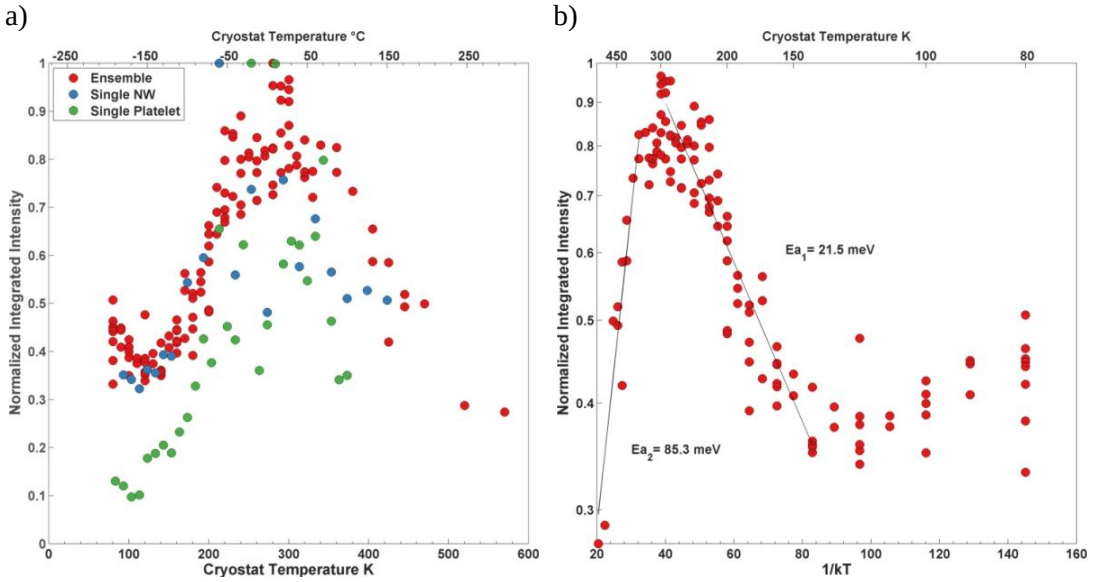

Figure 7-18 | Normalized integrated intensity as a function of temperature for the data shown in Figure 7-17(a). a) Linear scale; b) Logarithmic scale vs. $1/kT$. Note maximum intensity occurs around room temperature decreasing with an activation energy of 21.5 meV at lower temperatures and an activation energy of 85.3 meV at higher temperatures.

thermal phonons.

Interestingly, a step in the extracted carrier temperature is noted around 150K, the same point as there is an apparent increase in PL intensity. This temperature equates well with the exciton binding energy as calculated using the hydrogenic approximation:

$$E_x = \frac{-m_r^* q^4}{8h^2\epsilon^2}\frac{1}{n^2} \qquad \ldots(7\text{-}2)$$

where ϵ is the dielectric constant of the semiconductor and m_r^* is the reduced mass;

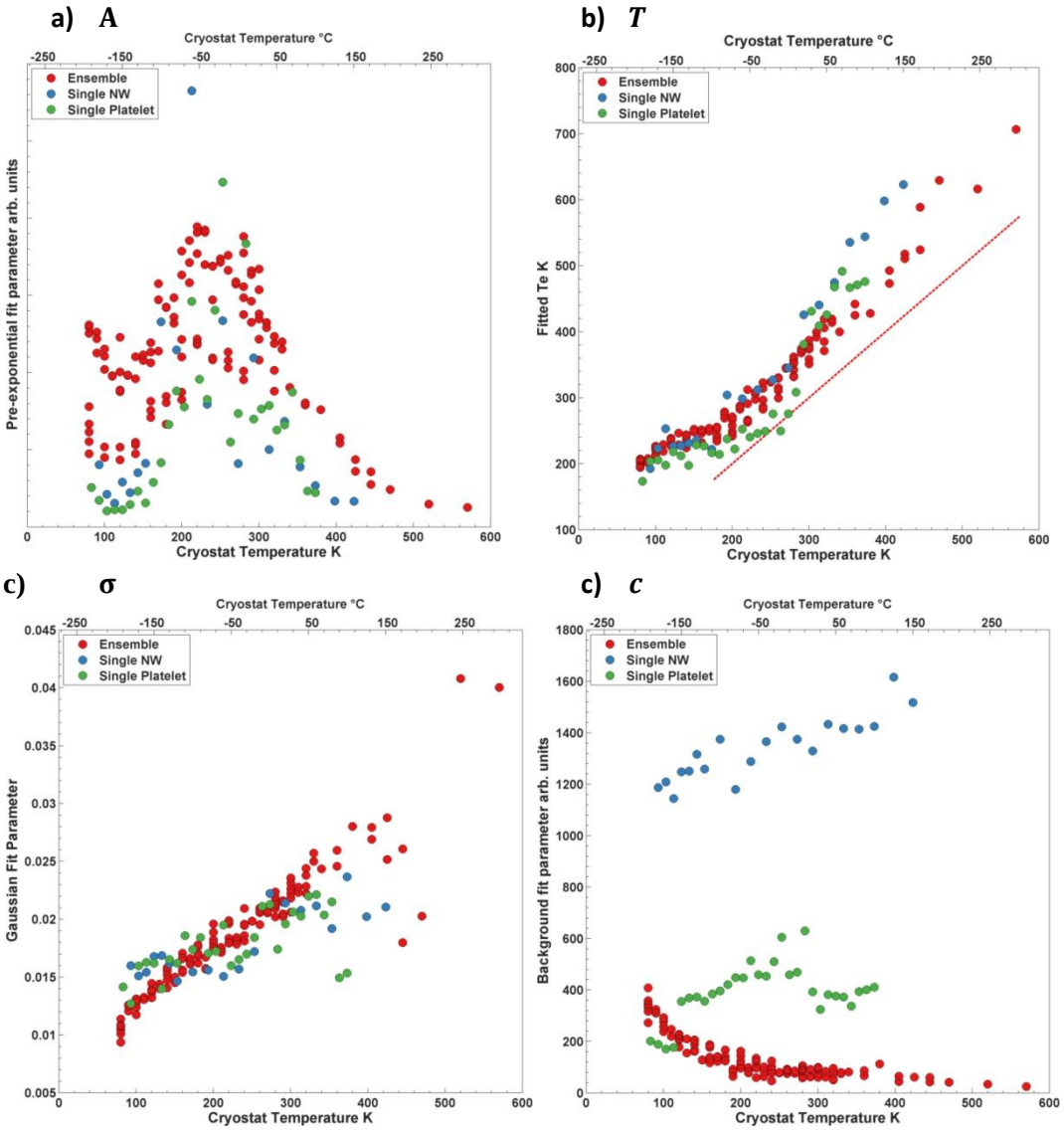

Figure 7-19 | Parameters determined for the fit of Equation 7-1 to the data shown in Figure 7-17(a). a) Pre-exponential term A; b) electronic temperature T; c) standard deviation of the Gaussian convolution σ; d) constant c.

$$\frac{1}{m_r^*} = \frac{1}{m_e^*} + \frac{1}{m_h^*} \qquad \ldots(7\text{-}3)$$

Substituting $m_e^* = 0.2m_0$ and $m_h^* = 0.36m_0$ [8] and $\epsilon = 11$ [9] gives an exciton binding energy of 14.4 meV, which equates to kT at 167 K. Similar values have been determined experimentally for the related semiconductor $ZnAs_2$.[10 11, 12]

In Figure 7-17(b) the fitted bandgap energy and its effective broadening is plotted as a function of lattice temperature for a single nanowire (SEM shown inset), a single platelet and the same ensemble of nanostructures studied in Fig. 2(a). Little variation is observed between datasets with a fit of the Varshni equation to the ensemble data in the

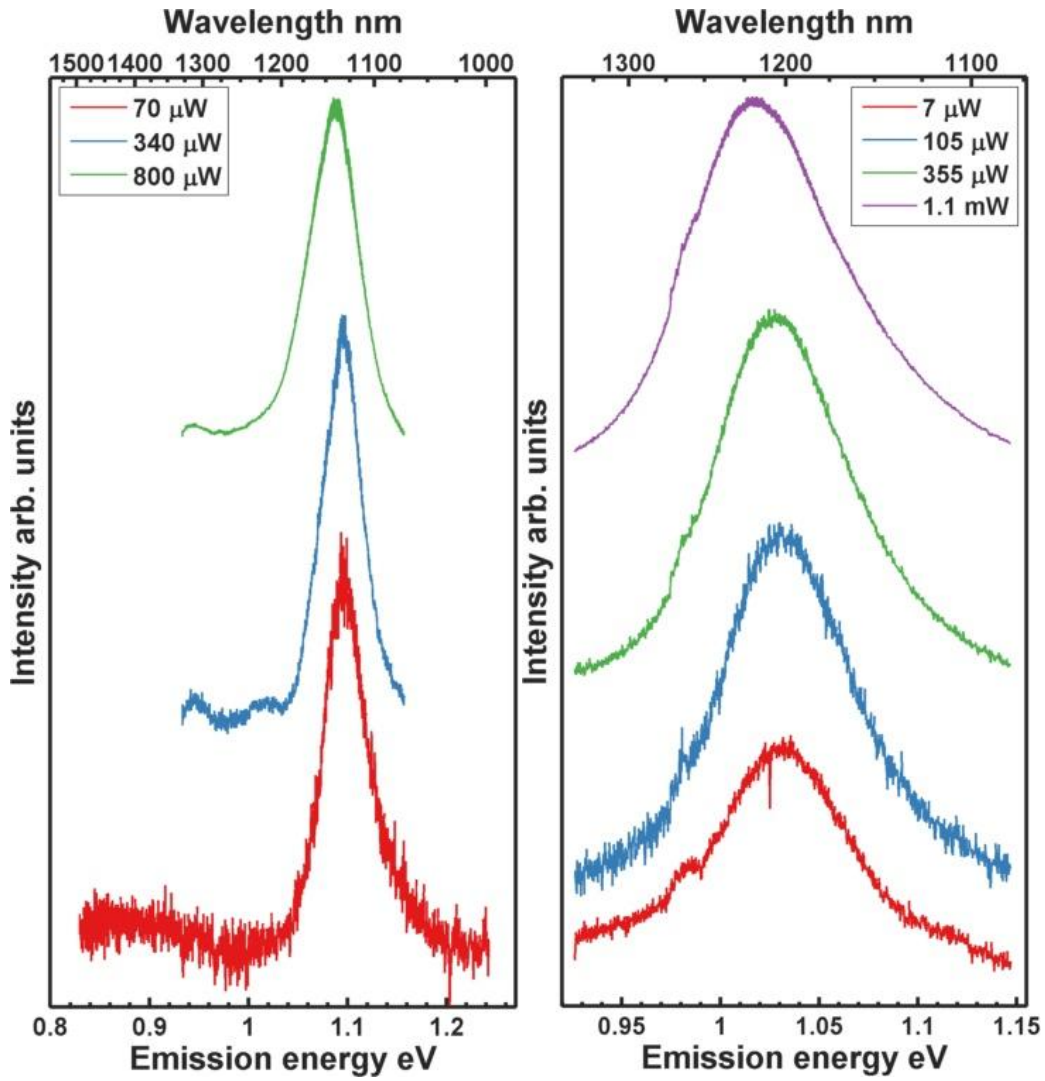

Figure 7-20 | Power dependence of PL emission from a single Zn_3As_2 nanowire at a) 80 K and b) 300 K. Note the consistency of the results over the power range investigated with a slight redshift occurring at the highest of pump powers.

temperature range of 80 to 570 K returning the coefficients; E_g = 1.094 eV, A = 5.087 x10^{-4} eV/K and B = 170.7 K. This fit and the underlying data is in good agreement with the behaviour of bulk Zn_3As_2.[308, 875] As discussed later, the fit also anticipates our low temperature measurements by both Rayleigh scattering and energy dependant photocurrent measurements.

Given that the band structure of Zn_3As_2 is poorly understood and previous studies have shown a power dependence to PL,[308] emission was assessed across a broad range of excitation intensities. Figure 7-20 presents the power dependence of PL emission from a single Zn_3As_2 nanowire at both 80 K and room temperature. The 830 nm excitation source was focused here to a spot size approaching the diffraction-limit giving areal power densities between approximately 0.25 and 39 kW/cm^2. Little variation was observed for excitation intensities less than those used in the experiments above suggesting artefacts due to band filling were not significant. At powers above several 100 µW (approximately 8 kW/cm^2) slight redshift and broadening was observed likely due to specimen heating.

7.3.4 Transient Rayleigh Scattering Spectroscopy

In order to further understand and quantify the efficiency of emission as observed by PL, transient Rayleigh scattering spectroscopy (TRS) experiments were performed on single Zn_3As_2 nanostructures. This technique provides insight into the carrier dynamics of a sample by measuring the time dependant photo-modulated polarization response of scattered light from a single nanowire following photoexcitation.[1069, 1098] By modelling this response parameters such as the band gap energy, background carrier concentration and minority carrier lifetime may be extracted.

Figure 7-21(a) presents a typical contour plot of the pump-induced variation in the photo-modulated polarization response, $\Delta R'/R' = \Delta(R_{\parallel} - R_{\perp})/(R_{\parallel} - R_{\perp})$, as a function of incident photon energy and time following photoexcitation. A strong response with a decay extending beyond 1 ns is immediately apparent in the energy range between 1.05 and 1.25 eV. As this measurement represents a derivative form at later times, the zero crossing point (dashed line, Figure 7-21(a)) of approximately 1.10 eV marks the band edge of these nanostructures.

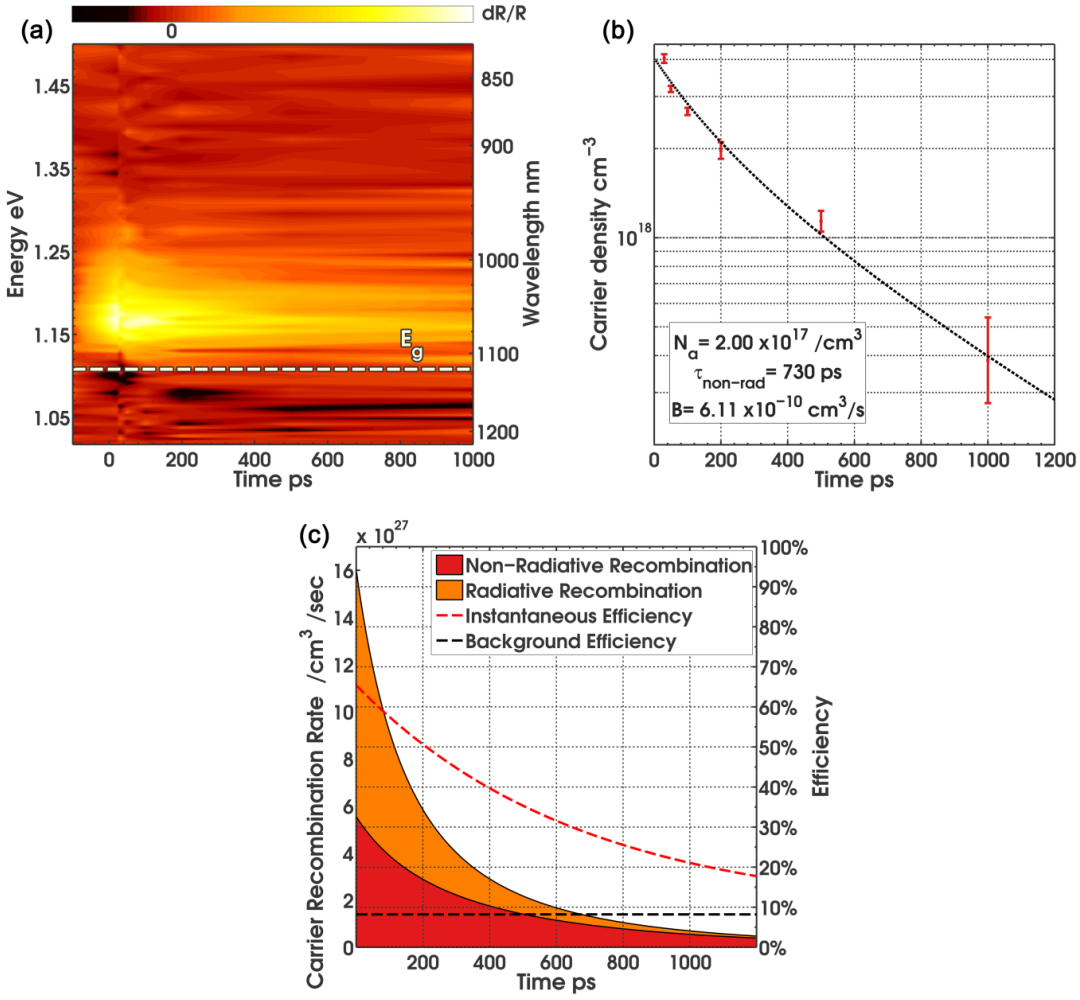

Figure 7-21 | Transient Rayleigh scattering spectroscopy of a single Zn_3As_2 nanowire: (a) Time dependant photo-modulated polarization response showing fitted bandgap. (b) Measured electron hole plasma density and fit extracting non-radiative lifetime and radiative recombination rate coefficient. (c) Plot of radiative and non-radiative recombination rates and the extracted internal quantum efficiency.

Using simple band-to-band transition theory to determine the carrier-dependent complex index of refraction, fits to the TRS spectral line shapes were made for given times following photoexcitation.

The fundamental band gap was thus determined to be at 1.108 eV at 10K with an effective broadening of 30 meV (FWHM). This energy and effective broadening correspond well to the PL results presented in Figure 7-17 and previous low temperature investigations of Zn_3As_2.[49, 875, 1143] Fits to the TRS lines shape required a free hole

density of $2x10^{17}$ cm^{-3} in the valence band, a concentration similar to that previously found from optical absorption and Hall measurements of nominally undoped Zn_3As_2 at low temperature.[49, 781, 875]

Figure 7-21(b) shows the extracted photoexcited carrier concentrations as a function of time following photoexcitation and These values are seen to decay from approximately 4 $x10^{18}$ to 4 $x10^{17}$ cm^{-3} in around 1 ns. Observed on the logarithmic axis, the non-linear nature of this decay at earlier times is suggestive of significant radiative recombination. Fitting this decay to bimolecular recombination which includes a linear non-radiative loss term, we find the lifetime of non-radiative decay to be 730 ps and the bimolecular recombination coefficient, B, to be $0.6x10^{-9}$ cm^3/s. The corresponding fitted temperature

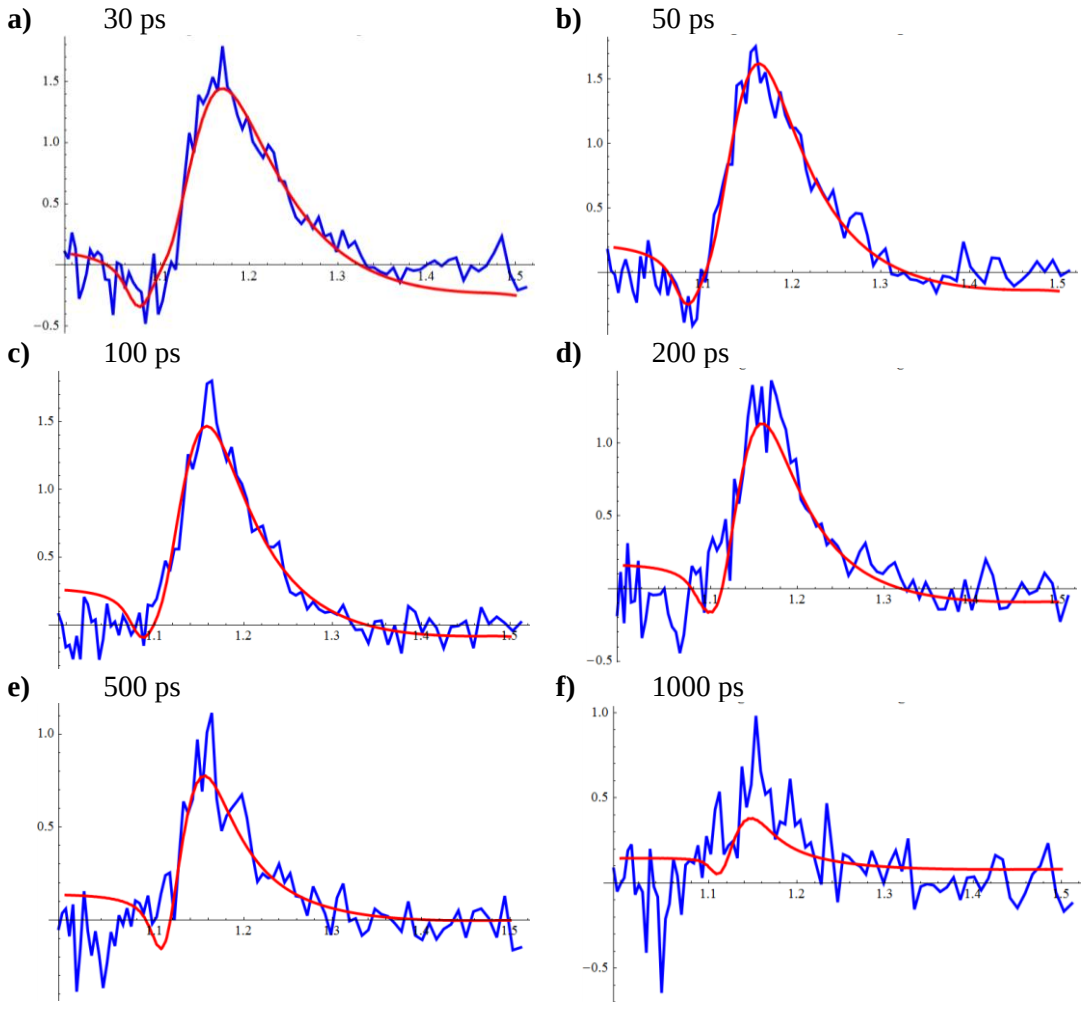

Figure 7-22 | Polarization response $\Delta R'/R' = \Delta(R_{\parallel} - R_{\perp})/(R_{\parallel} - R_{\perp})$ at various times following excitation (blue lines). a) 30 ps; b) 50 ps; c) 100 ps; d) 200 ps e) 500 ps f) 1000 ps. The fits to the raw data are shown (red).

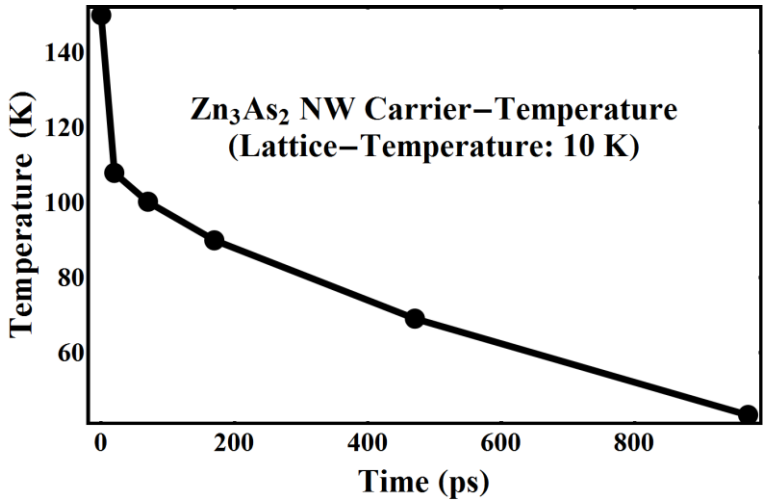

Figure 7-23 | Fitted carrier temperature as a function of time following photoexcitation.

decay is presented in supplementary Figure 7-23, where a rapid decay in the initial 100 ps likely relates to initial energy loss through LO-phonon emission followed by acoustic phonon emissions at later times.

The non-radiative lifetime found here is significantly longer than that measured previously for unpassivated GaAs nanowires and approaches values measured for InP nanowires.[1146, 1147] Given the nanowire geometry, such a long non-radiative lifetime is indicative of a low surface recombination velocity. The radiative recombination coefficient, B, is furthermore similar to that of direct bandgap semiconductors and likely incompatible with a phonon assisted transition. Taken together these two factors lead to a high IQE and may be considered responsible for the observation of a strong PL signal. Figure 7-21(c) plots the instantaneous non-radiative and radiative decay rates and their corresponding internal quantum efficiency (IQE) as a function of time following photoexcitation. Beginning at around 60%, the IQE is observed to decrease towards a background level of 8% as determined by the background carrier concentration.

7.3.5 Optoelectronic Characterization

In order to realize the optoelectronic potential of our Zn_3As_2 nanostructures we fabricated single nanowire and single nanoplatelet metal-semiconductor-metal (MSM) photoconductor devices (Figure 7-24 shows an example). Figure 7-25(a-b) present dark

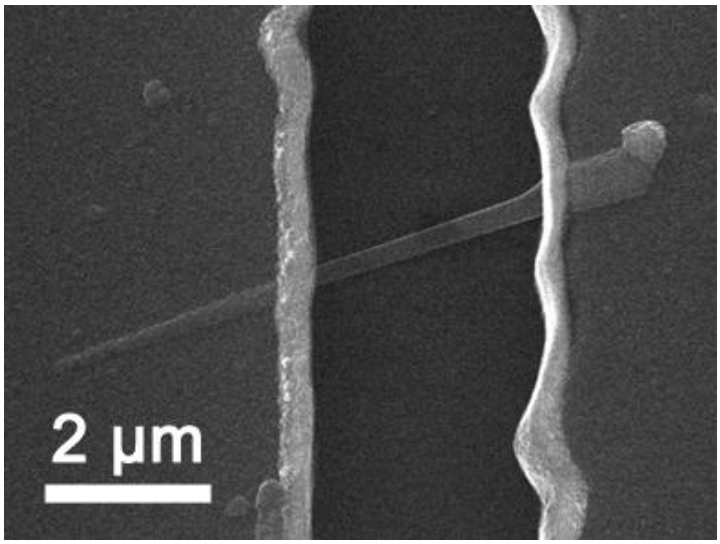

Figure 7-24 | SEM image of a single platelet MSM device.

I-V characteristics of a single platelet device at room temperature and a single nanowire device at both room and low temperature respectively. These IV curves show that both Ti-Al contacts to the nanowires and nanoplatelets form Schottky barriers.

To quantify the background carrier concentration of each device we adopted the approach of Zhang *et al.*[1148] The devices were modelled as a three element equivalent circuit consisting of an Ohmic resistance in series with Schottky barriers described by thermionic emission under forward bias and thermionic field emission[1149] under reverse bias. The forward-biased Schottky contact was described by an expression for thermionic emission:

$$I(V_f, \phi_b) = AA^{*}\mathrm{T}^2 \exp\left(\frac{-\phi_b}{k_B T}\right) \exp\left(\frac{qV_f}{nk_B T}\right)\left\{1 - \exp\left(\frac{-qV_f}{k_B T}\right)\right\} \qquad \ldots(7\text{-}4)$$

where A is contact area of the nanowire, $A^{*} = 4\pi \mathrm{m}^{*}\mathrm{qk}^2/\mathrm{h}^3$ is Richardson's constant ϕ_b the Schottky barrier height, k_B is the Boltzmann constant, T is the absolute temperature, q is the elementary charge and n is the ideality factor of the Schottky diode. The reverse-biased Schottky contact was further described by thermionic field emission (TFE)[1149]:

$$I(V_r, \phi_b) = AJ_{sr}(V_r, \phi_b) xp\left[V_r\left(\frac{q}{k_B T} - \frac{1}{E_0}\right)\right] \qquad \ldots(7\text{-}5)$$

with J_{sr} being the saturation current given by:

$$J_{sr} = \frac{A^{*}T(\pi q E_{00})^{1/2}}{k} exp\left(-\frac{\phi_b}{qE_0}\right)\left\{q(V-\zeta/q)+\frac{\phi_b}{cosh^2\left(\frac{qE_{00}}{kT}\right)}\right\}^{1/2} \quad \ldots(7\text{-}6)$$

where ζ is the difference between the Fermi energy and the top of the valence band, and

$$E_0 = E_{00}\coth\left(\frac{qE_{00}}{kT}\right) \quad \ldots(7\text{-}7)$$

with

$$E_{00} = \frac{\hbar}{2}\left[\frac{N_a}{m^{*}\varepsilon_s\varepsilon_0}\right]^{1/2} \quad \ldots(7\text{-}8)$$

Zn_3As_2 Properties

ε_s	10	Ref. 8
m^*	0.36 m_0	Ref. 9

Table 7-1 | Relevant properties of Zn_3As_2

	Nanowire Device	**Platelet Device**
l	3.65 µm	3.10 µm
d	92 nm	255 nm
A	6.66 x10^{-15} m^{-2}	1.28 x10^{-14} m^{-2}

Table 7-2 | Dimensions of the MSM devices

Nanowire Device

N_a	1.67 x10^{18} /cm^3
R_{NW}	5.39 x10^7 Ω
ϕ_1	0.498 eV
ϕ_2	0.558 eV
ζ	0.07 eV
n_1	5.82
n_2	4.50

Table 7-3 | Fit parameters for the nanowire device

Platelet Device

N_a	7.41 x10^{18} /cm^3
$R_{Platelet}$	3.62 x10^4 Ω
ϕ_1	0.361 eV
ϕ_2	0.399 eV
ζ	0.07 eV
n_1	0.593
n_2	0.799

Table 7-4 | Fit parameters for the platelet device

A self-consistent fit to the experimental IV data was achieved by taking the current through each contact and the nanowire to be equal to the source-drain current and the sum of the voltage drops across each contact and the nanowire to be equal to the total source-drain bias.

The relative permittivity of Zn_3As_2 and effective hole mass were taken from the literature.[1143] The spatial dimensions of each device were measured from SEM images [nanowire Figure 7-25(d), platelet Figure 7-24]. The contact area was defined as the cross sectional area of the Zn_3As_2 nanostructure.[13] Table 7-3 and Table 7-4 detail the parameters determined from the fits to the I-V characteristics of the nanowire and platelet device as presented in Figs. 4(a-b). As discussed by Zhang *et al.*[1148], the barrier heights found by this method are an effective value dependant upon other defined parameters, among which the contact area is particularly significant.

Fits to the I-V curves using this analysis are shown for the room-temperature plots, with

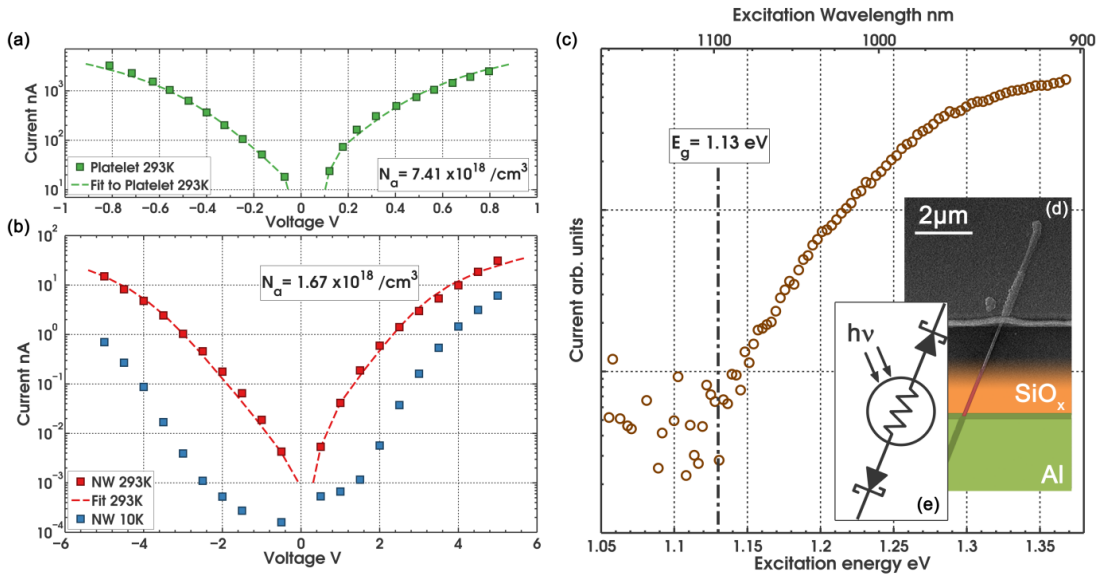

Figure 7-25 | Characterisation of single Zn_3As_2 nanostructure metal-semiconductor-metal photodetector devices. a) Room temperature dark I-V characteristic and fit of a single platelet device. b) Room temperature and low temperature dark I-V characteristics of a single nanowire device showing a fit to the room temperature data. c) Photocurrent normalized by incident power as a function of excitation energy for the single nanowire device imaged by SEM and illustrated schematically in d) and e) respectively.

the background carrier concentration of the nanowire determined to be 1.67×10^{18} cm^{-3}, and the platelet 7.41×10^{18} cm^{-3}. Although high, these values are consistent with previous studies which have found Zn_3As_2 to possess a significant p-type background[49, 314, 317] which has been related to shallow-level[310] native defects.[263] Compensation of this p-type character has been successfully achieved by doping with In.[781] In the case of the related semiconductor material, Zn_3P_2, a similar p-type background has been related to the formation of charged phosphorus interstitial defects.[311] Despite significant background hole concentrations, high room temperature hole mobilities of between 200-300 cm^2/Vs have previously been determined for Zn_3As_2.[317, 325]

All the Zn_3As_2 MSM devices investigated were found to be photosensitive giving useful photodetection down to approximately 1.0 eV. Figure 7-26 contrasts the light and dark I-V curves of a nanowire device under 550 nm illumination at room temperature where a clear photoresponse is shown across the voltage sweep.

As shown in Figure 7-25(c), the photocurrent versus excitation energy at low temperature displays a clear onset at approximately 1.13 eV. This energy is consistent with the band gap found by transient Rayleigh scattering spectroscopy and extrapolation of the Varshni fit to the PL data. It also accords well with previous measurements of the absorption edge at low temperature which were assigned to a direct bandgap

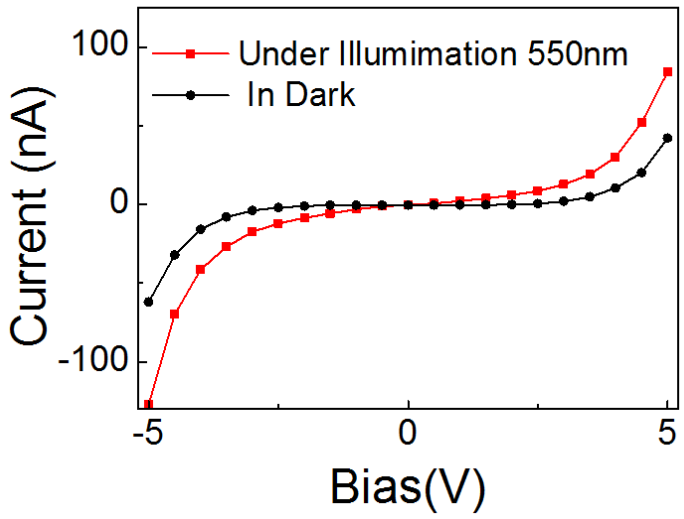

Figure 7-26 | Light and dark I-V characteristics of a nanowire MSM device at room temperature under 550 nm illumination.

transition.[1143, 1150, 1151]

7.3.6 Nickel-seeded growth of Zn_3As_2 Nanostructures.

Nickel thin films were found to seed the growth of Zn_3As_2 nanostructures across a similar parameter space to that found for Au nanoparticles. As described for Au in Section 7.3.1.2, at relatively low growth temperatures (below 400 °C) Ni seeding produced Zn_3As_2 nanocrystallites of several hundred nanometres in size [Figure 7-27(a)]. Above 400 °C, 0.5 nm thick Ni films typical gave a relatively low areal density of nanowires [Figure 7-27(b)]. Interestingly, Ni seeding was effective both with

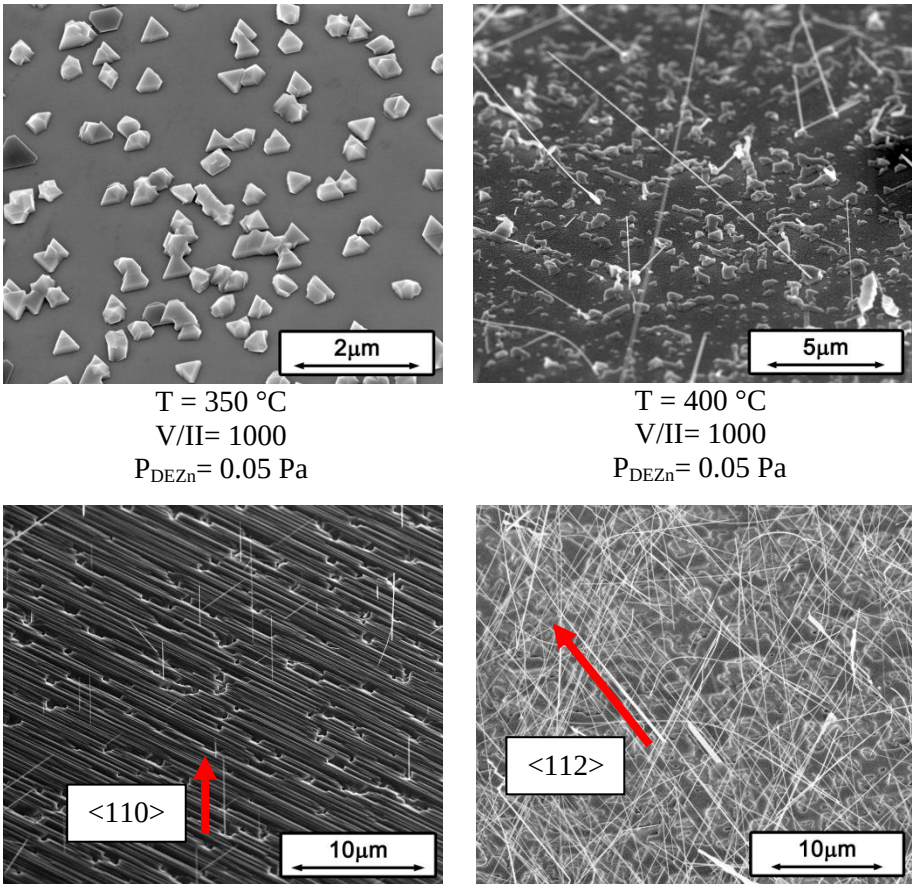

T = 350 °C
V/II= 1000
P_{DEZn}= 0.05 Pa

T = 400 °C
V/II= 1000
P_{DEZn}= 0.05 Pa

T = 500 °C
V/II= 34
P_{DEZn}= 3.6 Pa
Centre of substrate

T = 500 °C
V/II= 34
P_{DEZn}= 3.6 Pa
Edge of substrate

Figure 7-27 | Nickel-seeded Zn_3As_2 nanostructure growth at various reactor temperatures. a) 350 °C; b) 400 °C; c) 500 °C away from the edge of the growth substrate showing growth in a <110> pseudocubic equivalent direction; d) 500 °C close to the edge of the growth substrate showing growth in a <112> pseudocubic equivalent direction. All micrographs show the sample substrate tilted 45 ° to normal.

and without pre-annealing which was normally conducted at 600 °C under AsH_3 for ten minutes. Nickel seeded nanowires were significantly longer than Au seeded nanowires grown under the same conditions [contrast Figure 7-27(b) with Figure 7-3(c)] and showed little tapering. Both <440>/<408> and <114>/<421> growth directions (pseudocubic equivalents <110> and <112>) were observed from measurements of elevation angle by SEM. Significant variation was often visible across a single growth substrate as demonstrated by Figure 7-27(c,d). In this case, a low density of <110> type nanowires was observed away from the edges of the substrate and a high density of <112> type nanowires close to the edges. Similar 'edge-effects' reported for III-V nanowire growth have been related to local variations in effective V/III ratio.[1116, 1152] As the limiting reactant, zinc may well be in greater supply at the edge of the growth substrate. Relationships between growth conditions and growth direction have previously been established for a number of nanowire systems.[1126, 1130, 1131, 1153, 1154]

Like Au-assisted Zn_3As_2 growth, a VSS style mechanism[159, 183] is expected here as Ni has a relatively high melting point (1455 °C)[15] and does not form a low temperature eutectic with either Zn or As. Nickel does however form a variety of binary compounds ith each of these elements.[15, 1155] Previous investigations of Ni assisted growth have reported the formation of NiGa and $NiGe_x$ seed particles for GaAs and Ge nanowire growth respectively.[174, 175] In all cases here, post-growth TEM examination of Ni-assisted Zn_3As_2 nanowires revealed the seed particles to be NiAs. NiAs is a $P6_3/mmc$ prototype binary compound with a solid solubility range of 50.0-51.3 at.% As and a

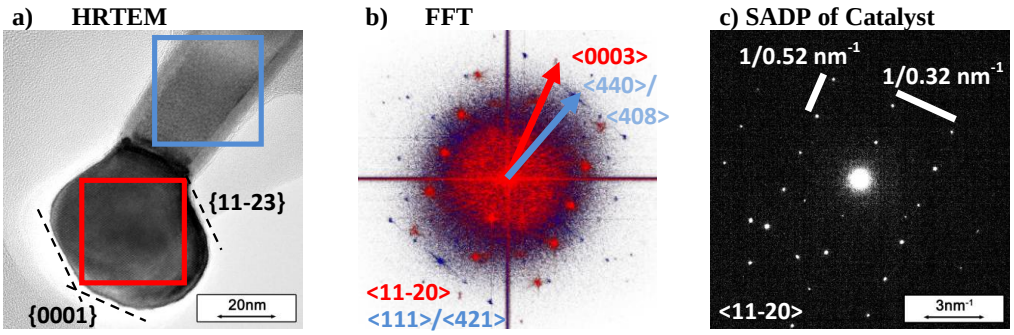

Figure 7-28 | TEM analysis of a Ni-seeded Zn_3As_2 nanowire. (a) HRTEM of the tip of the nanowire showing the areas chosen for (b) selected area FFTs where blue corresponds to the nanowire (on <111>/<421>) and red the seed particle (on <11-20>). (c) SADP of the seed particle giving spacings of 1/0.52 and 1/0.32 nm^{-1} which correlate well with the expected values for to NiAs[15].

melting point of 970 °C.[15]

Figure 7-28(a) presents a HRTEM image of the tip of a Ni-seeded Zn_3As_2 nanowire showing the NiAs seed particle aligned to a major zone axis. The presence of both Ni and As were confirmed through EDXS analysis and the SADP shown in Figure 7-28(c) can be indexed to the $\langle 11\bar{2}0 \rangle$ axis. The NiAs particle itself shows faceting corresponding to $\{11\bar{2}3\}$ and {0001} planes (Miller indices {111} and {001}) which was common across all the NiAs imaged [see for example: Figure 7-29(a)]. Nanowire growth is along a <440>/<408> axis (the orientation of the c-axis was not be determined here. The cubic equivilant is direction <110>) and no stacking faults were observed

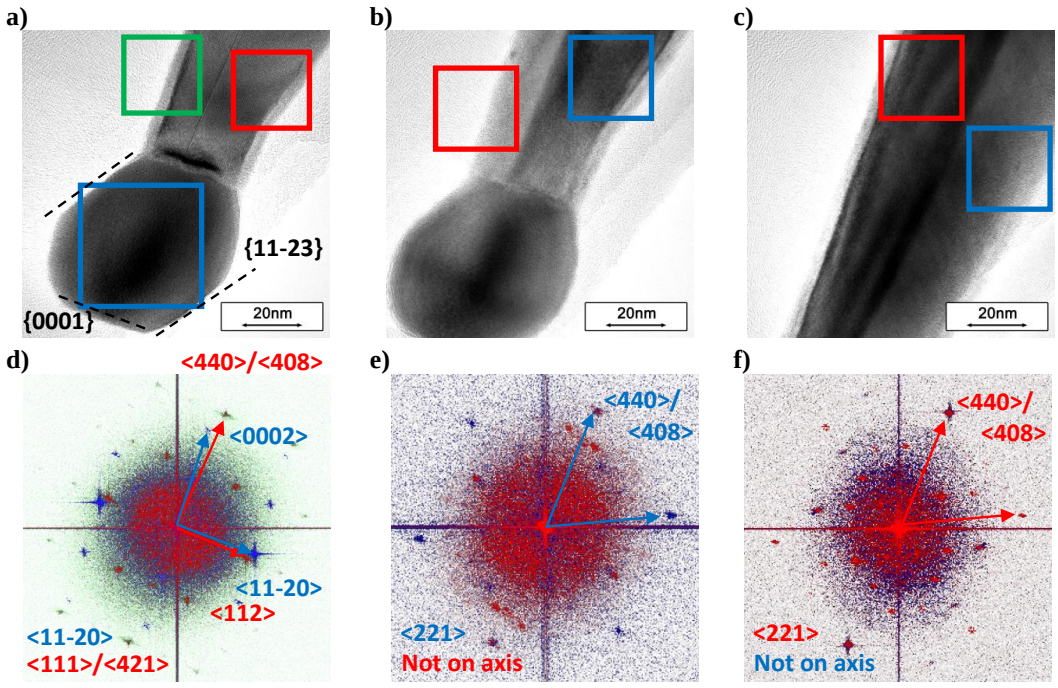

Figure 7-29 | TEM analysis of a Ni seeded Zn_3As_2 nanowire with a lamellar-type twin. (a-c) HRTEM images of the tip of the nanowire on various zone axes showing the areas chosen for selected area FFT. d) Composite of selected area FFTs taken from (a) where blue corresonds to the seed particle on <11-20>, red the twin to the right on <111>/<421> and green the twin to the left also on <111>/<421>. e) Compoisite of selected area FFTs taken from (b) where blue corresonds to the twin to the right on <221> and red the twin to the left which is not on a major zone axis. f) Composite of selected area FFTs taken from (c) where blue corresonds to the twin to the right which is not on a major zone axis and red the twin to the left which is on <221>.

along the length of the nanowire in any of the imaged zone axes. The NiAs seed and nanowire are simultaneously aligned on $\langle 11\bar{2}0 \rangle$ and <111>/<421> respectively with their <0001> and <440>/<408> directions close to alignment. A similar alignment was observed for all the Ni-assisted Zn_3As_2 nanowires analysed [see Figure 7-29(b) where the alignment between <0001> and <440>/<408> is even closer].

Unlike Au-assisted growth, some Ni-assisted Zn_3As_2 nanowires showed lamellar twinning. Figure 7-29 presents bright field TEM images showing three different orientations of the same nanowire along with FFTs of selected areas within those images. In each image a line running through the centre of the nanowire parallel to the growth direction may be identified as a lamellar twin. Lamellar twins have been reported for both group IV and III-V nanowires growing in the <112>[608, 1156-1160] and <110>[1161] directions and have been shown to be responsible for both a particular growth mode[1139] and several unique geometries.[1162-1164] Taking FFTs each side of the twin plane in Figure 7-29(a) reveals that both crystal orientations are on the <111>/<421> axis (the orientation of the c-axis was not determined. The cubic equivalent is direction <112>). Rotating approximately 19.5 degrees around the <110> growth axis gives Figure 7-29(b) where the region to the right of the plane is one the <221> axis (cubic equivalent <111>) and the region to the left is not on a major zone axis. This result is reversed for a rotation 19.5 degrees in the opposite direction Figure 7-29(c). Taken together, these findings are compatible with a rotational twin on the <221> axis (cubic equivalent <111>).

7.4 Zinc Phosphide

7.4.1 Growth parameters

7.4.1.1 Absolute diethylzinc flow rate

As was described for Zn_3As_2 in Section 7.3.1.1, Zn_3P_2 growth required DEZn partial pressures greater than a temperature dependant threshold level. Figure 7-30 presents the results of three Zn_3P_2 growth runs at a temperature of 475 °C and PH_3 molar fraction of 0.012. At a DEZn partial pressure of 0.47 Pa, no growth is observed and the Au seeds remain as nanoparticles on the InP (110) substrate [Figure 7-30(a)]. With a doubling of the DEZn partial pressure the threshold for growth is exceeded and a range of Zn_3P_2 nanostructures including nanowires are observed [Figure 7-30(b)]. A further doubling

leads to excessive planar growth with the nanostructures being somewhat buried [Figure 7-30(c)]. That this shift to planar growth is a direct result of the increase in DEZn partial pressure and not the changing V/II ratio is further discussed in Section 7.4.1.3.

The outcome of growth at various combinations of DEZn partial pressure and reactor temperature is indicated in Figure 7-31. As was discussed for the corresponding plot of Zn_3As_2 experiments (Figure 7-2), the ordinate here is plotted as the partial pressure of elemental Zn as DEZn is expected to fully decompose across the majority of the temperatures considered[1112] and zinc is further expected to be the limiting vapour phase reagent. Contrasting the parameters that produced Zn_3P_2 growth (green circles) with those that did not (red circles), the partial pressure of zinc required for growth is seen to increase rapidly with temperature. Relative to Zn_3As_2 (Figure 7-2), this threshold is slightly higher but its increase can again be approximated as a doubling every 25 °C. Close correlation is also again observed between the threshold for nanostructure growth found here and the partial pressure of zinc in equilibrium with bulk Zn_3P_2 (purple squares) reported in the literature. Unlike the Zn-As system, current thermodynamic assessments of the Zn-P system[16, 30] do not predict the vapour pressure of Zn_3P_2 with any accuracy and CALPHAD modelling of the zinc vapour pressure in equilibrium with Zn_3P_2 is not shown. The stability region for Zn_3P_2 is instead taken as the area above the experimentally determined vapour pressure curves of Schoonmaker and Lemmerman[10]

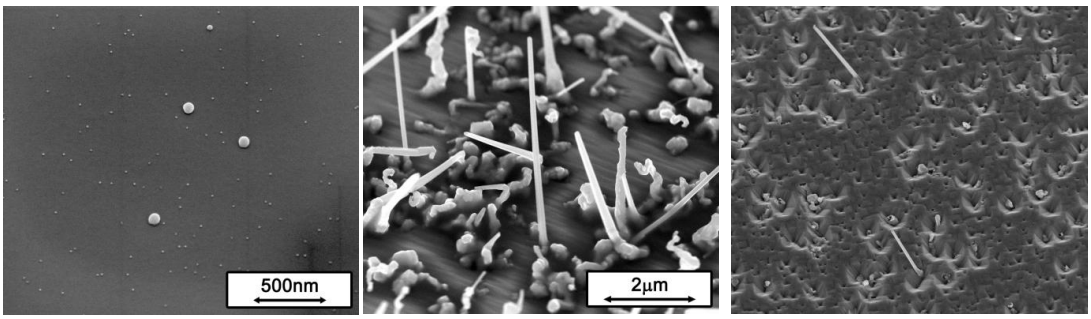

a) T = 475 °C, V/II= 256, P_{DEZn}= 0.47 Pa

c) **T = 475 °C**, V/II= 124, P_{DEZn}= 1 Pa

b) **T = 475 °C**, V/II= 35, P_{DEZn}= 1.90 Pa

Figure 7-30 | Sensitivity of Zn_3P_2 growth to the DEZn flow rate. a) Insufficient DEZn flow for growth. The Au seeds remain as nanoparticles on the substrate. b) A doubling of the DEZn flow rate produces Zn_3P_2 nanowire growth. c) A further doubling leads to excessive planar growth. All micrographs show the sample substrate tilted 45 ° to normal except (c) which is at 30 °.

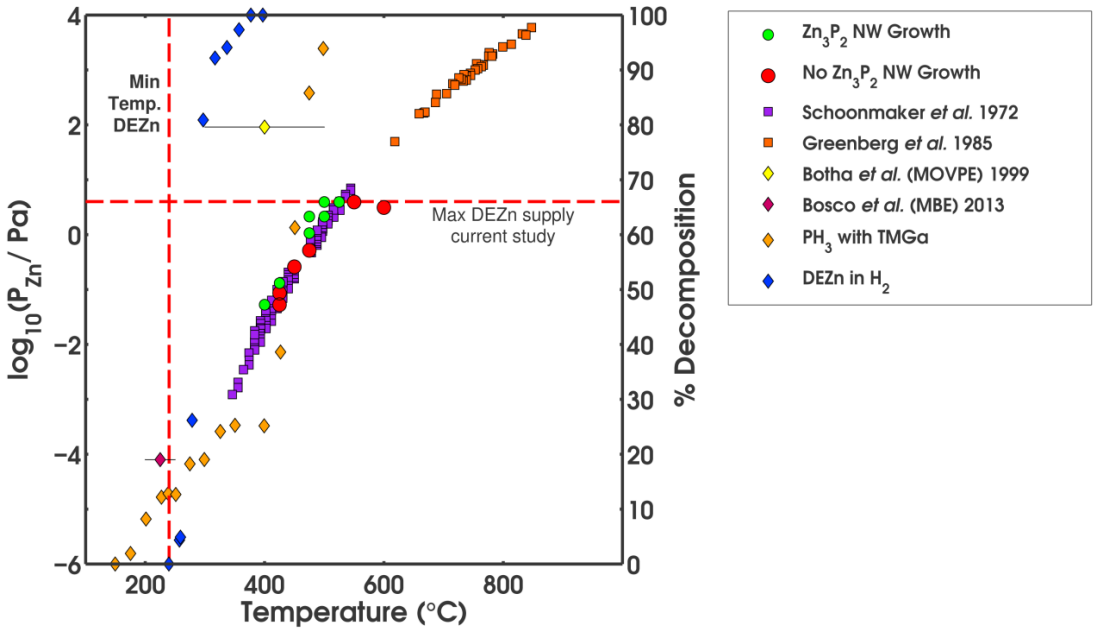

Figure 7-31 | Outcome of Zn_3P_2 nanowire growth for various zinc partial pressures and temperatures. The percentage decomposition of the precursors DEZn in H_2 and PH_3 with TMIn is further plotted as a function of temperature on the right-hand axis.[1, 2] Also plotted is the temperature dependence of zinc partial pressure in equilibrium with Zn_3P_2 as measured experimentally by Schoonmaker and Lemmerman[10] and Greenberg *et al.*[28]. For Zn_3P_2 growth to occur precursor decomposition is required and the partial pressure of zinc must exceed that in equilibrium with Zn_3P_2(s). The expected growth window for the current experimental setup is ~ 250-525 °C.

and Greenberg *et al.*[28]. The intersection of this data with the maximum partial pressure of zinc obtainable in the current experimental setup defines a maximum growth temperature of approximately 525 °C.

Also plotted on Figure 7-31 are heterogeneous decomposition curves for the precursors DEZn and PH_3 as a function of temperature.[1, 2] As material deposition requires some degree of precursor decomposition, these curves define the minimum growth temperature for Zn_3P_2 using the current precursors. In contrast to Zn_3As_2, DEZn is expected to be limiting with virtually no decomposition below 250 °C. Together with the maximum DEZn flow rate and the vapour pressure of Zn_3P_2, a growth parameter space is thus defined for Zn_3P_2 growth using the current experimental setup. This

parameter space covers a temperature range from approximately 250-525 °C and zinc partial pressures from around 0.01-3.6 Pa or equivalently, 0.5-136 sccm.

7.4.1.2 Growth Temperature

Figure 7-32 documents the morphology of Au-seeded Zn_3P_2 growth as a function of reactor temperature. In a similar manner to Au-seeded Zn_3As_2 growth (Section 7.3.1.2), relatively low reactor temperatures (<475 °C) are seen to promote the formation of nanocrystallites [Figure 7-32(a-c)]. As was discussed for Zn_3As_2, at lower temperatures zinc may act to disrupt VLS growth.[237, 243, 246, 539, 540, 578, 1113] Zn_3P_2 nanowire growth was first obtained at a temperature of 475 °C [Figure 7-32(d)]. From measurements of the elevation and azimuthal angles relative to the (110) substrate, both <110> and <112> type growth directions were identified. In addition to these geometrically straight nanowires, a large number of kinked nanowires, planar nanowires and other Zn_3P_2

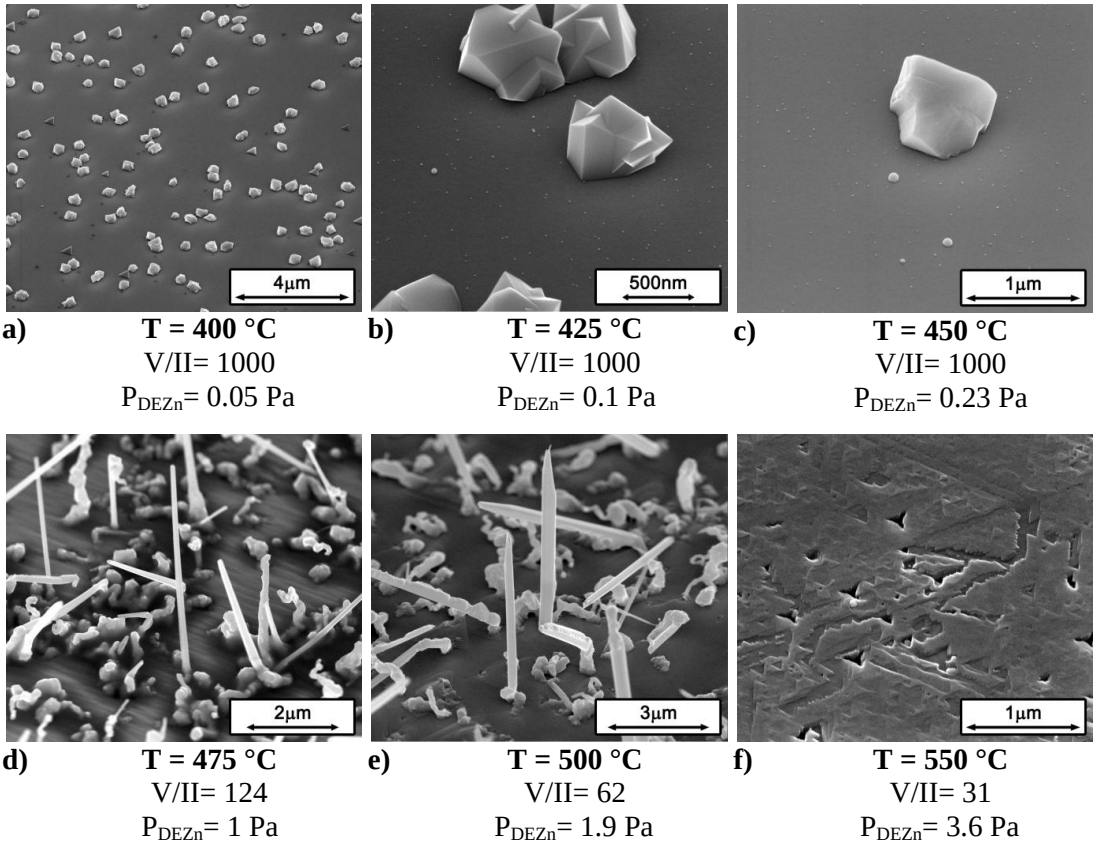

a) **T = 400 °C** V/II= 1000 P_{DEZn}= 0.05 Pa
b) **T = 425 °C** V/II= 1000 P_{DEZn}= 0.1 Pa
c) **T = 450 °C** V/II= 1000 P_{DEZn}= 0.23 Pa
d) **T = 475 °C** V/II= 124 P_{DEZn}= 1 Pa
e) **T = 500 °C** V/II= 62 P_{DEZn}= 1.9 Pa
f) **T = 550 °C** V/II= 31 P_{DEZn}= 3.6 Pa

Figure 7-32 | Effect of growth temperature on the morphology of Zn_3P_2 nanostructures. At the lowest temperatures investigated growth was not by the VLS mechanism. At the highest, no growth was obtained. The growth time in all cases was 20-30 minutes. a) 400 °C; b) 425 °C; c) 450 °C; d) 475 °C; e) 500 °C; f) 550 °C. All micrographs show the sample substrate tilted 45 ° to normal.

nanostructures were also formed [Figure 7-32(d)]. Unlike Zn_3As_2 growth however, no nanoplatelet structures were observed. Interestingly, the areal density of geometrically straight nanowires found here, 0.19 nanowires per square micron is similar to that found for Zn_3As_2 growth (see Section 7.3.1.2). At 500 °C Au-seeded Zn_3P_2 nanowires were observed to form with a similar areal density but vastly different morphology Figure 7-32(e). The diameter of these nanowires was larger with variable overgrowth and an often textured surface. The tips of these structures were particularly unusual with the seed apparently splitting to form a depression surrounded by sharp points. Unlike Zn_3As_2, a higher nanowire growth rate was not obtained at higher temperatures potentially due to the apparently reduced thermal stability of Zn_3P_2 (see Figure 7-33).Beyond 525 °C Zn_3P_2 growth was not obtained and substrates showed pitting relating to decomposition [Figure 7-32(f)]. Previous reports of Zn_3P_2 nanowire growth have employed thermal deposition and CVD techniques and the higher zinc partial pressures available through these techniques has enabled growth at temperatures of 600 °C and higher.[63, 329, 341, 1165]

In the experiments here, Zn_3P_2 showed reduced thermal stability relative to Zn_3As_2. Annealing at 500 °C for ten minutes under a phosphine molar fraction of 0.006 lead to total decomposition of Zn_3P_2 nanostructures and a return the substrate to a feature-less mirror-like appearance. Figure 7-33(a,b) contrasts Zn_3P_2 nanostructures cooled from

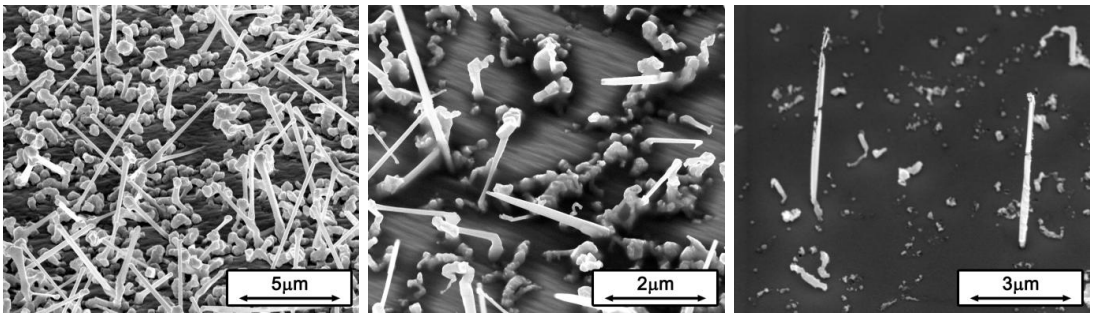

a) T = 475 °C
Both precursors supplied during cooling to 250 °C

b) T = 475 °C
Only phosphine supplied during cooling to 250 °C

c) T = 500 °C
Pulsed growth:
30s P_{DEZn}= 1.9 Pa
30s P_{DEZn}= 1.65 Pa

Figure 7-33 | Thermal stability of Zn_3P_2 nanostructures. a) Zn_3P_2 growth cooled under both DEZn and PH_3. b) Zn_3P_2 growth cooled under PH_3 only. c) Zn_3P_2 growth where the DEZn flow was alternatively varied to a value above and then below the threshold flow rate for growth. All micrographs show the sample substrate tilted 45 ° to normal.

their growth temperature of 475 °C under both PH_3 and DEZn [Figure 7-33(a)] with those cooled under PH_3 only [Figure 7-33(b)]. It is immediately apparent that the nanowires cooled under both precursors have a larger diameter and a greater amount of deposition is apparent. While some growth is expected when cooling under both precursors, the cooling window here is relatively short (around 15 minutes with 5 minutes below 300 °C) and deposition is not expected to be extensive.

Further evidence for the reduced thermal stability of Zn_3P_2 is provided by Figure 7-33(c). The nanowires in this figure were grown using a pulsing technique whereby the partial pressure of DEZn was cyclically increased to above the threshold for growth (1.9 Pa) and held for 30 seconds before being reduced to below the threshold (1.65 Pa) for the next 30 seconds. Cooling was under PH_3 only and the growth is otherwise comparable to that in Figure 7-32(e). The nanowires grown using this pulsing technique show clear evidence of decomposition with segments missing from along their length. Pulsed growth where the DEZn flow was totally suspended for 30 second intervals produced no Zn_3P_2 material.

7.4.1.3 V/II ratio

Growth was assessed at V/II ratios of between 34 and 1000. Figure 7-34 presents results for V/II ratios of 34, 124 and 434 at a temperature of 475 °C. Subtle effects are evident with the increasing V/II ratio appearing to favour planar growth and altering the geometry of the seed particle. Whereas the seed particle remains compact with a well-

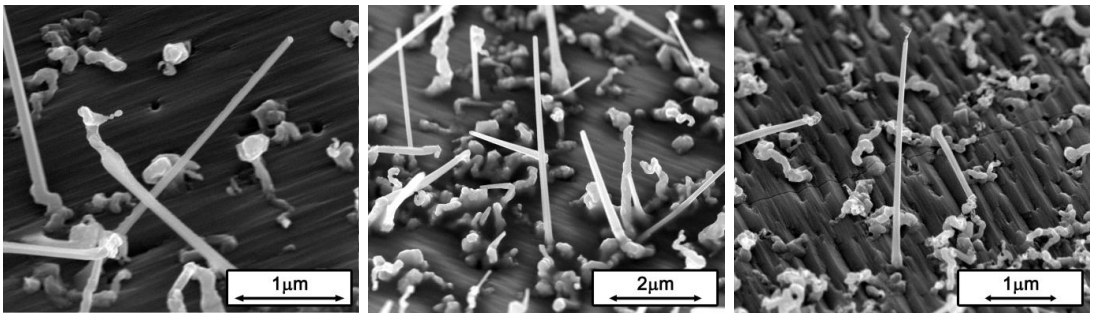

a) **T = 475 °C**
V/II= 34
P_{DEZn}= 1 Pa

b) **T = 475 °C**
V/II= 124
P_{DEZn}= 0.47 Pa

c) **T = 475 °C**
V/II= 434
P_{DEZn}= 1 Pa

Figure 7-34 | Effect of V/II on the morphology of Zn_3P_2 nanostructures grown at 475 °C. a) V/II=34; b) V/II=124; c) V/II=434. All micrographs show the sample substrate tilted 45 ° to normal.

defined interface at low V/II ratios [Figure 7-34(a)], increased phosphine supply appears to favour dewetting and complex faceting [Figure 7-34(c)]. Previous reports of Zn_3P_2 thin film growth by MBE have employed a Zn_3P_2 source and have therefore not been able to assess the effect of V/II ratio on growth.[320, 321]

7.4.1.4 Seed material

In addition to Au, a range of alternative seed materials were also investigated for the growth of Zn_3P_2 nanostructures. Limited success was achieved using Ag nanoparticles with the resultant structures being poorly faceted nanocrystallites [Figure 7-35(b)]. Thin

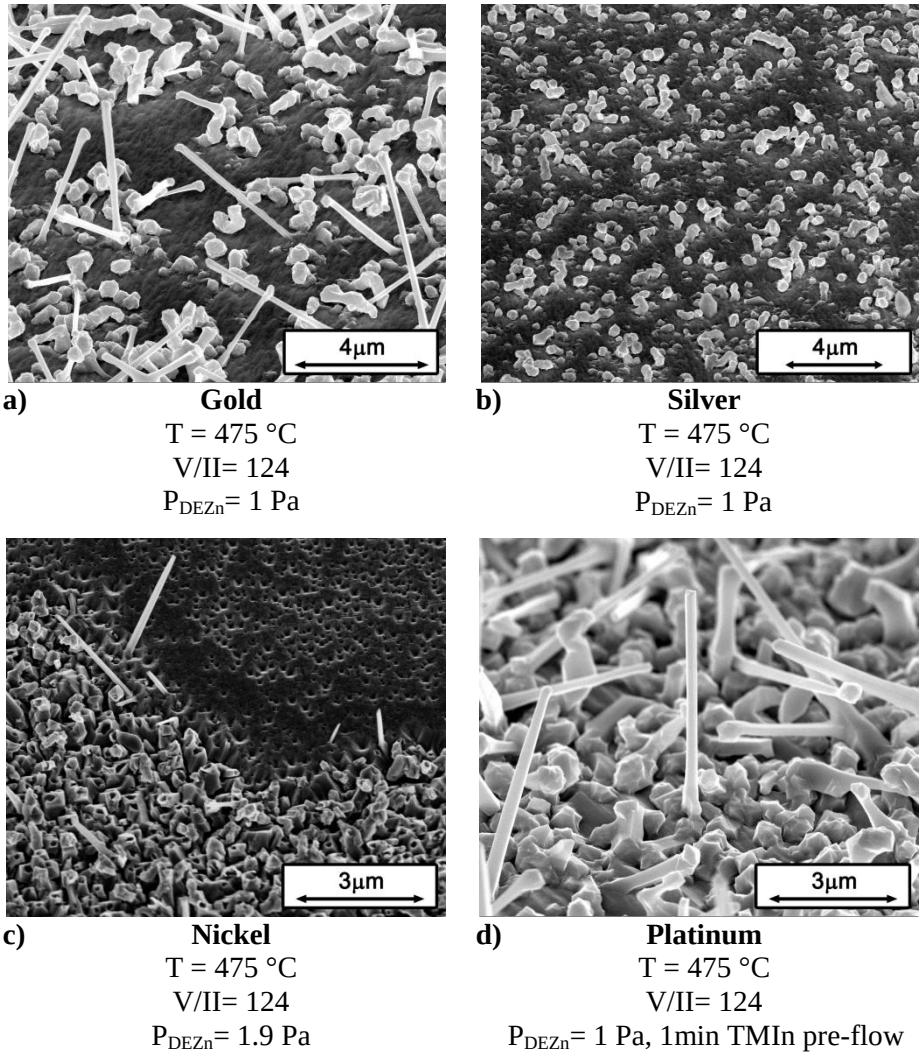

a) Gold
T = 475 °C
V/II= 124
P_{DEZn}= 1 Pa

b) Silver
T = 475 °C
V/II= 124
P_{DEZn}= 1 Pa

c) Nickel
T = 475 °C
V/II= 124
P_{DEZn}= 1.9 Pa

d) Platinum
T = 475 °C
V/II= 124
P_{DEZn}= 1 Pa, 1min TMIn pre-flow

Figure 7-35 | Zn_3P_2 nanostructure growth at 475 °C as seeded by various different metals. a) Gold (60 nm nanoparticles); b) Silver (60 nm nanoparticles); c) Nickel (0.5 nm thin film. Image here shows the edge of the film); d) Platinum (0.5 nm thin film. with a 1 minute TMIn pre-flow). All micrographs show the sample substrate tilted 45 ° to normal except (c) which is at 30 °.

films of Ni (0.5 nm) produced better results with a relatively low areal density of well facetted nanowire structures observed. Figure 7-35(c) presents an image of growth near the edge of the Ni thin film where the area towards the bottom left of the micrograph corresponds to the area which was covered by the Ni thin film. In addition to nanowire structures, a high areal density of nanotube structures is also observed. Growth was also achieved using a 0.5 nm thin film of Pt [Figure 7-35(d)]. In this case growth on InP and a short (1 minute) In pre-flow appeared to aid in nanowire growth. The Pt-assisted nanowires were characterized by relatively large diameters of around 200 nm and well defined facets. Some terracing was, however, observed by SEM especially towards the base of these structures.

Thin films of tin and zinc were not found to seed Zn_3P_2 growth under any of the parameters investigated despite Sn being reported to be an excellent catalyst for both IV and III-V nanostructure growth.[171, 172, 518] While the compound semiconductor Zn-Sn-P_2 is known, [1166, 1167] addition of tetraethyltin (TESn) was found to inhibit Zn_3P_2 nanowire growth and produce layer growth instead. Several previous publications have reported In seeded Zn_3P_2 nanowire growth by CVD methods,[63, 336, 1165] but attempts to induce In seeding through the decomposition of InP, TMIn pre-flow and even the continuous supply of TMIn throughout growth ultimately proved unsuccessful using the current MOVPE setup.

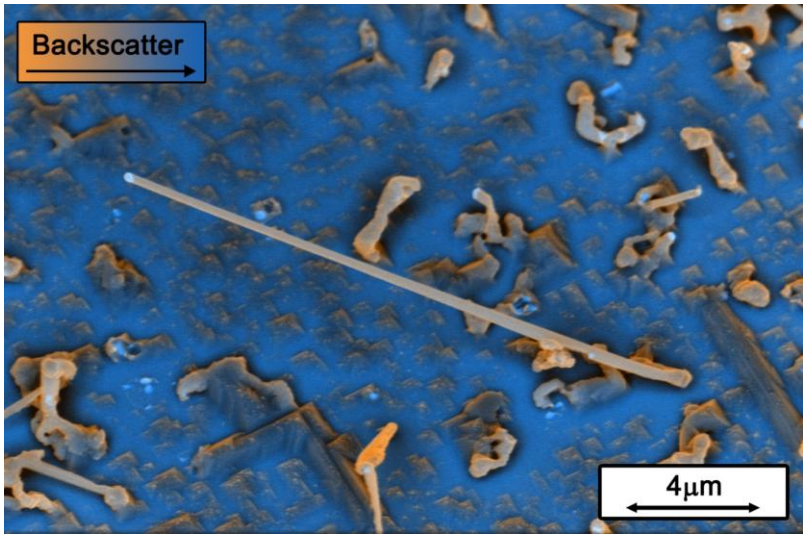

Figure 7-36 | Composite secondary electron (contrast) and backscattered electron (colour) image of Zn_3P_2 nanostructures demonstrating limited Au-seeded nucleation at 500 °C under a DEZn partial pressure of 1.9 Pa.

Although Au-seeding was found to be most successful approach to Zn_3P_2 nanostructure growth investigated here, the areal density of growth remained relatively low as is quantified in Section 7.4.1.2 and similarly for Au-assisted Zn_3As_2 nanostructures, in Section 7.3.1.2. Figure 7-36 is a composite secondary/backscatter SEM image of a typical Zn_3P_2 nanostructure growth where the Au particles can be readily identified. While many of the particles have clearly seeded VLS growth some remain as isolated nanoparticles. Statistical study of this image and similar revealed no difference in size between the Au nanoparticles that seeded growth and those that did not. It is likely in this situation that the nucleation of Zn_3P_2 nanostructures was determined by a stochastic process with relatively low probability.

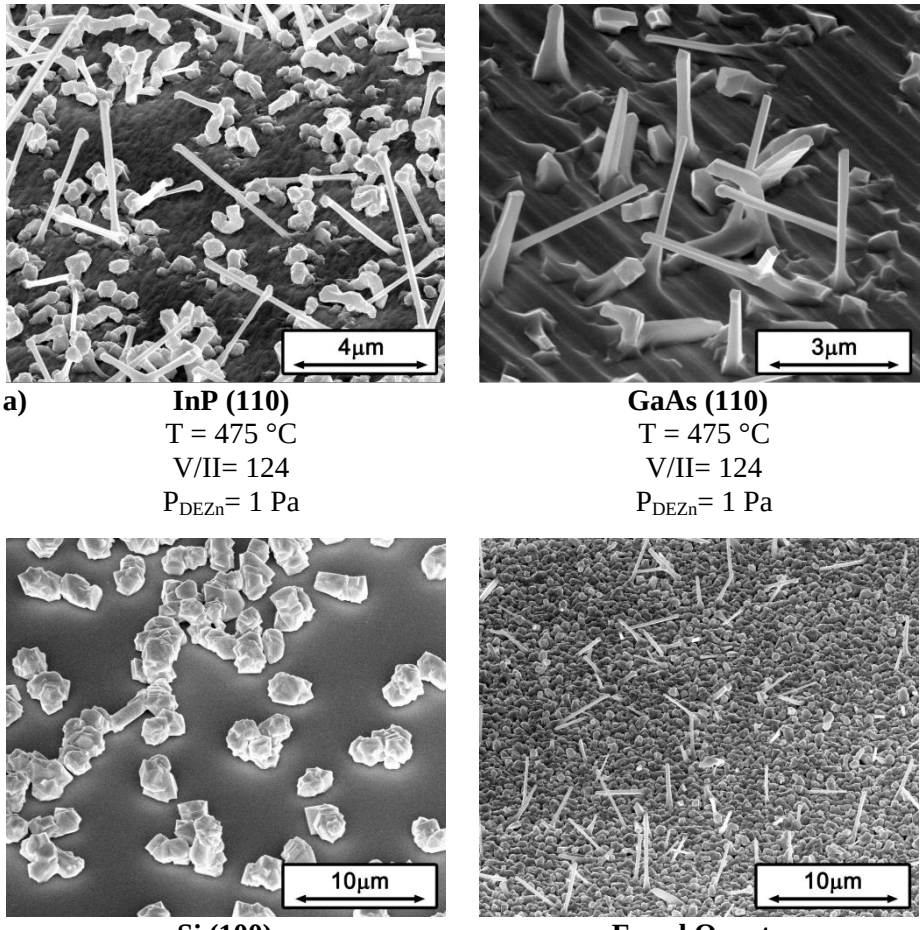

a) **InP (110)**
T = 475 °C
V/II= 124
P_{DEZn}= 1 Pa

GaAs (110)
T = 475 °C
V/II= 124
P_{DEZn}= 1 Pa

Si (100)
T = 475 °C
V/II= 124
P_{DEZn}= 1 Pa

Fused Quartz
T = 475 °C
V/II= 124
P_{DEZn}= 1 Pa

Figure 7-37 | Au seeded Zn_3P_2 nanostructure growth at 475 °C on various substrates. a) InP(110); b) GaAs(110); c) Si(100); d) Fused quartz. All micrographs show the sample substrate tilted 45 ° to normal.

7.4.1.5 Substrate

The studies here primarily employed InP(110) substrates. Indium phosphide was chosen as the most common binary phosphide wafer available and the (110) orientation was chosen as Zn_3As_2 nanowires had previously been found to take a <110> growth direction (see Section 7.3.2.3). In contrast to Zn_3P_2 growth on InP substrates [Figure 7-37(a)], growth on GaAs(110) produced nanowires of larger diameter and reduced height [Figure 7-37(b)]. While some terracing was still apparent by SEM, facets generally appeared smoother and better defined on the GaAs substrate and there appeared to be less kinking. As no AsH_3 was supplied during growth it is likely that substrate decomposition produced ternary $Zn_3P_{(2-x)}As_{(x)}$ material with As acting to improve faceting.[63] Alloying of the Au seed with In on the InP substrate likely also aided nanowire growth in a similar manner to that observed for Zn_3P_2 in Section 7.3.1.5.

Growth on Si substrates produced nanocrystallites [Figure 7-37(c)] similar to those formed on InP substrates at lower reactor temperatures [Figure 7-32(a-c)]. Without Au-seeding a highly porous layer formed on the Si. Despite the absence of nanowires on Si substrates, a moderate areal density of nanostructures was observed on the fused quartz substrates [Figure 7-37(d)]. It is however likely that an impurity in the quartz facilitated growth here as both the Au-treated and untreated quartz substrates presented structures with similar morphologies and areal densities.

7.4.2 Structural Characterization

The Zn_3P_2 nanowires synthesised in this study were found to exhibit a variety of unique morphological features. Of chief significance was the unusual appearance of many Au seed particles. In a large proportion of cases, the seed particles appeared with a flattened cylindrical morphology; their top facet being normal to the direction of growth in contrast to the usual rounded shape [Figure 7-38(a), Figure 7-40(a-c,f,g)]. Additional Zn_3P_2 growth tapering to a relatively sharp tip often accompanied this presentation. In other cases the Au seeds presented a more usual truncated spheroid geometry but with the growth interface oriented at an oblique angle to the growth direction [Figure 7-38(b)]. Non-perpendicular arrangements between growth interface and growth direction have been observed post-growth for a variety of VLS experiments, most commonly a (111) interface associated with non-<111> growth, and have been related to surface energy considerations or planar defects.[1124, 1134, 1139, 1163, 1168-1170] In a further

variation, some seed particles showed apparently poor wetting with the nanowire diameter at the growth interface being up to five times smaller than the diameter of the seed particle [Figure 7-38(c,f)]. For VLS-type growth, the wetting angle has been observed to vary with seed composition[243, 1126] affecting nanowire nucleation, diameter and phase.[243, 1120, 1126, 1130, 1171-1174]

In the current study it is likely that the natural size distribution of Au seed particles coupled with various stochastic processes worked to produce a variety of Au-Zn alloys assisting growth. The coexistence of differing seed particle compositions and phases and consequent variation in nanowire morphology has been reported by several

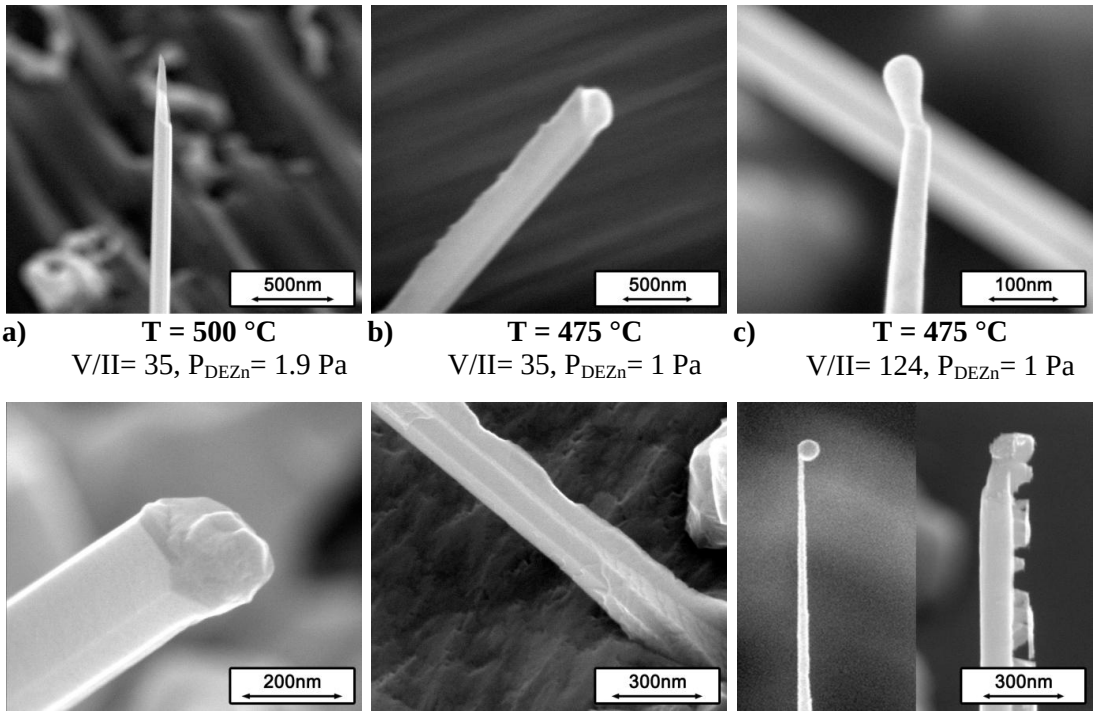

a) **T = 500 °C** V/II= 35, P_{DEZn}= 1.9 Pa

b) **T = 475 °C** V/II= 35, P_{DEZn}= 1 Pa

c) **T = 475 °C** V/II= 124, P_{DEZn}= 1 Pa

d) **T = 475 °C** V/II= 124, P_{DEZn}= 1 Pa Cooled under both precursors

e) **T = 475 °C** V/II= 124, P_{DEZn}= 1 Pa Cooled under both precursors

f,g) **T = 525 °C** V/II= 31, P_{DEZn}= 3.6 Pa GaAs Substrate

Figure 7-38 | SEM micrographs showing various morphological features of selected Zn_3P_2 nanowires. a) Growth tapering to a relatively sharp tip. b) Au seed with a post-growth interface which is not normal to the growth direction. The facet to the top of the nanowire shows significant roughness. c) Apparent dewetting of a Au seed. d) Nanowire tip showing re-entrant faceting e) Base of a nanowire showing a high density of growth steps. The diameter of the nanowire is observed to be non-uniform f) Likely decomposition in a nanowire grown at relatively high temperature. All micrographs show the sample substrate tilted 45 ° to normal.

authors.[1169, 1174-1176] In the case of Cu-seeded InP nanowires, Hillerich *et al.*[1176] proposed a dynamic interplay between VLS and VSS growth whereby VLS growth required but also consumed a greater In flux. A similar scenario is unlikely here as the lowest liquidus temperature in the Au-Zn system occurs for pure zinc at approximately 420 °C[21] and growth is therefore likely to have occurred by the VSS process.

Previous authors have associated some VSS growth modes with heavy kinking or a 'wormlike' geometry similar to that observed for many of the Zn_3P_2 nanowires reported here [see for example Figure 7-32(d,e),Figure 7-33(a,b),Figure 7-34(a-c)].[958, 1170, 1177-1179] Thombare *et al.*[1170] further suggested that the initial orientation of a solid seed and the consequent growth interface is critical in determining final nanowire morphology.

As observed in Figure 7-38(d), Zn_3P_2 nanowires generally exhibited an irregularly shaped cross-section. Most interestingly, re-entrant angles, most often associated with twin planes,[247, 616, 1043, 1139, 1180] were frequently visible. The presence of these features is consistent with lamellar twining which as discussed in Section 7.3.6, has been commonly observed for the <112> and to a lesser extent, <110> type growth directions. That the re-entrant geometry continued to the base of some nanowires [Figure 7-38(e)], is perhaps indicative of a low overgrowth rate, as a single re-entrant twin feature may be expected to outgrow itself.[1181] Poor overgrowth was also evident in the form of surface roughness as observed by SEM [Figure 7-38(e)] and in most cases could be linked to cooling under both DEZn and PH_3 to minimize decomposition (see Section 7.4.1.2.) Roughness at increased length scales was often observed for growth at relatively high temperatures (> 475 °C) and was related to the partial decomposition of the Zn_3P_2 nanostructures [Figure 7-38(e,g)]. Unlike previous observations for III-V nanowires where metallic droplets were taken as evidence of thermal decomposition,[1182] both zinc and phosphorus are expected to vaporise here. A phase transition from Zn_3P_2 to ZnP_2 may also be possible under PH_3.[40] Interestingly, variation in facet stability was apparent with examples of preferential decomposition as observed in Figure 7-38(g) being common.

Figure 7-39(a) presents a low magnification, bright field TEM image of a Zn_3P_2 nanowire grown at 475 °C under a DEZn partial pressure of 1 Pa and a V/II ratio of 124. The nanowire is approximately 6.5 μm long with a diameter of 360 nm at the base and 140 nm near the Au seed. Some tapering is evident closer to the tip of the nanowire.

Zn_3P_2 nanowires were found to be relatively beam sensitive and the nanowire here shows regions of beam damage on its lower right hand side and base.

Instead of a more usual truncated circular geometry, the Au seed presents as a relatively

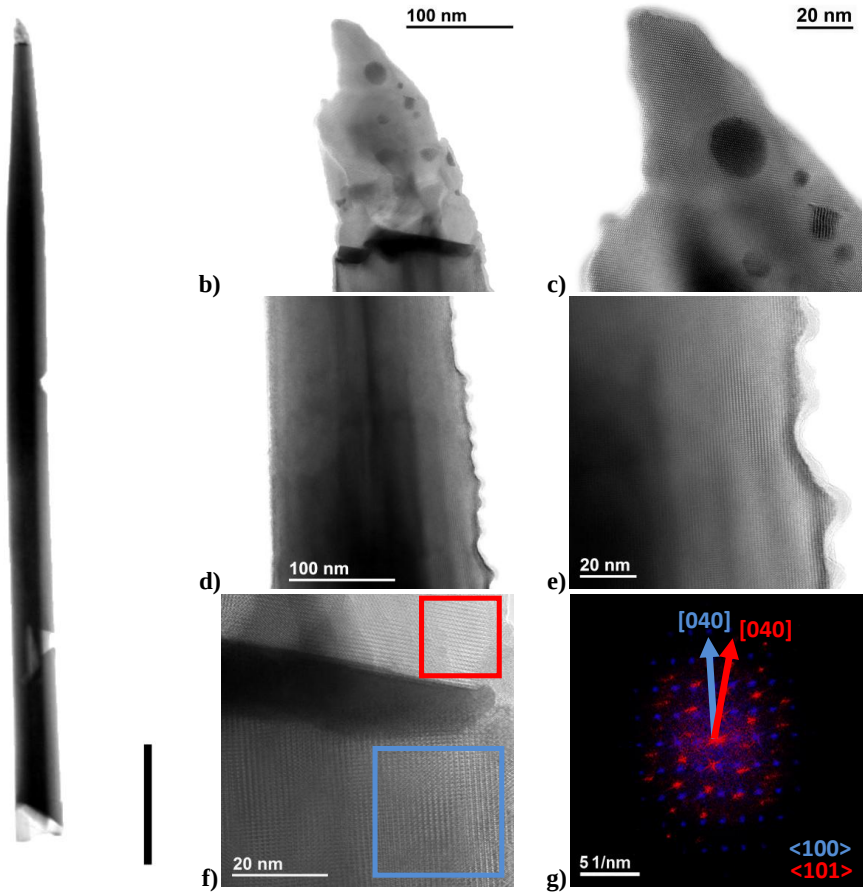

Figure 7-39 | TEM investigation of a Zn_3P_2 nanowire. a) Low magnification bright field image of the entire nanowire. Beam damage is visible at the base and two locations along the right-hand sidewall. b) A bright field image of the tip of the nanowire showing tapering growth above the Au nanoparticle. c) A high resolution bright field image of the tip of the nanowire showing Zn-P material with Au inclusions. Note the interference contrast apparent from the Au inclusion near the bottom left of the image. d) A bright field image taken close to the tip of the nanowire showing one sidewall to be relatively smooth and the other rough. e) A high resolution bright field image of the rough sidewall. f) A high resolution bright field image around the main Au nanoparticle. g) A composite of FFT from the two regions of (f) marked in red and blue. The zone axis and growth direction of the nanowire can be indexed to <100>/<010>. (Pseudocubic equivalent <110>) The zone axis of the material above the seed is tentatively identified as <101>.

thin dark band towards the tip of the nanowire with further tapered growth located above it. The border of the Au seed is highly irregular and no distinct orientational relationship was found between it and the nanowire. [As may be observed from (f), while the nanowire is on a low-index zone axis in the images presented, the Au seed is not.] Alloying with Zn was identified through EDXS analysis. The material above the seed was further identified through EDXS to be zinc phosphide with Au rich inclusions which appear as regions of darker contrast.

In Figure 7-39(c) lattice mismatch is evident between these two materials with clear translational-type Moiré fringes appearing for the larger inclusion towards to bottom right of the image. On the imaged zone axis the left hand facet of the nanowire appears relatively smooth while that on the right hand side presents significant roughness reminiscent of overgrowth on heavily twinned structures [Figure 7-39(d,e)].[247, 600, 670] No corresponding twin planes were however observed and FFT of Figure 7-39 (e) revealed no structural shifts across the width of the nanowire. It is therefore likely that the roughness observed at the right hand edge of the nanowire is the result of a complex faceting process with the preferred facet directions being geometrically frustrated. Partial decomposition coupled with poor surface diffusion during cooling may serve to accentuate this morphology. Figure 7-39 (f) presents a high resolution image of the interface between seed particle and nanowire. As discussed above, the seed particle is not on axis but FFTs of both the nanowire and the growth region above the seed produce cubic-like patterns [Figure 7-39(f)]. Considering first the blue pattern corresponding to the nanowire, the ratio between the two orthogonal directions is 1.43 which is indicative of a <110> type direction. Assuming the nanowire is lying in the plane of the images, its growth direction may also be indexed to <110>. A <110> growth direction has previously been reported for both Au-assisted[63, 331] and unassisted[326, 340] Zn_3P_2 nanowires grown by CVD methods. In the case of the red pattern which corresponds to the growth above the seed particle the ratio between the two orthogonal directions is 1.22 which is indicative of a <112> type direction.

Figure 7-40(a-c) presents diffraction patterns taken from three different zone axes of the nanowire imaged in Figure 7-39. In each case the pattern is aligned such that the growth direction of the nanowire as projected in the image plane points up. Cubic-like symmetry is evident in each of the patterns and the growth direction may be

unambiguously identified as <110> type. A further diffraction pattern from another nanowire [Figure 7-40(d)] presents a forth axis where the growth direction is again <110>. In Figure 7-40(e-h) simulated diffraction patterns for the room temperature α phase of Zn_3P_2 are presented as a match to the experimental patterns. While the relative intensities of the diffraction spots in Figure 7-40(b,d) display good agreement with the simulated pattern, those in Figure 7-40(a-c) do not. Relative intensity is expected to vary with a number of experimental factors including sample thickness but in this case it is likely that the experimental patterns are the result of diffraction by the lamellar twins noted in many of the Zn_3P_2 nanowires.

Despite being able to identify the nanowires as α Zn_3P_2, the growth above the seed

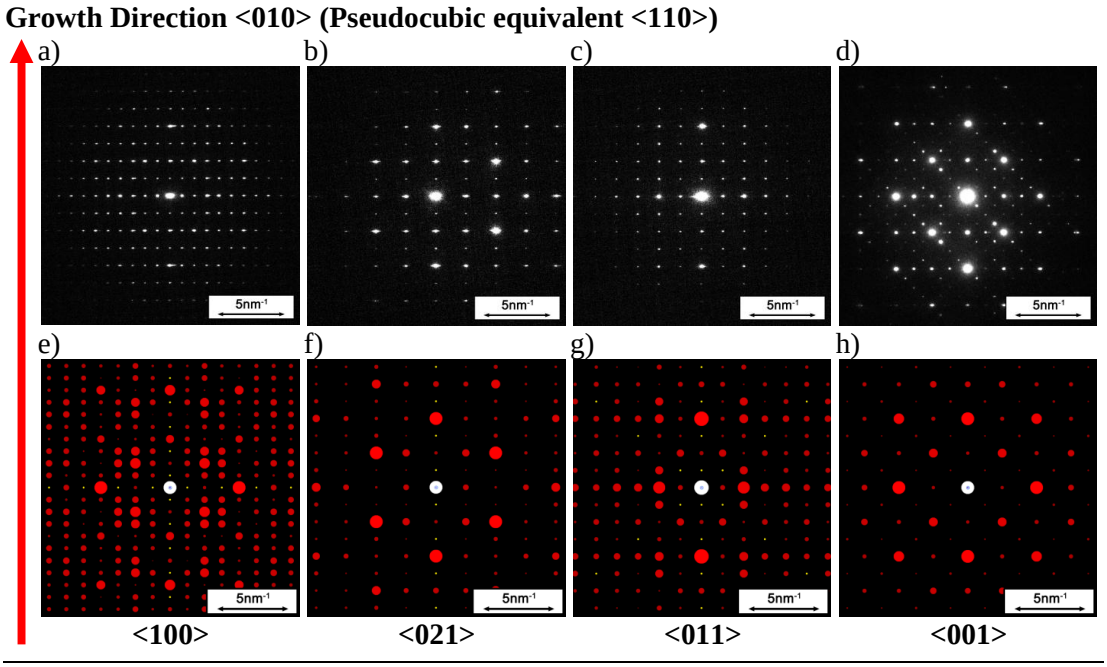

Figure 7-40 | Representative electron diffraction patterns taken from various crystallographic axes. (a-c) Electron diffraction patterns taken from the nanowire shown in Figure 7-39. d) Electron diffraction pattern taken from the nanowire shown in Figure 7-42(b,c). All patterns are oriented such that the nanowire growth direction is vertical in the page. The patterns may be indexed as (a) <100> axis (pseudocubic equivalent <110>), (b) <001> axis (pseudocubic equivalent <001>), (c) <021> axis (pseudocubic equivalent <111>) (d) <011> axis (pseudocubic equivalent <112>). (e-h) corresponding simulated electron diffraction patterns for α Zn_3P_2. In all cases the growth direction can be indexed to <010>/<111> or in the pseudocubic equivalent system: <110>.

observed in Figure 7-39 could not be positively identified. The lattice parameters as measured from the red FFT pattern shown in Figure 7-39(g) were not found to match any phase of Zn_3P_2, ZnP_2 or the Au-Zn alloys. These parameters were further found to vary within the region above the seed. Considering the high-Au inclusions and clear Moiré fringing it is likely that this material is variably strained. If the red FFT pattern is taken as the <011> axis of Zn_3P_2 (pseudocubic equivalent <112>) then a 7% compressive strain can be ascribed to both the <201> and <100> directions (pseudocubic equivalents <111> and <110> respectively). Interestingly, the <010> growth direction (pseudocubic equivalent <110>) appears perpendicular to the edge of the Au seed particle.

The room temperature α phase of Zn_3P_2 is tetragonal and belongs to the $P4_2$ /nmc space group with a=b=8.09 Å and c=11.45 Å.[12, 23] As was described for Zn_3As_2 in Section 7.3.2.2, the Zn_3P_2 lattice can be considered as a slightly distorted defective antifluorite structure consisting of a distorted face centred cubic anion lattice interpenetrated by a 75% filled simple cubic cation lattice. In this arrangement each zinc atom is surrounded by four phosphorus atoms, and each phosphorus atom by six zinc atoms and two

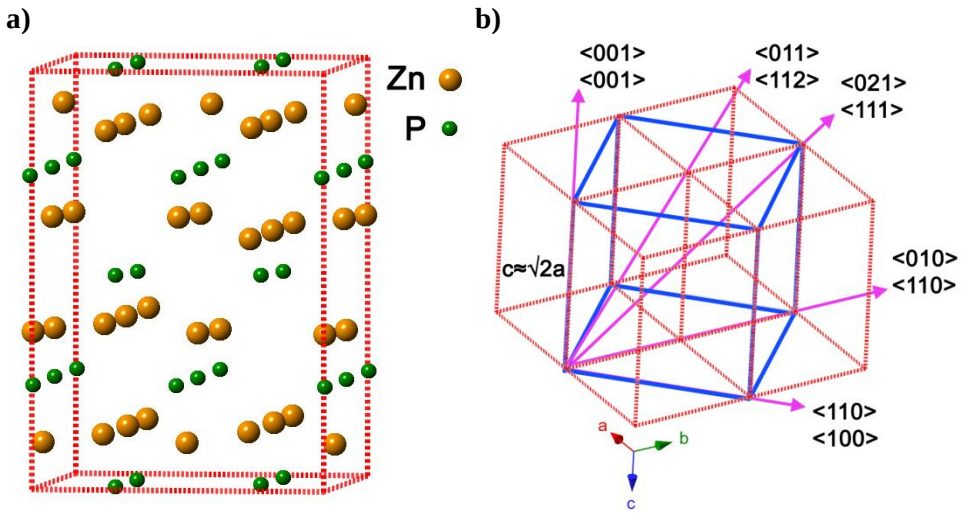

Figure 7-41 | Crystal structure of α Zn_3P_2. a) Tetragonal unit cell as described by Zanin[23]. Zinc atoms are shown in orange and phosphorus in green. Atoms slightly outside the unit cell are shown for clarity. b) Relationship between the tetragonal unit cell (red) and pseudocubic unit cell (blue) with selected high symmetry directions labelled. (In the manner of Zdanowicz *et al.*[33]) Equivalent cubic directions are listed below tetragonal directions.

vacancies. As for Zn_3As_2, the arrangement of the zinc vacancies is critical in defining the overall symmetry of the cell. Figure 7-41(a) depicts the Zn_3P_2 cell as was described most recently by Zanin *et al.*[12, 23] from XRD analysis. The cell itself contains 40 atoms with Figure 7-41(a) further depicting atoms immediately outside the cell to better illustrate the overall structure. As the axial ratio (c/a) ratio of the tetragonal cell is 1.415 the structure may also be described by a pseudocubic cell as is illustrated in Figure 7-41(b). The transformation from the tetragonal to pseudocubic lattice has the following form:

$$\begin{pmatrix} 1 & 1 & 0 \\ 1 & 1 & 0 \\ 0 & 0 & 1 \end{pmatrix} \qquad \ldots(7\text{-}9)$$

The high symmetry directions <010>, <001>, <110>, <021>, <011> correspond to the cubic directions <110>, <001>, <100>, <111>, <112> respectively. Figure 7-41(b) labels these high symmetry directions with indices corresponding to both the tetragonal and pseudocubic cells. Both indices are used throughout this work to aid comparison with the results for Zn_3As_2 in Section 7.3.2 and reports of zincblende nanostructures in the literature. Reconsidering Figure 7-40(a-d) these axes can be labelled with the tetragonal indices <100>, <021>, <011>, <001> respectively. As the projected

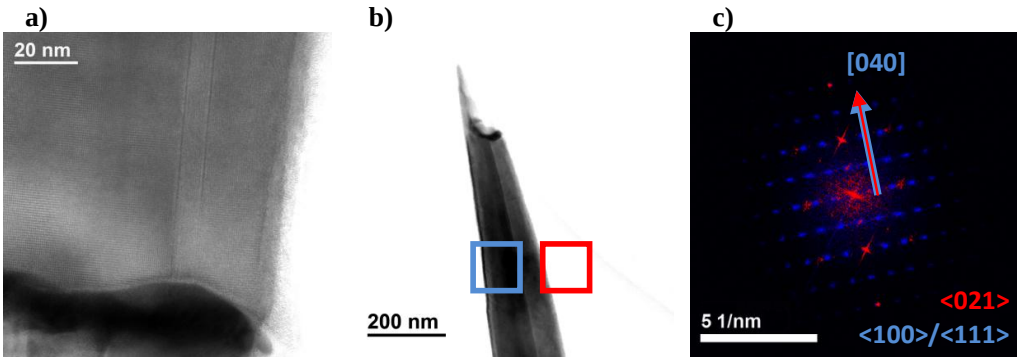

Figure 7-42 | Lamellar type defects in Zn_3P_2 nanowires. a) A bright field TEM micrograph of the nanowire featured in Figure 7-39 showing two lamellar defects. The nanowire is on the <011> zone axis (pseudocubic equivalent <112>). b) A bright field TEM micrograph of another Zn_3P_2 nanowire where FFTs have been taken from the two areas defined by blue and red boxes. c) Composite of the two FFT patterns obtained from (b). The blue pattern corresponds to the twin on the left and is on the <100> axis (pseudocubic equivalent <110>). The red pattern corresponds to the twin on the right and is on the <021> axis (pseudocubic equivalent <111>).

nanowire length was the same for Figure 7-40(a-c) the orientation of the c-axis can further be deduced and the zone axis and growth direction in Figure 7-39 be identified as [100] and [010] respectively (pseudocubic equivalent [110]). Figure 7-42(a) presents a high magnification bright field TEM image of the nanowire shown in Figure 7-39 aligned to the <101> zone axis (pseudocubic equivalent <112>). Unlike the bright field images shown in Figure 7-39, two lamellar defects are clearly visible. Their visibility on this zone axis is compatible with twinning on the <02-1> plane (pseudocubic equivalent <111>). Similar lamellar defects have been reported for <100> and <011> Zn_3P_2 nanowires grown by CVD,[63, 335] and are considered potential sources of charge trapping.[63] In this study, lamellar defects were often associated with disruptions to the shape of seed particle. Figure 7-42(b) presents a bright field TEM image of another Zn_3P_2 nanowire where the Au seed particle presents as a chevron-like shape. The tip of this chevron is met by a lamellar defect that bisects the nanowire. FFT transforms of regions to the left and right of the lamellar can be indexed to the <100>/<111> and <021> directions respectively (pseudocubic equivalents <110> and <111>. The orientation of the c-axis was not determined.)

7.4.3 Photoluminescence

The Zn_3P_2 nanowires grown in the current study were found to emit a strong PL signal in the near-infrared. Figure 7-43 presents representative spectra collected from a single nanowire. At room temperature under a pump fluence of 33 μJ /cm^2 /pulse emission is seen to peak at 1.52 eV with a FWHM of 70 meV [Figure 7-43(b)]. A relatively weak shoulder peak is also visible around 1.42 eV. With increasing pump fluence the relative intensity of this shoulder decreases and the high energy tail of the main peak is seen to widen likely due to both band filling and thermal effects.

At a pump fluence of 323 μJ /cm^2 /pulse emission of the main peak is slightly redshifted to 1.51 eV and the FWHM widened to 180 meV [Figure 7-43(b)]. As temperature is reduced the relative intensities of the main and shoulder peaks reverse such that by 150 K the only peak visible for a pump fluence of 65 μJ /cm^2 /pulse is the lower energy peak at 1.40 eV with a FWHM of 90 meV. This peak continues to redshift with decreasing temperature until at 6 K emission it is located at 1.38 eV with a FWHM of 40 meV. Interestingly, emission at low temperature is highly power sensitive blueshifting from 1.38 eV to 1.50 eV with an increase in pump fluence from 65 to

452 μJ /cm^2 /pulse. Similar temperature and power dependant PL results have been reported by Kimball *et al.*[45] for Zn_3P_2 thin films grown by CVD. The authors of that work assigned the peak at 1.50 eV to a direct transition and that at 1.38 eV to an indirect fundamental bandgap. This assignment follows considerable confusion in the literature regarding the band structure of Zn_3P_2.

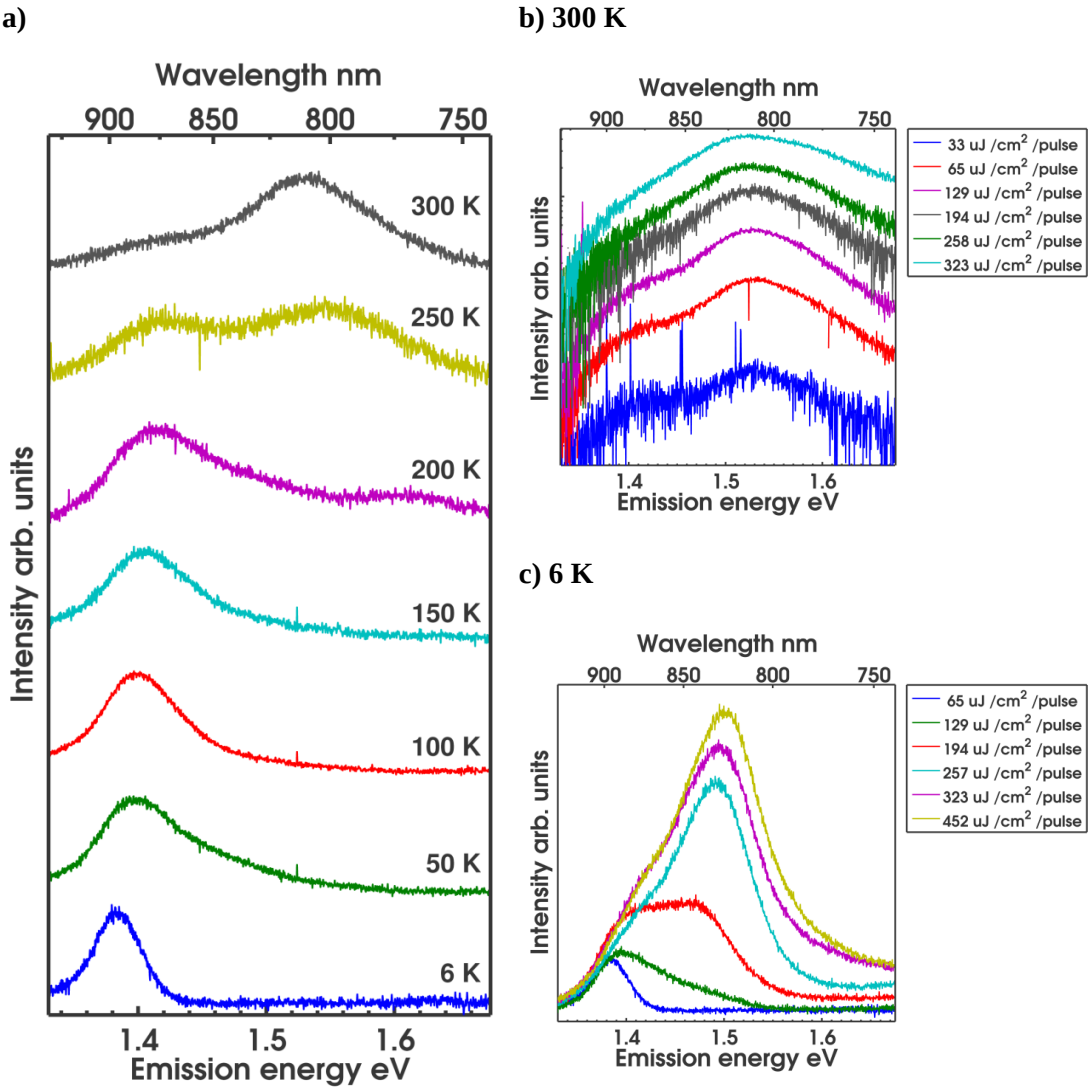

Figure 7-43 | Temperature and power dependant PL spectra collected from a single Zn_3P_2 nanowire. a) Temperature dependant measurements showing a redshift in peak emission from 1.38 to 1.53 eV with an increase in temperature from 6 to 300 K (fluence of 65 μJ /cm^2 /pulse.). b) Power dependant measurements at 300 K showing slight redshift as the pump power is increased from 22 to 215 μW. (Intensity is plotted on a logarithmic scale.) c) Power dependant measurements at 6 K showing a blueshift from 1.38 to 1.50 eV as the pump power is increased from 43 to 301 μW.

While the presence of a direct transition around 1.50 eV has been well established,[893] optical absorption between the energies of 1.30 to 1.50 eV has been variously ascribed to a direct transition,[783] indirect transition[305, 306] or defect states[307, 777]. Similar confusion has been generated from theoretical studies with different approaches variously finding direct[1183-1185] and indirect[1185, 1186] structures.

The dynamics of photoexcited carrier recombination were investigated by time correlated single photon counting (TCSPC). Figure 7-44 plots time resolved PL for a single Zn_3P_2 nanowire at various temperatures and pump fluences. In all cases these measurements were taken at the peak emission energy: 1.50 eV for room temperature and 1.38 eV for low temperature (6.5 K). While carrier decay could not be resolved at room temperature, monoexponential decay with a lifetime of approximately 200 ps was observed at low temperatures and pump fluence (65 μW μJ /cm^2 /pulse). With increased pump fluence (323 μW μJ /cm^2 /pulse) at low temperature, the system response again dominated.

Assuming that surface recombination dominates at low temperature Equation 6-3 gives a recombination velocity of 2.5 x10^4 cm/s for a 200 nm diameter nanowire at low pump fluences. As the system response of the TCSPC system can be estimated as 40 ps a

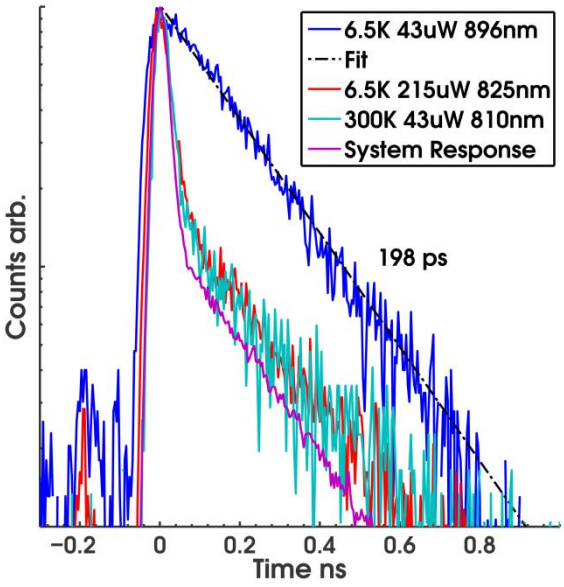

Figure 7-44 | Time resolved PL emission intensity of a single Zn_3P_2 nanowire. At low temperature and excitation powers a lifetime of up to 200 ps was measured. At room temperature the decay could not be deconvoluted from the system response suggesting a lifetime of less than 40 ps.

lower limit of 1.25 x10^5 cm/s can further be estimated for the surface recombination velocity of Zn_3P_2 nanowires at room temperature. Previous work has reported oxidation to passivate the surface of Zn_3P_2 substrates giving surface recombination velocities of 1.8±0.1 x10^3 cm/s and surface trap densities of 2 x10^{12} /cm^2.[847] Polishing and etching were both shown to increase the surface recombination velocity by at least an order of magnitude.

7.5 Zinc Antimonide

7.5.1 Growth parameters

As was discussed for Zn_3As_2 in Section 7.3.1.1 and Zn_3P_2 in Section 7.4.1.1, the growth of zinc antimonide by MOVPE also demands balance between precursor and product

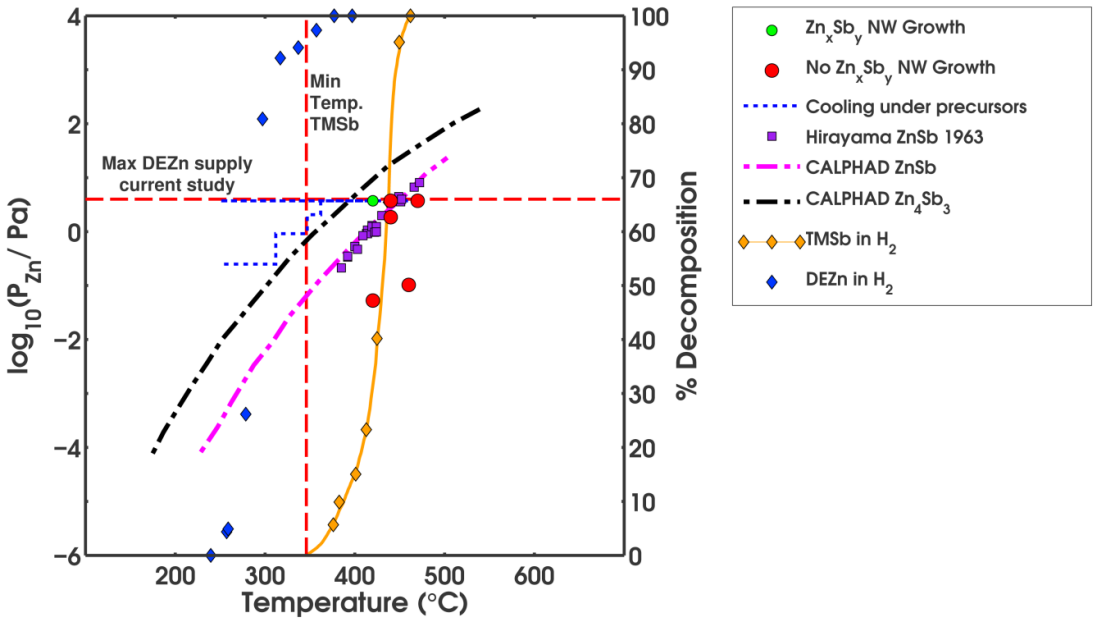

Figure 7-45 | Outcome of Zn_xSb_y nanowire growth under various combinations of zinc partial pressure and temperature. (Cooling under both precursors is indicated by dashed blue lines.) The percentage decomposition of the precursors DEZn and TMSb in H_2 is further plotted as a function of temperature on the right-hand axis.[1, 4] Also plotted is temperature dependence of zinc partial pressure in equilibrium with ZnSb and Zn_4Sb_3 as calculated by the CALPHAD method using the thermodynamic data of Liu *et al.*[20] and measured experimentally by Hirayama[32]. For Zn_xSb_y growth to occur, some precursor decomposition is required and the partial pressure of zinc must exceed that in equilibrium with Zn_xSb_y(s). The expected growth window for the current experimental setup is therefore approximately 350-440 °C.

decomposition. The thermal stability of the zinc antimonides is, however, even lower than that of the other II-V compounds investigated here[11, 32, 806, 849, 1187] and their growth window correspondingly smaller. There is furthermore evidence that the Zn-Sb phase diagram varies at the nanoscale with Schlecht *et al.* reporting the unexpected decomposition of Zn_4Sb_3 nanocrystals into Zn and ZnSb above 196 °C.[806]

Figure 7-45 plots the partial pressure of zinc in equilibrium with bulk ZnSb as measured by Hirayama[32] along with curves calculated for both bulk ZnSb and Zn_4Sb_3 using the CALPHAD method. (The calculations here employed the thermodynamic data of Liu *et al.*[20]) As was discussed for Zn_3As_2 and Zn_3P_2, growth will only occur where there is both precursor decomposition and product stability. In the case of Zn_4Sb_3, the growth window for the current experimental apparatus is seen to extend from 350 °C to 395 °C. The window for ZnSb is slightly larger, ranging to a maximum temperature of approximately 440 °C. A similarly small range of DEZn partial pressures are viable, 0.75 to 3.6 Pa for Zn_4Sb_3 and 0.065 to 3.6 Pa for ZnSb.

The minimal growth window here is a product of both the relatively low thermal stability of the zinc antimonides as well as the relatively high temperature of TMSb decomposition. While TMSb decomposition will vary with both liner condition and carrier gas,[1, 4] an Sb source with a lower decomposition temperature[1188-1190] has the potential to greatly extend the MOVPE growth window.

Further plotted in Figure 7-45 are the experimentally investigated parameters; red dots where growth was not obtained and green where it was. Unlike the other materials reported in this chapter, no steady state growth conditions were identified for zinc antimonide. Growth was instead obtained by cooling under both precursors to a temperature of 250 °C. This approach is represented in Figure 7-45 by dashed blue lines and was adopted in order to efficiently explore the available parameter space. Having demonstrated that the current experimental apparatus is capable of synthesising zinc antimonide it is expected that further study would reveal appropriate steady state growth conditions.

7.5.2 Structure and morphology

Figure **7-46** presents SEM micrographs of zinc antimonide grown from both substrate [Figure **7-46**(a-d)] and GaAs stems [Figure **7-46**(e,f)]. Where growth was on substrate, planar nanowires of up to several microns in length were generally observed to grow in

a <110> direction. [Figure **7-46**(c,d)]. An excess of Sb was required for growth with V/II ratios of less than one producing only nanoparticles [Figure **7-46**(b)]. Difficulty in obtaining vertical growth from substrate has previously been reported for III-antimonide nanowires and was related to a surfactant effect of Sb in decreasing the contact angle of the seed particle.[134, 1191-1193] The V/III ratio has further been shown to critically affect nucleation, growth rate and morphology.[193, 974, 1119, 1191] In the current work both Au and, to a lesser extent, Ag were found to seed zinc antimonide growth. Both metals have been previously reported to seed III-antimonide nanowire growth, albeit with significant group III alloying (greater than 50 at.%).[134, 164, 974, 1194-1196]

Due to both nucleation difficulties and the expense of native substrates, Au-seeded III-

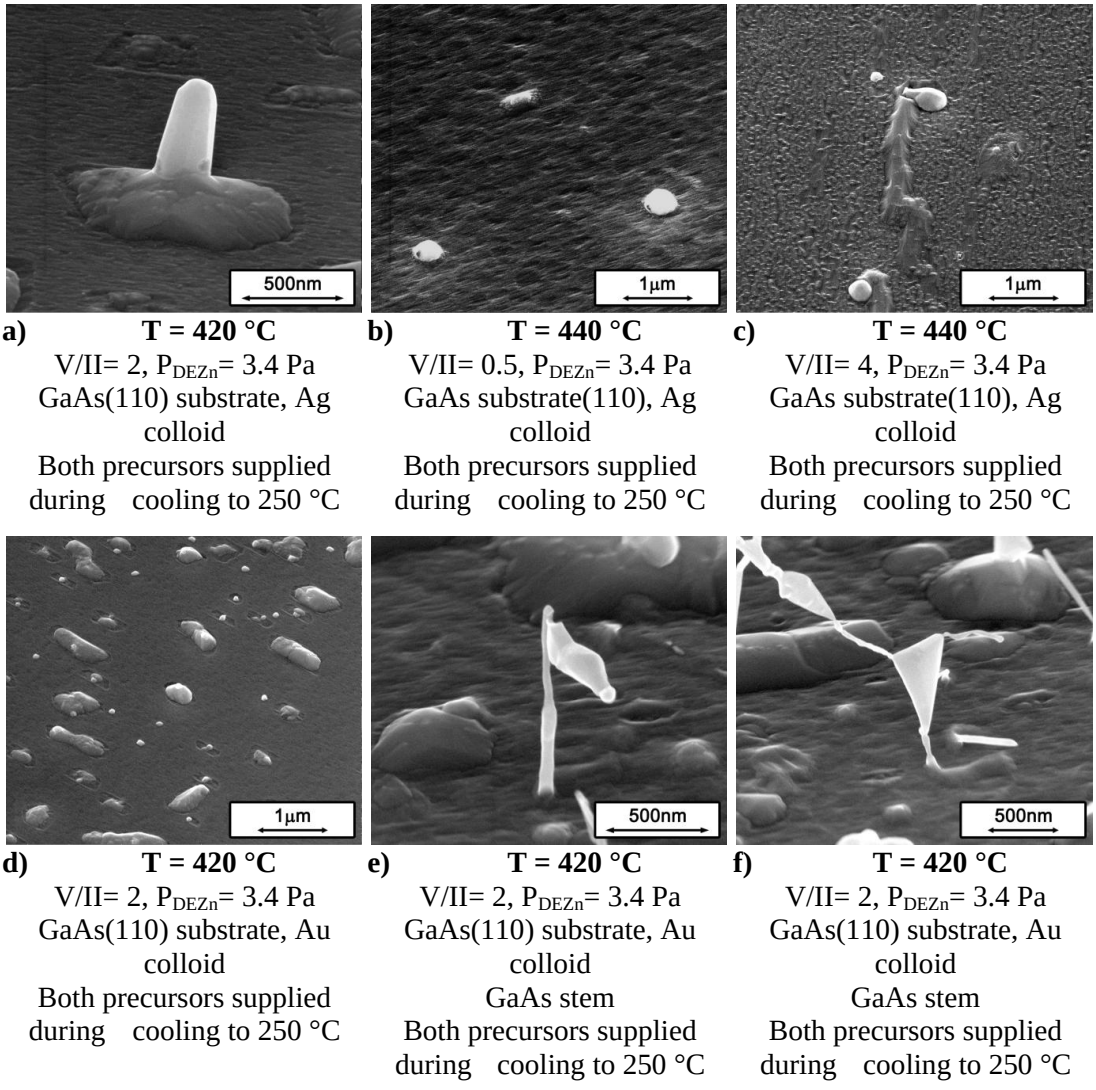

a) **T = 420 °C**
V/II= 2, P_{DEZn}= 3.4 Pa
GaAs(110) substrate, Ag colloid
Both precursors supplied during cooling to 250 °C

b) **T = 440 °C**
V/II= 0.5, P_{DEZn}= 3.4 Pa
GaAs substrate(110), Ag colloid
Both precursors supplied during cooling to 250 °C

c) **T = 440 °C**
V/II= 4, P_{DEZn}= 3.4 Pa
GaAs substrate(110), Ag colloid
Both precursors supplied during cooling to 250 °C

d) **T = 420 °C**
V/II= 2, P_{DEZn}= 3.4 Pa
GaAs(110) substrate, Au colloid
Both precursors supplied during cooling to 250 °C

e) **T = 420 °C**
V/II= 2, P_{DEZn}= 3.4 Pa
GaAs(110) substrate, Au colloid
GaAs stem
Both precursors supplied during cooling to 250 °C

f) **T = 420 °C**
V/II= 2, P_{DEZn}= 3.4 Pa
GaAs(110) substrate, Au colloid
GaAs stem
Both precursors supplied during cooling to 250 °C

Figure 7-46 | SEM micrographs of selected Zn_xSb_y nanostructures. a-d) Variations of planar growth; e,f) Growth following GaAs stem. All micrographs show the sample substrate tilted 45 ° to normal.

antimonide nanowires are often grown as axial heterostructures from III-V stems.[1191] In the current work, GaAs stems were found to deliver freestanding nanostructures [Figure 7-46(e,f)]. Like Zn_3As_2 and Zn_3P_2 growth however (see Sections 7.3.1.2 and 7.4.1.4 respectively), a variety of different morphologies were produced suggesting sensitivity to local conditions or perhaps a significant stochastic component to growth.

Examining Figure **7-46**(e), a vertical stem is observed to support a larger diameter non-vertical nanowire. Neither structure shows clear faceting. A similarly abrupt increase in diameter has been observed moving from III-arsenide stems to III-antimonide growth and related in those cases to group III accumulation in the seed particle.[134, 974] Here, in addition to this nanowire-like growth, 2D structures were also formed. Figure **7-46**(f)

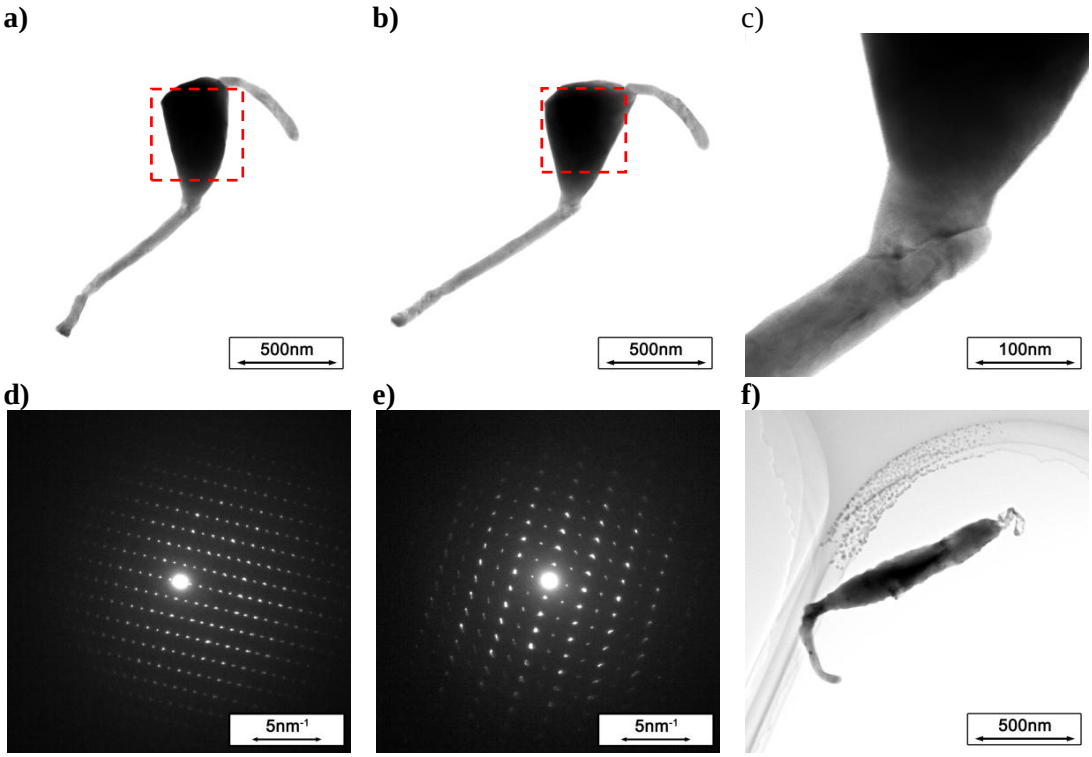

Figure 7-47 | TEM micrographs of Zn_xSb_y nanostructures grown from GaAs stems. a,b) Bright field TEM images of a Zn_xSb_y nanoplatelet with Zn_xAs_y nanowire structures emerging from either side. Dashed red lines enclose the regions corresponding to the SADPs shown in (d) and (e); c) Magnified view of the interface between nanoparticle and nanowire in (b). d,e) Diffraction patterns taken from the Zn_xSb_y nanoplatelet in (a) and (b). The rotation between these axes was approximately 30°. f) Zn_xSb_y showing beam damage at its top right end. Redeposited Zn and Sb is visible above the nanowire.

shows a triangular platelet with nanowires emerging from each of its three vertices. The formation of InSb platelets has been recently reported and linked to twinning coupled with VS growth.[1164, 1197] In this case however, the presence of VLS-like growth from each of the platelet's vertices is suggestive of seed-splitting.

Figure 7-47(a-e) presents bright field TEM images and corresponding SADPs of a zinc antimonide nanoplatelet similar to that shown in Figure **7-46**(f). Here, the images and diffraction patterns were collected from two different zone axes separated by a rotation of approximately 30°. The bright field image taken on the first axis [Figure 7-47(a)] shows a central region of darker contrast corresponding to the nanoplatelet with nanowire-like growths of lighter contrast emerging from either end. Considering EDXS spectra [Figure 7-48(c) – red spectrum] taken from a similar structure as shown in [Figure 7-48(a)], the nanoplatelet can be said to consist of zinc antimonide with a small amount of As contamination (the Cu signal derives from the sample holder). Arsenic contamination has previously been reported for III-antimonide nanowires grown from arsenide-based stems and related to the evaporation of arsenides during antimonide growth.[134, 1196, 1198] In contrast to the nanoplatelet, the nanowire structures are seen to consist of zinc arsenide with a small amount of Sb contamination [Figure 7-48(c) – green spectrum]. Despite GaAs stem growth, no Ga was detected in any of the

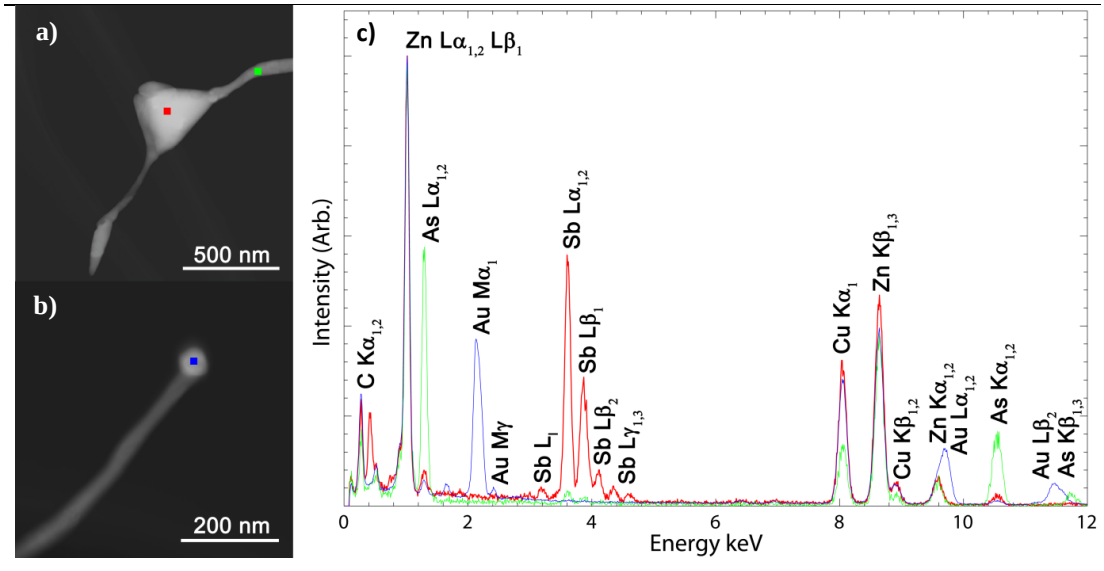

Figure 7-48 | HAADF STEM and corresponding EDXS of Zn_xSb_y grown from GaAs stems. a) HAADF STEM image of a structure similar to that shown in Figure 7-47. b) HAADF STEM image of a stem found in the same growth as (a). c) EDXS spectra collected from the locations indicated by coloured squares in (a) and (b).

structures analysed by EDXS.

Many of the zinc arsenide nanowires seen here were terminated by a Au-Zn alloy nanoparticle in a manner consistent with VLS growth (see Figure 7-48(b) and the blue spectrum of Figure 7-48(c)]. Arsenic was likely supplied through the evaporation of the GaAs substrate and nanowire stems. While only a low rate of evaporation is expected for bulk GaAs at the growth temperature of 420 °C, [1199-1201] an increased evaporation rate can be expected for nanowires due to the Gibbs-Thomson effect.[1202, 1203] Below approximately 650 °C, GaAs evaporation is furthermore stoichiometric and Ga droplets are not expected.[1200, 1201, 1204] Despite Ga not be detected by EDXS, the complete evaporation of the GaAs stems is however unlikely as stems of InAs, a material known to evaporate at a significantly higher rate than GaAs,[1205] have been reported to survive for at least half an hour under similar conditions.[134, 1119] One further possibility for the lack of a EDXS Ga signal may be a vapour-solid cation exchange reaction with Zn replacing Ga in the nanowires.[1206] Vapour-solid cation and anion exchange reactions have been reported for nanowire systems including $Cd_{(1-x)}Zn_xS$, $CdS_xSe_{(1-x)}$ and ZnO/ZnSe.[1207-1209]

Inspecting the first of the SADPs taken from the zinc antimonide platelet [Figure 7-47(d)], a pair of orthogonal planes can be identified with interplanar spacings of 13.15 and 7.79 Å respectively. A similar orthogonal arrangement is observed for the second zone axis [Figure 7-47(e)] with interplanar spacings of 7.46 and 7.90 Å. On this axis the direction corresponding to the longer interplanar spacing corresponds with the initial

Table 7-5 | Reported structures of selected Zn_xSb_y phases.

ZnSb [11] Pbca		**β-Zn_8Sb_7 [27] Pmn2_1**		**α-Zn_4Sb_3 [14] P$\bar{1}$ α=γ=90° β=98.77(3)°**		**β-Zn_4Sb_3 [19] R$\bar{3}$c**		**ζ-$Zn_{3-x}Sb_2$ [51] Pnna(α0)0s0 q=(α,0,0), a≈0.385**	
a	6.20393(8) Å	**a**	15.029(1) Å	**a**	32.536(5) Å	**a**	12.2282(3) Å,	**a**	7.283(3) Å
b	7.7408(1) Å	**b**	7.7310(5) Å	**b**	12.237(2) Å	**c**	12.4067(4) Å	**b**	15.398(5) Å
c	8.0977(1) Å	**c**	12.7431(9) Å	**c**	10.862(2) Å			**c**	25.06(1) Å

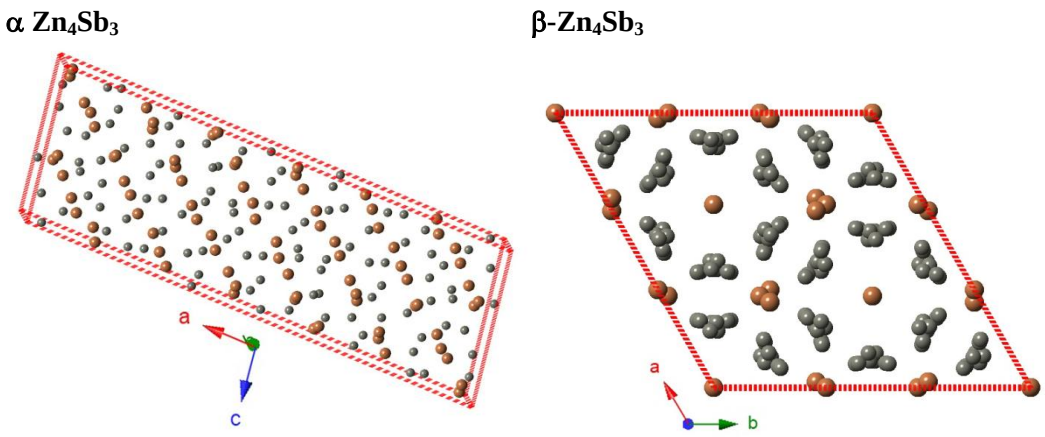

Figure 7-49 | Visual representation of the reported structures of Zn_4Sb_3. a) Unit cell of α-Zn_4Sb_3 as reported by Nylén;[14] b) Unit cell of β-Zn_4Sb_3 as reported by Snyder.[19]

growth direction of the nanoplatelet [Figure 7-47(c)] and the other with the initial sidewall facets. Comparing the measured spacings with the various reported polymorphs of zinc antimonide (summarised in Table 7-5 and depicted in Figure 7-49) does not give a complete match despite the majority of phases have low-index spacings of similar lengths. The structure that most closely approaches a match is the quasi-crystal ζ-$Zn_{3-x}Sb_2$,[51] where the planes $(0\bar{1}1)$, (020) and (021) have spacings of 13.11, 7.699 and 7.360 Å respectively. These planes are not however mutually orthogonal as is observed for the experimental patterns. The measured spacings of 7.79 Å and 7.90 Å are furthermore similar to the b-axes of ZnSb[11] and β-Zn_8Sb_7[27] (7.7408(1) Å and 7.7310(5) Å), the (111) direction of α-Zn_4Sb_3[14] (7.624 Å), and the (101) direction of β-Zn_4Sb_3[19] (8.055 Å).

While the current structure cannot be identified it is worth noting that zinc antimonide is known to crystallise in a variety of complex crystal structures, and that many of these structures have only recently been solved.[14, 19, 27] The large unit cell (one axis of at least 13.15 Å in length) and high degree of symmetry found in the current experiment are suggestive of a complex, relatively high temperature phase. Further study is required for a more full understanding of this phase.

7.6 Summary

Relatively unexplored, the II−V family of semiconductors holds appeal for a diverse range of applications. Examples include Zn_3As_2 for earth abundant IR, Zn_3P_2 for PV, Zn_4Sb_3 for thermoelectrics and Cd_3As_2 for topological physics. In addition to these unique binary compounds, the II-V family further offers scope for alloying to give band-gap and lattice parameter tuning. Integration with well-known III-V and silicon based materials is also possible.

The current chapter has explored the synthesis of Zn-V nanostructures by MOVPE using a reactor compatible with commercial III-V semiconductor production. With the aid of various thermodynamic analyses, a growth window has been established for the compounds zinc arsenide, zinc phosphide and zinc antimonide. Each of these compounds has furthermore been synthesised in various morphologies including nanowires and nanoplatelets. Detailed structural and optoelectronic characterization has revealed that the newly synthesised nanomaterials are of high quality and hold significant potential for both future research studies and commercial applications.

In using MOVPE, the current study both brings the highest levels of control and reproducibility to II-V material growth and introduces this novel semiconductor family to an existing community of researchers. Beyond the binary compounds investigated here, the door is now open for the MOVPE/MBE synthesis of nanostructured II−V semiconductor materials, II−V alloys, and novel II−V/III−V heterostructures for applications encompassing optoelectronics, thermoelectrics, high speed nanoelectronics, and topological physics.

8

Conclusion and Future Research Directions

An ongoing emphasis on device scaling has led to significant interest in 'bottom-up' fabrication methods. Among the various alternatives, VLS growth offers a convenient platform for realising complex geometries and heterostructures. The VLS mechanism is further well paired with MOVPE growth methods which combine a high degree of control with a wide variety of sources. This dissertation has considered various applications of the element Zn to VLS growth by MOVPE.

Chapter 4 considered the use of Zn in its conventional role as a III-V dopant. Higher DEZn flows were observed to affect the morphology of Au-seeded GaAs nanowires. Effects included an increase in planar defect density, and, both nanowire kinking and seed-splitting. Through a series of growth studies, the threshold for these morphological effects was established as a function of both nanowire diameter and growth temperature. These threshold values establish the maximum DEZn flows suitable for doping GaAs nanowires.

Having determined the range of DEZn flow rates useful for doping, dopant incorporation was assessed by APT. In a novel approach to APT, nanowires were synthesised at relatively low areal densities and then analysed on the growth substrate in the 'as-grown' condition. Detection of zinc in concentrations of up to 5.51 $x10^{20}$ Zn/cm^3 provided evidence for successful incorporation. The measured dopant distributions were, however, inhomogeneous with a significantly higher concentration of Zn found in VS shell growth relative to VLS core growth. This difference was related to solute partitioning in the Au seed. Dopant activity corresponding to the chemical concentration observed by APT was later shown through electrical characterisation.

While effective doping was achieved using DEZn, attempts to synthesise n-type material using SiH_4 were unsuccessful. Given the importance of p-n junctions to semiconductor devices, this failure provides an impetus for the current laboratory to investigate alternatives such as TESn. There is also significant scope for further nanowire doping studies by APT. The quantification of variations in dopant

concentration with variables such as temperature and V/III ratio has the potential to both deliver fundamental insights into the VLS process and provide a solid foundation for nanowire device design. Such an undertaking would, however, need to overcome significant difficulties relating to sample preparation. While the current approach was suitable for establishing dopant incorporation, a pick and place method would likely be required in order to analyse normal areal densities. Finally, it is noted that the observed morphological effects of Zn doping including twinning and kinking provide significant opportunities for tailoring nanowire structure and geometry. Study of the origin of these effects would further provide fundamental insight into the VLS growth process itself.

Chapter 5 focused on the synthesis of nanowire TSL structures using Zn as a morphological agent. Growth conditions leading to periodic twinning in GaAs nanowires of various different diameters were identified. The morphology and overgrowth of these nanowires was then studied. Nanowires were observed to form with {111} type facets which transformed to {110} with overgrowth. Initial overgrowth was faster on the {111}B relative to {111}A facets. Unlike previously reported examples of periodic twinning in III-V nanowires, twin spacing in the GaAs nanowires grown here was found to be a linear function of nanowire diameter. From an analysis within the context of classical nucleation theory, this result was related to the relatively higher twin plane and solid-liquid interface energies relevant to the GaAs nanowires. The analysis further enabled the extraction of values for the wetting angle and supersaturation operational during growth.

The development here of GaAs TSL nanowires opens the door to variety of future work. One concept of particular interest would be overgrowth on the serrated sidewalls of these nanowires to give unusual shell geometries. Reduction in the period between twin planes into the few nanometre regime could further generate detectable miniband structure. Such a reduction may be achieved by altering supersaturation and contact angle through the use of a different seed material such as Ga. Finally, the period between twin planes could be used as a metric to estimate variation in these parameters with growth conditions. In this way post-growth analysis of twin spacing could provide valuable insights into the fundamentals of the VLS growth process.

In chapter 6, Zn was used to massively increase the radiative efficiency of GaAs nanowires. Unlike more conventional passivation routes, doping here acted to reduce

the radiative lifetime rather than increase the non-radiative lifetime. In this way, strong luminescence was coupled with a picosecond lifetime. These performance gains were quantified using a calibrated PL setup to measure the absolute efficiency of individual nanowires. While the efficiency of undoped nanowires was observed to be an increasing function of pump power, that of the doped wires remained relatively constant. As such, the efficiency of the doped nanowires was found to be greater than that of the passivated nanowires for lower pump powers. Numerical modelling of these results enabled the extraction of values for carrier concentration that were similar to those found by APT and electrical measurements. Most importantly, the increase in radiative efficiency afforded through Zn doping enabled lasing from unpassivated GaAs nanowires at room temperature. The performance of these doped nano-lasers, including the non-linear transition into the lasing regime, was fully characterised with the lasing mode being identified from FDTD simulations as the TM01 mode. In addition to increasing radiative efficiency, p-type doping with Zn further acted to increase differential gain while also reducing the transparency carrier density. In this way, rate equation modelling showed the threshold pump power of a Zn doped nanowire to be less than that of an AlGaAs nanowire of similar dimensions.

The use of doping to increase the radiative efficiency of nanostructures here represents somewhat of a paradigm shift from more conventional passivation methods. Whereas passivation is aimed at achieving longer carrier lifetimes which are usually more characteristic of bulk devices, doping enables the relatively short lifetimes of nanostructures to be combined with greater radiative efficiency. These two approaches are not, however, mutually exclusive as each acts by a different mechanism. There is therefore scope for their combination in order to engineer both lifetime and IQE. Such a combination may be particularly relevant to future nanolaser devices which could take advantage of p-type doping in regards to differential gain and transparency carrier density. Doping is furthermore likely key to the development of electrically injected nanolasers.

Chapter 7 explored the use of DEZn as a source with the synthesis of the II-V nanostructures ZnAs, ZnP and ZnSb. These materials were grown on a variety of substrates such as GaAs, InP, Si and SiO_2. Several different seed metals including Au, Pt and Ni were explored. ZnAs was synthesised with two differing morphologies,

nanowire and nanoplate, corresponding to two different growth directions. Extensive TEM characterisation identified the phase of these nanomaterials to be α' Zn_3As_2. A strong room-temperature PL signal was obtained at around 1.0 eV with the radiative recombination coefficient calculated to be similar to that of a direct bandgap material. Electrical measurements found a high background carrier concentration. A variety of different growth morphologies were also identified for ZnP. Strong room temperature emission was observed from single nanowires at approximately 1.5 eV. Emission at low temperatures was found to be sensitive to pump power varying between 1.4 and 1.5 eV with a lifetime of less than 200 ps. ZnSb was grown from a GaAs stem and showed poor faceting which was possibly related to the small wetting angle of the seed particle.

The growth of II-V nanostructures by a standard MOVPE process unlocks this little known family of materials for the broader research community. Unlike In-based III-V semiconductors, the II-V nanostructures grown here may be considered earth abundant. This is of particular relevance for large scale applications such as photovoltaics. With strong emission at 1.0 and 1.5 eV respectively, ZnAs and ZnP hold significant potential for such applications. ZnSb is furthermore known to be one of the highest performing thermoelectric materials. Together these nanomaterials thus offer a range of properties having relevance to clean and efficient energy production. Alloying to engineer bandgap or lattice parameter will further extend these opportunities. Other possibilities include the combination of II-V nanostructures with III-V materials and Si to form complex heterostructures. Given that the II-V family is little explored, fundamental studies into the physical properties of these materials, particularly in regards to bandstructure, will be required to operate in tandem.

In conclusion, this dissertation has explored several applications of Zn to the growth of nanostructures by MOVPE. The framing of this work around a dopant rather than material or characterisation technique has provided the flexibility to visit a range of topics relating to the nanostructure growth. The varied contributions made here underline the vast possibilities offered by nanoscience, and more specifically, MOVPE growth.

References

1. Dumont, H.; Marbeuf, A.; Bouree, J.-E.; Gorochov, O. *J Mater Chem* **1993,** 3, (10), 1075-1079.
2. Buchan, N. I.; Larsen, C. A.; Stringfellow, G. B. *Journal of Crystal Growth* **1988,** 92, (3), 605-615.
3. Larsen, C. A.; Li, S. H.; Buchan, N. I.; Stringfellow, G. B.; Brown, D. W. *Journal of Crystal Growth* **1990,** 102, (1-2), 126-136.
4. Larsen, C. A.; Li, S. H.; Stringfellow, G. B. *Chemistry of Materials* **1991,** 3, (1), 39-44.
5. Williams, D. B.; Carter, C. B., *Transmission Electron Microscopy: A Textbook for Materials Science*. Plenum Press: New York, 1996.
6. Dinsdale, A. T. *Calphad* **1991,** 15, (4), 317-425.
7. Saxena, D. Design and Characterisation of III-V Semiconductor Nanowire Lasers. PhD thesis, Australian National University, Canberra, Australia, 2017.
8. Nelson, R. J.; Sobers, R. G. *J Appl Phys* **1978,** 49, (12), 6103-6108.
9. De Vries, G. C.; Frikkee, E.; Helmholdt, R. B.; Kopinga, K.; De Jonge, W. J. M. *Physica B: Condensed Matter* **1989,** 156–157, (0), 321-323.
10. Schoonmaker, R. C.; Venkitaraman, A.; Lee, P. K. *The Journal of Physical Chemistry* **1967,** 71, (8), 2676-2683.
11. Mozharivskyj, Y.; Pecharsky, A. O.; Bud'ko, S.; Miller, G. J. *Chemistry of Materials* **2004,** 16, (8), 1580-1589.
12. Zanin, I. E.; Aleinikova, K. B.; Antipin, M. Y.; Afanas'ev, M. M. *Crystallography Reports* **2004,** 49, (4), 579-584.
13. Ghasemi, M.; Johansson, J. *Journal of Alloys and Compounds* **2015,** 638, 95-102.
14. Nylén, J.; Andersson, M.; Lidin, S.; Häussermann, U. *Journal of the American Chemical Society* **2004,** 126, (50), 16306-16307.
15. Singleton, M.; Nash, P. *Journal of Phase Equilibria* **1987,** 8, (5), 419-422.
16. Tu, H.; Yin, F.; Su, X.; Liu, Y.; Wang, X. *Calphad* **2009,** 33, (4), 755-760.
17. Li, J.-B.; Record, M.-C.; Tedenac, J.-C. *Journal of Alloys and Compounds* **2007,** 438, (1–2), 171-177.
18. Aleinikova, K. B.; Kozlov, A. I.; Kozlova, S. G.; Sobolev, V. V. *Physics of the Solid State* **2002,** 44, (7), 1257-1262.
19. Snyder, G. J.; Christensen, M.; Nishibori, E.; Caillat, T.; Iversen, B. B. *Nat Mater* **2004,** 3, (7), 458-63.
20. Liu, X. J.; Wang, C. P.; Ohnuma, I.; Kainuma, R.; Ishida, K. *Journal of Phase Equilibria* **2000,** 21, (5), 432-442.
21. Okamoto, H.; Massalski, T. B. *Bulletin of Alloy Phase Diagrams* **1989,** 10, (1), 59-69.
22. Pietraszko, A.; Lukaszewicz, K. *Bulletin de l'Academie polonaise des sciences, Serie des sciences chimiques.* **1975,** 24, (6), 459-464.
23. Zanin, I. E.; Aleinikova, K. B.; Afanasiev, M. M.; Antipin, M. Y. *Journal of Structural Chemistry* **2004,** 45, (5), 844-848.
24. Algra, R. E.; Verheijen, M. A.; Feiner, L.-F.; Immink, G. G. W.; Enckevort, W. J. P. v.; Vlieg, E.; Bakkers, E. P. A. M. *Nano Letters* **2011,** 11, (3), 1259–1264.
25. Saxena, D.; Mokkapati, S.; Parkinson, P.; Jiang, N.; Gao, Q.; Tan, H. H.; Jagadish, C. *Nat Photon* **2013,** 7, (12), 963-968.
26. Ansara, I.; Chatillon, C.; Lukas, H. L.; Nishizawa, T.; Ohtani, H.; Ishida, K.; Hillert, M.; Sundman, B.; Argent, B. B.; Watson, A.; Chart, T. G.; Anderson, T. *Calphad* **1994,** 18, (2), 177-222.
27. Wang, J.; Kovnir, K. *Journal of the American Chemical Society* **2015,** 137, (39), 12474-12477.
28. Greenberg, J. H.; Lazarev, V. B.; Kozlov, S. E.; Shevchenko, V. J. *The Journal of Chemical Thermodynamics* **1974,** 6, (10), 1005-1012.
29. Sobolev, V. V.; Syrbu, N. N. *physica status solidi (b)* **1971,** 43, (1), K87-K91.
30. Liu, Y.; Zhou, B.; Lv, W.; Wu, C.; Su, X.; Wang, J. *Surface and Coatings Technology* **2016**.
31. Schoonmaker, R. C.; Lemmerman, K. J. *Journal of Chemical & Engineering Data* **1972,** 17, (2), 139-143.
32. Hirayama, C. *J Electrochem Soc* **1963,** 110, (1), 88-91.
33. Żdanowicz, W.; Kloc, K.; Kalińska, A.; Cisowska, E.; Burian, A. *Journal of Crystal Growth* **1975,** 31, 56-59.

34. Bachmann, K.; Buehler, E. *J Electrochem Soc* **1974,** 121, (6), 835-846.
35. Algra, R. E.; Verheijen, M. A.; Borgstrom, M. T.; Feiner, L. F.; Immink, G.; van Enckevort, W. J. P.; Vlieg, E.; Bakkers, E. *Nature* **2008,** 456, (7220), 369-372.
36. Lazarev, V. B.; Guskov, V. N.; Greenberg, J. H. *Mater Res Bull* **1981,** 16, (9), 1113-1120.
37. Dutkiewlcz, J. *Journal of Phase Equilibria* **1991,** 12, (4), 435-438.
38. Morozova, V.; Semenenya, T.; Marenkin, S.; Koshelev, O.; Raukhman, A.; Loseva, S. *Inorg Mater+* **1996,** 32, (1), 10-15.
39. Greenberg, J. H.; Guskov, V. N.; Lazarev, V. B. *The Journal of Chemical Thermodynamics* **1985,** 17, (8), 739-746.
40. Dutkiewicz, J.; Moser, Z.; Zabdyr, L.; Gohil, D.; Chart, T.; Ansara, I.; Girard, C. *Journal of Phase Equilibria* **1990,** 11, (1), 77-82.
41. Adjadj, F.; Belbacha, E.-d.; Bouharkat, M. *Journal of alloys and compounds* **2007,** 430, (1), 85-91.
42. Pawlikowski, J. M.; Misiewicz, J.; Sujak-Cyrul, B.; Wróbel, J. *physica status solidi (b)* **1979,** 92, (2), K123-K125.
43. Ali, M. N.; Gibson, Q.; Jeon, S.; Zhou, B. B.; Yazdani, A.; Cava, R. J. *Inorganic Chemistry* **2014,** 53, (8), 4062-4067.
44. Lisak, A.; Fitzner, K. *Journal of Phase Equilibria* **1994,** 15, (2), 151-154.
45. Kimball, G. M.; Müller, A. M.; Lewis, N. S.; Atwater, H. A. *Appl Phys Lett* **2009,** 95, (11), 112103.
46. Qiu, A. N.; Zhang, L. T.; Wu, J. S. *Physical Review B* **2010,** 81, (3), 035203.
47. Aubin, M. J.; Caron, L. G.; Jay-Gerin, J. P. *Physical Review B* **1977,** 15, (8), 3872-3878.
48. Klimova, A. M.; Ananichev, V. A.; Arif, M.; Blinov, L. N. *Glass Physics and Chemistry* **2005,** 31, (6), 760-762.
49. Chelluri, B.; Chang, T. Y.; Ourmazd, A.; Dayem, A. H.; Zyskind, J. L.; Srivastava, A. *Appl Phys Lett* **1986,** 49, (24), 1665-1667.
50. Hegyi, I. J.; Loebner, E. E.; Poor, E. W.; White, J. G. *J Phys Chem Solids* **1963,** 24, (2), 333-337.
51. Boström, M.; Lidin, S. *Journal of Alloys and Compounds* **2004,** 376, (1–2), 49-57.
52. Palkina, K. K.; Kuznetsov, V. G.; Lazarev, V. B. *Zhurnal Neorganicheskoj Khimii* **1975,** 20, (8), 2026-2028.
53. Aldred, A. T.; Pratt, J. N. *Journal of Chemical & Engineering Data* **1963,** 8, (3), 429-431.
54. Fleet, M. *Acta Crystallographica Section B* **1974,** 30, (1), 122-126.
55. Zanin, I. E.; Aleinikova, K. B.; Antipin, M. Y. *Crystallography Reports* **2003,** 48, (2), 199-204.
56. Carter, F. L.; Mazelsky, R. *J Phys Chem Solids* **1964,** 25, (6), 571-581.
57. Gelten, M. J.; Lieshout, A. v.; Es, C. v.; Blom, F. A. P. *Journal of Physics C: Solid State Physics* **1978,** 11, (1), 227.
58. Lazarev, V. B.; Marenkin, S. F.; Maksimova, S. I.; Khuseinov, B.; Shevchenko, V. Y. *Inorg Mater+* **1979,** 15, (5), 586-587.
59. Caron, L. G.; Jay-Gerin, J. P.; Aubin, M. J. *Physical Review B* **1977,** 15, (8), 3879-3887.
60. Munir, Z. A.; Searcy, A. W. *J Electrochem Soc* **1964,** 111, (10), 1170-1173.
61. Komiya, H.; Masumoto, K.; Fan, H. Y. *Physical Review* **1964,** 133, (6A), A1679-A1684.
62. Lyons, V. J. *The Journal of Physical Chemistry* **1959,** 63, (7), 1142-1144.
63. Im, H. S.; Park, K.; Jang, D. M.; Jung, C. S.; Park, J.; Yoo, S. J.; Kim, J.-G. *Nano Letters* **2015,** 15, (2), 990-997.
64. Pawlikowski, J. M. *Journal of Physics C: Solid State Physics* **1985,** 18, (29), 5605.
65. Morozova, V. A.; Marenkin, S. F.; Koshelev, O. G.; Chernoguzov, D. V.; Mikhailov, S. G.; Molchanov, A. V. *Inorg Mater+* **2007,** 43, (3), 215-220.
66. Radoff, P. L.; Bishop, S. G. *Physical Review B* **1972,** 5, (2), 442-448.
67. Schoonmaker, R. C.; Venkitaraman, A. R.; Lee, P. K. *The Journal of Physical Chemistry* **1967,** 71, (8), 2676-2683.
68. Richman, D. *J Phys Chem Solids* **1963,** 24, (9), 1131-1139.
69. Vogel, E. M. *Nat Nanotechnol* **2007,** 2, (1), 25-32.
70. Lu, W.; Lieber, C. M. *Nat Mater* **2007,** 6, (11), 841-850.
71. Theis, T. N.; Solomon, P. M. *Science* **2010,** 327, (5973), 1600-1601.
72. Samuelson, L. *Mater. Today* **2003,** 6, (10), 22-31.
73. Thelander, C.; Agarwal, P.; Brongersma, S.; Eymery, J.; Feiner, L. F.; Forchel, A.; Scheffler, M.; Riess, W.; Ohlsson, B. J.; Gosele, U.; Samuelson, L. *Mater Today* **2006,** 9, (10), 28-35.

74. Samuelson, L.; Thelander, C.; Bjork, M. T.; Borgstrom, M.; Deppert, K.; Dick, K. A.; Hansen, A. E.; Martensson, T.; Panev, N.; Persson, A. I.; Seifert, W.; Skold, N.; Larsson, M. W.; Wallenberg, L. R. *Physica E* **2004,** 25, (2-3), 313-318.
75. Law, M.; Goldberger, J.; Yang, P. D. *Annual Review of Materials Research* **2004,** 34, 83-122.
76. Kuchibhatla, S.; Karakoti, A. S.; Bera, D.; Seal, S. *Progress in Materials Science* **2007,** 52, (5), 699-913.
77. Dick, K. A.; Caroff, P. *Nanoscale* **2014,** 6, (6), 3006-3021.
78. Hu, Y. J.; Churchill, H. O. H.; Reilly, D. J.; Xiang, J.; Lieber, C. M.; Marcus, C. M. *Nat Nanotechnol* **2007,** 2, (10), 622-625.
79. Claudon, J.; Bleuse, J.; Malik, N. S.; Bazin, M.; Jaffrennou, P.; Gregersen, N.; Sauvan, C.; Lalanne, P.; Gerard, J. M. *Nat Photonics* **2010,** 4, (3), 174-177.
80. Bjork, M. T.; Thelander, C.; Hansen, A. E.; Jensen, L. E.; Larsson, M. W.; Wallenberg, L. R.; Samuelson, L. *Nano Letters* **2004,** 4, (9), 1621-1625.
81. Trivedi, K.; Yuk, H.; Floresca, H. C.; Kim, M. J.; Hu, W. *Nano Letters* **2011**, null-null.
82. Yu, H.; Li, J.; Loomis, R. A.; Wang, L.-W.; Buhro, W. E. *Nat Mater* **2003,** 2, (8), 517-520.
83. Arbiol, J.; de la Mata, M.; Eickhoff, M.; Morral, A. F. i. *Mater Today* **2013,** 16, (6), 213-219.
84. Garnett, E.; Yang, P. *Nano Letters* **2010,** 10, (3), 1082-1087.
85. Krogstrup, P.; Jorgensen, H. I.; Heiss, M.; Demichel, O.; Holm, J. V.; Aagesen, M.; Nygard, J.; Fontcuberta i Morral, A. *Nat Photonics* **2013,** 7, (4), 306-310.
86. Wallentin, J.; Anttu, N.; Asoli, D.; Huffman, M.; Åberg, I.; Magnusson, M. H.; Siefer, G.; Fuss-Kailuweit, P.; Dimroth, F.; Witzigmann, B.; Xu, H. Q.; Samuelson, L.; Deppert, K.; Borgström, M. T. *Science* **2013,** 339, (6123), 1057-1060.
87. Callahan, D. M.; Munday, J. N.; Atwater, H. A. *Nano Letters* **2011,** 12, (1), 214-218.
88. Mokkapati, S.; Catchpole, K. R. *J Appl Phys* **2012,** 112, (10), 101101.
89. Wang, Z. L.; Song, J. *Science* **2006,** 312, (5771), 242-246.
90. Feng, X.; He, R.; Yang, P.; Roukes, M. *Nano Letters* **2007,** 7, (7), 1953-1959.
91. Mile, E.; Jourdan, G.; Bargatin, I.; Labarthe, S.; Marcoux, C.; Andreucci, P.; Hentz, S.; Kharrat, C.; Colinet, E.; Duraffourg, L. *Nanotechnology* **2010,** 21, (16), 165504.
92. Zheng, G.; Patolsky, F.; Cui, Y.; Wang, W. U.; Lieber, C. M. *Nature biotechnology* **2005,** 23, (10), 1294-1301.
93. Stern, E.; Klemic, J. F.; Routenberg, D. A.; Wyrembak, P. N.; Turner-Evans, D. B.; Hamilton, A. D.; LaVan, D. A.; Fahmy, T. M.; Reed, M. A. *Nature* **2007,** 445, (7127), 519-522.
94. Zheng, G. F.; Patolsky, F.; Cui, Y.; Wang, W. U.; Lieber, C. M. *Nature Biotechnology* **2005,** 23, (10), 1294-1301.
95. Duan, X.; Li, Y.; Rajan, N. K.; Routenberg, D. A.; Modis, Y.; Reed, M. A. *Nat Nano* **2012,** 7, (6), 401-407.
96. Knopfmacher, O.; Tarasov, A.; Fu, W.; Wipf, M.; Niesen, B.; Calame, M.; Schönenberger, C. *Nano Letters* **2010**.
97. Offermans, P.; Crego-Calama, M.; Brongersma, S. H. *Nano Letters* **2010**.
98. Ng, H. T.; Han, J.; Yamada, T.; Nguyen, P.; Chen, Y. P.; Meyyappan, M. *Nano Letters* **2004,** 4, (7), 1247-1252.
99. Tomioka, K.; Yoshimura, M.; Fukui, T. *Nature* **2012,** 488, (7410), 189-192.
100. Xiang, J.; Lu, W.; Hu, Y. J.; Wu, Y.; Yan, H.; Lieber, C. M. *Nature* **2006,** 441, (7092), 489-493.
101. SalfiJ; Savelyev, I. G.; BluminM; Nair, S. V.; Ruda, H. E. *Nat Nanotechnol* **2010,** advance online publication.
102. Huang, Y.; Duan, X. F.; Cui, Y.; Lauhon, L. J.; Kim, K. H.; Lieber, C. M. *Science* **2001,** 294, (5545), 1313-1317.
103. Thelander, C.; Martensson, T.; Bjork, M. T.; Ohlsson, B. J.; Larsson, M. W.; Wallenberg, L. R.; Samuelson, L. *Appl Phys Lett* **2003,** 83, (10), 2052-2054.
104. Schmid, H.; Bessire, C.; Björk, M. T.; Schenk, A.; Riel, H. *Nano Letters* **2012,** 12, (2), 699-703.
105. Wallentin, J.; Persson, J. M.; Wagner, J. B.; Samuelson, L.; Deppert, K.; Borgstrom, M. T. *Nano Letters* **2010,** 10, (3), 974-979.
106. Ganjipour, B.; Dey, A. W.; Borg, B. M.; Ek, M.; Pistol, M.-E.; Dick, K. A.; Wernersson, L.-E.; Thelander, C. *Nano Letters* **2011,** 11, (10), 4222-4226.
107. Sadaf, S. M.; Ra, Y. H.; Nguyen, H. P. T.; Djavid, M.; Mi, Z. *Nano Letters* **2015,** 15, (10), 6696-6701.
108. Tchernycheva, M.; Lavenus, P.; Zhang, H.; Babichev, A. V.; Jacopin, G.; Shahmohammadi, M.; Julien, F. H.; Ciechonski, R.; Vescovi, G.; Kryliouk, O. *Nano Letters* **2014,** 14, (5), 2456-2465.
109. Qian, F.; Gradecak, S.; Li, Y.; Wen, C. Y.; Lieber, C. M. *Nano Letters* **2005,** 5, (11), 2287-2291.

110. Minot, E. D.; Kelkensberg, F.; van Kouwen, M.; van Dam, J. A.; Kouwenhoven, L. P.; Zwiller, V.; Borgstrom, M. T.; Wunnicke, O.; Verheijen, M. A.; Bakkers, E. *Nano Letters* **2007,** 7, (2), 367-371.
111. Tomioka, K.; Motohisa, J.; Hara, S.; Hiruma, K.; Fukui, T. *Nano Letters* **2010,** 10, (5), 1639-1644.
112. Huang, M. H.; Mao, S.; Feick, H.; Yan, H. Q.; Wu, Y. Y.; Kind, H.; Weber, E.; Russo, R.; Yang, P. D. *Science* **2001,** 292, (5523), 1897-1899.
113. Oulton, R. F.; Sorger, V. J.; Zentgraf, T.; Ma, R. M.; Gladden, C.; Dai, L.; Bartal, G.; Zhang, X. *Nature* **2009,** 461, (7264), 629-632.
114. Duan, X. F.; Huang, Y.; Agarwal, R.; Lieber, C. M. *Nature* **2003,** 421, (6920), 241-245.
115. Chu, S.; Wang, G.; Zhou, W.; Lin, Y.; Chernyak, L.; Zhao, J.; Kong, J.; Li, L.; Ren, J.; Liu, J. *Nat Nanotechnol* **2011,** 6, (8), 506-10.
116. Mayer, B.; Rudolph, D.; Schnell, J.; Morkotter, S.; Winnerl, J.; Treu, J.; Muller, K.; Bracher, G.; Abstreiter, G.; Koblmuller, G.; Finley, J. J. *Nat Commun* **2013,** 4, 2931.
117. Li, K. H.; Liu, X.; Wang, Q.; Zhao, S.; Mi, Z. *Nat Nanotechnol* **2015,** 10, (2), 140-144.
118. Chen, R.; Tran, T.-T. D.; Ng, K. W.; Ko, W. S.; Chuang, L. C.; Sedgwick, F. G.; Chang-Hasnain, C. *Nat Photon* **2011,** 5, (3), 170-175.
119. Pettersson, H.; Tragardh, J.; Persson, A. I.; Landin, L.; Hessman, D.; Samuelson, L. *Nano Letters* **2006,** 6, (2), 229-232.
120. Wang, J. F.; Gudiksen, M. S.; Duan, X. F.; Cui, Y.; Lieber, C. M. *Science* **2001,** 293, (5534), 1455-1457.
121. Rigutti, L.; Tchernycheva, M.; De Luna Bugallo, A.; Jacopin, G.; Julien, F. H.; Zagonel, L. F.; March, K.; Stephan, O.; Kociak, M.; Songmuang, R. *Nano Letters* **2010**, null-null.
122. Cao, L.; White, J. S.; Park, J.-S.; Schuller, J. A.; Clemens, B. M.; Brongersma, M. L. *Nat Mater* **2009,** 8, (8), 643-647.
123. Holm, J. V.; Jørgensen, H. I.; Krogstrup, P.; Nygård, J.; Liu, H.; Aagesen, M. *Nature Communications* **2013,** 4, 1498.
124. Mariani, G.; Scofield, A. C.; Hung, C.-H.; Huffaker, D. L. *Nat Commun* **2013,** 4, 1497.
125. Tian, B. Z.; Zheng, X. L.; Kempa, T. J.; Fang, Y.; Yu, N. F.; Yu, G. H.; Huang, J. L.; Lieber, C. M. *Nature* **2007,** 449, (7164), 885-889.
126. Thelander, C.; Nilsson, H. A.; Jensen, L. E.; Samuelson, L. *Nano Letters* **2005,** 5, (4), 635-638.
127. Bulgarini, G.; Reimer, M. E.; Bouwes Bavinck, M.; Jöns, K. D.; Dalacu, D.; Poole, P. J.; Bakkers, E. P. A. M.; Zwiller, V. *Nano Letters* **2014,** 14, (7), 4102-4106.
128. Dalacu, D.; Mnaymneh, K.; Lapointe, J.; Wu, X.; Poole, P. J.; Bulgarini, G.; Zwiller, V.; Reimer, M. E. *Nano Letters* **2012,** 12, (11), 5919-5923.
129. Kouwen, M. P. v.; Reimer, M. E.; Hidma, A. W.; van Weert, M. H. M.; Algra, R. E.; Bakkers, E. P. A. M.; Kouwenhoven, L. P.; Zwiller, V. *Nano Letters* **2010,** 10, (5), 1817-1822.
130. Heeres, E. C.; Bakkers, E.; Roest, A. L.; Kaiser, M.; Oosterkamp, T. H.; de Jonge, N. *Nano Letters* **2007,** 7, (2), 536-540.
131. Choi, Y.; Michan, M.; Johnson, J. L.; Naieni, A. K.; Ural, A.; Nojeh, A. *J Appl Phys* **2012,** 111, (4), 044308.
132. Lauhon, L. J.; Gudiksen, M. S.; Wang, C. L.; Lieber, C. M. *Nature* **2002,** 420, (6911), 57-61.
133. Mohan, P.; Motohisa, J.; Fukui, T. *Nanotechnology* **2005,** 16, (12), 2903.
134. Caroff, P.; Messing, M. E.; Borg, B. M.; Dick, K. A.; Deppert, K.; Wernersson, L. E. *Nanotechnology* **2009,** 20, (49), 95606.
135. de la Mata, M.; Magen, C.; Caroff, P.; Arbiol, J. *Nano Letters* **2014,** 14, (11), 6614-6620.
136. Ertekin, E.; Greaney, P. A.; Chrzan, D. C.; Sands, T. D. *J Appl Phys* **2005,** 97, (11), 14325.
137. Larsson, M. W.; Wagner, J. B.; Wallin, M.; Hakansson, P.; Froberg, L. E.; Samuelson, L.; Wallenberg, L. R. *Nanotechnology* **2007,** 18, (1), 15504.
138. Goldthorpe, I. A.; Marshall, A. F.; McIntyre, P. C. *Nano Lett* **2008,** 8, (11), 4081-4086.
139. Johansson, J.; Dick, K. A. *CrystEngComm* **2011,** 13, (24), 7175-7184.
140. Lauhon, L. J.; Gudiksen, M. S.; Lieber, C. M. *Philosophical Transactions of the Royal Society of London Series A-Mathematical Physical & Engineering Sciences* **2004,** 362, (1819), 1247-1260.
141. Martensson, T.; Svensson, C. P. T.; Wacaser, B. A.; Larsson, M. W.; Seifert, W.; Deppert, K.; Gustafsson, A.; Wallenberg, L. R.; Samuelson, L. *Nano Letters* **2004,** 4, (10), 1987-1990.
142. Roest, A. L.; Verheijen, M. A.; Wunnicke, O.; Serafin, S.; Wondergem, H.; Bakkers, E. *Nanotechnology* **2006,** 17, (11), S271-S275.
143. Mårtensson, T.; Svensson, C. P. T.; Wacaser, B. A.; Larsson, M. W.; Seifert, W.; Deppert, K.; Gustafsson, A.; Wallenberg, L. R.; Samuelson, L. *Nano Letters* **2004,** 4, (10), 1987-1990.

144. Hillerich, K.; Dick, K. A.; Wen, C.-Y.; Reuter, M. C.; Kodambaka, S.; Ross, F. M. *Nano Letters* **2013,** 13, (3), 903-908.
145. Akopian, N.; Patriarche, G.; Liu, L.; Harmand, J. C.; Zwiller, V. *Nano Letters* **2010,** 10, (4), 1198-1201.
146. Bouwes Bavinck, M.; Jöns, K. D.; Zieliński, M.; Patriarche, G.; Harmand, J.-C.; Akopian, N.; Zwiller, V. *Nano Letters* **2016,** 16, (2), 1081-1085.
147. Spirkoska, D.; Arbiol, J.; Gustafsson, A.; Conesa-Boj, S.; Glas, F.; Zardo, I.; Heigoldt, M.; Gass, M. H.; Bleloch, A. L.; Estrade, S.; Kaniber, M.; Rossler, J.; Peiro, F.; Morante, J. R.; Abstreiter, G.; Samuelson, L.; Fontcuberta i Morral, A. *Physical Review B* **2009,** 80, (24), 245325.
148. Dick, K. A.; Thelander, C.; Samuelson, L.; Caroff, P. *Nano Letters* **2010,** 10, (9), 3494–3499.
149. Mourik, V.; Zuo, K.; Frolov, S. M.; Plissard, S. R.; Bakkers, E. P. A. M.; Kouwenhoven, L. P. *Science* **2012,** 336, (6084), 1003-1007.
150. Deng, M. T.; Yu, C. L.; Huang, G. Y.; Larsson, M.; Caroff, P.; Xu, H. Q. *Nano Letters* **2012,** 12, (12), 6414-6419.
151. Das, A.; Ronen, Y.; Most, Y.; Oreg, Y.; Heiblum, M.; Shtrikman, H. *Nature Physics* **2012,** 8, (12), 887-895.
152. Stringfellow, G. B., *Organometallic vapor-phase epitaxy: theory and practice*. Academic Press: 1999.
153. Orton, J., *The Story of Semiconductors*. OXFORD UNIVERSITY PRESS: 2004.
154. Schubert, E. F., *Doping in III-V semiconductors*. E. Fred Schubert: 2015.
155. Dick, K. A. *Progress in Crystal Growth and Characterization of Materials* **2008,** 54, (3-4), 138-173.
156. Lu, W.; Lieber, C. M. *J Phys D Appl Phys* **2006,** 39, (21), R387-R406.
157. Gao, Q.; Tan, H. H.; Jackson, H. E.; Smith, L. M.; Yarrison-Rice, J. M.; Zou, J.; Jagadish, C. *Semiconductor Science and Technology* **2012,** 27, (5).
158. Joyce, H. J.; Gao, Q.; Tan, H. H.; Jagadish, C.; Kim, Y.; Zou, J.; Smith, L. M.; Jackson, H. E.; Yarrison-Rice, J. M.; Parkinson, P.; Johnston, M. B. *Prog Quant Electron* **2011,** 35, (2-3), 23-75.
159. Dick, K. A.; Deppert, K.; Martensson, T.; Mandl, B.; Samuelson, L.; Seifert, W. *Nano Letters* **2005,** 5, (4), 761-764.
160. Lensch-Falk, J. L.; Hemesath, E. R.; Perea, D. E.; Lauhon, L. J. *J Mater Chem* **2009,** 19, (7), 849-857.
161. Wen, C. Y.; Reuter, M. C.; Tersoff, J.; Stach, E. A.; Ross, F. M. *Nano Letters* **2009,** 10, (2), 514-519.
162. Dick, K. A.; Deppert, K.; Karlsson, L. S.; Wallenberg, L. R.; Samuelson, L.; Seifert, W. *Adv Funct Mater* **2005,** 15, (10), 1603-1610.
163. Lindberg, C.; Whiticar, A.; Dick, K. A.; Sköld, N.; Nygård, J.; Bolinsson, J. *Nano Letters* **2016**.
164. Vogel, A. T.; de Boor, J.; Becker, M.; Wittemann, J. V.; Mensah, S. L.; Werner, P.; Schmidt, V. *Nanotechnology* **2011,** 22, (1), 015605.
165. Boles, S. T.; Thompson, C. V.; Fitzgerald, E. A. *Journal of Crystal Growth* **2009,** 311, (5), 1446-1450.
166. Garnett, E. C.; Liang, W. J.; Yang, P. D. *Advanced Materials* **2007,** 19, (19), 2946-+.
167. Oh, E.; Lee, B. W.; Shim, S.; Lee, K.-Y.; Oh, H.; Choi, H.-J.; Son, B. H.; Ahn, Y. H.; Dang, L. S. *J Korean Phys Soc* **2010,** 56, (1), 100-103.
168. Li, Q.; Wang, G. T. *Appl Phys Lett* **2008,** 93, (4), 043119.
169. Wang, Y. W.; Schmidt, V.; Senz, S.; Gosele, U. *Nat Nanotechnol* **2006,** 1, (3), 186-189.
170. Moutanabbir, O.; Senz, S.; Scholz, R.; Alexe, M.; Kim, Y.; Pippel, E.; Wang, Y.; Wiethoff, C.; Nabbefeld, T.; Meyer zu Heringdorf, F.; Horn-von Hoegen, M. *ACS Nano* **2011,** 5, (2), 1313-20.
171. Mullane, E.; Kennedy, T.; Geaney, H.; Dickinson, C.; Ryan, K. M. *Chemistry of Materials* **2013,** 25, (9), 1816-1822.
172. Marcus, T.; Erik, K. M.; Reza, R. Z.; Sebastian, L.; Kimberly, A. D.; Sepideh Gorji, G. *Nanotechnology* **2016,** 27, (17), 175602.
173. Rong, S.; Neimantas, V.; Daniel, J.; Mats-Erik, P.; Sebastian, L.; Kimberly, A. D. *Nanotechnology* **2016,** 27, (21), 215603.
174. Ning, H.; et al. *Nanotechnology* **2011,** 22, (28), 285607.
175. Han, N.; Hui, A. T.; Wang, F.; Hou, J. J.; Xiu, F.; Hung, T.; Ho, J. C. *Appl Phys Lett* **2011,** 99, (8), 083114.
176. Ford, A. C.; Ho, J. C.; Fan, Z.; Ergen, O.; Altoe, V.; Aloni, S.; Razavi, H.; Javey, A. *Nano Res* **2008,** 1, (1), 32-39.

177. Tuan, H.-Y.; Lee, D. C.; Hanrath, T.; Korgel, B. A. *Chemistry of Materials* **2005,** 17, (23), 5705-5711.
178. Lu, X.; Harris, J. T.; Villarreal, J. E.; Chockla, A. M.; Korgel, B. A. *Chemistry of Materials* **2013,** 25, (10), 2172-2177.
179. Barth, S.; Koleśnik, M. M.; Donegan, K.; Krstić, V.; Holmes, J. D. *Chemistry of Materials* **2011,** 23, (14), 3335-3340.
180. Mattila, M.; Hakkarainen, T.; Jiang, H.; Kauppinen, E. I.; Lipsanen, H. *Nanotechnology* **2007,** 18, (15), 155301.
181. Pozuelo, M.; Zhou, H.; Lin, S.; Lipman, S. A.; Goorsky, M. S.; Hicks, R. F.; Kodambaka, S. *Journal of Crystal Growth* In Press, Accepted Manuscript.
182. Novotny, C. J.; Yu, P. K. L. *Appl Phys Lett* **2005,** 87, (20), 3111.
183. Mandl, B.; Stangl, J.; Hilner, E.; Zakharov, A. A.; Hillerich, K.; Dey, A. W.; Samuelson, L.; Bauer, G.; Deppert, K.; Mikkelsen, A. *Nano Letters* **2010,** 10, (11), 4443-4449.
184. Plissard, S.; et al. *Nanotechnology* **2011,** 22, (27), 275602.
185. Dick, K. A.; Bolinsson, J.; Borg, B. M.; Johansson, J. *Nano Letters* **2012,** 12, (6), 3200-3206.
186. Wen, C.-Y.; Reuter, M. C.; Bruley, J.; Tersoff, J.; Kodambaka, S.; Stach, E. A.; Ross, F. M. *Science* **2009,** 326, (5957), 1247-1250.
187. Perea, D. E.; Li, N.; Dickerson, R. M.; Misra, A.; Picraux, S. T. *Nano Letters* **2011,** 11, (8), 3117-3122.
188. Christesen, J. D.; Pinion, C. W.; Zhang, X.; McBride, J. R.; Cahoon, J. F. *ACS Nano* **2014,** 8, (11), 11790-11798.
189. Lim, S. K.; Tambe, M. J.; Brewster, M. M.; Gradečak, S. *Nano Letters* **2008,** 8, (5), 1386-1392.
190. Ameruddin, A. S.; Caroff, P.; Tan, H. H.; Jagadish, C.; Dubrovskii, V. G. *Nanoscale* **2015**.
191. Scuderi, M.; Prete, P.; Lovergine, N.; Spinella, C.; Nicotra, G. *Materials Science in Semiconductor Processing*.
192. Guo, Y. N.; Xu, H. Y.; Auchterlonie, G. J.; Burgess, T.; Joyce, H. J.; Gao, Q.; Tan, H. H.; Jagadish, C.; Shu, H. B.; Chen, X. S.; Lu, W.; Kim, Y.; Zou, J. *Nano Lett* **2013,** 13, (2), 643-50.
193. Conesa-Boj, S.; Kriegner, D.; Han, X.-L.; Plissard, S.; Wallart, X.; Stangl, J.; Fontcuberta i Morral, A.; Caroff, P. *Nano Letters* **2013**.
194. Shin, J. C.; Kim, D. Y.; Lee, A.; Kim, H. J.; Kim, J. H.; Choi, W. J.; Kim, H.-S.; Choi, K. J. *Journal of Crystal Growth* **2013,** 372, (0), 15-18.
195. Ameruddin, A. S.; Fonseka, H. A.; Caroff, P.; Wong-Leung, J.; Veld, R. L. M. O. H.; Boland, J. L.; Johnston, M. B.; Tan, H. H.; Jagadish, C. *Nanotechnology* **2015,** 26, (20).
196. Chi, C.-Y.; Chang, C.-C.; Hu, S.; Yeh, T.-W.; Cronin, S. B.; Dapkus, P. D. *Nano Letters* **2013,** 13, (6), 2506-2515.
197. Keitaro, I.; Takuya, S.; Hiroatsu, Y.; Kenji, H.; Junichi, M.; Shinjiroh, H.; Takashi, F. *Nanotechnology* **2008,** 19, (26), 265604.
198. Kelrich, A.; Dubrovskii, V. G.; Calahorra, Y.; Cohen, S.; Ritter, D. *Nanotechnology* **2015,** 26, (8), 085303.
199. Mohan, P.; Motohisa, J.; Fukui, T. *Nanotechnology* **2005,** 16, (12), 2903-2907.
200. Gao, Q.; Dubrovskii, V. G.; Caroff, P.; Wong-Leung, J.; Li, L.; Guo, Y.; Fu, L.; Tan, H. H.; Jagadish, C. *Nano Lett* **2016,** 16, (7), 4361-7.
201. Noborisaka, J.; Motohisa, J.; Fukui, T. *Appl Phys Lett* **2005,** 86, (21), 13102.
202. Joshua, N. S.; Andrew, L.; Christian, R.; Huffaker, D. L. *Nanotechnology* **2013,** 24, (47), 475601.
203. Borg, M.; Schmid, H.; Moselund, K. E.; Cutaia, D.; Riel, H. *J Appl Phys* **2015,** 117, (14), 144303.
204. Wang, F.; Gao, Q.; Peng, K.; Li, Z.; Li, Z.; Guo, Y.; Fu, L.; Smith, L. M.; Tan, H. H.; Jagadish, C. *Nano Letters* **2015**.
205. Treu, J.; Speckbacher, M.; Saller, K.; Morkötter, S.; Döblinger, M.; Xu, X.; Riedl, H.; Abstreiter, G.; Finley, J. J.; Koblmüller, G. *Appl Phys Lett* **2016,** 108, (5), 053110.
206. Berg, A.; Caroff, P.; Shahid, N.; Lockrey, M. N.; Yuan, X.; Borgström, M. T.; Tan, H. H.; Jagadish, C. *Nano Res* **2016**, 1-11.
207. Galli, G. *Nature* **2005,** 436, (7047), 32-33.
208. Bryan, J. D.; Gamelin, D. R., Doped Semiconductor Nanocrystals: Synthesis, Characterization, Physical Properties, and Applications. In *Progress in Inorganic Chemistry*, Karlin, K. D., Ed. 2005; Vol. 54, pp 47-126.
209. Castell, M. R.; Muller, D. A.; Voyles, P. M. *Nature Materials* **2003,** 2, (3), 129-131.
210. Mocatta, D.; Cohen, G.; Schattner, J.; Millo, O.; Rabani, E.; Banin, U. *Science* **2011,** 332, (6025), 77.

211. Norris, D. J.; Efros, A. L.; Erwin, S. C. *Science* **2008,** 319, (5871), 1776-1779.
212. Dalpian, G. M.; Chelikowsky, J. R. *Phys Rev Lett* **2006,** 96, (22), 226802.
213. Erwin, S. C.; Zu, L. J.; Haftel, M. I.; Efros, A. L.; Kennedy, T. A.; Norris, D. J. *Nature* **2005,** 436, (7047), 91-94.
214. Khanal, D. R.; Yim, J. W. L.; Walukiewicz, W.; Wu, J. *Nano Letters* **2007,** 7, (5), 1186-1190.
215. Xie, P.; Hu, Y.; Fang, Y.; Huang, J.; Lieber, C. M. *Proceedings of the National Academy of Sciences* **2009,** 106, (36), 15254-15258.
216. Du, M. H.; Erwin, S. C.; Efros, A. L.; Norris, D. J. *Phys Rev Lett* **2008,** 100, (17), -.
217. Chan, T.-L.; Kwak, H.; Eom, J.-H.; Zhang, S. B.; Chelikowsky, J. R. *Physical Review B* **2010,** 82, (11), 115421.
218. Connell, J. G.; Yoon, K.; Perea, D. E.; Schwalbach, E. J.; Voorhees, P. W.; Lauhon, L. J. *Nano Letters* **2012,** 13, (1), 199-206.
219. Koren, E.; Rosenwaks, Y.; Allen, J. E.; Hemesath, E. R.; Lauhon, L. J. *Appl Phys Lett* **2009,** 95, (9), 092105-3.
220. Perea, D. E.; Hemesath, E. R.; Schwalbach, E. J.; Lensch-Falk, J. L.; Voorhees, P. W.; Lauhon, L. J. *Nat Nanotechnol* **2009,** 4, (5), 315-319.
221. Peelaers, H.; Partoens, B.; Peeters, F. M. *Nano Letters* **2006,** 6, (12), 2781-2784.
222. Fernandez-Serra, M. V.; Adessi, C.; Blase, X. *Phys Rev Lett* **2006,** 96, (16), 166805-1-4.
223. Cui, Y.; Lauhon, L. J.; Gudiksen, M. S.; Wang, J. F.; Lieber, C. M. *Appl Phys Lett* **2001,** 78, (15), 2214-2216.
224. Yu, J. Y.; Chung, S. W.; Heath, J. R. *J. Phys. Chem. B* **2000,** 104, (50), 11864-11870.
225. Diarra, M.; Niquet, Y. M.; Delerue, C.; Allan, G. *Phys. Rev. B* **2007,** 75, (4), 5301.
226. Koenraad, P. M.; Flatte, M. E. *Nat Mater* **2011,** 10, (2), 91-100.
227. Chia, A. C. E.; Boulanger, J. P.; LaPierre, R. R. *Nanotechnology* **2013,** 24, (4), 045701.
228. Mikkelsen, A.; Skold, N.; Ouattara, L.; Borgstrom, M.; Andersen, J. N.; Samuelson, L.; Seifert, W.; Lundgren, E. *Nature Materials* **2004,** 3, (8), 519-523.
229. Hilner, E.; HaÌŠkanson, U.; FroÌˆberg, L. E.; Karlsson, M.; Kratzer, P.; Lundgren, E.; Samuelson, L.; Mikkelsen, A. *Nano Letters* **2008,** 8, (11), 3978-3982.
230. Schlitz, R. A.; Perea, D. E.; Lensch-Falk, J. L.; Hemesath, E. R.; Lauhon, L. J. *Appl Phys Lett* **2009,** 95, (16), 62101.
231. Koren, E.; Berkovitch, N.; Rosenwaks, Y. *Nano Letters* **2010,** 10, (4), 1163-1167.
232. Hultin, O.; Otnes, G.; Borgstrom, M. T.; Bjork, M.; Samuelson, L.; Storm, K. *Nano Lett* **2016,** 16, (1), 205-11.
233. Blömers, C.; Grap, T.; Lepsa, M. I.; Moers, J.; Trellenkamp, S.; Grützmacher, D.; Lüth, H.; Schäpers, T. *Appl Phys Lett* **2012,** 101, (15), 152106.
234. Daniel, W.; Axel, L.; Paola, P.; Nico, L.; Hannes, L. *Journal of Physics D: Applied Physics* **2016,** 49, (36), 364004.
235. Darbandi, A.; McNeil, J. C.; Akhtari-Zavareh, A.; Watkins, S. P.; Kavanagh, K. L. *Nano Lett* **2016,** 16, (7), 3982-8.
236. van Weert, M. H. M.; Helman, A.; van den Einden, W.; Algra, R. E.; Verheijen, M. A.; Borgström, M. T.; Immink, G.; Kelly, J. J.; Kouwenhoven, L. P.; Bakkers, E. P. A. M. *Journal of the American Chemical Society* **2009,** 131, (13), 4578-4579.
237. Regolin, I.; Gutsche, C.; Lysov, A.; Blekker, K.; Li, Z.-A.; Spasova, M.; Prost, W.; Tegude, F. J. *Journal of Crystal Growth* **2011,** 315, (1), 143-147.
238. Ihn, S. G.; Song, J. I.; Kim, T. W.; Leem, D. S.; Lee, T.; Lee, S. G.; Koh, E. K.; Song, K. *Nano Letters* **2007,** 7, (1), 39-44.
239. Dufouleur, J.; Colombo, C.; Garma, T.; Ketterer, B.; Uccelli, E.; Nicotra, M.; Fontcuberta i Morral, A. *Nano Letters* **2010,** 10, (5), 1734-1740.
240. Wang, H. H.; Baek, S.; Song, J. J.; Lee, J.; Lim, S. W. *Nanotechnology* **2008,** 19, (7), -.
241. Tutuc, E.; Guha, S.; Chu, J. O. *Appl Phys Lett* **2006,** 88, (4), 43113.
242. Pan, L.; Lew, K. K.; Redwing, J. M.; Dickey, E. C. *Journal of Crystal Growth* **2005,** 277, (1-4), 428-436.
243. Wallentin, J.; Ek, M.; Wallenberg, L. R.; Samuelson, L.; Deppert, K.; Borgström, M. T. *Nano Letters* **2010,** 10, (12), 4807–4812.
244. Wallentin, J.; Mergenthaler, K.; Ek, M.; Wallenberg, L. R.; Samuelson, L.; Deppert, K.; Pistol, M.-E.; Borgström, M. T. *Nano Letters* **2011,** 11, (6), 2286-2290.
245. Meng, C. Y.; Shih, B. L.; Lee, S. C. *Journal of Nanoparticle Research* **2005,** 7, (6), 615-620.
246. Borgstrom, M. T.; Norberg, E.; Wickert, P.; Nilsson, H. A.; Tragardh, J.; Dick, K. A.; Statkute, G.; Ramvall, P.; Deppert, K.; Samuelson, L. *Nanotechnology* **2008,** 19, 445602.

247. Burgess, T.; Breuer, S.; Caroff, P.; Wong-Leung, J.; Gao, Q.; Hoe Tan, H.; Jagadish, C. *ACS Nano* **2013,** 7, (9), 8105-8114.
248. Kuech, T., *Handbook of Crystal Growth: Thin Films and Epitaxy*. Elsevier: 2014.
249. Okamoto, K.; Mawatari, H.; Yamaguchi, K.; Noguchi, A. *Journal of Crystal Growth* **1989,** 98, (4), 630-636.
250. Hill, D. E. *J Appl Phys* **1970,** 41, (4), 1815-1818.
251. Ashen, D. J.; Dean, P. J.; Hurle, D. T. J.; Mullin, J. B.; White, A. M.; Greene, P. D. *J Phys Chem Solids* **1975,** 36, (10), 1041-1053.
252. White, A. M.; Dean, P. J.; Fairhurst, K. M.; Bardsley, W.; Williams, E. W.; Day, B. *Solid State Commun* **1972,** 11, (9), 1099-1103.
253. Fischbach, J. U.; Benz, G.; Stath, N.; Pilkuhn, M. H. *Solid State Commun* **1972,** 11, (5), 725-728.
254. Feng, M. S.; Ares Fang, C. S.; Chen, H. D. *Mater Chem Phys* **1995,** 42, (2), 143-147.
255. Li, G.; Linnarsson, M.; Jagadish, C. *Journal of Crystal Growth* **1995,** 154, (3-4), 231-239.
256. Gosele, U.; Morehead, F. *J Appl Phys* **1981,** 52, (7), 4617-4619.
257. Kadhim, M. A. H.; Tuck, B. *J Mater Sci* **1972,** 7, (1), 68-74.
258. Glew, R. W. *Journal of Crystal Growth* **1984,** 68, (1), 44-47.
259. Hahn, B.; Heindel, G.; Pschorr-Schoberer, E.; Gebhardt, W. *Semiconductor science and technology* **1998,** 13, (7), 788.
260. Shigeo, F.; Yoshitaka, T.; Akio, S. *Japanese Journal of Applied Physics* **1983,** 22, (9A), L583.
261. Hiroshi, M.; Iwao, M.; Masashi, M.; Hiroshi, K. *Japanese Journal of Applied Physics* **1985,** 24, (8A), L578.
262. Kuhn, W.; Wagner, H.; Stanzl, H.; Wolf, K.; Worle, K.; Lankes, S.; Betz, J.; Worz, M.; Lichtenberger, D.; Leiderer, H. *Semiconductor Science and Technology* **1991,** 6, (9A), A105.
263. Scriven, G. J.; Leitch, A. W. R.; Neethling, J. H.; Kozyrkov, V. V.; Watters, V. J. *Journal of Crystal Growth* **1997,** 170, (1-4), 813-816.
264. Wallentin, J.; Messing, M. E.; Trygg, E.; Samuelson, L.; Deppert, K.; Borgström, M. T. *Journal of Crystal Growth* **2011,** 331, (1), 8-14.
265. Stichtenoth, D.; Wegener, K.; Gutsche, C.; Regolin, I.; Tegude, F. J.; Prost, W.; Seibt, M.; Ronning, C. *Appl Phys Lett* **2008,** 92, (16), 163107.
266. Zhi-Min, L.; et al. *Nanotechnology* **2011,** 22, (37), 375201.
267. Han, N.; Wang, F.; Hou, J. J.; Xiu, F.; Yip, S.; Hui, A. T.; Hung, T.; Ho, J. C. *ACS Nano* **2012,** 6, (5), 4428-4433.
268. Ford, A. C.; Chuang, S.; Ho, J. C.; Chueh, Y.-L.; Fan, Z.; Javey, A. *Nano Letters* **2010,** 10, (2), 509-513.
269. Gutsche, C.; Regolin, I.; Blekker, K.; Lysov, A.; Prost, W.; Tegude, F. J. *J Appl Phys* **2009,** 105, (2), 024305-5.
270. Lysov, A.; Offer, M.; Gutsche, C.; Regolin, I.; Topaloglu, S.; Geller, M.; Prost, W.; Tegude, F. J. *Nanotechnology* **2011,** 22, (8), 085702.
271. Heurlin, M.; Wickert, P.; Falt, S.; Borgström, M. T.; Deppert, K.; Samuelson, L.; Magnusson, M. H. *Nano Letters* **2011,** 11, (5), 2028–2031.
272. Pettersson, H.; Zubritskaya, I.; Nghia, N. T.; Wallentin, J.; Borgstrom, M. T.; Storm, K.; Landin, L.; Wickert, P.; Capasso, F.; Samuelson, L. *Nanotechnology* **2012,** 23, (13), 135201.
273. Satoshi, M.; Katsuhiro, T.; Shinjiroh, H.; Junichi, M. *Japanese Journal of Applied Physics* **2012,** 51, (2S), 02BN03.
274. Algra, R. E.; Vonk, V.; Wermeille, D.; Szweryn, W. J.; Verheijen, M. A.; van Enckevort, W. J. P.; Bode, A. A. C.; Noorduin, W. L.; Tancini, E.; de Jong, A. E. F.; Bakkers, E. P. A. M.; Vlieg, E. *Nano Letters* **2010**, null-null.
275. Norman, A.; Olson, J.; Romero, M.; Al-Jassim, M. In *Electron Microscopy Studies of Potential 1-eV Bandgap Semiconductor Compounds AnGeAs2 and Zn3As2 Grown by MOVPE*, 2001 NCPV Program Review Meeting, Lakewood, Colorado, 2001; Lakewood, Colorado.
276. Engelbrecht, J. A. A.; Scriven, G. J.; Neethling, J. H.; Wagener, M. C. *Journal of Crystal Growth* **2000,** 216, (1-4), 235-244.
277. Burgess, T.; Caroff, P.; Wang, Y.; Badada, B. H.; Jackson, H. E.; Smith, L. M.; Guo, Y.; Tan, H. H.; Jagadish, C. *Nano Lett* **2015,** 15, (1), 378-85.
278. Green, M.; O'Brien, P. *Chemistry of Materials* **2001,** 13, (12), 4500-4505.
279. Venkatasubramanian, R.; Watko, E.; Colpitts, T. In *Thermoelectric properties of ZnSb films grown by MOCVD*, MRS Proceedings, 1997; Cambridge Univ Press: p 145.
280. Suda, T.; Kakishita, K. *J Appl Phys* **1992,** 71, (6), 3039.
281. Kakishita, K.; Aihara, K.; Suda, T. *Solar Energy Materials and Solar Cells* **1994,** 35, 333-340.

282. Kakishita, K.; Ikeda, S.; Suda, T. *Journal of Crystal Growth* **1991,** 115, (1-4), 793-797.
283. Kakishita, K.; Baba, T.; Suda, T. *Thin Solid Films* **1998,** 334, (1-2), 25-29.
284. Suda, T.; Nishimoto, T.; Kurita, S. *Journal of Crystal Growth* **1988,** 86, (1), 430-435.
285. Hermann, A. M.; Madan, A.; Wanlass, M. W.; Badri, V.; Ahrenkiel, R.; Morrison, S.; Gonzalez, C. *Solar Energy Materials and Solar Cells* **2004,** 82, (1–2), 241-252.
286. Vazquez-Mena, O.; Bosco, J. P.; Ergen, O.; Rasool, H. I.; Fathalizadeh, A.; Tosun, M.; Crommie, M.; Javey, A.; Atwater, H. A.; Zettl, A. *Nano Lett* **2014,** 14, (8), 4280-5.
287. Bosco, J. P.; Scanlon, D. O.; Watson, G. W.; Lewis, N. S.; Atwater, H. A. *J Appl Phys* **2013,** 113, (20), 203705.
288. Wadia, C.; Alivisatos, A. P.; Kammen, D. M. *Environmental Science & Technology* **2009,** 43, (6), 2072-2077.
289. Bhushan, M. *Appl Phys Lett* **1982,** 40, (1), 51-53.
290. Bhushan, M.; Catalano, A. *Appl Phys Lett* **1981,** 38, (1), 39-41.
291. Liu, Z. K.; Jiang, J.; Zhou, B.; Wang, Z. J.; Zhang, Y.; Weng, H. M.; Prabhakaran, D.; Mo, S. K.; Peng, H.; Dudin, P.; Kim, T.; Hoesch, M.; Fang, Z.; Dai, X.; Shen, Z. X.; Feng, D. L.; Hussain, Z.; Chen, Y. L. *Nat Mater* **2014,** 13, (7), 677-681.
292. Li, C. Z.; Wang, L. X.; Liu, H.; Wang, J.; Liao, Z. M.; Yu, D. P. *Nat Commun* **2015,** 6, 10137.
293. Neupane, M.; Xu, S. Y.; Sankar, R.; Alidoust, N.; Bian, G.; Liu, C.; Belopolski, I.; Chang, T. R.; Jeng, H. T.; Lin, H.; Bansil, A.; Chou, F.; Hasan, M. Z. *Nat Commun* **2014,** 5, 3786.
294. Pearson, W. B. *Acta Crystallographica* **1964,** 17, (1), 1-15.
295. Benson, D.; Sankey, O. F.; Häussermann, U. *Physical Review B* **2011,** 84, (12), 125211.
296. Mikhaylushkin, A. S.; Nylén, J.; Häussermann, U. *Chemistry – A European Journal* **2005,** 11, (17), 4912-4920.
297. Eklof, D.; Fischer, A.; Wu, Y.; Scheidt, E. W.; Scherer, W.; Haussermann, U. *Journal of Materials Chemistry A* **2013,** 1, (4), 1407-1414.
298. Partin, D. E.; Williams, D. J.; O'Keeffe, M. *Journal of Solid State Chemistry* **1997,** 132, (1), 56-59.
299. Yoo, S.-H.; Walsh, A.; Scanlon, D. O.; Soon, A. *RSC Advances* **2014,** 4, (7), 3306-3311.
300. Toyoura, K.; Tsujimura, H.; Goto, T.; Hachiya, K.; Hagiwara, R.; Ito, Y. *Thin Solid Films* **2005,** 492, (1–2), 88-92.
301. Zong, F.; Ma, H.; Du, W.; Ma, J.; Zhang, X.; Xiao, H.; Ji, F.; Xue, C. *Appl Surf Sci* **2006,** 252, (22), 7983-7986.
302. Kuriyama, K.; Takahashi, Y.; Sunohara, F. *Physical Review B* **1993,** 48, (4), 2781-2782.
303. Futsuhara, M.; Yoshioka, K.; Takai, O. *Thin Solid Films* **1998,** 322, (1–2), 274-281.
304. Zong, F.; Ma, H.; Ma, J.; Du, W.; Zhang, X.; Xiao, H.; Ji, F.; Xue, C. *Appl Phys Lett* **2005,** 87, (23), 233104.
305. Munoz, V.; Decroix, D.; Chevy, A.; Besson, J. M. *J Appl Phys* **1986,** 60, (9), 3282.
306. Pawlikowski, J. M.; Misiewicz, J.; Mirowska, N. *J Phys Chem Solids* **1979,** 40, (12), 1027-1033.
307. Pawlikowski, J. M. *Physical Review B* **1982,** 26, (8), 4711-4713.
308. Botha, J. R.; Scriven, G. J.; Engelbrecht, J. A. A.; Leitch, A. W. R. *J Appl Phys* **1999,** 86, (10), 5614-5618.
309. Roddaro, S.; Kristian, N.; Gvidas, A.; Lars, S.; Lars-Erik, W.; Olov, K.; Andreas, W. *Appl Phys Lett* **2008,** 92, (25), 253509.
310. Szatkowski, J.; Sierański, K. *J Phys Chem Solids* **1990,** 51, (3), 249-251.
311. Demers, S.; van de Walle, A. *Physical Review B* **2012,** 85, (19), 195208.
312. Nayar, P. S.; Catalano, A. *Appl Phys Lett* **1981,** 39, (1), 105-107.
313. Bosco, J. P.; Demers, S. B.; Kimball, G. M.; Lewis, N. S.; Atwater, H. A. *J Appl Phys* **2012,** 112, (9), 093703.
314. Chelluri, B.; Chang, T. Y.; Ourmazd, A.; Dayem, A. H.; Zyskind, J. L.; Srivastava, A. *Journal of Crystal Growth* **1987,** 81, (1–4), 530-535.
315. Neethling, J. H.; Scriven, G. J.; Krekels, T. *J Mater Sci* **2001,** 36, (16), 3997-4002.
316. Chang, T. Y.; Zyskind, J. L.; Dayem, A. H.; Ferguson, J. F.; Sulhoff, J. W.; Westerwick, E. H. *Journal of Crystal Growth* **1990,** 104, (2), 463-466.
317. Nagarajan, M.; Sudhakar, S.; Lourdudoss, S.; Baskar, K. *Journal of Crystal Growth* **2011,** 314, (1), 119-122.
318. Sudhakar, S.; Ganesh, V.; Indra, S.; Pawan, K. K.; Baskar, K. *Journal of Physics D: Applied Physics* **2007,** 40, (17), 5071.
319. Sudhakar, S.; Baskar, K. *Journal of Crystal Growth* **2009,** 311, (3), 798-801.
320. Jeon, S.; Bosco, J. P.; Wilson, S. S.; Rozeveld, S. J.; Kim, H.; Atwater, H. A. *The Journal of Physical Chemistry C* **2014,** 118, (24), 12717-12726.

321. Bosco, J. P.; Kimball, G. M.; Lewis, N. S.; Atwater, H. A. *Journal of Crystal Growth* **2013,** 363, (0), 205-210.
322. Suda, T.; Kakishita, K.; Sato, H.; Sasaki, K. *Appl Phys Lett* **1996,** 69, (16), 2426-2428.
323. Park, M. H.; Wang, L. C.; Cheng, J. Y.; Deng, F.; Lau, S. S.; Palmstro/m, C. J. *Appl Phys Lett* **1996,** 68, (7), 952-954.
324. Hwang, D. M.; Schwarz, S. A.; Mei, P.; Bhat, R.; Venkatesan, T.; Nazar, L.; Schwartz, C. L. *Appl Phys Lett* **1989,** 54, (12), 1160-1162.
325. Chen, G.; Liu, Z.; Liang, B.; Yu, G.; Xie, Z.; Huang, H.; Liu, B.; Wang, X.; Chen, D.; Zhu, M.-Q.; Shen, G. *Adv Funct Mater* **2013,** 23, (21), 2681-2690.
326. Shen, G.; Bando, Y.; Golberg, D. *The Journal of Physical Chemistry C* **2007,** 111, (13), 5044-5049.
327. Shen, G.; Bando, Y.; Ye, C.; Yuan, X.; Sekiguchi, T.; Golberg, D. *Angew Chem Int Ed Engl* **2006,** 45, (45), 7568-72.
328. Lance, B.; Venkata, V.; Sreeram, V. *Nanotechnology* **2014,** 25, (12), 125402.
329. Yu, G.; Liang, B.; Huang, H.; Chen, G.; Liu, Z.; Chen, D.; Shen, G. *Nanotechnology* **2013,** 24, (9), 095703.
330. Luber, E. J.; Mobarok, M. H.; Buriak, J. M. *ACS Nano* **2013,** 7, (9), 8136-8146.
331. Wu, P.; Sun, T.; Dai, Y.; Sun, Y.; Ye, Y.; Dai, L. *Cryst Growth Des* **2011,** 11, (5), 1417-1421.
332. Wu, P.; Dai, Y.; Ye, Y.; Yin, Y.; Dai, L. *J Mater Chem* **2011,** 21, (8), 2563-2567.
333. Sun, T.; Wu, P. C.; Guo, Z. D.; Dai, Y.; Meng, H.; Fang, X. L.; Shi, Z. J.; Dai, L.; Qin, G. G. *Phys Lett A* **2011,** 375, (21), 2118-2121.
334. Bae, I.-T.; Vasekar, P.; VanHart, D.; Dhakal, T. *J Mater Res* **2011,** 26, (12), 1464-1467.
335. Shen, G.; Chen, P.-C.; Bando, Y.; Golberg, D.; Zhou, C. *Chemistry of Materials* **2008,** 20, (23), 7319-7323.
336. Shen, G.; Chen, P. C.; Bando, Y.; Golberg, D.; Zhou, C. *J Phys Chem C* **2008,** 112, (42), 16405-16410.
337. Yang, R.; Chueh, Y. L.; Morber, J. R.; Snyder, R.; Chou, L. J.; Wang, Z. L. *Nano Lett* **2007,** 7, (2), 269-75.
338. Shen, G.; Ye, C.; Golberg, D.; Hu, J.; Bando, Y. *Appl Phys Lett* **2007,** 90, (7), 073115.
339. Shen, G.; Bando, Y.; Golberg, D. *J Phys Chem C* **2007,** 111, (13), 5044-5049.
340. Shen, G. Z.; Bando, Y.; Hu, J. Q.; Golberg, D. *Appl Phys Lett* **2006,** 88, (14), 143105.
341. Brockway, L.; Van Laer, M.; Kang, Y.; Vaddiraju, S. *Physical Chemistry Chemical Physics* **2013,** 15, (17), 6260-6267.
342. Omari, M.; Kouklin, N.; Lu, G.; Chen, J.; Gajdardziska-Josifovska, M. *Nanotechnology* **2008,** 19, (10), 105301.
343. Schönherr, P.; Hesjedal, T. *Appl Phys Lett* **2015,** 106, (1), 013115.
344. Omari, M.; Kouklin, N.; Lu, G.; Chen, J.; Gajdardziska-Josifovska, M. *Nanotechnology* **2008,** 19, (10), 105301.
345. Pan, H.; Zhang, K.; Wei, Z.; Zhao, B.; Wang, J.; Gao, M.; Pi, L.; Han, M.; Song, F.; Wang, X.; Wang, B.; Zhang, R. *Appl Phys Lett* **2016,** 108, (18), 183103.
346. Zhong, M.; Meng, X.; Li, J. *Appl Surf Sci* **2015,** 332, (0), 76-79.
347. Xu, J.; Wu, H.; Wang, F.; Xia, Y.; Zheng, G. *Advanced Energy Materials* **2013,** 3, (3), 286-289.
348. Lance, B.; Venkata, V.; Hasti, A.-A.; Reza, S.-Y.; Sreeram, V. *Nanotechnology* **2014,** 25, (14), 145401.
349. Birkel, C. S.; Mugnaioli, E.; Gorelik, T.; Kolb, U.; Panthöfer, M.; Tremel, W. *Journal of the American Chemical Society* **2010,** 132, (28), 9881-9889.
350. Smetana, J. *IEEE Transactions on Electronics Packaging Manufacturing* **2007,** 30, (1), 11-22.
351. Van De Ven, J.; Weyher, J.; Ikink, H.; Giling, L. *J Electrochem Soc* **1987,** 134, (4), 989-997.
352. McAleer, W.; Barkemeyer, H.; Pollak, P. *J Electrochem Soc* **1961,** 108, (12), 1168-1169.
353. Monchamp, R. R.; McAleer, W. J.; Pollak, P. I. *J Electrochem Soc* **1962,** 109, (11), 1108-1109.
354. Wagner, R. S.; Ellis, W. C. *Appl Phys Lett* **1964,** 4, (5), 89-90.
355. Wagner, R. S.; Ellis, W. C.; Jackson, K. A.; Arnold, S. M. *J Appl Phys* **1964,** 35, (10), 2993-3000.
356. Wagner, R. S.; Doherty, C. J. *J Electrochem Soc* **1966,** 113, (12), 1300-1305.
357. Komatsu, E.; Higuchi, Y.; Niina, T. *Appl Phys Lett* **1967,** 10, (2), 42-43.
358. Wagner, R. S. *J Appl Phys* **1967,** 38, (4), 1554-1560.
359. Wagner, R. S.; Doherty, C. J. *J Electrochem Soc* **1968,** 115, (1), 93-99.
360. Barns, R. L.; Ellis, W. C. *J Appl Phys* **1965,** 36, (7), 2296-2301.
361. Givargizov, E. *Journal of Crystal Growth* **1971,** 9, 326-329.
362. Givargizov, E. I.; Sheftal, N. N. *Kristall und Technik* **1972,** 7, (1-3), 37-41.

363. Givargizov, E. I. *Journal of Crystal Growth* **1973,** 20, (3), 217-226.
364. Givargizov, E., Growth of Whisker-and Plate-like Crystals from Vapour. Nauka, Moscow: 1977.
365. Givargizov, E.; Kostyuk, Y. G., Controlled Growth of Oriented Systems of Whisker Crystals. In *Growth of Crystals*, Springer: 1975; pp 276-283.
366. Givargizov, E. I. *Kristall und Technik* **1975,** 10, (5), 473-484.
367. Givargizov, E. I. *Journal of Crystal Growth* **1975,** 31, (Dec), 20-30.
368. Dubrovskii, V. G. *Technical Physics Letters* **2013,** 39, (2), 157-160.
369. Yazawa, M.; Koguchi, M.; Hiruma, K. *Appl Phys Lett* **1991,** 58, (10), 1080-1082.
370. Haraguchi, K.; Katsuyama, T.; Hiruma, K.; Ogawa, K. *Appl Phys Lett* **1992,** 60, (6), 745-747.
371. Hiruma, K.; Yazawa, M.; Haraguchi, K.; Ogawa, K.; Katsuyama, T.; Koguchi, M.; Kakibayashi, H. *J Appl Phys* **1993,** 74, (5), 3162-3171.
372. Hiruma, K.; Yazawa, M.; Katsuyama, T.; Ogawa, K.; Haraguchi, K.; Koguchi, M.; Kakibayashi, H. *J Appl Phys* **1995,** 77, (2), 447-462.
373. Hiruma, K.; Murakoshi, H.; Yazawa, M.; Katsuyama, T. *Journal of Crystal Growth* **1996,** 163, (3), 226-231.
374. Shimada, T.; Hiruma, K.; Shirai, M.; Yazawa, M.; Haraguchi, K.; Sato, T.; Matsui, M.; Katsuyama, T. *Superlattices & Microstructures* **1998,** 24, (6), 453-458.
375. Morales, A. M.; Lieber, C. M. *Science* **1998,** 279, (5348), 208-211.
376. Hu, J. T.; Min, O. Y.; Yang, P. D.; Lieber, C. M. *Nature* **1999,** 399, (6731), 48-51.
377. Cui, Y.; Lieber, C. M. *Science* **2001,** 291, (5505), 851-853.
378. Duan, X. F.; Lieber, C. M. *Advanced Materials* **2000,** 12, (4), 298-302.
379. Ohlsson, B. J.; Bjork, M. T.; Magnusson, M. H.; Deppert, K.; Samuelson, L.; Wallenberg, L. R. *Appl Phys Lett* **2001,** 79, (20), 3335-3337.
380. Bjork, M. T.; Ohlsson, B. J.; Sass, T.; Persson, A. I.; Thelander, C.; Magnusson, M. H.; Deppert, K.; Wallenberg, L. R.; Samuelson, L. *Appl Phys Lett* **2002,** 80, (6), 1058-1060.
381. Ohlsson, B. J.; Bjork, M. T.; Persson, A. I.; Thelander, C.; Wallenberg, L. R.; Magnusson, M. H.; Deppert, K.; Samuelson, L. *Physica A* **2002,** 13, (2-4), 1126-1130.
382. Bakkers, E.; Verheijen, M. A. *Journal of the American Chemical Society* **2003,** 125, (12), 3440-3441.
383. De Franceschi, S.; van Dam, J. A.; Bakkers, E.; Feiner, L. F.; Gurevich, L.; Kouwenhoven, L. P. *Appl Phys Lett* **2003,** 83, (2), 344-346.
384. Bakkers, E.; Van Dam, J. A.; De Franceschi, S.; Kouwenhoven, L. P.; Kaiser, M.; Verheijen, M.; Wondergem, H.; Van der Sluis, P. *Nature Materials* **2004,** 3, (11), 769-773.
385. Schwalbach, E. J.; Voorhees, P. W. *Appl Phys Lett* **2009,** 95, (6), 063105-3.
386. Dubrovskii, V. G. *Cryst Growth Des* **2015,** 15, (12), 5738-5743.
387. Moutanabbir, O.; Isheim, D.; Blumtritt, H.; Senz, S.; Pippel, E.; Seidman, D. N. *Nature* **2013,** 496, (7443), 78-82.
388. Durgun, E.; Akman, N.; Ataca, C.; Ciraci, S. *Physical Review B* **2007,** 76, (24), 245323.
389. Fernandez-Serra, M. V.; Adessi, C.; Blase, X. *Nano Letters* **2006,** 6, (12), 2674-2678.
390. Leao, C. R.; Fazzio, A.; da Silva, A. J. R. *Nano Letters* **2008,** 8, (7), 1866-1871.
391. Kim, S.; Park, J.-S.; Chang, K. J. *Nano Letters* **2012,** 12, (10), 5068-5073.
392. Wu, F.; Kan, E.; Wu, X. *Nanoscale* **2011,** 3, (9), 3620-3622.
393. Ng, M.-F.; Sullivan, M. B.; Tong, S. W.; Wu, P. *Nano Letters* **2011,** 11, (11), 4794-4799.
394. Han, J.; Chan, T.-L.; Chelikowsky, J. R. *Physical Review B* **2010,** 82, (15), 153413.
395. Petretto, G.; Debernardi, A.; Fanciulli, M. *Nano Lett* **2011,** 11, (11), 4509-14.
396. Yixi, Z.; Xi, Z.; Xin, L.; Gang, X. *Semiconductor Science and Technology* **2014,** 29, (7), 075023.
397. Peelaers, H.; Partoens, B.; Peeters, F. M. *Appl Phys Lett* **2007,** 90, (26), 63103.
398. Ghaderi, N.; Peressi, M.; Binggeli, N.; Akbarzadeh, H. *Physical Review B* **2010,** 81, (15), 155311.
399. Galicka, M.; Buczko, R.; Kacman, P. *The Journal of Physical Chemistry C* **2013,** 117, (39), 20361-20370.
400. Shu, H.; Yang, X.; Liang, P.; Cao, D.; Chen, X. *The Journal of Physical Chemistry C* **2016,** 120, (38), 22088-22095.
401. Song, C.; Wang, J.; Zhang, Z.; Mao, H.; Zhao, Q.; Yang, P.; Xing, H. *The Journal of Physical Chemistry C* **2014,** 118, (43), 25209-25214.
402. Cui, J.-g.; Zhang, X.; Huang, Y.-q.; Ren, X.-m. *Chinese Journal of Chemical Physics* **2014,** 27, (6), 685-689.
403. Besteiro, L. V.; Tortajada, L.; Souto, J.; Gallego, L. J.; Chelikowsky, J. R.; Alemany, M. M. G. *Physical Review B* **2013,** 88, (11), 115310.

404. Jiang, Q. G.; Wen, Z.; Jiang, Q. *Solid State Commun* **2012,** 152, (23), 2120-2122.
405. Shu, H.; Chen, X.; Ding, Z.; Dong, R.; Lu, W. *Journal of Physical Chemistry C* **2011,** 115, (30), 14449-14454.
406. dos Santos, C., L.; Schmidt, T. M.; Piquini, P. *Nanotechnology* **2011,** 22, (26), 265203.
407. Wang, H.; Zepeda-Ruiz, L. A.; Gilmer, G. H.; Upmanyu, M. *Nat Commun* **2013,** 4, 1956.
408. Hong, K. H.; Kim, J.; Lee, J. H.; Shin, J.; Chung, U. I. *Nano Letters* **2010,** 10, (5), 1671-1676.
409. Moon, C. Y.; Lee, W. J.; Chang, K. J. *Nano Lett* **2008,** 8, (10), 3086-91.
410. Rosini, M.; Magri, R. *ACS Nano* **2010,** 4, (10), 6021-31.
411. Chan, T.-L.; Zhang, S. B.; Chelikowsky, J. R. *Appl Phys Lett* **2011,** 98, (13), 133116.
412. Koren, E.; Hyun, J. K.; Givan, U.; Hemesath, E. R.; Lauhon, L. J.; Rosenwaks, Y. *Nano Lett.* **2011,** 11, (1), 183-7.
413. Garnett, E. C.; Tseng, Y.-C.; Khanal, D. R.; Wu, J.; Bokor, J.; Yang, P. *Nat Nanotechnol* **2009,** 4, (5), 311-314.
414. Yoon, J.; Girgis, A. M.; Shalish, I.; Ram-Mohan, L. R.; Narayanamurti, V. *Appl Phys Lett* **2009,** 94, (14), 142102.
415. Bjork, M. T.; Schmid, H.; Knoch, J.; Riel, H.; Riess, W. *Nat Nanotechnol* **2009,** 4, (2), 103-7.
416. Bryant, G. W. *Physical Review B* **1984,** 29, (12), 6632-6639.
417. Gold, A.; Ghazali, A. *Physical Review B* **1990,** 41, (11), 7626.
418. Osorio, F. A. P.; Degani, M. H.; Hipolito, O. *Physical Review B* **1988,** 37, (3), 1402-1405.
419. Rurali, R.; Aradi, B.; Frauenheim, T.; Gali, A. *Physical Review B (Condensed Matter and Materials Physics)* **2009,** 79, (11), 115303.
420. Rurali, R.; Palummo, M.; Cartoixà, X. *Physical Review B* **2010,** 81, (23), 235304.
421. Chan, T.-L.; Zhang, S. B.; Chelikowsky, J. R. *Physical Review B* **2011,** 83, (24), 245440.
422. Petretto, G.; Debernardi, A.; Fanciulli, M. *Nano Letters* **2013,** 13, (10), 4963-4968.
423. Durgun, E.; Bilc, D. I.; Ciraci, S.; Ghosez, P. *The Journal of Physical Chemistry C* **2012,** 116, (29), 15713-15722.
424. Lee, A. J.; Chan, T.-L.; Chelikowsky, J. R. *Physical Review B* **2014,** 89, (7), 075419.
425. Niquet, Y. M.; Genovese, L.; Delerue, C.; Deutsch, T. *Physical Review B* **2010,** 81, (16), 161301.
426. Niquet, Y. M.; Lherbier, A.; Quang, N. H.; Fernandez-Serra, M. V.; Blase, X.; Delerue, C. *Physical Review B* **2006,** 7316, (16), 5319.
427. Diarra, M.; Niquet, Y. M.; Delerue, C.; Allan, G. *Physical Review B* **2007,** 75, (4), 5301.
428. Corfdir, P.; Lefebvre, P. *J Appl Phys* **2012,** 112, (10), 106104.
429. Yan, B.; Frauenheim, T.; Gali, A. *Nano Lett* **2010,** 10, (9), 3791-5.
430. Oh, J. H.; Lee, S.-H.; Shin, M. *J Appl Phys* **2013,** 113, (23), 233706.
431. Guo, C.-S.; Luo, L.-B.; Yuan, G.-D.; Yang, X.-B.; Zhang, R.-Q.; Zhang, W.-J.; Lee, S.-T. *Angewandte Chemie International Edition* **2009,** 48, (52), 9896-9900.
432. Miranda-Duran, A.; Cartoixa, X.; Cruz Irisson, M.; Rurali, R. *Nano Lett* **2010,** 10, (9), 3590-5.
433. Shu, H.; Cao, D.; Liang, P.; Jin, S.; Chen, X.; Lu, W. *The Journal of Physical Chemistry C* **2012,** 116, (33), 17928-17933.
434. Xu, H.; Yang, X. B.; Zhang, C.; Lu, A. J.; Zhang, R. Q. *Appl Phys Lett* **2011,** 98, (7), 073115-3.
435. Blase, X.; Fernández-Serra, M. V. *Phys Rev Lett* **2008,** 100, (4), 046802.
436. Amato, G.; Cultrera, A.; Boarino, L.; Lamberti, C.; Bordiga, S.; Mercuri, F.; Cartoixà, X.; Rurali, R. *J Appl Phys* **2013,** 114, (20), 204302.
437. Luo, L. B.; Yang, X. B.; Liang, F. X.; Jie, J. S.; Wu, C. Y.; Wang, L.; Yu, Y. Q.; Zhu, Z. F. *The Journal of Physical Chemistry C* **2011,** 115, (49), 24293-24299.
438. Rurali, R. *Reviews of Modern Physics* **2010,** 82, (1), 427-449.
439. Markussen, T.; Rurali, R.; Cartoixà, X.; Jauho, A.-P.; Brandbyge, M. *Physical Review B* **2010,** 81, (12), 125307.
440. Markussen, T.; Rurali, R.; Jauho, A.-P.; Brandbyge, M. *Journal of Computational Electronics* **2008,** 7, (3), 324-327.
441. Persson, M. P.; Mera, H.; Niquet, Y.-M.; Delerue, C.; Diarra, M. *Physical Review B* **2010,** 82, (11).
442. Georgiev, V. P.; Towie, E. A.; Asenov, A. *Electron Devices, IEEE Transactions on* **2013,** 60, (3), 965-971.
443. Niquet, Y.-M.; Mera, H.; Delerue, C. *Appl Phys Lett* **2012,** 100, (15), 153119.
444. Wang, Y. F.; Lew, K. K.; Ho, T. T.; Pan, L.; Novak, S. W.; Dickey, E. C.; Redwing, J. M.; Mayer, T. S. *Nano Letters* **2005,** 5, (11), 2139-2143.
445. Schmid, H.; BjoÌˆrk, M. T.; Knoch, J.; Karg, S.; Riel, H.; Riess, W. *Nano Letters* **2009,** 9, (1), 173-177.

446. Zheng, G. F.; Lu, W.; Jin, S.; Lieber, C. M. *Advanced Materials* **2004,** 16, (21), 1890-1893.
447. Yang, C.; Zhong, Z. H.; Lieber, C. M. *Science* **2005,** 310, (5752), 1304-1307.
448. Yang, C.; Barrelet, C. J.; Capasso, F.; Lieber, C. M. *Nano Letters* **2006,** 6, (12), 2929-2934.
449. Schmid, H.; Bjork, M. T.; Knoch, J.; Riel, H.; Riess, W.; Rice, P.; Topuria, T. *J Appl Phys* **2008,** 103, (2), 024304.
450. Celle, C.; Mouchet, C. l.; Rouvière, E.; Simonato, J.-P.; Mariolle, D.; Chevalier, N.; Brioude, A. *The Journal of Physical Chemistry C* **2009,** 114, (2), 760-765.
451. Moselund, K. E.; Bjork, M. T.; Schmid, H.; Ghoneim, H.; Karg, S.; Lortscher, E.; Riess, W.; Riel, H. *Electron Devices, IEEE Transactions on* **2011,** 58, (9), 2911-2916.
452. Tian, B. Z.; Xie, P.; Kempa, T. J.; Bell, D. C.; Lieber, C. M. *Nat Nanotechnol* **2009,** 4, (12), 824-829.
453. Koo, T. W.; Kim, D. S.; Lee, J.-H.; Jung, Y. C.; Lee, J.-W.; Yu, Y. S.; Hwang, S. W.; Whang, D. *The Journal of Physical Chemistry C* **2011,** 115, (47), 23552-23557.
454. Fabbri, F.; Rotunno, E.; Lazzarini, L.; Cavalcoli, D.; Castaldini, A.; Fukata, N.; Sato, K.; Salviati, G.; Cavallini, A. *Nano Letters* **2013,** 13, (12), 5900-5906.
455. Allen, J. E.; Daniel E. Perea; Eric R. Hemesath; Lincoln J. Lauhon. *Advanced Materials* **2009,** 21, (30), 3067-3072.
456. Amit, I.; Givan, U.; Connell, J. G.; Paul, D. F.; Hammond, J. S.; Lauhon, L. J.; Rosenwaks, Y. *Nano Letters* **2013,** 13, (6), 2598-2604.
457. Nimmatoori, P.; Zhang, Q.; Dickey, E. C.; Redwing, J. M. *Nanotechnology* **2009,** 20, (2), 025607.
458. Lohn, A. J.; Cormia, R. D.; Fryauf, D. M.; Zhang, J.; Norris, K. J.; Kobayashi, N. P. *Japanese Journal of Applied Physics* **2012,** 51, (11S), 11PE04.
459. Schmidt, V.; Riel, H.; Senz, S.; Karg, S.; Riess, W.; Gosele, U. *Sml* **2006,** 2, (1), 85-88.
460. Cui, Y.; Duan, X. F.; Hu, J. T.; Lieber, C. M. *J. Phys. Chem. B* **2000,** 104, (22), 5213-5216.
461. Lew, K. K.; Pan, L.; Bogart, T. E.; Dilts, S. M.; Dickey, E. C.; Redwing, J. M.; Wang, Y. F.; Cabassi, M.; Mayer, T. S.; Novak, S. W. *Appl Phys Lett* **2004,** 85, (15), 3101-3103.
462. Kimukin, I.; Islam, M. S.; Williams, R. S. *Nanotechnology* **2006,** 17, (11), S240-S245.
463. Whang, S. J.; Lee, S.; Chi, D. Z.; Yang, W. F.; Cho, B. J.; Liew, Y. F.; Kwong, D. L. *Nanotechnology* **2007,** 18, (27), 275302.
464. Imamura, G.; Kawashima, T.; Fujii, M.; Nishimura, C.; Saitoh, T.; Hayashi, S. *Nano Letters* **2008,** 8, (9), 2620-2624.
465. Bjork, M. T.; Knoch, J.; Schmid, H.; Riel, H.; Riess, W. *Appl Phys Lett* **2008,** 92, (19), 93504.
466. Li, F.; Nellist, P. D.; Cockayne, D. J. H. *Appl Phys Lett* **2009,** 94, (26), 263111-3.
467. Chen, W. H.; Lardé, R.; Cadel, E.; Xu, T.; Grandidier, B.; Nys, J. P.; Stiévenard, D.; Pareige, P. *physica status solidi (c)* **2011,** 8, (3), 771-774.
468. Chen, W.; Dubrovskii, V. G.; Liu, X.; Xu, T.; Lardé, R.; Philippe Nys, J.; Grandidier, B.; Stiévenard, D.; Patriarche, G.; Pareige, P. *J Appl Phys* **2012,** 111, (9), 094909.
469. Vallett, A. L.; Minassian, S.; Kaszuba, P.; Datta, S.; Redwing, J. M.; Mayer, T. S. *Nano Lett* **2010,** 10, (12), 4813-8.
470. Goldberger, J.; Hochbaum, A. I.; Fan, R.; Yang, P. D. *Nano Letters* **2006,** 6, (5), 973-977.
471. He, R.; Yang, P. *Nat Nanotechnol* **2006,** 1, (1), 42-46.
472. Dávila, D.; Tarancón, A.; Fernández-Regúlez, M.; Calaza, C.; Salleras, M.; Paulo, A. S.; Fonseca, L. *Journal of Micromechanics and Microengineering* **2011,** 21, (10), 104007.
473. Lew, K. K.; Pan, L.; Dickey, E. C.; Redwing, J. M. *J Mater Res* **2006,** 21, (11), 2876-2881.
474. Ke, Y.; Weng, X. J.; Redwing, J. M.; Eichfeld, C. M.; Swisher, T. R.; Mohney, S. E.; Habib, Y. M. *Nano Letters* **2009,** 9, (12), 4494-4499.
475. Choi, S.-Y.; Fung, W. Y.; Lu, W. *Appl Phys Lett* **2011,** 98, (3), 033108-3.
476. Wacaser, B. A.; Reuter, M. C.; Khayyat, M. M.; Wen, C. Y.; Haight, R.; Guha, S.; Ross, F. M. *Nano Lett* **2009,** 9, (9), 3296-301.
477. Oehler, F.; Gentile, P.; Baron, T.; Hertog, M. D.; Rouviere, J.; Ferret, P. *Nanotechnology* **2009,** 20, (24), 245602.
478. Wang, D.; Wang, Q.; Javey, A.; Tu, R.; Dai, H.; Kim, H.; McIntyre, P. C.; Krishnamohan, T.; Saraswat, K. C. *Appl Phys Lett* **2003,** 83, (12), 2432-2434.
479. Greytak, A. B.; Lauhon, L. J.; Gudiksen, M. S.; Lieber, C. M. *Appl Phys Lett* **2004,** 84, (21), 4176-4178.
480. T. Le, S.; Jannaty, P.; Zaslavsky, A.; Dayeh, S. A.; Picraux, S. T. *Appl Phys Lett* **2010,** 96, (26), 262102-3.
481. Ahn, Y. H.; Park, J. *Appl Phys Lett* **2007,** 91, (16), 162102.
482. Tutuc, E.; Chu, J. O.; Ott, J. A.; Guha, S. *Appl Phys Lett* **2006,** 89, (26), 63101.

483. Fukata, N.; Sato, K.; Mitome, M.; Bando, Y.; Sekiguchi, T.; Kirkham, M.; Hong, J.-i.; Wang, Z. L.; Snyder, R. L. *ACS Nano* **2010,** 4, (7), 3807-3816.
484. Givan, U.; Kwiat, M.; Patolsky, F. *The Journal of Physical Chemistry C* **2010,** 114, (10), 4331-4335.
485. Dayeh, S. A.; Picraux, S. T. *Nano Lett* **2010,** 10, (10), 4032-9.
486. Wang, D. W.; Chang, Y. L.; Wang, Q.; Cao, J.; Farmer, D. B.; Gordon, R. G.; Dai, H. J. *Journal of the American Chemical Society* **2004,** 126, (37), 11602-11611.
487. Tutuc, E.; Appenzeller, J.; Reuter, M. C.; Guha, S. *Nano Letters* **2006,** 6, (9), 2070-2074.
488. Zhang, S.; Hemesath, E. R.; Perea, D. E.; Wijaya, E.; Lensch-Falk, J. L.; Lauhon, L. J. *Nano Lett* **2009,** 9, (9), 3268-74.
489. Wang, D.; Dai, H. *Appl. Phys. A* **2006,** 85, (3), 217-225.
490. Wallentin, J.; Ek, M.; Wallenberg, L. R.; Samuelson, L.; Borgström, M. T. *Nano Lett.* **2011,** 12, (1), 151-155.
491. Tuin, G.; Borgström, M.; Trägårdh, J.; Ek, M.; Wallenberg, L. R.; Samuelson, L.; Pistol, M.-E. *Nano Res* **2011,** 4, (2), 159-163.
492. Kriegner, D.; Wintersberger, E.; Kawaguchi, K.; Wallentin, J.; Borgström, M. T.; Stangl, J. *Nanotechnology* **2011,** 22, (42), 425704.
493. Mergenthaler, K.; Iqbal, A.; Wallentin, J.; Lehmann, S.; Borgström, M.; Samuelson, L.; Yartsev, A.; Pistol, M.-E. *Nano Res* **2013,** 6, (10), 752-757.
494. Azhar, I.; Jason, P. B.; Nicklas, A.; Mats-Erik, P.; Lars, S.; Magnus, T. B.; Arkady, Y. *Nanotechnology* **2013,** 24, (11), 115706.
495. Storm, K.; Halvardsson, F.; Heurlin, M.; Lindgren, D.; Gustafsson, A.; Wu, P. M.; Monemar, B.; Samuelson, L. *Nat Nano* **2012,** 7, (11), 718-722.
496. Jain, V.; Nowzari, A.; Wallentin, J.; Borgström, M.; Messing, M.; Asoli, D.; Graczyk, M.; Witzigmann, B.; Capasso, F.; Samuelson, L.; Pettersson, H. *Nano Res* **2014,** 7, (4), 1-9.
497. Hjort, M.; Wallentin, J.; Timm, R.; Zakharov, A. A.; Håkanson, U.; Andersen, J. N.; Lundgren, E.; Samuelson, L.; Borgström, M. T.; Mikkelsen, A. *ACS Nano* **2012,** 6, (11), 9679-9689.
498. Rigutti, L.; Bugallo, A. D.; Tchernycheva, M.; Jacopin, G.; Julien, F. H.; Cirlin, G.; Patriarche, G.; Lucot, D.; Travers, L.; Harmand, J. C. *Journal of Nanomaterials* **2009**, 35451.
499. Duan, X. F.; Huang, Y.; Cui, Y.; Wang, J. F.; Lieber, C. M. *Nature* **2001,** 409, (6816), 66-69.
500. De Franceschi, S.; van Dam, J. A.; Bakkers, E. P. A. M.; Feiner, L. F.; Gurevich, L.; Kouwenhoven, L. P. *Appl. Phys. Lett.* **2003,** 83, (2), 344-346.
501. van Weert, M. H. M.; Wunnicke, O.; Roest, A. L.; Eijkemans, T. J.; Yu Silov, A.; Haverkort, J. E. M.; t Hooft, G. W.; Bakkers, E. *Appl Phys Lett* **2006,** 88, (4), 043109.
502. Liu, C.; Dai, L.; You, L. P.; Xu, W. J.; Qin, G. G. *Nanotechnology* **2008,** 19, (46), 465203.
503. Wallentin, J.; Wickert, P.; Ek, M.; Gustafsson, A.; Reine Wallenberg, L.; Magnusson, M. H.; Samuelson, L.; Deppert, K.; Borgström, M. T. *Appl Phys Lett* **2011,** 99, (25), 253105.
504. Borgstrom, M. T.; Wallentin, J.; Heurlin, M.; Falt, S.; Wickert, P.; Leene, J.; Magnusson, M. H.; Deppert, K.; Samuelson, L. *Selected Topics in Quantum Electronics, IEEE Journal of* **2010,** 17, (4), 1050.
505. Cavalli, A.; Wang, J.; Esmaeil Zadeh, I.; Reimer, M. E.; Verheijen, M. A.; Soini, M.; Plissard, S. R.; Zwiller, V.; Haverkort, J. E.; Bakkers, E. P. *Nano Lett* **2016,** 16, (5), 3071-7.
506. Yee, R. J.; Gibson, S. J.; Dubrovskii, V. G.; LaPierre, R. R. *Appl Phys Lett* **2012,** 101, (26), 263106.
507. Tajik, N.; Haapamaki, C. M.; LaPierre, R. R. *Nanotechnology* **2012,** 23, (31), 315703.
508. Bertness, K. A.; Kendelewicz, T.; List, R. S.; Williams, M. D.; Lindau, I.; Spicer, W. E. *Journal of Vacuum Science & Technology A* **1986,** 4, (3), 1424-1426.
509. Hjort, M.; Wallentin, J.; Timm, R.; Zakharov, A. A.; Andersen, J. N.; Samuelson, L.; Borgström, M. T.; Mikkelsen, A. *Appl Phys Lett* **2011,** 99, (23), 233113.
510. Storm, K.; Nylund, G.; Borgstrom, M.; Wallentin, J.; Fasth, C.; Thelander, C.; Samuelson, L. *Nano Lett* **2011,** 11, (3), 1127-30.
511. Zhang, W.; Lehmann, S.; Mergenthaler, K.; Wallentin, J.; Borgström, M. T.; Pistol, M.-E.; Yartsev, A. *Nano Letters* **2015,** 15, (11), 7238-7244.
512. Heurlin, M.; Hultin, O.; Storm, K.; Lindgren, D.; Borgström, M. T.; Samuelson, L. *Nano Letters* **2014,** 14, (2), 749-753.
513. Cavalli, A.; Cui, Y.; Kolling, S.; Verheijen, M. A.; Plissard, S. R.; Wang, J.; Koenraad, P. M.; Haverkort, J. E.; Bakkers, E. P. *Nanotechnology* **2016,** 27, (45), 454003.
514. Yi, S. S.; Girolami, G.; Amano, J.; Islam, M. S.; Sharma, S.; Kamins, T. I.; Kimukin, I. *Appl Phys Lett* **2006,** 89, (13), 33121.

515. Vu, T. T. T.; Tilman, Z.; Verheijen, M. A.; Plissard, S. R.; Immink, G. W. G.; Haverkort, J. E. M.; Bakkers, E. P. A. M. *Nanotechnology* **2013,** 24, (11), 115705.
516. Lysov, A.; Vinaji, S.; Offer, M.; Gutsche, C.; Regolin, I.; Mertin, W.; Geller, M.; Prost, W.; Bacher, G.; Tegude, F.-J. *Nano Res* **2011,** 4, (10), 987-995.
517. Sager, D.; Gutsche, C.; Prost, W.; Tegude, F.-J.; Bacher, G. *J Appl Phys* **2013,** 113, (17), 174303.
518. Sun, R.; Jacobsson, D.; Chen, I. J.; Nilsson, M.; Thelander, C.; Lehmann, S.; Dick, K. A. *Nano Lett* **2015,** 15, (6), 3757-62.
519. Gutsche, C.; Lysov, A.; Regolin, I.; Münstermann, B.; Prost, W.; Tegude, F. J. *J Electron Mater* **2012,** 41, (5), 809-812.
520. Gutsche, C.; Niepelt, R.; Gnauck, M.; Lysov, A.; Prost, W.; Ronning, C.; Tegude, F.-J. *Nano Letters* **2012,** 12, (3), 1453-1458.
521. Gutsche, C.; Lysov, A.; Braam, D.; Regolin, I.; Keller, G.; Li, Z.-A.; Geller, M.; Spasova, M.; Prost, W.; Tegude, F.-J. *Adv Funct Mater* **2012,** 22, (5), 929-936.
522. Gutsche, C.; Lysov, A.; Regolin, I.; Blekker, K.; Prost, W.; Tegude, F.-J. *Nanoscale Res Lett* **2010**, 1-6.
523. Darbandi, A.; Salehzadeh, O.; Kuyanov, P.; LaPierre, R. R.; Watkins, S. P. *J Appl Phys* **2014,** 115, (23), 234305.
524. Salehzadeh, O.; Kavanagh, K. L.; Watkins, S. P. *J Appl Phys* **2012,** 112, (5), 054324.
525. Salehzadeh, O.; Chen, M. X.; Kavanagh, K. L.; Watkins, S. P. *Appl Phys Lett* **2011,** 99, (18), 182102.
526. Caram, J.; Sandoval, C.; Tirado, M.; Comedi, D.; Czaban, J.; Thompson, D. A.; LaPierre, R. R. *Nanotechnology* **2010,** 21, (13), 34007.
527. Czaban, J. A.; Thompson, D. A.; LaPierre, R. R. *Nano Letters* **2009,** 9, (1), 148-154.
528. Ketterer, B.; Uccelli, E.; Fontcuberta i Morral, A. *Nanoscale* **2012,** 4, (5), 1789-1793.
529. Lee, H. G.; Jeon, H. C.; Kang, T. W.; Kim, T. W. *Appl Phys Lett* **2001,** 78, (21), 3319-3321.
530. Matt, D.; Alan, T.; Marta, L.-K.; Lifan, Y.; Eun Seong, M.; Sara, B.; Cristina, G.; Vanessa, S.; Jamie, P.; Joanna Mirecki, M. *Nanotechnology* **2016,** 27, (49), 495605.
531. Boland, J. L.; Casadei, A.; Tutuncuoglu, G.; Matteini, F.; Davies, C. L.; Jabeen, F.; Joyce, H. J.; Herz, L. M.; Fontcuberta, I. M. A.; Johnston, M. B. *ACS Nano* **2016,** 10, (4), 4219-27.
532. Ihn, S.-G.; Ryu, M.-Y.; Song, J.-I. *Solid State Commun* **2010,** 150, (15–16), 729-733.
533. Xia, H.; Lu, Z.-Y.; Li, T.-X.; Parkinson, P.; Liao, Z.-M.; Liu, F.-H.; Lu, W.; Hu, W.-D.; Chen, P.-P.; Xu, H.-Y.; Zou, J.; Jagadish, C. *ACS Nano* **2012**.
534. Hilse, M.; Ramsteiner, M.; Breuer, S.; Geelhaar, L.; Riechert, H. *Appl Phys Lett* **2010,** 96, (19), 193104-3.
535. Ketterer, B.; Mikheev, E.; Uccelli, E.; Fontcuberta i Morral, A. *Appl Phys Lett* **2010,** 97, (22), 223103-3.
536. Piccin, M.; Bais, G.; Grillo, V.; Jabeen, F.; De Franceschi, S.; Carlino, E.; Lazzarino, M.; Romanato, F.; Businaro, L.; Rubini, S.; Martelli, F.; Franciosi, A. *Physica E: Low-dimensional Systems and Nanostructures* **2007,** 37, (1-2), 134-137.
537. Colombo, C.; Heibeta, M.; Gratzel, M.; Morral, A. F. i. *Appl Phys Lett* **2009,** 94, (17), 173108.
538. Qu, J.; Choi, W.; Katal Mohseni, P.; Li, X.; Zhang, Y.; Chen, H.; Ringer, S.; Zheng, R. *ACS Applied Materials & Interfaces* **2016,** 8, (39), 26244-26250.
539. Yang, F.; Messing, M. E.; Mergenthaler, K.; Ghasemi, M.; Johansson, J.; Wallenberg, L. R.; Pistol, M.-E.; Deppert, K.; Samuelson, L.; Magnusson, M. H. *Journal of Crystal Growth* **2015,** 414, 181-186.
540. Haggren, T.; Kakko, J. P.; Jiang, H.; Dhaka, V.; Huhtio, T.; Lipsanen, H. In *Effects of Zn doping on GaAs nanowires*, 14th IEEE International Conference on Nanotechnology 18-21 Aug. 2014, 2014; pp 825-829.
541. Dowdy, R. S.; Zhang, C.; Mohseni, P. K.; Fortuna, S. A.; Wen, J.-G.; Coleman, J. J.; Li, X. *Optical Materials Express* **2013,** 3, (10), 1687.
542. Dowdy, R.; Mohseni, P.; Fortuna, S. A.; Jianguo, W.; Xiuling, L. In *Twinning superlattice in VLS grown planar GaAs nanowires induced by impurity doping*, Photonics Conference (IPC), 2012 IEEE, Burlingame, CA 23-27 Sept. 2012, 2012; Burlingame, CA pp 693-694.
543. Ran, L.; Hui, H.; Xiaomin, R.; Jingwei, G.; Xiaolong, L.; Yongqing, H.; Shiwei, C. In *Optimization growth of P-type GaAs nanowires by metal-organic chemical vapor deposition*, Advances in Optoelectronics and Micro/Nano-Optics (AOM), 2010 OSA-IEEE-COS, 3-6 Dec. 2010, 2010; pp 1-4.
544. Vinaji, S.; Lochthofen, A.; Mertin, W.; Regolin, I.; Gutsche, C.; Prost, W.; Tegude, F. J.; Bacher, G. *Nanotechnology* **2009,** 20, (38), 385702.

545. Ullah, A. R.; Gluschke, J. G.; Krogstrup, P.; Sørensen, C. B.; Nygård, J.; Micolich, A. P. *Nanotechnology* **2017,** 28, (13), 134005.
546. Casadei, A.; Krogstrup, P.; Heiss, M.; Röhr, J. A.; Colombo, C.; Ruelle, T.; Upadhyay, S.; Sørensen, C. B.; Nygård, J.; Fontcuberta i Morral, A. *Appl Phys Lett* **2013,** 102, (1), 013117.
547. Casadei, A.; Schwender, J.; Russo-Averchi, E.; Rüffer, D.; Heiss, M.; Alarcó-Lladó, E.; Jabeen, F.; Ramezani, M.; Nielsch, K.; Morral, A. F. i. *physica status solidi (RRL) – Rapid Research Letters* **2013,** 7, (10), 890-893.
548. Salehzadeh, O.; Zhang, X.; Gates, B. D.; Kavanagh, K. L.; Watkins, S. P. *J Appl Phys* **2012,** 112, (9), 094323-5.
549. Breuer, S.; Pfuller, C.; Flissikowski, T.; Brandt, O.; Grahn, H. T.; Geelhaar, L.; Riechert, H. *Nano Lett* **2011,** 11, (3), 1276-9.
550. Bar-Sadan, M.; Barthel, J.; Shtrikman, H.; Houben, L. *Nano Letters* **2012,** 12, (5), 2352-2356.
551. Jiang, N.; Gao, Q.; Parkinson, P.; Wong-Leung, J.; Mokkapati, S.; Breuer, S.; Tan, H. H.; Zheng, C. L.; Etheridge, J.; Jagadish, C. *Nano Letters* **2013,** 13, (11), 5135-5140.
552. Jiang, N.; Parkinson, P.; Gao, Q.; Breuer, S.; Tan, H. H.; Wong-Leung, J.; Jagadish, C. *Appl Phys Lett* **2012,** 101, (2), 023111.
553. Smith, L. M.; Wolford, D. J.; Venkatasubramanian, R.; Ghandhi, S. K. *Appl Phys Lett* **1990,** 57, (15), 1572-1574.
554. Millea, M.; Silver, A. *Journal of Vacuum Science and Technology* **1978,** 15, (4), 1362-1369.
555. Mead, C.; Spitzer, W. *Phys Rev Lett* **1963,** 10, (11), 471.
556. Sørensen, B. S.; Aagesen, M.; Sørensen, C. B.; Lindelof, P. E.; Martinez, K. L.; Nygård, J. *Appl Phys Lett* **2008,** 92, (1), 012119.
557. Upadhyay, S.; Jespersen, T. S.; Madsen, M. H.; Krogstrup, P.; Nygård, J. *Appl Phys Lett* **2013,** 103, (16), 162104.
558. Hwang, J.; Shin, J. C. *J Korean Phys Soc* **2014,** 64, (11), 1621-1625.
559. Li, H. Y.; Wunnicke, O.; Borgstrom, M. T.; Immink, W. G. G.; van Weert, M. H. M.; Verheijen, M. A.; Bakkers, E. *Nano Letters* **2007,** 7, (5), 1144-1148.
560. Cui, Z.; Ishikura, T.; Jabeen, F.; Harmand, J. C.; Yoh, K. *Journal of Crystal Growth* **2013,** 378, 511-514.
561. Perea, D. E.; Allen, J. E.; May, S. J.; Wessels, B. W.; Seidman, D. N.; Lauhon, L. J. *Nano Letters* **2006,** 6, (2), 181-185.
562. Thelander, C.; Dick, K. A.; Borgstrom, M. T.; Froberg, L. E.; Caroff, P.; Nilsson, H. A.; Samuelson, L. *Nanotechnology* **2010,** 21, (20), 5703.
563. Ghoneim, H.; Mensch, P.; Schmid, H.; Bessire, C. D.; Rhyner, R.; Schenk, A.; Rettner, C.; Karg, S.; Moselund, K. E.; Riel, H.; Bjork, M. T. *Nanotechnology* **2012,** 23, (50), 505708.
564. Davydok, A.; Rieger, T.; Biermanns, A.; Saqib, M.; Grap, T.; Lepsa, M. I.; Pietsch, U. *Journal of Applied Crystallography* **2013,** 46, (4), 893-897.
565. Dimakis, E.; Ramsteiner, M.; Huang, C.-N.; Trampert, A.; Davydok, A.; Biermanns, A.; Pietsch, U.; Riechert, H.; Geelhaar, L. *Appl Phys Lett* **2013,** 103, (14), 143121.
566. Rolland, C.; Caroff, P.; Coinon, C.; Wallart, X.; Leturcq, R. *Appl Phys Lett* **2013,** 102, (22), 223105.
567. Park, D. W.; Jeon, S. G.; Lee, C.-R.; Lee, S. J.; Song, J. Y.; Kim, J. O.; Noh, S. K.; Leem, J.-Y.; Kim, J. S. *Sci Rep-Uk* **2015,** 5, 16652.
568. Jeon, S. G.; Park, D. W.; Shin, H. S.; Park, H. M.; Choi, S. Y.; Lee, S. J.; Yu, J.; Song, J. Y. *RSC Advances* **2016,** 6, (10), 7791-7797.
569. Zhang, G.; Tateno, K.; Suzuki, S.; Gotoh, H.; Sogawa, T. *Journal of Physical Chemistry C* **2011,** 115, (7), 2923-2930.
570. Astromskas, G.; Storm, K.; Karlstrom, O.; Caroff, P.; Borgstrom, M.; Wernersson, L.-E. *J Appl Phys* **2010,** 108, (5), 054306-5.
571. Viti, L.; Vitiello, M. S.; Ercolani, D.; Sorba, L.; Tredicucci, A. *Nanoscale Res Lett* **2012,** 7, (1), 159.
572. Otnes, G.; Heurlin, M.; Zeng, X.; Borgstrom, M. T. *Nano Lett* **2017,** 17, (2), 702-707.
573. Borg, B. M.; Ek, M.; Ganjipour, B.; Dey, A. W.; Dick, K. A.; Wernersson, L.-E.; Thelander, C. *Appl Phys Lett* **2012,** 101, (4), 043508.
574. Zhi-Gang, C.; Lina, C.; Gao Qing, L.; Jin, Z. *Nanotechnology* **2010,** 21, (37), 375701.
575. Standing, A.; Assali, S.; Gao, L.; Verheijen, M. A.; van Dam, D.; Cui, Y.; Notten, P. H.; Haverkort, J. E.; Bakkers, E. P. *Nat Commun* **2015,** 6, 7824.
576. Wallentin, J.; Kriegner, D.; Stangl, J.; Borgström, M. T. *Nano Letters* **2014,** 14, (4), 1707-1713.
577. Yazdi, S.; Berg, A.; Borgstrom, M. T.; Kasama, T.; Beleggia, M.; Samuelson, L.; Wagner, J. B. *Small* **2015,** 11, (22), 2687-95.

578. Novak, J.; Šoltýs, J.; Eliáš, P.; Hasenöhrl, S.; Stoklas, R.; Dujavová, A.; Mikulics, M. *physica status solidi (a)* **2012,** 209, (12), 2505-2509.
579. Yeh, C.-Y.; Lu, Z.; Froyen, S.; Zunger, A. *Physical Review B* **1992,** 46, (16), 10086.
580. Lawaetz, P. *Physical Review B* **1972,** 5, (10), 4039-4045.
581. Ito, T. *Japanese Journal of Applied Physics* **1998,** 37, (Copyright (C) 1998 Publication Board, Japanese Journal of Applied Physics), L1217.
582. Toru, A.; Kosuke, S.; Kohji, N.; Tomonori, I. *Japanese Journal of Applied Physics* **2006,** 45, (3L), L275.
583. Johansson, J.; Karlsson, L. S.; Svensson, C. P. T.; Martensson, T.; Wacaser, B. A.; Deppert, K.; Samuelson, L.; Seifert, W. *Nature Materials* **2006,** 5, (7), 574-580.
584. Caroff, P.; Bolinsson, J.; Johansson, J. *Ieee J Sel Top Quant* **2011,** 17, (4), 829-846.
585. Bolinsson, J.; Ouattara, L.; Hofer, W.; Sköld, N.; Lundgren, E.; Gustafsson, A.; Mikkelsen, A. *Journal of Physics: Condensed Matter* **2009,** 21, (5), 055404.
586. Fortuna, S. A.; Li, X. L. *Semiconductor Science & Technology 25(2 Special Issue* **2010,** 25, (2 Special Issue SI), 24005.
587. Hofmann, S.; Sharma, R.; Wirth, C. T.; Cervantes-Sodi, F.; Ducati, C.; Kasama, T.; Dunin-Borkowski, R. E.; Drucker, J.; Bennett, P.; Robertson, J. *Nature Materials* **2008,** 7, (5), 372-375.
588. Oh, S. H.; Chisholm, M. F.; Kauffmann, Y.; Kaplan, W. D.; Luo, W.; Ruhle, M.; Scheu, C. *Science* **2010,** 330, (6003), 489-493.
589. Jacobsson, D.; Panciera, F.; Tersoff, J.; Reuter, M. C.; Lehmann, S.; Hofmann, S.; Dick, K. A.; Ross, F. M. *Nature* **2016,** 531, (7594), 317-322.
590. Gil, E.; Dubrovskii, V. G.; Avit, G.; Andre, Y.; Leroux, C.; Lekhal, K.; Grecenkov, J.; Trassoudaine, A.; Castelluci, D.; Monier, G.; Ramdani, R. M.; Robert-Goumet, C.; Bideux, L.; Harmand, J. C.; Glas, F. *Nano Lett* **2014,** 14, (7), 3938-44.
591. Glas, F.; Harmand, J. C.; Patriarche, G. *Phys Rev Lett* **2007,** 99, 146101.
592. Dubrovskii, V. G.; Sibirev, N. V.; Harmand, J. C.; Glas, F. *Physical Review B* **2008,** 78, (23), 235301.
593. Johansson, J.; Karlsson, L. S.; Dick, K. A.; Bolinsson, J.; Wacaser, B. A.; Deppert, K.; Samuelson, L. *Cryst Growth Des* **2009,** 9, (2), 766-773.
594. Dubrovskii, V. G.; Grecenkov, J. *Cryst Growth Des* **2015,** 15, (1), 340-347.
595. Glas, F.; Ramdani, M. R.; Patriarche, G.; Harmand, J.-C. *Physical Review B* **2013,** 88, (19).
596. Dubrovskii, V. G. *The Journal of Chemical Physics* **2015,** 142, (20), 204702.
597. Johansson, J.; Bolinsson, J.; Ek, M.; Caroff, P.; Dick, K. A. *Acs Nano* **2012,** 6, (7), 6142-6149.
598. Joyce, H. J.; Wong-Leung, J.; Gao, Q.; Tan, H. H.; Jagadish, C. *Nano Letters* **2010,** 10, (3), 908-915.
599. Poole, P. J.; Dalacu, D.; Wu, X.; Lapointe, J.; Mnaymneh, K. *Nanotechnology* **2012,** 23, (38), 385205.
600. Ghalamestani, S. G.; Heurlin, M.; Wernersson, L.-E.; Lehmann, S.; Dick, K. A. *Nanotechnology* **2012,** 23, (28), 285601.
601. Yang, J.; Neudeck, G. W.; Denton, J. P. *J Appl Phys* **2002,** 91, (1), 420-426.
602. Stiles, M.; Hamann, D. *Physical Review B* **1990,** 41, (8), 5280.
603. Stiles, M.; Hamann, D. *Physical Review B* **1988,** 38, (3), 2021.
604. Sourribes, M. J. L.; Isakov, I.; Panfilova, M.; Liu, H.; Warburton, P. A. *Nano Letters* **2014,** 14, (3), 1643-1650.
605. Hörmann, N. G.; Zardo, I.; Hertenberger, S.; Funk, S.; Bolte, S.; Döblinger, M.; Koblmüller, G.; Abstreiter, G. *Physical Review B* **2011,** 84, (15), 155301.
606. Thelander, C.; Caroff, P.; Plissard, S. b.; Dey, A. W.; Dick, K. A. *Nano Letters* **2011,** 11, (6), 2424-2429.
607. Schroer, M. D.; Petta, J. R. *Nano Letters* **2010,** 10, (5), 1618-1622.
608. Lopez, F. J.; Hemesath, E. R.; Lauhon, L. J. *Nano Lett* **2009,** 9, (7), 2774-9.
609. Porter, A.; Tran, C.; Sansoz, F. *Physical Review B* **2016,** 93, (19), 195431.
610. Weathers, A.; Moore, A. L.; Pettes, M. T.; Salta, D.; Kim, J.; Dick, K.; Samuelson, L.; Linke, H.; Caroff, P.; Shi, L. *MRS Proceedings* **2012,** 1404.
611. Wallentin, J.; Ek, M.; Wallenberg, L. R.; Samuelson, L.; Borgstrom, M. T. *Nano Lett* **2012,** 12, (1), 151-5.
612. Murayama, M.; Nakayama, T. *Physical Review B* **1994,** 49, (7), 4710-4724.
613. Mattila, M.; Hakkarainen, T.; Mulot, M.; Lipsanen, H. *Nanotechnology* **2006,** 17, (6), 1580-1583.
614. Pemasiri, K.; Montazeri, M.; Gass, R.; Smith, L. M.; Jackson, H. E.; Yarrison-Rice, J.; Paiman, S.; Gao, Q.; Tan, H. H.; Jagadish, C.; Zhang, X.; Zou, J. *Nano Letters* **2009,** 9, (2), 648-654.

615. Koguchi, M.; Kakibayashi, H.; Yazawa, M.; Hiruma, K.; Katsuyama, T. *Jpn J Appl Phys 1* **1992,** 31, (7), 2061-2065.
616. Caroff, P.; Dick, K. A.; Johansson, J.; Messing, M. E.; Deppert, K.; Samuelson, L. *Nat Nanotechnol* **2009,** 4, (1), 50-55.
617. Krogstrup, P.; Popovitz-Biro, R.; Johnson, E.; Madsen, M. H.; Nygård, J.; Shtrikman, H. *Nano Letters* **2010,** 10, (11), 4475–4482.
618. Lehmann, S.; Wallentin, J.; Jacobsson, D.; Deppert, K.; Dick, K. A. *Nano Letters* **2013,** 13, (9), 4099-4105.
619. Lehmann, S.; Jacobsson, D.; Deppert, K.; Dick, K. *Nano Res* **2012**, 1-7.
620. Hjort, M.; Lehmann, S.; Knutsson, J.; Timm, R.; Jacobsson, D.; Lundgren, E.; Dick, K. A.; Mikkelsen, A. *Nano Letters* **2013,** 13, (9), 4492-4498.
621. Sebastian, L.; Daniel, J.; Kimberly, A. D. *Nanotechnology* **2015,** 26, (30), 301001.
622. Vainorius, N.; Lehmann, S.; Jacobsson, D.; Samuelson, L.; Dick, K. A.; Pistol, M.-E. *Nano letters* **2015,** 15, (4), 2652-2656.
623. Bolinsson, J.; Caroff, P.; Mandl, B.; Dick, K. A. *Nanotechnology* **2011,** 22, (26), 265606.
624. Assali, S.; Gagliano, L.; Oliveira, D. S.; Verheijen, M. A.; Plissard, S. R.; Feiner, L. F.; Bakkers, E. P. *Nano Lett* **2015,** 15, (12), 8062-9.
625. Jancu, J. M.; Gauthron, K.; Largeau, L.; Patriarche, G.; Harmand, J. C.; Voisin, P. *Appl Phys Lett* **2010,** 97, (4), 041910-3.
626. Kusch, P.; Grelich, E.; Somaschini, C.; Luna, E.; Ramsteiner, M.; Geelhaar, L.; Riechert, H.; Reich, S. *Physical Review B* **2014,** 89, (4), 045310.
627. Vainorius, N.; Jacobsson, D.; Lehmann, S.; Gustafsson, A.; Dick, K. A.; Samuelson, L.; Pistol, M.-E. *Physical Review B* **2014,** 89, (16), 165423.
628. Jaya Kumar, P.; Arup, C.; Daniele, E.; Mauro, G.; Lucia, S.; Anushree, R. *Nanotechnology* **2016,** 27, (41), 415201.
629. Bernhard, L.; Marcus, M.; Julia, W.; Peter, V.; Daniel, R.; Gerhard, A.; Jonathan, J. F.; Frank, B.; Jürgen, C.; Gregor, K. *New Journal of Physics* **2016,** 18, (6), 063009.
630. Nilsson, M.; Namazi, L.; Lehmann, S.; Leijnse, M.; Dick, K. A.; Thelander, C. *Physical Review B* **2016,** 93, (19), 195422.
631. Li, K.; Sun, H.; Ren, F.; Ng, K. W.; Tran, T.-T. D.; Chen, R.; Chang-Hasnain, C. J. *Nano Letters* **2013,** 14, (1), 183-190.
632. Heiss, M.; Conesa-Boj, S.; Ren, J.; Tseng, H.-H.; Gali, A.; Rudolph, A.; Uccelli, E.; Peiró, F.; Morante, J. R.; Schuh, D.; Reiger, E.; Kaxiras, E.; Arbiol, J.; Fontcuberta i Morral, A. *Physical Review B* **2011,** 83, (4), 045303.
633. Jahn, U.; Lähnemann, J.; Pfüller, C.; Brandt, O.; Breuer, S.; Jenichen, B.; Ramsteiner, M.; Geelhaar, L.; Riechert, H. *Physical Review B* **2012,** 85, (4), 045323.
634. Hoang, T. B.; Moses, A. F.; Zhou, H. L.; Dheeraj, D. L.; Fimland, B. O.; Weman, H. *Appl Phys Lett* **2009,** 94, (13), 133105.
635. Kim, D. C.; Dheeraj, D. L.; Fimland, B. O.; Weman, H. *Appl Phys Lett* **2013,** 102, (14), 142107.
636. Ketterer, B.; Heiss, M.; Uccelli, E.; Arbiol, J.; i Morral, A. F. *ACS Nano* **2011,** 5, (9), 7585-92.
637. Ahtapodov, L.; Todorovic, J.; Olk, P.; Mjåland, T.; Slåttnes, P.; Dheeraj, D. L.; van Helvoort, A. T. J.; Fimland, B.-O.; Weman, H. *Nano Letters* **2012,** 12, (12), 6090-6095.
638. Vainorius, N.; Lehmann, S.; Gustafsson, A.; Samuelson, L.; Dick, K. A.; Pistol, M.-E. *Nano Letters* **2016,** 16, (4), 2774-2780.
639. Mishra, A.; Titova, L. V.; Hoang, T. B.; Jackson, H. E.; Smith, L. M.; Yarrison-Rice, J. M.; Kim, Y.; Joyce, H. J.; Gao, Q.; Tan, H. H.; Jagadish, C. *Appl Phys Lett* **2007,** 91, 263104.
640. Gadret, E.; Dias, G.; Dacal, L.; de Lima, M.; Ruffo, C.; Iikawa, F.; Brasil, M.; Chiaramonte, T.; Cotta, M.; Tizei, L.; Ugarte, D.; Cantarero, A. *Physical Review B* **2010,** 82, (12).
641. Perera, S.; Pemasiri, K.; Fickenscher, M. A.; Jackson, H. E.; Smith, L. M.; Yarrison-Rice, J.; Paiman, S.; Gao, Q.; Tan, H. H.; Jagadish, C. *Appl Phys Lett* **2010,** 97, (2), 023106-3.
642. Montazeri, M.; Wade, A.; Fickenscher, M.; Jackson, H. E.; Smith, L. M.; Yarrison-Rice, J. M.; Gao, Q.; Tan, H. H.; Jagadish, C. *Nano Letters* **2011,** 11, (10), 4329-4336.
643. De, A.; Pryor, C. E. *Physical Review B* **2010,** 81, (15), 155210.
644. Tedeschi, D.; De Luca, M.; Granados del Águila, A.; Gao, Q.; Ambrosio, G.; Capizzi, M.; Tan, H. H.; Christianen, P. C. M.; Jagadish, C.; Polimeni, A. *Nano Letters* **2016**.
645. Rota, M. B.; Ameruddin, A. S.; Fonseka, H. A.; Gao, Q.; Mura, F.; Polimeni, A.; Miriametro, A.; Tan, H. H.; Jagadish, C.; Capizzi, M. *Nano Letters* **2016,** 16, (8), 5197-5203.
646. Trägårdh, J.; Persson, A. I.; Wagner, J. B.; Hessman, D.; Samuelson, L. *J Appl Phys* **2007,** 101, (12), 123701.

647. Chen, I. J.; Lehmann, S.; Nilsson, M.; Kivisaari, P.; Linke, H.; Dick, K. A.; Thelander, C. *Nano Letters* **2017,** 17, (2), 902-908.
648. Assali, S.; Zardo, I.; Plissard, S.; Kriegner, D.; Verheijen, M. A.; Bauer, G.; Meijerink, A.; Belabbes, A.; Bechstedt, F.; Haverkort, J. E. M.; Bakkers, E. P. A. M. *Nano Letters* **2013,** 13, (4), 1559-1563.
649. Panda, J. K.; Roy, A.; Gemmi, M.; Husanu, E.; Li, A.; Ercolani, D.; Sorba, L. *Appl Phys Lett* **2013,** 103, (2), 023108.
650. Assali, S.; Greil, J.; Zardo, I.; Belabbes, A.; de Moor, M. W. A.; Koelling, S.; Koenraad, P. M.; Bechstedt, F.; Bakkers, E. P. A. M.; Haverkort, J. E. M. *J Appl Phys* **2016,** 120, (4), 044304.
651. Greil, J.; Assali, S.; Isono, Y.; Belabbes, A.; Bechstedt, F.; Mackenzie, F. V.; Silov, A. Y.; Bakkers, E.; Haverkort, J. *Nano letters* **2016,** 16, (6), 3703.
652. Hauge, H. I.; Verheijen, M. A.; Conesa-Boj, S.; Etzelstorfer, T.; Watzinger, M.; Kriegner, D.; Zardo, I.; Fasolato, C.; Capitani, F.; Postorino, P.; Kolling, S.; Li, A.; Assali, S.; Stangl, J.; Bakkers, E. P. *Nano Lett* **2015,** 15, (9), 5855-60.
653. Leitsmann, R.; Bechstedt, F. *J Appl Phys* **2007,** 102, (6), 63528.
654. Cahangirov, S.; Ciraci, S. *Physical Review B (Condensed Matter and Materials Physics)* **2009,** 79, (16), 165118-8.
655. Magri, R.; Rosini, M.; Casetta, F. *physica status solidi (c)* **2010,** 7, (2), 374-377.
656. Yamashita, T.; Akiyama, T.; Nakamura, K.; Ito, T. *Physica E: Low-dimensional Systems and Nanostructures* **2010,** 42, (10), 2727-2730.
657. Dick, K. A.; Caroff, P.; Bolinsson, J.; Messing, M. E.; Johansson, J.; Deppert, K.; Wallenberg, L. R.; Samuelson, L. *Semiconductor Science & Technology* **2010,** 25, (2), 24009.
658. Dubrovskii, V. G.; Sibirev, N. V. *Physical Review B* **2008,** 77, (3), 035414.
659. Breuer, S.; Feiner, L.-F.; Geelhaar, L. *Cryst Growth Des* **2013,** 13, (7), 2749-2755.
660. Wacaser, B. A.; Dick, K. A.; Johansson, J.; Borgstrom, M. T.; Deppert, K.; Samuelson, L. *Advanced Materials* **2009,** 21, (2), 153-165.
661. Dubrovskii, V. G. *Cryst Growth Des* **2017**.
662. Nazarenko, M.; Sibirev, N.; Dubrovskii, V. *Technical Physics* **2011,** 56, (2), 311-315.
663. Dubrovskii, V. G. *Appl Phys Lett* **2014,** 104, (5), -.
664. Chou, Y.-C.; Hillerich, K.; Tersoff, J.; Reuter, M. C.; Dick, K. A.; Ross, F. M. *Science* **2014,** 343, (6168), 281-284.
665. Wen, C. Y.; Tersoff, J.; Hillerich, K.; Reuter, M. C.; Park, J. H.; Kodambaka, S.; Stach, E. A.; Ross, F. M. *Phys Rev Lett* **2011,** 107, (2), 025503.
666. Gamalski, A. D.; Ducati, C.; Hofmann, S. *The Journal of Physical Chemistry C* **2011,** 115, (11), 4413-4417.
667. Glas, F.; Harmand, J.-C.; Patriarche, G. *Phys Rev Lett* **2010,** 104, (13), 135501.
668. Joyce, H. J.; Gao, Q.; Tan, H. H.; Jagadish, C.; Kim, Y.; Fickenscher, M. A.; Perera, S.; Hoang, T. B.; Smith, L. M.; Jackson, H. E.; Yarrison-Rice, J. M.; Zhang, X.; Zou, J. *Adv Funct Mater* **2008,** 18, (23), 3794-3800.
669. Dick, K. A.; Bolinsson, J.; Messing, M. E.; Lehmann, S.; Johansson, J.; Caroff, P. *J Vac Sci Technol B* **2011,** 29, (4), 04D103.
670. Xu, T.; Dick, K. A.; Plissard, S.; Nguyen, T. H.; Makoudi, Y.; Berthe, M.; Nys, J.-P.; Wallart, X.; Grandidier, B.; Caroff, P. *Nanotechnology* **2012,** 23, (9), 095702.
671. Shtrikman, H.; Popovitz-Biro, R.; Kretinin, A.; Houben, L.; Heiblum, M.; Bukala, M.; Galicka, M.; Buczko, R.; Kacman, P. *Nano Lett* **2009,** 9, (4), 1506-10.
672. Berg, A.; Lehmann, S.; Vainorius, N.; Gustafsson, A.; Pistol, M.-E.; Wallenberg, L. R.; Samuelson, L.; Borgström, M. T. *Journal of Crystal Growth* **2014,** 386, 47-51.
673. Elena, H.; Daniele, E.; Mauro, G.; Lucia, S. *Nanotechnology* **2014,** 25, (20), 205601.
674. Mohseni, P. K.; LaPierre, R. R. *Nanotechnology* **2009,** 20, (2), 025610.
675. Plante, M.; LaPierre, R. *Nanotechnology* **2008,** 19, (49), 495603.
676. Cirlin, G. E.; Dubrovskii, V. G.; Samsonenko, Y. B.; Bouravleuv, A. D.; Durose, K.; Proskuryakov, Y. Y.; Mendes, B.; Bowen, L.; Kaliteevski, M. A.; Abram, R. A.; Zeze, D. *Physical Review B* **2010,** 82, (3), 035302.
677. Dheeraj, D.; Munshi, A.; Scheffler, M.; van Helvoort, A.; Weman, H.; Fimland, B. *Nanotechnology* **2012,** 24, (1), 015601.
678. Soda, M.; Rudolph, A.; Schuh, D.; Zweck, J.; Bougeard, D.; Reiger, E. *Physical Review B* **2012,** 85, (24), 245450.
679. Johansson, J.; Dick, K. A.; Caroff, P.; Messing, M. E.; Bolinsson, J.; Deppert, K.; Samuelson, L. *J Phys Chem C* **2010,** 114, (9), 3837-3842.

680. Kim, H. S.; Myung, Y.; Cho, Y. J.; Jang, D. M.; Jung, C. S.; Park, J.; Ahn, J.-P. *Nano Lett.* **2010,** 10, (5), 1682-1691.
681. Grap, T.; Rieger, T.; Ch, B.; Th, S.; Grützmacher, D.; Lepsa, M. I. *Nanotechnology* **2013,** 24, (33), 335601.
682. Ikonić, Z.; Srivastava, G. P.; Inkson, J. C. *Physical Review B* **1993,** 48, (23), 17181-17193.
683. Ikonić, Z.; Srivastava, G. P.; Inkson, J. C. *Physical Review B* **1995,** 52, (19), 14078-14085.
684. Tadic, M.; Ikonić, Z. *Journal of Physics: Condensed Matter* **1999,** 11, (36), 6891.
685. Tsuzuki, H.; Cesar, D. F.; Rebello de Sousa Dias, M.; Castelano, L. K.; Lopez-Richard, V.; Rino, J. P.; Marques, G. E. *ACS Nano* **2011,** 5, (7), 5519-5525.
686. Akiyama, T.; Yamashita, T.; Nakamura, K.; Ito, T. *Nano Letters* **2010,** 10, (11), 4614–4618.
687. Shimamura, K.; Yuan, Z.; Shimojo, F.; Nakano, A. *Appl Phys Lett* **2013,** 103, (2), 022105-4.
688. Moore, A. L.; Saha, S. K.; Prasher, R. S.; Shi, L. *Appl Phys Lett* **2008,** 93, (8), 083112.
689. Sansoz, F. *Nano Lett.* **2011,** 11, (12), 5378-82.
690. Nika, D. L.; Cocemasov, A. I.; Isacova, C. I.; Balandin, A. A.; Fomin, V. M.; Schmidt, O. G. *Physical Review B* **2012,** 85, (20), 205439.
691. Deng, C.; Sansoz, F. *ACS Nano* **2009,** 3, (10), 3001-3008.
692. Wang, J.; Sansoz, F.; Huang, J.; Liu, Y.; Sun, S.; Zhang, Z.; Mao, S. X. *Nat Commun* **2013,** 4, 1742.
693. Hill, M. T.; Gather, M. C. *Nat Photon* **2014,** 8, (12), 908-918.
694. Eaton, S. W.; Fu, A.; Wong, A. B.; Ning, C.-Z.; Yang, P. *Nature Reviews Materials* **2016,** 1, 16028.
695. Saxena, D.; Mokkapati, S.; Jagadish, C. *Ieee Photonics J* **2012,** 4, (2), 582-585.
696. Hill, M. T.; Marell, M.; Leong, E. S.; Smalbrugge, B.; Zhu, Y.; Sun, M.; Van Veldhoven, P. J.; Geluk, E. J.; Karouta, F.; Oei, Y.-S. *Opt Express* **2009,** 17, (13), 11107-11112.
697. Noginov, M. A.; Zhu, G.; Belgrave, A. M.; Bakker, R.; Shalaev, V. M.; Narimanov, E. E.; Stout, S.; Herz, E.; Suteewong, T.; Wiesner, U. *Nature* **2009,** 460, (7259), 1110-1112.
698. Berini, P.; De Leon, I. *Nat Photon* **2012,** 6, (1), 16-24.
699. Khurgin, J. B.; Sun, G. *Opt Express* **2012,** 20, (14), 15309-15325.
700. Khurgin, J. B.; Sun, G. *Appl Phys Lett* **2012,** 100, (1), 011105.
701. Khurgin, J. B.; Sun, G. *Nat Photonics* **2014,** 8, (6), 468-473.
702. Iga, K. *Ieee J Sel Top Quant* **2000,** 6, (6), 1201-1215.
703. Lee, Y.; Jewell, J.; Scherer, A.; McCall, S.; Harbison, J.; Florez, L. *Electron Lett* **1989,** 25, (20), 1377-1378.
704. Levi, A.; Slusher, R.; McCall, S.; Tanbun-Ek, T.; Coblentz, D.; Pearton, S. *Electron Lett* **1992,** 28, (11), 1010-1012.
705. Sun, L.; Ren, M.-L.; Liu, W.; Agarwal, R. *Nano Letters* **2014,** 14, (11), 6564-6571.
706. Saxena, D.; Wang, F.; Gao, Q.; Mokkapati, S.; Tan, H. H.; Jagadish, C. *Nano Lett* **2015,** 15, (8), 5342-8.
707. Gradecak, S.; Qian, F.; Li, Y.; Park, H. G.; Lieber, C. M. *Appl Phys Lett* **2005,** 87, (17), 73111.
708. Sun, H.; Ren, F.; Ng, K. W.; Tran, T.-T. D.; Li, K.; Chang-Hasnain, C. J. *ACS Nano* **2014,** 8, (7), 6833-6839.
709. Frost, T.; Jahangir, S.; Stark, E.; Deshpande, S.; Hazari, A.; Zhao, C.; Ooi, B. S.; Bhattacharya, P. *Nano Letters* **2014,** 14, (8), 4535-4541.
710. Johnson, J. C.; Yan, H.; Schaller, R. D.; Haber, L. H.; Saykally, R. J.; Yang, P. *The Journal of Physical Chemistry B* **2001,** 105, (46), 11387-11390.
711. Johnson, J. C.; Yan, H.; Yang, P.; Saykally, R. J. *The journal of physical chemistry B* **2003,** 107, (34), 8816-8828.
712. Roder, R.; Sidiropoulos, T. P.; Buschlinger, R.; Riediger, M.; Peschel, U.; Oulton, R. F.; Ronning, C. *Nano Lett* **2016,** 16, (4), 2878-84.
713. Röder, R.; Sidiropoulos, T. P. H.; Tessarek, C.; Christiansen, S.; Oulton, R. F.; Ronning, C. *Nano Letters* **2015,** 15, (7), 4637-4643.
714. Sidiropoulos, T. P. H.; Roder, R.; Geburt, S.; Hess, O.; Maier, S. A.; Ronning, C.; Oulton, R. F. *Nat Phys* **2014,** 10, (11), 870-876.
715. Versteegh, M. A. M.; van Capel, P. J. S.; Dijkhuis, J. I. *Appl Phys Lett* **2012,** 101, (2), 021101.
716. Agarwal, R.; Barrelet, C. J.; Lieber, C. M. *Nano Letters* **2005,** 5, (5), 917-920.
717. Robert, R.; Daniel, P.; Arian, K.; Robert, B.; Sebastian, G.; Ulf, P.; Carsten, R. *Journal of Physics D: Applied Physics* **2014,** 47, (39), 394012.
718. Liu, X.; Zhang, Q.; Xiong, Q.; Sum, T. C. *Nano Letters* **2013,** 13, (3), 1080-1085.
719. Geburt, S.; Thielmann, A.; Roder, R.; Borschel, C.; McDonnell, A.; Kozlik, M.; Kuhnel, J.; Sunter, K. A.; Capasso, F.; Ronning, C. *Nanotechnology* **2012,** 23, (36), 365204.

720. Ma, R. M.; Wei, X. L.; Dai, L.; Liu, S. F.; Chen, T.; Yue, S.; Li, Z.; Chen, Q.; Qin, G. G. *Nano Lett* **2009,** 9, (7), 2697-703.
721. Zhang, Y. F.; Russo, R. E.; Mao, S. S. *Appl Phys Lett* **2005,** 87, (4), 43106.
722. Johnson, J. C.; Choi, H. J.; Knutsen, K. R.; Schaller, R. D.; Yang, P. D.; Saykally, R. J. *Nature Materials* **2002,** 1, (2), 106-110.
723. Pan, A.; Liu, R.; Zhang, Q.; Wan, Q.; He, P.; Zacharias, M.; Zou, B. *The Journal of Physical Chemistry C* **2007,** 111, (38), 14253-14256.
724. Li, J.; Meng, C.; Liu, Y.; Wu, X.; Lu, Y.; Ye, Y.; Dai, L.; Tong, L.; Liu, X.; Yang, Q. *Advanced Materials* **2013,** 25, (6), 833-837.
725. Xiao, Y.; Meng, C.; Wu, X.; Tong, L. *Appl Phys Lett* **2011,** 99, (2), 023109.
726. Xiao, Y.; Meng, C.; Wang, P.; Ye, Y.; Yu, H.; Wang, S.; Gu, F.; Dai, L.; Tong, L. *Nano Lett.* **2011,** 11, (3), 1122-6.
727. Gao, Q.; Saxena, D.; Wang, F.; Fu, L.; Mokkapati, S.; Guo, Y.; Li, L.; Wong-Leung, J.; Caroff, P.; Tan, H. H.; Jagadish, C. *Nano Letters* **2014,** 14, (9), 5206-5211.
728. Wang, Z.; Tian, B.; Paladugu, M.; Pantouvaki, M.; Le Thomas, N.; Merckling, C.; Guo, W.; Dekoster, J.; Van Campenhout, J.; Absil, P.; Van Thourhout, D. *Nano Letters* **2013,** 13, (11), 5063-5069.
729. Wei, W.; Liu, Y.; Zhang, X.; Wang, Z.; Ren, X. *Appl Phys Lett* **2014,** 104, (22), 223103.
730. Tatebayashi, J.; Kako, S.; Ho, J.; Ota, Y.; Iwamoto, S.; Arakawa, Y. *Nat Photon* **2015,** 9, (8), 501-505.
731. Stettner, T.; Zimmermann, P.; Loitsch, B.; Döblinger, M.; Regler, A.; Mayer, B.; Winnerl, J.; Matich, S.; Riedl, H.; Kaniber, M. *Appl Phys Lett* **2016,** 108, (1), 011108.
732. Mayer, B.; Janker, L.; Loitsch, B.; Treu, J.; Kostenbader, T.; Lichtmannecker, S.; Reichert, T.; Morkotter, S.; Kaniber, M.; Abstreiter, G.; Gies, C.; Koblmuller, G.; Finley, J. J. *Nano Lett* **2016,** 16, (1), 152-6.
733. Chin, A. H.; Vaddiraju, S.; Maslov, A. V.; Ning, C. Z.; Sunkara, M. K.; Meyyappan, M. *Appl Phys Lett* **2006,** 88, (16), 63115.
734. Heo, J.; Guo, W.; Bhattacharya, P. *Appl Phys Lett* **2011,** 98, (2), 021110-3.
735. Gao, H.; Fu, A.; Andrews, S. C.; Yang, P. *Proceedings of the National Academy of Sciences* **2013,** 110, (3), 865-869.
736. Li, C.; Liu, S.; Luk, T. S.; Figiel, J. J.; Brener, I.; Brueck, S. R. J.; Wang, G. T. *Nanoscale* **2016,** 8, (10), 5682-5687.
737. Wright, J. B.; Campione, S.; Liu, S.; Martinez, J. A.; Xu, H.; Luk, T. S.; Li, Q.; Wang, G. T.; Swartzentruber, B. S.; Lester, L. F.; Brener, I. *Appl Phys Lett* **2014,** 104, (4), 041107.
738. Hurtado, A.; Xu, H.; Wright, J. B.; Liu, S.; Li, Q.; Wang, G. T.; Luk, T. S.; Figiel, J. J.; Cross, K.; Balakrishnan, G.; Lester, L. F.; Brener, I. *Appl Phys Lett* **2013,** 103, (25), 251107.
739. Heo, J.; Jahangir, S.; Xiao, B.; Bhattacharya, P. *Nano Letters* **2013,** 13, (6), 2376-2380.
740. Xu, H.; Wright, J. B.; Luk, T.-S.; Figiel, J. J.; Cross, K.; Lester, L. F.; Balakrishnan, G.; Wang, G. T.; Brener, I.; Li, Q. *Appl Phys Lett* **2012,** 101, (11), 113106.
741. Qian, F.; Li, Y.; Gradecak, S.; Park, H.-G.; Dong, Y.; Ding, Y.; Wang, Z. L.; Lieber, C. M. *Nat Mater* **2008,** 7, (9), 701-706.
742. Pauzauskie, P. J.; Sirbuly, D. J.; Yang, P. D. *Phys Rev Lett* **2006,** 9614, (14), 3903.
743. Pan, A.; Zhou, W.; Leong, E. S. P.; Liu, R.; Chin, A. H.; Zou, B.; Ning, C. Z. *Nano Letters* **2009,** 9, (2), 784-788.
744. Liu, Z.; Yin, L.; Ning, H.; Yang, Z.; Tong, L.; Ning, C.-Z. *Nano Letters* **2013,** 13, (10), 4945-4950.
745. Yang, Z.; Wang, D.; Meng, C.; Wu, Z.; Wang, Y.; Ma, Y.; Dai, L.; Liu, X.; Hasan, T.; Liu, X.; Yang, Q. *Nano Letters* **2014,** 14, (6), 3153-3159.
746. Guo, P.; Zhuang, X.; Xu, J.; Zhang, Q.; Hu, W.; Zhu, X.; Wang, X.; Wan, Q.; He, P.; Zhou, H.; Pan, A. *Nano Letters* **2013,** 13, (3), 1251-1256.
747. Yan, X.; Zhang, X.; Li, J.; Wu, Y.; Cui, J.; Ren, X. *Nanoscale* **2015,** 7, (3), 1110-1115.
748. Zimmler, M. A.; Bao, J.; Capasso, F.; Müller, S.; Ronning, C. *Appl Phys Lett* **2008,** 93, (5), 051101.
749. Hua, B.; Motohisa, J.; Kobayashi, Y.; Hara, S.; Fukui, T. *Nano Letters* **2009,** 9, (1), 112-116.
750. Saxena, D.; Jiang, N.; Yuan, X.; Mokkapati, S.; Guo, Y.; Tan, H. H.; Jagadish, C. *Nano Letters* **2016,** 16, (8), 5080-5086.
751. Chand, N.; Becker, E.; Van der Ziel, J.; Chu, S. G.; Dutta, N. *Appl Phys Lett* **1991,** 58, (16), 1704-1706.
752. Kirstaedter, N.; Ledentsov, N.; Grundmann, M.; Bimberg, D.; Ustinov, V.; Ruvimov, S.; Maximov, M.; Kop'ev, P. S.; Alferov, Z. I.; Richter, U. *Electron Lett* **1994,** 30, (17), 1416-1417.

753. Caroff, P.; Paranthoen, C.; Platz, C.; Dehaese, O.; Folliot, H.; Bertru, N.; Labbé, C.; Piron, R.; Homeyer, E.; Le Corre, A.; Loualiche, S. *Appl Phys Lett* **2005,** 87, (24), 243107.
754. Huffaker, D.; Park, G.; Zou, Z.; Shchekin, O.; Deppe, D. *Appl Phys Lett* **1998,** 73, (18), 2564-2566.
755. Wu, J.; Chen, S.; Seeds, A.; Liu, H. *Journal of Physics D: Applied Physics* **2015,** 48, (36), 363001.
756. von Stackelberg, M.; Paulus, R. *Z. Phys. Chem. B-Chem. Elem. Aufbau. Mater.* **1935,** 28, (6), 427-460.
757. Heike, W. *Zeitschrift Fur Anorganische Und Allgemeine Chemie* **1921,** 118, (3), 264-268.
758. Curry, B. E. *The Journal of Physical Chemistry* **1908,** 13, (8), 589-605.
759. Smith, A. W. *Physical Review (Series I)* **1911,** 32, (2), 178-200.
760. Cooke, J. P. *Memoirs of the American Academy of Arts and Sciences* **1855,** 5, (2), 337-371.
761. Cooke, J. P. *Philosophical Magazine Series 4* **1860,** 19, (129), 405-416.
762. Cole, H.; Chambers, F.; Dunn, H. *Acta Crystallographica* **1956,** 9, (8), 685-685.
763. Silvey, G. A. *J Appl Phys* **1958,** 29, (2), 226-227.
764. Żdanowicz, L.; Żdanowicz, W. *physica status solidi (b)* **1964,** 6, (1), 227-234.
765. Zdanowic.W; Henkie, Z. *B Acad Pol Sci-Chim* **1964,** 12, (10), 729-&.
766. Turner, W. J.; Fischler, A. S.; Reese, W. E. *J Appl Phys* **1961,** 32, (10), 2241.
767. Nasledov, D. N.; Shevchenko, V. Y. *physica status solidi (a)* **1973,** 15, (1), 9-38.
768. Żdanowicz, W.; Żdanowicz, L. *Annual Review of Materials Science* **1975,** 5, (1), 301-328.
769. Castellion, G. A.; Beegle, L. C. *J Phys Chem Solids* **1965,** 26, (4), 767-773.
770. Naake, H. J.; Belcher, S. C. *J Appl Phys* **1964,** 35, (10), 3064-3065.
771. Jayaraman, A.; Anantharaman, T. R.; Klement Jr, W. *J Phys Chem Solids* **1966,** 27, (10), 1605-1609.
772. Spitzer, D. P.; Castellion, G. A.; Haacke, G. *J Appl Phys* **1966,** 37, (10), 3795-3801.
773. Iwami, M.; Fujishima, K.; Kawabe, K. *Journal of the Physical Society of Japan* **1973,** 35, (4), 1261.
774. Marenkin, S. F.; Huseynov, B.; Shevchenko, V. Y.; Belyskiy, N. K. *Journal of Crystal Growth* **1978,** 44, (2), 259-261.
775. Almin, K. E. *Acta Chem. Scand* **1948,** 2, 400-407.
776. Bokii, G. B.; Klevtsova, R. F. *Journal of Structural Chemistry* **1965,** 6, (6), 830-834.
777. Fagen, E. A. *J Appl Phys* **1979,** 50, (10), 6505-6515.
778. Tapiero, M.; Tarabichi, S.; Gies, J. G.; Noguet, C.; Zielinger, J. P.; Joucla, M.; Loison, J. L.; Robino, M.; Herion, J. *Solar Energy Materials* **1985,** 12, (4), 257-274.
779. Rogers, L. M.; Jenkins, R. M.; Crocker, A. J. *Journal of Physics D: Applied Physics* **1971,** 4, (6), 793.
780. Wagner, R. J.; Palik, E. D.; Swiggard, E. M. *Phys Lett A* **1969,** 30, (3), 175-176.
781. Iwami, M.; Fujishima, K.; Kawabe, K. *Journal of the Physical Society of Japan* **1976,** 41, (2), 521.
782. Ito, T.; Wada, M.; Iwami, M.; Kawabe, K. *Journal of the Physical Society of Japan* **1977,** 43, (5), 1672-1678.
783. Sobolev, V. V.; Syrbu, N. N. *physica status solidi (b)* **1974,** 64, (2), 423-429.
784. Palatnik, L. S.; Fedorov, G. V.; Kornienko, L. A.; Bogdanova, A. F.; Toptygin, A. L. *Soviet Physics Journal* **1968,** 11, (11), 37-41.
785. Freik, D. M.; Gaiduchok, G. M.; Oles'kiv, S. P.; Voitkiv, V. V. *Soviet Physics Journal* **1970,** 13, (5), 678-679.
786. Catalano, A. *Journal of Crystal Growth* **1980,** 49, (4), 681-686.
787. Catalano, A.; Hall, R. B. *J Phys Chem Solids* **1980,** 41, (6), 635-640.
788. Bendett, M. P.; Hunsperger, R. G. *J Electron Mater* **1981,** 10, (3), 559-569.
789. Faa-Ching, W.; Bube, R. H.; Feigelson, R. S.; Route, R. K. *Journal of Crystal Growth* **1981,** 55, (2), 268-272.
790. Elrod, U.; Lux-Steiner, M.; Bucher, E.; Hönigschmid, J.; Bickmann, K.; Gain, L. *Journal of Crystal Growth* **1984,** 67, (2), 195-201.
791. Kloc, K.; Żdanowicz, W. *Journal of Crystal Growth* **1984,** 66, (2), 451-458.
792. Murali, K. R.; Vaya, P. R.; Sobhanadri, J. *Journal of Crystal Growth* **1985,** 73, (1), 196-198.
793. Murali, K. R.; Jayachandran, M. *Mater Chem Phys* **1987,** 16, (5-6), 561-567.
794. Marenkin, S. F.; Morozova, V. A.; Yur'ev, G. S.; Vol'fkovich, A. Y.; Astakhov, V. V.; Kondakov, N. B. *Inorg Mater+* **2002,** 38, (8), 781-783.
795. Kouklin, N.; Sen, S.; Gajdardziska-Josifovska, M. *J Appl Phys* **2006,** 89, (7), 071901.
796. Li, J.; Wang, L. S.; Buchholz, D. B.; Chang, R. P. *Nano Lett* **2009,** 9, (5), 1764-9.

797. Sathyamoorthy, R.; Sharmila, C.; Natarajan, K.; Velumani, S. *Materials Characterization* **2007,** 58, (8–9), 745-749.
798. Liu, Y.-B.; Zhou, S.-M.; Yuan, X.-Y.; Lou, S.-Y.; Gao, T.; Shi, X.-J.; Wu, X.-P. *Materials Letters* **2012,** 84, 116-119.
799. Xu, J.; Wu, H.; Wang, F.; Xia, Y.; Zheng, G. *Advanced Energy Materials* **2013,** 3, (3), 286-289.
800. Suda, T. *Journal of Crystal Growth* **1990,** 99, (1), 625-629.
801. Long, J. *J Electrochem Soc* **1983,** 130, (3), 725-728.
802. Kakishita, K.; Aihara, K.; Suda, T. *Appl Surf Sci* **1994,** 79-80, 281-286.
803. Pangilinan, G.; Sooryakumar, R.; Chelluri, B.; Chang, T. Y. *Phys Rev Lett* **1989,** 62, (5), 551.
804. Yeshchenko, O. A.; Dmitruk, I. M.; Koryakov, S. V.; Galak, M. P.; Pundyk, I. P.; Hohlova, L. M. *Physica B: Condensed Matter* **2005,** 368, (1–4), 8-15.
805. Yeshchenko, O. A.; Dmitruk, I. M.; Koryakov, S. V.; Galak, M. P.; Pundyk, I. P.; Hohlova, L. M. *Materials Science and Engineering: C* **2007,** 27, (5–8), 1364-1367.
806. Schlecht, S.; Erk, C.; Yosef, M. *Inorganic Chemistry* **2006,** 45, (4), 1693-1697.
807. Saadat, S.; Zhu, J.; Shahjamali, M. M.; Maleksaeedi, S.; Tay, Y. Y.; Tay, B. Y.; Hng, H. H.; Ma, J.; Yan, Q. *Chemical Communications* **2011,** 47, (35), 9849-9851.
808. Mai, N. T.; Mott, D. M.; Higashimine, K.; Maenosono, S. *Chemistry Letters* **2012,** 41, (11), 1529-1531.
809. Nie, A.; Gan, L.-y.; Cheng, Y.; Tao, X.; Yuan, Y.; Sharifi-Asl, S.; He, K.; Asayesh-Ardakani, H.; Vasiraju, V.; Lu, J.; Mashayek, F.; Klie, R.; Vaddiraju, S.; Schwingenschlögl, U.; Shahbazian-Yassar, R. *Adv Funct Mater* **2016,** 26, (4), 543-552.
810. Trukhan, V. M.; Izotov, A. D.; Shoukavaya, T. V. *Inorg Mater+* **2014,** 50, (9), 868-873.
811. Trukhan, V. M.; Marenkin, S. F.; Shoukavaya, T. V. *Crystallography Reports* **2014,** 59, (1), 53-59.
812. Trzebiat.W; Krolicki, F.; Zdanowic.W. *B Acad Pol Sci-Chim* **1968,** 16, (7), 343-&.
813. Gates, O. R.; Black, R. W. *Report of Nrl Progress* **1970**, (SEP), 27-&.
814. Cisowski, J.; Żdanowicz, W. *physica status solidi (a)* **1973,** 19, (2), 741-745.
815. Nakamura, M.; Iwami, M.; Kawabe, K. *Japanese Journal of Applied Physics* **1973,** 12, (10), 1649.
816. Caron, L. G.; Aubin, M. J.; Jay-Gerin, J. P. *Solid State Commun* **1977,** 23, (7), 493-498.
817. GUBANOVA, A.; CHUIKO, G. *Sov Phys Semicond+* **1984,** 18, (7), 794-795.
818. Arushanov, E. K.; Gubanova, A. A.; Knyazev, A. F.; Lashkul, A. V.; Lisunov, K. G.; Sologub, V. V. *Sov Phys Semicond+* **1988,** 22, (2), 208-209.
819. Yakimovich, V. N.; Rubtsov, V. A.; Trukhan, V. M. *Inorg Mater+* **1996,** 32, (6), 579-582.
820. Yakimovich, V. N.; Rubtsov, V. A.; Trukhan, V. M. *Inorg Mater+* **1996,** 32, (7), 705-709.
821. Gremenok, V. F.; Trukhan, V. M.; Marenkin, S. F. *Inorg Mater+* **1999,** 35, (7), 658-660.
822. Marenkin, S. F.; Trukhan, V. M. *Russian Journal of Inorganic Chemistry* **2001,** 46, S187-S202.
823. Marenkin, S. F.; Mikhailov, S. G.; Morozova, V. A.; Palkina, K. K.; Koshelev, O. G. *Inorg Mater+* **2003,** 39, (10), 1024-1027.
824. Marenkin, S. F.; Vol'fkovich, A. Y.; Mikhailov, S. G.; Astakhov, V. V. *Inorg Mater+* **2003,** 39, (9), 911-915.
825. Morozova, V. A.; Marenkin, S. F.; Mikhailov, S. G.; Koshelev, O. G. *Inorg Mater+* **2005,** 41, (3), 212-216.
826. Sanygin, V. P.; Mikhailov, S. G.; Palkina, K. K.; Steblevskii, A. V.; Kvardakov, A. M.; Marenkin, S. F. *Inorg Mater+* **2005,** 41, (1), 3-6.
827. Morozova, V. A.; Marenkin, S. F.; Koshelev, O. G.; Chernoguzov, D. V.; Mikhailov, S. G.; Molchanov, A. V. *Inorg Mater+* **2006,** 42, (12), 1289-1293.
828. Mollaev, A. Y.; Kamilov, I. K.; Arslanov, R. K.; Saipulaeva, L. A.; Dzhamamedov, R. G.; Marenkin, S. F.; Babushkin, A. N. *Russian Journal of Inorganic Chemistry* **2009,** 54, (1), 121-124.
829. Marenkin, S. F.; Morozova, V. A.; Koshelev, O. G. *Inorg Mater+* **2010,** 46, (9), 1001-1006.
830. Soshnikov, L. E.; Trukhan, V. M.; Marenkin, S. F. *Inorg Mater+* **2003,** 39, (4), 317-322.
831. Jeon, S.; Zhou, B. B.; Gyenis, A.; Feldman, B. E.; Kimchi, I.; Potter, A. C.; Gibson, Q. D.; Cava, R. J.; Vishwanath, A.; Yazdani, A. *Nat Mater* **2014,** 13, (9), 851-856.
832. Rosenberg, A. J.; Harman, T. C. *J Appl Phys* **1959,** 30, (10), 1621-1622.
833. Trukhan, V.; Izotov, A.; Shoukavaya, T. *Inorg Mater+* **2014,** 50, (9), 868-873.
834. Masumoto, K.; Isomura, S.; Sasaki, K. *Physica Status Solidi (a)* **1971,** 6, (2), 515-523.
835. Nayak, A.; Rao, D. R. *Appl Phys Lett* **1993,** 63, (5), 592-593.
836. Nayak, A.; Banerjee, H. *Mater Chem Phys* **1999,** 60, (1), 95-98.
837. Nayak, A.; Rao, D. *Mater Chem Phys* **1994,** 37, (3), 225-229.

838. Rao, D.; Nayak, A. *J Mater Sci* **1992,** 27, (16), 4389-4392.
839. Vitkina, T. Z.; Orlik, L. K.; Smolyarenko, E. M.; Ttrukhan, V. M. *Cryst Res Technol* **1986,** 21, (11), 1409-1412.
840. Palkina, K. K.; Mikhailov, S. G.; Marenkin, S. F.; Molchanov, A. V.; Vol'fkovich, A. Y. *Inorg Mater+* **2005,** 41, (9), 906-910.
841. Trukhan, V.; Yakimovich, V.; Rubtsov, V.; Vitkina, Z.; Orlik, L.; Roze, M. *physica status solidi (a)* **1992,** 130, (1), 83-89.
842. Mollaev, A. Y.; Arslanov, R.; Khokhlachev, P.; Dzhamamedov, R.; Marenkin, S.; Palkina, K.; Mikhailov, S. *Inorg Mater+* **2003,** 39, (8), 780-782.
843. Morozova, V.; Marenkin, S.; Mikhailov, S.; Koshelev, O. *Inorg Mater+* **2005,** 41, (10), 1039-1042.
844. Smolyarenko, E.; Trukhan, V.; Bologa, A. *physica status solidi (a)* **1985,** 87, (2), K123-K126.
845. Turner, W. J.; Fischler, A. S.; Reese, W. E. *Physical Review* **1961,** 121, (3), 759.
846. Roura, P.; Lousa, A.; Cornet, A.; Morenza, J. L.; Morante, J. R. *physica status solidi (a)* **1986,** 94, (1), K47-K50.
847. Kimball, G. M.; Bosco, J. P.; Müller, A. M.; Tajdar, S. F.; Brunschwig, B. S.; Atwater, H. A.; Lewis, N. S. *J Appl Phys* **2012,** 112, (10), 106101.
848. Ahn, J. H.; Oh, M. W.; Kim, B. S.; Park, S. D.; Min, B. K.; Lee, H. W.; Shim, Y. J. *Mater Res Bull* **2011,** 46, (9), 1490-1495.
849. Rouessac, F.; Ayral, R. M. *Journal of Alloys and Compounds* **2012,** 530, (0), 56-62.
850. Song, X.; Böttger, P. H. M.; Karlsen, O. B.; Finstad, T. G.; Taftø, J. *Physica Scripta* **2012,** 2012, (T148), 014001.
851. Shai, X.; Deng, S.; Shen, L.; Meng, D.; Li, D.; Zhang, Y.; Jiang, X. *physica status solidi (b)* **2015,** 252, (4), 795-799.
852. Tang, D.; Zhu, W.; Wei, P.; Zhou, H.; Liu, Z.; Yu, J.; Zhao, W. *J Electron Mater* **2015**, 1-7.
853. Jund, P.; Viennois, R.; Tao, X.; Niedziolka, K.; Tédenac, J.-C. *Physical Review B* **2012,** 85, (22), 224105.
854. Alireza, F.; Cynthia, S. L. *Journal of Physics: Condensed Matter* **2015,** 27, (12), 125502.
855. Niedziółka, K.; Jund, P. *J Electron Mater* **2015,** 44, (6), 1540-1546.
856. Murali, K. R.; Rao, D. R. *J Mater Sci Lett* **1983,** 2, (3), 132-136.
857. Catalano, A.; Bhushan, M. *Appl Phys Lett* **1980,** 37, (6), 567-569.
858. Yin, W.-J.; Yan, Y. *J Appl Phys* **2013,** 113, (1), 013708.
859. Bhushan, M. *J Appl Phys* **1982,** 53, (1), 514.
860. Kimball, G. M.; Lewis, N. S.; Atwater, H. A. In *Mg doping and alloying in Zn_3P_2 heterojunction solar cells*, Photovoltaic Specialists Conference (PVSC), 2010 35th IEEE, 20-25 June 2010, 2010; pp 001039-001043.
861. Januškevičius, Z.; Marceniuk, L.; Sakalas, A.; Sodeika, A. *physica status solidi (a)* **1980,** 59, (2), K139-K142.
862. Stamov, I. G.; Tkachenko, D. V. *Semiconductors* **2008,** 42, (6), 662-668.
863. Babu, V. S.; Vaya, P. R.; Sobhanadri, J. *Semiconductor Science and Technology* **1989,** 4, (7), 521.
864. Decroix, D.; Muñoz, V.; Chevy, A. *J Mater Sci* **1987,** 22, (4), 1265-1270.
865. Kato, Y.; Kurita, S.; Suda, T. *J Appl Phys* **1987,** 62, (9), 3733-3739.
866. Okamoto, H. *Journal of Phase Equilibria* **1992,** 13, (2), 155-161.
867. Yamaguchi, K.; Mikula, A.; Komarek, K.; Itagaki, K. *Zeitschrift für Metallkunde* **1991,** 82, (8), 591-598.
868. Marenkin, S.; Raukhman, A.; Pishchikov, D.; Lazarev, V. *Izvestiya Akademii Nauk-Rossijskaya Akademiya Nauk. Neorganicheskie Materialy* **1992,** 28, (9), 1813-1828.
869. Ugai, Y. A.; Zyubina, T. *IZV AKAD NAUK SSSR NEORGAN MATERIALY* **1966,** 2, (1), 9-16.
870. Nadtochii, Y.; Pischikov, D.; BURSTEV, Y.; Zakharov, S.; MARENKIN, S.; LAZAREV, V. *Inorg Mater+* **1992,** 28, (2), 208-212.
871. Stamov, I. G.; Syrbu, N. N.; Ursaki, V. V.; Dorogan, A. V. *Opt Commun* **2012,** 285, (13-14), 3104-3110.
872. Pietraszko, A.; Łukaszewicz, K. *physica status solidi (a)* **1973,** 18, (2), 723-730.
873. Pistorius, C. *High Temperatures-High Pressures* **1975,** 7, 441-449.
874. Greenberg, J. H.; Guskov, V. N.; Lazarev, V. B.; Kotliar, A. A. *Mater Res Bull* **1982,** 17, (10), 1329-1335.
875. Misiewicz, J.; Pawlikowski, J. M. *Solid State Commun* **1979,** 32, (8), 687-690.
876. Ugay, Y.; Gukov, O.; Domashevskaya, E.; Ozerov, L. *Neorg. Mater.* **1968,** 4, 147-148.
877. Berak, J.; Pruchnik, Z. *Roczniki Chemii* **1969,** 43, (6), 1141-&.

878. Schneider, M.; Krumnacker, M. *Neue Hütte* **1973,** 18, 715-718.
879. Tanaka, Y. **1969**.
880. Mowles, T. A. *Synthesis of monoclinic zinc diphosphide single crystals*; LBL-7661 United States 10.2172/6486530 Dep. NTIS, PC A04/MF A01. LBNL English; ; California Univ., Berkeley (USA). Lawrence Berkeley Lab.: 1978; p Medium: ED.
881. Fleet, M. E.; Mowles, T. A. *Acta Crystallographica Section C: Crystal Structure Communications* **1984,** 40, (11), 1778-1779.
882. Trukhan, V. M.; Yakimovich, V. N.; Rubtsov, V. A.; Z.Vitkina, T.; Orlik, L. K.; Roze, M. V. *Physica Status Solidi (a)* **1992,** 130, (1), 83-89.
883. Rubenstein, M.; DEAN, P. J. *J Appl Phys* **1970,** 41, (4), 1777-1786.
884. Gorban, I. S.; Grishchenko, G. A.; Sakalas, A. P.; Sodeika, A. S.; Tychina, I. I.; Tkachenko, A. K. *physica status solidi (a)* **1978,** 48, (2), 329-334.
885. Ryan, M. A.; Parkinson, B. A. *Appl Phys Lett* **1986,** 48, (25), 1754-1755.
886. Ray, B.; Burnet, P. *physica status solidi (b)* **1969,** 32, (1), K113-K115.
887. Sobolev, V. V.; Syrbu, N. N. *physica status solidi (b)* **1972,** 51, (2), 863-872.
888. Aleynikova, K.; Kozlov, A.; Kozlova, S.; Sobolev, V. *Moldavian Journal of the Physical Sciences* **2004,** 3, 137-148.
889. Morozova, V. A.; Marenkin, S. F.; Koshelev, O. G.; Trukhan, V. M. *Inorg Mater+* **2006,** 42, (3), 221-225.
890. Sobolev, V. V.; Kozlov, A. I.; Polygalov, Y. I.; Tupitsyn, V. E.; Poplavnoi, A. S. *physica status solidi (b)* **1989,** 154, (1), 377-388.
891. Lazarev, V. B.; Shevchenko, V. J.; Marenkin, S. F.; Magomedgadghiev, G. *Journal of Crystal Growth* **1977,** 38, (2), 275-276.
892. Pistorius, C.; Clark, J.; Geotzer, J. *High Press. High Temp* **1977,** 9, 471-482.
893. Misiewicz, J. *Journal of Physics: Condensed Matter* **1990,** 2, (8), 2053.
894. Kurbatov, L. N.; Dirochka, A. I.; Sinitsyn, E. V.; Lazarev, V. B.; Shevchenko, V. Y.; Kozlov, S. E. *Soviet Journal of Quantum Electronics* **1976,** 6, (2), 166.
895. Huldt, L.; Nilsson, N. G.; Sundström, B. O.; Żdanowicz, W. *Physica Status Solidi (a)* **1979,** 53, (1), K15-K18.
896. Kazmerski, L. L.; Ireland, P. J.; Catalano, A. *Journal of Vacuum Science & Technology* **1981,** 18, (2), 368-371.
897. Kentaro, I.; Yoshihiro, M.; Tatsuo, N.; Hidemi, T. *Japanese Journal of Applied Physics* **1981,** 20, (S2), 109.
898. Känel, H. v.; Hauger, R.; Wachter, P. *Solid State Commun* **1982,** 43, (8), 619-621.
899. Toshikazu, S.; Masahisa, S.; Shoichi, K. *Japanese Journal of Applied Physics* **1983,** 22, (10A), L656.
900. Pawlikowski, J. M. *Infrared Phys* **1988,** 28, (3), 177-182.
901. Kimball, G. M.; Lewis, N. S.; Atwater, H. A. In *Direct evidence of Mg-Zn-P alloy formation in Mg/Zn_3P_2 solar cells*, Photovoltaic Specialists Conference (PVSC), 2011 37th IEEE, 19-24 June 2011, 2011; pp 003381-003381.
902. DeWitt, B.; Seltz, H. *Journal of the American Chemical Society* **1939,** 61, (11), 3170-3173.
903. Tydlitat, V. *Czechoslovak Journal of Physics* **1959,** 9, (5), 638-640.
904. Takei, T. *Tohoku Imperial Univ. Sci. Rep* **1927,** 16, (8), 1031-1056.
905. Izard, V.; Record, M. C.; Tedenac, J. C.; Fries, S. G. *Calphad* **2001,** 25, (4), 567-581.
906. Gierlotka, W. *J Electron Mater* **2016,** 45, (4), 2216-2221.
907. Vuillard, G.; Piton, J. *COMPT REND ACAD SCI* **1966,** 263, (17), 1018-1021.
908. KONESKA, S. *Fizika* **1980,** 12, 143.
909. Pomrehn, G. S.; Toberer, E. S.; Snyder, G. J.; van de Walle, A. *J Am Chem Soc* **2011,** 133, (29), 11255-61.
910. He, A.; Svitlyk, V.; Chernyshov, D.; Mozharivskyj, Y. *Dalton Transactions* **2015,** 44, (48), 20983-20990.
911. Psarev, V.; Kuznetsov, A.; Kirii, V. *Soviet Physics Journal* **1980,** 23, (3), 254-256.
912. Zabdyr, L. A. *Journal of Phase Equilibria* **1992,** 13, (2), 130-135.
913. Minić, D.; Manasijević, D.; Ćosovic, V.; Talijan, N.; Živković, Ž.; Živković, D.; Premović, M. *Journal of Alloys and Compounds* **2012,** 517, 31-39.
914. Gierlotka, W. *Journal of Mining and Metallurgy B: Metallurgy* **2014,** 50, (2), 149-155.
915. Fedorov, M. I.; Prokof'eva, L. V.; Pshenay-Severin, D. A.; Shabaldin, A. A.; Konstantinov, P. P. *J Electron Mater* **2014,** 43, (6), 2314-2319.
916. Shaver, P.; Blair, J. *Physical Review* **1966,** 141, (2), 649.
917. Závêtová, M. *physica status solidi (b)* **1964,** 5, (1), K19-K21.

918. Keloglu, Y. P.; Fedorko, A. S. *Journal of Structural Chemistry* **1965,** 5, (2), 213-217.
919. Seebeck, T. J. *Annalen der Physik* **1826,** 82, (3), 253-286.
920. Okamura, C.; Ueda, T.; Hasezaki, K. *Materials transactions* **2010,** 51, (5), 860-862.
921. Xiong, D.-B.; Okamoto, N. L.; Inui, H. *Scripta Mater* **2013,** 69, (5), 397-400.
922. Toberer, E. S.; Rauwel, P.; Gariel, S.; Tafto, J.; Jeffrey Snyder, G. *J Mater Chem* **2010,** 20, (44), 9877-9885.
923. Caillat, T.; Fleurial, J. P.; Borshchevsky, A. *J Phys Chem Solids* **1997,** 58, (7), 1119-1125.
924. Ur, S.-C.; Kim, I.-H.; Nash, P. *J Mater Sci* **2007,** 42, (6), 2143-2149.
925. Haussermann, U.; Mikhaylushkin, A. S. *Dalton Transactions* **2010,** 39, (4), 1036-1045.
926. Bhattacharya, S.; Hermann, R. P.; Keppens, V.; Tritt, T. M.; Snyder, G. J. *Physical Review B* **2006,** 74, (13), 134108.
927. Toberer, E. S.; Sasaki, K. A.; Chisholm, C. R. I.; Haile, S. M.; Goddard, W. A.; Snyder, G. J. *physica status solidi (RRL) – Rapid Research Letters* **2007,** 1, (6), 253-255.
928. Qi, D.; Tang, X.; Li, H.; Yan, Y.; Zhang, Q. *J Electron Mater* **2010,** 39, (8), 1159-1165.
929. Rauwel, P.; Løvvik, O. M.; Rauwel, E.; Toberer, E. S.; Snyder, G. J.; Taftø, J. *physica status solidi (a)* **2011,** 208, (7), 1652-1657.
930. Zou, T. H.; Qin, X. Y.; Li, D.; Sun, G. L.; Dou, Y. C.; Wang, Q. Q.; Ren, B. J.; Zhang, J.; Xin, H. X.; Li, Y. Y. *Appl Phys Lett* **2014,** 104, (1), 013904.
931. Tsutsui, M.; Zhang, L.; Ito, K.; Yamaguchi, M. *Intermetallics* **2004,** 12, (7), 809-813.
932. Pedersen, B. L.; Birkedal, H.; Nygren, M.; Frederiksen, P. T.; Iversen, B. B. In *The effect of Mg doping on the thermoelectric performance of Zn 4 Sb 3*, Thermoelectrics, 2007. ICT 2007. 26th International Conference on, 2007; IEEE: pp 382-385.
933. Nakamoto, G.; Akai, N.; Kurisu, M.; Kim, I.-H.; Ur, S.-C.; Kuznetsov, V. *Journal of alloys and compounds* **2007,** 432, (1), 116-121.
934. Didchenko, R.; Alix, J.; Toeniskoetter, R. *Journal of Inorganic and Nuclear Chemistry* **1960,** 14, (1-2), 35-37.
935. Manasevit, H. *Journal of Crystal Growth* **1972,** 13, 306-314.
936. Manasevit, H.; Simpson, W. I. *J Electrochem Soc* **1969,** 116, (12), 1725-1732.
937. Manasevit, H. M. *Appl Phys Lett* **1968,** 12, (4), 156-159.
938. Cui, Y.; Lauhon, L. J.; Gudiksen, M. S.; Wang, J.; Lieber, C. M. *Appl Phys Lett* **2001,** 78, (15), 2214-2216.
939. Hochbaum, A. I.; Fan, R.; He, R. R.; Yang, P. D. *Nano Letters* **2005,** 5, (3), 457-460.
940. De Broglie, L. Recherches sur la théorie des quanta. Migration-université en cours d'affectation, 1924.
941. Knoll, M.; Ruska, E. *Zeitschrift für Physik A Hadrons and Nuclei* **1932,** 78, (5), 318-339.
942. Spurr, A. R. *Journal of ultrastructure research* **1969,** 26, (1-2), 31-43.
943. Müller, E. W. *Zeitschrift für Physik A Hadrons and Nuclei* **1937,** 106, (9), 541-550.
944. Müller, E. W.; Bahadur, K. *Physical Review* **1956,** 102, (3), 624.
945. Panitz, J. A. *Rev Sci Instrum* **1973,** 44, (8), 1034-1038.
946. Miller, M. K.; Kelly, T. F.; Rajan, K.; Ringer, S. P. *Mater Today* **2012,** 15, (4), 158-165.
947. Seidman, D. N. *Annual Review of Materials Research* **2007,** 37, 127-158.
948. Gault, B.; Moody, M. P.; Cairney, J. M.; Ringer, S. P., *Atom probe microscopy*. Springer Science & Business Media: 2012; Vol. 160.
949. Gilliland, G. D. *Materials Science and Engineering: R: Reports* **1997,** 18, (3-6), 99-399.
950. Wallentin, J.; Borgström, M. T. *J Mater Res* **2011,** 26, (17), 2142-2156.
951. Dalpian, G. M.; Chelikowsky, J. R. *Phys Rev Lett* **2006,** 96, (22), -.
952. Zhang, S. B. *Journal of Physics: Condensed Matter* **2002,** 14, (34), R881.
953. Rojo, M. M.; Calero, O. C.; Lopeandia, A. F.; Rodriguez-Viejo, J.; Martin-Gonzalez, M. *Nanoscale* **2013,** 5, (23), 11526-11544.
954. Perea, D. E.; Wijaya, E.; Lensch-Falk, J. L.; Hemesath, E. R.; Lauhon, L. J. *Journal of Solid State Chemistry* **2008,** 181, (7), 1642-1649.
955. Park, H.; Beresford, R.; Hong, S.; Xu, J. *J Appl Phys* **2010,** 108, (9), 094308-9.
956. Sladek, K.; Klinger, V.; Wensorra, J.; Akabori, M.; Hardtdegen, H.; Grützmacher, D. *Journal of Crystal Growth* **2010,** 312, (5), 635-640.
957. Burgess, T.; Saxena, D.; Mokkapati, S.; Li, Z.; Hall, C. R.; Davis, J. A.; Wang, Y.; Smith, L. M.; Fu, L.; Caroff, P.; Tan, H. H.; Jagadish, C. *Nat Commun* **2016,** 7, 11927.
958. Joyce, H. J.; Gao, Q.; Tan, H. H.; Jagadish, C.; Kim, Y.; Zhang, X.; Guo, Y. N.; Zou, J. *Nano Letters* **2007,** 7, (4), 921-926.
959. Du, S.; Burgess, T.; Tjing Loi, S.; Gault, B.; Gao, Q.; Bao, P.; Li, L.; Cui, X.; Kong Yeoh, W.; Hoe Tan, H.; Jagadish, C.; Ringer, S. P.; Zheng, R. *Ultramicroscopy* **2013,** 124, (0), 96-101.

960. Xudong, W.; Christopher, J. S.; Zhong Lin, W., Self-attraction among aligned Au/ZnO nanorods under electron beam. AIP: 2005; Vol. 86, p 013111.
961. Dai, X.; Dayeh, S. A.; Veeramuthu, V.; Larrue, A.; Wang, J.; Su, H.; Soci, C. *Nano Letters* **2011,** 11, (11), 4947-4952.
962. Jinzhang, L.; Soonil, L.; Kyungmoon, L.; Ahn, Y. H.; Ji-Yong, P.; Ken Ha, K. *Nanotechnology* **2008,** 19, (18), 185607.
963. Sun, Z.; Wang, D.; Xiang, J. *ACS Nano* **2014,** 8, (11), 11261-11267.
964. Zhou, M.; Tian, Y.; Zeng, H.; Pesika, N.; Israelachvili, J. *Advanced Materials Interfaces* **2015,** 2, (5), 1400466.
965. Krogstrup, P.; Curiotto, S.; Johnson, E.; Aagesen, M.; Nyg; aring; rd, J.; Chatain, D. *Phys Rev Lett* **2011,** 106, (12), 125505.
966. Dheeraj, D. L.; Patriarche, G.; Zhou, H.; Harmand, J. C.; Weman, H.; Fimland, B. O. *Journal of Crystal Growth* **2009,** 311, (7), 1847-1850.
967. Jabeen, F.; Patriarche, G.; Glas, F.; Harmand, J. C. *Journal of Crystal Growth* **2011,** 323, (1), 293-296.
968. Boulanger, J. P.; LaPierre, R. R. *Journal of Crystal Growth* **2014,** 388, 116-123.
969. Paladugu, M.; Zou, J.; Guo, Y. N.; Zhang, X.; Kim, Y.; Joyce, H. J.; Gao, Q.; Tan, H. H.; Jagadish, C. *Appl Phys Lett* **2008,** 93, (10), 1911.
970. Krogstrup, P.; Yamasaki, J.; Sorensen, C. B.; Johnson, E.; Wagner, J. B.; Pennington, R.; Aagesen, M.; Tanaka, N.; Nygard, J. *Nano Letters* **2009,** 9, (11), 3689-3693.
971. Bauer, J.; Gottschalch, V.; Paetzelt, H.; Wagner, G. *Journal of Crystal Growth* **2008,** 310, (23), 5106-5110.
972. Hocevar, M.; Immink, G.; Verheijen, M.; Akopian, N.; Zwiller, V.; Kouwenhoven, L.; Bakkers, E. *Nat Commun* **2012,** 3, 1266.
973. Boulanger, J. P.; LaPierre, R. R. *Journal of Crystal Growth* **2011,** 332, (1), 21-26.
974. Jeppsson, M.; Dick, K. A.; Wagner, J. B.; Caroff, P.; Deppert, K.; Samuelson, L.; Wernersson, L.-E. *Journal of Crystal Growth* **2008,** 310, (18), 4115-4121.
975. Verheijen, M. A.; Immink, G.; de Smet, T.; Borgstrom, M. T.; Bakkers, E. *Journal of the American Chemical Society* **2006,** 128, (4), 1353-1359.
976. Guoqiang, Z.; Kouta, T.; Hideki, G.; Tetsuomi, S.; Hidetoshi, N. *Japanese Journal of Applied Physics* **2010,** 49, (1R), 015001.
977. Borgstrom, M. T.; Verheijen, M. A.; Immink, G.; de Smet, T.; Bakkers, E. *Nanotechnology* **2006,** 17, (16), 4010-4013.
978. Priante, G.; Patriarche, G.; Oehler, F.; Glas, F.; Harmand, J.-C. *Nano Letters* **2015**.
979. Okamoto, H.; Massalski, T. B. *Bulletin of Alloy Phase Diagrams* **1984,** 5, (4), 378-379.
980. Kuech, T. F.; Tischler, M. A.; Wang, P. J.; Scilla, G.; Potemski, R.; Cardone, F. *Appl Phys Lett* **1988,** 53, (14), 1317-1319.
981. van de Ven, J.; Schoot, H. G.; Giling, L. J. *J Appl Phys* **1986,** 60, (5), 1648-1660.
982. Lee, B. J.; Houng, Y. M.; Miller, J. N.; Turner, J. E. *Journal of Crystal Growth* **1990,** 105, (1), 168-177.
983. Borgstrom, M. T.; Wallentin, J.; Tragardh, J.; Ramvall, P.; Ek, M.; Wallenberg, L. R.; Samuelson, L.; Deppert, K. *Nano Res* **2010,** 3, (4), 264-270.
984. Joyce, H. J.; Gao, Q.; Tan, H. H.; Jagadish, C.; Kim, Y.; Fickenscher, M. A.; Perera, S.; Hoang, T. B.; Smith, L. M.; Jackson, H. E.; Yarrison-Rice, J. M.; Zhang, X.; Zou, J. *Nano Letters* **2009,** 9, (2), 695-701.
985. Zou, J.; Paladugu, M.; Wang, H.; Auchterlonie, G. J.; Guo, Y. N.; Kim, Y.; Gao, Q.; Joyce, H. J.; Tan, H. H.; Jagadish, C. *Sml* **2007,** 3, (3), 389-393.
986. Jiang, N.; Wong-Leung, J.; Joyce, H. J.; Gao, Q.; Tan, H. H.; Jagadish, C. *Nano Letters* **2014,** 14, (10), 5865-72.
987. Zhou, H. L.; Hoang, T. B.; Dheeraj, D. L.; Helvoort, A. T. J. v.; Liu, L.; Harmand, J. C.; Fimland, B. O.; Weman, H. *Nanotechnology* **2009,** 20, (41), 415701.
988. Montazeri, M.; Fickenscher, M.; Smith, L. M.; Jackson, H. E.; Yarrison-Rice, J.; Kang, J. H.; Gao, Q.; Tan, H. H.; Jagadish, C.; Guo, Y. N.; Zou, J.; Pistol, M. E.; Pryor, C. E. *Nano Letters* **2010,** 10, (3), 880-886.
989. Grönqvist, J.; Søndergaard, N.; Boxberg, F.; Guhr, T.; Åberg, S.; Xu, H. Q. *J Appl Phys* **2009,** 106, (5), 053508.
990. Brune, H.; Bromann, K.; Röder, H.; Kern, K.; Jacobsen, J.; Stoltze, P.; Jacobsen, K.; No/rskov, J. *Physical Review B* **1995,** 52, (20), R14380-R14383.
991. Penev, E.; Kratzer, P.; Scheffler, M. *Physical Review B* **2001,** 64, (8), 085401.

992. Dubrovskii, V. G.; Sibirev, N. V.; Cirlin, G. E.; Soshnikov, I. P.; Chen, W. H.; Larde, R.; Cadel, E.; Pareige, P.; Xu, T.; Grandidier, B.; Nys, J.-P.; Stievenard, D.; Moewe, M.; Chuang, L. C.; Chang-Hasnain, C. *Physical Review B* **2009,** 79, (20), 205316.
993. Froberg, L. E.; Seifert, W.; Johansson, J. *Physical Review B* **2007,** 76, (15), 3401.
994. Johansson, J.; Svensson, C. P. T.; Martensson, T.; Samuelson, L.; Seifert, W. *J. Phys. Chem. B* **2005,** 109, (28), 13567-13571.
995. Allen, J. E.; Hemesath, E. R.; Perea, D. E.; Lensch-Falk, J. L.; Li, Z. Y.; Yin, F.; Gass, M. H.; Wang, P.; Bleloch, A. L.; Palmer, R. E.; Lauhon, L. J. *Nat Nanotechnol* **2008,** 3, (3), 168-73.
996. Schwalbach, E. J.; Voorhees, P. W. *Nano Letters* **2008,** 8, (11), 3739-3745.
997. Guo, Y. N.; Burgess, T.; Gao, Q.; Tan, H. H.; Jagadish, C.; Zou, J. *Nano Lett* **2013,** 13, (11), 5085-9.
998. Agrawal, R.; Bernal, R. A.; Isheim, D.; Espinosa, H. D. *The Journal of Physical Chemistry C* **2011,** 115, (36), 17688-17694.
999. Xu, T.; Nys, J. P.; Grandidier, B.; Stievenard, D.; Coffinier, Y.; Boukherroub, R.; Larde, R.; Cadel, E.; Pareige, P. *J Vac Sci Technol B* **2008,** 26, (6), 1960-1963.
1000. Du, S.; Burgess, T.; Gault, B.; Gao, Q.; Bao, P.; Li, L.; Cui, X.; Kong Yeoh, W.; Liu, H.; Yao, L.; Ceguerra, A. V.; Hoe Tan, H.; Jagadish, C.; Ringer, S. P.; Zheng, R. *Ultramicroscopy* **2013,** 132, (0), 186-92.
1001. Kingham, D. R. *Surf Sci* **1982,** 116, (2), 273-301.
1002. Leonard, F.; Talin, A. A. *Nat Nano* **2011,** 6, (12), 773-783.
1003. Suyatin, D. B.; Jain, V.; Nebol'sin, V. A.; Tragardh, J.; Messing, M. E.; Wagner, J. B.; Persson, O.; Timm, R.; Mikkelsen, A.; Maximov, I.; Samuelson, L.; Pettersson, H. *Nat Commun* **2014,** 5, 3221.
1004. Gutsche, C.; Lysov, A.; Regolin, I.; Brodt, A.; Liborius, L.; Frohleiks, J.; Prost, W.; Tegude, F.-J. *J Appl Phys* **2011,** 110, (1), 014305.
1005. Torkhov, N. A. *Semiconductors* **2003,** 37, (10), 1177-1184.
1006. Sawada, T.; Hasegawa, H. *Thin Solid Films* **1979,** 56, (1–2), 183-200.
1007. Demichel, O.; Heiss, M.; Bleuse, J.; Mariette, H.; Fontcuberta i Morral, A. *Appl Phys Lett* **2010,** 97, (20), 201907.
1008. Han, N.; Wang, F.; Yip, S.; Hou, J. J.; Xiu, F.; Shi, X.; Hui, A. T.; Hung, T.; Ho, J. C. *Appl Phys Lett* **2012,** 101, (1), 013105.
1009. Schricker, A. D.; Davidson, F. M.; Wiacek, R. J.; Korgel, B. A. *Nanotechnology* **2006,** 17, (10), 2681-2688.
1010. Ryoichi, F.; Moriaki, W.; Kimihiro, O.; Hajime, O. *Japanese Journal of Applied Physics* **1986,** 25, (4R), 652.
1011. LaPierre, R. R. *J Appl Phys* **2011,** 109, (3), 034311-9.
1012. Tajik, N.; Chia, A. C. E.; LaPierre, R. R. *Appl Phys Lett* **2012,** 100, (20), 203122.
1013. Chang, C.-C.; Chi, C.-Y.; Yao, M.; Huang, N.; Chen, C.-C.; Theiss, J.; Bushmaker, A. W.; LaLumondiere, S.; Yeh, T.-W.; Povinelli, M. L.; Zhou, C.; Dapkus, P. D.; Cronin, S. B. *Nano Letters* **2012,** 12, (9), 4484-4489.
1014. Sze, S. M.; Irvin, J. C. *Solid State Electron* **1968,** 11, (6), 599-602.
1015. Cavallini, A.; Polenta, L.; Rossi, M.; Stoica, T.; Calarco, R.; Meijers, R. J.; Richter, T.; Lüth, H. *Nano Letters* **2007,** 7, (7), 2166-2170.
1016. Baumgartner, P.; Engel, C.; Böhm, G.; Abstreiter, G. *Appl Phys Lett* **1997,** 70, (21), 2876-2878.
1017. Thunich, S.; Prechtel, L.; Spirkoska, D.; Abstreiter, G.; Fontcuberta i Morral, A.; Holleitner, A. W. *Appl Phys Lett* **2009,** 95, (8), 083111-3.
1018. Casey, H. C.; Stern, F. *J Appl Phys* **1976,** 47, (2), 631-643.
1019. Casey, H. C.; Sell, D. D.; Wecht, K. W. *J Appl Phys* **1975,** 46, (1), 250-257.
1020. Meng, Q.; Jiang, C.; Mao, S. X. *Journal of Crystal Growth* **2008,** 310, (20), 4481-4486.
1021. Li, Q.; Gong, X.; Wang, C.; Wang, J.; Ip, K.; Hark, S. *Advanced Materials* **2004,** 16, (16), 1436-1440.
1022. Fan, X.; Meng, X. M.; Zhang, X. H.; Zhang, M. L.; Jie, J. S.; Zhang, W. J.; Lee, C. S.; Lee, S. T. *J Phys Chem C* **2009,** 113, (3), 834-838.
1023. Wang, Y. Q.; Philipose, U.; Xu, T.; Ruda, H. E.; Kavanagh, K. L. *Semiconductor Science and Technology* **2007,** 22, (3), 175.
1024. Hao, Y. F.; Meng, G. W.; Wang, Z. L.; Ye, C. H.; Zhang, L. D. *Nano Letters* **2006,** 6, (8), 1650-1655.
1025. Wang, J.; Sun, X. W.; Xie, S.; Zhou, W.; Yang, Y. *Cryst Growth Des* **2007,** 8, (2), 707-710.
1026. Kim, S.; Na, S.; Jeon, H.; Lee, B.; Yang, J.; Kim, H.; Lee, H. J. *Nanotechnology* **2013,** 24, (6), 065703.

1027. Wang, D.-H.; Di, X.; Qing, W.; Ya-Juan, H.; Guo-Qiang, J.; Xiang-Yun, G.; Tu, K. N. *Nanotechnology* **2008,** 19, (21), 215602.
1028. Verheijen, M. A.; Algra, R. E.; Borgstrom, M. T.; Immink, G.; Sourty, E.; van Enckevort, W. J. P.; Vlieg, E.; Bakkers, E. *Nano Letters* **2007,** 7, (10), 3051-3055.
1029. Dayeh, S. A.; Yu, E. T.; Wang, D. L. *Nano Letters* **2009,** 9, (5), 1967-1972.
1030. Avramov, I. *Nanoscale Res Lett* **2007,** 2, (5), 235-239.
1031. Landre, O.; Bougerol, C.; Renevier, H.; Daudin, B. *Nanotechnology* **2009,** 20, (41), 415602.
1032. Lin, P. A.; Liang, D.; Reeves, S.; Gao, X. P. A.; Sankaran, R. M. *Nano Letters* **2012,** 12, (1), 315-320.
1033. Froeberg, L. E.; Wacaser, B. A.; Wagner, J. B.; Jeppesen, S.; Ohlsson, B. J.; Deppert, K.; Samuelson, L. *Nano Letters* **2008,** 8, (11), 3815-3818.
1034. Pan, D.; Fu, M.; Yu, X.; Wang, X.; Zhu, L.; Nie, S.; Wang, S.; Chen, Q.; Xiong, P.; von Molnár, S.; Zhao, J. *Nano Letters* **2014,** 14, (3), 1214-1220.
1035. Paiman, S.; Gao, Q.; Tan, H. H.; Jagadish, C.; Pemasiri, K.; Montazeri, M.; Jackson, H. E.; Smith, L. M.; Yarrison-Rice, J. M.; Zhang, X.; Zou, J. *Nanotechnology* **2009,** 20, (22), 25606.
1036. Jensen, L. E.; Bjork, M. T.; Jeppesen, S.; Persson, A. I.; Ohlsson, B. J.; Samuelson, L. *Nano Letters* **2004,** 4, (10), 1961-1964.
1037. Dubrovskiĭ, V.; Sibirev, N.; Suris, R.; Cirlin, G.; Ustinov, V.; Tchernysheva, M.; Harmand, J. *Semiconductors* **2006,** 40, (9), 1075-1082.
1038. Peter, K.; Henrik, I. J.; Erik, J.; Morten Hannibal, M.; Claus, B. S.; Anna Fontcuberta i, M.; Martin, A.; Jesper, N.; Frank, G. *Journal of Physics D: Applied Physics* **2013,** 46, (31), 313001.
1039. Bao, J. M.; Bell, D. C.; Capasso, F.; Wagner, J. B.; Martensson, T.; Tragardh, J.; Samuelson, L. *Nano Letters* **2008,** 8, (3), 836-841.
1040. Ikejiri, K.; Kitauchi, Y.; Tomioka, K.; Motohisa, J.; Fukui, T. *Nano Letters* **2011,** 11, (10), 4314-4318.
1041. Ek, M.; Borgström, M. T.; Karlsson, L. S.; Hetherington, C. J. D.; Wallenberg, L. R. *Microscopy and Microanalysis* **2011,** 17, (05), 752-758.
1042. de la Mata, M.; Magen, C.; Gazquez, J.; Utama, M. I. B.; Heiss, M.; Lopatin, S.; Furtmayr, F.; Fernández-Rojas, C. J.; Peng, B.; Morante, J. R.; Rurali, R.; Eickhoff, M.; Fontcuberta i Morral, A.; Xiong, Q.; Arbiol, J. *Nano Letters* **2012,** 12, (5), 2579-2586.
1043. Karlsson, L. S.; Dick, K. A.; Wagner, J. B.; Malm, J. O.; Deppert, K.; Samuelson, L.; Wallenberg, L. R. *Nanotechnology* **2007,** 18, (48), 85717.
1044. Chiaramonte, T.; Tizei, L. H. G.; Ugarte, D.; Cotta, M. n. A. *Nano Letters* **2011**, null-null.
1045. Harmand, J. C.; Patriarche, G.; Pere-Laperne, N.; Merat-Combes, M. N.; Travers, L.; Glas, F. *Appl Phys Lett* **2005,** 87, (20), 3101.
1046. Persson, A. I.; Larsson, M. W.; Stenstrom, S.; Ohlsson, B. J.; Samuelson, L.; Wallenberg, L. R. *Nature Materials* **2004,** 3, (10), 677-681.
1047. Bolinsson, J.; Caroff, P.; Mandl, B.; Dick, K. A. *Nanotechnology* **2011,** 22, (26), 265606.
1048. Moll, N.; Kley, A.; Pehlke, E.; Scheffler, M. *Physical Review B* **1996,** 54, (12), 8844-8855.
1049. Heiss, M.; Fontana, Y.; Gustafsson, A.; Wüst, G.; Magen, C.; O'Regan, D. D.; Luo, J. W.; Ketterer, B.; Conesa-Boj, S.; Kuhlmann, A. V.; Houel, J.; Russo-Averchi, E.; Morante, J. R.; Cantoni, M.; Marzari, N.; Arbiol, J.; Zunger, A.; Warburton, R. J.; Fontcuberta i Morral, A. *Nat. Mater.* **2013,** 12, (5), 439-444.
1050. Zheng, C.; Wong-Leung, J.; Gao, Q.; Tan, H. H.; Jagadish, C.; Etheridge, J. *Nano Letters* **2013,** 13, (8), 3742-3748.
1051. Ross, F. M.; Tersoff, J.; Reuter, M. C. *Phys Rev Lett* **2005,** 9514, (14), 6104.
1052. Shim, H. W.; Zhang, Y.; Huang, H. *J Appl Phys* **2008,** 104, (6), 063511.
1053. Xiaolong, L.; Dubrovskii, V. G.; Xiaomin, R. *Journal of Physics: Condensed Matter* **2013,** 25, (21), 215302.
1054. Gottschalk, H.; Patzer, G.; Alexander, H. *physica status solidi (a)* **1978,** 45, (1), 207-217.
1055. Liu, Q. K. K.; Moll, N.; Scheffler, M.; Pehlke, E. *Physical Review B* **1999,** 60, (24), 17008-17015.
1056. Glas, F. *J Appl Phys* **2010,** 108, (7), 073506-6.
1057. Chatillon, C.; Hodaj, F.; Pisch, A. *Journal of Crystal Growth* **2009,** 311, (14), 3598-3608.
1058. Dubrovskii, V. G.; Sibirev, N. V. *Journal of Crystal Growth* **2007,** 304, (2), 504-513.
1059. Wen, C. Y.; Tersoff, J.; Reuter, M. C.; Stach, E. A.; Ross, F. M. *Phys Rev Lett* **2010,** 105, (19), 195502.
1060. Dubrovskii, V. G. *Physical Review B* **2013,** 87, (19), 195426.
1061. Ma, R.-M.; Yin, X.; Oulton, R. F.; Sorger, V. J.; Zhang, X. *Nano Letters* **2012,** 12, (10), 5396-5402.

1062. Miller, D. A. B. *P Ieee* **2009,** 97, (7), 1166-1185.
1063. Piccione, B.; Cho, C.-H.; van Vugt, L. K.; Agarwal, R. *Nat Nano* **2012,** 7, (10), 640-645.
1064. Garcia-Vidal, F. J.; Moreno, E. *Nature* **2009,** 461, (7264), 604-605.
1065. Lu, Y.-J.; Kim, J.; Chen, H.-Y.; Wu, C.; Dabidian, N.; Sanders, C. E.; Wang, C.-Y.; Lu, M.-Y.; Li, B.-H.; Qiu, X.; Chang, W.-H.; Chen, L.-J.; Shvets, G.; Shih, C.-K.; Gwo, S. *Science* **2012,** 337, (6093), 450-453.
1066. Das, A.; Heo, J.; Jankowski, M.; Guo, W.; Zhang, L.; Deng, H.; Bhattacharya, P. *Phys Rev Lett* **2011,** 107, (6), 066405.
1067. Chu, S.; Wang, G.; Zhou, W.; Lin, Y.; Chernyak, L.; Zhao, J.; Kong, J.; Li, L.; Ren, J.; Liu, J. *Nat Nanotechnol* **2011,** advance online publication.
1068. Ho, J.; Tatebayashi, J.; Sergent, S.; Fong, C. F.; Iwamoto, S.; Arakawa, Y. *ACS Photonics* **2015,** 2, (1), 165-171.
1069. Montazeri, M.; Jackson, H. E.; Smith, L. M.; Yarrison-Rice, J. M.; Kang, J.-H.; Gao, Q.; Tan, H. H.; Jagadish, C. *Nano Letters* **2012,** 12, (10), 5389-5395.
1070. Paniagua-Dominguez, R.; Grzela, G.; Rivas, J. G.; Sanchez-Gil, J. A. *Nanoscale* **2013,** 5, (21), 10582-10590.
1071. Li, Z.; Wenas, Y. C.; Fu, L.; Mokkapati, S.; Tan, H. H.; Jagadish, C. *Ieee J Photovolt* **2015,** 5, (3), 854-864.
1072. Ohno, Y.; Francis, P.; Nogome, M.; Yuji, T. *Electron Devices, IEEE Transactions on* **1999,** 46, (1), 214-219.
1073. Kazuyuki, H.; Takao, N.; Akihiko, U.; Masayuki, U. *Japanese Journal of Applied Physics* **1991,** 30, (12S), 3741.
1074. Capiod, P.; Xu, T.; Nys, J. P.; Berthe, M.; Patriarche, G.; Lymperakis, L.; Neugebauer, J.; Caroff, P.; Dunin-Borkowski, R. E.; Ebert, P.; Grandidier, B. *Appl Phys Lett* **2013,** 103, (12), 122104.
1075. Darling, R. B. *Physical Review B* **1991,** 43, (5), 4071-4083.
1076. Yin, X.; Chen, H. M.; Pollak, F. H.; Chan, Y.; Montano, P. A.; Kirchner, P. D.; Pettit, G. D.; Woodall, J. M. *Journal of Vacuum Science & Technology A* **1992,** 10, (1), 131-136.
1077. Joyce, H. J.; Docherty, C. J.; Gao, Q.; Tan, H. H.; Jagadish, C.; Lloyd-Hughes, J.; Herz, L. M.; Johnston, M. B. *Nanotechnology* **2013,** 24, (21), 214006.
1078. Ito, H.; Ishibashi, T. *Japanese Journal of Applied Physics* **1994,** 33, (1R), 88.
1079. Parkinson, P.; Lloyd-Hughes, J.; Gao, Q.; Tan, H. H.; Jagadish, C.; Johnston, M. B.; Herz, L. M. *Nano Letters* **2007,** 7, (7), 2162-2165.
1080. Lundstrom, M. S.; Klausmeier-Brown, M. E.; Melloch, M. R.; Ahrenkiel, R. K.; Keyes, B. M. *Solid State Electron* **1990,** 33, (6), 693-704.
1081. Wolfe, C. M.; Stillman, G. E.; Lindley, W. T. *J Appl Phys* **1970,** 41, (7), 3088-3091.
1082. Saito, K.; Tokumitsu, E.; Akatsuka, T.; Miyauchi, M.; Yamada, T.; Konagai, M.; Takahashi, K. *J Appl Phys* **1988,** 64, (8), 3975-3979.
1083. Ahrenkiel, R. K.; Dunlavy, D. J.; Keyes, B.; Vernon, S. M.; Dixon, T. M.; Tobin, S. P.; Miller, K. L.; Hayes, R. E. *Appl Phys Lett* **1989,** 55, (11), 1088-1090.
1084. Lush, G. B.; MacMillan, H. F.; Keyes, B. M.; Levi, D. H.; Melloch, M. R.; Ahrenkiel, R. K.; Lundstrom, M. S. *J Appl Phys* **1992,** 72, (4), 1436-1442.
1085. Ahrenkiel, R. K.; Ellingson, R.; Metzger, W.; Lubyshev, D. I.; Liu, W. K. *Appl Phys Lett* **2001,** 78, (13), 1879-1881.
1086. Strauss, U.; Rühle, W. W.; Köhler, K. *Appl Phys Lett* **1993,** 62, (1), 55-57.
1087. Capizzi, M.; Modesti, S.; Frova, A.; Staehli, J. L.; Guzzi, M.; Logan, R. A. *Physical Review B* **1984,** 29, (4), 2028-2035.
1088. Benz, G.; Conradt, R. *Physical Review B* **1977,** 16, (2), 843-855.
1089. Faustino, M.; Giacomo, P.; Silvia, R. *Semiconductor Science and Technology* **2015,** 30, (5), 055020.
1090. Moewe, M.; Chuang, L. C.; Crankshaw, S.; Chase, C.; Chang-Hasnain, C. *Appl Phys Lett* **2008,** 93, (2), 023116.
1091. Kusch, P.; Breuer, S.; Ramsteiner, M.; Geelhaar, L.; Riechert, H.; Reich, S. *Physical Review B* **2012,** 86, (7), 075317.
1092. Signorello, G.; Lörtscher, E.; Khomyakov, P. A.; Karg, S.; Dheeraj, D. L.; Gotsmann, B.; Weman, H.; Riel, H. *Nat Commun* **2014,** 5.
1093. Ettenberg, M.; Nuese, C. J. *J Appl Phys* **1975,** 46, (8), 3500-3508.
1094. Lu, Z. H.; Hanna, M. C.; Majerfeld, A. *Appl Phys Lett* **1994,** 64, (1), 88-90.
1095. Lysov, A.; et al. *Nanotechnology* **2011,** 22, (8), 085702.

1096. Leonard, F.; Talin, A. A.; Swartzentruber, B. S.; Picraux, S. T. *Phys Rev Lett* **2009,** 102, (10), 106805.
1097. Büyükköse, S.; Hernández-Mínguez, A.; Vratzov, B.; Somaschini, C.; Geelhaar, L.; Riechert, H.; Wiel, W. G. v. d.; Santos, P. V. *Nanotechnology* **2014,** 25, (13), 135204.
1098. Wang, Y.; Montazeri, M.; Jackson, H. E.; Smith, L. M.; Burgess, T.; Paiman, S.; Gao, Q.; Tan, H. H.; Jagadish, C. *In preparation* **2014**.
1099. Titova, L. V.; Hoang, T. B.; Jackson, H. E.; Smith, L. M.; Yarrison-Rice, J. M.; Kim, Y.; Joyce, H. J.; Tan, H. H.; Jagadish, C. *Appl Phys Lett* **2006,** 89, (17), 73126.
1100. Hoang, T. B.; Titova, L. V.; Yarrison-Rice, J. M.; Jackson, H. E.; Govorov, A. O.; Kim, Y.; Joyce, H. J.; Tan, H. H.; Jagadish, C.; Smith, L. M. *Nano Letters* **2007,** 7, (3), 588-595.
1101. Mayer, G.; Maile, B. E.; Germann, R.; Forchel, A.; Meier, H. P. *Superlattice Microst* **1989,** 5, (4), 579-582.
1102. Izrael, A.; Sermage, B.; Marzin, J. Y.; Ougazzaden, A.; Azoulay, R.; Etrillard, J.; Thierry-Mieg, V.; Henry, L. *Appl Phys Lett* **1990,** 56, (9), 830-832.
1103. Wang, P. D.; Sotomayor Torres, C. M.; Benisty, H.; Weisbuch, C.; Beaumont, S. P. *Appl Phys Lett* **1992,** 61, (8), 946-948.
1104. Clausen, E. M.; Craighead, H. G.; Worlock, J. M.; Harbison, J. P.; Schiavone, L. M.; Florez, L.; Van der Gaag, B. *Appl Phys Lett* **1989,** 55, (14), 1427-1429.
1105. Ogawa, K.; Haraguchi, K.-i.; Hiruma, K.; Fujisaki, Y.; Katsuyama, T.; Fasol, G. *J Lumin* **1992,** 53, (1–6), 387-390.
1106. Henry, C. H.; Lang, D. V. *Physical Review B* **1977,** 15, (2), 989-1016.
1107. Henry, C. *J Electron Mater* **1975,** 4, (5), 1037-1052.
1108. Chang, G. S.; Hwang, W. C.; Wang, Y. C.; Yang, Z. P.; Hwang, J. S. *J Appl Phys* **1999,** 86, (3), 1765-1767.
1109. Peters, G. I.; Allen, L. *Journal of Physics A: General Physics* **1971,** 4, (2), 238.
1110. Coldren, L. A.; Corzine, S. W.; Mashanovitch, M. L., *Diode lasers and photonic integrated circuits*. John Wiley & Sons: 2012; Vol. 218.
1111. Tan, F.; Bambery, R.; Feng, M.; Holonyak, N. *Appl Phys Lett* **2011,** 99, (6), 061105.
1112. Dumont, H.; Marbeuf, A.; Bouree, J. E.; Gorochov, O. *J Mater Chem* **1992,** 2, (9), 923-930.
1113. Hasenöhrl, S.; Eliáš, P.; Šoltýs, J.; Stoklas, R.; Dujavová-Laurenčíková, A.; Novák, J. *Appl Surf Sci* **2013,** 269, 72-76.
1114. Samuel, C. C.; Sema, E.; Georg, H.; Eric, J. J.; Silvija, G. *Nanotechnology* **2015,** 26, (22), 225604.
1115. Soci, C.; Bao, X.-Y.; Aplin, D. P. R.; Wang, D. *Nano Letters* **2008,** 8, (12), 4275-4282.
1116. Dayeh, S. A.; Yu, E. T.; Wang, D. *Nano Letters* **2007,** 7, (8), 2486-2490.
1117. Persson, A. I.; Ohlsson, B. J.; Jeppesen, S.; Samuelson, L. *Journal of Crystal Growth* **2004,** 272, (1-4), 167-174.
1118. Sébastien, P.; et al. *Nanotechnology* **2010,** 21, (38), 385602.
1119. Plissard, S. R.; Slapak, D. R.; Verheijen, M. A.; Hocevar, M.; Immink, G. W. G.; van Weperen, I.; Nadj-Perge, S.; Frolov, S. M.; Kouwenhoven, L. P.; Bakkers, E. P. A. M. *Nano Letters* **2012,** 12, (4), 1794-1798.
1120. Zannier, V.; Grillo, V.; Martelli, F.; Plaisier, J. R.; Lausi, A.; Rubini, S. *Nanoscale* **2014,** 6, (14), 8392-8399.
1121. Asubar, J. T.; Nakamura, S.; Jinbo, Y.; Uchitomi, N. In *Fabrication and structural characterization of nearly lattice-matched p-ZnSnAs2/n-InP heterojunctions*, Indium Phosphide & Related Materials, 2009. IPRM '09. IEEE International Conference on, 10-14 May 2009, 2009; pp 255-258.
1122. Manimaran, M.; Kalkura, S. N.; Ramasamy, P. *J Mater Sci Lett* **1995,** 14, (19), 1366-1368.
1123. Mikkelsen, A.; Skold, N.; Ouattara, L.; Lundgren, E. *Nanotechnology* **2006,** 17, (11), S362-S368.
1124. Fortuna, S. A.; Wen, J.; Chun, I. S.; Li, X. *Nano Letters* **2008,** 8, (12), 4421-4427.
1125. Dowdy, R. S.; Walko, D. A.; Li, X. *Nanotechnology* **2013,** 24, (3), 035304.
1126. Yuan, X.; Caroff, P.; Wong-Leung, J.; Fu, L.; Tan, H. H.; Jagadish, C. *Advanced Materials* **2015,** 27, (40), 6096-6103.
1127. Paladugu, M.; Zou, J.; Guo, Y. N.; Auchterlonie, G. J.; Joyce, H. J.; Gao, Q.; Tan, H. H.; Jagadish, C.; Kim, Y. *Sml* **2007,** 3, (11), 1873-1877.
1128. Zhang, X.; Zou, J.; Paladugu, M.; Guo, Y. A.; Wang, Y.; Kim, Y.; Joyce, H. J.; Gao, Q.; Tan, H. H.; Jagadish, C. *Sml* **2009,** 5, (3), 366-369.
1129. Dick, K. A.; Deppert, K.; Samuelson, L.; Wallenberg, L. R.; Ross, F. M. *Nano Letters* **2008,** 8, (11), 4087-4091.

1130. Wang, J.; Plissard, S. R.; Verheijen, M. A.; Feiner, L.-F.; Cavalli, A.; Bakkers, E. P. A. M. *Nano Letters* **2013,** 13, (8), 3802-3806.
1131. Fonseka, H. A.; Caroff, P.; Wong-Leung, J.; Ameruddin, A. S.; Tan, H. H.; Jagadish, C. *ACS Nano* **2014,** 8, (7), 6945-6954.
1132. Ghosh, S. C.; Kruse, P.; LaPierre, R. R. *Nanotechnology* **2009,** 20, (11), 115602.
1133. Hanrath, T.; Korgel, B. A. *Small* **2005,** 1, (7), 717-721.
1134. Xu, H.; Wang, Y.; Guo, Y.; Liao, Z.; Gao, Q.; Tan, H. H.; Jagadish, C.; Zou, J. *Nano Letters* **2012,** 12, (11), 5744-5749.
1135. Wu, Z. H.; Mei, X.; Kim, D.; Blumin, M.; Ruda, H. E.; Liu, J. Q.; Kavanagh, K. L. *Appl Phys Lett* **2003,** 83, (16), 3368-3370.
1136. Wacaser, B. A.; Deppert, K.; Karlsson, L. S.; Samuelson, L.; Seifert, W. *Journal of Crystal Growth* **2006,** 287, (2), 504-508.
1137. Billinge, S. J. L.; Levin, I. *Science* **2007,** 316, (5824), 561-565.
1138. Ma, D. D. D.; Lee, C. S.; Au, F. C. K.; Tong, S. Y.; Lee, S. T. *Science* **2003,** 299, (5614), 1874-1877.
1139. Gamalski, A. D.; Voorhees, P. W.; Ducati, C.; Sharma, R.; Hofmann, S. *Nano Letters* **2014,** 14, (3), 1288-1292.
1140. Wang, Y. W.; Zhang, L. D.; Wang, G. Z.; Peng, X. S.; Chu, Z. Q.; Liang, C. H. *Journal of Crystal Growth* **2002,** 234, (1), 171-175.
1141. Campos, L. C.; Tonezzer, M.; Ferlauto, A. S.; Grillo, V.; Magalhães-Paniago, R.; Oliveira, S.; Ladeira, L. O.; Lacerda, R. G. *Advanced Materials* **2008,** 20, (8), 1499-1504.
1142. Lin-Chung, P. *Physical Review* **1969,** 188, (3), 1272-1280.
1143. Barbara Sujak-Cyrul, B. K., Jan Misiewicz, Janusz M. Pawlikowski. *Journal of Physical and Chemical Solids* **1982,** 43, (11), 1045-1051.
1144. De-Sheng, J.; Makita, Y.; Ploog, K.; Queisser, H. J. *J Appl Phys* **1982,** 53, (2), 999-1006.
1145. Pelant, I.; Dian, J.; Matoušková, J.; Valenta, J.; Hála, J.; Ambrož, M.; Vácha, M.; Kohlová, V.; Vojtěchovský, K.; Kašlík, K. *J Appl Phys* **1993,** 73, (7), 3477-3481.
1146. Joyce, H., J.; Callum, J. D.; Qiang, G.; Tan, H. H.; Chennupati, J.; James, L.-H.; Laura, M. H.; Michael, B. J. *Nanotechnology* **2013,** 24, (21), 214006.
1147. Cui, Y.; Wang, J.; Plissard, S. R.; Cavalli, A.; Vu, T. T. T.; van Veldhoven, R. P. J.; Gao, L.; Trainor, M.; Verheijen, M. A.; Haverkort, J. E. M.; Bakkers, E. P. A. M. *Nano Letters* **2013,** 13, (9), 4113-4117.
1148. Zhang, Z.; Yao, K.; Liu, Y.; Jin, C.; Liang, X.; Chen, Q.; Peng, L. M. *Adv Funct Mater* **2007,** 17, (14), 2478-2489.
1149. Padovani, F. A.; Stratton, R. *Solid State Electron* **1966,** 9, (7), 695-707.
1150. Misiewicz, J.; Pawlikowski, J. M. *Solid State Commun.* **1979,** 32, 687-690.
1151. Mudryi, A. V.; Patuk, A. I.; Shakin, I. A.; Kalmykov, A. E.; Marenkin, S. F.; Raukhman, A. M. *Mater Chem Phys* **1996,** 44, (2), 151-155.
1152. Jung, K.; Mohseni, P. K.; Li, X. *Nanoscale* **2014,** 6, (24), 15293-15300.
1153. Zhang, Z.; Zheng, K.; Lu, Z.-Y.; Chen, P.-P.; Lu, W.; Zou, J. *Nano Letters* **2015,** 15, (2), 876-882.
1154. Car, D.; Wang, J.; Verheijen, M. A.; Bakkers, E. P. A. M.; Plissard, S. R. *Advanced Materials* **2014,** 26, (28), 4875-4879.
1155. Nash, P.; Pan, Y. Y. *Journal of Phase Equilibria* **1987,** 8, (5), 422-430.
1156. Davidson, F. M.; Lee, D. C.; Fanfair, D. D.; Korgel, B. A. *The Journal of Physical Chemistry C* **2007,** 111, (7), 2929-2935.
1157. Chen, W.; Yu, L.; Misra, S.; Fan, Z.; Pareige, P.; Patriarche, G.; Bouchoule, S.; Cabarrocas, P. R. i. *Nat Commun* **2014,** 5.
1158. Barth, S.; Boland, J. J.; Holmes, J. D. *Nano Letters* **2011**, null-null.
1159. Wang, Z. W.; Li, Z. Y. *Nano Letters* **2009,** 0, (0).
1160. Jeon, N.; Dayeh, S. A.; Lauhon, L. J. *Nano Letters* **2013,** 13, (8), 3947-3952.
1161. Perumal, R.; Zhixin, C.; Patniarche, G.; Jean-Christophe, H.; Kanji, Y. *Semiconductor Science and Technology* **2014,** 29, (11), 115005.
1162. Oliveira, D. S.; Tizei, L. H. G.; Li, A.; Vasconcelos, T. L.; Senna, C. A.; Archanjo, B. S.; Ugarte, D.; Cotta, M. A. *Nanoscale* **2015**.
1163. Soo, M. T.; Zheng, K.; Gao, Q.; Tan, H. H.; Jagadish, C.; Zou, J. *Nano Res* **2016**, 1-8.
1164. de la Mata, M.; Leturcq, R.; Plissard, S. R.; Rolland, C.; Magén, C.; Arbiol, J.; Caroff, P. *Nano Letters* **2016,** 16, (2), 825-833.
1165. Kim, H. S.; Myung, Y.; Cho, Y. J.; Jang, D. M.; Jung, C. S.; Park, J.; Ahn, J. P. *Nano Lett.* **2010,** 10, (5), 1682-91.

1166. Miyauchi, K.; Minemura, T.; Nakatani, K.; Nakanishi, H.; Sugiyama, M.; Shirakata, S. *physica status solidi (c)* **2009,** 6, (5), 1116-1119.
1167. Peña-Pedraza, H.; López-Rivera, S. A.; Martin, J. M.; Delgado, J. M.; Power, C. *Materials Science and Engineering: B* **2012,** 177, (16), 1465-1469.
1168. Wu, Y.; Cui, Y.; Huynh, L.; Barrelet, C. J.; Bell, D. C.; Lieber, C. M. *Nano Letters* **2004,** 4, (3), 433-436.
1169. Xu, H. Y.; Guo, Y. N.; Liao, Z. M.; Sun, W.; Gao, Q.; Tan, H. H.; Jagadish, C.; Zou, J. *Appl Phys Lett* **2013,** 102, (20).
1170. Thombare, S. V.; Marshall, A. F.; McIntyre, P. C. *J Appl Phys* **2012,** 112, (5), 054325.
1171. Lim, S. K.; Crawford, S.; Haberfehlner, G.; Gradečak, S. *Nano Letters* **2012,** 13, (2), 331-336.
1172. Fonseka, H. A.; Caroff, P.; Guo, Y.; Wang, F.; Wong-Leung, J.; Tan, H. H.; Jagadish, C. In *InP-based radial heterostructures grown on [100] nanowires*, Optoelectronic and Microelectronic Materials & Devices (COMMAD), 2014 Conference on, 14-17 Dec. 2014, 2014; pp 168-170.
1173. Gamalski, A. D.; Perea, D. E.; Yoo, J.; Li, N.; Olszta, M. J.; Colby, R.; Schreiber, D. K.; Ducati, C.; Picraux, S. T.; Hofmann, S. *ACS Nano* **2013,** 7, (9), 7689-7697.
1174. Kodambaka, S.; Tersoff, J.; Reuter, M. C.; Ross, F. M. *Science* **2007,** 316, (5825), 729-732.
1175. Heun, S.; Radha, B.; Ercolani, D.; Kulkarni, G. U.; Rossi, F.; Grillo, V.; Salviati, G.; Beltram, F.; Sorba, L. *Sml* **2010**, n/a-n/a.
1176. Hillerich, K.; Dick, K. A.; Messing, M. E.; Deppert, K.; Johansson, J. *Nano Res* **2012,** 5, (5), 297-306.
1177. Kim, J. H.; Moon, S. R.; Kim, Y.; Chen, Z. G.; Zou, J.; Choi, D. Y.; Joyce, H. J.; Gao, Q.; Tan, H. H.; Jagadish, C. *Nanotechnology* **2012,** 23, (11).
1178. Zannier, V.; Grillo, V.; Rubini, S. *Journal of Physics D: Applied Physics* **2014,** 47, (39), 394005.
1179. Jordi, A.; Billel, K.; Pere Roca i, C.; Joan Ramon, M.; Anna Fontcuberta i, M. *Nanotechnology* **2007,** 18, (30), 305606.
1180. Lofton, C.; Sigmund, W. *Adv Funct Mater* **2005,** 15, (7), 1197-1208.
1181. Hamilton, D. R.; Seidensticker, R. G. *J Appl Phys* **1960,** 31, (7), 1165-1168.
1182. Westover, T.; Jones, R.; Huang, J. Y.; Wang, G.; Lai, E.; Talin, A. A. *Nano Letters* **2009,** 9, (1), 257-263.
1183. Lin-Chung, P. J. *physica status solidi (b)* **1971,** 47, (1), 33-39.
1184. Misiewicz, J.; Andrzejewski, J. *physica status solidi (b)* **1994,** 184, (1), K7-K10.
1185. Andrzejewski, J.; Misiewicz, J. *physica status solidi (b)* **2001,** 227, (2), 515-540.
1186. Sierański, K.; Szatkowski, J.; Misiewicz, J. *Physical Review B* **1994,** 50, (11), 7331-7337.
1187. Sun, Y.; Christensen, M.; Johnsen, S.; Nong, N. V.; Ma, Y.; Sillassen, M.; Zhang, E.; Palmqvist, A. E. C.; Bøttiger, J.; Iversen, B. B. *Advanced Materials* **2012,** 24, (13), 1693-1696.
1188. Dimroth, F.; Agert, C.; Bett, A. W. *Journal of Crystal Growth* **2003,** 248, 265-273.
1189. Jones, A. C. *Chemical Society Reviews* **1997,** 26, (2), 101-110.
1190. Graham, R. M.; Jones, A. C.; Mason, N. J.; Rushworth, S.; Salesse, A.; Seong, T. Y.; Booker, G.; Smith, L.; Walker, P. J. *Semiconductor Science and Technology* **1993,** 8, (10), 1797.
1191. Borg, B. M.; Lars-Erik, W. *Nanotechnology* **2013,** 24, (20), 202001.
1192. Nebol'sin, V. A.; Shchetinin, A. A. *Inorg Mater+* **2003,** 39, (9), 899-903.
1193. Farzinpour, P.; Sundar, A.; Gilroy, K. D.; Eskin, Z. E.; Hughes, R. A.; Neretina, S. *Nanotechnology* **2012,** 23, (49), 495604.
1194. Vogel, A. T.; de Boor, J.; Wittemann, J. V.; Mensah, S. L.; Werner, P.; Schmidt, V. *Cryst Growth Des* **2011,** 11, (5), 1896-1900.
1195. Weng, X. J.; Burke, R. A.; Dickey, E. C.; Redwing, J. M. *Journal of Crystal Growth* **2010,** 312, (4), 514-519.
1196. Caroff, P.; Wagner, J. B.; Dick, K. A.; Nilsson, H. A.; Jeppsson, M.; Deppert, K.; Samuelson, L.; Wallenberg, L. R.; Wernersson, L.-E. *Small* **2008,** 4, (7), 878-882.
1197. Pan, D.; Fan, D. X.; Kang, N.; Zhi, J. H.; Yu, X. Z.; Xu, H. Q.; Zhao, J. H. *Nano Letters* **2016,** 16, (2), 834-841.
1198. Li, T.; Gao, L.; Lei, W.; Guo, L.; Pan, H.; Yang, T.; Chen, Y.; Wang, Z. *Nanoscale Res Lett* **2013,** 8, (1), 1-6.
1199. Haynes, T. E.; Chu, W. K.; Aselage, T. L.; Picraux, S. T. *Appl Phys Lett* **1986,** 49, (11), 666-668.
1200. Arthur, J. R. *J Phys Chem Solids* **1967,** 28, (11), 2257-2267.
1201. Goldstein, B.; Szostak, D. J.; Ban, V. S. *Surf Sci* **1976,** 57, (2), 733-740.
1202. Kamins, T. I.; Li, X.; Williams, R. S. *Appl Phys Lett* **2003,** 82, (2), 263-265.

1203. Dubrovskii, V. G.; Sibirev, N. V.; Cirlin, G. E.; Bouravleuv, A. D.; Samsonenko, Y. B.; Dheeraj, D. L.; Zhou, H. L.; Sartel, C.; Harmand, J. C.; Patriarche, G.; Glas, F. *Physical Review B* **2009,** 80, (20), 205305.
1204. Foxon, C. T.; Harvey, J. A.; Joyce, B. A. *J Phys Chem Solids* **1973,** 34, (10), 1693-1701.
1205. Woodall, J. M.; Rupprecht, H.; Chicotka, R. J.; Wicks, G. *Appl Phys Lett* **1981,** 38, (8), 639-641.
1206. Wright, A. C.; Ng, T.-L.; Maung, N. *Philosophical Magazine A* **1999,** 79, (11), 2691-2710.
1207. Zhang, B.; Jung, Y.; Chung, H.-S.; Vugt, L. V.; Agarwal, R. *Nano Letters* **2010,** 10, (1), 149-155.
1208. Li, G.; Jiang, Y.; Wang, Y.; Wang, C.; Sheng, Y.; Jie, J.; Zapien, J. A.; Zhang, W.; Lee, S.-T. *The Journal of Physical Chemistry C* **2009,** 113, (39), 17183-17188.
1209. Wang, Y.; Liu, M.-X.; Ling, T.; Tang, C.-C.; Zhi, C.-Y.; Du, X.-W. *J Mater Chem C* **2014,** 2, (15), 2793-2798.